The Unique Formation and Evolution of Magnetars and Constraining Fast Radio Burst Progenitors with Polarization

Thesis by
Myles Bradford Sherman

In Partial Fulfillment of the Requirements for the
Degree of
Doctor of Philosophy

CALIFORNIA INSTITUTE OF TECHNOLOGY
Pasadena, California

2026
Defended April 28, 2026

© 2026

Myles Bradford Sherman
ORCID: 0000-0002-6573-7316

All rights reserved except where otherwise noted

ACKNOWLEDGEMENTS

I would like to thank my family — my mother Bonita, my father Michael, my sister Mikayla, my grandparents, and my entire extended family — for their unwavering love and support throughout my PhD journey. In turbulent times you have been my refuge, and I would have never reached this point without you.

I would also like to thank my advisor, Vikram Ravi, and my mentors, Casey Law, Liam Connor, Jim Cordes, Dana Simard, Dean Howarth, Stella Koch Ocker, and Kaitlyn Shin, for guiding me into the world of astronomy and academia.

I thank the National Science Foundation whose Graduate Research Fellowship Program has funded this research under Grant No. 2139433.

Thank you to my Physics, Math, and Astronomy graduate cohort, especially Kritti Sharma, Jakob Faber, Jean Somalwar, and Frank Verdi, whose friendship and passion for science have been instrumental to my success. Thank you to Denise Lin and Edgardo Menvielle, for your patience, kindness, and understanding.

I thank the Caltech Y, Pasadena PAL, and the National Council of Negro Women for allowing me to participate in tutoring programs for the youth of Pasadena; I'm inspired always by my students' hard work and dedication to learning in the classroom. I am honored to have had the chance to help them in their educational journey.

Thank you to my fellow organizers, for fighting for human rights, public safety, equitable education, and science research and literacy in the face of increasing authoritarianism: Beth Fabinsky, Kaden Ouimet, Rosemary Lee, AnnMarie Kolakowski, Catalina McFarland, Katie Davos, Ingrid Shan, and the entire *Students Rise Up* coalition; our community watch network *Grupo Autodefensa*; our United Auto Workers Local 2478 graduate and postdoc union and JPL Workers United; Kitty Cahalan and the Caltech Teaching and Learning Office; Tashiana Bryant Malick, Lindsey Malcom-Piqueux and the Caltech Center for Inclusion and Diversity; Erin Burkett, Josh Schneiderman, and the Caltech Hixon Writing Center; the Caltech Y, *The California Tech*, and the Science and Engineering Policy At Caltech Club.

For my late grandfather, James Joe, who always believed in me.

ABSTRACT

Magnetars, the most highly magnetized subset of neutron stars, remain enigmatic in nature; while likely formed through Core-collapse Supernovae (CCSNe), the origin of their large ($> 10^{13}$ G) magnetic fields and relationship to radio pulsars are unclear. Beyond the wide variety of emission states observed in Galactic magnetars, including periodic short bursts, Giant Flares, and outbursts, magnetars are considered the leading candidates for the origins of multiple unidentified phenomena, such as Long Period Radio Transients (LPRTs) and extragalactic Fast Radio Bursts (FRBs). In this thesis, I use multi-wavelength data to explore the formation of magnetars, and investigate the origins and emission properties of FRBs and LPRTs.

Through an archival search of radio, optical, and infrared data, we identify two new candidates for magnetar-massive star binaries that have been disrupted by CCSNe. We find the CCSNe formation scenario requires a high progenitor merger rate ($\sim 70-80\%$) to explain the lack of such unbound systems, and suggests they may preferentially form from massive stellar mergers.

We then use the 64-antenna prototype Deep Synoptic Array (DSA-110) radio telescope to explore the polarization properties of FRBs. With a custom baseband analysis pipeline, we find that FRBs' high ($> 70\%$) linear polarization closely resembles that of young (< 100 kyr) Galactic pulsars, suggesting that they inhabit similar environments. This supports the magnetar scenario, as they have typical characteristic ages below < 100 kyr. FRB rotation measures also indicate that FRB environments are more highly magnetized than those of typical Galactic pulsars.

To investigate the magnetar origin of LPRTs, Galactic events which have periods from minutes to hours and burst widths up to 30 seconds, I have implemented a real-time search for single-pulses between 0.134 - 160.8 seconds for the completed 96-antenna DSA-110. A pilot survey of the galactic plane (GP) region (> 1.2 Jy flux limit at 25σ) places constraints on the White-Dwarf binary model while failing to rule-out the magnetar model, a result which supports the multiple-progenitor LPRT theory.

Looking ahead, we use population synthesis to predict that the next-generation DSA-2000 radio telescope will detect $\sim 23,000$ new radio pulsars and radio magnetars with full polarization information. This sample will enable a more holistic view of magnetar evolution and their relationship to radio pulsars, FRBs, and LPRTs.

PUBLISHED CONTENT AND CONTRIBUTIONS

Sherman, M. B. et al. (2026). "Deep Synoptic Array Science: Searching for Long Duration Radio Transients with the DSA-110". In: *Publications of the Astronomical Society of the Pacific* 138.2, p. 024501. DOI: 10.1088/1538-3873/ae390e.

M. B. Sherman designed the Not-So-Fast Radio Burst (NSFRB) search pipeline for the DSA-110, developed calibration routines, operated the offline system, monitored the realtime system, and devised the mathematical methods to constrain the Galactic Long Period Radio Transient population using the DSA-110 upper limit.

Sherman, M. B. et al. (2024a). "Searching for magnetar binaries disrupted by core-collapse supernovae". In: *Monthly Notices of the Royal Astronomical Society* 531.2, pp. 2379–2414. DOI: 10.1093/mnras/stae1289.

– (2024b). "Correction to: Searching for magnetar binaries disrupted by core-collapse supernovae". In: *Monthly Notices of the Royal Astronomical Society* 534.2, pp. 1414–1419. DOI: 10.1093/mnras/stae2124.

M. B. Sherman implemented the Monte Carlo trajectory sampling technique and applied it to each magnetar, compiled the point source and image catalogue data on each magnetar sightline, and interpreted the results within the Core Collapse formation hypothesis.

Sherman, M. B. et al. (2024c). "Deep Synoptic Array Science: Polarimetry of 25 New Fast Radio Bursts Provides Insights into Their Origins". In: *The Astrophysical Journal 964.2*, p. 131. DOI: 10.3847/1538-4357/ad275e.

M. B. Sherman developed the polarization analysis pipeline, applied it to each FRB to estimate linear and circular polarization fractions, compiled the literature sample of FRB polarization data, and designed the polarization classification scheme.

Sherman, M. B. et al. (2023). "Deep Synoptic Array Science: Implications of Faraday Rotation Measures of Fast Radio Bursts Localized to Host Galaxies". In: *The Astrophysical Journal Letters* 957.1, p. L8. DOI: 10.3847/2041-8213/ad0380.

M. B. Sherman developed the Faraday Rotation Measure Synthesis pipeline, applied it to each FRB and conducted Markov-Chain Monte Carlo simulations to search for correlations.

TABLE OF CONTENTS

Acknowledgements . . . iii
Abstract . . . iv
Published Content and Contributions . . . v
Table of Contents . . . vi
List of Illustrations . . . ix
List of Tables . . . xxix
Chapter I: Introduction . . . 1
1.1 Stellar Evolution: Neutron Star Origins . . . 1
1.2 Stellar Binaries, Stellar Mergers, and Alternative Neutron Star Formation Channels . . . 2
1.3 The Neutron Star Zoo . . . 2
1.4 The Magnetar Census . . . 7
1.5 Galactic Magnetar Candidates . . . 12
1.6 Extragalactic Magnetar Candidates . . . 16
1.7 Outline and Questions Addressed in this Thesis . . . 23
1.8 Chapter I Bibliography . . . 24
Chapter II: Searching for Magnetar Binaries Disrupted By Core-Collapse Supernovae (CCSNe) . . . 41
2.1 Abstract . . . 41
2.2 Introduction . . . 42
2.3 Magnetar Sample . . . 46
2.4 *Gaia* Catalog Search For Unbound Companions . . . 47
2.5 Optical and IR Search for Bound Companions . . . 56
2.6 Radio Search for SNR Shells . . . 63
2.7 Discussion . . . 72
2.8 Conclusion . . . 88
2.9 Data Availability . . . 89
2.10 Acknowledgements . . . 89
2.11 Appendix . . . 91
2.12 Chapter II Bibliography . . . 111
Chapter III: Magnetar Population Synthesis Under the Stellar Merger Formation Hypothesis . . . 135
3.1 Introduction . . . 135
3.2 Methods . . . 137
3.3 Results . . . 140
3.4 Discussion . . . 141
3.5 Conclusion . . . 144
3.6 Chapter III Bibliography . . . 145

Chapter IV: An Updated Magnetar Scale Height and Implications for their Stellar Progenitors . . . 149
4.1 Introduction . . . 149
4.2 Methods . . . 151
4.3 Results . . . 153
4.4 Discussion . . . 153
4.5 Conclusion . . . 159
4.6 Chapter IV Bibliography . . . 161
Chapter V: Searching for Long Duration Radio Transients with the DSA-110 . 165
5.1 Abstract . . . 165
5.2 Introduction . . . 166
5.3 NSFRB System Design . . . 168
5.4 Commissioning Injection and Pulsar Tests . . . 175
5.5 The DSA-110 NSFRB galactic plane Survey (DN-GPS) . . . 178
5.6 Discussion . . . 184
5.7 Conclusion . . . 188
5.8 Data Availability . . . 190
5.9 Acknowledgments . . . 190
5.10 Appendix . . . 190
5.11 Chapter V Bibliography . . . 193
Chapter VI: Polarimetry of 25 New Fast Radio Bursts Provides Insights into Their Origins . . . 198
6.1 Abstract . . . 198
6.2 Introduction . . . 198
6.3 Observations and data analysis . . . 202
6.4 Discussion of Individual Burst Polarization Properties . . . 204
6.5 Comparisons . . . 216
6.6 Conclusions . . . 222
6.7 Acknowledgements . . . 224
6.8 Appendix . . . 225
6.9 Chapter VI Bibliography . . . 260
Chapter VII: Implications of Faraday Rotation Measures of Fast Radio Bursts Localized to Host Galaxies . . . 271
7.1 Abstract . . . 271
7.2 Motivation and background . . . 271
7.3 Estimation of host DM and RM . . . 274
7.4 The origin of FRB rotation measures . . . 276
7.5 Magnetic fields in FRB environments and host galaxies . . . 280
7.6 Discussion . . . 283
7.7 Conclusions . . . 284
7.8 Acknowledgments . . . 285
7.9 Chapter VII Bibliography . . . 286
Chapter VIII: Forecasts for Pulsar Searching with the DSA-2000 . . . 292
8.1 Introduction . . . 292
8.2 DSA-2000 Pulsar Search Design . . . 293

8.3 Pulsar Detection Forecasts 294
8.4 CASS Target Selection and Multi-Wavelength Cross-Matching 296
8.5 Cadence, Follow-up, and Confirmation Strategy 300
8.6 Conclusion 302
8.7 Appendix 303
8.8 Chapter VIII Bibliography 309
Chapter IX: Conclusions and Outlook 314
9.1 Stellar Merger Channels and OB Associations Contribute to the Magnetar Population 314
9.2 $10-50$ s White Dwarf-M Dwarf Binary LPTs are Rare in the galactic plane 315
9.3 FRBs Inhabit Highly-Magnetized Environments Resembling those of Young (< 10 kyr) Pulsars 315
9.4 The DSA-2000 will Increase the Known Pulsar Population by Orders of Magnitude 316
9.5 Chapter IX Bibliography 318
Appendix A: PARSEC: A Custom DSA-110 Polarization Analysis Interface . . 320
Appendix B: DSA-110 Real-time NSFRB Quick Start Guide 339

LIST OF ILLUSTRATIONS

Number *Page*

1.1 Period-Spindown ("P vs. $\dot{P}$", or "P-Pdot") diagram populated with the neutron star zoo and candidates. Slow, or "Canonical" Pulsars (CPs; blue) and Millisecond Pulsars (MSPs; red) are from the ATNF catalog (Manchester et al., 2005). The "Magnificent Seven" x-ray Dim Isolated Neutron Stars are shown in teal (XDINSs Haberl, 2007) while Rotating RAdio Transients from the RRATalog (Agarwal et al., 2026), including the FAST sample (Han et al., 2025) are in yellow. Magnetars and candidates from the McGill Catalog (Olausen & Kaspi, 2014) and the updated sample discussed in Sections 1.4 and 1.5 are in green. Long Period Radio Transients (LPRTs or LPTs) as discussed in Section 1.5 are in magenta with the two confirmed White Dwarf-M Dwarf binary LPTs outlined in black. Lines of constant magnetic field B_S and characteristic age τ_C are dashed black and grey, respectively, while the quantum critical field strength $B_{\rm QC}$ is in red. . 8

1.2 Periodic Emission Luminosity Limits from GBT Observations (GBT25A-328) of Low B-Field Magnetars. Limits are shown as a function of pulse duty cycle and colored by each magnetars magnetic field strength. Luminosity measurements from the six confirmed radio magnetars are shown as points (Camilo et al., 2008, 2016; Esposito et al., 2020; Levin et al., 2010; Pennucci et al., 2015; Zhu et al., 2023). 11

2.1 (*Top*) Locations of *Gaia* search sample in Celestial coordinates. The tangential velocity magnitude in km s^{-1} is indicated by the colorbar. The *Bayestar19* Dust Map is used for sources at $\delta > -30°$ (red outline), and the *Gaia* photometric extinction is used for $\delta < -30°$ (black outline; Green, 2019; Vallenari et al., 2022). The 5° radius cones queried around each magnetar are shown in red, and those around each pulsar used for the test sample (see Section 2.4) are shown in violet. Lower transverse velocities are found in the galactic plane (GP), meaning that the unbound companions of GP magnetars can be found at smaller angular separations. (*Bottom*) Color-Magnitude Diagrams for the *Gaia* search sample. The *left* plot shows the apparent $G-$band magnitude m_G plotted against the apparent $m_{G_{BP}} - m_{G_{RP}}$ color. The *right* plot shows absolute $V-$band magnitude M_V for each source against the absolute color $G_{BP} - G_{RP}$. M_V is derived using the Johnson-Cousins relationships in Equations 2.1-2.8 (see Appendix 2.11). Sources with $\delta > -30°$ are again outlined in black while those with $\delta \geq -30°$ are outlined in red. The parallax of each source is indicated by the colorbar in milliarcseconds (mas). Sources from the initial query (see Appendix 2.11) which were cut by the magnitude (black) and color (red) limits are shown in grey. GSP-Aeneas extinction estimates may be unreliable in the galactic plane according to the *Gaia* DR3 Documentation (Section 11.3.3), resulting in a rough color cutoff near $G_{\rm BP} - G_{\rm RP} \approx -0.5$ (Andrae et al., 2022; Fouesneau et al., 2022; Vallenari et al., 2022). 50

2.2 (*Left*) Monte Carlo sampled trajectories for candidate *Gaia* DR3 sources with p-values $p < 5\%$ possibly associated with three magnetars (*right*, *bottom*), PSR J0538+2817 (*top left*), and PSR B1951+32 (*middle left*). Each figure includes only *Gaia* OB star candidates with association p-value $p < 5\%$, including the unbound companion of CXOU J164710.2-455216 proposed by Clark et al. (2014), WR 77F (*top right*). Present-day magnetar/pulsar and GDR3 source locations are shown as red stars and circular markers, respectively; the latter has colorbar corresponding to the total p-value p, except for PSR 0538+2817 and CXOU J164710.2-455216, for which we exclude p_1 (see Section 2.4). Red lines show the initial magnetar/pulsar trajectory samples while thin lines extrapolate the magnetar/pulsar and source trajectories to their past intersection. Note for these initial trajectories extend farther for pulsars (*top left*, *middle left*) than for magnetars (*right*, *bottom*) since travel time samples were drawn from a uniform distribution up to 1 Myr for pulsars in contrast to 10 kyr for magnetars. If proper motion measurements are available, the proper motion direction is indicated by a purple arrow. Each GDR3 source is shown with its source ID, 2D travel time difference $\Delta\tau_{2D}$, the magnetar's/pulsar's 3D travel time $\mathcal{T}_{3D,mag/psr}$, an upper limit age estimate $\mathcal{T}_{SNR/decay/rot}$, and the relevant p-value. (*Right*) Contour plot of Monte Carlo samples in $\{\Theta - M_V\}$ space. The 95% contour region is in beige, and candidates with search statistic $\hat{f}$ less than the critical threshold, $\hat{f}_c$, have colorbar corresponding to $\hat{f}$ (see Appendix 2.11). $\hat{f}_c$ is indicated by a red horizontal line on each colorbar. We recover the proposed companions of CXOU J164710.2-455216 (WR 77F; *upper right*) and PSR J0538+2817 (HD 37424; *top left*) with $p < 5\%$. We also identify potential runaway companions of SGR 1822.3-1606 and PSR B1951+32 (*middle row*) with $p < 5\%$. The companions shown for 3XMM J185246.6+003317 (*bottom*) are most likely false positives as discussed in Appendix 2.11. 57

2.3 Optical (*Left*) and Infrared (*Right*) $1' \times 1'$ image cutouts for 2 magnetars and 1 magnetar candidate. Each image is in grayscale where RGB channels are combined using $0.2989R + 0.5870G + 0.1140B$. Optical images use the $g-$, $i-$, and $y-$band filters for PS1 images (CXOU J1714) and the $g-$, $r-$, and $i-$band filters for SkyMapper images (SGR 0755 and SGR J1822). Infrared images use the $J-$, $H-$, and $K-$band filters for UKIDSS images (SGR 1822) and the $J-$, $H-$, and K_s-band filters for VVV (CXOU J1714) and 2MASS (SGR 0755) images. The magnetar location is indicated by red cursors and the 3σ error ellipse is shown in red. Note the error ellipse is much larger than the image for SGR 0755-2933. Each marker indicates a point source from the optical or infrared catalogs with colorbar corresponding to the association p-value, p. Sources with insufficient data to determine a p-value are grey. Sources with $p < 5\%$ are outlined in green, while those with $p > 5\%$ are outlined in red. (*Left*) PS1 sources are shown as circles, SkyMapper sources are shown as triangles, and sources identified 'by-eye' are shown as squares. (*Right*) 2MASS sources are shown as circles, VVV sources are shown as triangles, UKIDSS sources are shown as diamonds, and sources idenified 'by-eye' are shown as squares. Sources with no corresponding marker were not identified in the catalogs considered, and could not be well-fit with an ellipse. The Be-star companion of SGR 0755 is recovered in the optical and infrared searches, and candidates are identified for SGR 1822. The proposed companion of CXOU J1714 is not recovered, but cannot be ruled out as a bound companion due to uncertainty in the extinction estimate. Note that the axes for CXOU J1714 differ between optical and infrared due to the use of different World Coordinate System (WCS) projections (ZPN) for VVV data (e.g. Greisen & Calabretta, 2002). 62

2.4 Radio Image and Trajectory Analysis of 3XMM J185246.6+00317. (*Top left*) A RACS DR1 888 MHz continuum $1^\circ \times 1^\circ$ image cutout is shown for 3XMM J185246.6+00317 with $25'' \times 25''$ pixels. The magnetar and pulsar locations are indicated by red and blue pointers, while circular and square markers show known and 'by-eye' identified radio sources, respectively. Note that no markers are shown for catalogued Active Galactic Nuclei or radio galaxies, as they were not included in this search. Other extended sources without markers were not identified in SIMBAD and could not be well-fit with an ellipse. The colorbar corresponds to the association p-value. The purple shaded region indicates the 1, 2, and 3σ past travel distances based on the Hobbs et al. (2005) velocity distribution. The angular extent of Kes 79 (labelled) is shown as a blue circle. (*Bottom*) The cartoon demonstrates how a bound massive stellar binary (orange) may evolve into an unbound magnetar (red) and pulsar (blue) following two CCSNe. (*Top right*) The trajectory plot for 3XMM J185246.6+00317 and the x-ray pulsar CXOU J185238.6+004020 is shown with 468 valid trajectories (out of 10,000 trials). Blue traces show the pulsar's trajectory prior to the second CCSN, and yellow traces show its trajectory after the CCSN. The blue circle indicates the location and extent of Kes 79. 70

2.5 Radio continuum image cutouts for four magnetars (*middle, bottom*), and two magnetar candidates (*top*) with possible SNR associations. Red pointers indicate each magnetar's location and the 1σ, 2σ, and 3σ magnetar error ellipses are shown in red (although they are too small to be visible except for SGR 1808-20 and SGR 1801-23. For the latter, the 3.8° error ellipse is too large to be effectively shown.). Note the difference in axis extents for each image. RACS 888 MHz continuum images with $25'' \times 25''$ pixels are shown for SGR 1808-20, SGR 1801-23, SGR J1745-2900, and SGR 0526-66 (*top, middle*). For SGR 0501+4516, a 3 GHz $1' \times 1'$ VLASS image with $1'' \times 1''$ pixels (smoothed to $25'' \times 25''$ with a boxcar kernel) is shown enclosed in a red box indicating the queried region, while the remainder of the image is from the 1.4 GHz NVSS survey to show SNR HBH 9 (e.g. Göğüş et al., 2010b). However, NVSS is only sensitive to angular sizes $< 970''$ ($\lesssim 16.7'$), making SNR HBH9 ($120 - 140'$) unobservable in the image shown. No radio images from RACS, VLASS, or NVSS were available at SGR 1627-41's position (*bottom left*). Circular markers indicate the locations of known radio sources while square markers indicate unknown sources identified by-eye. Note that no markers are shown for catalogued Active Galactic Nuclei or radio galaxies, as they were not included in this search. Other extended sources without markers were not identified in SIMBAD and could not be well-fit with an ellipse. The colorbar corresponds to the association p-value; sources outlined in red (green) have $p > 5\%$ ($p \leq 5\%$). The most likely or previously proposed SNRs (see Section 2.6) are labelled. 'Source 1' (*top left*) is S24-RACS J180842-202849. The angular extents of SNRs, if available, are shown as ellipses. For SGR 1745-2900 (*middle left*), the proper motion direction is marked by a purple arrow, and the purple shaded region indicates the 1σ, 2σ, and 3σ past travel direction and extent; for SGR 1627-41, SGR 0501+4516, and SGR 0526-66 (*bottom, middle right*), the Hobbs et al. (2005) velocity distribution is used to show possible past travel direction and extent. 73

2.6 Completeness plots versus distance modulus for (*rows 1 and 2*) the *Gaia* search, (*row 3*) the optical and (*row 4*) IR searches, and (*row 5*) the radio search. Circular, square, and diamond markers with errorbars indicate known companions or remnants of magnetars, pulsars, and HMXBs, respectively. Proper motion, apparent magnitude, and 1 GHz flux ranges, are shown as vertical lines, with color relating to the survey used for the search. The sensitivity limits of each survey are indicated by horizontal lines. We expect most magnetars with SNR shells or stellar companions would have been detected if present. Sensitivity limits for past searches are shown as black dotted lines for comparison (see Appendix 2.11 for references). 76

2.7 (*Upper Left:*) Corner Plots from the Magnetar Binary Fraction Simulation in Section 2.7. The 'SNR complete', 'SNR incomplete', and 'SNR/unbound complete' cases as defined in Section 2.7 and Table 2.4 are shown in black, red, and blue, respectively. Vertical lines indicate the median values from Table 2.4 in each case. The 'SNR complete' and 'SNR/unbound complete' cases would suggest that $f_{nc} \approx 45 - 55\%$ of magnetars to descend from non-CCSN channels, whereas the 'SNR incomplete' case suggests a higher stellar merger rate $f_m \approx 70\%$ among OB stars is sufficient to produce the observed sample. The merger rates displayed assume a massive star binary fraction $F_0 = 84 \pm 9\%$ (Moe & Di Stefano, 2017). (*Upper Right:*) 90% Confidence Regions for the merger fraction f_m and OB star binary fraction F_0. The colors for each region correspond to the cases in the contour plot, and vertical purple lines show F_0 predicted for different stellar types through population synthesis (Moe & Di Stefano, 2017). The green and yellow dashed lines indicate the median merger fractions from Renzo et al. (2019) and Kochanek et al. (2019); the teal dashed line indicates the f_m vs. F_0 curve inferred from f_b and f_u in Chrimes et al. (2022). The green and teal shaded regions indicate the 1σ errors for the Renzo et al. (2019) and Chrimes et al. (2022) cases. Each of these appear to underestimate the true fraction for early B-type stars. 84

2.8 x-ray Luminosity (L_X) vs. Dipole Magnetic Field Strength (B_d) for Known Magnetars using the Decay Model of Ferrario & Wickramasinghe (2006, 2008). The magnetic field estimate is derived from the pulse period P and spindown rate $\dot{P}$ using $B_d \approx (3.2 \times 10^{19} G)\sqrt{P\dot{P}/1\,\mathrm{s}}$ as reported in the McGill catalog (Olausen & Kaspi, 2014). The x-ray luminosity is derived from the $2-10$ keV flux and reported distance, also from the McGill catalog. The colorbar corresponds to the decay age $\mathcal{T}_{\mathrm{decay}}$ derived from Equation 2.9, and lines of constant age are shown in grey. This estimate is preferred to the spindown age, $\mathcal{T}_{\mathrm{rot}}$, which likely overestimates magnetar ages through neglect of field decay and glitching (e.g. Kaspi & Beloborodov, 2017; Nakano et al., 2015). 108

3.1 Hopf Function Beaming Model Centered on the Magnetar. The emitted intensity profile is shown as a grey dashed line while the foreshortened observed intensity profile is in blue. The angular range within which bursts will be in the 10^{th} percentile of intensity is shaded red, with the arrow indicating the observer's direction for peak intensity. The black shaded region highlights disallowed beaming directions for an emission area at 0°. 139

4.1 Spatial Distribution in Galactic Coordinates (Top), Cumulative Distribution Functions (cdfs), and Best-Fit Exponential Models (Bottom). Magnetars (red) and OB Associations (teal) are shown with best-fit curves from this work's MCMC analysis. LPTs are in magenta. 10% errorbars are assumed for sources without error estimates. Pulsar (gold Levin et al., 2013; Lorimer et al., 2006) and White Dwarf (brown Wegg & Phinney, 2012) scale height ranges are shaded, while the OB star scale height (teal Quintana et al., 2025) is a dashed line. The cdf from Olausen & Kaspi (2014) is in black. The galactic plane position $z_{\odot,BB19}$ from (Bennett & Bovy, 2019) and Sun are indicated by purple and black dashed lines, respectively. 160

5.1 Diagram of the NSFRB Search System. Voltages for $N_{\rm ant} = 97$ antennas, $N_t = 25$ time samples, $N_p = 2$ polarizations, and $N_f = 384$ frequency channels are pulled from a rotating PSRDADA buffer, cross-correlated, down-channelized to $n_f = 8$, and calibrated. $N_{\rm pix} = 175 \times 175$ images are formed for each of $N_c = 16$ sub-bands and sent to the Process Server which assigns search and post-processing tasks. Image data and candidate metadata are saved to disk along with 26.8-second of voltage data triggered from the PSRDADA buffer if candidates above the 6σ threshold are identified. We outline in green the post-processor which is *not* required to operate in real-time. . . . 169

5.2 Pulse width and $6\sigma_{\rm srch}$ Fluence Sensitivity to $\Delta t = 134$ ms Bursts of the DSA-110 FRB (light blue; ~ 840 mJy ms) and NSFRB (dark blue hatched; ~ 40 Jy ms) searches. For each search we assume the fluence threshold is fixed; thus the lower border indicates the corresponding flux density threshold $6\sigma_{\rm th}\Delta t/W$ where W is the width measured at 1.4 GHz (note that in some cases (e.g. ASKAP J1832-09 Li et al., 2024; Z. Wang et al., 2025), only sub-pulses were detected at 1.4 GHz while a broader profile was detected at lower frequencies. In these cases, we still use the 1.4 GHz sub-pulse width). The dark blue dashed line shows the 90% completeness limit $25\sigma \approx 1200$ mJy ($25\sigma\Delta t \approx 160$ Jy ms; see Section 5.4). The purple dashed line shows the theoretical radiometer $6\sigma_{\rm th}$ sensitivity of the NSFRB survey. 1.4 GHz fluences and widths are shown for radio pulsars in the ATNF catalog (diamonds), FRBs from the literature (triangles), and LPRTs (circles). DSA-110 FRBs have dark blue outlines and show their detection pulse widths and S/N rather than refined estimates from baseband analysis. The colorbar indicates distance estimates in kpc (FRB luminosity distances are computed from host Galaxy redshifts; pulsar, magnetar, and LPRT distances are from parallaxes where available, and DM distance limits for the rest of the sample). Note that only pulsars, FRBs, and LPRTs with 1.4 GHz detections are shown. 173

5.3 Relative S/N Loss (Equation 5.1) of NSFRB Search on the Three `cerberus` Timescales (134 ms, 670 ms, and 10.05 s) as a Function of DM. Each line corresponds to an intrinsic pulse width $W_{\rm int}$, and solid points indicate each trial DM. 174

5.4 Detection Rate vs. Input S/N for Injection Test. The blue curve includes any candidates detected with S/N> 6σ while the red curves include only candidates classified as sources by the CNN classifier using probability thresholds $p_{\rm rfi} < 50\%$ (dashed) and $p_{\rm rfi} < 15\%$ (solid). The black line indicates the 6σ threshold determined in Section 5.4. 177

5.5 Example NSFRB candidate plot from detections of pulsar B0329+54. (top left) Position of the candidate (shaded circle) in reference to the pulsar's catalogued position (open blue square) and other field NVSS continuum sources (open blue circles). The colorbar corresponds to the S/N. (top right) S/N as a function of search DM and pulse width. (middle) DM=0 0.134 ms-sampled time series of the peak candidate in arbitrary units. (bottom) Dynamic spectrum of the peak candidate with coarse 12 MHz channels. The title gives the UTC time of the first time sample, RA and declination after systematic error correction, detected DM, pulse width, and S/N, and the CNN classifier's p-value. 179

5.6 Summary of Pulsar B0329+54 Monitoring Observations. (Top) The S/N of all pulses measured from predicted Times-of-Arrival (TOAs) are in blue. Initial candidates above the 8.5σ threshold are in grey, remaining candidates after PSF-based reduction are in black, and final candidates after classification are in red. (Bottom right) The S/N distribution of all single-pulses above 3σ are in blue, while 'non-detections' below 3σ are in grey. The median of the $> 3\sigma$ distribution is indicated in red and compared to the predicted S/N in black. (Bottom left) The folded pulse profile (S/N-weighted histogram of full timeseries) with 1,036 phase bins is shown in red while a histogram of peak TOAs is shown in blue. Note that the folded profile TOAs are not phase connected between days, nor are they phase connected to past observations (e.g. A. Deller et al., 2019). The profile from the European Pulsar Network (EPN) database is shown in black (Seiradakis et al., 1995). The TOA histogram is normalized such that the sum equals the mean TOA S/N, while the EPN and folded profiles are scaled to match the TOA histogram peak. The sampling time 134 ms, which limits the pulse profile resolution, is shown in phase units as black dashed lines. 180

5.7 Coverage and Rate Limits for the DN-GPS pilot survey. (top) Each sub-plot shows one of six passes of the galactic plane (dashed black line). Center coordinates for each 3.35 s pointing are shown in red. The positions of known pulsars and magnetars are shown as diamonds; non-pulsar LPRTs detected to date are circles. A sample of White Dwarf-M Dwarf binaries from Rebassa-Mansergas et al. (2021) are shown as triangles. (bottom) 95% Poissonian burst rate upper limits are indicated by the colorbar for each $3^\circ \times 3^\circ$ grid region as discussed in Section 5.5. Sources of interest covered by the DN-GPS search region are labeled; of these, only B0329+54 is confidently detected. 182

5.8 Flux and Astrometry Calibration Observations from the DSA-110 NSFRB galactic plane Survey (DN-GPS). (Left) Measured vs. NVSS catalogued flux for the 16 calibrators selected from DN-GPS data are shown as circles. Individual measurements are in grey, while the mean measurements have colorbar equal to the observed signal-to-noise. Additional calibrator observations from the real-time pipeline are shown as triangles. The red line shows the conversion curve constrained from the brightest source, J060351+215937, and the sensitivity limit $\sigma_{\rm srch}$ is shown in blue. The range of theoretical sensitivity limits from natural to approximately uniform $\mathcal{R} = -2$ imaging weights is shown in purple. (Right) Measured position errors of the 16 calibrators, after subtracting the mean systematic offsets $\epsilon_\alpha = -1.77' \pm 2''$, $\epsilon_\delta = -1.15' \pm 1''$ from RFC positions, are shown as circles with colorbar equal to the observed signal-to-noise. The 3σ error ellipse ($72'' \times 42''$) is outlined in red. 185

5.9 A Time- (3.35 s) and Frequency- (187.5 MHz) Averaged Dirty Image of Calibrator J060351+215937 where PSF and central sidelobes are visible. Dark regions are positive and light regions are negative in arbitrary units. J060351+215937 was the brightest calibrator observed during the DSA-110 NSFRB galactic plane Survey (DN-GPS) and was used to estimate the flux curve shown in Figure 5.8. 186

5.10 $P - \dot{P}$ Constraints from the DN-GPS Survey Using a Neutron Star Model (top; Cooper & Wadiasingh, 2024) and a White Dwarf Model (bottom; Qu & B. Zhang, 2025). In each plot the thick red lines bound the allowed emission ranges for each model. Vertical grey lines indicate hard limits from the DN-GPS search due to the sampling time and Poissonian burst rate. Pulsars (diamonds), WD binary LPRTs (squares) and all other LPRTs (circles) are colored with their distance estimates, while those without distances are in red. The colorbar also highlights the maximum detectable distance ($d_{\max}(P, \dot{P})$) for each model (see Section 5.5) given the DN-GPS $25\sigma_{\mathrm{srch},P<5\,\mathrm{min}} \approx 1030\,\mathrm{mJy}$ and $25\sigma_{\mathrm{srch},P>5\,\mathrm{min}} \approx 1200\,\mathrm{mJy}$ detection limits for $P < 2\,\mathrm{min}$ and $P > 2\,\mathrm{min}$, respectively. Red dashed lines are contours of constant $d_{\max}(P, \dot{P})$). 189

5.11 Candidate Plots for RFI Detected in the 134 ms (left) 670 ms (middle) and 10.07 s (right) Searches. Subplots for the left and middle plots are the same as described in Figure 5.5, while the right plot omits the dynamic spectrum since de-dispersion is omitted for the 10.07 s search. 192

6.1 Comparison of the pulse profile of PSR J1935 + 1616 observed with the DSA-110 (left) to an archival profile from the European Pulsar Network (right). The observed profile was formed by centroiding and stacking 26 single-pulse detections automatically triggered and processed identically to DSA-110 FRBs. The top panels show the PA of the average profile (blue), and for the DSA-110 bursts, the PA of single pulses (grey). The bottom panels show the Stokes parameters and linear-polarization fraction (L/I) as labeled. Besides a PA offset of unknown origin, the profiles are otherwise similar. 202

6.2 Summary of polarization and RM data on FRB 20220207C (***Zach***). Identical plots on all FRBs presented herein are shown in Appendix 6.8. *Left:* From top, we show the PPA (with 1σ errorbars) measured after correcting for RM, and frequency averaged time series of Stokes I, L, and V. The PPA is highlighted in bins with linear-polarization S/N $> 3\sigma$. The dynamic spectrum is shown at center, to the right of which are shown optimally summed spectra (Appendix 6.8) and the spectrally resolved PPA with $> 3\sigma$ bins highlighted. *Right:* The top panel shows the RM spectra evaluated over the full range of sensitivity using two different methods (Appendix 6.8), and the bottom panel shows a detailed analysis of the S/N of the peak. 203

6.3 Linear and Absolute Value Circular Polarization for DSA-110 FRBs. Each FRB is color-coded by its polarization class as reported in Table 6.3. **Single Component** FRBs are shown as circles and **Multi-Component** FRBs are shown as triangles. The errorbars shown are 1σ uncertainties. The black line indicates where the total-polarization fraction $T/I = \sqrt{(|V|/I)^2 + (L/I)^2} = 100\%$. While all **Consistent with 100%** (blue) and most **Intermediate** (green) FRBs have $L/I > 50\%$, FRB 20220121B and FRB 20220506D also show significant circular polarization. FRB 20220319D is the only FRB in either class with less than 50% total polarization. All **Consistent with 0%** FRBs (orange) have L/I and $|V|/I$ below 25%. 210

6.4 Projection of the polarization state of FRB 20220310F onto the Poincaré sphere. The position angle (χ) and longitude (ψ) are related to the Stokes parameters by $Q = \sin(2\psi)\sin(2\chi)$, $U = \sin(2\psi)\cos(2\chi)$, and $V = \cos(2\psi)$. Note the position angle axis has been shifted by 90° for ease of viewing. Data are displayed in windows of eight and ten 32.768 μs samples for the first and second components of the burst. 216

6.5 Comparison between the linear- and circular-polarization fractions of various FRB sub-samples. The top and right panels show empirical cumulative distribution functions (CDFs) for the DSA-110 sample (pink), published non-repeaters (brown), published repeaters (purple), and FRBs with measurements only at < 1 GHz (green). Arrows indicate upper limits in $|V/I|$ estimated from the measured values of L/I. See Appendix 6.8 for a summary of the literature data. In general, no significant differences between sub-samples are found. . 218

6.6 Comparison between the linear- and circular- polarization fractions of FRBs, pulsar APs, and RRATs. *Top:* FRBs (grey) are observed to have much higher linear-polarization fractions than MSPs (blue), CPs (orange) and RRATs (gold). Arrows indicate upper limits in $|V/I|$ estimated from the measured values of L/I. Somewhat higher circular-polarization fractions are also observed for FRBs. *Bottom:* We compare FRBs with canonical pulsars ($P > 30$ ms) with various characteristic ages. Young pulsars (blue) have remarkable similarity to FRBs (grey) in linear polarization, while older pulsars (orange, green) are more depolarized. 220

6.7 Comparison between the linear- and circular- polarization fractions of FRBs with pulsar single pulses (SPs). Pulsar SPs (red) have similar average linear polarization fraction ($\sim$ 60%), but cover a narrower range than FRBs (grey). Arrows indicate upper limits in $|V/I|$ estimated from the measured values of L/I. 222

6.8 Simulated error in the linear polarization position angle (PA), as a function of linear-polarization S/N. See text for details of the simulation. The simulated error (blue) is taken as the standard deviation of the PA across the width of each boxcar pulse. The red lines indicate the piecewise exponential fit of the simulated error, while the red markers show the resulting error for each trial when computed using the fit. The error derived from the PA distribution of Naghizadeh-Khouei & Clarke (1993), shown in orange, appears to underestimate the error, especially at high S/N. 233

6.9 Jones matrix solutions on four epochs. *Left:* Frequency dependent $r(\nu)$, $\phi(\nu)$, and $|g_{yy}(\nu)|$ after removing birdies, downsampling and interpolating. *Right:* Solutions averaged over frequency for each observation. The violin plots show the distribution of the frequency dependent points while the red line shows the average value over all epochs. 238

6.10 Violin plots of leakage estimates. The mean values are shown as markers, while the distributions are values from all calibrated voltage dumps and all frequency channels in each observation. 239

6.11 Linear (*top*), absolute value circular (*middle*), and signed circular polarization (*bottom*) measurements of J1935+1616. Polarization fractions for individual pulses are shown in blue, and the weighted mean is shown in purple, with the shaded area indicating the weighted error. The expected polarization fractions from Gould & Lyne (1998) (18%, 15%, and 2% from top to bottom) are shown in black. The linear and absolute value circular polarization fractions measured from the folded profiles, shown in red, are in good agreement with expectation within the 1σ errorbar. 241

6.12 Simulated error in the recovered RM through RM Synthesis, as a function of linear-polarization S/N. See text for details of the simulation. For each true S/N, the mean analytic RM-uncertainty estimate from Brentjens & De Bruyn (2005) is shown as an orange curve. The blue points show the standard deviations of the recovered RMs, which are fit by the green line. 244

6.13 Fractional depolarization the DSA-110 as a function of RM, for different frequencies within the DSA-110 band. 245

6.14 Summary of polarization data for each DSA-110 FRB. For each FRB, from top, we show the PPA (with 1σ errorbars) measured after correcting for RM, and frequency averaged time series of Stokes I, L, and V. The PPA is highlighted in bins with linear-polarization S/N $> 3\sigma$. The dynamic spectrum is shown at center, to the right of which are shown optimally summed spectra (Appendix 6.8) and the spectrally resolved PPA with $> 3\sigma$ bins highlighted. For FRBs with no measured RM, the PA without RM correction, rather than the PPA is shown. 249

6.15 Same as Figure 6.14. 250

6.16 Same as Figure 6.14. 251

6.17 Same as Figure 6.14. 252

6.18 Summary of RM data on each FRB with significant detection. For each FRB, the top panel shows the RM spectra evaluated over the full range of sensitivity using two different methods (Appendix 6.8), and the bottom panel shows a detailed analysis of the S/N of the peak. The horizontal purple line indicates the 9σ significance threshold applied to the S/N Method spectrum (yellow). 253

6.19 Same as Figure 6.18. 254

6.20 Same as Figure 6.18. 255
6.21 Time evolution of RM in FRB 20220207C; *Right:* The top plot shows the measured RM from the S/N method for each time bin; the polarized profile showing Stokes I (black), linear polarization (blue) and circular polarization (orange) is shown in the middle plot. The bottom plot shows the RM spectrum in each time bin, referred to as the Rotation Measure Transform. In the top plot, the color of each point corresponds to the peak S/N in the RM spectrum for that time bin, and correlates with the colormap in the RM transform. The red line is drawn at the average RM value from both sub-components, $162.48 \pm 0.04\,\mathrm{rad\,m^{-2}}$. *Right:* The RM synthesis summary plots are shown for sub-bursts 1 (top) and 2 (bottom) individually. See the caption for Figure 6.18 for a description of each trace in the RM synthesis plots. 256
6.22 Same as Figure 6.21 for FRB 20220310F. The red line is drawn at the average RM value from both sub-components, $11.4 \pm 0.2\,\mathrm{rad\,m^{-2}}$. . . . 257
6.23 Same as Figure 6.21 for FRB 20220418A. The red line is drawn at the average RM value from all sub-components, $6.1 \pm 7.5\,\mathrm{rad\,m^{-2}}$. For the individual components, a significant RM is found only for the first. 258
6.24 Same as Figure 6.21 for FRB 20221101B. The red line is drawn at the average RM value from both sub-components, $-13.1 \pm 10.5\,\mathrm{rad\,m^{-2}}$. 259
7.1 Estimates of $\mathrm{RM_{host}}$ and $\mathrm{DM_{host}}$ for as yet non-repeating (brown triangles) and repeating FRBs (purple circles). Solid lines show the best fit from a Markov-Chain Monte Carlo (MCMC) analysis for non-repeaters (brown), repeaters (purple), and the full sample (grey). Random draws from each MCMC simulation are shown by faint lines for non-repeaters (brown), repeaters (purple) and all FRBs (grey). The best fit slopes with 1-σ errors are displayed in the legend in each case. 276

7.2 Estimates of RM_{exgal} at different redshifts for as yet non-repeating (brown triangles) and repeating FRBs (purple circles). Solid lines show the best fit from an MCMC analysis for non-repeaters (brown), repeaters (purple), and the full sample (grey). Note that redshift errorbars are omitted. The green line indicates the expected scaling from redshift suppression, i.e. $RM_{exgal} \propto (1+z)^{-2}$. Samples from each MCMC simulation are shown by faint lines for non-repeaters (brown), repeaters (purple) and all FRBs (grey). The best fit slopes with 1-σ errors are displayed in the legend in each case. Significant negative correlation is found for non-repeaters ($p = 0.006$) using a Spearman Rho test, although the median slope $m = -8.1^{6.9}_{6.1}$ is only marginally consistent with redshift suppression. The two repeaters with the highest values of RM_{exgal}, FRB 20121102A and FRB 20190520B, are known to have highly magnetized, dynamic local environments that may dominate their RMs (Anna-Thomas et al., 2022; Plavin et al., 2022). 278

7.3 ***Top:*** Comparison of FRB RM_{host} and DM_{host} estimates with the RMs and DMs of pulsars, RRATs, and radio-loud magnetars. As yet non-repeating (brown triangles) and repeating FRBs (purple circles) are distinguished, as are canonical pulsars (CPs; $P > 30$ ms; blue circles) and millisecond pulsars (MSPs; $P < 30$ ms; orange circles). RRATs (yellow diamonds), pulsars in the Large and Small Magellanic Clouds (LMC, SMC; green squares), and radio magnetars (**cyan** squares) are included to complete the sample. Dotted grey lines of constant magnetic field, $\bar{B}_{\parallel,\mathrm{host}}$, are shown. *Bottom:* Empirical cumulative distribution functions (CDF) for the line-of-sight magnetic field $\bar{B}_{\parallel,\mathrm{host}}$. CDFs for CPs (blue) MSPs (orange), repeating (purple) and as yet non-repeating (brown) FRBs, and RRATs (yellow) are shown. Note that radio magnetars and Magellanic Cloud pulsars are included in the CP distribution. Both repeaters and non-repeaters are found to have distinct $\bar{B}_{\parallel,\mathrm{host}}$ from CPs and MSPs using a Kolmogorov-Smirnov (K-S) test and an Anderson-Darling (A-D) test with > 99% confidence. FRBs in general appear to occupy slightly more magnetized environments than pulsars. K-S and A-D tests find similarity between FRB and RRAT distributions. Data on literature samples of neutron stars were compiled according to Appendix A of the companion paper Sherman et al. (2024) 281

7.4 Estimates of $\bar{B}_{\parallel,\mathrm{host}}$ for FRBs at different redshifts, including as yet non-repeating sources (triangles) and repeaters (circles). FRBs are grouped by the (logarithmic) specific star-formation rates (lSSFR) of the host galaxies, scaled by $10^{10} M_{\odot}$: lSSFR < -1.25 (orange), $-1.25 \leq$ lSSFR < 0 (green) and lSSFR ≥ 0 (purple). FRBs 20121102A and 20190520B, both associated with persistent radio sources (PRSs; C. J. Law et al., 2022), are circled in black. No correlation is found between $\bar{B}_{\parallel,\mathrm{host}}$ and redshift for any subgroup, nor are there significant differences between the subgroups. 282

8.1 Histogram of Galactic Latitude of Simulated Pulsar Population. The inset plot shows the population in Cartesian coordinates projected into the galactic plane. For both plots, the full simulated sample is in grey, the $\delta > 30^{\circ}$ population is in blue, the 25,902 pulsars detectable by CASS are in orange, and the 10,879 detectable by periodicity search are in green. 297

8.2 Simulated DSA-2000 Detections from a Blind Periodicity Search as a Function of Observing Bandwidth. 1σ errorbars are shown. Each trial bandwidth uses 700 MHz as the lower limit; the nominal 312.5 MHz design bandwidth is indicated in red. The right-hand axis indicates the percent of the total pulsar population detected. The solid horizontal lines indicate the number of pulsars detectable in the CASS. The known pulsar population (3838 total) from the ATNF catalog is shown in yellow, as of May 10^{th}, 2025. 298

8.3 Example Pulsar Target Selection Using the COSMOS Deep Field. The underlying image is from the MeerKAT MIGHTEE survey. MIGHTEE/VLAC20 sources excluded as extended in radio or optical are grey circles. COSMOS2015 and VLAC20 Galaxies are marked with purple triangles and orange squares, respectively. The final target sample is indicated by red circles. 301

8.4 Example 25-Pointing Grid for DSA-2000 CASS. Pointing centers are indicated by an "x", and each circle indicates the FWHM of the primary beam at 2 GHz (1.68°). 303

8.5 (top right) Number of adjacent pointings that overlap each point within example pulsar search FOVs. Each row corresponds to a different search region size and each column corresponds to a different frequency band. The pink circle indicates the edge of the search region, while the colorscale indicates the number of times a point can be visited within a 25-pointing grid. (bottom right) Sensitivity increase factor from re-visiting a point the maximum number of times. The rows and columns are identical to the bottom left plot. The top left and bottom left plots are zoomed in on the FOV= 1.848° example. 304

8.6 (top) Detection Probability Curves for the Baseline Search. The red line indicates the 50% detection probability corresponding to the S/N threshold. The purple line indicates the threshold η set by the false positive rate α used as the detection criteria on the search statistic. (bottom) S/N Threshold for Baseline Search. Linear interpolation is shown as a solid line, which is used for constraint of PSRPop.py simulations. 307

8.7 Baseline Search Sensitivity Plot and PSRPoppy Simulated Detections with Revised S/N Threshold. Sensitivity curves with the original constant S/N threshold of 9 are shown as solid lines. 308

LIST OF TABLES

Number *Page*

1.1 New Galactic Magnetars and Candidates 17
2.1 Magnetars and Magnetar Candidates from the McGill Catalog 48
2.2 Magnetar Age Upper Limits Used for the *Gaia* Search 52
2.3 Search Results and Completeness Ratios 77
2.4 Constraints on magnetar binaries from this work 81
2.5 Critical Thresholds for Magnetar Association Tests 102
3.1 Results of BPASS Monte Carlo Magnetar Generation 141
4.1 Magnetar Galactic Latitudes (b) with Errors (σ_b), Distances, and Vertical Distances (z) from galactic plane ($b = 0°$) 151
4.2 Results of MCMC Fit of Magnetar Scale Height 154
6.1 Table of Frequently Used Symbols and Abbreviations 201
6.2 DSA-110 FRB Sample Polarization Properties 205
6.3 Polarization-based FRB subgroups from DSA-110 data. 208
6.4 Previously Published FRB Sample Polarization Properties 230
6.5 Polarization Calibration Observations and Jones Matrix Parameters . 237
7.1 DSA-110 FRB Sample Rotation Measure Properties 277
8.1 Baseline Design Parameters for Pulsar Search 295

Chapter 1

INTRODUCTION

1.1 Stellar Evolution: Neutron Star Origins

The neutron star species central to this work are the second life of massive stars; thus, I start my thesis with a summary of their first.

Low-mass ($\lesssim 7M_\odot$) stars like our Sun, initially formed through gravitational collapse of proto-stellar dust, will not form neutron stars. These stars begin on the Main Sequence (MS) with cores composed primarily of neutral Hydrogen (H), which it fuses to form Helium (He) through the proton-proton (p-p) chain or Carbon-Nitrogen-Oxygen (CNO) cycle reaction. Exhausting this H reservoir, radiation pressure fails to support the core against gravitational contraction. This leads to heating of the core, and thus expansion of the outer H and He envelope into the Red Giant (RG) phase. Some stars lack sufficient material to collapse further, radiating away their outer layers to leave behind a He White Dwarf (He-WD) star. More massive stars will continue to contract and heat until they ignite the next fusion processes to form heavier Carbon (C) and Oxygen (O) atoms. Another giant phase follows the exhaustion of He fuel, and again the lower mass stars radiate away their outer layers, leaving a CO-WD while higher mass stars will repeat the cycle to become ONeMg-WD (see e.g., Acharya et al., 2025; Hansen & Kawaler, 1994, for reviews). The WDs left behind by low-mass stars are supported by electron degeneracy pressure, and have typical radii around $\sim 0.01R_\odot$, masses of $\sim 0.6M_\odot$, and dipole-like magnetic fields $\sim 10^6$ G (see e.g., Ferrario et al., 2015; Wickramasinghe & Ferrario, 2005, for reviews).

I have described this evolution primarily to contrast with that of high-mass ($\gtrsim 7M_\odot$) stars relevant to this work. After traversing the same fusion and giant phases as low-mass stars, high-mass stars can continue fusing much heavier elements until forming Iron (Fe), which can no longer be fused without consuming energy. The core continues to collapse under gravity, dissociating Fe atoms whose protons $\beta-$decay into neutrons. This neutron-rich core continues to contract until supported only by neutron degeneracy pressure. Finally, the star's outer core layers can no longer expand against gravity; they collapse and 'bounce' off of the core, ejected in an energetic explosion that collides with still-infalling lighter elements: a Core-

Collapse Supernova (CCSN). The event leaves behind only the stellar core, a newly formed neutron star; these have masses $\gtrsim 1.4M_\odot$, radii of ~ 10 km, and the strongest magnetic fields in the universe $\sim 10^{12-15}$ G. The most massive stars can collapse into Black Holes, singularities whose gravitational pull prevents light from escaping. Thus, the long-lived (kyr−Myr after CCSN) neutron stars we see in the Milky Way are generally concentrated at the Chandrasekhar mass limit $\sim 1.4M_\odot$ (see e.g., Smartt, 2009, for a review).

1.2 Stellar Binaries, Stellar Mergers, and Alternative Neutron Star Formation Channels

According to statistical constraints from observations of early-type binary stars by Moe & Di Stefano (2017), roughly $\sim 85\%$ of massive stars form in binary, triple, or higher-order systems. Interaction between a star and its companions can influence its evolution, even dictating its fate as a WD, neutron star, or black hole. Through simulation, mass loss has been found to impact the formation of neutron stars and black holes, whether via stable accretion of the less massive star's inflated envelope to the more massive star during one of the former's Giant phases, or through stellar winds of charged particles propelled by radiation pressure (e.g., Dorozsmai & Toonen, 2024; Eldridge & Stanway, 2016; Laplace et al., 2021). In addition, WDs can undergo Accretion Induced Collapse (AIC) into neutron stars or black holes by transferring their companion stars' envelope to their own, effectively making them behave as high-mass Giant stars (Nomoto & Kondo, 1991; Ruiter et al., 2019). Mergers of intermediate-mass stars ($4-8M_\odot$), either with stellar or WD companions, can similarly incite a Merger Induced Collapse (MIC) into neutron stars and black holes on later timescales (R.-C. Hu & B. Zhang, 2026; Zapartas et al., 2017). Binary stellar evolution thus plays an important role in our understanding of CCSNe and neutron star formation.

1.3 The Neutron Star Zoo

In this following section, we explore the variety of confirmed neutron star species, their unique properties, and the parameters used to characterize them.

1.3.1 Slow/Canonical Radio Pulsars (CPs)

Although neutron stars were theorized as a possible leftover of stellar supernovae by Baade & Zwicky (1934), it was not until the discovery of the first radio pulsar by Jocelyn Bell-Burnell in 1967 that their existence was confirmed (and not until

2004 that she was properly recognized for her discovery which won her advisor the 1974 Nobel Prize in Physics; Bell Burnell, 2004; Hewish, 1968; Hewish et al., 1979). Radio pulsars are rapidly rotating ($P \approx 30 - 1000$ ms) neutron stars with strong magnetic fields ($B \approx 10^{12}$ G) that emit beams of coherent radio emission in their magnetic polar regions. Roughly 4,000 slow radio pulsars have been discovered at the time of writing according to the Australia Telescope National Facility (ATNF) catalog[1] (Manchester et al., 2005). Before describing the most probable emission mechanism and geometry, we take a brief aside to distinguish 'coherent' and 'incoherent' radiation in this context.

Consider a single particle with charge q accelerating at rate a. The power radiated by this charge is given by Larmor's formula:

$$P = \frac{2}{3}\frac{q^2a^2}{c^3} \tag{1.1}$$

where c is the speed of light. Instead, if N charges radiate independently, the total power is computed as the sum of the individual particle's power. This is because the individual Poynting vectors ($\overrightarrow{S} = \frac{1}{\mu_0}(\overrightarrow{E} \times \overrightarrow{B})$ where $\overrightarrow{E}$ and $\overrightarrow{B}$ are the radiated electric and magnetic fields and μ_0 is the vacuum permeability), which measure the radiated power per unit area, are superimposed. Thus, the total power for N *incoherently* radiating particles is given by:

$$P_{IC} = \frac{2}{3}\frac{Nq^2a^2}{c^3} \tag{1.2}$$

In contrast, if N charges radiate such that $\overrightarrow{E}$ and $\overrightarrow{B}$ are in-phase, then the fields themselves are super-imposed. The total Poynting vector is then $\overrightarrow{S}_C = \frac{1}{\mu_0}(N\overrightarrow{E} \times N\overrightarrow{B}) = \frac{N^2}{\mu_0}(\overrightarrow{E} \times \overrightarrow{B})$ and the power is increased by N^2; the total power for N *coherently* radiating particles is given by:

$$P_C = \frac{2}{3}\frac{N^2q^2a^2}{c^3} = NP_{IC} \tag{1.3}$$

This means that coherently radiating particles can radiate significantly more power (higher brightness temperatures) than incoherently radiating particles (e.g., Condon & Ransom, 2016).

[1] `https://www.atnf.csiro.au/research/pulsar/psrcat`

Pulsars' polar emission is coherent and therefore extremely luminous ($L'_{1.4\,\mathrm{GHz}} \lesssim 10\,\mathrm{Jy\,kpc^2}$)[2], with multiple pulsars observed in the Magellanic Clouds roughly 50 kpc away (Crawford et al., 2001). Pulsar emission is powered by their rotational energy, causing their rotation periods to change at a rate $\dot{P} = dP/dt$ measured through pulsar timing. The exact triggering and emission mechanism is unclear; the simplified magnetic dipole radiation model was introduced by Goldreich & Julian (1969) and has persisted as a useful analog for decades. By assuming a pulsar has a dipolar magnetic field structure, one can estimate the minimum surface magnetic field strength B_S, the characteristic pulsar age (time since CCSNe) τ_C, and the maximum spin-down luminosity that can be produced from rotational energy allowance, $L_{\max}$, as follows:

$$B_S \gtrsim 3.2 \times 10^{19}\ \mathrm{G}\left(\frac{P\dot{P}}{\mathrm{s}}\right)^{1/2} \tag{1.4}$$

$$\tau_C \leq \frac{P}{2\dot{P}} \tag{1.5}$$

$$L_{\max} = -\frac{4\pi^2 I \dot{P}}{P^3} \tag{1.6}$$

where the moment of inertia $I = 2MR^2/5 \approx 10^{45}\,\mathrm{g\,cm^2}$ ($M \sim 1.4 M_\odot$ and $R \sim 10\,\mathrm{km}$ are the neutron star mass and radius). Notably, this model relies on the assumptions that the field is purely dipolar and the initial rotation period is infinitesimally small. The latter assumption is reasonable for $P >> P_0$; however, simulations of neutron star magnetospheres suggest a toroidal component is necessary to form a stable magnetic field (e.g., Braithwaite & Spruit, 2006).

Here I will briefly and qualitatively describe the more realistic model of pulsar emission, the Partially-Screened Vacuum Gap (PSVG) model; for a detailed description see Szary et al. (2015), Gil et al. (2003), Cheng & Ruderman (1980), Ruderman & Sutherland (1975) and references therein. The neutron star geometry consists of an iron crust and an electron-positron pair plasma-filled magnetosphere with mean co-rotational charge density $\bar{\rho} = \rho_{GJ} \equiv -(2\pi c)^{-1}(\overrightarrow{\Omega} \cdot \overrightarrow{B_S})$ (Goldreich & Julian, 1969). Recall that the magnetic field can be non-dipolar. Throughout

[2]Throughout this paper, I will use L' to denote pseudo-luminosity, defined as the observed flux density (power per unit area per unit bandwidth) scaled by distance squared. I will use L to denote real luminosity, the power emitted by the source.

the magnetosphere, an electric field $\overrightarrow{E}$ is induced perpendicular to the magnetic field $\overrightarrow{B}$ ($\overrightarrow{E} \cdot \overrightarrow{B} = 0$), whereas in the polar cap region, defined as the surface area where open, non-corotating magnetic field lines terminate, $\overrightarrow{E} \cdot \overrightarrow{B} \neq 0$. Above the polar cap, positive charges stream out of the magnetosphere along open field lines. This creates a vertical voltage potential drop in the polar cap region; loosely bound electrons in the crust are then discharged, or 'sparked', across the gap, which regulates the maximum gap voltage. As discharging electrons accelerate, they radiate high-energy photons that pair-create electron-positron pairs. Some pairs will radiate and pair-create themselves, inducing a discharge avalanche that rapidly fills the gap region with positrons which stream out of the gap and electrons which stream back to the surface. The escaping positrons then radiate via a coherent mechanism (such as coherent curvature radiation or synchrotron maser emission) to produce the observed pulsar beam. Gil et al. (2003) extend this picture to allow both parallel ($\overrightarrow{\Omega} \cdot \overrightarrow{B} > 0$) and anti-parallel ($\overrightarrow{\Omega} \cdot \overrightarrow{B} < 0$) rotators, and further explain how the sparking process can result in sub-pulse drifting behavior observed in many pulsars.

1.3.2 Slow/Canonical High-Energy Pulsars (HEPs)

A subset of 207 slow pulsars have been detected in hard X-rays ($\sim 20-50$ keV) and/or Gamma rays ($\sim$ 50 keV-10 GeV; Kuiper & Hermsen, 2015; Philippov & Kramer, 2022; von Kienlin et al., 2020). These High-Energy Pulsars (HEPs) are generally young ($10 - 100$ kyr) with high spin-down luminosities ($L_{\rm max} \gtrsim 10^{45}$erg s^{-1}), and around 100 also exhibit radio emission in conjunction with HE emission. Unlike radio pulsars, HEPs' inferred geometries suggest an outer magnetospheric origin; one model requires magnetic reconnection within the equatorial current sheet to heat particles which radiate Gamma rays, while the photons also pair-create IR, optical, and X-ray emitting particles (e.g., Lyubarskii, 1996; Philippov & Kramer, 2022). Thirty-six HEPs are associated with Pulsar Wind Nebulae (PWNe) and/or Supernova Remnants (SNRs) at X-ray and radio wavelengths. PWNe are relativistic outflows of charged particles expanding as particles cool either adiabatically or via synchrotron radiation in the local magnetic field (Granot et al., 2017). SNRs, in contrast are bright shells formed when CCSNe ejecta collide with the surrounding Interstellar Medium (ISM) gas and create a turbulent "shock" front in which charged particles radiate synchrotron photons (Salpeter, 1955; Schenck et al., 2016; Truelove & McKee, 1999). As evidenced by the large fraction ($\sim 35\%$) of HEPs with PWNe and SNRs, these are observable only on short timescales ($\lesssim$ 10 kyr and $\lesssim$ 100 kyr, respectively). Only ~ 60 of the $\sim 4,000$ slow radio pulsars (typically $0.1 - 1$ Myr

old) have PWNe or SNRs by comparison.

1.3.3 Recycled Millisecond Pulsars (MSPs)

Millisecond Pulsars (MSPs), of which around 800 are known, have rotation periods $P < 30\,\mathrm{ms}$ and typically have stellar companions. MSPs first evolved as canonical pulsars before passing the 'death line' or 'death valley' where they could no longer pair-produce to create radio emission (e.g., K. Chen & Ruderman, 1993). Their stellar companions then evolve off of the main sequence into a Giant Phase, filling their Roche Lobes and allowing the pulsar to accrete material. In addition to producing bright X-ray and IR emission from the accretion disk (observable as an X-ray binary; e.g., Schatz & Rehm, 2006), the pulsar's rotational energy will increase, 'spinning-up' to millisecond rotation periods where it can again produce radio emission (e.g., Lorimer, 2008). As a result, MSPs are much older than canonical pulsars, with ages $\sim 0.1 - 1\,\mathrm{Gyr}$. Notably, neutron stars cannot rotate faster than $P \sim 1\,\mathrm{ms}$ without breaking apart.

1.3.4 X-ray Dim Isolated Neutron Stars (XDINSs)

Only 7 X-ray Dim Isolated Neutron Stars (XDINSs) are known to date; the so-called 'Magnificent Seven' exhibit no radio or Gamma ray pulses, and are instead only detectable by their faint thermal ($T \sim 10^6\,\mathrm{K}$) X-ray luminosity. This X-ray emission is modulated by the XDINS rotation period from inhomogeneities of the surface temperature (e.g., Dessert et al., 2020; E. F. Keane & Kramer, 2008; Turolla, 2009). It is unclear if XDINS have never exhibited pulsar-like magnetospheric emission, or if they are the remnant of a pulsar which expended its available energy. However, their rotation period and $\dot{P}$ upper limits suggest they have not yet passed the death line.

1.3.5 Rotating RAdio Transients (RRATs)

Rotating RAdio Transients (RRATs) are the most recently discovered neutron star species, exhibiting $0.1 - 10\,\mathrm{s}$ periods and significant pulse-to-pulse amplitude variations. Their extreme variability limits detectability in traditional periodicity search pipelines, such that RRATs are predominantly discovered in single-pulse searches (E. Keane & M. McLaughlin, 2011; M. A. McLaughlin et al., 2006). According to the RRATalog[3] (Agarwal et al., 2026), over 336 RRATs have been discovered since 2006, including 41 discovered recently in the Five-Hundred Meter Aperture

[3] `https://rratalog.github.io/rratalog/`

Telescope (FAST) galactic plane Snapshot Survey (FAST; Han et al., 2021, 2025). Their intermediate rotation periods suggest they may be a transitional neutron star phase, e.g., between radio pulsars and XDINSs (e.g., E. F. Keane & Kramer, 2008).

1.3.6 Magnetars & the Magnetar Model

Magnetars, proposed as slow ($P \sim 1 - 10\,\mathrm{s}$), strongly magnetized ($B_S \sim 10^{14-15}\,\mathrm{G}$) X-ray and Gamma-ray emitting neutron stars by Duncan & Thompson (1992), were initially distinguished observationally as two unique species: Soft Gamma Repeaters (SGRs) and Anomalous X-ray pulsars (AXPs). The former were characterized by periodic hard X-ray/Gamma rays observed in the decaying tails of "giant flares" (GFs; Mazets et al., 1979a); the latter exhibited softer periodic X-ray pulsations (Gregory & Fahlman, 1980). Both appeared to enter and exit "outburst" phases during which they were observable for weeks or months before returning to quiescence. AXPs and SGRs were finally linked by Gavriil et al. (2002) when SGR-like bursts were observed from AXP 1E1048.1-5937, solidifying magnetars as a unique class of neutron star. For a complete review, see e.g., Kaspi & Beloborodov (2017).

Unlike radio and high-energy pulsars, magnetars usually exhibit high luminosities that exceed their rotational energy allowance, $L > L_{\mathrm{max}} \sim 10^{29-35}\,\mathrm{erg\,s^{-1}}$. The quantum critical field strength:

$$B_{\mathrm{QC}} = \frac{m_e^2 c^3}{q\hbar} = 4.413 \times 10^{13}\mathrm{G} \tag{1.7}$$

where m_e is the electron mass and $\hbar$ is the reduced Planck's constant, is often applied as an approximate threshold to distinguish highly magnetized magnetars from pulsars and other neutron stars (e.g., Baring & Harding, 1996; Duncan & Thompson, 1992). X-ray burst spectra can display a thermal component associated with the neutron star crust, contrasting with pulsars' non-thermal power law spectra (e.g., Halpern et al., 2008). Bright intermediate and giant flares with $L > 10^{40}\,\mathrm{erg\,s^{-1}}$ often lead to magnetars' initial discovery, and further distinguish them from the stable periodic emission of pulsars (e.g., Anderson et al., 2012; Camilo et al., 2007; Levin et al., 2012; Woods et al., 1999). In Section 1.4.1, we explore the criteria that define the magnetar class in more detail. The Period-Spindown ("P vs. $\dot{P}$", or "P-Pdot") diagram in Figure 1.1 summarizes the current census of neutron stars, indicating the B_{QC} threshold as a red dashed line.

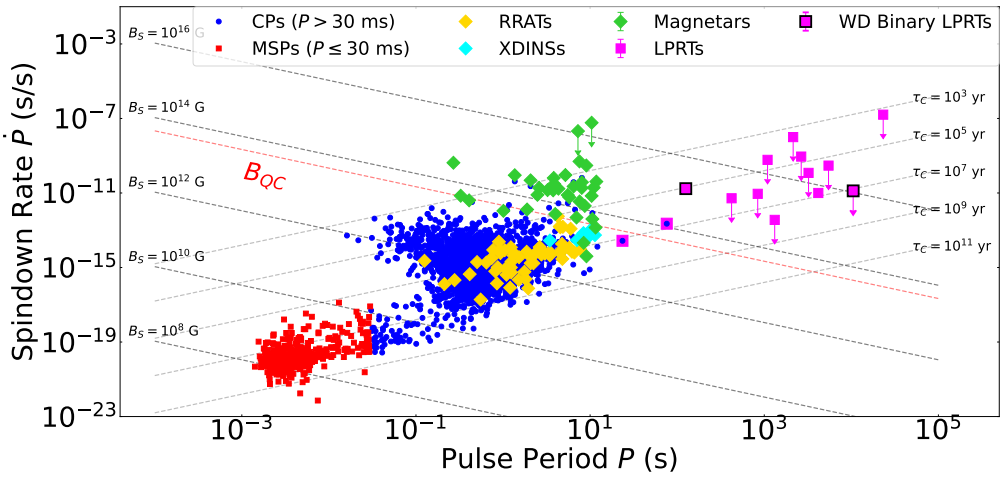

Figure 1.1: Period-Spindown ("P vs. $\dot{P}$", or "P-Pdot") diagram populated with the neutron star zoo and candidates. Slow, or "Canonical" Pulsars (CPs; blue) and Millisecond Pulsars (MSPs; red) are from the ATNF catalog (Manchester et al., 2005). The "Magnificent Seven" X-ray Dim Isolated Neutron Stars are shown in teal (XDINSs; Haberl, 2007) while Rotating RAdio Transients from the RRATalog (Agarwal et al., 2026), including the FAST sample (Han et al., 2025) are in yellow. Magnetars and candidates from the McGill Catalog (Olausen & Kaspi, 2014) and the updated sample discussed in Sections 1.4 and 1.5 are in green. Long Period Radio Transients (LPRTs or LPTs) as discussed in Section 1.5.3 are in magenta with the two confirmed White Dwarf-M Dwarf binary LPTs outlined in black. Lines of constant magnetic field B_S and characteristic age τ_C are dashed black and grey, respectively, while the quantum critical field strength $B_{\rm QC}$ is in red. Uncertainties are not shown, but typically range from $10^{-17} - 10^{-3}$ s for P and from $10^{-26} - 10^{-11}$ s/s for $\dot{P}$, increasing for larger P and $\dot{P}$.

1.4 The Magnetar Census

The McGill Magnetar Catalog[4] compiled a census of 24 magnetars and 6 magnetar candidates starting in 2014, but has not been actively managed since 2020 (Olausen & Kaspi, 2014). Since then, two additional magnetars have been confirmed: SGR J1830-0645 (Page et al., 2020; R. Sharma et al., 2023; Younes et al., 2022a; Zelati et al., 2021) and Swift J1555.2-5402 (Borghese et al., 2025; Demirer et al., 2025; Enoto et al., 2021). At least 24 additional Galactic magnetar candidates have been identified including novel Long Period Radio Transients (LPTs or LPRTs; Beniamini et al., 2023), while Fast Radio Bursts (FRBs) and some short Gamma Ray Bursts (sGRBs), and X-ray Transients (XTs) compose a growing population of extragalactic magnetar candidates. We summarize these in the following sections. Some Super-luminous supernovae (SLSNe) and long Gamma Ray Bursts (lGRBs)

[4] `https://www.physics.mcgill.ca/~pulsar/magnetar/main.html`

have also been proposed to be powered by newborn millisecond magnetars, which we will not discuss in detail here.

1.4.1 The McGill Magnetar Sample: Review of Selection Criteria

As noted above, the criteria for identifying magnetars varies among sources and has evolved over the decades. We have conducted a review of the 24 McGill magnetars' discovery papers to summarize the most common identifying features. Note that periodicity is taken as a default condition to confirm a magnetar. SNRs have also informed magnetar identification, but are limited by observational selection effects and can indicate the presence of compact objects other than magnetars. Therefore, we do not include SNR asociation as a condition in this analysis.

The X-ray spectrum properties are the most common discriminating features, and were included in 20 of 24 magnetars' identification criteria. Kouveliotou et al. (1993b), for example, summarizes SGR (magnetar) spectra as being "much harder than those of X-ray bursts and much softer than those of classical GRBs." Indeed, around 10 magnetars, such as the SMC magnetar CXOU J010043.1-721134, were confirmed in part due to their "soft" or "steep" spectra (e.g., R. C. Lamb et al., 2002). Many of these, like SGR J1935+54, found that the power-law model typically fit to pulsar spectra is insufficient, requiring instead a thermal blackbody, thermal bremsstrahlung, or multi-component (e.g., blackbody component and power law component or 2 blackbodies) spectra for acceptable fits (e.g., R. C. Lamb et al., 2002). This likely relates to localized heating of the neutron star crust that forms "hotspots," proposed as the energy source in magnetospheric emission models (e.g., Kaspi & Beloborodov, 2017).

Nearly as common as spectral uniqueness, time variability was cited in the identification of 17 magnetars. In most cases, this is related to the observed flux brightening at onset of an outburst or its gradual decay, as for magnetars XTE J1810-197 and 3XMM J185246.6+003317 (Gotthelf et al., 2004; Zhou et al., 2014). Earlier discoveries placed significant weight on short flaring emission, which contrasted with the constant diffuse emission flux and one-off GRBs. For example, (Kouveliotou et al., 1993b) first collected SGR 0526-66, SGR 1900+14, and SGR 1806-20 into a unique SGR class because "Of the one thousand or so detected sources of cosmic $\gamma-$ray bursts (GRBs), only three are known to have exhibited recurrent activity," coupled with their soft spectra. After the magnetar population was large enough to denote in $P - \dot{P}$ space, the long rotation periods, or "slow variations" as stated for

3XMM J185246.6+003317, became a distinguishing feature as well (Zhou et al., 2014).

Perhaps unexpectedly, requirements that $L_X \gtrsim L_{\rm max}$ or that $B_S \gtrsim B_{QC}$ (or an arbitrary threshold) were only invoked for 12 of the 24 magnetars; 6 of these used both criteria. A few, like 1E 1547.05408 and SGR J1745-2900, more generally note that the "rotational parameters" or "timing properties" resemble those of the magnetar sample (Levin et al., 2010; Mori et al., 2013). The introduction of the magnetar model by (Duncan & Thompson, 1992) may denote the transition to include X-ray luminosity and magnetic field strength among identification criteria, having established the prediction that rapidly rotating, strongly magnetized neutron stars could produce X-ray and gamma ray bursts. Rather than discounting these criteria, this may actually bolster the strength of the magnetar model; remarkably, all five magnetars discovered before 1992 (1E 1048.1-5937, SGR 1806-20, SGR 1900+14, 1E 2259+586, SGR 0526-66) have $L_X \gtrsim L_{\rm max}$ and $B_S \gtrsim B_{QC}$ despite neglecting these criteria upon discovery (Laros et al., 1987; Mazets et al., 1979a,b; Seward et al., 1986). The Venn diagram in Figure 1.2 summarizes the criteria used to confirm each magnetar, demonstrating that multiple criteria are used in most cases. Spectral uniqueness is the only property that has been used independently to confirm a magnetar.

The apparent qualitative correlation between high X-ray luminosity and magnetic field strength with spectral softness and thermal content highlight magnetars' uniqueness from the pulsar class. Magnetars may form or evolve in a manner distinct from pulsars to achieve their unique spectral and magnetic properties (Duncan & Thompson, 1992).

This is further confirmed by magnetars near the threshold magnetic field strength of $\sim 10^{13}$ G, which display no radio pulsar-like properties. In proposal GBT25A-328[5], we used the Green Bank Telescope to search for L-band radio emission from the four magnetars with the lowest magnetic field strengths (low B-field magnetars): SGR J1822-1606 ($B_S = 1.4 \times 10^{13}$ G), SGR J0418+5729 ($B_S = 6.1 \times 10^{12}$ G), CXOU J1647-45 ($B_S < 6.6 \times 10^{13}$ G), and 3XMM J1852+0033 ($B_S < 4.1 \times 10^{13}$ G). Using the VEGAS pulsar backend and searching for periodic (at the known rotation periods and with unconstrained priors) and single-pulse emission with the PRESTO[6] software (Ransom, 2001), we find no confident radio candidates, placing the tightest

[5] https://library.nrao.edu/proposals/catalog/22139
[6] https://github.com/scottransom/presto

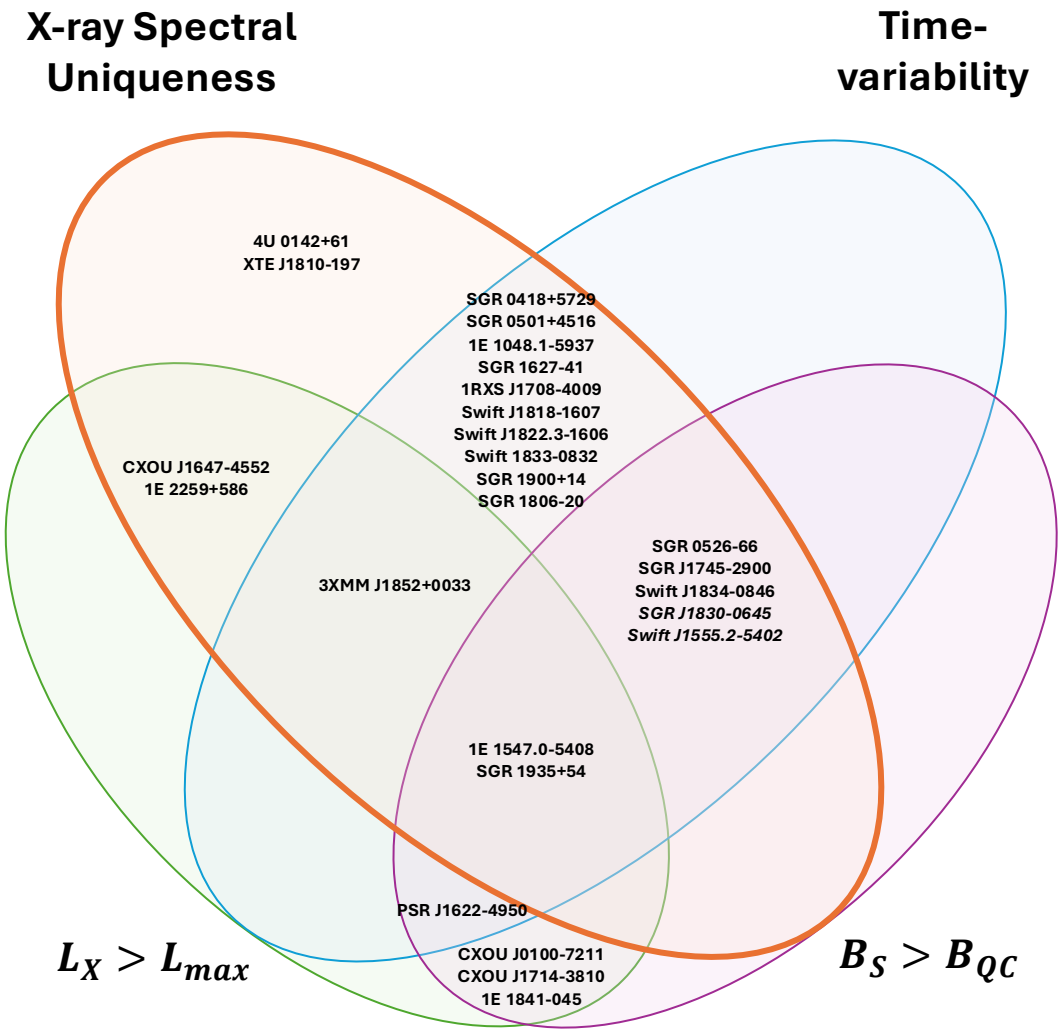

Figure 1.2: Venn Diagram of Four Magnetar Identification Criteria: X-ray Spectral Uniqueness (orange, upper left), Time-variability (blue, upper right), X-ray luminosity (green, lower left), and magnetic field strength (purple, lower right). The 24 confirmed McGill magnetars are shown, as well as the two more recently identified magnetars discussed in Section 1.4.2. X-ray spectral uniqueness is the most robust condition, and the only one used independently to identify a magnetar.

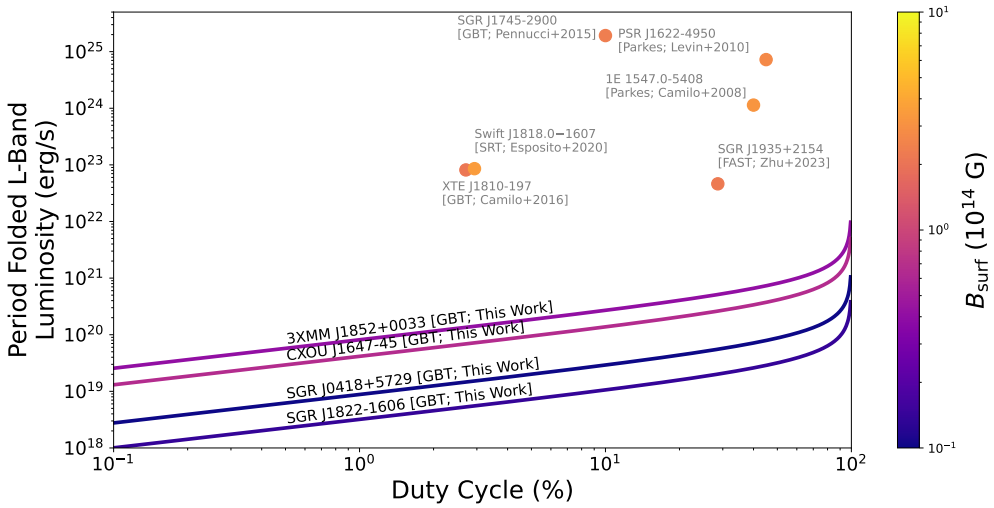

Figure 1.3: Periodic Emission Luminosity Limits from GBT Observations (GBT25A-328) of Low B-Field Magnetars. Limits are shown as a function of pulse duty cycle and colored by each magnetars magnetic field strength. Luminosity measurements from the six confirmed radio magnetars are shown as points (Camilo et al., 2008, 2016; Esposito et al., 2020; Levin et al., 2010; Pennucci et al., 2015; Zhu et al., 2023).

radio upper limits (10^{18-20} erg s^{-1}) on these magnetars to date as shown in Figure 1.3. Over 100 radio pulsars have magnetic fields of similar magnitude to this sample (Manchester et al., 2005); thus our non-detection demonstrates that the magnetar-pulsar threshold is not solely dependent on the magnetic field strength.

Szary et al. (2015) attempt to address this within the Partially-Screened Gap (PSG) model, which requires the blackbody temperature to be lower than $T_{\rm crit} \approx 2 \times 10^6\, K \frac{B_S}{10^{14}\, G}$ and the polar-cap heating power $L_{\rm heat} = \sigma A_{\rm pc} T_{\rm crit}^4$ (where σ is the Stefan-Boltzmann constant and $A_{\rm pc}$ is the polar cap area) to be less than 1% of the spindown luminosity. This is an elegant solution; four of the six radio magnetars satisfy both requirements, while the other two lack blackbody temperature measurements but satisfy the luminosity condition. Meanwhile, three of the four low-B field magnetars satisfy only the luminosity condition, while the other lacks a blackbody temperature measurement. However, there is a strong dependence on the magnetic field strength B_S, which Szary et al. (2015) note can vary by up to a factor of 2 depending on assumptions about the magnetic field axis angle with respect to the rotation angle and whether the field is assumed to be a dipole (e.g., Spitkovsky, 2006). Despite deep searches with the Five-Hundred metre Aperture Spherical Telescope (FAST; Bai et al., 2025; Lu et al., 2024), MeerKAT (Bause et al., 2025), and the Parkes *Murriyang* Telescope (Crawford et al., 2007), radio emission has not been detected

from the other magnetars which could satisfy the Szary et al. (2015) conditions under different B_S assumptions, such as SGR J1627-41. Thus the magnetar-pulsar relationship remains complex.

Twenty-one of the 24 magnetars in total satisfy $B_S \gtrsim B_{QC}$, while only 12 satisfy $L_X \gtrsim L_{\max}$. Radio magnetars, like XTE J1810-197, have lower X-ray luminosities and are less likely to fulfill the luminosity condition (Gotthelf et al., 2004). Thus, it is essential to consider magnetar candidates' properties holistically (burst morphology, magnetic field, luminosity, and spectra), rather than relying on a strict cutoff for any one criterion, in order to make a confident confirmation.

1.4.2 Recently Confirmed Magnetars

The McGill Magnetar catalog has not been actively maintained since at least 2020; since then, two candidates have been confirmed as magnetars based on their spectral and timing properties: SGR J1830-0645 and SGR J1555.2-5402.

Both SGR J1830-0645 and SGR J1555.2-5402 were discovered during X-ray outbursts in 2020 and 2021, respectively, flagged as candidate SGRs due to their short ($\lesssim$ 8 ms) durations and, for SGR J1830-0645, soft spectrum (Page et al., 2020; Palmer et al., 2021). Prompt follow-up revealed periodic short bursts at $P = 10.4$ s for SGR J1830-0645 and $P = 3.86$ s for SGR J1555.2-5402 (Enoto et al., 2021; Younes et al., 2022a; Zelati et al., 2021). While the former's outburst decayed over a month, exhibiting apparent pulse peak drift, the latter remained bright for over $\sim$ 500 days before returning to quiescence (Borghese et al., 2026).

SGR J1830-0645's burst spectra are best fit with two blackbody components and a power law, resembling other magnetars, and the inferred magnetic field $5.5 \times 10^{14} > B_{QC}$ (R. Sharma et al., 2023). Only a single blackbody component is required to model Swift J1555.2-5402's spectrum, and its large field $3.15 \times 10^{14} > B_{QC}$ also resembles magnetars' (Enoto et al., 2021). While distance measurements are required to constrain the intrinsic X-ray luminosities for both magnetars, their timinig and spectral properties are consistent with the magnetar population. We summarize the properties of these magnetars in Table 1.1.

1.5 Galactic Magnetar Candidates

1.5.1 Flaring Candidates

Eight magnetar candidates were detected through soft X-ray flares with short durations ($\lesssim$ 1 s) distinguishable from GRBs ($\gtrsim$ 1 s); rotational periods and spin-down

rates have not been detected, and thus magnetic field estimates and spin-down luminosities are unavailable to confirm their nature. Furthermore, their large positional uncertainties ranging from arcminute to degree scales make confirmation through follow-up and association with optical or IR counterparts difficult (e.g., Chrimes et al., 2022). For example, SGR 0755-2933 was detected by the *Swift* Burst Analysis Telescope (BAT), and its origin from the direction of a High-Mass X-ray Binary led to proposals of the first magnetar binary discovery. However, the lack of subsequent bursts and the large $3'$ error ellipse render this model significantly uncertain (Barthelmy et al., 2016; Doroshenko et al., 2021; Richardson et al., 2023).

SGR 1808-20 (D. Lamb et al., 2003), SGR 2013+34 (Sakamoto et al., 2011), and SGR 150228213 (R.-C. Chen et al., 2023) similarly were identified as single bursts with magnetar-like spectra. SGR 150228213 has some evidence of quasi-periodic oscillations (QPOs) as seen in some magnetar flares (e.g., Kaspi & Beloborodov, 2017). AX J1818.8-1559 (Mereghetti et al., 2012) and SGR 1801-23 (Cline et al., 2000) exhibited multiple bursts, but no sign of periodicity (see also; Pacholski et al., 2025).

4XMM J175136.8-275858 was detected in archival 50 s binned XMM-Newton data when it brightened by two orders of magnitude in X-ray luminosity (Webbe et al., 2025). Its high column density suggests it is distant with a high intrinsic brightness, though no periodic emission has been detected. Swift J195509.6+261406 is a unique flaring transient which was initially detected as a luminous X-ray burst, while follow-up observations with the high time resolution photometer OPTIMA-burst identified aperiodic optical flares lasting 50-100 seconds (Stefanescu et al., 2007, 2008). No X-ray or γ-ray emission coincided with the optical flares, though their pulse profiles resemble giant flares from magnetars, with moderately significant evidence for $6-8$ second QPOs. In Table 1.1, we list the most recently discovered flaring magnetar candidates.

1.5.2 Periodic Short Burst Candidates

Four X-ray pulsars have been proposed as magnetars based on their long ($6-8$ second) pulse periods and soft X-ray spectra. AX J1845.0-0258 exhibits these features, with $P = 6.97$ s and an upper limit $\dot{P} < 5 \times 10^{-8}$ which leaves the magnetic field and spin-down luminosity relatively unconstrained (Torii et al., 1998). Its location within SNR G29.6+0.1 strengthens the magnetar argument, but its high variability compared to other AXPs have left uncertainty about its nature (Gaensler et

al., 1999; Tam et al., 2006). In the decades since, the SGRs and AXPs were conflated into the magnetar class, as SGR-like outbursts and variability were increasingly observed among AXPs such as XTE J1810-197 and 1E 1547-5408 (Bernardini et al., 2009; Halpern et al., 2008). Thus, a confident measurement of a spindown rate below the X-ray luminosity would confirm AX J1845.0-0258 as a magnetar.

PSR J1846-0258, located within SNR Kes 75, was discovered as a rotationally-powered X-ray pulsar with a magnetic field marginally exceeding B_{QC}, but a short 0.3 s period compared to other magnetars (Gotthelf et al., 2000). The pulsar then exhibited a 2-month long outburst in which the X-ray flux increased by $\sim 5.5\times$ and five ~ 0.1 s bursts with soft X-ray power-law spectra similar to magnetar bursts were observed; the brightest exceeded the spin-down luminosity with $L_X \approx 1.5\times10^{38}$ erg s^{-1} (Gavriil et al., 2008). PSR J1846-0258 is thus theorized to be a 'transitional' neutron star, supporting unified models of an evolutionary relationship between pulsars and magnetars.

1E 161348-5055, an X-ray pulsar discovered within SNR RCW 103 in 1979, has an extremely long 6.67 hour period. This, coupled with long-term X-ray variability, suggests the presence of an accretion disk and has led to speculation that it is a low-mass X-ray binary, but no optical or IR stellar companion has been detected to support this (D'Aì et al., 2016; Garmire et al., 2000; Pizzolato et al., 2008; Reynoso et al., 2004; Xu & X.-D. Li, 2019). Makishima et al. (2026) recently detected a secondary X-ray pulse period at $P \approx 1.001$ s after applying a novel demodulation periodicity search technique to archival ASCA and XMM-Newton data. This is likely the compact object's rotation rate while the refined 6.5 ± 0.05 hour period is the orbital period, suggesting a young ($\tau_C = 14.7 \pm 0.1$ kyr) pulsar with a typical magnetic field $B_S = 4.6 \times 10^{13}$ G. The spindown luminosity is only $\dot{E}_{\rm max} \approx 4.2\times10^{34}$ erg s^{-1}, whereas the X-ray luminosity ranges from 10^{33-35} erg s^{-1}. Thus the brightest emission suggests that 1E 161348-5055 may be a magnetar despite its pulsar-like rotation rate. If so, the detected orbital period would make this the third and most convincing binary magnetar candidate to date.

A search through archival *XMM-Newton* data revealed a second magnetar candidate in the Large Magellanic Cloud (LMC), 4XMM J045626.3-694723, through $P = 7.25$ s pulses with long duty cycles (Imbrogno et al., 2023). A spin-down rate has not been measured due to the source's slow rotation, and the spectrum, while soft like other magnetars, shows roughly equal goodness-of-fit results for power-law, double blackbody, and blackbody + power-law models, limiting interpretation.

The candidate's ~ 50 kpc distance also prevents ruling out a low-mass companion, though its low rotation rate suggests it is unlikely to be an accreting system. No X-ray flares or radio pulses were detected in searches by *IBIS* and MeerKAT, respectively (Pacholski et al., 2026; Prayag et al., 2026). A proper estimate of $\dot{P}$ would likely lead to confirmation of 4XMM J045626.3-694723.

Four radio pulsars have been proposed as magnetars based on their radio properties alone, exhibiting large magnetic fields ($\gtrsim 10^{13}$ G) and magnetar-like outbursts, glitches, and intermittency. PSR 1119-6127, in addition to its 4.4×10^{13} G field, exhibited a glitch upon discovery, rapidly changing its pulse period by $\Delta P/P = -4.4 \times 10^{-9}$. While glitches occur in pulsars, the phenomenon is related to crustal disruptions common among magnetars due to their large magnetic fields (Camilo et al., 2000). PSR 1119-6127 also underwent a 6-month outburst, further promoting the magnetar model (H.-H. Wang et al., 2020). PSR J1710-3452 was discovered to have an extremely long pulse period, $P = 10.4$ s, with unique intermittency motivating a magnetar source despite its unconstrained spin-down magnetic field (Surnis et al., 2023). PSR J1814-1744 and PSR J1746-2829 have long periods (3.975 s and 1.89 s, respectively) and strong magnetic fields (5.5×10^{13} G and 5.2×10^{13} G, respectively), but appear rotationally-powered given the lack of X-ray detection (Camilo et al., 2000; Pivovaroff et al., 2000; Wongphechauxsorn et al., 2024).

Finally, two X-ray Binaries, LS I +61°303 and LS 5039, were proposed to have magnetar primaries based on the detection of secondary periods. The former has 0.3 s radio pulsations and soft gamma-ray flares (Suvorov & Glampedakis, 2022; Weng et al., 2022; P. Zhang, 2024), while the latter based on $P = 9$ s modulations in its X-ray emission (Yoneda et al., 2020). The complication of an accreting companion must be reconciled with expected magnetar properties to confirm these. The most recently discovered periodic candidates are also in Table 1.1.

1.5.3 Long Period Radio Transients

Discovered in 2022, Long Period Radio Transients (LPTs, or LPRTs) have been identified at a rapid pace, with a sample of 14 LPRTs constructed in only 3 years (see Rea et al., 2026, for a detailed review). LPRTs are radio sources denoted by pulse periods ranging from 20 seconds to 8.7 hours and pulse durations from 1-100 s (e.g., Caleb et al., 2022; Hurley-Walker et al., 2022). OIR follow-up of two LPRTs, GLEAM-X J0704-37 and ILT J1101+5521, have revealed M-dwarf stars at their

location, with spectroscopically measured radial velocities and blue optical excess suggesting they are white dwarf-M-dwarf polars (de Ruiter et al., 2025a,b; Horváth et al., 2025; Hurley-Walker et al., 2024; Rodriguez, 2025). Two other LPRTs, CHIME J1634+44 and ASKAP J144834-685644 have OIR counterpart candidates, but have not been confirmed as White Dwarf-M-Dwarf systems (Anumarlapudi et al., 2025; Bloot et al., 2025). Similar radio emission has been seen from intermediate polars like AR Scorpii, though the lack of a beat period (as expected from a unique orbital and rotational rate) suggests a magnetically-locked configuration (Qu & B. Zhang, 2025).

In contrast, no OIR companions have been identified for the other 12 LPRTs despite their close proximity within 6 kpc of Earth (e.g., Hurley-Walker et al., 2023). However, most are within the galactic plane, leaving open the possibility of a highly extincted M-dwarf companion. Alternatively, LPRTs' sub-pulse structure, apparent outburst phases, one SNR association, and, in two cases, persistent X-ray counterparts resemble radio pulsars (e.g., Dong et al., 2025a,b; D. Li et al., 2024a; Z. Wang et al., 2025). Beniamini et al. (2023) further suggested that LPRTs could be a rare population of Ultra-Long Period Magnetars (ULPMs) which experienced enhanced spin-down through extreme glitches, fallback accretion, or a rapid initial spin-down process. Thus, while the white-dwarf M-dwarf model is likely for two cases, additional evidence is required to definitively rule out the magnetar model for others.

We list 12 LPRTs in Table 1.1, excluding those confidently identified as WD-M Dwarf binaries. We add to this list the Galactic Center transient GCRT J1745-3009, which was discovered during an outburst with 77 minute periodic radio emission (Hyman et al., 2005) and retroactively identified as an LPRT by Rea et al. (2026). The P-Pdot diagram in Figure 1.1 illustrates the unique periods of LPTs compared to the rest of the neutron star population.

1.6 Extragalactic Magnetar Candidates

Multiple species of high-luminosity, extragalactic transients are thought to originate from magnetars, including Fast Radio Bursts (FRBs), short Gamma Ray Bursts (sGRBs), and Rapid X-ray Transients (RXTs). We discuss their observed properties and evidence for magnetar origins in the following sections.

Table 1.1: New Galactic Magnetars and Candidates

Magnetar or Candidate	J2000 Position	$\sigma('')^{\dagger}$	d (kpc)	P (s)	P (10^{-11})	L_{max} (10^{33} erg s^{-1})	B_{surf} (10^{14} G)	SNR	Refs.
Confirmed Magnetars									
SGR J1830-0645	$18^h30^m41^s.64 - 06°45'16''.9$	0.73	~ 4	10.415724(1)	0.7(1)	0.24	5.5	–	1-4
SGR J1555.2-5402	$15^h55^m08^s.66 - 54°03'41''.1$	2.2	~ 10	3.86104705(12)	3.05(7)	20.9(5)	3.47(4)	–	5,6
Periodic Short Burst Candidates									
4XMM J045626.3-694723	$04^h56^m26^s.36 - 69°47'23''.1$	1.9	~ 50	7.25243(4)	< 2100	–	–	–	16
PSR J1119–6127	$11^h19^m14^s.30 - 61°27'40''.5$	0.15, 0.2	~ 8.4	0.40796298356(2)	0.40202200(17)	2300	0.41	–	17-19
PSR J1814-1744	$18^h14^m43^s.10 - 17°44'48''$	0.7, 8	~ 5.118	3.975905188(16)	0.07447(4)	0.47	0.41	–	17,20
PSR J1746-2829	$17^h46^m15^s - 28°29'32''$	184, 40	~ 8.235	1.888928609337(9)	0.130(3)	7.6	0.501	–	22
PSR J1710-3452	$17^h10^m22^s.81 - 34°52'57''.5$	0.4, 0.5	~ 4	10.412(1)	< 5900	–	< 250	–	23
LS I +61°303	$02^h40^m31^s.66 + 61°13'45''.59$	$7.3, 9.2 \times 10^{-6}$	2.65(9)	0.26915508(16)	42(12)	–	7.0	–	24-28
LS 5039	$18^h26^m15^s.06 - 14°50'54''.25$	$12.7, 11.3 \times 10^{-6}$	2.9(8)	9.050(16)	~ 30	–	–	–	29-31
1E 161348–5055‡	$16^h17^m36^s.26 - 51°02'25''.0$	0.2	~ 3.3	1.0094300(2)	0.1097(2)	42	0.46	RCW 103	7-12,51
Flaring Candidates									
SGR 150228213	$01^h46^m23^s.18 - 61°45'06''.8$	5.2	–	–	–	–	–	–	13-15
4XMM J175136.8-275858	$17^h51^m36^s.8 - 27°58'58''$	1.9	–	–	–	–	–	–	21
Swift J195509.6+261406	$19^h55^m11^s - 26°12'49''$	120	$\gtrsim 3.7$	–	–	–	–	–	32-35
LPT Candidates									
GLEAM-X J162759.5-523504.3	$16^h27^m59^s.5 - 52°35'04''.3$	2	~ 1.3	1091.1690(5)	60	1.2×10^{-5}	–	–	38
PSR J0901-4046	$09^h01^m29^s.249 - 40°46'02''984$	0.01,0.001	0.327	75.88554711(6)	0.0225(12)	2.0×10^{-5}	1.32	–	35
PSR J0250+5854	$02^h50^m17^s.78 + 58°54'01''3$	0.2	1.558	23.5353784760(10)	0.002716(7)	8.2×10^{-5}	0.256	–	36,37
ASKAP J1935+2184	$19^h35^m05^s.12 + 21°48'41''.047$	1.5	~ 4.5	3225.313(2)	$< 12 \pm 15$	–	–	–	39
CHIME J0630+25	$06^h30^m38^s.40 + 25°26'23''$	60	$0.17^{+0.31}_{-0.10}$	421.35584(8)	0.52(11)	2.76×10^{-6}	15	–	40
GPM J1839-10	$18^h39^m02^s - 10°31'49.37''$	0.15	5.7(2.9)	1318.1957(2)	< 0.036	–	–	–	41
ASKAP J1832-0911/ DART J1832-0911	$18^h32^m48^s.4589 - 09°11'15''297$	0.0005	$4.5^{+1.2}_{-0.5}$	2656.2412(3)	< 90	4.6×10^{-6}	–	G22.7-0.2	42,43
ASKAP J183950.5-075635.0	$18^h39^m50^s.57 - 07°56'39''.17$	0.33,0.15	4.0(1.2)	23221.7(1)	$< 1.6 \times 10^4$	$< 10^{-7}$	$< 3 \times 10^4$	–	44
CHIME J1634+44	$16^h34^m29^s.96 + 44°50'13''.5$	0.5,1.1	1.4 – 3	841.245895(6)	−0.903(11)	–	–	–	45,46
ASKAP J175534.9-252749	$17^h55^m34''.9 - 25°27'49''.1$	1.4,0.1	~ 4.7	4186.3285(2)	−1.0(9.2)	–	–	–	47,48
ASKAP J144834–685644	$16^h34^m29^s.96 - 68°56'44''.1$	0.1,0.3	–	5472(1080)	$< 2 \times 10^3$	–	–	–	49
ASKAP J142431.2–612611	$14^h24^m31^s.2 - 61°26'11''$	0.9 – 1.9	–	2147.27(1)	$< 10^3$	–	–	–	50
GCRT J1745-3009‡	$17^h45^m05^s.09 - 30°09'56''.04$	2.2,2.0	~ 8.5	~ 4620.72	–	–	–	G359.1-0.5	52,53

From left to right, J2000 coordinates and position errors, distance d (constrained from dispersion measure, parallax, or association with SNR), period P, spin down rate $\dot{P}$, maximum spin down luminosity limit $L_{\rm max}$ and surface magnetic field strength B_S constrained from P and $\dot{P}$, associated SNR, and relevant references.

†Position Uncertainties are given as the 1σ error radius or σ_α, σ_δ (RA, declination error) if the RA and declination error are different.

‡GCRT J1745-3009 and 1E 161348–5055 were discovered before 2020, but were proposed as magnetars more recently (Beniamini et al., 2023; Rea et al., 2026).

Relevant citations referenced in the rightmost column are below: (1) R. Sharma et al. (2023) (2) Zelati et al. (2021) (3) Younes et al. (2022b) (4) Page et al. (2020) (5) Enoto et al. (2021) (6) Borghese et al. (2026) (7) Beniamini et al. (2023) (8) Garmire et al. (2000) (9) De Luca et al. (2006) (10) De Luca et al. (2008) (11) D'Aì et al. (2016) (12) Esposito et al. (2011) (13) R.-C. Chen et al. (2023) (14) Barthelmy et al. (2015) (15) O. J. Roberts (2015) (16) Imbrogno et al. (2023) (17) Camilo et al. (2000) (18) H.-H. Wang et al. (2020) (19) Weltevrede et al. (2011) (20) Janssen & Stappers (2006) (21) Webbe et al. (2025) (22) Wongphechauxsorn et al. (2024) (23) Surnis et al. (2023) (24) Suvorov & Glampedakis (2022) (25) Weng et al. (2022) (26) LS (n.d.) (27) Esposito et al. (2007) (28) P. Zhang (2024) (29) Yoneda et al. (2020) (30) Volkov et al. (2021) (31) Makishima et al. (2023) (32) Stefanescu et al. (2008) (33) Pagani et al. (2007) (34) Castro-Tirado et al. (2008) (35) Caleb et al. (2022) (36) Tan et al. (2018) (37) Tan et al. (2023) (38) Hurley-Walker et al. (2022) (39) Caleb et al. (2024) (40) Dong et al. (2025b) (41) Hurley-Walker et al. (2023) (42) Z. Wang et al. (2025) (43) D. Li et al. (2024b) (44) Lee et al. (2025) (45) Dong et al. (2025a) (46) Bloot et al. (2025) (47) Dobie et al. (2024) (48) McSweeney et al. (2025) (49) Anumarlapudi et al. (2025) (50) Pritchard et al. (2026) (51) Makishima et al. (2026) (52) Hyman et al. (2005) (53) Hyman et al. (2007)

1.6.1 Short Gamma Ray Bursts (sGRBs) and Rapid X-ray Transients (RXTs)

Since the Compton Gamma Ray Observatory's Burst and Transient Source Experiment's (BATSE) first light in 1990, succeeded by the *Swift* Burst Analysis Telescope (BAT) and *Fermi* Gamma-Ray Burst Monitor (GBM), over 10,000 GRBs, $1-100$ s bursts with energies $\sim 10^{51}$ ergs, have been detected between $\sim 10\,\mathrm{keV}-100\,\mathrm{GeV}$ (Lien et al., 2016; Paciesas et al., 1999; von Kienlin et al., 2020). Some have multiwavelength afterglows, while others are only observed in gamma rays. Kouveliotou et al. (1993a) identified two distinct classes: short ($\lesssim 2$ s) GRBs with hard spectra and long ($\gtrsim 2$ s) GRBs with soft spectra (see Gehrels & Mészáros, 2012, for a review). As the population grew, their extragalactic nature was confirmed by their uniform all-sky spatial distribution, and follow-up optical/IR observations were used to identify host galaxies (Meegan et al., 1992).

Most short and long GRBs' are thought to form via the merger of two compact stellar remnants which release gravitational energy as gamma rays and form a black hole. However, Hurley et al. (2005) noted that a recent giant flare from SGR 1806-20 would appear like a short GRB if placed in another galaxy. Some subset of short GRBs are then likely produced by magnetar giant flares, but confirming them would require detection of periodic $1-10$ s modulations in short GRBs' tails, a phenomenon observable only from extremely luminous flares within nearby galaxies.

Nonetheless, at least seven short GRBs have been proposed as giant flares from extragalactic magnetars. GRB 051103 was detected from the nearby M81/M82 galaxy group, possibly from a known star forming region, but its large $\sim 10' \times 1^\circ$ error region makes the association tenuous (Ofek et al., 2006). GRB 070201, likely originating from the Andromeda galaxy (M31), was similarly proposed based on its location near the galaxy's star-forming spiral arms (Ofek et al., 2008). In addition, the Laser Interferometer Gravitational-Wave Observatory (LIGO; Abramovici et al., 1992), now known to be sensitive to compact object binary mergers since its groundbreaking detection in Abbott et al. (2016), ruled out the presence of a compact binary merger in M31 temporally coincident with GRB 070201 with 99% confidence. No periodic modulations were detected for either GRB.

GRB 200415A, detected from NGC 253, shared a similar magnetar flare-like temporal profile with no evidence of periodicity or optical afterglow, but also displays a unique spectral evolution, hardening over the first ~ 7 ms before softening again (O. Roberts et al., 2021). While such spectral evolution has not been observed in Galactic magnetar flares, they propose that a relativistically moving emitting plasma

within the magnetar magnetosphere could produce such an effect. GRB 180128A, also from NGC 253, and GRB 231115A from M82, exhibited similar spectral evolution and were proposed as magnetar giant flares (Trigg et al., 2024, 2025).

GRB 070222A from M83 was added to the candidate magnetar flare sample based on its coincidence with a star forming galaxy, but Burns et al. (2021) claim that it, along with three GRBs mentioned above, has unique rise time and energy compared to the remaining short GRB sample, potentially supporting a magnetar origin.

Only one short GRB has evidence of periodic structure, GRB 970110 from the Firework galaxy (NGC 6946). Conducting a periodicity search for modulations in the tails of 358 BATSE short GRBs, Crider (2006) identify a statistically significant $P = 13.8\,\mathrm{s}$ using a Lomb periodogram. Visual inspection of the lightcurve is less convincing, and it is unlikely that such modulations would be detectable at the galaxy's 5.9 Mpc distance. Nonetheless, GRB 970110 demonstrates that giant flare features may be detectable in GRBs beyond the local ($\lesssim 1\,\mathrm{Mpc}$) universe.

More recently, Y. Zhang & H. Feng (2023) discovered 11 'single-frame' soft ($0.5 - 10\,\mathrm{keV}$) X-ray transients within archival $0.1 - 3.3\,\mathrm{s}$ resolution image data from the *Chandra* Advanced CCD Imaging Spectrometer (ACIS). These Rapid X-ray Transients (RXTs) appear uniformly distributed across the sky and have fluxes $\sim 10^{-11} - 10^{-10}\,\mathrm{erg\,cm^{-2}\,s^{-1}}$, suggesting high, magnetar flare-like intrinsic luminosities $\gtrsim 10^{34}\,\mathrm{erg\,s^{-1}}$ if they are extragalactic. While the RXTs have not been confidently localized yet, with only arcminute-scale position errors, two have extragalactic candidate associations to M31 (RXT 070602) and the SMC (RXT 130305), two have Galactic candidate associations to the Carina Nebula (RXT 080723) and the M37 cluster (RXT 111115), and two have cautious optical counterparts (RXT 110123 and RXT 140323). RXTs' luminosities resemble those of magnetar short bursts ($\sim 10^{29-35}$), but spectral characterization is required to investigate further.

1.6.2 Fast Radio Bursts (FRBs)

FRB 20010824 was discovered in archival data from the Parkes *Murriyang* Telescope as a $\sim 15\,\mathrm{ms}$ radio pulse at 1.4 GHz (Lorimer et al., 2007). The FRB was proposed as extragalactic in origin based on the significant frequency-dependent dispersive delay due to the light's propagation through the ionized Interstellar Medium (ISM). Quantified by the dispersion measure (DM):

$$\mathrm{DM} = \int_0^D \frac{n_e}{1+z(l)} dl \tag{1.8}$$

where n_e is the free electron number density, D is the distance, z is the redshift, and l integrates along the line-of-sight, FRB 20010824's DM= $375 \pm 1\,\mathrm{pc\,cm^{-3}}$ was much larger than the estimated Galactic contribution as constrained by Galactic radio pulsars (Cordes & Lazio, 2002; Yao et al., 2017). Additional highly dispersed, wideband FRBs were revealed in archival data, including the first repeating FRB, FRB 20121102, which was localized to a z=0.2 galaxy and confirmed FRBs' extragalactic origins (Spitler et al., 2014; Tendulkar et al., 2017). To date, around $\sim$ 1000 FRBs have been detected, with $\sim$ 100 localized to host galaxies and $\sim$ 100 observed to repeat (see sample papers such as Gordon et al., 2023; K. Sharma et al., 2024).

Unlike GRBs, whose profile and high-energy emission closely resemble magnetar giant flares, FRBs are detected only at radio frequencies. Their association with magnetars is based predominantly on their high $L \sim 10^{40-43}\,\mathrm{erg\,s^{-1}}$ luminosities (brightness temperature $T_b \sim 10^{34-38}$ K) which exceed typical neutron star rotational energy allowances L_{max} (e.g., Petroff et al., 2019). This suggests that FRBs originate from a compact source with a coherent emission process driven by magnetic energy stored in a strong, magnetar-like magnetic field. Thus, while they don't resemble typical Galactic magnetar emission, predominant models invoke a magnetar origin for FRBs.

Coherent emission is intrinsically highly linearly polarized, meaning that the electric field is oriented in a fixed direction. However, if the line-of-sight is at an angle relative to the emission direction, the observed radiation will have circular components, in which the electric field direction rotates about the propagation axis, due to the charge bunch's trajectory. This is accompanied by $\sim$ 50% reduction in intensity, and therefore is unlikely to be the source of FRBs' high circular polarization fractions (e.g., Qu & B. Zhang, 2023; W.-Y. Wang et al., 2022). Instead, propagation effects can alter the observed polarization properties. We summarize polarization using Stokes parameters, which are composed of conjugate combinations of electric field components as detected by orthogonally oriented antenna feeds:

$$I = \frac{1}{2}(< V_A V_A^* > + < V_B V_B* >) \tag{1.9}$$

$$Q = \frac{1}{2}(< V_A V_A^* > - < V_B V_B* >) \tag{1.10}$$

$$U = Re(< V_A V_B* >) \tag{1.11}$$

$$V = Im(< V_A V_B* >) \tag{1.12}$$

where V_A and V_B are the complex voltages from the antenna feeds, I corresponds to the total intensity, Q and U describe the linear polarization, and V describes right (>0) and left (<0) hand circular polarization. Light propagating within an ionized medium along a line-of-sight magnetic field $\overrightarrow{B}_{||}$ with electron density n_e will undergo Faraday Rotation, in which the electric field direction, or position angle $\chi = 0.5 \tan^{-1}(U/Q)$, is rotated as a function of emission wavelength squared (Brentjens & De Bruyn, 2005; Burn, 1966). This effect will reduce the band-averaged linear polarization, and is described by the Rotation Measure:

$$RM = 0.81 \int_0^D \frac{n_e B_{||}}{(1 + z(l))^2} dl \tag{1.13}$$

FRBs have been measured with a wide range of RM magnitudes from $0-10^5$ rad m^{-2}, suggesting they can inhabit diverse magnetoionic environments (Anna-Thomas et al., 2023; Ravi et al., 2025). Furthermore, if light propagates through a turbulent medium in which different regions impart unique RMs scattered with variation σ_{RM}, it can disperse along multiple propagation paths and incoherently recombine, lowering the observed linear polarization. Y. Feng et al. (2022b) demonstrate that this model appears consistent with some repeating FRBs' polarization fractions. A strong perpendicular magnetic field $B_\perp$ can induce circular polarization through birefringence, or slowing of one linear polarization mode relative to another (Suresh & Cordes, 2019). Thus, the broad diversity of polarization properties exhibited by FRBs more readily support inner magnetospheric emission and propagation through circumstellar media with unique electron densities and magnetic fields, whereas maser models would imply a more uniform polarization behavior across the population. Despite this, distinguishing the emission properties, circumstellar propagation effects, and ISM propagation effects remains an open research area, as will be discussed in Section 6 and Section 7.

Emission models (see Qu & B. Zhang, 2023, for a review) broadly fall into two categories: maser mechanisms and antenna mechanisms. While both originate from breaks in magnetic tension within the magnetar crust which release energy from the

twisted magnetic field, the maser mechanism requires the energy to propagate as an Alfvén plasma wave 'pulse' through the outer magnetosphere until encountering the shock front between CCSN ejecta or magnetized pair-plasma wind and circumstellar gas $\sim 10^9$ km from the magnetar. The pulse induces a contact instability by displacing the shocked plasma, inverting the population and causing turbulent, relativistic charges to coherently produce synchrotron radiation at low radio frequencies (e.g., Lyubarsky, 2014):

$$\nu_0 = \frac{qB}{2\pi m_e c \Gamma_{cd}} \approx 50\,\mathrm{M}Hz \tag{1.14}$$

where $\Gamma_{cd} \sim 10^4$ is the bulk Lorentz factor of the plasma. However, recent observations of circular polarization, pulsar-like linear polarization position angle swings, and scintillation from turbulent screens near the emission site support inner-magnetosphere antenna mechanisms instead (Y. Feng et al., 2022a; Mckinven et al., 2025; Nimmo et al., 2025). Coherent curvature radiation shares a similar 'sparking' mechanism as the pulsar emission model (see Section 1.3.1), in which electrons are discharged across a vacuum gap. However, FRBs' extreme luminosities require larger bunches of coherently radiating charges moving at higher speeds γ than in pulsar magnetospheres. Charge bunches then stream along curved magnetic field lines, possibly sustained by a parallel electric field, with their centripetal acceleration inducing curvature radiation (W.-Y. Wang et al., 2022). Coherent Inverse Compton Scattering (ICS) postulates that low frequency electromagnetic waves triggered by crust disruptions could scatter off of relativistic charge bunches, boosting the frequency by γ^2 to GHz frequencies (Qu & B. Zhang, 2024; Rybicki & Lightman, 2024; B. Zhang, 2022).

Beyond energetics and polarization, FRBs are linked to magnetars by a series of FRB-like radio bursts produced by the Galactic magnetar SGR J1935+54. Simultaneously detected on April 28, 2020 by the Canadian Hydrogen Intensity Mapping Experiment (CHIME), the Survey for Transient Astronomical Radio Emission 2 (STARE2), and the Five-Hundred Metre Aperture Spherical Telescope (FAST), the first event lasted 0.61 ± 0.09 ms with isotropic luminosity $\sim 3.6 \times 10^{38}\,\mathrm{erg\,s^{-1}}$. While the flare, referred to as FRB 20200428, was around two orders of magnitude fainter than the weakest FRBs, it remains the most energetic magnetar radio flare detected to date (Bochenek et al., 2020; CHIME/FRB Collaboration et al., 2020). Unlike FRBs, which have never been associated with X-ray, gamma-ray, UV, or OIR counterparts, FRB 20200428 was coincident with a ~ 0.6 s X-ray burst.

While other SGR J1935+54 flares have had softer spectra (steepen below 200 keV) and fit equally to double blackbody and power law models (e.g., Kozlova et al., 2016), the coincident $\sim 10^{38}\,\mathrm{erg\,s^{-1}}$ X-ray burst is best-fit to a power law which hardens across the triple-peaked burst profile, more closely resembling some short GRBs (see Section 1.6.1; C. Li et al., 2021; Mereghetti et al., 2020; Ridnaia et al., 2021). The FRB and X-ray burst followed a glitch in which the rotation frequency increased by $\Delta\nu/\nu = 5.8^{+2.6}_{-1.6} \times 10^{-6}$, suggesting its unique properties were triggered by a disruption in the magnetar crust (Younes et al., 2023). Two weaker radio bursts were detected in late 2020 with no simultaneous X-ray emission, kicking off a month-long outburst phase in which periodic radio pulsations were detected for the first time from SGR J1935+54 (Kirsten et al., 2021; Zhu et al., 2023). Finally, two FRB-like bursts were detected in October Dong & Chime/Frb Collaboration (2022), Maan et al. (2022), and Mereghetti et al. (2022) and December 2022 (Pearlman & Chime/Frb Collaboration, 2022), respectively; the former (FRB 20221014) was recently associated with another glitch (C.-P. Hu et al., 2025) and an X-ray burst (C.-W. Wang et al., 2026). These follow-up FRBs indicate that magnetars could feasibly be the source of repeating FRBs in addition to non-repeaters. Since no other Galactic magnetars have produced FRBs, it is unclear whether SGR J1935+54 is a unique neutron star or if all magnetars can produce FRB-like events. Association of an FRB with an X-ray flare would confirm the magnetar-FRB model, but prospects are limited since the SGR J1935+54 X-ray burst luminosity would not be detectable at extragalactic distances.

1.7 Outline and Questions Addressed in this Thesis

In this thesis, I strive to understand the unique formation and evolution of magnetars and their connection to radio transients including FRBs and LPRTs. To this end, we explore the following questions.

1.7.1 What factors cause magnetars to have large magnetic field strengths?

In Chapter 2, we probe the progenitor and formation process of the 30 magnetars and candidates from the McGill sample using archival radio and OIR catalog data. Using statistical methods, we place constraints on the magnetar binary fraction and CCSN formation scenario. In Chapter 3, we extend these results using simulations to predict the magnetar population based on the binary and merger fractions derived in Chapter 2. In Chapter 4, we re-estimate the magnetar scale height and compare it to other Galactic populations to investigate formation scenarios.

1.7.2 Are all LPTs White Dwarf-M-dwarf Binaries?

In Chapter 5, we search for LPTs in the galactic plane using the Deep Synoptic Array (DSA-110) radio interferometer at the Owens Valley Radio Observatory (OVRO). Beyond testing single-pulse search strategies for $\gtrsim$ 134 ms transients, we place limits on the LPT burst rate within the plane and consider the implications for White Dwarf-M-dwarf binary models and magnetar models for LPT emission.

1.7.3 What process drives FRB emission, and which propagation effects result from the local and galactic environment?

In Chapter 6 we use one of the largest uniform samples of FRB linear and circular polarization to determine the most common properties among the FRB population. By investigating individual cases and comparing the population properties to those of Galactic pulsars, we determine the impact of the magnetized circumstellar and interstellar media on FRB polarization. In Chapter 7 we use FRBs' RMs, DMs, and host galaxy redshifts to learn about their magnetic environments, again comparing to Milky Way pulsars to search for unique trends that hint towards their progenitors' natures.

1.7.4 What is the future of pulsar, magnetar, LPRT, and FRB astronomy?

In Chapter 8, we look ahead, quantifying the promise of next-generation telescopes like the DSA-2000 by forecasting the pulsar yields. We summarize the thesis in Chapter 9 and look towards future prospects for FRB and LPRT searches.

CHAPTER 1 BIBLIOGRAPHY

Abbott, B. P. et al. (2016). "Observation of gravitational waves from a binary black hole merger". In: *Physical review letters* 116.6, p. 061102.

Abramovici, A. et al. (1992). "LIGO: The laser interferometer gravitational-wave observatory". In: *science* 256.5055, pp. 325–333.

Acharya, B. et al. (2025). "Solar fusion III: New data and theory for hydrogen-burning stars". In: *Reviews of Modern Physics* 97.3, p. 035002.

Agarwal, D. et al. (2026). "The RRATalog: a Galactic census of rotating radio transients". In: *Monthly Notices of the Royal Astronomical Society*, stag787.

Anderson, G. E. et al. (May 2012). "Multi-wavelength Observations of the Radio Magnetar PSR J1622-4950 and Discovery of Its Possibly Associated Supernova Remnant". In: *The Astrophysical Journal* 751.1, 53, p. 53. DOI: 10.1088/0004-637X/751/1/53. arXiv: 1203.2719 [astro-ph.HE].

Anna-Thomas, R. et al. (2023). "Magnetic field reversal in the turbulent environment around a repeating fast radio burst". In: *Science* 380.6645, pp. 599–603.

Anumarlapudi, A. et al. (2025). "ASKAP J144834- 685644: a newly discovered long period radio transient detected from radio to X-rays". In: *Monthly Notices of the Royal Astronomical Society* 542.2, pp. 1208–1232.

Baade, W. & F. Zwicky (1934). "Remarks on super-novae and cosmic rays". In: *Physical Review* 46.1, p. 76.

Bai, J. et al. (Feb. 2025). "Deep Searches for Radio Pulsations and Bursts from Four Magnetar and a Magnetar-like Pulsar with FAST". In: *The Astrophysical Journal* 979.2, 122, p. 122. DOI: 10.3847/1538-4357/ada3c4. arXiv: 2412.20050 [astro-ph.HE].

Baring, M. G. & A. K. Harding (1996). "Photon splitting in magnetar models of soft gamma repeaters". In: *AIP Conference Proceedings*. Vol. 366. 1. American Institute of Physics, pp. 129–133.

Barthelmy, S. D. et al. (Jan. 2015). "Trigger 632888: Swift detection of the magnetar 4U 0142+61." In: *GRB Coordinates Network* 17507, p. 1.

Barthelmy, S. D. et al. (Mar. 2016). "Swift detection of a likely new SGR: SGR 0755-2933". In: *The Astronomer's Telegram* 8831, p. 1.

Bause, M. L. et al. (Sept. 2025). "Searching for radio emission from radio quiet magnetars with MeerKAT". In: *arXiv e-prints*, arXiv:2509.14043, arXiv:2509.14043. DOI: 10.48550/arXiv.2509.14043. arXiv: 2509.14043 [astro-ph.HE].

Bell Burnell, S. J. (2004). *So few pulsars, so few females*.

Beniamini, P. et al. (2023). “Evidence for an abundant old population of Galactic ultra-long period magnetars and implications for fast radio bursts”. In: *Monthly Notices of the Royal Astronomical Society* 520.2, pp. 1872–1894.

Bernardini, F. et al. (2009). “From outburst to quiescence: the decay of the transient AXP XTE J1810-197”. In: *Astronomy & Astrophysics* 498.1, pp. 195–207.

Bloot, S. et al. (2025). “Strongly polarised radio pulses from a new white-dwarf-hosting long-period transient”. In: *Astronomy & Astrophysics* 699, A341.

Bochenek, C. D. et al. (2020). “A fast radio burst associated with a Galactic magnetar”. In: *Nature* 587.7832, pp. 59–62.

Borghese, A. et al. (2025). “A magnetar outburst with atypical evolution: the case of Swift J1555. 2-5402”. In: *arXiv preprint arXiv:2512.08692*.

– (2026). “A magnetar outburst with atypical evolution: The case of Swift J1555. 2–5402”. In: *Astronomy & Astrophysics* 706, A28.

Braithwaite, J. & H. Spruit (2006). “Evolution of the magnetic field in magnetars”. In: *Astronomy & Astrophysics* 450.3, pp. 1097–1106.

Brentjens, M. A. & A. De Bruyn (2005). “Faraday rotation measure synthesis”. In: *Astronomy & Astrophysics* 441.3, pp. 1217–1228.

Burn, B. (1966). “On the depolarization of discrete radio sources by Faraday dispersion”. In: *Monthly Notices of the Royal Astronomical Society* 133.1, pp. 67–83.

Burns, E. et al. (Feb. 2021). “Identification of a Local Sample of Gamma-Ray Bursts Consistent with a Magnetar Giant Flare Origin”. In: *The Astrophysical Journal Letters* 907.2, L28, p. L28. DOI: 10.3847/2041-8213/abd8c8. arXiv: 2101.05144 [astro-ph.HE].

Caleb, M. et al. (May 2022). “Discovery of a radio-emitting neutron star with an ultra-long spin period of 76 s”. In: *Nature Astronomy* 6, pp. 828–836. DOI: 10.1038/s41550-022-01688-x. arXiv: 2206.01346 [astro-ph.HE].

Caleb, M. et al. (2024). “An emission-state-switching radio transient with a 54-minute period”. In: *Nature Astronomy* 8.9, pp. 1159–1168.

Camilo, F. et al. (2008). “The Magnetar 1E 1547.0–5408: Radio Spectrum, Polarimetry, and Timing”. In: *The Astrophysical Journal* 679.1, pp. 681–686.

Camilo, F. et al. (2016). “Radio disappearance of the magnetar XTE J1810–197 and continued X-ray timing”. In: *The Astrophysical Journal* 820.2, p. 110.

Camilo, F. et al. (Sept. 2000). “Discovery of Two High Magnetic Field Radio Pulsars”. In: *The Astrophysical Journal* 541.1, pp. 367–373. DOI: 10.1086/309435. arXiv: astro-ph/0004330 [astro-ph].

Camilo, F. et al. (Sept. 2007). “1E 1547.0-5408: A Radio-emitting Magnetar with a Rotation Period of 2 Seconds”. In: *The Astrophysical Journal Letters* 666.2, pp. L93–L96. DOI: 10.1086/521826. arXiv: 0708.0002 [astro-ph].

Castro-Tirado, A. J. et al. (2008). "Flares from a candidate Galactic magnetar suggest a missing link to dim isolated neutron stars". In: *Nature* 455.7212, pp. 506–509.

Chen, K. & M. Ruderman (1993). "Pulsar death lines and death valley". In: *Astrophysical Journal, Part 1 (ISSN 0004-637X), vol. 402, no. 1, p. 264-270.* 402, pp. 264–270.

Chen, R.-C. et al. (2023). "Detection of Quasi-periodic Oscillations in SGR 150228213". In: *Research in Astronomy and Astrophysics* 23.8, p. 085018.

Cheng, A. F. & M. Ruderman (1980). "Particle acceleration and radio emission above pulsar polar caps". In: *Astrophysical Journal, Part 1, vol. 235, Jan. 15, 1980, p. 576-586. NSF-supported research.* 235, pp. 576–586.

CHIME/FRB Collaboration et al. (Nov. 2020). "A bright millisecond-duration radio burst from a Galactic magnetar". In: *Nature* 587.7832, pp. 54–58. DOI: 10.1038/s41586-020-2863-y. arXiv: 2005.10324 [astro-ph.HE].

Chrimes, A. et al. (2022). "New candidates for magnetar counterparts from a deep search with the Hubble Space Telescope". In: *Monthly Notices of the Royal Astronomical Society* 512.4, pp. 6093–6103.

Cline, T. et al. (Mar. 2000). "Observations of a Possible New Soft Gamma Repeater, SGR 1801-23". In: *The Astrophysical Journal* 531.1, pp. 407–410. DOI: 10.1086/308470. arXiv: astro-ph/9909054 [astro-ph].

Condon, J. J. & S. M. Ransom (2016). *Essential radio astronomy*. Princeton University Press.

Cordes, J. M. & T. J. W. Lazio (2002). "NE2001. I. A new model for the galactic distribution of free electrons and its fluctuations". In: *arXiv preprint astro-ph/0207156*.

Crawford, F., J. W. T. Hessels, & V. M. Kaspi (June 2007). "Deep Searches for Radio Pulsations and Bursts from Four Southern Anomalous X-Ray Pulsars". In: *The Astrophysical Journal* 662.2, pp. 1183–1187. DOI: 10.1086/517991. arXiv: astro-ph/0703246 [astro-ph].

Crawford, F. et al. (2001). "Radio pulsars in the magellanic clouds". In: *The Astrophysical Journal* 553.1, p. 367.

Crider, A. (2006). "A magnetar flare in the BATSE catalog?" In: *AIP Conference Proceedings*. Vol. 836. 1. American Institute of Physics, pp. 64–67.

D'Aì, A. et al. (2016). "Evidence for the magnetar nature of 1E 161348- 5055 in RCW 103". In: *Monthly Notices of the Royal Astronomical Society* 463.3, pp. 2394–2404.

De Luca, A. et al. (Aug. 2006). "A Long-Period, Violently Variable X-ray Source in a Young Supernova Remnant". In: *Science* 313.5788, pp. 814–817. DOI: 10.1126/science.1129185. arXiv: astro-ph/0607173 [astro-ph].

De Luca, A. et al. (Aug. 2008). "Deep Infrared Observations of the Puzzling Central X-Ray Source in RCW 103". In: *The Astrophysical Journal* 682.2, pp. 1185–1194. DOI: 10.1086/588600. arXiv: 0803.2885 [astro-ph].

de Ruiter, I. et al. (May 2025a). "Publisher Correction: Sporadic radio pulses from a white dwarf binary at the orbital period". In: *Nature Astronomy* 9, pp. 747–747. DOI: 10.1038/s41550-025-02540-8.

– (May 2025b). "Sporadic radio pulses from a white dwarf binary at the orbital period". In: *Nature Astronomy* 9, pp. 672–684. DOI: 10.1038/s41550-025-02491-0. arXiv: 2408.11536 [astro-ph.HE].

Demirer, M. et al. (2025). "Detailed Time Resolved Spectral and Temporal Investigations of SGR J1550-5418 Bursts Detected with Fermi/Gamma-ray Burst Monitor". In: *arXiv preprint arXiv:2506.04414*.

Dessert, C., J. W. Foster, & B. R. Safdi (2020). "Hard X-ray excess from the magnificent seven neutron stars". In: *The Astrophysical Journal* 904.1, p. 42.

Dobie, D. et al. (2024). "A two-minute burst of highly polarized radio emission originating from low Galactic latitude". In: *Monthly Notices of the Royal Astronomical Society* 535.1, pp. 909–923.

Dong, F. A. & Chime/Frb Collaboration (Oct. 2022). "CHIME/FRB Detection of a Bright Radio Burst from SGR 1935+2154". In: *The Astronomer's Telegram* 15681, p. 1.

Dong, F. A. et al. (July 2025a). "CHIME/Fast Radio Burst Discovery of an Unusual Circularly Polarized Long-period Radio Transient with an Accelerating Spin Period". In: *The Astrophysical Journal Letters* 988.1, L29, p. L29. DOI: 10.3847/2041-8213/adeaab. arXiv: 2507.05139 [astro-ph.HE].

Dong, F. A. et al. (Sept. 2025b). "CHIME/Fast Radio Burst/Pulsar Discovery of a Nearby Long-period Radio Transient with a Timing Glitch". In: *The Astrophysical Journal Letters* 990.2, L49, p. L49. DOI: 10.3847/2041-8213/adfa8e. arXiv: 2407.07480 [astro-ph.HE].

Doroshenko, V. et al. (2021). "SGR 0755- 2933: a new high-mass X-ray binary with the wrong name". In: *Astronomy & Astrophysics* 647, A165.

Dorozsmai, A. & S. Toonen (2024). "Importance of stable mass transfer and stellar winds for the formation of gravitational wave sources". In: *Monthly Notices of the Royal Astronomical Society* 530.4, pp. 3706–3739.

Duncan, R. C. & C. Thompson (1992). "Formation of very strongly magnetized neutron stars-Implications for gamma-ray bursts". In: *Astrophysical Journal, Part 2-Letters (ISSN 0004-637X), vol. 392, no. 1, June 10, 1992, p. L9-L13. Research supported by NSERC.* 392, pp. L9–L13.

Eldridge, J. & E. R. Stanway (2016). "BPASS predictions for binary black hole mergers". In: *Monthly Notices of the Royal Astronomical Society* 462.3, pp. 3302–3313.

Enoto, T. et al. (Oct. 2021). "A Month of Monitoring the New Magnetar Swift J1555.2-5402 during an X-Ray Outburst". In: *The Astrophysical Journal Letters* 920.1, L4, p. L4. DOI: 10.3847/2041-8213/ac2665. arXiv: 2108.02939 [astro-ph.HE].

Esposito, P. et al. (Nov. 2011). "Swift monitoring of the central X-ray source in RCW 103". In: *Monthly Notices of the Royal Astronomical Society* 418.1, pp. 170–175. DOI: 10.1111/j.1365-2966.2011.19473.x. arXiv: 1107.3770 [astro-ph.HE].

Esposito, P. et al. (2007). "Swift/XRT monitoring of five orbital cycles of LS I+ 61° 303". In: *Astronomy & Astrophysics* 474.2, pp. 575–578.

Esposito, P. et al. (2020). "A very young radio-loud magnetar". In: *The Astrophysical Journal Letters* 896.2, p. L30.

Feng, Y. et al. (2022a). "Circular polarization in two active repeating fast radio bursts". In: *Science Bulletin* 67.23, pp. 2398–2401.

Feng, Y. et al. (2022b). "Frequency-dependent polarization of repeating fast radio bursts—implications for their origin". In: *Science* 375.6586, pp. 1266–1270.

Ferrario, L., D. de Martino, & B. T. Gänsicke (2015). "Magnetic white dwarfs". In: *Space Science Reviews* 191.1, pp. 111–169.

Gaensler, B. M., E. V. Gotthelf, & G. Vasisht (Nov. 1999). "A New Supernova Remnant Coincident with the Slow X-Ray Pulsar AX J1845-0258". In: *The Astrophysical Journal Letters* 526.1, pp. L37–L40. DOI: 10.1086/312362. arXiv: astro-ph/9909400 [astro-ph].

Garmire, G. P. et al. (Jan. 2000). "1E 161348-5055". In: *International Astronomical Union Circulars* 7350, p. 2.

Gavriil, F. P., V. Kaspi, & P. Woods (2002). "Magnetar-like X-ray bursts from an anomalous X-ray pulsar". In: *Nature* 419.6903, pp. 142–144.

Gavriil, F. P. et al. (2008). "Magnetar-like emission from the young pulsar in Kes 75". In: *Science* 319.5871, pp. 1802–1805.

Gehrels, N. & P. Mészáros (2012). "Gamma-ray bursts". In: *Science* 337.6097, pp. 932–936.

Gil, J., G. I. Melikidze, & U. Geppert (2003). "Drifting subpulses and inner acceleration regions in radio pulsars". In: *Astronomy & Astrophysics* 407.1, pp. 315–324.

Goldreich, P. & W. H. Julian (1969). "Pulsar electrodynamics". In: *Astrophysical Journal, vol. 157, p. 869* 157, p. 869.

Gordon, A. C. et al. (2023). "The demographics, stellar populations, and star formation histories of fast radio burst host galaxies: implications for the progenitors". In: *The Astrophysical Journal* 954.1, p. 80.

Gotthelf, E. V. et al. (Oct. 2000). "A 700 Year-old Pulsar in the Supernova Remnant Kesteven 75". In: *The Astrophysical Journal Letters* 542.1, pp. L37–L40. DOI: 10.1086/312923. arXiv: astro-ph/0008097 [astro-ph].

Gotthelf, E. V. et al. (Apr. 2004). "Imaging X-Ray, Optical, and Infrared Observations of the Transient Anomalous X-Ray Pulsar XTE J1810-197". In: *The Astrophysical Journal* 605.1, pp. 368–377. DOI: 10.1086/382232. arXiv: astro-ph/0309745 [astro-ph].

Granot, J. et al. (2017). "Learning about the magnetar Swift J1834. 9- 0846 from its wind nebula". In: *Monthly Notices of the Royal Astronomical Society* 464.4, pp. 4895–4926.

Gregory, P. & G. Fahlman (1980). "An extraordinary new celestial X-ray source". In: *Nature* 287.5785, pp. 805–806.

Haberl, F. (2007). "The magnificent seven: magnetic fields and surface temperature distributions". In: *Astrophysics and Space Science* 308, pp. 181–190.

Halpern, J. et al. (2008). "Outburst of the 2 s Anomalous X-Ray Pulsar 1E 1547.0–5408". In: *The Astrophysical Journal* 676.2, p. 1178.

Han, J. et al. (2021). "The FAST Galactic Plane Pulsar Snapshot survey: I. Project design and pulsar discoveries". In: *Research in Astronomy and Astrophysics* 21.5, p. 107.

Han, J. et al. (2025). "The FAST Galactic Plane Pulsar Snapshot Survey. VI. The Discovery of 473 New Pulsars". In: *Research in Astronomy and Astrophysics* 25.1, p. 014001.

Hansen, C. J. & S. D. Kawaler (1994). "An Overview of Stellar Evolution". In: *Stellar Interiors: Physical Principles, Structure, and Evolution*, pp. 35–108.

Hewish, A. (1968). "Pulsars". In: *Scientific American* 219.4, pp. 25–35.

Hewish, A. et al. (1979). "Observation of a rapidly pulsating radio source". In: *A Source Book in Astronomy and Astrophysics, 1900–1975*. Harvard University Press, pp. 498–504.

Horváth, C. et al. (Sept. 2025). "A long period transient search method for the Murchison Widefield Array". In: *Publications of the Astronomical Society of Australia* 42, e129, e129. DOI: 10.1017/pasa.2025.10093. arXiv: 2509.06315 [astro-ph.IM].

Hu, C.-P. et al. (2025). "Rapid Spectral Evolution of SGR 1935+ 2154 during Its 2022 Outburst". In: *The Astrophysical Journal* 989.1, p. 63.

Hu, R.-C. & B. Zhang (2026). "Formation Channels of Magnetars". In: *The Astrophysical Journal* 999.1, p. 102.

Hurley, K. et al. (2005). "An exceptionally bright flare from SGR 1806–20 and the origins of short-duration γ-ray bursts". In: *Nature* 434.7037, pp. 1098–1103.

Hurley-Walker, N. et al. (Jan. 2022). "A radio transient with unusually slow periodic emission". In: *Nature* 601.7894, pp. 526–530. DOI: 10.1038/s41586-021-04272-x. arXiv: 2503.08033 [astro-ph.HE].

Hurley-Walker, N. et al. (July 2023). "A long-period radio transient active for three decades". In: *Nature* 619.7970, pp. 487–490. DOI: 10.1038/s41586-023-06202-5. arXiv: 2503.08036 [astro-ph.HE].

Hurley-Walker, N. et al. (2024). "A 2.9 hr Periodic Radio Transient with an Optical Counterpart". In: *The Astrophysical Journal Letters* 976.2, L21, p. L21. DOI: 10.3847/2041-8213/ad890e. arXiv: 2408.15757 [astro-ph.SR].

Hyman, S. D. et al. (2005). "A powerful bursting radio source towards the Galactic Centre". In: *nature* 434.7029, pp. 50–52.

Hyman, S. D. et al. (2007). "A faint, steep-spectrum burst from the radio transient GCRT J1745–3009". In: *The Astrophysical Journal Letters* 660.2, pp. L121–L124.

Imbrogno, M. et al. (Oct. 2023). "Discovery of a magnetar candidate X-ray pulsar in the Large Magellanic Cloud". In: *Monthly Notices of the Royal Astronomical Society* 524.4, pp. 5566–5574. DOI: 10.1093/mnras/stad2173. arXiv: 2307.09224 [astro-ph.HE].

Janssen, G. H. & B. W. Stappers (2006). "30 glitches in slow pulsars". In: *aap* 457, pp. 611–618. DOI: 10.1051/0004-6361:20065267.

Kaspi, V. M. & A. M. Beloborodov (2017). "Magnetars". In: *Annual Review of Astronomy and Astrophysics* 55.1, pp. 261–301.

Keane, E. & M. McLaughlin (2011). "Rotating radio transients". In: *arXiv preprint arXiv:1109.6896*.

Keane, E. F. & M. Kramer (2008). "On the birthrates of Galactic neutron stars". In: *Monthly Notices of the Royal Astronomical Society* 391.4, pp. 2009–2016.

Kirsten, F. et al. (2021). "Detection of two bright radio bursts from magnetar SGR 1935+ 2154". In: *Nature Astronomy* 5.4, pp. 414–422.

Kouveliotou, C. et al. (Aug. 1993a). "Identification of Two Classes of Gamma-Ray Bursts". In: *The Astrophysical Journal Letters* 413, p. L101. DOI: 10.1086/186969.

Kouveliotou, C. et al. (Apr. 1993b). "Recurrent burst activity from the soft γ-ray repeater SGR 1900+14". In: *Nature* 362.6422, pp. 728–730. DOI: 10.1038/362728a0.

Kozlova, A. et al. (2016). "The first observation of an intermediate flare from SGR 1935+ 2154". In: *Monthly Notices of the Royal Astronomical Society* 460.2, pp. 2008–2014.

Kuiper, L. & W. Hermsen (2015). "The soft γ-ray pulsar population: a high-energy overview". In: *Monthly Notices of the Royal Astronomical Society* 449.4, pp. 3827–3866.

Lamb, D. et al. (Aug. 2003). "SGR 1808-20 (=H2802): A Possible new SGR". In: *GRB Coordinates Network* 2351, p. 1.

Lamb, R. C. et al. (July 2002). "Discovery of a Possible Anomalous X-Ray Pulsar in the Small Magellanic Cloud". In: *The Astrophysical Journal Letters* 574.1, pp. L29–L32. DOI: 10.1086/342352. arXiv: astro-ph/0205310 [astro-ph].

Laplace, E. et al. (2021). "Different to the core: The pre-supernova structures of massive single and binary-stripped stars". In: *Astronomy & Astrophysics* 656, A58.

Laros, J. G. et al. (Sept. 1987). "A New Type of Repetitive Behavior in a High-Energy Transient". In: *The Astrophysical Journal Letters* 320, p. L111. DOI: 10.1086/184985.

Lee, Y. et al. (2025). "The emission of interpulses by a 6.45-h-period coherent radio transient". In: *Nature Astronomy* 9.3, pp. 393–405.

Levin, L. et al. (Sept. 2010). "A Radio-loud Magnetar in X-ray Quiescence". In: *ApJ* 721.1, pp. L33–L37. DOI: 10.1088/2041-8205/721/1/L33. arXiv: 1007.1052 [astro-ph.HE].

– (2012). "Radio emission evolution, polarimetry and multifrequency single pulse analysis of the radio magnetar PSR J1622- 4950". In: *Monthly Notices of the Royal Astronomical Society* 422.3, pp. 2489–2500.

Li, C. et al. (2021). "HXMT identification of a non-thermal X-ray burst from SGR J1935+ 2154 and with FRB 200428". In: *Nature Astronomy* 5.4, pp. 378–384.

Li, D. et al. (Nov. 2024a). "A 44-minute periodic radio transient in a supernova remnant". In: *arXiv e-prints*, arXiv:2411.15739, arXiv:2411.15739. DOI: 10.48550/arXiv.2411.15739. arXiv: 2411.15739 [astro-ph.HE].

– (2024b). "A 44-minute periodic radio transient in a supernova remnant". In: *arXiv preprint arXiv:2411.15739*.

Lien, A. et al. (Sept. 2016). "The Third Swift Burst Alert Telescope Gamma-Ray Burst Catalog". In: *The Astrophysical Journal* 829.1, 7, p. 7. DOI: 10.3847/0004-637X/829/1/7. arXiv: 1606.01956 [astro-ph.HE].

Lorimer, D. R. (2008). "Binary and millisecond pulsars". In: *Living reviews in relativity* 11.1, p. 8.

Lorimer, D. R. et al. (2007). "A bright millisecond radio burst of extragalactic origin". In: *Science* 318.5851, pp. 777–780.

LS, I. (n.d.). "Bayesian Analysis of Radio Observations of the Be X-ray Binary". In: ().

Lu, W.-J. et al. (2024). "Upper limits on the radio pulses from magnetars and a central compact object with FAST". In: *The Astrophysical Journal* 963.2, p. 151.

Lyubarskii, Y. E. (July 1996). "A model for the energetic emission from pulsars." In: *Astronomy & Astrophysics* 311, pp. 172–178.

Lyubarsky, Y. (2014). "A model for fast extragalactic radio bursts". In: *Monthly Notices of the Royal Astronomical Society: Letters* 442.1, pp. L9–L13.

Maan, Y. et al. (Oct. 2022). "GBT detection of bright 5 GHz radio bursts from SGR 1935+2154, coincident with X-ray and 600 MHz bursts". In: *The Astronomer's Telegram* 15697, p. 1.

Makishima, K., N. Uchida, & T. Enoto (2026). "Evidence for 1.01 s pulsations of the Central Compact Object in the supernova remnant RCW 103 with ASCA, XMM-Newton, and NuSTAR". In: *Publications of the Astronomical Society of Japan* 78.2, pp. 688–709.

Makishima, K. et al. (2023). "Further Evidence for the 9 s Pulsation in LS 5039 from NuSTAR and ASCA". In: *The Astrophysical Journal* 959.2, p. 79.

Manchester, R. N. et al. (2005). "The Australia telescope national facility pulsar catalogue". In: *The Astronomical Journal* 129.4, p. 1993.

Mazets, E. P., S. V. Golenetskij, & Y. A. Guryan (1979a). "Soft gamma-ray bursts from the source B1900+14". In: *Soviet Astronomy Letters* 5, p. 343.

Mazets, E. P. et al. (1979b). "Observations of a flaring X-ray pulsar in Dorado". In: *Nature* 282.5739, pp. 587–589. DOI: 10.1038/282587a0.

Mckinven, R. et al. (2025). "A pulsar-like polarization angle swing from a nearby fast radio burst". In: *Nature* 637.8044, pp. 43–47.

McLaughlin, M. A. et al. (2006). "Transient radio bursts from rotating neutron stars". In: *Nature* 439.7078, pp. 817–820.

McSweeney, S. J. et al. (2025). "A new long-period radio transient: discovery of pulses repeating every 1.16 h from ASKAP J175534. 9- 252749.1". In: *Monthly Notices of the Royal Astronomical Society* 542.1, pp. 203–214.

Meegan, C. et al. (1992). "Spatial distribution of γ-ray bursts observed by BATSE". In: *Nature* 355.6356, pp. 143–145.

Mereghetti, S. et al. (2020). "INTEGRAL discovery of a burst with associated radio emission from the magnetar SGR 1935+ 2154". In: *The Astrophysical Journal Letters* 898.2, p. L29.

Mereghetti, S. et al. (2022). "INTEGRAL detection of a burst from SGR J1935+ 2154". In: *GRB Coordinates Network* 32698, p. 1.

Mereghetti, S. et al. (Oct. 2012). "The magnetar candidate AX J1818.8-1559". In: *Astronomy & Astrophysics* 546, A30, A30. DOI: 10.1051/0004-6361/201219907. arXiv: 1208.0249 [astro-ph.HE].

Moe, M. & R. Di Stefano (2017). “Mind your Ps and Qs: the interrelation between period (P) and mass-ratio (Q) distributions of binary stars”. In: *The Astrophysical Journal Supplement Series* 230.2, p. 15.

Mori, K. et al. (Apr. 2013). “NuSTAR discovery of a 3.76 second pulsar in the Sgr A* region”. In: *The Astronomer’s Telegram* 5020, p. 1.

Nimmo, K. et al. (2025). “Magnetospheric origin of a fast radio burst constrained using scintillation”. In: *Nature* 637.8044, pp. 48–51.

Nomoto, K. & Y. Kondo (1991). “Conditions for accretion-induced collapse of white dwarfs”. In: *Astrophysical Journal, Part 2-Letters (ISSN 0004-637X), vol. 367, Jan. 20, 1991, p. L19-L22.* 367, pp. L19–L22.

Ofek, E. et al. (2006). “The short-hard GRB 051103: observations and implications for its nature”. In: *The Astrophysical Journal* 652.1, p. 507.

Ofek, E. et al. (2008). “GRB 070201: a possible soft gamma-ray repeater in M31”. In: *The Astrophysical Journal* 681.2, p. 1464.

Olausen, S. A. & V. M. Kaspi (May 2014). “The McGill Magnetar Catalog”. In: *The Astrophysical Journal Supplement Series* 212.1, 6, p. 6. DOI: 10.1088/0067-0049/212/1/6. arXiv: 1309.4167 [astro-ph.HE].

Pacholski, D., S. Mereghetti, & M. Topinka (2025). “INTEGRAL IBIS catalog of magnetar bursts”. In: *arXiv preprint arXiv:2512.14356*.

– (2026). “INTEGRAL IBIS catalog of magnetar bursts”. In: *The Astrophysical Journal* 997.2, p. 272.

Paciesas, W. S. et al. (June 1999). “The Fourth BATSE Gamma-Ray Burst Catalog (Revised)”. In: *The Astrophysical Journal Supplement Series* 122.2, pp. 465–495. DOI: 10.1086/313224. arXiv: astro-ph/9903205 [astro-ph].

Pagani, C. et al. (Jan. 2007). “GRB 070610: Swift detection of a burst.” In: *GRB Coordinates Network* 6489, p. 1.

Page, K. L. et al. (Oct. 2020). “Swift detection of a new SGR 1830-0645 or a short GRB 201010A”. In: *The Astronomer’s Telegram* 14083, p. 1.

Palmer, D. M. et al. (June 2021). “Swift Detection of probable new Swift SGR J1555.2-5402”. In: *GRB Coordinates Network* 30120, p. 1.

Pearlman, A. B. & Chime/Frb Collaboration (2022). “CHIME/FRB Detection of Another Bright Radio Burst from SGR 1935+2154”. In: *The Astronomer’s Telegram* 15792, p. 1.

Pennucci, T. T. et al. (2015). “Simultaneous multi-band radio and X-ray observations of the galactic center magnetar SGR 1745–2900”. In: *The Astrophysical Journal* 808.1, p. 81.

Petroff, E., J. Hessels, & D. Lorimer (2019). “Fast radio bursts”. In: *The Astronomy and Astrophysics Review* 27.1, p. 4.

Philippov, A. & M. Kramer (2022). “Pulsar magnetospheres and their radiation”. In: *Annual Review of Astronomy and Astrophysics* 60.1, pp. 495–558.

Pivovaroff, M. J., V. M. Kaspi, & F. Camilo (May 2000). “X-Ray Observations of the High Magnetic Field Radio Pulsar PSR J1814-1744”. In: *The Astrophysical Journal* 535.1, pp. 379–384. DOI: 10.1086/308848. arXiv: astro-ph/0001091 [astro-ph].

Pizzolato, F. et al. (2008). “1E 161348–5055 in the Supernova Remnant RCW 103: A Magnetar in a Young Low-Mass Binary System?” In: *The Astrophysical Journal* 681.1, p. 530.

Prayag, V. et al. (2026). “The TRAPUM Large Magellanic Cloud pulsar survey with MeerKAT–II. 12 new discoveries and timing solutions for 7 pulsars”. In: *Monthly Notices of the Royal Astronomical Society* 545.4, staf2193.

Pritchard, J. et al. (2026). “Discovery of a 36-minute long-period transient ASKAP J142431. 2-612611”. In: *arXiv preprint arXiv:2603.07857*.

Qu, Y. & B. Zhang (2023). “Polarization of fast radio bursts: radiation mechanisms and propagation effects”. In: *Monthly Notices of the Royal Astronomical Society* 522.2, pp. 2448–2477.

– (2024). “Coherent inverse compton scattering in fast radio bursts revisited”. In: *The Astrophysical Journal* 972.1, p. 124.

– (Mar. 2025). “Magnetic Interactions in White Dwarf Binaries as Mechanism for Long-period Radio Transients”. In: *The Astrophysical Journal* 981.1, 34, p. 34. DOI: 10.3847/1538-4357/adb1b5. arXiv: 2409.05978 [astro-ph.HE].

Ransom, S. M. (2001). *New search techniques for binary pulsars*. Harvard University.

Ravi, V. et al. (2025). “Deep Synoptic Array science: a 50 Mpc fast radio burst constrains the mass of the Milky Way circumgalactic medium”. In: *The Astronomical Journal* 169.6, p. 330.

Rea, N., N. Hurley-Walker, & M. Caleb (2026). “Long Period Transients (LPTs): a comprehensive review”. In: *Journal of High Energy Astrophysics*, p. 100566.

Reynoso, E. M. et al. (2004). “Influence of the Neutron Star 1E 161348–5055 in RCW 103 on the Surrounding Medium”. In: *Publications of the Astronomical Society of Australia* 21.1, pp. 82–88.

Richardson, N. D. et al. (2023). “A high-mass X-ray binary descended from an ultra-stripped supernova”. In: *Nature* 614.7946, pp. 45–47.

Ridnaia, A. et al. (2021). “A peculiar hard X-ray counterpart of a Galactic fast radio burst”. In: *Nature Astronomy* 5.4, pp. 372–377.

Roberts, O. J. (Jan. 2015). “Fermi GBM Observations of Magnetar 4U 0142+61.” In: *GRB Coordinates Network* 17508, p. 1.

Roberts, O. et al. (2021). “Rapid spectral variability of a giant flare from a magnetar in NGC 253”. In: *Nature* 589.7841, pp. 207–210.

Rodriguez, A. C. (Mar. 2025). “Spectroscopic detection of a 2.9-hour orbit in a long-period radio transient”. In: *Astronomy & Astrophysics* 695, L8, p. L8. DOI: 10.1051/0004-6361/202553684. arXiv: 2501.03315 [astro-ph.SR].

Ruderman, M. & P. G. Sutherland (1975). “Theory of pulsars-Polar caps, sparks, and coherent microwave radiation”. In: *Astrophysical Journal, vol. 196, Feb. 15, 1975, pt. 1, p. 51-72.* 196, pp. 51–72.

Ruiter, A. et al. (2019). “On the formation of neutron stars via accretion-induced collapse in binaries”. In: *Monthly Notices of the Royal Astronomical Society* 484.1, pp. 698–711.

Rybicki, G. B. & A. P. Lightman (2024). *Radiative processes in astrophysics*. John Wiley & Sons.

Sakamoto, T. et al. (Apr. 2011). “Probing the nature of short swift bursts via deep INTEGRAL monitoring of GRB 050925”. In: *Advances in Space Research* 47.8, pp. 1346–1352. DOI: 10.1016/j.asr.2010.08.004. arXiv: 1008.0226 [astro-ph.HE].

Salpeter, E. E. (1955). “The luminosity function and stellar evolution.” In: *Astrophysical Journal, vol. 121, p. 161* 121, p. 161.

Schatz, H. & K. Rehm (2006). “X-ray binaries”. In: *Nuclear physics A* 777, pp. 601–622.

Schenck, A., S. Park, & S. Post (2016). “A Chandra Study of the Interstellar Metallicity in the Large Magellanic Cloud Using Supernova Remnants”. In: *The Astronomical Journal* 151.6, p. 161.

Seward, F. D., P. A. Charles, & A. P. Smale (June 1986). “A 6 Second Periodic X-Ray Source in Carina”. In: *The Astrophysical Journal* 305, p. 814. DOI: 10.1086/164294.

Sharma, K. et al. (2024). “Preferential occurrence of fast radio bursts in massive star-forming galaxies”. In: *Nature* 635.8037, pp. 61–66.

Sharma, R. et al. (2023). “AstroSat observation of the magnetar SGR J1830- 0645 during its first detected X-ray outburst”. In: *Monthly Notices of the Royal Astronomical Society* 526.4, pp. 4877–4884.

Smartt, S. J. (2009). “Progenitors of core-collapse supernovae”. In: *Annual Review of Astronomy and Astrophysics* 47.1, pp. 63–106.

Spitkovsky, A. (Sept. 2006). “Time-dependent Force-free Pulsar Magnetospheres: Axisymmetric and Oblique Rotators”. In: *The Astrophysical Journal Letters* 648.1, pp. L51–L54. DOI: 10.1086/507518. arXiv: astro-ph/0603147 [astro-ph].

Spitler, L. et al. (2014). "Fast radio burst discovered in the Arecibo pulsar ALFA survey". In: *The Astrophysical Journal* 790.2, p. 101.

Stefanescu, A. et al. (Sept. 2007). "OPTIMA-Burst – Catching GRB Afterglows (and other Transients) with High Time Resolution". In: *Astronomische Nachrichten* 328.7, p. 620.

Stefanescu, A. et al. (Sept. 2008). "Very fast optical flaring from a possible new Galactic magnetar". In: *Nature* 455.7212, pp. 503–505. DOI: 10.1038/nature07308. arXiv: 0809.4043 [astro-ph].

Suresh, A. & J. M. Cordes (2019). "Induced polarization from birefringent pulse splitting in magneto-ionic media". In: *The Astrophysical Journal* 870.1, p. 29.

Surnis, M. P. et al. (Nov. 2023). "Discovery of an extremely intermittent periodic radio source". In: *Monthly Notices of the Royal Astronomical Society* 526.1, pp. L143–L148. DOI: 10.1093/mnrasl/slad082. arXiv: 2306.10817 [astro-ph.HE].

Suvorov, A. G. & K. Glampedakis (2022). "Does the Gamma-Ray Binary LS I + 61°303 Harbor a Magnetar?" In: *The Astrophysical Journal* 940.2, 128, p. 128. DOI: 10.3847/1538-4357/ac9b48. arXiv: 2210.09471 [astro-ph.HE].

Szary, A., G. I. Melikidze, & J. Gil (2015). "On the origin of radio emission from magnetars". In: *The Astrophysical Journal* 800.1, p. 76.

Tam, C. R. et al. (Nov. 2006). "Chandra Observations of the Transient 7 s X-ray Pulsar AX J1845.0-0258". In: *The Astrophysical Journal* 652.1, pp. 548–553. DOI: 10.1086/507262. arXiv: astro-ph/0602522 [astro-ph].

Tan, C. et al. (2018). "LOFAR Discovery of a 23.5 s Radio Pulsar". In: *The Astrophysical Journal* 866.1, p. 54.

Tan, C. et al. (2023). "X-ray non-detection of PSR J0250+ 5854". In: *Monthly Notices of the Royal Astronomical Society* 520.4, pp. 5960–5963.

Tendulkar, S. P. et al. (2017). "The host galaxy and redshift of the repeating fast radio burst FRB 121102". In: *The Astrophysical Journal Letters* 834.2, p. L7.

Torii, K. et al. (Aug. 1998). "Discovery of a 7 Second X-Ray Pulsar, AX J1845.0-0300". In: *The Astrophysical Journal* 503.2, pp. 843–847. DOI: 10.1086/306038.

Trigg, A. C. et al. (July 2024). "GRB 180128A: A second magnetar giant flare candidate from the Sculptor Galaxy". In: *Astronomy & Astrophysics* 687, A173, A173. DOI: 10.1051/0004-6361/202348858. arXiv: 2311.09362 [astro-ph.HE].

Trigg, A. C. et al. (Feb. 2025). "Extragalactic magnetar giant flare GRB 231115A: Insights from Fermi/GBM observations". In: *Astronomy & Astrophysics* 694, A323, A323. DOI: 10.1051/0004-6361/202452268. arXiv: 2409.06056 [astro-ph.HE].

Truelove, J. K. & C. F. McKee (1999). "Evolution of nonradiative supernova remnants". In: *The Astrophysical Journal Supplement Series* 120.2, p. 299.

Turolla, R. (2009). “Isolated neutron stars: the challenge of simplicity”. In: *Neutron stars and pulsars*. Springer, pp. 141–163.

Volkov, I. et al. (2021). “NuSTAR observation of LS 5039”. In: *The Astrophysical Journal* 915.1, p. 61.

von Kienlin, A. et al. (Apr. 2020). “The Fourth Fermi-GBM Gamma-Ray Burst Catalog: A Decade of Data”. In: *The Astrophysical Journal* 893.1, 46, p. 46. DOI: 10.3847/1538-4357/ab7a18. arXiv: 2002.11460 [astro-ph.HE].

Wang, C.-W. et al. (Mar. 2026). “GECAM discovery of the second FRB-associated magnetar X-ray burst from SGR J1935+2154”. In: *MNRAS* 546.4, stag312, stag312. DOI: 10.1093/mnras/stag312. arXiv: 2602.10895 [astro-ph.HE].

Wang, H.-H. et al. (Oct. 2020). “A Multiwavelength Study of PSR J1119-6127 after 2016 Outburst”. In: *The Astrophysical Journal* 902.2, 96, p. 96. DOI: 10.3847/1538-4357/abb3c4. arXiv: 2008.12585 [astro-ph.HE].

Wang, W.-Y. et al. (2022). “Polarization of magnetospheric curvature radiation in repeating fast radio bursts”. In: *Monthly Notices of the Royal Astronomical Society* 517.4, pp. 5080–5089.

Wang, Z. et al. (June 2025). “Detection of X-ray emission from a bright long-period radio transient”. In: *Nature* 642.8068, pp. 583–586. DOI: 10.1038/s41586-025-09077-w. arXiv: 2411.16606 [astro-ph.HE].

Webbe, R. et al. (2025). “4XMM J175136. 8- 275858: a new magnetar candidate?” In: *Monthly Notices of the Royal Astronomical Society* 539.4, pp. 3046–3057.

Weltevrede, P., S. Johnston, & C. M. Espinoza (2011). “The glitch-induced identity changes of PSR J1119- 6127”. In: *Monthly Notices of the Royal Astronomical Society* 411.3, pp. 1917–1934.

Weng, S.-S. et al. (Mar. 2022). “Radio pulsations from a neutron star within the gamma-ray binary LS I +61° 303”. In: *Nature Astronomy* 6, pp. 698–702. DOI: 10.1038/s41550-022-01630-1. arXiv: 2203.09423 [astro-ph.HE].

Wickramasinghe, D. & L. Ferrario (2005). “The origin of the magnetic fields in white dwarfs”. In: *Monthly Notices of the Royal Astronomical Society* 356.4, pp. 1576–1582.

Wongphechauxsorn, J. et al. (Jan. 2024). “The High Time Resolution Universe Pulsar survey - XVIII. The reprocessing of the HTRU-S Low Lat survey around the Galactic Centre using a Fast Folding Algorithm pipeline for accelerated pulsars”. In: *Monthly Notices of the Royal Astronomical Society* 527.2, pp. 3208–3219. DOI: 10.1093/mnras/stad3283. arXiv: 2310.14008 [astro-ph.HE].

Woods, P. M. et al. (1999). “Discovery of a New Soft Gamma Repeater, SGR 1627–41”. In: *The Astrophysical Journal* 519.2, p. L139.

Xu, K. & X.-D. Li (2019). “On the Fallback Disk around the Slowest Isolated Pulsar, 1E 161348-5055”. In: *The Astrophysical Journal* 877.2, p. 138.

Yao, J., R. Manchester, & N. Wang (2017). "A new electron-density model for estimation of pulsar and FRB distances". In: *The Astrophysical Journal* 835.1, p. 29.

Yoneda, H. et al. (Sept. 2020). "Sign of Hard-X-Ray Pulsation from the γ -Ray Binary System LS 5039". In: *Physical Review Letters* 125.11, 111103, p. 111103. DOI: 10.1103/PhysRevLett.125.111103. arXiv: 2009.02075 [astro-ph.HE].

Younes, G. et al. (2022a). "Pulse peak migration during the outburst decay of the magnetar SGR 1830-0645: crustal motion and magnetospheric untwisting". In: *The Astrophysical Journal Letters* 924.2, p. L27.

Younes, G. et al. (2022b). "X-ray burst and persistent emission properties of the magnetar SGR 1830-0645 in outburst". In: *The Astrophysical Journal* 924.2, p. 136.

Younes, G. et al. (2023). "Magnetar spin-down glitch clearing the way for FRB-like bursts and a pulsed radio episode". In: *Nature Astronomy* 7.3, pp. 339–350.

Zapartas, E. et al. (2017). "Delay-time distribution of core-collapse supernovae with late events resulting from binary interaction". In: *Astronomy & Astrophysics* 601, A29.

Zelati, F. C. et al. (2021). "The new magnetar SGR J1830- 0645 in outburst". In: *The Astrophysical Journal Letters* 907.2, p. L34.

Zhang, B. (2022). "Coherent inverse compton scattering by bunches in fast radio bursts". In: *The Astrophysical Journal* 925.1, p. 53.

Zhang, P. (Sept. 2024). "A New Puzzling Periodic Signal in GeV Energies of the γ-Ray Binary LS I+61°303". In: *The Astrophysical Journal* 972.1, 80, p. 80. DOI: 10.3847/1538-4357/ad6a16. arXiv: 2406.02042 [astro-ph.HE].

Zhang, Y. & H. Feng (2023). "Searching for single-frame rapid X-ray transients detected with Chandra". In: *Monthly Notices of the Royal Astronomical Society* 523.2, pp. 2513–2518.

Zhou, P. et al. (Jan. 2014). "Discovery of the Transient Magnetar 3XMM J185246.6+003317 near Supernova Remnant Kesteven 79 with XMM-Newton". In: *The Astrophysical Journal Letters* 781.1, L16, p. L16. DOI: 10.1088/2041-8205/781/1/L16. arXiv: 1310.7705 [astro-ph.HE].

Zhu, W. et al. (2023). "A radio pulsar phase from SGR J1935+ 2154 provides clues to the magnetar FRB mechanism". In: *Science Advances* 9.30, eadf6198.

1.6.1 Short Gamma Ray Bursts (sGRBs) and Rapid X-ray Transients (RXTs)

Since the Compton Gamma Ray Observatory's Burst and Transient Source Experiment's (BATSE) first light in 1990, succeeded by the *Swift* Burst Analysis Telescope (BAT) and *Fermi* Gamma-Ray Burst Monitor (GBM), over 10,000 GRBs, $1-100$ s bursts with energies $\sim 10^{51}$ ergs, have been detected between $\sim 10\,\mathrm{keV}-100\,\mathrm{GeV}$ (Lien et al., 2016; Paciesas et al., 1999; von Kienlin et al., 2020). Some have multiwavelength afterglows, while others are only observed in gamma rays. Kouveliotou et al. (1993a) identified two distinct classes: short ($\lesssim 2$ s) GRBs with hard spectra and long ($\gtrsim 2$ s) GRBs with soft spectra (see Gehrels & Mészáros, 2012, for a review). As the population grew, their extragalactic nature was confirmed by their uniform all-sky spatial distribution, and follow-up optical/IR observations were used to identify host galaxies (Meegan et al., 1992).

Most short and long GRBs' are thought to form via the merger of two compact stellar remnants which release gravitational energy as gamma rays and form a black hole. However, Hurley et al. (2005) noted that a recent giant flare from SGR 1806-20 would appear like a short GRB if placed in another galaxy. Some subset of short GRBs are then likely produced by magnetar giant flares, but confirming them would require detection of periodic $1-10$ s modulations in short GRBs' tails, a phenomenon observable only from extremely luminous flares within nearby galaxies.

Nonetheless, at least seven short GRBs have been proposed as giant flares from extragalactic magnetars. GRB 051103 was detected from the nearby M81/M82 galaxy group, possibly from a known star forming region, but its large $\sim 10' \times 1^\circ$ error region makes the association tenuous (Ofek et al., 2006). GRB 070201, likely originating from the Andromeda galaxy (M31), was similarly proposed based on its location near the galaxy's star-forming spiral arms (Ofek et al., 2008). In addition, the Laser Interferometer Gravitational-Wave Observatory (LIGO; Abramovici et al., 1992), now known to be sensitive to compact object binary mergers since its groundbreaking detection in Abbott et al. (2016), ruled out the presence of a compact binary merger in M31 temporally coincident with GRB 070201 with 99% confidence. No periodic modulations were detected for either GRB.

GRB 200415A, detected from NGC 253, shared a similar magnetar flare-like temporal profile with no evidence of periodicity or optical afterglow, but also displays a unique spectral evolution, hardening over the first ~ 7 ms before softening again (O. Roberts et al., 2021). While such spectral evolution has not been observed in Galactic magnetar flares, they propose that a relativistically moving emitting plasma

within the magnetar magnetosphere could produce such an effect. GRB 180128A, also from NGC 253, and GRB 231115A from M82, exhibited similar spectral evolution and were proposed as magnetar giant flares (Trigg et al., 2024, 2025).

GRB 070222A from M83 was added to the candidate magnetar flare sample based on its coincidence with a star forming galaxy, but Burns et al. (2021) claim that it, along with three GRBs mentioned above, has unique rise time and energy compared to the remaining short GRB sample, potentially supporting a magnetar origin.

Only one short GRB has evidence of periodic structure, GRB 970110 from the Firework galaxy (NGC 6946). Conducting a periodicity search for modulations in the tails of 358 BATSE short GRBs, Crider (2006) identify a statistically significant $P = 13.8\,\mathrm{s}$ using a Lomb periodogram. Visual inspection of the lightcurve is less convincing, and it is unlikely that such modulations would be detectable at the galaxy's 5.9 Mpc distance. Nonetheless, GRB 970110 demonstrates that giant flare features may be detectable in GRBs beyond the local ($\lesssim 1\,\mathrm{Mpc}$) universe.

More recently, Y. Zhang & H. Feng (2023) discovered 11 'single-frame' soft ($0.5 - 10\,\mathrm{keV}$) X-ray transients within archival $0.1 - 3.3\,\mathrm{s}$ resolution image data from the *Chandra* Advanced CCD Imaging Spectrometer (ACIS). These Rapid X-ray Transients (RXTs) appear uniformly distributed across the sky and have fluxes $\sim 10^{-11} - 10^{-10}\,\mathrm{erg\,cm^{-2}\,s^{-1}}$, suggesting high, magnetar flare-like intrinsic luminosities $\gtrsim 10^{34}\,\mathrm{erg\,s^{-1}}$ if they are extragalactic. While the RXTs have not been confidently localized yet, with only arcminute-scale position errors, two have extragalactic candidate associations to M31 (RXT 070602) and the SMC (RXT 130305), two have Galactic candidate associations to the Carina Nebula (RXT 080723) and the M37 cluster (RXT 111115), and two have cautious optical counterparts (RXT 110123 and RXT 140323). RXTs' luminosities resemble those of magnetar short bursts ($\sim 10^{29-35}$), but spectral characterization is required to investigate further.

1.6.2 Fast Radio Bursts (FRBs)

FRB 20010824 was discovered in archival data from the Parkes *Murriyang* Telescope as a $\sim 15\,\mathrm{ms}$ radio pulse at 1.4 GHz (Lorimer et al., 2007). The FRB was proposed as extragalactic in origin based on the significant frequency-dependent dispersive delay due to the light's propagation through the ionized Interstellar Medium (ISM). Quantified by the dispersion measure (DM):

$$\mathrm{DM} = \int_0^D \frac{n_e}{1+z(l)} dl \tag{1.8}$$

where n_e is the free electron number density, D is the distance, z is the redshift, and l integrates along the line-of-sight, FRB 20010824's DM= $375 \pm 1\,\mathrm{pc\,cm^{-3}}$ was much larger than the estimated Galactic contribution as constrained by Galactic radio pulsars (Cordes & Lazio, 2002; Yao et al., 2017). Additional highly dispersed, wideband FRBs were revealed in archival data, including the first repeating FRB, FRB 20121102, which was localized to a z=0.2 galaxy and confirmed FRBs' extragalactic origins (Spitler et al., 2014; Tendulkar et al., 2017). To date, around $\sim$ 1000 FRBs have been detected, with $\sim$ 100 localized to host galaxies and $\sim$ 100 observed to repeat (see sample papers such as Gordon et al., 2023; K. Sharma et al., 2024).

Unlike GRBs, whose profile and high-energy emission closely resemble magnetar giant flares, FRBs are detected only at radio frequencies. Their association with magnetars is based predominantly on their high $L \sim 10^{40-43}\,\mathrm{erg\,s^{-1}}$ luminosities (brightness temperature $T_b \sim 10^{34-38}$ K) which exceed typical neutron star rotational energy allowances L_{max} (e.g., Petroff et al., 2019). This suggests that FRBs originate from a compact source with a coherent emission process driven by magnetic energy stored in a strong, magnetar-like magnetic field. Thus, while they don't resemble typical Galactic magnetar emission, predominant models invoke a magnetar origin for FRBs.

Coherent emission is intrinsically highly linearly polarized, meaning that the electric field is oriented in a fixed direction. However, if the line-of-sight is at an angle relative to the emission direction, the observed radiation will have circular components, in which the electric field direction rotates about the propagation axis, due to the charge bunch's trajectory. This is accompanied by $\sim$ 50% reduction in intensity, and therefore is unlikely to be the source of FRBs' high circular polarization fractions (e.g., Qu & B. Zhang, 2023; W.-Y. Wang et al., 2022). Instead, propagation effects can alter the observed polarization properties. We summarize polarization using Stokes parameters, which are composed of conjugate combinations of electric field components as detected by orthogonally oriented antenna feeds:

$$I = \frac{1}{2}(< V_A V_A^* > + < V_B V_B* >) \tag{1.9}$$

$$Q = \frac{1}{2}(< V_A V_A^* > - < V_B V_B* >) \tag{1.10}$$

$$U = Re(< V_A V_B* >) \tag{1.11}$$

$$V = Im(< V_A V_B* >) \tag{1.12}$$

where V_A and V_B are the complex voltages from the antenna feeds, I corresponds to the total intensity, Q and U describe the linear polarization, and V describes right (>0) and left (<0) hand circular polarization. Light propagating within an ionized medium along a line-of-sight magnetic field $\overrightarrow{B}_{||}$ with electron density n_e will undergo Faraday Rotation, in which the electric field direction, or position angle $\chi = 0.5 \tan^{-1}(U/Q)$, is rotated as a function of emission wavelength squared (Brentjens & De Bruyn, 2005; Burn, 1966). This effect will reduce the band-averaged linear polarization, and is described by the Rotation Measure:

$$RM = 0.81 \int_0^D \frac{n_e B_{||}}{(1 + z(l))^2} dl \tag{1.13}$$

FRBs have been measured with a wide range of RM magnitudes from $0-10^5$ rad m^{-2}, suggesting they can inhabit diverse magnetoionic environments (Anna-Thomas et al., 2023; Ravi et al., 2025). Furthermore, if light propagates through a turbulent medium in which different regions impart unique RMs scattered with variation σ_{RM}, it can disperse along multiple propagation paths and incoherently recombine, lowering the observed linear polarization. Y. Feng et al. (2022b) demonstrate that this model appears consistent with some repeating FRBs' polarization fractions. A strong perpendicular magnetic field $B_\perp$ can induce circular polarization through birefringence, or slowing of one linear polarization mode relative to another (Suresh & Cordes, 2019). Thus, the broad diversity of polarization properties exhibited by FRBs more readily support inner magnetospheric emission and propagation through circumstellar media with unique electron densities and magnetic fields, whereas maser models would imply a more uniform polarization behavior across the population. Despite this, distinguishing the emission properties, circumstellar propagation effects, and ISM propagation effects remains an open research area, as will be discussed in Section 6 and Section 7.

Emission models (see Qu & B. Zhang, 2023, for a review) broadly fall into two categories: maser mechanisms and antenna mechanisms. While both originate from breaks in magnetic tension within the magnetar crust which release energy from the

twisted magnetic field, the maser mechanism requires the energy to propagate as an Alfvén plasma wave 'pulse' through the outer magnetosphere until encountering the shock front between CCSN ejecta or magnetized pair-plasma wind and circumstellar gas $\sim 10^9$ km from the magnetar. The pulse induces a contact instability by displacing the shocked plasma, inverting the population and causing turbulent, relativistic charges to coherently produce synchrotron radiation at low radio frequencies (e.g., Lyubarsky, 2014):

$$\nu_0 = \frac{qB}{2\pi m_e c \Gamma_{cd}} \approx 50\,\mathrm{M}Hz \tag{1.14}$$

where $\Gamma_{cd} \sim 10^4$ is the bulk Lorentz factor of the plasma. However, recent observations of circular polarization, pulsar-like linear polarization position angle swings, and scintillation from turbulent screens near the emission site support inner-magnetosphere antenna mechanisms instead (Y. Feng et al., 2022a; Mckinven et al., 2025; Nimmo et al., 2025). Coherent curvature radiation shares a similar 'sparking' mechanism as the pulsar emission model (see Section 1.3.1), in which electrons are discharged across a vacuum gap. However, FRBs' extreme luminosities require larger bunches of coherently radiating charges moving at higher speeds γ than in pulsar magnetospheres. Charge bunches then stream along curved magnetic field lines, possibly sustained by a parallel electric field, with their centripetal acceleration inducing curvature radiation (W.-Y. Wang et al., 2022). Coherent Inverse Compton Scattering (ICS) postulates that low frequency electromagnetic waves triggered by crust disruptions could scatter off of relativistic charge bunches, boosting the frequency by γ^2 to GHz frequencies (Qu & B. Zhang, 2024; Rybicki & Lightman, 2024; B. Zhang, 2022).

Beyond energetics and polarization, FRBs are linked to magnetars by a series of FRB-like radio bursts produced by the Galactic magnetar SGR J1935+54. Simultaneously detected on April 28, 2020 by the Canadian Hydrogen Intensity Mapping Experiment (CHIME), the Survey for Transient Astronomical Radio Emission 2 (STARE2), and the Five-Hundred Metre Aperture Spherical Telescope (FAST), the first event lasted 0.61 ± 0.09 ms with isotropic luminosity $\sim 3.6 \times 10^{38}\,\mathrm{erg\,s^{-1}}$. While the flare, referred to as FRB 20200428, was around two orders of magnitude fainter than the weakest FRBs, it remains the most energetic magnetar radio flare detected to date (Bochenek et al., 2020; CHIME/FRB Collaboration et al., 2020). Unlike FRBs, which have never been associated with X-ray, gamma-ray, UV, or OIR counterparts, FRB 20200428 was coincident with a ~ 0.6 s X-ray burst.

While other SGR J1935+54 flares have had softer spectra (steepen below 200 keV) and fit equally to double blackbody and power law models (e.g., Kozlova et al., 2016), the coincident $\sim 10^{38}\,\mathrm{erg\,s^{-1}}$ X-ray burst is best-fit to a power law which hardens across the triple-peaked burst profile, more closely resembling some short GRBs (see Section 1.6.1; C. Li et al., 2021; Mereghetti et al., 2020; Ridnaia et al., 2021). The FRB and X-ray burst followed a glitch in which the rotation frequency increased by $\Delta\nu/\nu = 5.8^{+2.6}_{-1.6} \times 10^{-6}$, suggesting its unique properties were triggered by a disruption in the magnetar crust (Younes et al., 2023). Two weaker radio bursts were detected in late 2020 with no simultaneous X-ray emission, kicking off a month-long outburst phase in which periodic radio pulsations were detected for the first time from SGR J1935+54 (Kirsten et al., 2021; Zhu et al., 2023). Finally, two FRB-like bursts were detected in October Dong & Chime/Frb Collaboration (2022), Maan et al. (2022), and Mereghetti et al. (2022) and December 2022 (Pearlman & Chime/Frb Collaboration, 2022), respectively; the former (FRB 20221014) was recently associated with another glitch (C.-P. Hu et al., 2025) and an X-ray burst (C.-W. Wang et al., 2026). These follow-up FRBs indicate that magnetars could feasibly be the source of repeating FRBs in addition to non-repeaters. Since no other Galactic magnetars have produced FRBs, it is unclear whether SGR J1935+54 is a unique neutron star or if all magnetars can produce FRB-like events. Association of an FRB with an X-ray flare would confirm the magnetar-FRB model, but prospects are limited since the SGR J1935+54 X-ray burst luminosity would not be detectable at extragalactic distances.

1.7 Outline and Questions Addressed in this Thesis

In this thesis, I strive to understand the unique formation and evolution of magnetars and their connection to radio transients including FRBs and LPRTs. To this end, we explore the following questions.

1.7.1 What factors cause magnetars to have large magnetic field strengths?

In Chapter 2, we probe the progenitor and formation process of the 30 magnetars and candidates from the McGill sample using archival radio and OIR catalog data. Using statistical methods, we place constraints on the magnetar binary fraction and CCSN formation scenario. In Chapter 3, we extend these results using simulations to predict the magnetar population based on the binary and merger fractions derived in Chapter 2. In Chapter 4, we re-estimate the magnetar scale height and compare it to other Galactic populations to investigate formation scenarios.

1.7.2 Are all LPTs White Dwarf-M-dwarf Binaries?

In Chapter 5, we search for LPTs in the galactic plane using the Deep Synoptic Array (DSA-110) radio interferometer at the Owens Valley Radio Observatory (OVRO). Beyond testing single-pulse search strategies for $\gtrsim$ 134 ms transients, we place limits on the LPT burst rate within the plane and consider the implications for White Dwarf-M-dwarf binary models and magnetar models for LPT emission.

1.7.3 What process drives FRB emission, and which propagation effects result from the local and galactic environment?

In Chapter 6 we use one of the largest uniform samples of FRB linear and circular polarization to determine the most common properties among the FRB population. By investigating individual cases and comparing the population properties to those of Galactic pulsars, we determine the impact of the magnetized circumstellar and interstellar media on FRB polarization. In Chapter 7 we use FRBs' RMs, DMs, and host galaxy redshifts to learn about their magnetic environments, again comparing to Milky Way pulsars to search for unique trends that hint towards their progenitors' natures.

1.7.4 What is the future of pulsar, magnetar, LPRT, and FRB astronomy?

In Chapter 8, we look ahead, quantifying the promise of next-generation telescopes like the DSA-2000 by forecasting the pulsar yields. We summarize the thesis in Chapter 9 and look towards future prospects for FRB and LPRT searches.

CHAPTER 1 BIBLIOGRAPHY

Abbott, B. P. et al. (2016). "Observation of gravitational waves from a binary black hole merger". In: *Physical review letters* 116.6, p. 061102.

Abramovici, A. et al. (1992). "LIGO: The laser interferometer gravitational-wave observatory". In: *science* 256.5055, pp. 325–333.

Acharya, B. et al. (2025). "Solar fusion III: New data and theory for hydrogen-burning stars". In: *Reviews of Modern Physics* 97.3, p. 035002.

Agarwal, D. et al. (2026). "The RRATalog: a Galactic census of rotating radio transients". In: *Monthly Notices of the Royal Astronomical Society*, stag787.

Anderson, G. E. et al. (May 2012). "Multi-wavelength Observations of the Radio Magnetar PSR J1622-4950 and Discovery of Its Possibly Associated Supernova Remnant". In: *The Astrophysical Journal* 751.1, 53, p. 53. DOI: 10.1088/0004-637X/751/1/53. arXiv: 1203.2719 [astro-ph.HE].

Anna-Thomas, R. et al. (2023). "Magnetic field reversal in the turbulent environment around a repeating fast radio burst". In: *Science* 380.6645, pp. 599–603.

Anumarlapudi, A. et al. (2025). "ASKAP J144834- 685644: a newly discovered long period radio transient detected from radio to X-rays". In: *Monthly Notices of the Royal Astronomical Society* 542.2, pp. 1208–1232.

Baade, W. & F. Zwicky (1934). "Remarks on super-novae and cosmic rays". In: *Physical Review* 46.1, p. 76.

Bai, J. et al. (Feb. 2025). "Deep Searches for Radio Pulsations and Bursts from Four Magnetar and a Magnetar-like Pulsar with FAST". In: *The Astrophysical Journal* 979.2, 122, p. 122. DOI: 10.3847/1538-4357/ada3c4. arXiv: 2412.20050 [astro-ph.HE].

Baring, M. G. & A. K. Harding (1996). "Photon splitting in magnetar models of soft gamma repeaters". In: *AIP Conference Proceedings*. Vol. 366. 1. American Institute of Physics, pp. 129–133.

Barthelmy, S. D. et al. (Jan. 2015). "Trigger 632888: Swift detection of the magnetar 4U 0142+61." In: *GRB Coordinates Network* 17507, p. 1.

Barthelmy, S. D. et al. (Mar. 2016). "Swift detection of a likely new SGR: SGR 0755-2933". In: *The Astronomer's Telegram* 8831, p. 1.

Bause, M. L. et al. (Sept. 2025). "Searching for radio emission from radio quiet magnetars with MeerKAT". In: *arXiv e-prints*, arXiv:2509.14043, arXiv:2509.14043. DOI: 10.48550/arXiv.2509.14043. arXiv: 2509.14043 [astro-ph.HE].

Bell Burnell, S. J. (2004). *So few pulsars, so few females*.

Beniamini, P. et al. (2023). “Evidence for an abundant old population of Galactic ultra-long period magnetars and implications for fast radio bursts”. In: *Monthly Notices of the Royal Astronomical Society* 520.2, pp. 1872–1894.

Bernardini, F. et al. (2009). “From outburst to quiescence: the decay of the transient AXP XTE J1810-197”. In: *Astronomy & Astrophysics* 498.1, pp. 195–207.

Bloot, S. et al. (2025). “Strongly polarised radio pulses from a new white-dwarf-hosting long-period transient”. In: *Astronomy & Astrophysics* 699, A341.

Bochenek, C. D. et al. (2020). “A fast radio burst associated with a Galactic magnetar”. In: *Nature* 587.7832, pp. 59–62.

Borghese, A. et al. (2025). “A magnetar outburst with atypical evolution: the case of Swift J1555. 2-5402”. In: *arXiv preprint arXiv:2512.08692*.

– (2026). “A magnetar outburst with atypical evolution: The case of Swift J1555. 2–5402”. In: *Astronomy & Astrophysics* 706, A28.

Braithwaite, J. & H. Spruit (2006). “Evolution of the magnetic field in magnetars”. In: *Astronomy & Astrophysics* 450.3, pp. 1097–1106.

Brentjens, M. A. & A. De Bruyn (2005). “Faraday rotation measure synthesis”. In: *Astronomy & Astrophysics* 441.3, pp. 1217–1228.

Burn, B. (1966). “On the depolarization of discrete radio sources by Faraday dispersion”. In: *Monthly Notices of the Royal Astronomical Society* 133.1, pp. 67–83.

Burns, E. et al. (Feb. 2021). “Identification of a Local Sample of Gamma-Ray Bursts Consistent with a Magnetar Giant Flare Origin”. In: *The Astrophysical Journal Letters* 907.2, L28, p. L28. DOI: 10.3847/2041-8213/abd8c8. arXiv: 2101.05144 [astro-ph.HE].

Caleb, M. et al. (May 2022). “Discovery of a radio-emitting neutron star with an ultra-long spin period of 76 s”. In: *Nature Astronomy* 6, pp. 828–836. DOI: 10.1038/s41550-022-01688-x. arXiv: 2206.01346 [astro-ph.HE].

Caleb, M. et al. (2024). “An emission-state-switching radio transient with a 54-minute period”. In: *Nature Astronomy* 8.9, pp. 1159–1168.

Camilo, F. et al. (2008). “The Magnetar 1E 1547.0–5408: Radio Spectrum, Polarimetry, and Timing”. In: *The Astrophysical Journal* 679.1, pp. 681–686.

Camilo, F. et al. (2016). “Radio disappearance of the magnetar XTE J1810–197 and continued X-ray timing”. In: *The Astrophysical Journal* 820.2, p. 110.

Camilo, F. et al. (Sept. 2000). “Discovery of Two High Magnetic Field Radio Pulsars”. In: *The Astrophysical Journal* 541.1, pp. 367–373. DOI: 10.1086/309435. arXiv: astro-ph/0004330 [astro-ph].

Camilo, F. et al. (Sept. 2007). “1E 1547.0-5408: A Radio-emitting Magnetar with a Rotation Period of 2 Seconds”. In: *The Astrophysical Journal Letters* 666.2, pp. L93–L96. DOI: 10.1086/521826. arXiv: 0708.0002 [astro-ph].

Castro-Tirado, A. J. et al. (2008). "Flares from a candidate Galactic magnetar suggest a missing link to dim isolated neutron stars". In: *Nature* 455.7212, pp. 506–509.

Chen, K. & M. Ruderman (1993). "Pulsar death lines and death valley". In: *Astrophysical Journal, Part 1 (ISSN 0004-637X), vol. 402, no. 1, p. 264-270.* 402, pp. 264–270.

Chen, R.-C. et al. (2023). "Detection of Quasi-periodic Oscillations in SGR 150228213". In: *Research in Astronomy and Astrophysics* 23.8, p. 085018.

Cheng, A. F. & M. Ruderman (1980). "Particle acceleration and radio emission above pulsar polar caps". In: *Astrophysical Journal, Part 1, vol. 235, Jan. 15, 1980, p. 576-586. NSF-supported research.* 235, pp. 576–586.

CHIME/FRB Collaboration et al. (Nov. 2020). "A bright millisecond-duration radio burst from a Galactic magnetar". In: *Nature* 587.7832, pp. 54–58. DOI: 10.1038/s41586-020-2863-y. arXiv: 2005.10324 [astro-ph.HE].

Chrimes, A. et al. (2022). "New candidates for magnetar counterparts from a deep search with the Hubble Space Telescope". In: *Monthly Notices of the Royal Astronomical Society* 512.4, pp. 6093–6103.

Cline, T. et al. (Mar. 2000). "Observations of a Possible New Soft Gamma Repeater, SGR 1801-23". In: *The Astrophysical Journal* 531.1, pp. 407–410. DOI: 10.1086/308470. arXiv: astro-ph/9909054 [astro-ph].

Condon, J. J. & S. M. Ransom (2016). *Essential radio astronomy*. Princeton University Press.

Cordes, J. M. & T. J. W. Lazio (2002). "NE2001. I. A new model for the galactic distribution of free electrons and its fluctuations". In: *arXiv preprint astro-ph/0207156*.

Crawford, F., J. W. T. Hessels, & V. M. Kaspi (June 2007). "Deep Searches for Radio Pulsations and Bursts from Four Southern Anomalous X-Ray Pulsars". In: *The Astrophysical Journal* 662.2, pp. 1183–1187. DOI: 10.1086/517991. arXiv: astro-ph/0703246 [astro-ph].

Crawford, F. et al. (2001). "Radio pulsars in the magellanic clouds". In: *The Astrophysical Journal* 553.1, p. 367.

Crider, A. (2006). "A magnetar flare in the BATSE catalog?" In: *AIP Conference Proceedings*. Vol. 836. 1. American Institute of Physics, pp. 64–67.

D'Aì, A. et al. (2016). "Evidence for the magnetar nature of 1E 161348- 5055 in RCW 103". In: *Monthly Notices of the Royal Astronomical Society* 463.3, pp. 2394–2404.

De Luca, A. et al. (Aug. 2006). "A Long-Period, Violently Variable X-ray Source in a Young Supernova Remnant". In: *Science* 313.5788, pp. 814–817. DOI: 10.1126/science.1129185. arXiv: astro-ph/0607173 [astro-ph].

De Luca, A. et al. (Aug. 2008). "Deep Infrared Observations of the Puzzling Central X-Ray Source in RCW 103". In: *The Astrophysical Journal* 682.2, pp. 1185–1194. DOI: 10.1086/588600. arXiv: 0803.2885 [astro-ph].

de Ruiter, I. et al. (May 2025a). "Publisher Correction: Sporadic radio pulses from a white dwarf binary at the orbital period". In: *Nature Astronomy* 9, pp. 747–747. DOI: 10.1038/s41550-025-02540-8.

– (May 2025b). "Sporadic radio pulses from a white dwarf binary at the orbital period". In: *Nature Astronomy* 9, pp. 672–684. DOI: 10.1038/s41550-025-02491-0. arXiv: 2408.11536 [astro-ph.HE].

Demirer, M. et al. (2025). "Detailed Time Resolved Spectral and Temporal Investigations of SGR J1550-5418 Bursts Detected with Fermi/Gamma-ray Burst Monitor". In: *arXiv preprint arXiv:2506.04414*.

Dessert, C., J. W. Foster, & B. R. Safdi (2020). "Hard X-ray excess from the magnificent seven neutron stars". In: *The Astrophysical Journal* 904.1, p. 42.

Dobie, D. et al. (2024). "A two-minute burst of highly polarized radio emission originating from low Galactic latitude". In: *Monthly Notices of the Royal Astronomical Society* 535.1, pp. 909–923.

Dong, F. A. & Chime/Frb Collaboration (Oct. 2022). "CHIME/FRB Detection of a Bright Radio Burst from SGR 1935+2154". In: *The Astronomer's Telegram* 15681, p. 1.

Dong, F. A. et al. (July 2025a). "CHIME/Fast Radio Burst Discovery of an Unusual Circularly Polarized Long-period Radio Transient with an Accelerating Spin Period". In: *The Astrophysical Journal Letters* 988.1, L29, p. L29. DOI: 10.3847/2041-8213/adeaab. arXiv: 2507.05139 [astro-ph.HE].

Dong, F. A. et al. (Sept. 2025b). "CHIME/Fast Radio Burst/Pulsar Discovery of a Nearby Long-period Radio Transient with a Timing Glitch". In: *The Astrophysical Journal Letters* 990.2, L49, p. L49. DOI: 10.3847/2041-8213/adfa8e. arXiv: 2407.07480 [astro-ph.HE].

Doroshenko, V. et al. (2021). "SGR 0755- 2933: a new high-mass X-ray binary with the wrong name". In: *Astronomy & Astrophysics* 647, A165.

Dorozsmai, A. & S. Toonen (2024). "Importance of stable mass transfer and stellar winds for the formation of gravitational wave sources". In: *Monthly Notices of the Royal Astronomical Society* 530.4, pp. 3706–3739.

Duncan, R. C. & C. Thompson (1992). "Formation of very strongly magnetized neutron stars-Implications for gamma-ray bursts". In: *Astrophysical Journal, Part 2-Letters (ISSN 0004-637X), vol. 392, no. 1, June 10, 1992, p. L9-L13. Research supported by NSERC.* 392, pp. L9–L13.

Eldridge, J. & E. R. Stanway (2016). "BPASS predictions for binary black hole mergers". In: *Monthly Notices of the Royal Astronomical Society* 462.3, pp. 3302–3313.

Enoto, T. et al. (Oct. 2021). "A Month of Monitoring the New Magnetar Swift J1555.2-5402 during an X-Ray Outburst". In: *The Astrophysical Journal Letters* 920.1, L4, p. L4. DOI: 10.3847/2041-8213/ac2665. arXiv: 2108.02939 [astro-ph.HE].

Esposito, P. et al. (Nov. 2011). "Swift monitoring of the central X-ray source in RCW 103". In: *Monthly Notices of the Royal Astronomical Society* 418.1, pp. 170–175. DOI: 10.1111/j.1365-2966.2011.19473.x. arXiv: 1107.3770 [astro-ph.HE].

Esposito, P. et al. (2007). "Swift/XRT monitoring of five orbital cycles of LS I+ 61° 303". In: *Astronomy & Astrophysics* 474.2, pp. 575–578.

Esposito, P. et al. (2020). "A very young radio-loud magnetar". In: *The Astrophysical Journal Letters* 896.2, p. L30.

Feng, Y. et al. (2022a). "Circular polarization in two active repeating fast radio bursts". In: *Science Bulletin* 67.23, pp. 2398–2401.

Feng, Y. et al. (2022b). "Frequency-dependent polarization of repeating fast radio bursts—implications for their origin". In: *Science* 375.6586, pp. 1266–1270.

Ferrario, L., D. de Martino, & B. T. Gänsicke (2015). "Magnetic white dwarfs". In: *Space Science Reviews* 191.1, pp. 111–169.

Gaensler, B. M., E. V. Gotthelf, & G. Vasisht (Nov. 1999). "A New Supernova Remnant Coincident with the Slow X-Ray Pulsar AX J1845-0258". In: *The Astrophysical Journal Letters* 526.1, pp. L37–L40. DOI: 10.1086/312362. arXiv: astro-ph/9909400 [astro-ph].

Garmire, G. P. et al. (Jan. 2000). "1E 161348-5055". In: *International Astronomical Union Circulars* 7350, p. 2.

Gavriil, F. P., V. Kaspi, & P. Woods (2002). "Magnetar-like X-ray bursts from an anomalous X-ray pulsar". In: *Nature* 419.6903, pp. 142–144.

Gavriil, F. P. et al. (2008). "Magnetar-like emission from the young pulsar in Kes 75". In: *Science* 319.5871, pp. 1802–1805.

Gehrels, N. & P. Mészáros (2012). "Gamma-ray bursts". In: *Science* 337.6097, pp. 932–936.

Gil, J., G. I. Melikidze, & U. Geppert (2003). "Drifting subpulses and inner acceleration regions in radio pulsars". In: *Astronomy & Astrophysics* 407.1, pp. 315–324.

Goldreich, P. & W. H. Julian (1969). "Pulsar electrodynamics". In: *Astrophysical Journal, vol. 157, p. 869* 157, p. 869.

Gordon, A. C. et al. (2023). "The demographics, stellar populations, and star formation histories of fast radio burst host galaxies: implications for the progenitors". In: *The Astrophysical Journal* 954.1, p. 80.

Gotthelf, E. V. et al. (Oct. 2000). "A 700 Year-old Pulsar in the Supernova Remnant Kesteven 75". In: *The Astrophysical Journal Letters* 542.1, pp. L37–L40. DOI: 10.1086/312923. arXiv: astro-ph/0008097 [astro-ph].

Gotthelf, E. V. et al. (Apr. 2004). "Imaging X-Ray, Optical, and Infrared Observations of the Transient Anomalous X-Ray Pulsar XTE J1810-197". In: *The Astrophysical Journal* 605.1, pp. 368–377. DOI: 10.1086/382232. arXiv: astro-ph/0309745 [astro-ph].

Granot, J. et al. (2017). "Learning about the magnetar Swift J1834. 9- 0846 from its wind nebula". In: *Monthly Notices of the Royal Astronomical Society* 464.4, pp. 4895–4926.

Gregory, P. & G. Fahlman (1980). "An extraordinary new celestial X-ray source". In: *Nature* 287.5785, pp. 805–806.

Haberl, F. (2007). "The magnificent seven: magnetic fields and surface temperature distributions". In: *Astrophysics and Space Science* 308, pp. 181–190.

Halpern, J. et al. (2008). "Outburst of the 2 s Anomalous X-Ray Pulsar 1E 1547.0–5408". In: *The Astrophysical Journal* 676.2, p. 1178.

Han, J. et al. (2021). "The FAST Galactic Plane Pulsar Snapshot survey: I. Project design and pulsar discoveries". In: *Research in Astronomy and Astrophysics* 21.5, p. 107.

Han, J. et al. (2025). "The FAST Galactic Plane Pulsar Snapshot Survey. VI. The Discovery of 473 New Pulsars". In: *Research in Astronomy and Astrophysics* 25.1, p. 014001.

Hansen, C. J. & S. D. Kawaler (1994). "An Overview of Stellar Evolution". In: *Stellar Interiors: Physical Principles, Structure, and Evolution*, pp. 35–108.

Hewish, A. (1968). "Pulsars". In: *Scientific American* 219.4, pp. 25–35.

Hewish, A. et al. (1979). "Observation of a rapidly pulsating radio source". In: *A Source Book in Astronomy and Astrophysics, 1900–1975*. Harvard University Press, pp. 498–504.

Horváth, C. et al. (Sept. 2025). "A long period transient search method for the Murchison Widefield Array". In: *Publications of the Astronomical Society of Australia* 42, e129, e129. DOI: 10.1017/pasa.2025.10093. arXiv: 2509.06315 [astro-ph.IM].

Hu, C.-P. et al. (2025). "Rapid Spectral Evolution of SGR 1935+ 2154 during Its 2022 Outburst". In: *The Astrophysical Journal* 989.1, p. 63.

Hu, R.-C. & B. Zhang (2026). "Formation Channels of Magnetars". In: *The Astrophysical Journal* 999.1, p. 102.

Hurley, K. et al. (2005). "An exceptionally bright flare from SGR 1806–20 and the origins of short-duration γ-ray bursts". In: *Nature* 434.7037, pp. 1098–1103.

Hurley-Walker, N. et al. (Jan. 2022). "A radio transient with unusually slow periodic emission". In: *Nature* 601.7894, pp. 526–530. DOI: 10.1038/s41586-021-04272-x. arXiv: 2503.08033 [astro-ph.HE].

Hurley-Walker, N. et al. (July 2023). "A long-period radio transient active for three decades". In: *Nature* 619.7970, pp. 487–490. DOI: 10.1038/s41586-023-06202-5. arXiv: 2503.08036 [astro-ph.HE].

Hurley-Walker, N. et al. (2024). "A 2.9 hr Periodic Radio Transient with an Optical Counterpart". In: *The Astrophysical Journal Letters* 976.2, L21, p. L21. DOI: 10.3847/2041-8213/ad890e. arXiv: 2408.15757 [astro-ph.SR].

Hyman, S. D. et al. (2005). "A powerful bursting radio source towards the Galactic Centre". In: *nature* 434.7029, pp. 50–52.

Hyman, S. D. et al. (2007). "A faint, steep-spectrum burst from the radio transient GCRT J1745–3009". In: *The Astrophysical Journal Letters* 660.2, pp. L121–L124.

Imbrogno, M. et al. (Oct. 2023). "Discovery of a magnetar candidate X-ray pulsar in the Large Magellanic Cloud". In: *Monthly Notices of the Royal Astronomical Society* 524.4, pp. 5566–5574. DOI: 10.1093/mnras/stad2173. arXiv: 2307.09224 [astro-ph.HE].

Janssen, G. H. & B. W. Stappers (2006). "30 glitches in slow pulsars". In: *aap* 457, pp. 611–618. DOI: 10.1051/0004-6361:20065267.

Kaspi, V. M. & A. M. Beloborodov (2017). "Magnetars". In: *Annual Review of Astronomy and Astrophysics* 55.1, pp. 261–301.

Keane, E. & M. McLaughlin (2011). "Rotating radio transients". In: *arXiv preprint arXiv:1109.6896*.

Keane, E. F. & M. Kramer (2008). "On the birthrates of Galactic neutron stars". In: *Monthly Notices of the Royal Astronomical Society* 391.4, pp. 2009–2016.

Kirsten, F. et al. (2021). "Detection of two bright radio bursts from magnetar SGR 1935+ 2154". In: *Nature Astronomy* 5.4, pp. 414–422.

Kouveliotou, C. et al. (Aug. 1993a). "Identification of Two Classes of Gamma-Ray Bursts". In: *The Astrophysical Journal Letters* 413, p. L101. DOI: 10.1086/186969.

Kouveliotou, C. et al. (Apr. 1993b). "Recurrent burst activity from the soft γ-ray repeater SGR 1900+14". In: *Nature* 362.6422, pp. 728–730. DOI: 10.1038/362728a0.

Kozlova, A. et al. (2016). "The first observation of an intermediate flare from SGR 1935+ 2154". In: *Monthly Notices of the Royal Astronomical Society* 460.2, pp. 2008–2014.

Kuiper, L. & W. Hermsen (2015). "The soft γ-ray pulsar population: a high-energy overview". In: *Monthly Notices of the Royal Astronomical Society* 449.4, pp. 3827–3866.

Lamb, D. et al. (Aug. 2003). "SGR 1808-20 (=H2802): A Possible new SGR". In: *GRB Coordinates Network* 2351, p. 1.

Lamb, R. C. et al. (July 2002). "Discovery of a Possible Anomalous X-Ray Pulsar in the Small Magellanic Cloud". In: *The Astrophysical Journal Letters* 574.1, pp. L29–L32. DOI: 10.1086/342352. arXiv: astro-ph/0205310 [astro-ph].

Laplace, E. et al. (2021). "Different to the core: The pre-supernova structures of massive single and binary-stripped stars". In: *Astronomy & Astrophysics* 656, A58.

Laros, J. G. et al. (Sept. 1987). "A New Type of Repetitive Behavior in a High-Energy Transient". In: *The Astrophysical Journal Letters* 320, p. L111. DOI: 10.1086/184985.

Lee, Y. et al. (2025). "The emission of interpulses by a 6.45-h-period coherent radio transient". In: *Nature Astronomy* 9.3, pp. 393–405.

Levin, L. et al. (Sept. 2010). "A Radio-loud Magnetar in X-ray Quiescence". In: *ApJ* 721.1, pp. L33–L37. DOI: 10.1088/2041-8205/721/1/L33. arXiv: 1007.1052 [astro-ph.HE].

– (2012). "Radio emission evolution, polarimetry and multifrequency single pulse analysis of the radio magnetar PSR J1622- 4950". In: *Monthly Notices of the Royal Astronomical Society* 422.3, pp. 2489–2500.

Li, C. et al. (2021). "HXMT identification of a non-thermal X-ray burst from SGR J1935+ 2154 and with FRB 200428". In: *Nature Astronomy* 5.4, pp. 378–384.

Li, D. et al. (Nov. 2024a). "A 44-minute periodic radio transient in a supernova remnant". In: *arXiv e-prints*, arXiv:2411.15739, arXiv:2411.15739. DOI: 10.48550/arXiv.2411.15739. arXiv: 2411.15739 [astro-ph.HE].

– (2024b). "A 44-minute periodic radio transient in a supernova remnant". In: *arXiv preprint arXiv:2411.15739*.

Lien, A. et al. (Sept. 2016). "The Third Swift Burst Alert Telescope Gamma-Ray Burst Catalog". In: *The Astrophysical Journal* 829.1, 7, p. 7. DOI: 10.3847/0004-637X/829/1/7. arXiv: 1606.01956 [astro-ph.HE].

Lorimer, D. R. (2008). "Binary and millisecond pulsars". In: *Living reviews in relativity* 11.1, p. 8.

Lorimer, D. R. et al. (2007). "A bright millisecond radio burst of extragalactic origin". In: *Science* 318.5851, pp. 777–780.

LS, I. (n.d.). "Bayesian Analysis of Radio Observations of the Be X-ray Binary". In: ().

Lu, W.-J. et al. (2024). "Upper limits on the radio pulses from magnetars and a central compact object with FAST". In: *The Astrophysical Journal* 963.2, p. 151.

Lyubarskii, Y. E. (July 1996). "A model for the energetic emission from pulsars." In: *Astronomy & Astrophysics* 311, pp. 172–178.

Lyubarsky, Y. (2014). "A model for fast extragalactic radio bursts". In: *Monthly Notices of the Royal Astronomical Society: Letters* 442.1, pp. L9–L13.

Maan, Y. et al. (Oct. 2022). "GBT detection of bright 5 GHz radio bursts from SGR 1935+2154, coincident with X-ray and 600 MHz bursts". In: *The Astronomer's Telegram* 15697, p. 1.

Makishima, K., N. Uchida, & T. Enoto (2026). "Evidence for 1.01 s pulsations of the Central Compact Object in the supernova remnant RCW 103 with ASCA, XMM-Newton, and NuSTAR". In: *Publications of the Astronomical Society of Japan* 78.2, pp. 688–709.

Makishima, K. et al. (2023). "Further Evidence for the 9 s Pulsation in LS 5039 from NuSTAR and ASCA". In: *The Astrophysical Journal* 959.2, p. 79.

Manchester, R. N. et al. (2005). "The Australia telescope national facility pulsar catalogue". In: *The Astronomical Journal* 129.4, p. 1993.

Mazets, E. P., S. V. Golenetskij, & Y. A. Guryan (1979a). "Soft gamma-ray bursts from the source B1900+14". In: *Soviet Astronomy Letters* 5, p. 343.

Mazets, E. P. et al. (1979b). "Observations of a flaring X-ray pulsar in Dorado". In: *Nature* 282.5739, pp. 587–589. DOI: 10.1038/282587a0.

Mckinven, R. et al. (2025). "A pulsar-like polarization angle swing from a nearby fast radio burst". In: *Nature* 637.8044, pp. 43–47.

McLaughlin, M. A. et al. (2006). "Transient radio bursts from rotating neutron stars". In: *Nature* 439.7078, pp. 817–820.

McSweeney, S. J. et al. (2025). "A new long-period radio transient: discovery of pulses repeating every 1.16 h from ASKAP J175534. 9- 252749.1". In: *Monthly Notices of the Royal Astronomical Society* 542.1, pp. 203–214.

Meegan, C. et al. (1992). "Spatial distribution of γ-ray bursts observed by BATSE". In: *Nature* 355.6356, pp. 143–145.

Mereghetti, S. et al. (2020). "INTEGRAL discovery of a burst with associated radio emission from the magnetar SGR 1935+ 2154". In: *The Astrophysical Journal Letters* 898.2, p. L29.

Mereghetti, S. et al. (2022). "INTEGRAL detection of a burst from SGR J1935+ 2154". In: *GRB Coordinates Network* 32698, p. 1.

Mereghetti, S. et al. (Oct. 2012). "The magnetar candidate AX J1818.8-1559". In: *Astronomy & Astrophysics* 546, A30, A30. DOI: 10.1051/0004-6361/201219907. arXiv: 1208.0249 [astro-ph.HE].

Moe, M. & R. Di Stefano (2017). “Mind your Ps and Qs: the interrelation between period (P) and mass-ratio (Q) distributions of binary stars”. In: *The Astrophysical Journal Supplement Series* 230.2, p. 15.

Mori, K. et al. (Apr. 2013). “NuSTAR discovery of a 3.76 second pulsar in the Sgr A* region”. In: *The Astronomer’s Telegram* 5020, p. 1.

Nimmo, K. et al. (2025). “Magnetospheric origin of a fast radio burst constrained using scintillation”. In: *Nature* 637.8044, pp. 48–51.

Nomoto, K. & Y. Kondo (1991). “Conditions for accretion-induced collapse of white dwarfs”. In: *Astrophysical Journal, Part 2-Letters (ISSN 0004-637X), vol. 367, Jan. 20, 1991, p. L19-L22.* 367, pp. L19–L22.

Ofek, E. et al. (2006). “The short-hard GRB 051103: observations and implications for its nature”. In: *The Astrophysical Journal* 652.1, p. 507.

Ofek, E. et al. (2008). “GRB 070201: a possible soft gamma-ray repeater in M31”. In: *The Astrophysical Journal* 681.2, p. 1464.

Olausen, S. A. & V. M. Kaspi (May 2014). “The McGill Magnetar Catalog”. In: *The Astrophysical Journal Supplement Series* 212.1, 6, p. 6. DOI: 10.1088/0067-0049/212/1/6. arXiv: 1309.4167 [astro-ph.HE].

Pacholski, D., S. Mereghetti, & M. Topinka (2025). “INTEGRAL IBIS catalog of magnetar bursts”. In: *arXiv preprint arXiv:2512.14356*.

– (2026). “INTEGRAL IBIS catalog of magnetar bursts”. In: *The Astrophysical Journal* 997.2, p. 272.

Paciesas, W. S. et al. (June 1999). “The Fourth BATSE Gamma-Ray Burst Catalog (Revised)”. In: *The Astrophysical Journal Supplement Series* 122.2, pp. 465–495. DOI: 10.1086/313224. arXiv: astro-ph/9903205 [astro-ph].

Pagani, C. et al. (Jan. 2007). “GRB 070610: Swift detection of a burst.” In: *GRB Coordinates Network* 6489, p. 1.

Page, K. L. et al. (Oct. 2020). “Swift detection of a new SGR 1830-0645 or a short GRB 201010A”. In: *The Astronomer’s Telegram* 14083, p. 1.

Palmer, D. M. et al. (June 2021). “Swift Detection of probable new Swift SGR J1555.2-5402”. In: *GRB Coordinates Network* 30120, p. 1.

Pearlman, A. B. & Chime/Frb Collaboration (2022). “CHIME/FRB Detection of Another Bright Radio Burst from SGR 1935+2154”. In: *The Astronomer’s Telegram* 15792, p. 1.

Pennucci, T. T. et al. (2015). “Simultaneous multi-band radio and X-ray observations of the galactic center magnetar SGR 1745–2900”. In: *The Astrophysical Journal* 808.1, p. 81.

Petroff, E., J. Hessels, & D. Lorimer (2019). “Fast radio bursts”. In: *The Astronomy and Astrophysics Review* 27.1, p. 4.

Philippov, A. & M. Kramer (2022). “Pulsar magnetospheres and their radiation”. In: *Annual Review of Astronomy and Astrophysics* 60.1, pp. 495–558.

Pivovaroff, M. J., V. M. Kaspi, & F. Camilo (May 2000). “X-Ray Observations of the High Magnetic Field Radio Pulsar PSR J1814-1744”. In: *The Astrophysical Journal* 535.1, pp. 379–384. DOI: 10.1086/308848. arXiv: astro-ph/0001091 [astro-ph].

Pizzolato, F. et al. (2008). “1E 161348–5055 in the Supernova Remnant RCW 103: A Magnetar in a Young Low-Mass Binary System?” In: *The Astrophysical Journal* 681.1, p. 530.

Prayag, V. et al. (2026). “The TRAPUM Large Magellanic Cloud pulsar survey with MeerKAT–II. 12 new discoveries and timing solutions for 7 pulsars”. In: *Monthly Notices of the Royal Astronomical Society* 545.4, staf2193.

Pritchard, J. et al. (2026). “Discovery of a 36-minute long-period transient ASKAP J142431. 2-612611”. In: *arXiv preprint arXiv:2603.07857*.

Qu, Y. & B. Zhang (2023). “Polarization of fast radio bursts: radiation mechanisms and propagation effects”. In: *Monthly Notices of the Royal Astronomical Society* 522.2, pp. 2448–2477.

– (2024). “Coherent inverse compton scattering in fast radio bursts revisited”. In: *The Astrophysical Journal* 972.1, p. 124.

– (Mar. 2025). “Magnetic Interactions in White Dwarf Binaries as Mechanism for Long-period Radio Transients”. In: *The Astrophysical Journal* 981.1, 34, p. 34. DOI: 10.3847/1538-4357/adb1b5. arXiv: 2409.05978 [astro-ph.HE].

Ransom, S. M. (2001). *New search techniques for binary pulsars*. Harvard University.

Ravi, V. et al. (2025). “Deep Synoptic Array science: a 50 Mpc fast radio burst constrains the mass of the Milky Way circumgalactic medium”. In: *The Astronomical Journal* 169.6, p. 330.

Rea, N., N. Hurley-Walker, & M. Caleb (2026). “Long Period Transients (LPTs): a comprehensive review”. In: *Journal of High Energy Astrophysics*, p. 100566.

Reynoso, E. M. et al. (2004). “Influence of the Neutron Star 1E 161348–5055 in RCW 103 on the Surrounding Medium”. In: *Publications of the Astronomical Society of Australia* 21.1, pp. 82–88.

Richardson, N. D. et al. (2023). “A high-mass X-ray binary descended from an ultra-stripped supernova”. In: *Nature* 614.7946, pp. 45–47.

Ridnaia, A. et al. (2021). “A peculiar hard X-ray counterpart of a Galactic fast radio burst”. In: *Nature Astronomy* 5.4, pp. 372–377.

Roberts, O. J. (Jan. 2015). “Fermi GBM Observations of Magnetar 4U 0142+61.” In: *GRB Coordinates Network* 17508, p. 1.

Roberts, O. et al. (2021). “Rapid spectral variability of a giant flare from a magnetar in NGC 253”. In: *Nature* 589.7841, pp. 207–210.

Rodriguez, A. C. (Mar. 2025). “Spectroscopic detection of a 2.9-hour orbit in a long-period radio transient”. In: *Astronomy & Astrophysics* 695, L8, p. L8. DOI: 10.1051/0004-6361/202553684. arXiv: 2501.03315 [astro-ph.SR].

Ruderman, M. & P. G. Sutherland (1975). “Theory of pulsars-Polar caps, sparks, and coherent microwave radiation”. In: *Astrophysical Journal, vol. 196, Feb. 15, 1975, pt. 1, p. 51-72.* 196, pp. 51–72.

Ruiter, A. et al. (2019). “On the formation of neutron stars via accretion-induced collapse in binaries”. In: *Monthly Notices of the Royal Astronomical Society* 484.1, pp. 698–711.

Rybicki, G. B. & A. P. Lightman (2024). *Radiative processes in astrophysics*. John Wiley & Sons.

Sakamoto, T. et al. (Apr. 2011). “Probing the nature of short swift bursts via deep INTEGRAL monitoring of GRB 050925”. In: *Advances in Space Research* 47.8, pp. 1346–1352. DOI: 10.1016/j.asr.2010.08.004. arXiv: 1008.0226 [astro-ph.HE].

Salpeter, E. E. (1955). “The luminosity function and stellar evolution.” In: *Astrophysical Journal, vol. 121, p. 161* 121, p. 161.

Schatz, H. & K. Rehm (2006). “X-ray binaries”. In: *Nuclear physics A* 777, pp. 601–622.

Schenck, A., S. Park, & S. Post (2016). “A Chandra Study of the Interstellar Metallicity in the Large Magellanic Cloud Using Supernova Remnants”. In: *The Astronomical Journal* 151.6, p. 161.

Seward, F. D., P. A. Charles, & A. P. Smale (June 1986). “A 6 Second Periodic X-Ray Source in Carina”. In: *The Astrophysical Journal* 305, p. 814. DOI: 10.1086/164294.

Sharma, K. et al. (2024). “Preferential occurrence of fast radio bursts in massive star-forming galaxies”. In: *Nature* 635.8037, pp. 61–66.

Sharma, R. et al. (2023). “AstroSat observation of the magnetar SGR J1830- 0645 during its first detected X-ray outburst”. In: *Monthly Notices of the Royal Astronomical Society* 526.4, pp. 4877–4884.

Smartt, S. J. (2009). “Progenitors of core-collapse supernovae”. In: *Annual Review of Astronomy and Astrophysics* 47.1, pp. 63–106.

Spitkovsky, A. (Sept. 2006). “Time-dependent Force-free Pulsar Magnetospheres: Axisymmetric and Oblique Rotators”. In: *The Astrophysical Journal Letters* 648.1, pp. L51–L54. DOI: 10.1086/507518. arXiv: astro-ph/0603147 [astro-ph].

Spitler, L. et al. (2014). "Fast radio burst discovered in the Arecibo pulsar ALFA survey". In: *The Astrophysical Journal* 790.2, p. 101.

Stefanescu, A. et al. (Sept. 2007). "OPTIMA-Burst – Catching GRB Afterglows (and other Transients) with High Time Resolution". In: *Astronomische Nachrichten* 328.7, p. 620.

Stefanescu, A. et al. (Sept. 2008). "Very fast optical flaring from a possible new Galactic magnetar". In: *Nature* 455.7212, pp. 503–505. DOI: 10.1038/nature07308. arXiv: 0809.4043 [astro-ph].

Suresh, A. & J. M. Cordes (2019). "Induced polarization from birefringent pulse splitting in magneto-ionic media". In: *The Astrophysical Journal* 870.1, p. 29.

Surnis, M. P. et al. (Nov. 2023). "Discovery of an extremely intermittent periodic radio source". In: *Monthly Notices of the Royal Astronomical Society* 526.1, pp. L143–L148. DOI: 10.1093/mnrasl/slad082. arXiv: 2306.10817 [astro-ph.HE].

Suvorov, A. G. & K. Glampedakis (2022). "Does the Gamma-Ray Binary LS I + 61°303 Harbor a Magnetar?" In: *The Astrophysical Journal* 940.2, 128, p. 128. DOI: 10.3847/1538-4357/ac9b48. arXiv: 2210.09471 [astro-ph.HE].

Szary, A., G. I. Melikidze, & J. Gil (2015). "On the origin of radio emission from magnetars". In: *The Astrophysical Journal* 800.1, p. 76.

Tam, C. R. et al. (Nov. 2006). "Chandra Observations of the Transient 7 s X-ray Pulsar AX J1845.0-0258". In: *The Astrophysical Journal* 652.1, pp. 548–553. DOI: 10.1086/507262. arXiv: astro-ph/0602522 [astro-ph].

Tan, C. et al. (2018). "LOFAR Discovery of a 23.5 s Radio Pulsar". In: *The Astrophysical Journal* 866.1, p. 54.

Tan, C. et al. (2023). "X-ray non-detection of PSR J0250+ 5854". In: *Monthly Notices of the Royal Astronomical Society* 520.4, pp. 5960–5963.

Tendulkar, S. P. et al. (2017). "The host galaxy and redshift of the repeating fast radio burst FRB 121102". In: *The Astrophysical Journal Letters* 834.2, p. L7.

Torii, K. et al. (Aug. 1998). "Discovery of a 7 Second X-Ray Pulsar, AX J1845.0-0300". In: *The Astrophysical Journal* 503.2, pp. 843–847. DOI: 10.1086/306038.

Trigg, A. C. et al. (July 2024). "GRB 180128A: A second magnetar giant flare candidate from the Sculptor Galaxy". In: *Astronomy & Astrophysics* 687, A173, A173. DOI: 10.1051/0004-6361/202348858. arXiv: 2311.09362 [astro-ph.HE].

Trigg, A. C. et al. (Feb. 2025). "Extragalactic magnetar giant flare GRB 231115A: Insights from Fermi/GBM observations". In: *Astronomy & Astrophysics* 694, A323, A323. DOI: 10.1051/0004-6361/202452268. arXiv: 2409.06056 [astro-ph.HE].

Truelove, J. K. & C. F. McKee (1999). "Evolution of nonradiative supernova remnants". In: *The Astrophysical Journal Supplement Series* 120.2, p. 299.

Turolla, R. (2009). “Isolated neutron stars: the challenge of simplicity”. In: *Neutron stars and pulsars*. Springer, pp. 141–163.

Volkov, I. et al. (2021). “NuSTAR observation of LS 5039”. In: *The Astrophysical Journal* 915.1, p. 61.

von Kienlin, A. et al. (Apr. 2020). “The Fourth Fermi-GBM Gamma-Ray Burst Catalog: A Decade of Data”. In: *The Astrophysical Journal* 893.1, 46, p. 46. DOI: 10.3847/1538-4357/ab7a18. arXiv: 2002.11460 [astro-ph.HE].

Wang, C.-W. et al. (Mar. 2026). “GECAM discovery of the second FRB-associated magnetar X-ray burst from SGR J1935+2154”. In: *MNRAS* 546.4, stag312, stag312. DOI: 10.1093/mnras/stag312. arXiv: 2602.10895 [astro-ph.HE].

Wang, H.-H. et al. (Oct. 2020). “A Multiwavelength Study of PSR J1119-6127 after 2016 Outburst”. In: *The Astrophysical Journal* 902.2, 96, p. 96. DOI: 10.3847/1538-4357/abb3c4. arXiv: 2008.12585 [astro-ph.HE].

Wang, W.-Y. et al. (2022). “Polarization of magnetospheric curvature radiation in repeating fast radio bursts”. In: *Monthly Notices of the Royal Astronomical Society* 517.4, pp. 5080–5089.

Wang, Z. et al. (June 2025). “Detection of X-ray emission from a bright long-period radio transient”. In: *Nature* 642.8068, pp. 583–586. DOI: 10.1038/s41586-025-09077-w. arXiv: 2411.16606 [astro-ph.HE].

Webbe, R. et al. (2025). “4XMM J175136. 8- 275858: a new magnetar candidate?” In: *Monthly Notices of the Royal Astronomical Society* 539.4, pp. 3046–3057.

Weltevrede, P., S. Johnston, & C. M. Espinoza (2011). “The glitch-induced identity changes of PSR J1119- 6127”. In: *Monthly Notices of the Royal Astronomical Society* 411.3, pp. 1917–1934.

Weng, S.-S. et al. (Mar. 2022). “Radio pulsations from a neutron star within the gamma-ray binary LS I +61° 303”. In: *Nature Astronomy* 6, pp. 698–702. DOI: 10.1038/s41550-022-01630-1. arXiv: 2203.09423 [astro-ph.HE].

Wickramasinghe, D. & L. Ferrario (2005). “The origin of the magnetic fields in white dwarfs”. In: *Monthly Notices of the Royal Astronomical Society* 356.4, pp. 1576–1582.

Wongphechauxsorn, J. et al. (Jan. 2024). “The High Time Resolution Universe Pulsar survey - XVIII. The reprocessing of the HTRU-S Low Lat survey around the Galactic Centre using a Fast Folding Algorithm pipeline for accelerated pulsars”. In: *Monthly Notices of the Royal Astronomical Society* 527.2, pp. 3208–3219. DOI: 10.1093/mnras/stad3283. arXiv: 2310.14008 [astro-ph.HE].

Woods, P. M. et al. (1999). “Discovery of a New Soft Gamma Repeater, SGR 1627–41”. In: *The Astrophysical Journal* 519.2, p. L139.

Xu, K. & X.-D. Li (2019). “On the Fallback Disk around the Slowest Isolated Pulsar, 1E 161348-5055”. In: *The Astrophysical Journal* 877.2, p. 138.

Yao, J., R. Manchester, & N. Wang (2017). "A new electron-density model for estimation of pulsar and FRB distances". In: *The Astrophysical Journal* 835.1, p. 29.

Yoneda, H. et al. (Sept. 2020). "Sign of Hard-X-Ray Pulsation from the γ -Ray Binary System LS 5039". In: *Physical Review Letters* 125.11, 111103, p. 111103. DOI: 10.1103/PhysRevLett.125.111103. arXiv: 2009.02075 [astro-ph.HE].

Younes, G. et al. (2022a). "Pulse peak migration during the outburst decay of the magnetar SGR 1830-0645: crustal motion and magnetospheric untwisting". In: *The Astrophysical Journal Letters* 924.2, p. L27.

Younes, G. et al. (2022b). "X-ray burst and persistent emission properties of the magnetar SGR 1830-0645 in outburst". In: *The Astrophysical Journal* 924.2, p. 136.

Younes, G. et al. (2023). "Magnetar spin-down glitch clearing the way for FRB-like bursts and a pulsed radio episode". In: *Nature Astronomy* 7.3, pp. 339–350.

Zapartas, E. et al. (2017). "Delay-time distribution of core-collapse supernovae with late events resulting from binary interaction". In: *Astronomy & Astrophysics* 601, A29.

Zelati, F. C. et al. (2021). "The new magnetar SGR J1830- 0645 in outburst". In: *The Astrophysical Journal Letters* 907.2, p. L34.

Zhang, B. (2022). "Coherent inverse compton scattering by bunches in fast radio bursts". In: *The Astrophysical Journal* 925.1, p. 53.

Zhang, P. (Sept. 2024). "A New Puzzling Periodic Signal in GeV Energies of the γ-Ray Binary LS I+61°303". In: *The Astrophysical Journal* 972.1, 80, p. 80. DOI: 10.3847/1538-4357/ad6a16. arXiv: 2406.02042 [astro-ph.HE].

Zhang, Y. & H. Feng (2023). "Searching for single-frame rapid X-ray transients detected with Chandra". In: *Monthly Notices of the Royal Astronomical Society* 523.2, pp. 2513–2518.

Zhou, P. et al. (Jan. 2014). "Discovery of the Transient Magnetar 3XMM J185246.6+003317 near Supernova Remnant Kesteven 79 with XMM-Newton". In: *The Astrophysical Journal Letters* 781.1, L16, p. L16. DOI: 10.1088/2041-8205/781/1/L16. arXiv: 1310.7705 [astro-ph.HE].

Zhu, W. et al. (2023). "A radio pulsar phase from SGR J1935+ 2154 provides clues to the magnetar FRB mechanism". In: *Science Advances* 9.30, eadf6198.

Chapter 2

SEARCHING FOR MAGNETAR BINARIES DISRUPTED BY CORE-COLLAPSE SUPERNOVAE (CCSNE)

Sherman, M. B. et al. (2024a). "Searching for magnetar binaries disrupted by core-collapse supernovae". In: *Monthly Notices of the Royal Astronomical Society* 531.2, pp. 2379–2414. DOI: 10.1093/mnras/stae1289.

– (2024b). "Correction to: Searching for magnetar binaries disrupted by core-collapse supernovae". In: *Monthly Notices of the Royal Astronomical Society* 534.2, pp. 1414–1419. DOI: 10.1093/mnras/stae2124.

2.1 Abstract

Core-collapse Supernovae (CCSNe) are considered the primary magnetar formation channel, with 15 magnetars associated with supernova remnants (SNRs)[1]. A large fraction of these should occur in massive stellar binaries that are disrupted by the explosion, meaning that $\sim 45\%$ of magnetars should be nearby high-velocity stars. Here we conduct a multi-wavelength search for unbound stars, magnetar binaries, and SNR shells using public optical ($uvgrizy-$bands), infrared ($J-$, $H-$, $K-$, and K_s-bands), and radio (888 MHz, 1.4 GHz, and 3 GHz) catalogs. We use Monte Carlo analyses of candidates to estimate the probability of association with a given magnetar based on their proximity, distance, proper motion, and magnitude. In addition to recovering a proposed magnetar binary, a proposed unbound binary, and 13 of 15 magnetar SNRs, we identify two new candidate unbound systems: an OB star from the *Gaia* catalog we associate with SGR J1822.3-1606, and an X-ray pulsar we associate with 3XMM J185246.6+003317. Using a Markov-Chain Monte Carlo simulation that assumes all magnetars descend from CCSNe, we constrain the fraction of magnetars with unbound companions to $5 \lesssim f_u \lesssim 24\%$, which disagrees with neutron star population synthesis results. Alternate formation channels are unlikely to wholly account for the lack of unbound binaries as this would require $31 \lesssim f_{nc} \lesssim 66\%$ of magnetars to descend from such channels. Our results support a high fraction ($48 \lesssim f_m \lesssim 86\%$) of pre-CCSN mergers, which can amplify fossil magnetic fields to preferentially form magnetars.

[1] After publication, Cotton et al. (2024) discovered a new supernova remnant, MCSNR J0100-7211, associated with the Small Magellanic Cloud magnetar CXOU J0110043.1-721134.

2.2 Introduction

Magnetars are highly magnetized ($B \gtrsim 10^{14}$ G) neutron stars which emit X-ray, gamma ray, or radio emission driven by their magnetic fields (Kaspi & Beloborodov, 2017). At the time of submission, there are 24 confirmed magnetars and 7 magnetar candidates identified based on their high-energy X-ray and gamma ray bursts (T. Cline et al., 2000; D. Lamb et al., 2003; Leahy & W. Tian, 2007; Mereghetti et al., 2012; Richardson et al., 2023; Sakamoto et al., 2011; Torii et al., 1998)[2]. With burst events initially categorized as either Anomalous X-ray Pulsars (AXPs) or Soft Gamma Repeaters (SGRs), magnetars were later identified as the common source of their emission (Gavriil et al., 2002).

Magnetar birth rates $\beta \approx N_{\mathrm{m}ag}\mathcal{T}^{-1} \sim 0.3\,\mathrm{century}^{-1}$ are difficult to constrain due to less confident age $\mathcal{T}$ and population size $N_{\mathrm{m}ag}$ estimates. Most notably, the characteristic spindown age $\mathcal{T}_{\mathrm{rot}} \propto P(2\dot{P})^{-1} \sim 10\,\mathrm{kyr}{-}10\,\mathrm{Myr}$ used for radio pulsars (where P is the pulse period and $\dot{P}$ is the spindown rate) does not incorporate the magnetic field decay on $\sim 10\,\mathrm{kyr}$ timescales thought to drive magnetar emission[3]. Therefore, $\mathcal{T}_{\mathrm{rot}}$ can significantly overestimate the true age (e.g., Ferrario & Wickramasinghe, 2008; Nakano et al., 2015; Pons & Geppert, 2007). While this is the major effect, 'glitches', or abrupt decreases in rotation period P (e.g., Livingstone et al., 2011a; Tong & Huang, 2020; Younes et al., 2023), can also complicate magnetar age estimation when data is limited (e.g., for transient magnetars as discussed in Ibrahim et al., 2024; Lower et al., 2023; Rea et al., 2016; Scholz et al., 2017), as can 'anti-glitches' and 'glitch recovery' for which P increases (e.g., Archibald et al., 2013; Olausen & Kaspi, 2014; Scholz et al., 2014). For these reasons, magnetic field decay ages $\mathcal{T}_{\mathrm{decay}} \sim 1 - 100\,\mathrm{kyr}$ derived from X-ray luminosity and magnetic field strength may be preferred, although these are model-dependent, and may not account for rapid initial spindown models (see Appendix 2.11.4.1 in this work, and e.g., Arras et al., 2004; Ferrario & Wickramasinghe, 2008; Mondal, 2021, for examples of decay models). The ages of associated SNRs $\mathcal{T}_{\mathrm{SNR}} \sim 1\,\mathrm{kyr}{-}100\,\mathrm{kyr}$ are more accurate, but can cover a wide range and are only known for a small fraction of magnetars (Borkowski & Reynolds, 2017; B. M. Gaensler et al., 1999; Lyman

[2]While a number of Gamma Ray Bursts (GRBs) in nearby galaxies have been proposed as magnetar Giant Flares (e.g. Burns et al., 2021; Frederiks et al., 2007; Mazets et al., 2008; Mereghetti et al., 2024; Minaev et al., 2024; Svinkin et al., 2021; Trigg et al., 2024), we focus this work on magnetars and candidates within the Galaxy and Magellanic Clouds.

[3]In this work, we adopt the notation $\mathcal{T}_{\mathrm{rot}}$ for the characteristic age as opposed to the more widely used τ_c to distinguish it from estimates of the angular travel time used in Section 2.4 and Appendix 2.11.2.4.

et al., 2022; Suzuki et al., 2021).

While M. Muno et al. (2008) estimate that $N_{mag} \lesssim 540$ magnetars reside in the Galaxy, a number of factors make this uncertain. First, it is unclear how magnetar beaming affects the observed population, particularly due to the small sample size (e.g., Keane & Kramer, 2008). Furthermore, the detection of a globular cluster (M81) Fast Radio Burst (FRB), thought to originate in a magnetar's magnetosphere, offers a counterexample to our assumption that $N_{\rm mag}$ scales with star formation, and supports the notion of multiple magnetar formation channels (Kirsten et al., 2022; Lu et al., 2022; Petroff et al., 2022). The evolutionary connections among magnetars, pulsars, XDINs, RRATs, and isolated neutron stars are also unclear, leading to potential double-counting errors in the Keane & Kramer (2008) birthrates. Thus, the continued search for and recovery of CCSNe and SNRs will help inform our models and improve age estimates.

SNR radio emission surrounding a magnetar is the most direct indicator of a CCSN progenitor (e.g., Kaspi, 1996). Supernova shells are detectable in radio and X-rays expanding from a young ($1 - 10\,$kyr) magnetar's birth site at its center; most of the known magnetar-SNR associations were identified by their remnant shell radio emission (e.g., G. E. Anderson et al., 2012; Gelfand & B. M. Gaensler, 2007). The significant increase in data from radio all-sky surveys will boost the sensitivity considerably. The Rapid ASKAP Continuum Survey (RACS), for example, uses the 36-antenna Australian Square Kilometre Array Pathfinder (ASKAP) telescope to survey the southern sky (declination range $-80^\circ < \delta < +30^\circ$) from 700–1800 MHz (McConnell et al., 2020). The Karl G. Jansky Very Large Array (VLA) Sky Survey (VLASS) and National Radio Astronomy Observatory (NRAO) VLA Sky Survey (NVSS) similarly cover the northern sky above $\delta > -40^\circ$ at 1.4 and 3 GHz (J. J. Condon et al., 1998; Y. A. Gordon et al., 2020, 2021, 2023), while the Low Frequency Array (LOFAR) covers lower frequencies near 135 MHz (J. J. Condon et al., 1998; Y. A. Gordon et al., 2020, 2021, 2023; Shimwell, 2016; Shimwell et al., 2022). Identifying supernova shells through radio emission relies on the magnetar being young enough that the shell has not yet dissipated; for expansion rates up to $\sim 1000\,\mathrm{km\,s^{-1}}$, SNRs with ages $\lesssim 100\,$kyr may be detected (e.g., G. E. Anderson et al., 2012; Sedov, 2018; Truelove & McKee, 1999).

In recent years, the presence (or absence) of binary magnetar systems has become a powerful probe of CCSN formation channels for the broader neutron star population. Chrimes et al. (2022b), Renzo et al. (2019), C. Kochanek et al. (2019), and Moe

& Di Stefano (2017) conducted population synthesis simulations with massive stellar binaries to estimate what fraction of primary stars would remain bound to their secondaries as neutron stars following their CCSN. Moe & Di Stefano (2017) estimate that $F_0 \sim 84\%$ of massive stars should initially be in binaries, while C. Kochanek et al. (2019) predicts that $f_m \sim 48\%$ of these merge prior to core-collapse[4]; the other $1 - f_m \sim 52\%$ undergo CCSNe as non-merged binaries. Renzo et al. (2019) suggest a lower merger rate $f_m \sim 22^{+26}_{-9}\%$. They also find that $\sim 14^{+22}_{-10}\%$ of the binaries that do not merge remain bound following the CCSN. Thus only $f_b \sim 6-9\%$ of all neutron stars should have massive binary companions. Chrimes et al. (2022b) affirm these results, obtaining a bound neutron star fraction $f_b \sim 5\%$. Notably, the binary statistics of magnetars may deviate from those above if they form from distinct progenitor populations, such as those with enhanced rotation or magnetic fields, though this has not been explored extensively through population synthesis (e.g., S. Popov & Prokhorov, 2006)[5].

Taking a census of young, non-degenerate neutron star-massive star binaries, 7 pulsars with bound OB star companions have been reported in the Australia Telescope National Facility[6] (ATNF) catalog, while SGR 0755-2933 is a tentatively confirmed magnetar binary (Chrimes et al., 2022b; Doroshenko et al., 2021; Richardson et al., 2023). A candidate stellar companion was also proposed for magnetar CXOU J171405.7-381031 using Infrared (IR) Hubble Space Telescope (HST) images, though the IR counterpart's stellar nature is unconfirmed (Chrimes et al., 2022b). The two proposed binaries out of 31 magnetars are marginally consistent with the $f_b \sim 5-9\%$ expected to be in bound systems, while the 9 total neutron stars with massive companions out of the total catalog of $\sim 2,950$ neutron stars marginally underestimate the binary fraction due to selection effects (D. R. Lorimer, 2008)[7].

[4]Note this fraction includes only mergers where both stars are massive OB stars. For a discussion of CCSNe from mergers of intermediate mass stars, see Zapartas et al. (2017).

[5]We caution that the results of S. Popov & Prokhorov (2006) may be biased by their definition of 'magnetars', which they define as evolutionary paths that include "Coalescence prior to NS formation" or "Roche lobe overflow", rather than using an independent condition on their magnetic field strength. Therefore, the merger fractions and binary fractions from Tables 1 and 2 of S. Popov & Prokhorov (2006) should not be directly compared to those from Chrimes et al. (2022b), Renzo et al. (2019), C. Kochanek et al. (2019), Moe & Di Stefano (2017), or this work.

[6]`https://www.atnf.csiro.au/research/pulsar/psrcat/`

[7]Our young neutron star census includes 2,903 slow (period $P > 30$ ms) pulsars from the ATNF catalog, ~ 10 thermally discovered isolated neutron stars including the *Magnificent Seven* ROSAT sample (Avakyan et al., 2023; Haberl, 2007; Pires et al., 2009; Schwope et al., 1998; Tetzlaff et al., 2011; Turolla, 2009), and 31 magnetars and magnetar candidates from the McGill magnetar catalog. We acknowledge this may be incomplete; for example, not all pulsars have sufficient timing solutions to rule out binary companions, and some may be old enough that their companions have undergone

However, one expects a much larger fraction ($f_u \sim 38-56\%$) of 'unbound' neutron star binaries disrupted by the CCSN, motivating a search for 'walkaway' or 'runaway' stellar companions (Renzo et al., 2019). Considering a physical scenario, a massive companion ejected at $\sim 30\,\mathrm{km\,s^{-1}}$ (Renzo et al., 2019) could travel ~ 0.03 pc over ~ 1 kyr. At a distance of $5-10$ kpc, this should appear only $\sim 1.2-2.5''$ away from its previously bound magnetar. C. Kochanek et al. (2019) and C. Kochanek (2018, 2021, 2023) have used the *Gaia* optical catalog to search for both runaway and bound stars nearby 43 SNRs with compact objects, including central pulsars, HMXBs, LMXBs, radio sources, and gamma ray sources. Only the pulsar PSR J0538+2817 was confidently associated with a runaway companion star (Dinçel et al., 2015; C. Kochanek, 2021). Clark et al. (2014) note that the Wolf-Rayet star WR 77F (Wd1-5) may be a runaway unbound companion of magnetar CXOU 164710.2-455216, but the absence of a magnetar proper motion measurement make this difficult to confirm. More general searches for runaway stars with high velocities relative to field stars have also been carried out, but haven't identified magnetar or pulsar companions (e.g., Carretero-Castrillo et al., 2023). With $\sim 2,950$ neutron stars and 31 magnetars, one expects $\sim 1,100-1,700$ and $\sim 11-18$ unbound companions, respectively[8].

A comprehensive search of archived data can leverage catalogs like *Gaia*, the Two Micron All Sky Survey (2MASS), and Panoramic Survey Telescope and Rapid Response System (Pan-STARRS or PS1), as well as surveys such as the SkyMapper Southern Survey (SMSS), UKIRT Infrared Deep Sky Survey (UKIDSS) and the Visible and Infrared Survey Telescope for Astronomy (VISTA) Variables in the Vía Láctea (VVV) to find stellar companions (Brown et al., 2021; Chambers et al., 2019; Flewelling et al., 2020; Kaiser et al., 2002; Lawrence et al., 2007; Nikzat et al., 2022; Onken et al., 2024; Skrutskie et al., 2006; Wolf et al., 2018). For example, Chrimes et al. (2023) predict the ability of *Gaia* Data Release 3 (DR3), as well as future releases from HST, the James Webb Space Telescope (JWST), *Euclid*, and the Nancy Grace Roman Space Telescope (NGRST) to detect unbound stellar objects. They find that while *Gaia* is limited by extinction ($A_V \lesssim 10$), its absolute reference capability and proper motion measurements could increase the number of unbound

supernovae, as well. However, this provides a reasonable estimate of the number of known young neutron stars to date. We exclude older populations such as High- and Low-Mass X-ray Binaries (HMXBs, LMXBs) and millisecond pulsars since they are only observable in binary systems, and are therefore subject to selection effects (e.g., D. R. Lorimer, 2008).

[8]See Table 2.4 for definitions of f_b, f_m, f_u, and other relevant fractions. These will be discussed in detail in Section 2.7.2.

companion discoveries by $\sim 8\times$ when combined with next generation IR telescope data. *Gaia* data have also been used effectively to search for unbound companions of White Dwarfs and neutron stars (El-Badry et al., 2023; C. Kochanek et al., 2019; Shen et al., 2018).

In this paper, we conduct a search for unbound binary companions of magnetars using the *Gaia* catalog, supplemented by a search for bound companions and CCSN remnants. In Section 2.3 we describe the magnetar sample used for the search. Section 2.4 describes the search and trajectory analysis of sources in the *Gaia* archive for unbound magnetar companions and results. In Section 2.5 we describe the methods and results of the optical and IR search for bound magnetar companions. In Section 2.6 we summarize the radio image search using the RACS, VLASS, and NVSS catalogs. Section 2.7 discusses the sensitivity, completeness, and implications of our search. Section 2.8 concludes with a summary and outlook on next steps for analyzing magnetar formation. Section 2.9 provides information regarding data availability. Details on the statistical analysis are included in the appendices.

2.3 Magnetar Sample

In Table 2.1, we present the sample of 24 magnetars listed in the McGill magnetar catalog[9], as well as 7 unconfirmed magnetar candidates (Olausen & Kaspi, 2014). For each we list the Right Ascension (α), declination (δ), distance (d), and proper motion (μ) from the available literature. We also provide the V-band dust extinction estimates along each magnetar's line-of-sight, which we derive using the *Bayestar19*[10] dust map for magnetars above declination $\delta \gtrsim -30^\circ$ (G. M. Green et al., 2015, 2018, 2019; E. Schlafly et al., 2015). For magnetars outside this range we use the Predehl & Schmitt (1995) relation between the X-ray column density, N_H, and A_V if an N_H measurement is available. If not, the average photometric extinction from *Gaia* Data Release 3 (DR3) sources within 1° is given (Collaboration et al., 2022; Gaia Collaboration et al., 2016). This will likely underestimate the true extinction, since most *Gaia* sources are in the foreground. Twelve magnetars and 3 magnetar candidates have secure or proposed SNR associations.

[9] `http://www.physics.mcgill.ca/~pulsar/magnetar/main.html`
[10] `https://dustmaps.readthedocs.io/en/latest/modules.html`

Table 2.1: Magnetars and Magnetar Candidates from the McGill Catalog

Magnetar	α	σ_α ($''$)	δ	σ_δ ($''$)	**Distance (kpc)**	$\mu_\alpha \cos(\delta)$ (mas yr^{-1})	μ_δ (mas yr^{-1})	A_V	**Refs.**
CXOU J010(043.1-721134)	$01^h00^m43^s.14$	0.60	$-72°11'33''.80$	0.60	62.4 ± 1.6	–	–	$0.35^{+0.11}_{-0.09}$ ‡	1,2
4U 0142(+61)	$01^h46^m22^s.407$	0.50	$+61°45'03''.19$	0.50	3.6 ± 0.4	-4.1 ± 1.0	1.9 ± 1	$3.81^{+0.51}_{-0.16}$	3,4,5
SGR 0418(+5729)	$04^h18^m33^s.867$	0.35	$+57°32'22''.91$	0.35	~ 2	–	–	1.60	6
SGR 0501(+4516)*	$05^h01^m08^s.00$	0.11	$+45°16'31''.00$	0.11	2.0 ± 0.3	–	–	$2.82^{+0.10}_{-0.42}$	7,8,9,73
SGR 0526(-66)*	$05^h26^m00^s.89$	0.60	-66°04'36''.30	0.60	53.6 ± 1.2	–	–	$3.37^{+0.32}_{-0.33}$ ‡	1,10,11
1E 1048.1(-5937)	$10^h50^m07^s.14$	0.60	-59°53'21''.40	0.60	9.0 ± 1.7	–	–	5.42 ± 0.06‡	3,12,13,76,77,78,79
1E 1547.0(-5408)	$15^h50^m54^s.12$	0.0056	-54°18'24''.11	0.0020	3.91 ± 0.07	4.8 ± 0.5	-7.9 ± 0.3	17.88 ± 1.12‡	14,15,16
PSR J1622(-4950)	$16^h22^m44^s.89$	0.80	-49°50'52''.70	0.80	9.00 ± 1.35	–	–	$30.17^{+8.94}_{-7.82}$ ‡	17,18
SGR 1627(-41)	$16^h35^m51^s.84$	0.60	-47°35'23''.31	0.60	11.0 ± 0.3	–	–	55.87 ± 11.17‡	19,20
CXOU J1647(10.2-455216)	$16^h47^m10^s.20$	0.30	-45°52'16''.90	0.30	3.9 ± 0.7	–	–	13.35 ± 0.28‡	21,22
1RXS J1708(49.0-400910)	$17^h08^m46^s.87$	0.80	-40°08'52''.44	0.80	3.8 ± 0.5	–	–	7.60 ± 0.22‡	3,23
CXOU J1714(05.7-381031)	$17^h14^m05^s.74$	0.60	-38°10'30''.90	0.60	9.8 ± 1.5	–	–	$22.07^{+0.84}_{-0.78}$ ‡	24,25,26,69
SGR J1745(-2900)*	$17^h45^m40^s.16$	0.02	-29°00'29''.82	0.09	8.3 ± 0.3	2.44 ± 0.33	5.89 ± 0.11	3.01	27,28,29,30,74,75
SGR 1806(-20)	$18^h08^m39^s.34$	0.04	-20°24'39''.85	0.04	$8.7^{+1.8}_{-1.5}$	-4.5 ± 1.4	-6.9 ± 2.0	6.66 ± 0.06	31,32,33
XTE J1810(-197)	$18^h09^m51^s.08$	0.0003	$-19°43'52''.14$	0.0005	$2.5^{+0.4}_{-0.3}$	-3.79 ± 0.04	-16.2 ± 0.1	$3.71^{+0.03}_{-0.10}$	34,35,70,87
Swift 1818(.0-1607)	$18^h18^m03^s.70$	2.70	-16°07'31''.80	2.70	~ 4.8	-3.54 ± 0.05	-7.65 ± 0.09	~ 3.78	36,37,38
Swift J1822(.3-1606)	$18^h22^m18^s.00$	1.80	-16°04'26''.80	1.80	1.6 ± 0.3	–	–	$2.02^{+1.47}_{-1.09}$	39,40
SGR 1833(-0832)	$18^h33^m44^s.37$	0.30	-08°31'07''.50	0.30	–	–	–	$\sim 3.16^{\dagger}$	41
Swift J1834(.9-0846)	$18^h34^m52^s.12$	0.60	-08°45'56''.02	0.60	4.2 ± 0.3	–	–	4.03 ± 0.06	42,43
1E 1841(-045)	$18^h41^m19^s.34$	0.30	-04°56'00''.69	0.30	8.5 ± 1.3	–	–	3.76 ± 0.06	44,45,46,80,81
3XMM J1852(46.6+003317)	$18^h52^m46^s.67$	2.4	+00°33'17''.80	2.4	~ 7.1	–	–	~ 6.30	47
SGR 1900(+14)	$19^h07^m14^s.33$	0.15	+09°19'20''.1	0.15	12.5 ± 1.7	-2.1 ± 0.4	-0.6 ± 0.5	$10.94^{+0.06}_{-0.03}$	48,49,33
SGR 1935(+2154)	$19^h34^m55^s.60$	0.70	+21°53'47''.79	0.70	9.0 ± 2.5	–	–	$8.58^{+0.16}_{-1.98}$	50,51,52,82,83
1E 2259(+586)	$23^h01^m08^s.30$	0.70	+58°52'44''.45	0.70	3.2 ± 2.0	-6.4 ± 0.6	-2.3 ± 0.6	$2.59^{+0.38}_{-1.79}$	53,54,55,5,84
SGR 0755(-2933)	$07^h55^m42^s.48$	180	-29°33'53''.46	180	3.5 ± 2.0	–	–	$1.82^{+0.32}_{-1.18}$	56,57,58,72
SGR 1801(-23)*	18^h00^m59s	13680	-22°56'48''.00	13680	–	–	–	$\sim 1.95^{\dagger}$	59
SGR 1808(-20)	$18^h08^m11^s.20$	414	-20°38'49''.00	414	–	–	–	$\sim 2.82^{\dagger}$	60
AX J1818(.8-1559)	$18^h18^m51^s.38$	0.60	-15°59'22''.62	0.60	–	–	–	20.11 ± 2.79‡	61
AX J1845(-0258)	$18^h44^m54^s.70$	0.60	-02°56'53''.10	0.60	8.5	–	–	~ 5.15	62,63,64
SGR 2013(+34)	$20^h13^m56^s.90$	2.7	+34°19'48''	2.7	8.5 ± 1.32	–	–	~ 4.38	65,71
PSR J1846(-0258)	$18^h46^m24^s.94$	0.15	-02°58'30''.10	0.20	$6.0^{+1.5}_{-0.9}$	–	–	$5.00^{+0.13}_{-0.06}$	66,67,68,85,86

Abbreviated magnetar names are given with full names in parentheses, which are used throughout this work. RA (α), declination (δ), and distance are taken from the McGill Magnetar Catalog (Olausen & Kaspi, 2014), while proper motions ($\mu_\alpha \cos(\delta)$ and μ_δ) were found in the available literature. Italicized entries are unconfirmed magnetar candidates and boldfaced entries have confirmed or proposed supernova remnant associations. Proposed associations are indicated by a *. A_V extinction estimates are from the *Bayestar19* map for magnetars with $\delta \gtrsim -30°$. Magnetars outside this range have A_V from the X-ray column density N_H (indicated by a ‡) using the Predehl & Schmitt (1995) relation: $A_V \approx (5.59 \times 10^{-22}\ \mathrm{cm}^2) N_H$. If no N_H measurement is available, we list the median A_V from *Gaia* GSP photometry for massive sources within 1° (indicated by a †; see Section 2.4 for details).

Relevant citations referenced in the rightmost column are below: (1) Haschke et al. (2012) (2) R. C. Lamb et al. (2002) (3) Durant & van Kerkwijk (2006) (4) Hulleman et al. (2004) (5)Tendulkar et al. (2013) (6) van der Horst et al. (2010) (7) L. Lin et al. (2011) (8) Göğüş et al. (2010b) (9) B. Gaensler & Chatterjee (2008) (10) Kulkarni et al. (2003) (11) Klose et al. (2004) (12) Wang & Chakrabarty (2002) (13) B. M. Gaensler et al. (2005) (14) Tiengo et al. (2010) (15) Deller et al. (2012) (16) Gelfand & B. M. Gaensler (2007) (17) Levin et al. (2010) (18) G. E. Anderson et al. (2012) (19) Corbel et al. (1999) (20) Wachter et al. (2004) (21) Kothes & Dougherty (2008) (22) M. P. Muno et al. (2006) (23) G. L. Israel et al. (2003) (24) W. W. Tian & Leahy (2012) (25) J. P. Halpern & Gotthelf (2010b) (26) J. P. Halpern & Gotthelf (2010a) (27) Bower et al. (2014) (28) Mori et al. (2013a) (29) Shannon & Johnston (2013) (30) Bower et al. (2015) (31) Bibby et al. (2008) (32) G. Israel et al. (2005) (33) Tendulkar et al. (2012) (34) Minter et al. (2008) (35) Helfand et al. (2007) (36) Karuppusamy et al. (2020) (37) Stamatikos et al. (2020) (38) Ding et al. (2020b) (39) Scholz et al. (2012) (40) Pagani et al. (2011) (41) Göğüş et al. (2010a) (42) Leahy & W. W. Tian (2008) (43) Kargaltsev et al. (2012) (44) W. W. Tian & Leahy (2008) (45) Wachter et al. (2004) (46) Vasisht & Gotthelf (1997) (47) Zhou et al. (2014) (48) Davies et al. (2009) (49) D. A. Frail et al. (1999) (50) B. Gaensler (2014) (51) G. L. Israel et al. (2016) (52) Zhong et al. (2020) (53) Kothes & Foster (2012) (54) Fahlman & Gregory (1981) (55) Hulleman et al. (2001) (56) Barthelmy et al. (2016) (57) Doroshenko et al. (2021) (58) Richardson et al. (2023) (59) T. Cline et al. (2000) (60) D. Lamb et al. (2003) (61) Mereghetti et al. (2012) (62) Torii et al. (1998) (63) B. M. Gaensler et al. (1999) (64) Tam et al. (2006) (65) Sakamoto et al. (2011) (66) Leahy & W. Tian (2007) (67) Gotthelf et al. (2000) (68) Helfand et al. (2003) (69) Blumer et al. (2019) (70) D. Lin et al. (2012) (71) Roming et al. (2008) (72) Barthelmy et al. (2016) (73) Jing et al. (2023) (74) Ponti et al. (2015) (75) Yalinewich et al. (2017) (76) T. L. Cline et al. (1982) (77) Park et al. (2012) (78) Park et al. (2020) (79) Sano et al. (2023) (80) Borkowski & Reynolds (2017) (81) Zhou et al. (2019) (82) Kothes et al. (2018) (83) Zhou et al. (2020) (84) Nakano et al. (2017) (85) Leahy & W. Tian (2008) (86) Straal et al. (2023) (87) Ding et al. (2020a)

2.4 *Gaia* Catalog Search For Unbound Companions

2.4.1 Gaia Data

The *Gaia* DR3 catalog was queried to search for unbound magnetar companions ejected by the CCSN (Collaboration et al., 2022; Gaia Collaboration et al., 2016). As is highlighted in Chrimes et al. (2023), the *Gaia* catalog is a unique tool given its absolute reference frame which allows for comparison of proper motion data. We build upon previous magnitude-based searches (e.g., Chrimes et al., 2022b) by analyzing the trajectories for each GDR3 source in reference to the magnetars'. Chrimes et al. (2023) note the *Gaia* survey depth $m_{G,\,\mathrm{min}} = 20.7$ and proper motion uncertainty ranging from $9.6 \leq \mu_{\mathrm{min}} \leq 801.6\,\mu\mathrm{as\,yr}^{-1}$ for $13 \leq m_G \leq 20.7$ limit the survey's detection of walkaway or runaway stars to those with low extinction ($A_V \lesssim 10$; Lindegren et al., 2021)[11]. Despite this, our combination of magnitude analysis with proper motion data will still make a marked improvement over previous searches, seen for example in El-Badry et al. (2023) and inferred through simulations by Chrimes et al. (2023, Figure 8 row 1).

The *Gaia* query is limited to potential O and B type stars, as we expect many of the companions of magnetars to be massive stars, and removing dim stars significantly reduces contamination by false positives. To do this we impose an upper limit on the absolute V-band magnitude $M_V < -2.5\log_{10}(L_{OB}/L_\odot) + 4.68 = 1.185$, where we use $L_{OB} \approx 25L_\odot$, and color $G_{BP} - G_{RP} < 2$. Appendix 2.11.1 contains the Astronomical Data Query Language (ADQL) query used to compile the initial *Gaia* sample.

Following the initial query, extinction corrections and cutoffs were re-applied using the *Bayestar19*[12] dust map (G. M. Green et al., 2018, 2019) for any *Gaia* sources above declination $\delta \gtrsim -30°$. From *Bayestar19* we obtain the $B - V$ color excess, E_{B-V}, which is converted to $V-$band extinction with $A_V \approx 3.2E_{B-V}$ and the $G - V$ excess using the Johnson-Cousins Relations[13]. These are used along with the parallax distance d from the C. Bailer-Jones (2023) catalog (see also C. A. L. Bailer-Jones et al., 2021) to obtain the absolute $G-$ and $V-$band magnitudes, M_G and M_V. Details on conversions between photometric systems are in Appendix 2.11.1.

For sources with $\delta \lesssim -30°$, M_V is computed with Equations 2.15-2.18 using A_G and $E_{G_{BP}-G_{RP}}$ reported in *Gaia*, which are derived from $G_{BP} - G_{RP}$ spectra in the

[11] `https://www.cosmos.esa.int/web/gaia/science-performance` Section 1

[12] `https://dustmaps.readthedocs.io/en/latest/modules.html`

[13] See the *Gaia* DR3 Documentation at `https://gea.esac.esa.int/archive/documentation/GDR3/` Section 5.5.1 Table 5.9 for details.

GSP-Aeneas library (Vallenari et al., 2022). However, we proceed cautiously with the GSP extinction estimates, which are known to be unreliable within the galactic plane where the effective temperature is overestimated (see Andrae et al., 2022; Fouesneau et al., 2022, Section 3.4, and the *Gaia* DR3 Documentation Section 11.3.3 for details).

Sources were constrained to have parallax $0.008 < \omega \pm \sigma_\omega < 1.25$ mas based on the distances of the farthest (CXOU J010043.1-721134, 62.4 ± 1.6 kpc) and nearest (Swift J1822.3-16.06, 1.6 ± 3 kpc) magnetars in the McGill catalog, placing an upper limit ~ 125 kpc on the sample. The query was further constrained to Galactic longitudes $-80^\circ \leq b \leq 20^\circ$ based on magnetar locations. Figure 2.1 shows the resulting *Gaia* sample of 156,572 potential OB star sources.

We use a Monte Carlo simulation to estimate p-values for the *Gaia* search. The criteria for association for a given sampled trajectory are below:

1. When the magnetar and source are extrapolated back in time over a sampled travel time (between $1 - 10$ kyr), their initial angular separation $\Theta \approx 0^\circ$.
2. The absolute $V-$band magnitude of the *Gaia* source is consistent with that of an OB (possibly A) star ($-10 \lesssim M_V \lesssim 3$)[14].
3. The difference in 2D travel time for the magnetar and source to travel from their past intersection point to their present positions is $\Delta\tau_{2D} \approx 0$.
4. The magnetar's physical travel time $\mathcal{T}_{3D,mag}$ is consistent with its age $\mathcal{T}$.
5. The source's parallax distance is consistent with magnetar's distance, such that $\Delta d \approx 0$.

These are used to define p-values p_1, p_2, p_3, and p_4 respectively (the first two criteria are combined to define p_1). Note that the *Gaia* radial velocity measurements are not used in our search since they have not been confirmed through spectroscopic follow-up and would over-constrain the sampled velocity vectors. Appendix 2.11.2.4 describes the definition of p_1, p_2, p_3, and p_4 in more detail, which are combined as shown below:

[14]While we expect most OB stars to have $M_V \lesssim 0$, we use a wider range that also includes A stars to avoid missing dim companions.

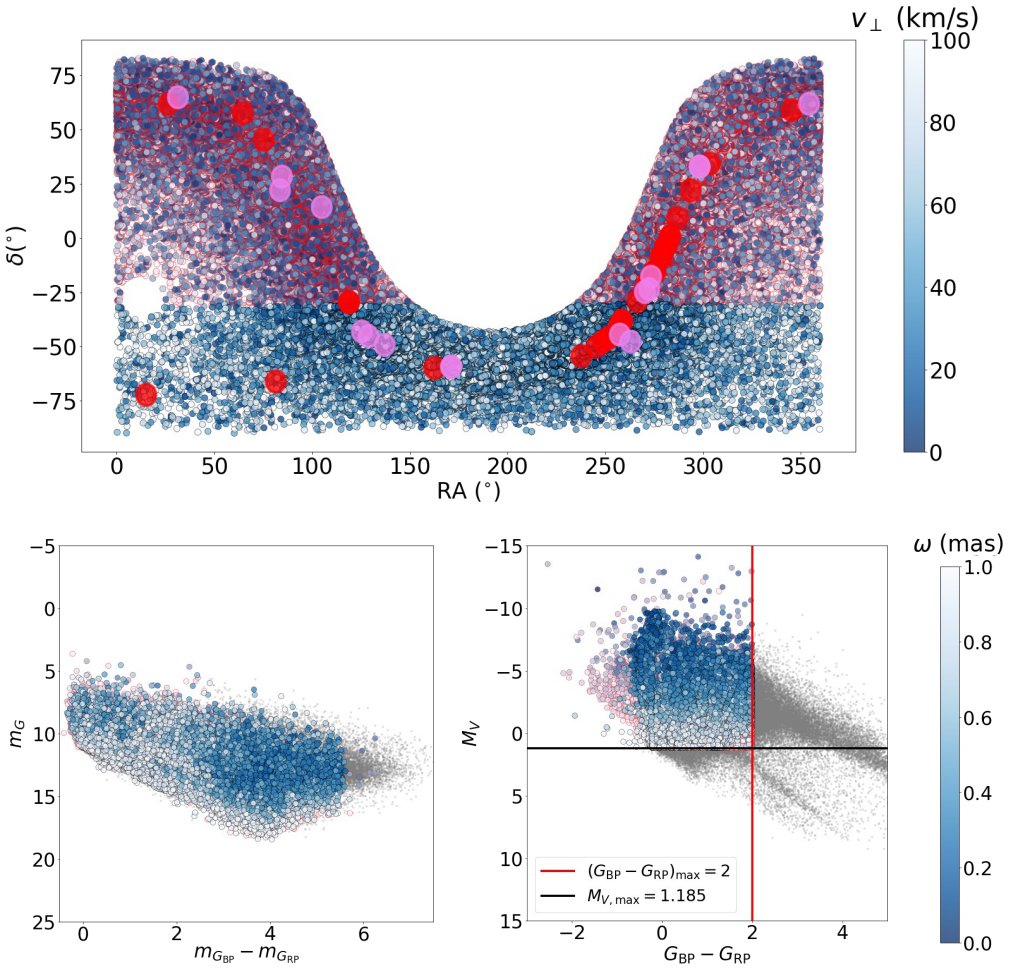

Figure 2.1: (*Top*) Locations of *Gaia* search sample in Celestial coordinates. The tangential velocity magnitude in km s^{-1} is indicated by the colorbar. The *Bayestar19* Dust Map is used for sources at $\delta > -30°$ (red outline), and the *Gaia* photometric extinction is used for $\delta < -30°$ (black outline; D. Green, 2019; Vallenari et al., 2022). The 5° radius cones queried around each magnetar are shown in red, and those around each pulsar used for the test sample (see Section 2.4.2) are shown in violet. Lower transverse velocities are found in the galactic plane (GP), meaning that the unbound companions of GP magnetars can be found at smaller angular separations. (*Bottom*) Color-Magnitude Diagrams for the *Gaia* search sample. The *left* plot shows the apparent $G-$band magnitude m_G plotted against the apparent $m_{G_{BP}} - m_{G_{RP}}$ color. The *right* plot shows absolute $V-$band magnitude M_V for each source against the absolute color $G_{BP} - G_{RP}$. M_V is derived using the Johnson-Cousins relationships in Equations 2.11-2.18 (see Appendix 2.11.1). Sources with $\delta > -30°$ are again outlined in black while those with $\delta \geq -30°$ are outlined in red. The parallax of each source is indicated by the colorbar in milliarcseconds (mas). Sources from the initial query (see Appendix 2.11.1) which were cut by the magnitude (black) and color (red) limits are shown in grey. GSP-Aeneas extinction estimates may be unreliable in the galactic plane according to the *Gaia* DR3 Documentation (Section 11.3.3), resulting in a rough color cutoff near $G_{\rm BP} - G_{\rm RP} \approx -0.5$ (Andrae et al., 2022; Fouesneau et al., 2022; Vallenari et al., 2022).

$$p = 1 - (1 - p_1)(1 - p_2)(1 - p_3)(1 - p_4) \tag{2.1}$$

We choose this definition (as opposed to e.g., the Fisher statistic, Lancaster statistic, or a direct average) for its intuitive application to this search, as all four criteria must be met with $p_i << 5\%$ to obtain $p < 5\%$. This also makes it straightforward to interpret p-values by tracing back each p_i to its criterion.

Each magnetar's age is estimated as the age of its associated SNR $\mathcal{T}_{\rm SNR}$ (Suzuki et al., 2021). If no SNR is associated, its X-ray luminosity decay age $\mathcal{T}_{\rm decay}$ is used, which adopts the Ferrario & Wickramasinghe (2008) field model and is derived in Appendix 2.11.4.1. For magnetars with no persistent X-ray emission or magnetic field estimates, the characteristic spin-down age $\mathcal{T}_{\rm rot}$ is used (Olausen & Kaspi, 2014). In Table 2.2 we provide the derived or reported timescales for each magnetar.

2.4.2 *Gaia* Search Test Using High Velocity Pulsars with Supernova Remnants

In order to test the search pipeline, we applied the Monte Carlo simulation to a sample of 15 pulsars with known SNR associations and proper motion measurements compiled from the ATNF catalog (Andersen et al., 2023; Dinçel et al., 2015; C. Kochanek, 2021; Lyne et al., 2015; Stairs et al., 2001; Wateren et al., 2023). Within this sample, only PSR J0538+2817 is known to have a runaway companion B0.5V-type star, as discovered by Dinçel et al. (2015) and confirmed by C. Kochanek (2021). The upper limit on the travel time τ is set to 100 kyr, the maximum age of SNR shells before they dissipate (e.g., D. Frail et al., 1994), given that pulsars can have ages > 100 kyr (e.g., Kaspi & Beloborodov, 2017; D. R. Lorimer, 2008). The initial Monte Carlo simulation (criteria 1 and 2) identifies between 2 and 800 potential candidates with $p_1 < 5\%$ for each of the 15 pulsars. Following the trajectory analysis, only 1 pulsar, PSR B1951+32, remains with $p < 5\%$ and a sufficient fraction of valid trajectories[15]. The companion of PSR J0538+2817 is not initially recovered. In this section we discuss the likelihood of PSR B1951+32's candidate companion, and the reasons for PSR J0538+2817's omission. Figure 2.2 shows the trajectory plots for both pulsars.

[15]Three other pulsars had candidates with $p < 5\%$, but used only one valid trajectory, for which the source and pulsar paths intersect, out of 100 trials, and they are considered false positives.

Table 2.2: Magnetar Age Upper Limits Used for the *Gaia* Search

Magnetar	Age Method	$\mathcal{T}_{\rm decay/rot/SNR}$	Reference
CXOU J010	Decay	7.7 kyr	This work
4U 0142	Decay	3.8 kyr	This work
SGR 0418	Decay	8.3 Myr	This work
SGR 0501	Decay	59.4 kyr	This work
SGR 0526	Decay	2.9 kyr	This work
1E 1048.1	Decay	8.9 kyr	This work
1E 1547.0	Decay	30.4 kyr	This work
PSR J1622	Decay	44.2 kyr	This work
SGR 1627	Decay	37.0 kyr	This work
CXOU J1647	Decay	2.1 Myr	This work
1RXS J1708	Decay	8.1 kyr	This work
CXOU J1714	SNR	6.2 kyr	Blumer et al. (2019)
SGR J1745	Decay	64.9 kyr	This work
SGR 1806	Decay	1.3 kyr	This work
XTE J1810	Decay	81.1 kyr	This work
Swift 1818	Spindown	0.86 kyr	Rajwade et al. (2022)
Swift J1822	Decay	0.2 Myr	This work
SGR 1833	Spindown	34 kyr	Esposito et al. (2011)
Swift J1834	Decay	0.2 Myr	This work
1E 1841	SNR	1.8 kyr	Borkowski & Reynolds (2017)
3XMM J1852	Decay	0.7 Myr	This work
SGR 1900	Decay	4.1 kyr	This work
SGR 1935	SNR	16.0 kyr	Lyman et al. (2022)
1E 2259	Decay	62.0 kyr	This work
SGR 0755	–	–	–
SGR 1801	–	–	–
SGR 1808	–	–	–
AX J1818	–	–	–
AX J1845	SNR	1.4 kyr	B. M. Gaensler et al. (1999)
SGR 2013	–	–	–
PSR J1846	Spindown	0.73 kyr	Livingstone et al. (2011b)

$\mathcal{T}_{\rm decay}$ is estimated in this work (see Appendix 2.11.4.1 in this work and Ferrario & Wickramasinghe, 2008) using the magnetic field B_d and X-ray luminosity L_X reported in the McGill Magnetar Catalog (Olausen & Kaspi, 2014, and references therin). Spindown ages are those from the McGill catalog, and are approximated as the characteristic age $\mathcal{T}_{\rm rot} = P(2\dot{P})^{-1}$. SNR ages $\mathcal{T}_{\rm SNR}$ are used only for magnetars with confident SNR associations. References for the spindown and SNR ages are in the rightmost column.

2.4.2.1 PSR J0538+2817

For PSR J0538+2817, we initially do not recover the runaway companion star, HD 37424, which was identified by Dinçel et al. (2015) and C. Kochanek (2021). The corresponding *Gaia* source, *Gaia* DR3 3441732292729818752, was assigned a p-value $p > 99\%$[16] and therefore was not identified as a candidate. Upon further inspection, we find the high p-value is the result of a high false positive rate; among the simulated sources used to estimate the *H0* distribution, $\sim 95\%$ are

[16]The minimum and maximum p-values are set by the number of trials, which varies for each magnetar depending on what constraints on its position, distance, and proper motion are available. One-thousand and 100 trials were used for PSR B1951+32 and PSR J0538+2817, respectively.

found with all Monte Carlo samples within the $\{\Theta, M_V\}$ association region ($\hat{f} = 0$; see Appendix 2.11.3.1). We attribute this to the large association region in $\{\Theta, M_V\}$ space which extends to $\gtrsim 1'$ (see Figure 2.2). While pulsars have larger confidence regions in $\{\Theta, M_V\}$ space than magnetars due to the higher age limit and lower distances, the high proper motions of PSR J0538+2817, PSR J1809-2332, and PSR B2334+61 further extend the region, resulting in unusually high false positive rates $\gtrsim 99\%$, $\gtrsim 91\%$, and $\gtrsim 76\%$, respectively.

We therefore increase the p-value thresholds for these three sources to match their minimum false positive rates. We use a threshold $p_1 < 100\%$ for PSR J0538+2817 since the false positive rate is $\gtrsim 99\%$. For PSR B2334+61 and PSR J1809-2332, no additional sources are identified with the new threshold, whereas HD 37424 is identified as a candidate for PSR J0538+2817 after increasing the threshold. This scenario also justifies our use of the search statistic $\hat{f} < \hat{f}_c$ to identify candidates initially, as it implicitly accounts for this false-positive rate bias. Our conditional recovery of PSR J0538+2817's runaway star demonstrates the accuracy and sensitivity of our search method, but indicates we must be wary of false positives and sources along unique sightlines. We address completeness of the magnetar search in detail in Section 2.7.

2.4.2.2 PSR B1951+32

One *Gaia* companion candidate is identified for PSR B1951+32 with $p < 0.1\%$, Gaia DR3 2035109887486067456 (catalogued as TYC 2673-414-1; Høg et al., 2000a). The parallax distance 1.13 ± 0.02 kpc is only marginally consistent with the pulsar's ~ 3 kpc distance, which has an uncertainty that is not well defined (Kulkarni et al., 1988). The pulsar's dispersion measure (DM) and more recent estimates of the associated SNR CTB 80 suggest a closer ~ 2 kpc distance, which would be more consistent with TYC 2673-414-1 (Kramer et al., 2000; Migliazzo et al., 2002; Yao et al., 2017). From the 2MASS counterpart, 2MASS J19544429+3327472, we estimate absolute $H-$band magnitude $M_H \approx -4.5$ and $J - H$ color $J - H \approx -0.1$ when placed at the pulsar distance 3 kpc. While these are reasonable, they do fall outside of the expected ranges of IR magnitude and color from Chrimes et al. (2022b)'s simulations. From the valid trajectory samples, TYC 2673-414-1 is required to have velocity $|\overrightarrow{v}| \approx 75^{+14}_{-6}$ km s^{-1}, which would be consistent with a more rare runaway star if ejected from the pulsar's CCSN (Renzo et al., 2019). While pulsar companions are not the focus of this search, we encourage follow-up of TYC 2673-414-1 as

a possible unbound companion of PSR B1951+32.

2.4.3 *Gaia* Search Results

Through the *Gaia* Monte Carlo search, we identify potential candidates with $p < 5\%$ for 2 magnetars. In Figure 2.2, we show the trajectory plots and contour plots of the Monte Carlo samples for these, along with CXOU J164710.2-455216, whose proposed companion WR 77F we recover with $p = 0.6\%$ (Clark et al., 2014). We rule out one of the two candidates, 3XMM J185246.6+003317, as a false positive based on detailed analysis of its candidates' velocities and distances, which we discuss in Appendix 2.11.3.1. Having not recovered the proposed binaries SGR 0755-2933 and CXOU J171405.7-38131, we find this search method is relatively insensitive to bound stellar companions due to their position within magnetars' error ellipses (Chrimes et al., 2022b; Doroshenko et al., 2021; Richardson et al., 2023). However, it is a useful tool to identify which candidates are likely to be bound companions (see Section 2.5.3). In the following sections, we focus on the unbound companion candidates for SGR J1822.3-1606 and CXOU J164710.2-455216.

2.4.3.1 SGR J1822.3-1606

The primary candidate for an unbound system is SGR J1822.3-1606 and *Gaia* DR3 4097832458955594880, which is assigned a p-value $p < 0.1\%$. Its distance, $d = 1.00^{+0.03}_{-0.02}$ kpc, is consistent with that of the magnetar, 1.6 ± 0.3 kpc, at the 2σ level, and from the IR counterpart, 2MASS 18230515-1600296, we estimate absolute magnitudes $M_J = -3.9 \pm 0.5$ and $M_H = -4.6^{+0.5}_{-0.4}$, and color $J - H = 0.7 \pm 0.1$[17], which are both reasonable for a low-mass B-type star. SGR J1822.3-1606 does not have a measured proper motion, and our simulation suggests $\mu_\alpha \cos(\delta) = -29^{+15}_{-24}$ mas yr^{-1}, $\mu_\delta = -25^{+13}_{-19}$ mas yr^{-1} are required for the magnetar to have a valid trajectory[18]. A wide range of magnetar velocities are permitted for this association, with $|\overrightarrow{v}_{\rm mag}| = 413^{+184}_{-175}$ km s^{-1}. Notably, the permitted stellar velocity $|\overrightarrow{v}| = 60^{+7}_{-5}$ km s^{-1} would classify this as a rare 'runaway' companion star (Renzo et al., 2019). This is roughly consistent with the source's high transverse velocity, ~ 55 km s^{-1}, making the association achievable without a significant radial component. While it is unlikely that such velocities can be reached from CCSN disruption alone,

[17]Uncertainties are estimated from the 16$^{\rm th}$ and 84$^{\rm th}$ percentiles of the magnitude and color samples, which take into account distance and apparent magnitude errors.

[18]Estimates of the proper motion and velocity are derived from Monte Carlo samples found to produce 'valid' trajectories which are found to intersect through our iterative analysis. Uncertainties are from the 16$^{\rm th}$ and 84$^{\rm th}$ percentiles of these 'valid' samples.

other mechanisms may contribute to the source's and magnetar's space motion, such as dynamical ejection from an OB association (e.g., Poveda et al., 1967; Tetzlaff et al., 2011). Therefore, we identify this as a promising candidate, and further characterization from follow-up observations would be of great interest.

2.4.3.2 CXOU J164710.2-455216

Next, we consider the Wolf-Rayet star WR 77F (or Wd1-5), which Clark et al. (2014) suggest as an unbound companion of CXOU 164710.2-455216 based on the position, radial velocity, and chemical content of the star. WR 77F is associated with *Gaia* DR3 5940106797374726784 which was not included in the initial *Gaia* query, possibly due to an underestimated *Gaia* extinction from GSP photometry. We add this candidate to the sample and run the simulation with an increased 1000 trials after finding a low fraction of valid trajectories with 100 samples. Given that the candidate is an evolved Wolf-Rayet star rather than a main-sequence OB star, and that magnetar CXOU J164710.2-455216 lies along a high extinction sightline with $A_V = 13.35 \pm 0.28$, we omit p_1 from this analysis (which initially was $p_1 > 99.9\%$). With this adjustment, we recover a p-value $p_{2,3,4} = 0.6\%$. The magnetar's derived physical travel time $\mathcal{T}_{\rm 3D,mag} \approx 16.0^{+25.6}_{-10.0}\,$kyr, is consistent with its decay age $\mathcal{T}_{\rm decay} \approx 0.2\,$Myr within $\sim 1\sigma$. Finally, the valid trajectories require velocities $|\overrightarrow{v}_{\rm mag}| \approx 390 \pm 170\,{\rm km\,s^{-1}}$ and $|\overrightarrow{v}| \approx 80^{+20}_{-13}\,{\rm km\,s^{-1}}$ for CXOU 164710.2-455216 and WR 77F, respectively. The former is consistent with Hobbs et al. (2005) while the latter suggests that WR 77F is a runaway star ($|\overrightarrow{v}| \gtrsim 30\,{\rm km\,s^{-1}}$; Renzo et al., 2019). However, the localization of CXOU J164710.2-455216 and WR 77F to the Westerlund-1 massive star cluster implies that dynamical ejection may have contributed to the large observed velocities, as well. We conclude it is likely that CXOU J164710.2-455216 are WR 77F are an unbound magnetar binary disrupted by the former's CCSN, potentially supplemented by dynamical ejection, supporting the results of Clark et al. (2014).

2.5 Optical and IR Search for Bound Companions

In this section, we search for bound OB star-magnetar binaries using optical and near-IR images. As discussed in Section 2.2, bound companions should have negligible ($\lesssim 1'$) separation from the magnetar in high resolution ($\sim 0.25'' - 0.4''$) images. Chrimes et al. (2022a) conducted a similar search using HST Wide Field

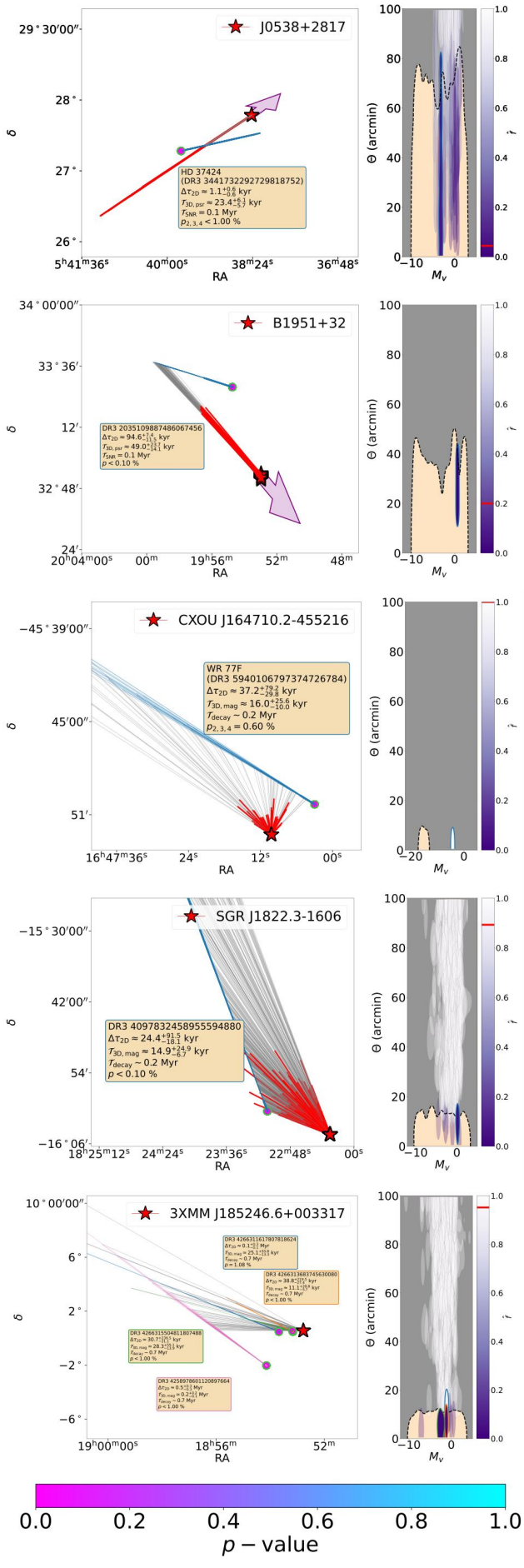

Figure 2.2: (*Left*) Monte Carlo sampled trajectories for candidate *Gaia* DR3 sources with p-values $p < 5\%$ possibly associated with three magnetars (*right*, *bottom*), PSR J0538+2817 (*top left*), and PSR B1951+32 (*middle left*). Each figure includes only *Gaia* OB star candidates with association p-value $p < 5\%$, including the unbound companion of CXOU J164710.2-455216 proposed by Clark et al. (2014), WR 77F (*top right*). Present-day magnetar/pulsar and GDR3 source locations are shown as red stars and circular markers, respectively; the latter has colorbar corresponding to the total p-value p, except for PSR 0538+2817 and CXOU J164710.2-455216, for which we exclude p_1 (see Section 2.4). Red lines show the initial magnetar/pulsar trajectory samples while thin lines extrapolate the magnetar/pulsar and source trajectories to their past intersection. Note for these initial trajectories extend farther for pulsars (*top left*, *middle left*) than for magnetars (*right*, *bottom*) since travel time samples were drawn from a uniform distribution up to 1 Myr for pulsars in contrast to 10 kyr for magnetars. If proper motion measurements are available, the proper motion direction is indicated by a purple arrow. Each GDR3 source is shown with its source ID, 2D travel time difference $\Delta\tau_{2D}$, the magnetar's/pulsar's 3D travel time $\mathcal{T}_{3D,mag/psr}$, an upper limit age estimate $\mathcal{T}_{SNR/decay/rot}$, and the relevant p-value. (*Right*) Contour plot of Monte Carlo samples in $\{\Theta - M_V\}$ space. The 95% contour region is in beige, and candidates with search statistic $\hat{f}$ less than the critical threshold, $\hat{f}_c$, have colorbar corresponding to $\hat{f}$ (see Appendix 2.11.2.4). $\hat{f}_c$ is indicated by a red horizontal line on each colorbar. We recover the proposed companions of CXOU J164710.2-455216 (WR 77F; *upper right*) and PSR J0538+2817 (HD 37424; *top left*) with $p < 5\%$. We also identify potential runaway companions of SGR 1822.3-1606 and PSR B1951+32 (*middle row*) with $p < 5\%$. The companions shown for 3XMM J185246.6+003317 (*bottom*) are most likely false positives as discussed in Appendix 2.11.3.1.

Camera 3[19] images with $\sim$ 27 magnitude depth and 0.1265″ resolution. They place tight constraints with milliarcsecond precision on $\sim$ 15 magnetar NIR counterpart candidates using $H-$band HST data, laying the foundation for the Chrimes et al. (2022b) search.

While Chrimes et al. (2022b) discuss that searching in NIR is more effective than optical due to the $\sim 7\times$ lower extinction, searching optical data is still beneficial. The massive, un-evolved OB star companions we expect are intrinsically fainter in the NIR than optical wavelengths. The magnitude depth of the PS1 ($\sim$ 24) and SkyMapper ($\sim$ 18) catalogs therefore makes them powerful resources for this search (Kaiser, 2004; Maund et al., 2016; Onken et al., 2024; Wolf et al., 2018). We also note that since the resolution (0.4″, 0.34″, and 3″, respectively) and depth ($\sim$ 18, $\sim$ 15, and $\sim$ 19.3, respectively) of the UKIDSS, VVV, and 2MASS images are far exceeded by HST, any additional data to supplement the breadth of the search is valuable.

2.5.1 Pan-STARRS and SkyMapper Data and Optical Search Method

The Pan-STARRS Data Release 2 (PS1 DR2) catalog contains optical images of the northern sky (above $\delta > -30°$) in 5 passbands ($g-$,$r-$,$i-$,$z-$,and $y-$bands, or '$grizy$') with 0.25″ pixels (Chambers et al., 2019; Flewelling et al., 2020). $1' \times 1'$ image cutouts were obtained from the PS1 Image Server[20] at the position of each magnetar and candidate. Seventeen magnetars and all 7 magnetar candidates fall within the PS1 survey range. For the remaining 7 with $\delta \leq -30°$, we use images from the SkyMapper Southern Survey Data Release 4 (SkyMapper DR4[21]), which records in $u-$,$v-$,$g-$,$r-$,$i-$, and $z-$bands ('$uvgriz$') with 0.5″ pixels (Onken et al., 2024; Wolf et al., 2018). Note the point source detection limit is $\sim$ 18.0 in comparison to $\sim$ 21.5 for PS1.

In addition to image cutouts, the PS1 and SkyMapper point source catalogs were queried to obtain known sources within a 30″ search cone of each magnetar. We also include any bright sources identified 'by-eye' within the image that do not appear to coincide with catalogued point sources (see Appendix 2.11.2.3). We then use the catalogued magnitudes and position of each source to conduct a Monte Carlo simulation. Similarly to the *Gaia* search we define the association p-value using

[19] See the WFC3 Instrument Handbook for details: https://hst-docs.stsci.edu/wfc3ihb/chapter-7-ir-imaging-with-wfc3/7-8-ir-sensitivity

[20] https://ps1images.stsci.edu/ps1image.html

[21] https://skymapper.anu.edu.au/, doi.org/10.25914/5M47-S621

three criteria:

1. The PS1 source and magnetar are located at the same RA and declination.
2. If we assume the source absolute magnitude is that of an OB star ($-10 \lesssim M_V \lesssim 3$), the distance is equal to the magnetar's distance.
3. The difference of the Kron and point source (PSF) magnitude ($M_{x,\mathrm{Kron}} - M_{x,\mathrm{PSF}}$) exceeds the Farrow et al. (2014) point source cutoff for x = '$uvgrizy$' bands as available (Kron, 1980):

$$\Delta M_{\mathrm{min}}(M_{x,\mathrm{Kron}}) = -0.319+0.129(M_{x,\mathrm{Kron}}-21)+0.007(M_{x,\mathrm{Kron}}-21)^2 \quad (2.2)$$

for which we define p-values p_1, p_2, and p_3, respectively. The three p-values are combined to get the total association p-value:

$$p = 1 - (1 - p_1)(1 - p_2)(1 - p_3) \quad (2.3)$$

An explicit derivation of p_1, p_2, and p_3 is provided in Appendix 2.11.2.1.

The method above was applied only for magnetars with errors defined for the RA, declination and distance, and only for point sources with at least $g-$ and $r-$ band PSF and Kron magnitudes[22], and errors defined for RA and declination. Note that our evaluation of p_2 contrasts with the Chrimes et al. (2022b) search, which uses the magnetar distance to estimate extinction values for nearby candidate stars. However, magnetar distances are not well-constrained, with errors of order $\sim$ kpc. In this work, we invert this process to obtain a distance estimate whose uncertainty is driven by the expected absolute magnitude range. Through this, we avoid making assumptions about the source distance beyond the requirement that it be an OB star.

2.5.2 UKIDSS, VVV, and 2MASS Data and IR Search Method

Infrared images were obtained from the UKIDSS survey catalog, which is a superset of the Large Area Survey (LAS), galactic plane Survey (GPS), Galactic Clusters Survey (GCS), Deep Extragalactic Survey (DES), and Ultra Deep Survey (UDS)

[22]This unfortunately means that p-values are not estimated for 'by-eye' sources in the optical and IR searches. However, most lie at a large angular separation relative to the magnetars' $\sim 1''$ position errors, making them unlikely candidates.

catalogs (Dye et al., 2006). Collectively, this covers the declination range from $-60^\circ < \delta < +40^\circ$, including sightlines for 12 magnetars and 6 magnetar candidates from this sample. We obtained $1' \times 1'$ image cutouts with $0.2''$ pixels in the $J-$, $H-$, and $K-$bands (390 − 1220 nm) for each magnetar to search for binary companions. For 8 magnetars in the southern portion of the galactic disk, the VISTA Variables in the Via Lactea (VVV) survey was queried for $J-$, $H-$, and K_s-band images with $0.2''$ pixels (Nikzat et al., 2022). Images for the five remaining magnetars were obtained from the Two-Micron All-Sky Survey (2MASS)[23], which surveys the full sky in the $J-$, $H-$, and K_s-bands at much lower $\sim 3''$ resolution ($\sim 2''$ pixels; Skrutskie et al., 2006). The UKIDSS galactic plane Survey (UGPS)[24] catalog, 2MASS point source catalog, and VVV Infrared Astrometric Catalogue (VIRAC)[25] were queried in a cone search for discrete objects within $0.5'$ of each magnetar (Lawrence et al., 2012, 2013; Lucas et al., 2008; Nikzat et al., 2022; Skrutskie et al., 2006; Smith et al., 2018). Additional sources were identified 'by-eye' in each image to include in the search.

The criteria used for the IR search are below:

1. The source and magnetar are located at the same RA and declination;
2. If we assume the source's absolute $H-$band magnitude and $J - H$ color are stellar in nature and resemble that of a bound OB star ($-2.76 \lesssim M_H \lesssim 3.34$, $-0.14 \lesssim J-H \lesssim 0.31$ are 95% confidence ranges from Chrimes et al. (2022b) population synthesis), the distance is equal to the magnetar's distance;

for which we define p-values p_1 and p_2, respectively. Kron magnitudes are not available from the included IR catalogs. The p-values are combined using:

$$p = 1 - (1 - p_1)(1 - p_2) \tag{2.4}$$

An explicit derivation of these p-values is provided in Appendix 2.11.2.2. Note the p-value is only evaluated for magnetars and sources with position errors, and only for 2MASS and VVV sources with at least $H-$ and $J-$ band magnitudes. Chrimes et al. (2022b) revealed that magnetar surface IR emission can be easily

[23] https://irsa.ipac.caltech.edu/Missions/2mass.html
[24] https://vizier.cfa.harvard.edu/viz-bin/VizieR?-source=II/316
[25] https://vizier.cfa.harvard.edu/viz-bin/VizieR?-source=II/364

mistaken for a companion star, with IR magnitudes $M_H \gtrsim 2.5$ (see Chrimes et al., 2022b, Figure 5). Although interacting binaries such as SGR 0755-2933 can be far brighter (its companion CPD-29 2076 has $M_H \sim -4$), passive binaries like PSR J0210+5845 are much fainter in the absence of mass transfer (its companion B0V star has $M_H \sim 0.5$; Tan et al., 2020). Both magnitude and color must be considered to distinguish massive stellar companions from surface emission, which we account for in p_2.

2.5.3 Optical and IR Search Results

Using a 95% confidence level, we recover the proposed Be star bound companion of magnetar candidate SGR 0755-2933, CPD-29 2176, through the optical (PS1) and IR (UKIDSS) searches with $p < 0.1\%$[26] (Chrimes et al., 2022b; Richardson et al., 2023). In the following sections, we discuss the association of a PS1 source with the companion of SGR 0755-2933's error circle and the non-recovery of the proposed counterpart of CXOU J171405.7-38131. Figure 2.3 shows optical and IR images for these three magnetars. Candidate companions were identified with $p < 5\%$ for PSR J1622-4950 and SGR J1822.3-1606, but are most likely false positives as discussed in Appendix 2.11.3.3.

2.5.3.1 PS1 Counterpart of SGR 0755-2933's Be Star Companion

Five IR candidates and three optical candidates were recovered with $p < 5\%$ as potential companions of SGR 0755-2933. The abundance of sources is due to its large $3'$ position error (Barthelmy et al., 2016). This sample includes the known 2MASS counterpart to the proposed companion star CPD-29 2176, 2MASS J07554248-2933535. We also recover a PS1 source within the 2MASS source's 60 mas error circle, PSO J118.9270-29.5649, and therefore conclude this is the optical counterpart of CPD-29 2176.

However, we note that the association of SGR 0755-2933 with CPD-29 2176 is tenuous due to the former's lack of activity; only one burst localized to a $3'$ region by the *Swift* telescope has been detected (Barthelmy et al., 2016). While a revised position uncertainty $0.4''$ was derived by Richardson et al. (2023) by assuming its association with CPD-29 2176, Doroshenko et al. (2021) identify 8 persistent X-ray sources within the $3'$ error circle. This prevents a confident association of the burst with any persistent source, including CPD-29 2176. Although Richardson

[26]For the optical and IR searches we use 1,000 trials, setting lower an upper limits of $0.1 < p < 99.9\%$ on the p-value.

et al. (2023)'s spectral analysis confirms the presence of an HMXB containing CPD-29 2176 (formally 2SXPS J075542.5-293353), a second burst localized to the binary is required to confirm that it contains SGR 0755-2933.

2.5.3.2 CXOU J171405.7-38131

We do not recover the infrared source, VIRAC 384090103, proposed by Chrimes et al. (2022b) as a potential stellar companion to CXOU J171405.7-38131 (Nikzat et al., 2022; Smith et al., 2018). If placed at the distance of the magnetar, 3.8 ± 0.5 kpc, the source has an $H-$band magnitude $M_H \approx -0.9 \pm 0.1$ consistent with an OB star and its color $J - H \approx -0.5 \pm 0.3$ differs only marginally. We note that the magnetar lies along a highly extincted sightline outside of the *Bayestar19* range, making its $A_V \approx 22.1 \pm 0.8$ from the $N_H - A_V$ relation an upper limit (Predehl & Schmitt, 1995). This biases the Monte Carlo p-value test since the extinction cannot be estimated as a function of distance. Therefore, the location of the magnetar and source make this analysis inconclusive, and we cannot rule out VIRACS 384090103 as a potential companion of CXOU J171405.7-38131.

2.6 Radio Search for SNR Shells

2.6.1 RACS, VLASS, and NVSS Data and Search Method

While numerous continuum radio searches for SN shells have been conducted (see e.g., Dubner & Giacani, 2015; D. Green, 2019; D. Lorimer et al., 1998, for comprehensive reviews) as have searches for compact objects near SNRs (e.g., C. Kochanek, 2018, 2021, 2023; C. Kochanek et al., 2019), few targeted searches for SNRs near compact objects have been carried out beyond individual sources. Leveraging the young ages ($\lesssim$ 1 Myr, e.g., Suzuki et al., 2021) we search for evidence of SNRs among the magnetar sample.

The RACS-low Data Release 1 (DR1) contains images with 15″ resolution at 888 MHz, with a limiting sensitivity of 0.25 mJy beam^{-1} (Hale et al., 2021; McConnell et al., 2020). Public images are smoothed to a common pixel scale 25″. Twenty magnetars and 6 magnetar candidates without confirmed SNRs fall within the survey region $-80^\circ < \delta < +30^\circ$. We obtained $1^\circ \times 1^\circ$ radio image cutouts via the RACS Data Access Portal[27]. For two magnetars (SGR 0501+4516 and 1E 2259+586) with $\delta > +30^\circ$, images from the Karl G. Jansky Very Large Array Sky Survey (VLASS), which covers $\delta > -40^\circ$ with 0.12 mJy sensitivity, were obtained using the Canadian

[27] `https://data.csiro.au/`

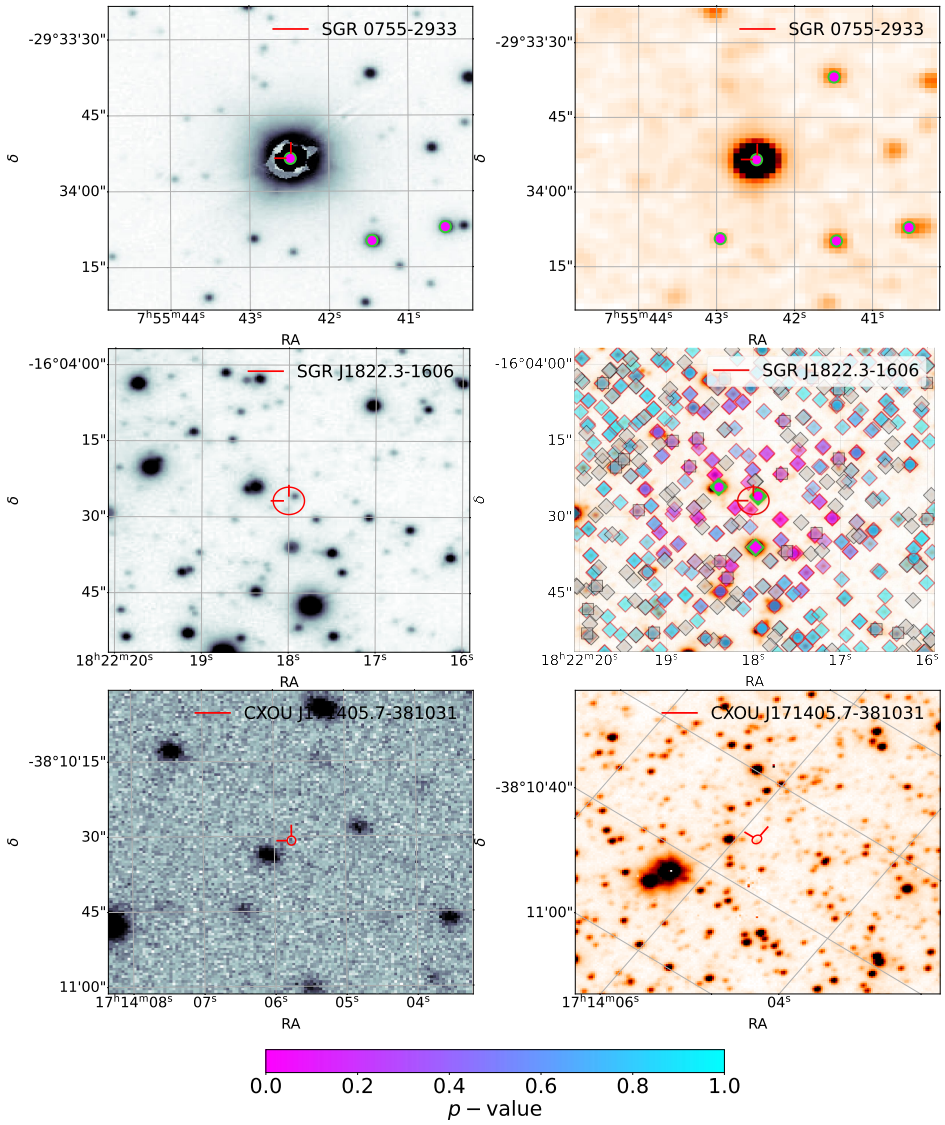

Figure 2.3: Optical (*Left*) and Infrared (*Right*) $1' \times 1'$ image cutouts for 2 magnetars and 1 magnetar candidate. Each image is in grayscale where RGB channels are combined using $0.2989R + 0.5870G + 0.1140B$. Optical images use the $g-$, $i-$, and $y-$band filters for PS1 images (CXOU J1714) and the $g-$, $r-$, and $i-$band filters for SkyMapper images (SGR 0755 and SGR J1822). Infrared images use the $J-$, $H-$, and $K-$band filters for UKIDSS images (SGR 1822) and the $J-$, $H-$, and K_s-band filters for VVV (CXOU J1714) and 2MASS (SGR 0755) images. The magnetar location is indicated by red cursors and the 3σ error ellipse is shown in red. Note the error ellipse is much larger than the image for SGR 0755-2933. Each marker indicates a point source from the optical or infrared catalogs with colorbar corresponding to the association p-value, p. Sources with insufficient data to determine a p-value are grey. Sources with $p < 5\%$ are outlined in green, while those with $p > 5\%$ are outlined in red. (*Left*) PS1 sources are shown as circles, SkyMapper sources are shown as triangles, and sources identified 'by-eye' are shown as squares. (*Right*) 2MASS sources are shown as circles, VVV sources are shown as triangles, UKIDSS sources are shown as diamonds, and sources idenified 'by-eye' are shown as squares. Sources with no corresponding marker were not identified in the catalogs considered, and could not be well-fit with an ellipse. The Be-star companion of SGR 0755 is recovered in the optical and infrared searches, and candidates are identified for SGR 1822. The proposed companion of CXOU J1714 is not recovered, but cannot be ruled out as a bound companion due to uncertainty in the extinction estimate. Note that the axes for CXOU J1714 differ between optical and infrared due to the use of different World Coordinate System (WCS) projections (ZPN) for VVV data (e.g., Greisen & Calabretta, 2002).

Initiative for Radio Astronomy Data Analysis (CIRADA[28]) cutout service (Y. A. Gordon et al., 2020, 2021, 2023). VLASS Quick-Look images[29] are taken at 3 GHz with 1″ pixel scale, which we bin to 25″ to search for extended emission. For three magnetars covered by neither VLASS nor RACS (4U 0142+61, SGR 0418+5729, and SGR 2013+34), we obtain cutouts from the 1.4 GHz National Radio Astronomy and VLA Sky Survey (NVSS)[30], a precursor to VLASS (J. J. Condon et al., 1998). This catalog contains images with 15″ pixels and RMS noise 0.5 mJy beam^{-1}, or $\sim$ 0.8 mJy beam^{-1} for 25″ pixels[31]. One magnetar, SGR 1627-41, is not covered by any of the radio surveys discussed [32].

The Set of Identifications, Measurements and Bibliography for Astronomical Data (SIMBAD[33]) database was queried for known SNRs, SNR candidates, and unidentified radio sources with 'ISM' object-types[34] within the same $1^\circ \times 1^\circ$ region for each magnetar (Egret et al., 1991). If a previously proposed SNR candidate was not found in the initial SIMBAD query, it was added manually to the sample for the association test (for example, SNR HBH 9 is associated with SGR 0501+4516, but falls more than 1.3° away and was missed in the query). Additional sources which may be SNRs are identified 'by eye' to include in the search (see Appendix 2.11.2.3). Sources identified as known radio galaxies or AGN were removed from the sample. While a radio image is not available for SGR 1627-41, we proceed with the association test using SIMBAD radio sources within 1°. Through a Monte Carlo search, p-values are estimated with the criteria below:

1. The SNR and magnetar are located at the same RA and declination;
2. The magnetar's proper motion direction is consistent with the direction required to intersect the SNR;
3. The magnetar's proper motion and age are consistent with the observed angular separation of the magnetar and SNR;

[28] `https://cirada.ca/vlasscatalogueql0`

[29] Epochs 3.1 and 2.2 are used for magnetars SGR 0501+4516 and 1E 2259+586, respectively.

[30] `https://www.cv.nrao.edu/nvss/postage.shtml`

[31] VLASS data is taken in the B configuration which is sensitive to angular scales between 2.1 – 58″. NVSS data is taken in the D and DnC configurations which are sensitive to angular scales between 14 – 970″ and 46 – 970″, respectively. See `https://science.nrao.edu/facilities/vla/docs/manuals/oss/performance/resolution` for details.

[32] While this magnetar does fall in the survey range of RACS-DR1, no continuum images are available that contain SGR 1627-41 in its field-of-view.

[33] `https://simbad.u-strasbg.fr/simbad/sim-fbasic`

[34] See `https://simbad.cds.unistra.fr/guide/otypes.htx` for details on SIMBAD object-types.

4. The SNR's dynamical age is consistent with an SNR shell rather than a point source;

for which we define p-values p_1, p_2, p_3, and p_4, respectively. Appendix 2.11.2.3 contains a derivation of these p-values explicitly. Unlike in the binary companion searches, criteria (i)-(iii) relate to two independent cases: first that the magnetar is located within the SNR shell (i), and then that the magnetar has travelled some distance away from the SNR during its lifetime (ii and iii). Therefore, unless $p_1 < 0.1\%$ or $1 - (1 - p_2)(1 - p_3) < 0.1\%$[35], we combine p_1, p_2, and p_3 using the Fisher statistic[36]:

$$\hat{\chi}^2_4 = -2(\ln(p_1) + \ln(1 - (1 - p_2)(1 - p_3))) \tag{2.5}$$

This follows a χ^2 distribution with 4 degrees of freedom, from which we compute the p-value p_χ using the inverse survival function. We then combine this with p_4 using:

$$p = 1 - (1 - p_\chi)(1 - p_4) \tag{2.6}$$

Note that p_1 requires definition of the RA and declination errors for the magnetar and either the RA and declination errors or angular size and position angle for the SNR. p_2 and p_3 additionally require definition of the magnetar proper motion errors and the X-ray decay or characteristic age. p_4 requires the angular size or position error to be defined.

2.6.2 Radio SNR Search Test with Known Magnetar-SNR Associations

Eight magnetars and 2 magnetar candidates with confirmed SNR associations are used to test the radio image search method. With the analysis above, we accurately recover the associated SNRs with $p < 5\%$ for 7 magnetars and both magnetar candidates. SGR 1627-41 is the only confirmed SNR association that we fail to recover in the radio search (SNR G337.0-00.1; Corbel et al., 1999), which is likely due to the large angular offset $\sim 15.5'$. No proper motion is known for SGR 1627-41, but a velocity $\sim 1275\,\mathrm{km\,s^{-1}}$ would be required given its $\mathcal{T}_{\rm decay} \approx 37.0\,\mathrm{kyr}$, which is in marginal agreement with the Hobbs et al. (2005) distribution. Given that

[35] The minimum p-value is set by the 1,000 trials used for the SNR search.

[36] `https://en.wikipedia.org/wiki/Fisher%27s_method`

9 of the 10 trials were successful in recovering the associated SNRs, we proceed with confidence that the image-plane and Monte Carlo search methods are effective. Radio images for five magnetars with proposed SNR associations are shown in Figure 2.5.

2.6.3 Radio SNR Search Results

Among the 13 magnetars and magnetar candidates with no previous SNR associations, we identify two candidates which have $p < 5\%$. One of these, associated with SGR 0755-2933 is most likely a false positive which we discuss in Appendix 2.11.3.2. For SGR 1808-20, we find two viable SNR association candidates which require proper motion and distance measurements to properly assess. Of the eight magnetars and magnetar candidates with proposed but unconfirmed or rejected SNRs we recover five (and marginally recover a sixth with $p = 5.6\%$), one of which is nearby the Galactic Center magnetar SGR J1745-2900 and another of which would suggest 3XMM J185246.6+003317 has an ejected pulsar companion. In this section, we discuss the SNR candidates for SGR 1808-20 and the recovered unconfirmed SNR candidates in detail.

2.6.3.1 SGR 1808-20

For SGR 1808-20, we find multiple candidate radio sources (29) with $p < 0.1\%$, 10 of which were selected for analysis 'by-eye' rather than through the SIMBAD query. The large number of sources comes from the loose position ($\sim 7'$ error) and distance (no measurement) constraints, as only one burst has been detected from the magnetar since its discovery (D. Lamb et al., 2003). $2' \times 2'$ VLASS cutouts at $1''$ scales were obtained for each candidate, revealing that 6 of the 29 sources were resolved and unlikely to be SNRs. One source is a known Young Stellar Object (YSO) while another is an unidentified sub-millimetric source, both of which are unlikely to be SNRs (Eden et al., 2017). Fourteen are labelled as 'dense cores', or InfraRed Dark Clouds (IRDCs) which are pre-star forming regions that may be the birthplaces of massive stars (Jiao et al., 2023). IRDCs are distinguished from SNRs based on their high masses ($\sim 100 M_\odot$) and hydrogen column densities ($N_H \sim 10^{23}\,\mathrm{cm}^{-2}$), essentially ruling out these candidates (e.g., Güver & Özel, 2009).

Six of the seven remaining sources are 'by-eye' candidates; we query the SIMBAD database within $1'$ of each source to identify potentially missed sources of radio emission. One is nearby PSR J1808-2057 which has a radio flux 2.3 mJy and

is likely responsible for the observed emission (Hobbs et al., 2004). Another is coincident with a $\sim 532 M_\odot$ molecular cloud discovered through sub-millimeter ($\sim 0.1 - 1$ THz) emission, making it a plausible radio source (Duarte-Cabral et al., 2021). One is coincident with an infrared-bright 'bubble'; these are star-forming sites in HII regions and are therefore also plausible radio sources (Simpson et al., 2012). Two others are coincident with stars, one an AGB star and the other an eclipsing binary system, both of which are potentially radio bright, though no radio flux has yet been catalogued (Cutri et al., 2003; Heinze et al., 2018; Spangler et al., 1977). While these five sources cannot be confidently ruled out, we will assume they are not associated given the possible contamination by nearby objects. This leaves two sources as candidates for association: SNR G009.7-00.0 and an unidentified radio source, which we formally label S24-RACS J180842-202849, with no SIMBAD objects within $1'$. For the remaining discussion, we will refer to the latter source as 'Source 1'.

Source 1 was identified by eye at $18^{\mathrm{h}}08^{\mathrm{m}}42^{\mathrm{s}} - 20°28'45''$ and fit with an ellipse of approximate major and minor axes $a \sim b \sim 18''$. This lies very near the position of another magnetar, SGR 1806-20, and the W31 HII region (e.g., Corbel & Eikenberry, 2004; D. Frail & Clifton, 1989; Moisés et al., 2011). The distance to W31 has been disputed in the literature; if we adopt the distance of SGR 1806-20, $8.7^{+1.8}_{-1.5}$ kpc, Source 1 would have a radius ~ 0.8 pc. At this size the SNR would be in the free-expansion phase, and assuming $n_0 \sim 1\,\mathrm{cm}^{-3}$, we estimate the age of the remnant to be between $0.3 - 1.2$ kyr (Sedov, 2018). This is roughly consistent with $\mathcal{T}_{\mathrm{rot}}$ and $\mathcal{T}_{\mathrm{decay}}$ for magnetars, but the lack of data for SGR 1808-20 prevents a direct comparison. A detailed composition analysis is required to confirm Source 1 as a supernova remnant, though its morphological similarity to other false positives implies it is unlikely to be an SNR.

SNR G009.7-00.0, on the contrary, was detected by D. Frail et al. (1994) and confirmed through its OH maser by Hewitt & Yusef-Zadeh (2009), which constrained its distance to ~ 4.7 kpc. Yeung et al. (2016) find its distance is inconsistent with W31 and SGR 1806-20. At ~ 4.7 kpc, the $\sim 11 - 15'$ angular size corresponds to a radius $\sim 8 - 10$ pc, suggesting a free-expansion age of ~ 10 kyr. Both Source 1 and SNR G009.7-00.0 appear to be viable candidates for association with SGR 1808-20, but a magnetar distance measure and more tightly constrained position are necessary to investigate further. The radio image is shown in Figure 2.5.

2.6.3.2 3XMM J185246.6+003317 and CXOU J185238.6+004020 as an Unbound Double Neutron Star Binary

For 3XMM J185246.6+003317 we recover the Kes 79 SNR (SNR G033.6+00.1) with $p < 0.1\%$, which is associated with a central X-ray pulsar CXOU J185238.6+004020 (PSR J1852+0040; e.g., Bogdanov, 2014; Gotthelf et al., 2005; Malofeev et al., 2005). Bogdanov (2014) derive a Sedov-Taylor expansion age of ~ 5 kyr for the SNR which contrasts with both the decay age $\mathcal{T}_{\rm decay} \approx 0.7$ Myr[37] and spindown age $\mathcal{T}_{\rm rot} \gtrsim 1.3$ Myr of 3XMM J185246.6+003317.[38] Magnetars are typically expected to be unobservable beyond $\sim 10^4$ years; however, the spindown age $\mathcal{T}_{\rm rot}$ is a well-constrained lower limit derived by Rea et al. (2014) from an X-ray timing solution. They find a pulse period $P = 11.55871346(6)$ s with no discernible spindown, leading to upper limits of $\dot{P} < 1.4 \times 10^{-13}\,{\rm s\,s^{-1}}$ and $B_{\rm dip} \lesssim 10^{13}$ G. on the spindown rate and magnetic field. While these paramters are reminiscent of typical radio pulsars, Zhou et al. (2014) noted in their initial discovery that the X-ray luminosity ($\sim 10^{33-34}\,{\rm erg\,s^{-1}}$) far exceeds its spindown luminosity ($\sim 10^{30}\,{\rm erg\,s^{-1}}$), making its magnetar nature robust. Therefore we take both the spindown age and the decay age to be reasonable age estimates. This suggests that Kes 79 is associated with CXOU J185238.6+004020, but allows a scenario wherein the pulsar and magnetar were gravitationally bound in the past (Zhou et al., 2014).

Considering this case, let the initially bound massive star progenitors of 3XMM J185246.6+003317 and CXOU J185238.6+004020 be called stars 1 and 2, respectively. When the CCSN of star 1 disrupts the binary[39], the remnant magnetar (3XMM J185246.6+003317) and star 2 are ejected at $\sim 300\,{\rm km\,s^{-1}}$ and $\sim 6\,{\rm km\,s^{-1}}$, respectively (Hobbs et al., 2005; Renzo et al., 2019). After travelling for ~ 0.7 Myr based on the magnetar's age, the CCSN of star 2 would then kick the remnant pulsar (CXOU J185238.6+004020) at $\sim 300\,{\rm km\,s^{-1}}$, leaving behind the remnant shell Kes 79. This sequence of events is shown in Figure 2.4. We investigate this scenario by applying a modified *Gaia* unbound companion search pipeline to the magnetar and CXOU J185238.6+004020's *Gaia* counterpart, *Gaia* DR3 4266508881354196736.

[37] More recent constraints on the magnetic field from ray-tracing simulations by Lima et al. (2024) suggest $\mathcal{T}_{\rm decay} \gtrsim 1.2$ Myr, though they caution not to over-interpret their initial estimates.

[38] While the spindown age of CXOU J185238.6+004020 is ~ 192 Myr, 'anti-magnetars' or 'compact central objects' (CCO) like this are known to have overestimated spindown ages due to the complex relation of their low magnetic fields to a dynamo process (Gotthelf & J. P. Halpern, 2008; Gotthelf et al., 2013; J. P. Halpern et al., 2007).

[39] The alternate case in which star 2 undergoes the first CCSN is equally likely, but we we focus the discussion on this scenario which is more consistent with the age estimate for 3XMM J185246.6+003317.

We split the companion's trajectory into two parts with different velocities to account for the two CCSN events, assume the absolute magnitude of the companion is $M_V > 0$, and neglect p_2 since the magnetar's and pulsar's travel times no longer coincide directly. Ten thousand trials (rather than 100) are used since the magnetar has no proper motion measurment.

The resulting trajectory plot is shown in Figure 2.4; we find a p-value $p_{1,3} = 0.02\%$, suggesting that this scenario is likely. From the 497 valid samples out of 10,000, the scenario requires the magnetar to have velocity $|\overrightarrow{v}_{\rm mag}| \approx 398^{+208}_{-165}\,{\rm km\,s^{-1}}$ (proper motion $\mu_\alpha \cos(\delta) \approx -2.1^{+1.2}_{-5.8}\,{\rm mas\,yr^{-1}}$, $\mu_\delta \approx -9.8^{+4.9}_{-20.8}\,{\rm mas\,yr^{-1}}$) and a travel time $\mathcal{T}_{\rm 3D,mag} \approx 40.1^{+56.1}_{-21.8}\,{\rm kyr}$, which is consistent with expected magnetar ages, but disagrees with Rea et al. (2014), Zhou et al. (2014), and $\mathcal{T}_{\rm decay}$. Despite the robustness of the X-ray timing solution, magnetars are known to glitch, anti-glitch, and slowly recover from glitches during outbursts such as the one used for timing analysis (e.g., Archibald et al., 2013; Scholz et al., 2014; Tong & Huang, 2020; Younes et al., 2023). Coupled with Rea et al. (2014) observing the outburst at a late time, this implies that 3XMM J185245.6+003317 may have experienced a glitch event leading to its undetectable spindown. If we impose $\mathcal{T}_{\rm 3D,mag}$ as an age constraint, then using the period $P = 11.55871346(6)$ s we derive a revised spindown rate of $\dot{P} \approx 4.6^{+5.4}_{-2.7} \times 10^{-12}\,{\rm s\,s^{-1}}$, and dipolar magnetic field $B_{\rm dip} \approx 2.3^{+1.1}_{-0.2} \times 10^{14}\,{\rm G}$, both of which are more consistent with the magnetar sample.

The pulsar requires a velocity $|\overrightarrow{v}_{\rm psr,1}| \approx 8^{+11}_{-4}\,{\rm km\,s^{-1}}$ following the first CCSN, and $|\overrightarrow{v}_{\rm psr,2}| \approx 422^{+192}_{-172}\,{\rm km\,s^{-1}}$ following the second. The most supportive evidence for this scenario is the position of the pulsar's CCSN, estimated from valid samples as $18^{\rm h}52^{\rm m}38\overset{\rm s}{.}60 + 00°40'20\overset{''}{.}09$ with 1σ errors of $0.2'$ and $0.4'$ in RA and declination respectively. This is roughly 8σ away from the centroid of Kes 79, $18^{\rm h}52^{\rm m}48^{\rm s} + 00°41'00''$, but is well within its $\sim 5'$ radius. We obtain an estimate of $18^{\rm h}52^{\rm m}56\overset{\rm s}{.}5 + 00°43'57\overset{''}{.}5$ with errors $\sigma_\alpha \sim 3'$ and $\sigma_\delta \sim 6'$ for the position of the first CCSN. This also lies within the extent of Kes 79, and suggests that its unique multi-shell structure may result from interactions between the magnetar and pulsar SNR shock fronts. Other single-SNR scenarios have been presented to explain this structure as, for example, the interaction of the SNR with a molecular cloud or the progenitor's stellar wind (Giacani et al., 2009; Sato et al., 2016; Sun et al., 2004; Velusamy et al., 1991; Zhou et al., 2016). We conclude that it is likely that the progenitors of 3XMM J185246.6+003317 and CXOU J185238.6+004020 began in a bound system prior to the former's CCSN, and a proper motion measurement for

3XMM J185246.6+003317 would further constrain their formation history.

2.6.3.3 SGR J1745-2900, the Galactic Center Magnetar

SGR J1745-2900 is a unique magnetar at the Galactic Center (GC) of the Milky Way (Mori et al., 2013b). The radio emission from the supermassive black hole Sag A* and high density of radio sources in this region make it difficult to identify any associations with confidence. The black hole would also distort an SNR shell from SGR J1745-2900 (e.g., Yalinewich et al., 2017). However, Ponti et al. (2015) used high resolution X-ray observations to catalog extended regions near the GC, identifying the GC X-ray/radio lobes as a warped and mirrored SNR. SGR J1745-2900 lies near the intersection of the two lobes, and Yalinewich et al. (2017) use numerical simulations to demonstrate that an 'engulfing' SNR explosion at this location could produce the observed SNR structure.

Given this analysis, the radio lobes were added to the simulation using the centroid position ($17^{\rm h}45^{\rm m}32\overset{\rm s}{.}3$ – $29°2'32\overset{''}{.}5$) and angular diameter $\sim 5.8'$ from Ponti et al. (2015). Through the Monte Carlo simulation, we recover the radio lobes, as well as a gamma-ray source 0FGL J1746.0-2900 found not to be an SNR (Acero et al., 2016) and an HII region (Nguyen et al., 2015), with $p < 0.1\%$. In our simplified model of the lobes, we do not account for the irregular structure of the SNR, but instead assume the SNR is centered at the lobes' centroid with angular size equal to a single lobe. This simplification should not greatly impact the results since only a lower limit is imposed on the SNR's dynamical age based on the angular size. The position of the radio lobes' centroid is marginally consistent with the trajectory of SGR J1745+1900 (see Figure 2.5). With a proper motion magnitude ~ 6.4 mas yr^{-1}, the $\sim 2.7'$ separation suggests an SNR age ~ 25 kyr, which is slightly lower than the decay age estimate $\mathcal{T}_{\rm decay} \approx 64.9$ kyr. Further interpretation requires a more detailed analysis of the GC lobe geometry, but our results support a scenario where the bipolar radio lobes are the SNR of SGR J1745+1900.

2.6.3.4 Other Magnetars with Unconfirmed SNRs

Five other magnetars in the sample were identified in previous searches as potential associations of nearby supernovae, but have not yet been confirmed: SGR 1900+14, SGR 1806-20, SGR 0526-66, SGR 0501+4516, and SGR 1801-23. SGR 1900+14's association with SNR G042.8+00.6 (for which we find $p = 5.6\%$) was rejected by Vrba et al. (2000) given the former's more likely association with a star cluster.

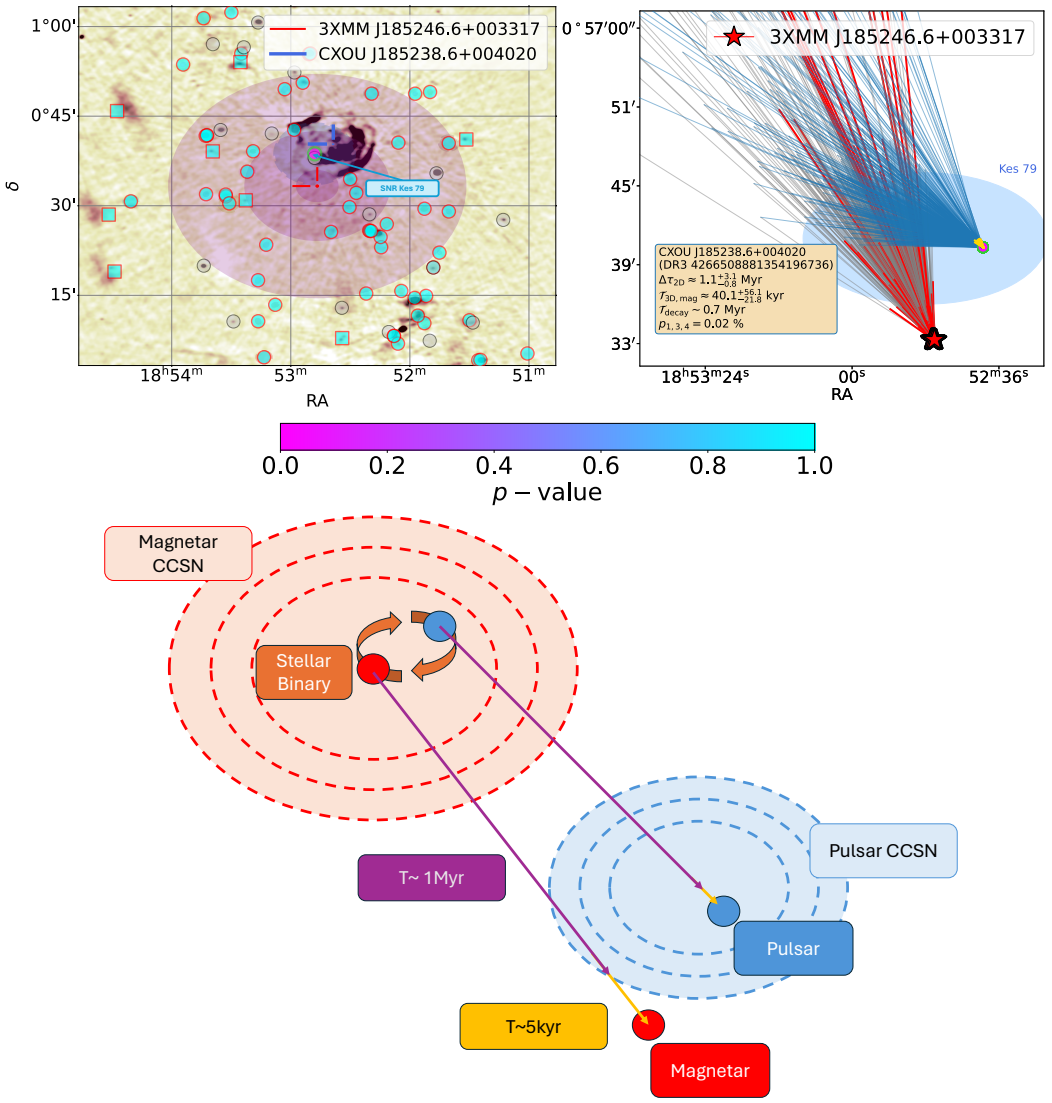

Figure 2.4: Radio Image and Trajectory Analysis of 3XMM J185246.6+00317. (*Top left*) A RACS DR1 888 MHz continuum $1^\circ \times 1^\circ$ image cutout is shown for 3XMM J185246.6+00317 with $25'' \times 25''$ pixels. The magnetar and pulsar locations are indicated by red and blue pointers, while circular and square markers show known and 'by-eye' identified radio sources, respectively. Note that no markers are shown for catalogued Active Galactic Nuclei or radio galaxies, as they were not included in this search. Other extended sources without markers were not identified in SIMBAD and could not be well-fit with an ellipse. The colorbar corresponds to the association p-value. The purple shaded region indicates the 1, 2, and 3σ past travel distances based on the Hobbs et al. (2005) velocity distribution. The angular extent of Kes 79 (labelled) is shown as a blue circle. (*Bottom*) The cartoon demonstrates how a bound massive stellar binary (orange) may evolve into an unbound magnetar (red) and pulsar (blue) following two CCSNe. (*Top right*) The trajectory plot for 3XMM J185246.6+00317 and the X-ray pulsar CXOU J185238.6+004020 is shown with 468 valid trajectories (out of 10,000 trials). Blue traces show the pulsar's trajectory prior to the second CCSN, and yellow traces show its trajectory after the CCSN. The blue circle indicates the location and extent of Kes 79.

We identify one additional by-eye source, S24-RACS J190707+091737, as an SNR candidate with $p < 0.1\%$, but rule it a false positive as it disagrees with the proper motion direction of SGR 1900+14. SGR 1806-20's association with AX J1808.6-2024 (SNR G10.0-0.3) was also rejected by Hurley et al. (1999), suggesting it is not an SNR but a radio nebula powered by its central LBV star. While there is insufficient position data to estimate a p-value for the nebula, we do recover it when using the angular size of its potentially associated gamma ray emission, Fermi J1808.2-2029 (H. E. S. S. Collaboration et al., 2018). Finally, we do not recover XTE J1810-197's association with SNR G11.0-0.0, supporting the age considerations which ruled out the candidate in Ding et al. (2020a).

SGR 0526-66 is located within the Large Magellanic Cloud (LMC) near SNR N49 (SNR J052559-660453; Klose et al., 2004). However, its association with SNR N49 could not be confirmed as the magnetar's proper motion is unknown, which is necessary to localize its birth place to SNR N49's host star cluster, SL 463. With our pipeline, we obtain a p-value $p < 0.1\%$ for this association. Notably, five other 'by-eye' radio sources were recovered with $p < 5\%$; however, each of these fall within $1'$ of possible known radio sources that are not within the LMC. While SGR 0526-66 does not have a proper motion measurement, its position error of $0.6''$ compared to the $1.4'$ angular size result in a highly confident association. The large distance 53.6 ± 1.2 kpc suggests N49 has a tranverse size of roughly 22 pc, while the $0.6''$ position error for the magnetar corresponds to ~ 0.1 pc. Therefore it is likely that N49 contains SGR 0526-66, supporting Klose et al. (2004)'s claim of association.

For SGR 0501+4516, B. Gaensler & Chatterjee (2008) localized the magnetar to the outer rim of SNR HBH 9 (HB9 or SNR G160.9+2.6) at a position $\sim 15'$ from the next nearest SNR. The large angular separation $\sim 1.3°$, however, initially excluded SNR HBH 9 from the test sample. After adding this as a bye-eye radio source, we obtain a p-value $p = 7.0\%$, providing insufficient evidence to confirm the association. This is most likely due to the large angular separation $\sim 1.3°$; at the magnetar's distance 2 ± 0.3 kpc, this corresponds to a transverse separation of ~ 45 pc. For the magnetar's decay age $\mathcal{T}_{\rm decay} \approx 59.4$ kyr, this would require a velocity $\sim 730\,{\rm km\,s^{-1}}$ for the magnetar, which agrees well with the Hobbs et al. (2005) distribution expected for neutron stars. Therefore, given the marginal p-value recovered and the achievable kick velocity, we find this association remains possible, and a proper motion measurement is required to confirm or reject it.

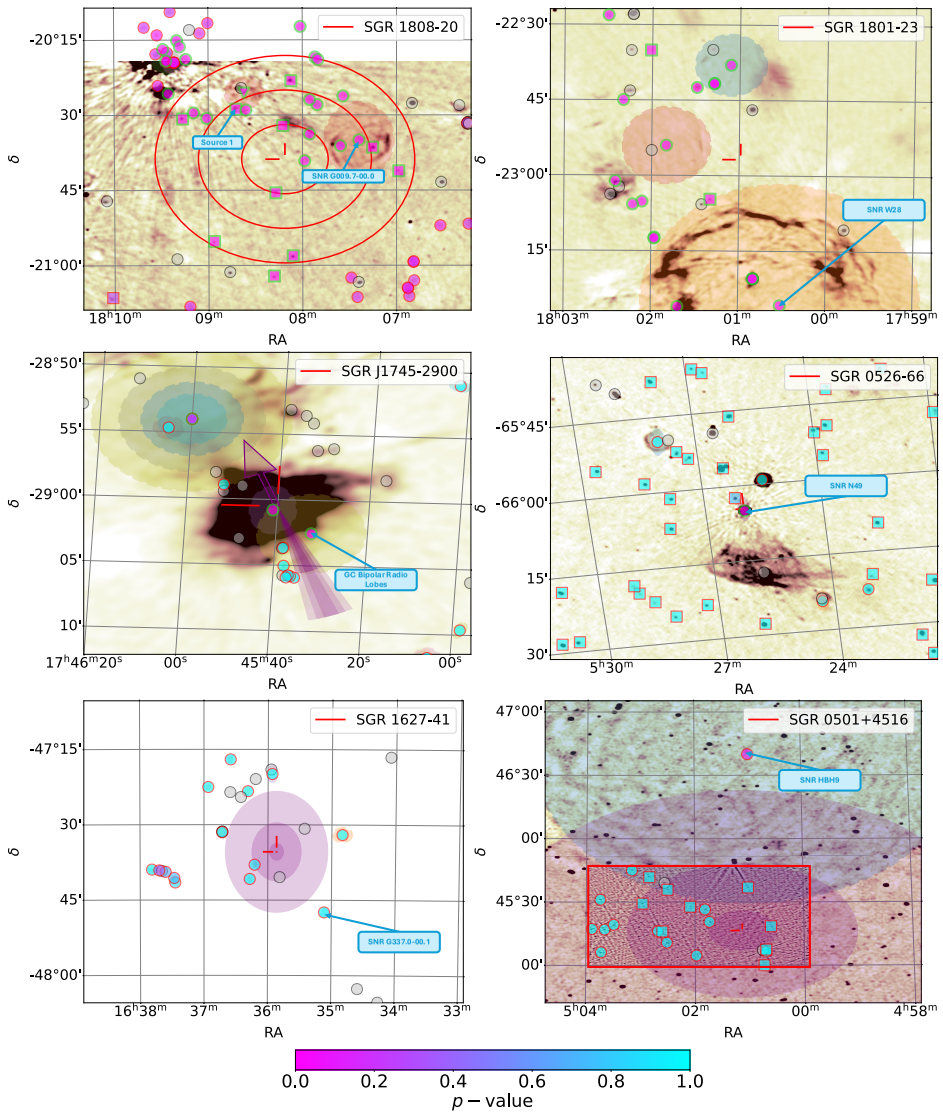

Figure 2.5: Radio continuum image cutouts for four magnetars (*middle, bottom*), and two magnetar candidates (*top*) with possible SNR associations. Red pointers indicate each magnetar's location and the 1σ, 2σ, and 3σ magnetar error ellipses are shown in red (although they are too small to be visible except for SGR 1808-20 and SGR 1801-23. For the latter, the 3.8° error ellipse is too large to be effectively shown.). Note the difference in axis extents for each image. RACS 888 MHz continuum images with $25'' \times 25''$ pixels are shown for SGR 1808-20, SGR 1801-23, SGR J1745-2900, and SGR 0526-66 (*top, middle*). For SGR 0501+4516, a 3 GHz $1' \times 1'$ VLASS image with $1'' \times 1''$ pixels (smoothed to $25'' \times 25''$ with a boxcar kernel) is shown enclosed in a red box indicating the queried region, while the remainder of the image is from the 1.4 GHz NVSS survey to show SNR HBH 9 (e.g., Göğüş et al., 2010b). However, NVSS is only sensitive to angular sizes $< 970''$ ($\lesssim 16.7'$), making SNR HBH9 ($120 - 140'$) unobservable in the image shown. No radio images from RACS, VLASS, or NVSS were available at SGR 1627-41's position (*bottom left*). Circular markers indicate the locations of known radio sources while square markers indicate unknown sources identified by-eye. Note that no markers are shown for catalogued Active Galactic Nuclei or radio galaxies, as they were not included in this search. Other extended sources without markers were not identified in SIMBAD and could not be well-fit with an ellipse. The colorbar corresponds to the association p-value; sources outlined in red (green) have $p > 5\%$ ($p \leq 5\%$). The most likely or previously proposed SNRs (see Section 2.6.3) are labelled. 'Source 1' (*top left*) is S24-RACS J180842-202849. The angular extents of SNRs, if available, are shown as ellipses. For SGR 1745-2900 (*middle left*), the proper motion direction is marked by a purple arrow, and the purple shaded region indicates the 1σ, 2σ, and 3σ past travel direction and extent; for SGR 1627-41, SGR 0501+4516, and SGR 0526-66 (*bottom, middle right*), the Hobbs et al. (2005) velocity distribution is used to show possible past travel direction and extent.

2.7 Discussion

Through this multiwavelength search of 31 magnetars and magnetar candidates, we identify one magnetar with a potential unbound OB star companion, SGR J1822.3-1606, but require proper motion data to explore further. We note that magnetar 3XMM J185246.6+003317 may be an unbound system whose progenitor was bound to that of an X-ray pulsar, CXOU J185238.6+004020. While we recover the Be star companion of SGR 0755-2933 proposed by Richardson et al. (2023) and the unbound Wolf-Rayet star companion of CXOU J164710.2-455216 proposed by Clark et al. (2014), we are unable to confidently associate the IR counterpart of CXOU J171405.7–381031 proposed as a bound companion by Chrimes et al. (2022b). Through the radio search, we recover nine of ten confirmed SNR associations, propose scenarios supporting four of five unconfirmed SNR associations, and identify a new candidate SNR associated with SGR 1808-20 which requires a proper motion and distance measurement for confirmation.

Table 2.3 summarizes our results, which prompt a discussion of the CCSN model for magnetar formation. The recovery of only two unbound binary candidates is inconsistent with Chrimes et al. (2022b) and Renzo et al. (2019) simulations predicting that $f_u \sim 38 - 56\%$ of magnetars should be nearby unbound companion stars. We begin this section by analyzing our search's sensitivity before exploring the implications of the search on magnetars' massive star progenitors. We then consider potential limitations in our work and investigate the possibility of more exotic magnetar formation channels.

2.7.1 Completeness and Sensitivity Considerations

For each search, we estimate the expected ranges of intrinsic parameters and derive the ranges of their corresponding observables in order to compare to our sensitivity thresholds. For the bound companion search, we search for OB stars with intrinsic magnitudes in the following ranges:

1. $-2.76 \lesssim M_H \lesssim 4.34$ (Chrimes et al., 2022b)
2. $-2.61 \lesssim M_i \lesssim 5.55$ [40]

Similarly in the *Gaia* search for unbound companions we expect:

[40] Derived by converting the Chrimes et al. (2022b) constraints on M_H and $J - H$ using the 2MASS relationships. See also Section 5.5 of *Gaia* DR3 Documentation (`https://gea.esac.esa.int/archive/documentation/GDR3/`.

1. $-10 \lesssim M_V \lesssim 1.185$
2. $v_{\rm mag}$ following the Hobbs et al. (2005) distribution
3. v_{src} following the Renzo et al. (2019) distribution

and for the SNR search:

1. Radio luminosity $L \approx 10^{42}\,{\rm erg\,s^{-1}}$ in the Rayleigh-Jeans limit (Barker et al., 2023, 2022; Hamuy, 2003)
2. Angular size $25'' \lesssim \Delta\Theta \lesssim 1^\circ$ (from observed SNR sizes in the D. A. Green (1987) catalog and considerations of free- and Sedov-Taylor-expansion in Truelove & McKee (1999))

By combining these constraints with the distance, extinction, and proper motion of each magnetar (see Table 2.1), we estimate the expected range of apparent magnitudes ($V-$, $i-$, and $H-$band), SNR flux at 1 GHz, and relative proper motion $\Delta\mu$ between the magnetar and an unbound companion. Figure 2.6 and Table 2.3 summarize the results. Four magnetars have no distance measurements and are not included in this analysis.

For the *Gaia* search we observe that the relative proper motion of each magnetar and a walk/runaway companion should be detectable down to $M_G \sim 21$ given the proper motion uncertainty $\sigma_\mu \approx 1.4\,{\rm mas\,yr^{-1}}$ (Collaboration et al., 2022). Only the SMC magnetar CXOU J010043.1-721134 is partially incomplete for faint stars due to its large distance. However, four magnetars lie along high-extinction sightlines with $A_V \gtrsim 17$ (CXOU J171405.7-381031, 1E 1547.0-5408, PSR J1622-4950, SGR 1627-41), making unbound companions undetectable at *Gaia*'s $M_V < 20.7$ sensitivity. Nineteen magnetars are partially complete, meaning that our search may miss fainter B-star companions. These results are more promising than indicated by the simulations of Chrimes et al. (2023), which determined that without the aid of next generation deep-field surveys, *Gaia* may recover only a small fraction of unbound neutron star companions. This demonstrates that incorporating a trajectory search into our Monte Carlo analysis can make significant improvements to our search sensitivity.

The bound search is complete or partially complete for most magnetars covered by the IR survey; only SGR 1627-41, which has a large extinction $A_V \approx 55.87 \pm$

11.17, and the two magnetars in Magellanic Clouds, CXOU J010043.1-721134 and SGR 0526-66 are incomplete. The optical search, on the other hand, is incomplete for six magnetars due to their high extinction. This is in agreement with Chrimes et al. (2022b), which concluded that IR searches are more effective for OB stars due to the $\sim 4\times$ lower extinction in $H-$band compared to $i-$band (e.g., D. Green, 2019).

Finally, the SNR search is complete in all cases for typical radio luminosities and angular sizes in the free- or Sedov-Taylor expansion phases (e.g., Salpeter, 1955; Truelove & McKee, 1999). We note, however, that a bright synchrotron radio shell may not be produced if the magnetar inhabits a low-density local environment or lacks a significant internal energy source (e.g., Chevalier & Clegg, 1985; D. Frail et al., 1995; Leung et al., 2020; Nomoto, 1987). Future work may expand on this sensitivity analysis with detailed forward modelling of SNRs, but this is beyond the scope of this work. Table 2.3 indicates whether each magnetar's search is considered 'partially or fully complete' (✓) or 'incomplete' (✗) in the above analysis. We conclude that our search for companion stars and SNRs is reasonably sensitive along sightlines with typical extinction and distances $< 10\,\mathrm{kpc}$.

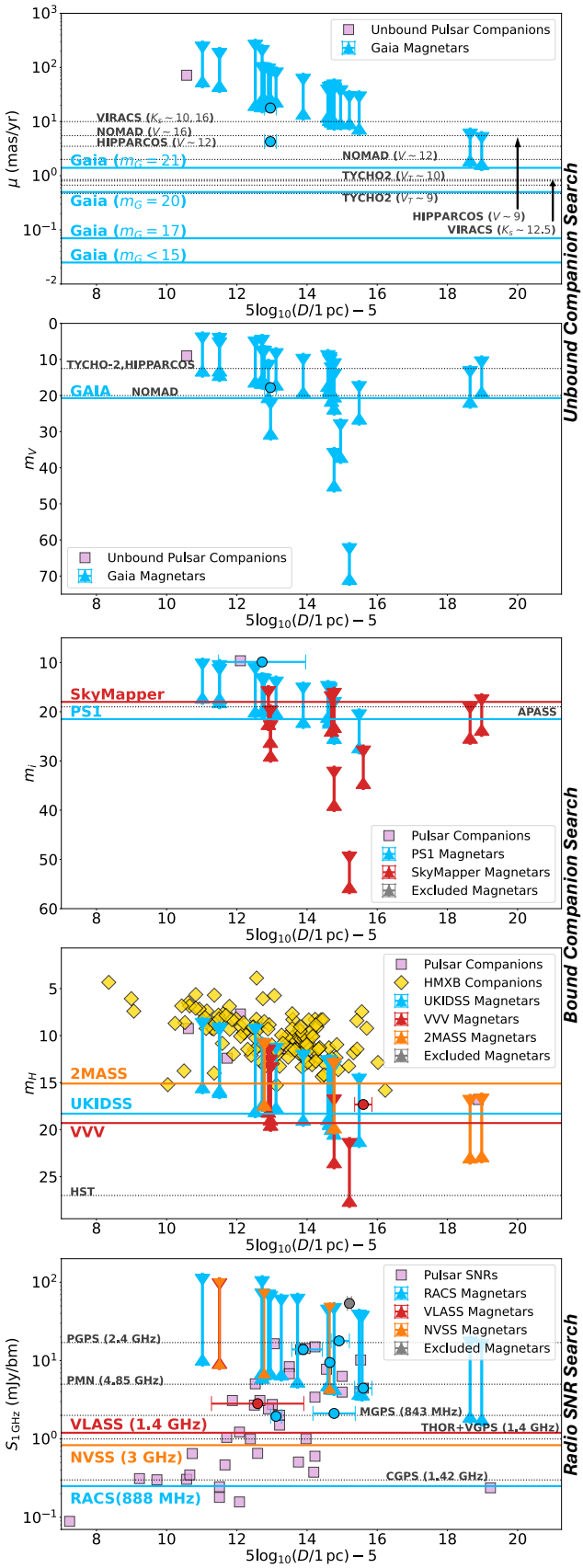

Figure 2.6: Completeness plots versus distance modulus for (*rows 1 and 2*) the *Gaia* search, (*row 3*) the optical and (*row 4*) IR searches, and (*row 5*) the radio search. Circular, square, and diamond markers with errorbars indicate known companions or remnants of magnetars, pulsars, and HMXBs, respectively. Proper motion, apparent magnitude, and 1 GHz flux ranges, are shown as vertical lines, with color relating to the survey used for the search. The sensitivity limits of each survey are indicated by horizontal lines. We expect most magnetars with SNR shells or stellar companions would have been detected if present. Sensitivity limits for past searches are shown as black dotted lines for comparison (see Appendix 2.11.5 for references).

Table 2.3: Search Results and Completeness Ratios

Magnetar	SNR Candidate	Radio SNR Complete?	Bound Companion Candidate	Optical/IR Bound Complete?	Unbound Companion Candidate	*Gaia* Unbound Complete?	Prior Association Candidate(s)
CXOU J0100	*None*	✓(R)	None	✓(S,T)	–	✓	–
4U 0142	*None*	✓(N)	*None*	✓(P,T)	*None*	✓	–
SGR 0418	*None*	✓(N)	*None*	✓(P,U)	*None*	✓	–
SGR 0501	*None*	✓(V)	*None*	✓(P,U)	*None*	✓	HBH 9 (1)
SGR 0526	N49 {p<0.1%}	✓(R)	*None*	✗(S,U)	*None*	✓	N49 (2)
1E 1048	*None*	✓(R)	*None*	✓(S,T)	*None*	✓	–
1E 1547	G327.2-00.1 {p=1.5%}	✓(R)	*None*	✓(S,V)	–	✗	G327.2-00.1 (3)
PSR J1622	G333.9+00.0 {p<0.1%}	✓(R)	*SMSS J162244.99-495055.7 {p<0.1%}*	✓(S,V)	–	✗	G333.9+00.0 (4)
SGR 1627	*None*	✓(R)	*None*	✗(S,V)	–	✗	G337.0-00.1 (5)
CXOU J1647	*None*	✓(R)	*None*	✓(S,V)	*None*	✓	WR 77F (6)
1RXS J1708	*None*	✓(R)	*None*	✓(S,V)	*None*	✓	–
CXOU J1714	CTB 37B {p<0.1%}	✓(R)	*None*	✓(S,V)	*None*	✗	{CTB 37B, VIRAC 384090103 (7,8)}
SGR J1745	*{0FGL J1746.0-2900 {p<0.1%}* GC Bipolar Radio Lobes {p<0.1%} *NNM2015 {p<0.1%}}*	✓(R)	*None*	✓(P,V)	*None*	✓	GC Bipolar Radio Lobes (13,14)
SGR 1806	*Fermi J1808.2-2029 {p<0.1%}*	✓(R)	*None*	✓(S,V)	*None*	✓	{G10.0-0.3 (9) Fermi J1808.2-2029 (21)}
XTE J1810	*None*	✓(R)	*None*	✓(P,U)	*None*	✓	G11.0-0.0 (22)
Swift 1818	*None*	✓(R)	*None*	✓(P,U)	*None*	✓	–
Swift J1822	*None*	✓(R)	*{2MASS J18221794-1604259 {p<0.1%} UKIDSS J182217.94-160425.9 {p<0.1%} UKIDSS J182217.94-160426.0 {p<0.1%} 2MASS J18221839-1604241 {p<0.1%} UKIDSS J182218.39-160424.1 {p<0.1%} UKIDSS J182218.39-160424.0 {p<0.1%} UKIDSS J182217.97-160436.0 {p=2.0%} UKIDSS J182217.97-160435.9 {p=1.0%} }*	✓(P,U)	GDR3 4097832458955594880 {p<0.1%}	✓	–
SGR 1833	*None*	– (R)	*None*	– (P,T)	*None*	–	–
Swift J1834	W41 {p<0.1%}	✓(R)	*None*	✓(P,U)	*None*	✓	W41 (10)
1E 1841-045	4C-04.71 {p<0.1%}	✓(R)	*None*	✓(P,U)	*None*	✓	4C-04.71 (11)

3XMM J1852	Kes 79 {p<0.1%}	✓(R)	*None*	✓(P,U)	*{DR3 4266311617807818624 {p=1.08%}, DR3 4266313683745630080 {p<1.0%}, DR3 4266315504811807488 {p<1.0%}, DR3 4258978601120897664 {p<1.0%}* CXOU J185238.6+004020* {p=0.02%}}	✓	Kes 79 (17)
SGR 1900	*S24-RACS J190707+091737{p<0.1%}*	✓(R)	*None*	✓(P,U)	*None*	✓	G042.8+00.6 (12)
SGR 1935	G057.2+00.8 {p<0.1%}	✓(R)	*None*	✓(P,U)	*None*	✓	G057.2+00.8 (13)
1E 2259	CTB 109 {p<0.1}	✓(V)	*None*	✓(P,U)	*None*	✓	G109.1-01.0 (14)
SGR 0755	{ *S24-RACS J075552-293709 {p<0.1%}* *S24-RACS J230208+585020{p<0.1%}* *S24-RACS J075520-293531 {p<0.1%}* *S24-RACS J075523-292928 {p<0.1%}* *S24-RACS J075603-292541 {p<0.1%}* *S24-RACS J075613-293630 {<0.1%}* *NVSS J075522-293937 {p<0.1%}* *NVSS J075529-294201 {p<0.1%}* }	✓(R)	{ PSO J118.9270-29.5649 {p<0.1%} 2MASS J07554248-2933535 {p<0.1%} *PSO J118.9228-29.5694 {p=2.0%}* *PSO J118.9189-29.5686 {p=4.0%}* *2MASS J07554146-2934098 {p<0.1%}* *2MASS J07554053-2934071 {p<0.1%}* *2MASS J07554295-2934093 {p=2.0%}* *2MASS J07554149-2933368 {p<0.1%}*}	✓(P,T)	*None*	✓	CPD-29 2176 (8)
SGR 1801	{W28 {p<0.1%} *18 sources‡ {p<0.1%}*}	– (R)	*None*	–(P,U)	*None*	–	W28 (20)
SGR 1808	{G009.7-00.0 {p<0.1%} *S24-RACS J180842-202849 {p<0.1%}* *28 sources‡ {p<0.1%}*}	– (R)	*None*	–(P,U)	*None*	–	–
AX J1818.8-1559	*None*	– (R)	*None*	–(P,U)	*None*	–	–
AX J1845-0258	G029.6+00.1 {p<0.1%}	✓(R)	*None*	✓(P,U)	*None*	✓	G029.6+00.1 (15)
SGR 2013+34	*None*	✓(N)	*None*	✓(P,U)	*None*	✓	–
PSR J1846-0258	Kes 75 {p=1.0%}	✓(R)	*None*	✓(P,U)	*None*	✓	Kes 75 (16)

For each magnetar (written with its abbreviated name), the SNR candidates, bound companion candidates, and unbound companion candidates with $p < 5\%$ are given, with p-values in brackets. Candidates suspected to be false positives are given in italics. Sources identified 'by-eye' which are not confidently associated with any known object are labelled using the format, 'S24-*survey*-J*hhmmss±ddmmss*', where *survey* is the survey used and the italicized portion is the J2000 RA and declination of the centroid. For each search, the completeness along each magnetar's sightline is indicated by a ✓, meaning the search is either partially or fully sensitive to stars or remnants, or by an ✗, meaning that even the brightest expected stars or remnants would not be detectable. The radio search completeness is labelled with 'R', 'V', or 'N' to indicate whether the RACS, VLASS, or NVSS survey is used. The optical/IR bound search is considered partially or fully complete if either the optical or IR search are complete. These are labelled with 'P' or 'S', to indicate whether the PS1 or SkyMapper survey is used, and 'T', 'U', or 'V' to indicate whether the 2MASS, PS1, or VVV survey is used. The *Gaia* search is considered partially or fully complete if both the $V-$band magnitude and expected relative proper motion are detectable. Four magnetars or candidates have no distance measures and the completeness cannot be determined; these are marked with '–'.Candidates for SNR, bound, or unbound companions from previous analyses are provided in the last column with references matched to the following: (1) B. Gaensler & Chatterjee (2008) (2) Klose et al. (2004) (3) Gelfand & B. M. Gaensler (2007) (4) G. E. Anderson et al. (2012) (5) Corbel et al. (1999) (6) Clark et al. (2014) (7) J. P. Halpern & Gotthelf (2010b) (8) Chrimes et al. (2022b) (9) Corbel & Eikenberry (2004) (10) Kargaltsev et al. (2012) (11) Vasisht & Gotthelf (1997) (12) Vrba et al. (2000) (13) B. Gaensler (2014) (14) Fahlman & Gregory (1981) (15) B. M. Gaensler et al. (1999) (16) Gotthelf et al. (2000) (17) Zhou et al. (2014) (18) Ponti et al. (2015) (19) Yalinewich et al. (2017) (20) T. Cline et al. (2000) (21) H. E. S. S. Collaboration et al. (2018) (22) Ding et al. (2020a)

†For the *Gaia* search for unbound companions, we consider the proper motion sensitivity in four magnitude bins as described in Collaboration et al. (2022): $m_G > 15$ ($\mu_{\rm min} = 0.025\,{\rm mas\,yr^{-1}}$), $m_G = 17$ ($\mu_{\rm min} = 0.07\,{\rm mas\,yr^{-1}}$), $m_G = 20$ ($\mu_{\rm min} = 0.5\,{\rm mas\,yr^{-1}}$), and $m_G = 21$ ($\mu_{\rm min} = 1.4\,{\rm mas\,yr^{-1}}$).

‡For conciseness, we omit the names of the 17 and 28 false positives found for SGR 1801-23 and SGR 1808-20, respectively. For the former, the false positives are rejected in favor of W28 identified by T. Cline et al. (2000). Detailed discussion for the latter is provided in Section 2.6.3.

*CXOU J185238.6+004020 is an X-ray pulsar associated with Kes 79. We explore the scenario that the progenitors of 3XMM J1852 and this pulsar were bound in Section 2.6.3.

2.7.2 The Magnetar Binary and Massive Star Merger Fractions

2.7.2.1 Markov-Chain Monte Carlo Analysis of Magnetar Binary Fractions

With more well defined estimates of our search completeness, we next determine the implications of our results on the CCSN model. We adapt the method of C. Kochanek (2023) to constrain the binary parameters of the magnetar progenitor population using a Markov-Chain Monte Carlo (MCMC) simulation. Uniform priors are chosen to estimate the fraction of systems which were not binaries at death, f_n; the fraction that were unbound at death, f_u; and the fraction of interacting binaries remaining bound after the CCSN, f_i. We relate these to the total fraction of binaries remaining bound after the CCSN, f_b, and the fraction of non-interacting binaries remaining bound after the CCSN, f_p, by $f_n = 1 - f_u - f_b$ and $f_b = f_i + f_p$.

The likelihood is the joint multinomial probability of the observed samples; we define the sample for this analysis by incorporating the completeness ratios in Table 2.3. Of the 31 magnetars and candidates, three systems, CXOU J164710.2-455216, 3XMM J185246.6+003317, and SGR J1822.3-1606, were proposed as unbound binary systems. The candidate companion of CXOU J171405.7-381031 from Chrimes et al. (2022b) is unconfirmed based on the optical and IR search results. For the purpose of our analysis, we will accept SGR 0755-2933 and CPD-29 2176 as a bound interacting binary system based on the results of Richardson et al. (2023). Of the remaining sample, three magnetars are constrained to be not currently bound, two are constrained not to have unbound companions, and the remaining 21 are considered not to be binaries at the time of the CCSN. With this, the likelihood can be written as:

$$\mathcal{P}_{\rm i} = f_n^{21} f_u^3 f_i^1 (1 - f_u)^2 (f_n + f_u)^3 \tag{2.7}$$

where $(1 - f_u)$ is the fraction that are not unbound systems and $(f_n + f_u)$ is the fraction that are not bound systems. The sampled posteriors are used to estimate the median values and 90% confidence intervals for f_n, f_u, and f_i.

In keeping with the notation of C. Kochanek (2023), we define the case above as 'SNR incomplete', where we assume that all magnetars in the sample originate in CCSNe. While this is likely the primary formation channel, it is possible that other processes may form magnetars at lower rates. Considering this, we define the 'SNR complete' case, in which magnetars without confirmed or proposed SNR

associations are not formed via CCSNe, and therefore do not contribute to the binary fractions above. In this case, the likelihood becomes:

$$\mathcal{P}_{\rm c} = f_n^{10} f_u^1 f_{nc}^{15} (f_n + f_u)^2 (1 - f_u)^2 (1 - f_{nc})^1 \tag{2.8}$$

where f_{nc} is the fraction of magnetars which do not originate in CCSNe. This modifies the definition for f_n to $f_n = 1 - f_u - f_b - f_{nc}$. Note this case is more restrictive, as SGR 0755+2933, SGR J1822.3-1606, and 13 other magnetars for which the radio search is $> 75\%$ complete have no confirmed SNR in this or any other work. A final case, 'SNR/unbound complete' is defined if we also take unbound magnetar binaries as evidence of CCSNe; in this case, we include CXOU J164710.2-455216, SGR J1822.3-1606, and 3XMM J185246.6+003317 as unbound systems, and the likelihood becomes:

$$\mathcal{P}_{\rm uc} = f_n^{10} f_u^3 f_{nc}^{13} (f_n + f_u)^2 (1 - f_u)^2 (1 - f_{nc})^1 \tag{2.9}$$

Results for the three cases are summarized in Table 2.4. In the 'SNR incomplete' case, we find a median bound binary fraction $f_b \approx 9^{+6}_{-4}\%$, and unbound binary fraction $f_u \approx 12^{+6}_{-5}\%$, where the errors are 1σ uncertainties. While the bound fraction is marginally consistent with the predictions from Chrimes et al. (2022b), C. Kochanek et al. (2019), and Renzo et al. (2019) population synthesis results, the unbound fraction significantly disagrees with their prediction of $f_u \sim 38 - 56\%$. Furthermore, we find that a median of only $1 - f_n \approx 22^{+8}_{-7}\%$ of magnetars were binaries at death, which disagrees with the estimate of $\sim 50 - 60\%$ from population synthesis with 90% confidence.

In the 'SNR complete' case, we estimate a median unbound fraction $f_u \approx 3^{+3}_{-2}\%$, and a 90% upper limit on the bound fraction of $f_b \lesssim 12\%$, the former of which also disagrees with the Chrimes et al. (2022b), C. Kochanek et al. (2019), and Renzo et al. (2019) population synthesis estimates. We find a median $1 - f_n \approx 63^{+9}_{-8}\%$ of magnetars undergo CCSNe while in binaries, which more closely agrees with population synthesis than the 'SNR incomplete' case. Most significantly, we constrain the fraction of magnetars formed by channels other than CCSNe to $f_{nc} \approx 53^{+8}_{-10}\%$, with a 90% confidence interval from $37-66\%$. This would contradict the view that CCSNe are the dominant formation pathway (e.g., Keane & Kramer, 2008; F. R. Schneider et al., 2019; White et al., 2022). Furthermore, no magnetars have been confirmed to form from non-CCSN channels.

Table 2.4: Constraints on magnetar binaries from this work

Sub-Sample[†]	**Symbol**	**SNR incomplete**		**SNR complete**		**SNR/unbound complete**	
		Median	90% C.I.	Median	90% C.I.	Median	90% C.I.
Not binary at death	f_n	78^{+7}_{-8}%	64 – 88%	37^{+9}_{-8}%	24 – 52%	39 ± 9%	25 – 54%
Bound binary	f_b	9^{+6}_{-4}%	3 – 20%	–	< 12%	–	< 13%
Interacting binary	f_i	6^{+5}_{-3}%	1 – 15%	–	< 8%	–	< 8%
Non-interacting binary	f_p	–	< 8%	–	< 7%	–	< 7%
Unbound binary	f_u	12^{+6}_{-5}%	5 – 24%	3^{+3}_{-2}%	1 – 10%	8^{+5}_{-3}%	3 – 16%
Not CCSN Progenitor	f_{nc}	–	–	53^{+8}_{-10}%	37 – 66%	46 ± 9%	31 – 60%
Pre-CCSN Merger[‡]	f_m	70^{+10}_{-12}%	48 – 86%	88^{+5}_{-8}%	73 – 96%	82^{+7}_{-9}%	65 – 92%

Note: We define two broad cases based on the completeness of the RACS SNR search: 'SNR incomplete' assumes that all magnetars originate in CCSNe, whether one is detected or not. 'SNR complete' assumes that magnetars with RACS search completeness ratios > 75% which had no SNR detected did not form through CCSNe. We also consider the 'SNR/unbound complete' case in which unbound magnetar binaries are evidence of the CCSN progenitor channel as well. Median values are reported with 1σ errors and 90% confidence intervals (C.I.) are shown.

[†] f_n, f_b, f_u, and f_{nc} are defined such that $f_n + f_b + f_u = 1$ in the 'SNR incomplete' case, and $f_n + f_b + f_u + f_{nc} = 1$ in the 'SNR complete' and 'SNR/unbound complete' cases. f_i and f_p sum to the total binary fraction $f_p + f_i = f_b$. The merger rate f_m is the fraction of binary stars that merge, while the other fractions are taken out of the total number of CCSNe.

[‡] f_m is estimated assuming the progenitor stars are early B-type stars ($9M_\odot < M_* < 16M_\odot$) with binary fraction $F_0 = 84 \pm 9\%$ (Moe & Di Stefano, 2017).

A similar result is obtained in the 'SNR/unbound complete' case; notably, the larger unbound fraction $f_u \approx 8^{+5}_{-3}\%$ allows a lower non-CCSN fraction $f_{nc} \approx 46 \pm 9\%$, while the fraction of magnetars from binaries $1 - f_n \approx 61 \pm 9\%$ still agrees with population synthesis results. While the 'SNR/unbound complete' and 'SNR complete' cases do not differ in their underlying assumptions about alternate formation channels, they demonstrate that the detection of unbound magnetar binaries allows for tighter constraints to be placed on f_{nc}. Furthermore, these cases motivate discussion of alternate formation channels, such as Accretion Induced Collapse (AIC) of magnetized White Dwarfs, electron-capture supernovae of less massive stars, or binary Neutron Star mergers, to which we return in Section 2.7.3 (C. Fryer et al., 1999; Giacomazzo & Perna, 2013; Giacomazzo et al., 2015; Miyaji et al., 1980; Ruiter et al., 2019).

2.7.2.2 Implications for Massive OB Star Binary and Merger Fractions

Many models of magnetar formation attribute their strong magnetic fields to a dynamo process driven by accretion from ablated stellar companions (e.g., Fuller & Lu, 2022; S. B. Popov, 2020; Revnivtsev & Mereghetti, 2016, and references

therein). The low f_b and f_u fractions in Table 2.4 may indicate that other magnetic field growth mechanisms are more common, such as the merger of massive stars. In this scenario, the magnetic field of the primary star is first amplified up to $\lesssim 10^8$ G through accretion before further amplification through merger of the cores, producing a highly magnetized massive star such as τ Sco and the Wolf-Rayet star in the HD 45166 binary (F. R. Schneider et al., 2019; Shenar et al., 2023). If magnetic flux is conserved during the CCSN event, a neutron star remnant with a magnetar-like surface magnetic field ($\sim 10^{14}$ G) could be achieved (e.g., Obergaulinger et al., 2014; S. B. Popov, 2020; F. R. Schneider et al., 2019, and references therein). A high frequency of such pre-CCSN mergers could potentially explain the lack of magnetars with bound or unbound companions.

The fraction of massive stellar binaries that merge prior to CCSNe, f_m, can be inferred by assuming an initial massive star companion fraction $F_0 \approx 84 \pm 9\%$, derived in Moe & Di Stefano (2017), for early B-type stars. [41] While some simulations suggest that CCSNe can form from mergers of intermediate mass stars ($5 - 8 M_\odot$), we focus this discussion on binaries where both stars are $> 7.5 M_\odot$ (e.g., Zapartas et al., 2017). Relating the initial companion fraction to the fraction of systems in binaries at death:

$$\frac{f_u + f_b}{1 - (f_b + f_u) f_q} = F_0 (1 - f_m) \tag{2.10}$$

where $f_q = 0.426$ is the fraction of binaries with a secondary star less massive than the primary [42]. f_q effectively estimates the fraction of CCSNe from explosions of the secondary star, which are excluded from this analysis since we consider CCSN of stars with *stellar* companions[43] (see Kobulnicky & C. L. Fryer, 2007; C. S. Kochanek, 2009; C. Kochanek et al., 2019, for detailed discussions). If we

[41] Note that this fraction includes binary, tertiary, and higher order systems with primary early B-type stars ($9 M_\odot < M_* < 16 M_\odot$), but we will collectively refer to them as 'binaries' (Moe & Di Stefano, 2017). Any higher order system can lead to a compact remnant with bound or unbound companion stars, regardless of multiplicity.

[42] This is derived by integrating a Salpeter-like ($\alpha = -2.35$) initial mass function (IMF; Moe & Di Stefano, 2017; Salpeter, 1955); see Section 1 and Equation 1 of C. Kochanek et al. (2019), and references therein. Note that in C. Kochanek et al. (2019) Equation 1, f_b is defined as the fraction of CCSNe that occur in stellar binaries, whereas we here define f_b as the fraction of systems for which the binary remains bound following the CCSN.

[43] We assume that magnetar 3XMM J185246.6+003317 was formed from the first explosion, as is implied from our analysis in Section 2.5.

adopt f_b and f_u from Table 2.4 and use a Gaussian distribution[44] for F_0, we obtain median values $f_m \approx 70^{+10}_{-12}\%$ for the 'SNR complete' case, $f_m \approx 88^{+5}_{-8}\%$ for the 'SNR incomplete' case, and $f_m \approx 82^{+7}_{-9}\%$ for the 'SNR/unbound complete' case. In all three cases, f_m is significantly higher than the merger fractions estimated for neutron star progenitors in population synthesis from C. Kochanek et al. (2019) ($\sim 48\%$) and Renzo et al. (2019) ($\sim 22^{+26}_{-9}\%$). It is also possible that magnetar progenitors have an above average merger rate compared to other neutron star species. Corner plots summarizing this analysis are shown in the left-hand plot of Figure 2.7.

The 'SNR incomplete' case does not allow for alternate formation channels, suggesting instead that a large fraction $f_n \approx 80\%$ were formed from single stars. For a fixed binary fraction F_0, this requires an inflated merger rate $f_m \approx 75\%$. The 'SNR/unbound complete' case is one step removed, taking unbound companions as evidence of a disruption event (CCSN) but also allowing for $f_{\rm nc} \approx 45\%$ to form from other formation channels (e.g., AIC, neutron star merger). For this reason, $f_n \approx 40\%$ is lowered, but the unbound fraction $f_u \approx 10\%$ is relatively unchanged and the merger rate $f_m \approx 80\%$ increases only marginally ($< 1\sigma$ change). The 'SNR complete' case, however, excludes both SGR 1822.3-1606 and CXOU J164710.2-455216, which do not have SNR detections, from the unbound sample. SGR 0755-2933, the only proposed bound system, is excluded for the same reason. Therefore, both the merger fraction $f_m \approx 90\%$ and the fraction from alternate channels $f_{\rm nc} \approx 55\%$ increase to accommodate the lowered unbound fraction $f_u \approx 5\%$. In all three cases, the merger fraction f_m is larger than expected, requiring us to reconsider the conditions that lead to massive OB star mergers. However, a more strict interpretation ('complete' cases) is consistent with $f_{\rm nc} \approx 31 - 66\%$ forming from alternate channels.

Alternatively, we can allow both F_0 and f_m to vary, leaving the progenitor mass and stellar type unconstrained. Under this assumption, the right-hand plot of Figure 2.7 shows the 90% confidence regions for F_0 and f_m in each case. This demonstrates that a wider range of merger rates can be tolerated if magnetars can form from the mergers of less massive stars (Moe & Di Stefano, 2017). This would marginally support the analysis of Zapartas et al. (2017), which identified a population of CCSNe from the mergers of intermediate mass stars ($5 - 7.5 M_\odot$). However, a reliable comparison requires a broader search that targets both massive and intermediate mass stars, which we leave to future work. Figure 2.7 summarizes the results of this analysis in a flowchart showing the evolution of stellar progenitors to magnetar remnants.

[44] More rigorously, F_0 follows a binomial distribution, but we find this makes little difference to

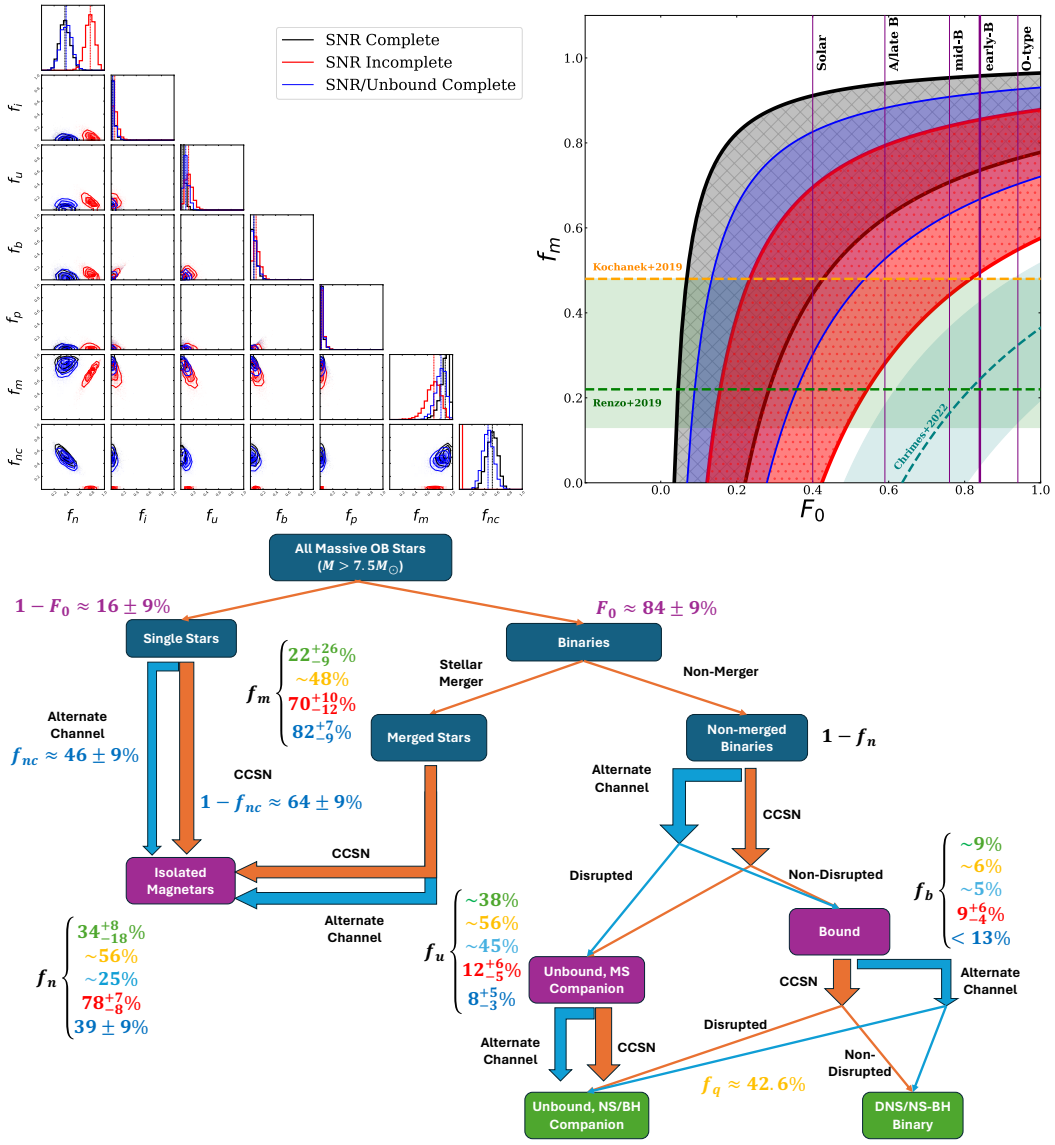

Figure 2.7: (*Upper Left:*) Corner Plots from the Magnetar Binary Fraction Simulation in Section 2.7.2. The 'SNR complete', 'SNR incomplete', and 'SNR/unbound complete' cases as defined in Section 2.7 and Table 2.4 are shown in black, red, and blue, respectively. Vertical lines indicate the median values from Table 2.4 in each case. The 'SNR complete' and 'SNR/unbound complete' cases would suggest that $f_{nc} \approx 45 - 55\%$ of magnetars to descend from non-CCSN channels, whereas the 'SNR incomplete' case suggests a higher stellar merger rate $f_m \approx 70\%$ among OB stars is sufficient to produce the observed sample. The merger rates displayed assume a massive star binary fraction $F_0 = 84 \pm 9\%$ (Moe & Di Stefano, 2017). (*Upper Right:*) 90% Confidence Regions for the merger fraction f_m and OB star binary fraction F_0. The colors for each region correspond to the cases in the contour plot, and vertical purple lines show F_0 predicted for different stellar types through population synthesis (Moe & Di Stefano, 2017). The green and yellow dashed lines indicate the median merger fractions from Renzo et al. (2019) and C. Kochanek et al. (2019); the teal dashed line indicates the f_m vs. F_0 curve inferred from f_b and f_u in Chrimes et al. (2022b). The green and teal shaded regions indicate the 1σ errors for the Renzo et al. (2019) and Chrimes et al. (2022b) cases. Each of these appear to underestimate the true fraction for early B-type stars.

(*Bottom:*) Flowchart showing the progression of massive stars into magnetars with constraints from population synthesis and observations in this work. CCSNe are indicated by orange arrows while alternate formation channels are indicated by blue arrows. Constraints on f_m, f_n, f_u, f_b, and F_0 (see Section 2.4.3) are shown from simulations by Moe & Di Stefano (2017, purple), Renzo et al. (2019, green), C. Kochanek et al. (2019, yellow), and Chrimes et al. (2022b, teal). Observational constraints from this work are shown in red for the 'SNR incomplete' case and blue for the 'SNR/unbound complete' case. A lower binary fraction would allow for a lower merger fraction for magnetar progenitors, but would require lower mass progenitors.

2.7.2.3 Limitations in Comparison to Population Synthesis Results

While we compare our resulting binary, merger, and CCSN fractions to population synthesis simulations, a discussion of the limitations of such analysis is warranted. We focus this discussion on the Chrimes et al. (2022b) simulations, though similar comparisons can be made with the C. Kochanek et al. (2019) and Renzo et al. (2019) simulations. Chrimes et al. (2022b) utilized Binary Population and Spectral Synthesis (BPASS) models and imposed constraints on the total mass ($> 2.0 M_\odot$), CO core mass ($> 1.38 M_\odot$), and remnant mass ($1.38 < M_{\rm rem} < 3.0$) to identify stellar models that evolve into magnetars. One potential source of error is the Initial Mass Function (IMF), for which Chrimes et al. (2022b) use the two-component Kroupa et al. (1993) broken power law model with index $\alpha = -1.30$ for masses $0.1 - 0.5\,M_\odot$ and $\alpha = -2.35$ for masses $0.5 - 300\,M_\odot$. Alternatively, some analyses have proposed a smoothly varying IMF with a mass-dependent α which is steeper for high mass stars (e.g., Chabrier, 2001; Kroupa, 2002; Kroupa & Weidner, 2003; Miller & Scalo, 1979; Weidner & Kroupa, 2005). This could lead to a larger ratio of low mass to high mass stars. The relationship of the IMF to the binary fraction also has a complex dependency on the mass-ratio (M_2/M_1) distribution. While a uniform distribution is assumed to compute $f_q \approx 0.426$ (e.g., C. Kochanek, 2018; C. Kochanek et al., 2019; Kouwenhoven et al., 2005), Renzo et al. (2019) find that a negative power law distribution results in a larger merger fracton f_m. This demonstrates that both the IMF and mass ratio distribution can have a significant impact on the massive star binary fraction, and motivates detailed consideration in future studies.

An additional caveat is that relatively loose constraints were used to gather the magnetar sample for this work in comparison to previous analyses. For example,

the results. The Gaussian method is adopted to more easily incorporate the uncertainty on F_0.

Chrimes et al. (2022b) excludes magnetars in Magellanic Clouds, as well as those without distance estimates, imaging data, or photometric data. With the small 31-magnetar sample, we have chosen not to place arbitrary limits beyond the completeness constraints discussed in Section 2.7.1. The reported p-values provide quantitative measures of confidence that incorporate large distances, errors, and accuracy of imaging data. Furthermore, the irregularity of transient magnetar outbursts could have marginal effects on our analysis; for example, both SGR 1935+2154 and PSR J1846-0258 have recently entered X-ray outburst phases which may tighten constraints on their ages (Ibrahim et al., 2024; Krimm et al., 2020; Laha et al., 2020; Sathyaprakash et al., 2024). SGR 0755-2933 and SGR 1808-20, contrarily have only one burst detection, each (Barthelmy et al., 2016; D. Lamb et al., 2003). Future tests may benefit from partitioning the sample based on their distance, proper motion, extinction properties, or outburst phase to characterize its affect on the search.

2.7.2.4 Comparing Magnetar Binary Statistics to the Neutron Star Population

The apparent differences between the magnetar and neutron star formation processes limit the generalization of our results to the full neutron star population. Magneto-hydrodynamic (MHD) plasma simulations of CCSNe demonstrate that the magneto-rotational instability (MRI) or a dynamo action can amplify the progenitor stars' fossil fields during collapse (e.g., Akiyama et al., 2003; Obergaulinger et al., 2009; Obergaulinger et al., 2014, 2018; Raynaud et al., 2020). However both MRI and dynamos require either high progenitor magnetic fields ($\gtrsim 10^{8-11}$ G core magnetic field; Obergaulinger et al., 2018; F. R. Schneider et al., 2019) or high specific angular momentum ($\gtrsim 9 \times 10^{14}\,\mathrm{cm^2\,s^{-1}}$; Obergaulinger et al., 2018). Such conditions were considered at a high level by S. Popov & Prokhorov (2006), whose population synthesis experiment estimates that $\sim 8-9\%$ of neutron stars would be magnetars, though the details of MRI and dynamo evolution were not incorporated. Thus magnetars and neutron stars probe different progenitor star populations that are not well-defined. Such a partition of the progenitor star population would also disfavor models presenting magnetar emission as a continuum among neutron stars.

Furthermore, some evidence suggests that highly magnetized massive stars can be formed through the merger of stars with standard surface magnetic field strengths ($\sim 1-100$ G; e.g., F. R. Schneider et al., 2019). This is presented as a possible origin of blue straggler stars with ~ 1 kG surface fields (e.g., τ Sco; Donati et al., 2006;

F. Schneider et al., 2016), which are thought to be magnetar progenitors. The high merger rate found in this work, $f_m \sim 70-80\%$, supports this scenario since it implies neutron stars with typical field strengths may have a smaller progenitor merger rate. This may also explain the discrepancy between our work and the $\sim 22^{+26}_{-9}\%$ merger rate suggested by Renzo et al. (2019)'s population synthesis. Without a more detailed understanding of the partitioning of magnetar and pulsar progenitors, our results are confined to the magnetar population and cannot be confidently applied to neutron stars as a whole.

2.7.3 Alternate Magnetar Formation Channels

In this section, we consider the implications of the 'SNR complete' and 'SNR/unbound complete' cases which require large contributions $f_{nc} \sim 45-55\%$ from non-CCSN formation channels. First, consider how this alters the birth rate assumptions for the neutron star population. Keane & Kramer (2008) predicted that the Galactic CCSN rate ($1.9 \pm 1.1\,\mathrm{century}^{-1}$) is too low to source the observed population of magnetars, pulsars, XDINS, and RRATs (total $10.8^{+7.0}_{-5.0}\,\mathrm{century}^{-1}$). If we incorporate the results of the 'SNR complete' and 'SNR/unbound complete' cases, which predict $f_{nc} \approx 55\%$ and $f_{nc} \approx 45\%$ of magnetars are formed by alternate channels, respectively, then the total neutron star birth rate from CCSNe is decreased to $\sim 5\,\mathrm{century}^{-1}$ and $\sim 6\,\mathrm{century}^{-1}$. This is still inconsistent with the CCSN rate, and suggests that alternate channels are unlikely to wholly explain the observed binary fractions.

It is possible that alternate formation channels are partially responsible for our observations. One such channel is Accretion Induced Collapse (AIC), in which ONe White Dwarfs accrete from Helium burning giant companions before collapsing (e.g., C. Fryer et al., 1999; Ruiter et al., 2019). Following AIC, either a bound neutron star-white dwarf binary is formed, or the donor star is ejected as a runaway. While the ejected mass from AIC is expected to be lower than that of a CCSN ($\sim 10^{-3} - 0.05 M_\odot$), low mass white dwarf companions would require less energy to become unbound than massive stars (El-Badry et al., 2023; Ruiter et al., 2019; Shen et al., 2018).

Direct evidence for AIC has not yet been observed, making them unlikely to make up the required $f_{nc} \sim 45-55\%$; however, Sharma et al. (2023) observed that long delay times and high-mass host galaxies for two Fast Radio Bursts (FRBs) support origins from neutron stars or magnetars formed through AIC (see also A. C. Gordon

et al., 2023; Woodland et al., 2023, for comparisons of offset and host galaxy flux distributions between FRBs and CCSNe). More unique formation processes such as neutron star mergers require gravitational wave detection and followup, but are unlikely to supercede CCSNe in magnetar production (e.g., Giacomazzo & Perna, 2013; Giacomazzo et al., 2015). Electron-capture supernovae, which occur in less massive ($8 - 11 M_{\odot}$) stars, also are unlikely to produce magnetars as they impart weaker explosion kicks to their companions, resulting in a higher surviving binary fraction, f_b (Leung et al., 2020; Miyaji et al., 1980; Nomoto, 1987; Poelarends et al., 2017). Therefore, the results of this search continue to support CCSNe as the most common magnetar formation channel, and we expect future improvements on radio survey sensitivity to recover any remaining SNRs with sufficient local density and explosion energy (e.g., D. Frail et al., 1995).

2.8 Conclusion

In this work, we have searched optical, IR, and radio image and point source catalogs for evidence of CCSNe and massive OB stars associated with magnetars. Out of the 31 known magnetars and candidates, we identify two candidates for unbound magnetar binaries at > 95% confidence: a massive OB star in association with SGR 1822.3-1606, and an X-ray pulsar in association with 3XMM J185246.6+003317. We also recover the proposed Be star companion of SGR 0755-2933 and marginally detect the proposed unbound companion of CXOU J164710.2-455216. Through the radio search we recover nine out of ten confirmed SNR associations and four of five unconfirmed associations; additional SNR candidates for SGR 1808-20 are identified but require a distance and proper motion measurement for the magnetar to confirm. Through an MCMC analysis, we find only $5 - 24\%$ of magnetars have unbound massive star companions with 90% confidence. This is much lower than is predicted by neutron star population synthesis simulations from Chrimes et al. (2022b), C. Kochanek et al. (2019), and Renzo et al. (2019).

Our results support a high merger rate for massive OB star progenitors between $48 - 86\%$. It is unclear if only magnetars or neutron stars as a whole preferentially form from mergers. While alternate formation channels such as AIC and neutron star mergers may account for a small fraction of magnetars, it is unlikely that they are solely responsible for the lack of observed unbound binaries, as this would require $\sim 45 - 55\%$ of magnetars to follow such channels and would not entirely solve the neutron star birth rate problem.

Significant improvements to this search can be made with proper motion measurements for the 23 magnetars without constraints. This may be achieved with next-generation, high sensitivity infrared telescopes like the JWST and NGRST. Similarly, Very Long Baseline Interferometry (VLBI) parallax measurements are available for only two magnetars; targeting the remaining sample will provide independent distance measurements to better inform the association tests. Next generation radio telescopes like the Deep Synoptic Array (DSA-2000) and the SKA will also detect a large sample of FRBs to investigate their origins, potentially constraining the magnetar birth rate from an extragalactic perspective.

2.9 Data Availability

The data underlying this article, including the magnetar parameters in Tables 2.1 and Tables 2.2 as well as derived values and p-values for each optical, IR, and radio source included in the search, are available in machine-readable format in the *CaltechDATA* repository, at `https://data.caltech.edu/records/fbdqe-hez98`.

2.10 Acknowledgements

The authors would like to thank the members of the Deep Synoptic Array (DSA-110) team for their support and insight with regards to this search effort. The authors thank staff members of the Owens Valley Radio Observatory and the Caltech radio group, including Kristen Bernasconi, Stephanie Cha-Ramos, Sarah Harnach, Tom Klinefelter, Lori McGraw, Corey Posner, Andres Rizo, Michael Virgin, Scott White, and Thomas Zentmyer. Their tireless efforts were instrumental to the success of the DSA-110. The DSA-110 is supported by the National Science Foundation Mid-Scale Innovations Program in Astronomical Sciences (MSIP) under grant AST-1836018. The authors would also like to thank Casey Law, Alexa Gordon, Alice Curtin, Maxim Lyutikov, and an anonymous referee for their insightful discussions and feedback on the early draft of this manuscript. This material is based upon work supported by the National Science Foundation Graduate Research Fellowship under Grant No. DGE-1745301.

The Pan-STARRS1 Surveys (PS1) and the PS1 public science archive have been made possible through contributions by the Institute for Astronomy, the University of Hawaii, the Pan-STARRS Project Office, the Max-Planck Society and its participating institutes, the Max Planck Institute for Astronomy, Heidelberg and the Max Planck Institute for Extraterrestrial Physics, Garching, The Johns Hopkins University, Durham University, the University of Edinburgh, the Queen's Univer-

sity Belfast, the Harvard-Smithsonian Center for Astrophysics, the Las Cumbres Observatory Global Telescope Network Incorporated, the National Central University of Taiwan, the Space Telescope Science Institute, the National Aeronautics and Space Administration under Grant No. NNX08AR22G issued through the Planetary Science Division of the NASA Science Mission Directorate, the National Science Foundation Grant No. AST-1238877, the University of Maryland, Eotvos Lorand University (ELTE), the Los Alamos National Laboratory, and the Gordon and Betty Moore Foundation. The UKIDSS project is defined in Lawrence et al. (2007). The national facility capability for SkyMapper has been funded through ARC LIEF grant LE130100104 from the Australian Research Council, awarded to the University of Sydney, the Australian National University, Swinburne University of Technology, the University of Queensland, the University of Western Australia, the University of Melbourne, Curtin University of Technology, Monash University and the Australian Astronomical Observatory. SkyMapper is owned and operated by The Australian National University's Research School of Astronomy and Astrophysics. The survey data were processed and provided by the SkyMapper Team at ANU. The SkyMapper node of the All-Sky Virtual Observatory (ASVO) is hosted at the National Computational Infrastructure (NCI). Development and support of the SkyMapper node of the ASVO has been funded in part by Astronomy Australia Limited (AAL) and the Australian Government through the Commonwealth's Education Investment Fund (EIF) and National Collaborative Research Infrastructure Strategy (NCRIS), particularly the National eResearch Collaboration Tools and Resources (NeCTAR) and the Australian National Data Service Projects (ANDS).

UKIDSS uses the UKIRT Wide Field Camera (WFCAM; Casali et al. (2007)). The photometric system is described in Hewett et al. (2006), and the calibration is described in Hodgkin et al. (2009). The pipeline processing and science archive are described in Irwin et al. (2004) and Hambly et al. (2008). The VISTA Data Flow System pipeline processing and science archive are described in Irwin et al. (2004), Hambly et al. (2008) and Cross et al. (2012). We have used data from the 5th data release of the Vista Variables in the Via Lactea (VVV) Survey, which is described in detail in Nikzat et al. (2022), and the VVV Infrared Astrometric Catalogue, described in detail in Smith et al. (2018). This publication makes use of data products from the Two Micron All Sky Survey, which is a joint project of the University of Massachusetts and the Infrared Processing and Analysis Center/California Institute of Technology, funded by the National Aeronautics and Space Administration and the National Science Foundation.

This work also uses data obtained from Inyarrimanha Ilgari Bundara / the Murchison Radio-astronomy Observatory. We acknowledge the Wajarri Yamaji People as the Traditional Owners and native title holders of the Observatory site. CSIRO's ASKAP radio telescope is part of the Australia Telescope National Facility (https://ror.org/05qajvd42). Operation of ASKAP is funded by the Australian Government with support from the National Collaborative Research Infrastructure Strategy. ASKAP uses the resources of the Pawsey Supercomputing Research Centre. Establishment of ASKAP, Inyarrimanha Ilgari Bundara, the CSIRO Murchison Radio-astronomy Observatory and the Pawsey Supercomputing Research Centre are initiatives of the Australian Government, with support from the Government of Western Australia and the Science and Industry Endowment Fund. This paper includes archived data obtained through the CSIRO ASKAP Science Data Archive, CASDA (https://data.csiro.au). This work has utilized data from the LoTSS survey and image archive, which is described in detail in Shimwell et al. (2022). This work has made use of data from the European Space Agency (ESA) mission *Gaia* (https://www.cosmos.esa.int/gaia), processed by the *Gaia* Data Processing and Analysis Consortium (DPAC, https://www.cosmos.esa.int/web/gaia/dpac/consortium). Funding for the DPAC has been provided by national institutions, in particular the institutions participating in the *Gaia* Multilateral Agreement. This research has made use of the CIRADA cutout service at cutouts.cirada.ca, operated by the Canadian Initiative for Radio Astronomy Data Analysis (CIRADA). CIRADA is funded by a grant from the Canada Foundation for Innovation 2017 Innovation Fund (Project 35999), as well as by the Provinces of Ontario, British Columbia, Alberta, Manitoba and Quebec, in collaboration with the National Research Council of Canada, the US National Radio Astronomy Observatory and Australia's Commonwealth Scientific and Industrial Research Organisation.

2.11 Appendix

2.11.1 *Gaia* ADQL Query and Photometric Conversions

Below is the ADQL query used to compile the initial sample of *Gaia* sources:

```
select * from (
    select *,phot_g_mean_mag_absolute - (-0.02704 + 0.1424*bp_rp_absolute -
                    0.2156*POWER(bp_rp_absolute,2) +
                    0.01426*POWER(bp_rp_absolute,3))
                AS phot_v_mean_mag_absolute from (
            select source_id,
            ra,ra_error,dec,dec_error,
            parallax,parallax_error,parallax_over_error,pm,
            pmra,pmra_error,pmdec,pmdec_error,
            ruwe,phot_g_n_obs,
            phot_g_mean_flux,phot_g_mean_flux_error,
            phot_g_mean_flux_over_error,phot_g_mean_mag,
            phot_bp_n_obs,phot_bp_mean_flux,
            phot_bp_mean_flux_error,phot_bp_mean_flux_over_error,
            phot_bp_mean_mag,phot_rp_n_obs,
            phot_rp_mean_flux,phot_rp_mean_flux_error,
            phot_rp_mean_flux_over_error,phot_rp_mean_mag,
            phot_bp_rp_excess_factor,bp_rp,bp_g,g_rp,
            radial_velocity,radial_velocity_error,
            teff_gspphot,teff_gspphot_lower,
            teff_gspphot_upper,logg_gspphot,
            logg_gspphot_lower,logg_gspphot_upper,
            mh_gspphot,distance_gspphot,
            distance_gspphot_lower,distance_gspphot_upper,
            azero_gspphot,azero_gspphot_upper,
            ag_gspphot,ag_gspphot_lower,
            ag_gspphot_upper,ebpminrp_gspphot,
            ebpminrp_gspphot_lower,ebpminrp_gspphot_upper,l,b,
            phot_g_mean_mag-ag_gspphot-(5*LOG10(1000*ABS(parallax))-5) AS
                        phot_g_mean_mag_absolute,
            bp_rp - ebpminrp_gspphot
                    AS bp_rp_absolute
                    from gaiadr3.gaia_source
        AS m)
    AS mm)
AS mmm
WHERE parallax+parallax_error>0.008
    and parallax-parallax_error<1 and phot_v_mean_mag_absolute<1.18
    and b>-80 and b<20
```

The magnitude limit was re-applied, along with the color limit, after the initial query to incorporate the *Bayestar19* extinction estimates. From *Bayestar19* we obtain the E_{B-V} color excess and convert it to E_{G-V} using the Johnson-Cousins Relations[45]:

$$E_{G-V} = -0.04749 - 0.0124E_{B-V} - 0.2901E_{B-V}^2 + 0.02008E_{B-V}^3 + 0.04772E_{B-V}^4 \tag{2.11}$$

and similarly the $G_{BP} - G_{RP}$ excess:

$$E_{G_{BP}-G_{RP}} = 0.06483 + 1.575E_{B-V} - 0.7815E_{B-V}^2 + 0.5707E_{B-V}^3 - 0.176E_{B-V}^4 + 0.01916E_{B-V}^5 \tag{2.12}$$

(e.g., Fernie, 1983; Stetson, 2000). The V- and G- band extinction are then computed using:

$$A_V \approx 3.2E_{B-V} \tag{2.13}$$

$$A_G \approx A_V + E_{G-V} \tag{2.14}$$

(e.g., Savage & Mathis, 1979; Seaton, 1979). The G-band absolute magnitude is then:

$$M_G = m_G - A_G - (5\log_{10}(d) - 5) \tag{2.15}$$

while the absolute color is:

$$G_{BP} - G_{RP} = m_{G_{BP}} - m_{G_{RP}} - E_{G_{BP}-G_{RP}} \tag{2.16}$$

Finally, we derive the absolute $G - V$ color from the Johnson-Cousins relations:

$$G-V = -0.027 + 0.01424(G_{BP}-G_{RP}) - 0.2156(G_{BP}-G_{RP})^2 + 0.07426(G_{BP}-G_{RP})^3 \tag{2.17}$$

[45]See the *Gaia* DR3 Documentation at `https://gea.esac.esa.int/archive/documentation/GDR3/` Section 5.5.1 Table 5.9 for details.

which is used to get the absolute V-band magnitude:

$$M_V = M_G - (G - V) \tag{2.18}$$

For source with $\delta \leq -30°$, the extinction and color excess from *Gaia* GSP-Aeneas photometry are used as described in Section 2.4.

2.11.2 Definition of Association P-values

In this appendix, we explicitly define p-values for association of magnetars with SNRs, bound companions, and unbound companions from the radio, optical, IR, and *Gaia* searches. The p-values are based on the criteria defined in Sections 2.5.1-2.4, and are estimated through Monte Carlo simulations.

2.11.2.1 Optical Search for Bound Companions

Recall for the bound companion search, the null hypothesis (*H0*) is that the magnetar and source are not bound in a binary system, and we use the position, distance, and difference between PSF and Kron magnitudes ('$grizy$' for PS1, '$uvgriz$' for SkyMapper) as association criteria. For each source, we draw 1,000 samples of the RA and declination of the source and magnetar ($\alpha_{\rm PS1}, \delta_{\rm PS1}, \alpha_{\rm mag}, \delta_{\rm mag}$), and the distance of the magnetar ($d_{\rm mag}$), assuming each are normally distributed. Using $\Delta\alpha = |\alpha_{\rm PS1} - \alpha_{\rm mag}|$, $\Delta\delta = |\delta_{\rm PS1} - \delta_{\rm mag}|$, we compute the search statistic $\hat{g}_1$ as the fraction of samples that fall below the 95$^{\rm th}$ percentiles of folded zero-mean normal distributions with $\sigma_\alpha = (\sigma^2_{\alpha,\rm PS1} + \sigma^2_{\alpha,\rm mag})^{1/2}$ and $\sigma_\delta = (\sigma^2_{\delta,\rm PS1} + \sigma^2_{\delta,\rm mag})^{1/2}$, respectively. The *H0* distribution of $\hat{g}_1$ is estimated by repeating the simulation 100 times with mean $\Delta\alpha, \Delta\delta$ selected uniformly between $1 - 5\sigma_{\alpha/\delta}$, and the p-value p_1 is taken as the percentile of $\hat{g}_1$ given the resulting $\hat{g}_1$ distribution.

p_2 is computed by a similar process; since the errors on apparent magnitudes are small, we assume they are negligible, and use $g-$ and $r-$band magnitudes to derive the apparent $V-$band magnitude:

$$m_V = m_r + 0.005 + 0.462(m_g - m_r) + 0.013(m_g - m_r)^2 \tag{2.19}$$

(Tonry et al., 2012). From *Bayestar19* we obtain the $B - V$ color excess[46] along

[46]Note that *Bayestar19* reports reddening in arbitrary units and is converted to E_{B-V} by multiplying by 0.995 as described at `http://argonaut.skymaps.info/usage`(E. F. Schlafly & Finkbeiner, 2011). We proceed assuming this factor is approximately 1, which is accurate to the first decimal place.

the source's sightline, E_{B-V}, for distances between 60 pc−60 kpc, converting to the $V-$band extinction with $A_V \approx 3.2E_{B-V}$. If *Bayestar19* extinction estimates are not available, we use the $N_H - A_V$ relation from Predehl & Schmitt (1995) from Table 2.1. Then, after samples of the absolute magnitude are drawn from a uniform distribution between $-10 \lesssim M_V \lesssim 3$, linear interpolation is used to obtain a sample of the PS1 source distance, $d_{\rm PS1}$, from the difference $m_V - M_V$. Finally, we use the magnetar distance samples to get samples of $\Delta d = |d_{\rm PS1} - d_{\rm mag}|$, which is again compared to the 95^{th} percentile of a folded zero-mean distribution and *H0* samples between $1 - 10\sigma_{\Delta d}$ to get the statistic $\hat{g}_2$ and p-value p_2.

Finally, the Kron magnitude describes the flux of extended sources within a characteristic Kron radius (Kron, 1980). As described by Farrow et al. (2014), the difference $m_{x,\rm Kron} - m_{x,\rm PSF}$ can be used to distinguish between point sources and extended sources by imposing a cutoff $m_{x,cutoff}(m_{x,\rm Kron})$. Point sources are expected to exceed this limit, and we adopt the Farrow et al. (2014) fit equation for the cutoff:

$$m_{x,cutoff}(m_{x,\rm Kron}) = -0.319 + 0.129(m_{x,\rm Kron} - 21) + 0.007(m_{x,\rm Kron} - 21)^2 \quad (2.20)$$

Since the apparent magnitude error is negligible, we set the p-value $p_{3,x} = 0$ if $m_{x,\rm Kron} - m_{x,\rm PSF} > m_{x,cutoff}(m_{x,\rm Kron})$ and $p_{3,x} = 1$ if $m_{x,\rm Kron} - m_{x,\rm PSF} \leq m_{x,cutoff}(m_{x,\rm Kron})$, combining results in all available passbands to get p_3:

$$p_3 = 1 - \prod_{x}^{\text{`}uvgrizy\text{'}} (1 - p_{3,x}) \quad (2.21)$$

For SkyMapper sources, multiple measurements for the Kron and PSF magnitudes are available in each band, each of which is used to compute p_3. We additionally exclude SkyMapper sources with stellar classification probability (*class_star*) < 90% to avoid extended objects (Onken et al., 2024; Wolf et al., 2018).

2.11.2.2 Infrared Search for Bound Companions

Like the optical search, the IR search uses the position, distance, and PSF $J-$ and $H-$band magnitudes as criteria for association, with *H0* that the magnetar and source are not bound in a binary system. p_1 is computed in a similar way to the optical data for UKIDSS and VVV using their respective PSF FWHMs, 1″ and 0.75″, as errors in RA and declination. For 2MASS sources, the RA and declination are sampled as

a bi-normal distribution using the reported major axis ($a_{\rm IR}$), minor axis ($b_{\rm IR}$), and position angle ($\phi_{\rm IR}$) of the error ellipse. The covariance matrix of the bi-normal distribution is given by:

$$\sigma_{\rm pos} = \begin{bmatrix} (a_{\rm IR} sin(\phi_{\rm IR}))^2 + (b_{\rm IR}\cos(\phi_{\rm IR}))^2 & (a_{\rm IR}^2 - b_{\rm IR}^2)\cos(\phi_{\rm IR})sin(\phi_{\rm IR}) \\ (a_{\rm IR}^2 - b_{\rm IR}^2)\cos(\phi_{\rm IR})sin(\phi_{\rm IR}) & (a_{\rm IR}\cos(\phi_{\rm IR}))^2 + (b_{\rm IR} sin(\phi_{\rm IR}))^2 \end{bmatrix} \tag{2.22}$$

We proceed as in the PS1 search to compute the search statistic $\hat{g}_1$ and its p-value p_1, utilizing the 95$^{\rm th}$ percentile contour as a threshold and simulating the *H0* distribution of angular separation, $\Delta\theta$, using mean separations between $1 - 5\sigma_{\rm pos}\{1, 1\}$ for RA and $1 - 5\sigma_{\rm pos}\{0, 0\}$ for declination.

For the second condition we follow the same method as for PS1 sources using instead the $J-$ band and $H-$ band magnitudes, m_J and m_H. Following Chrimes et al. (2022b), we expect OB stars to have $H-$band magnitudes in the range $-2.76 \lesssim M_H \lesssim 3.34$ and $J - H$ colors between $-0.14 \lesssim J - H \lesssim 0.31$. After drawing samples of M_H and $J - H$ from uniform distributions in these ranges, we compute $M_J = (J - H) + M_H$. The *Bayestar19* extinction library is again queried, using $A_H \approx 0.4690E_{B-V}$ and $A_J \approx 0.7927E_{B-V}$, and the inferred distance is estimated from both the $J-$ and $H-$ bands, $d_{{\rm IR},J}$ and $d_{{\rm IR},H}$. The search statistic is taken as the fraction of sources for which either $d_{{\rm IR},J}$ or $d_{{\rm IR},H}$ falls outside the 95$^{\rm th}$ percentile of the *H1* distribution.

2.11.2.3 Radio Search for SNR Shells

The radio search uses the position, proper motion, and angular size to define association p-values, which cover two independent cases: first, that the magnetar resides within the SNR shell, and second, that the magnetar was kicked from the center of the SNR. *H0* in both cases is that the magnetar did not originate at the center of the SNR. p_1 is derived similarly to the IR case; when the angular size of the SNR is known, we assume the semi-major ($a_{\rm SNR}/2$) and semi-minor axes ($b_{\rm SNR}/2$) are the 3σ half-widths of the error ellipse. If not, the error ellipse is used to derive the binormal distribution. We again derive the search statistic $\hat{g}_1$ using the 95$^{\rm th}$ percentile contour, and the p-value p_1 by comparing to the *H0* distribution of $\hat{g}_1$, which is derived using mean angular separations between $1 - 5\sigma_{\alpha/\delta}$ of the origin.

The second criteria is similar to that above, but instead compares the angle of the line connecting the magnetar location and the SNR, $\rho_{\rm SNR} = \tan^{-1}(\Delta\delta/\Delta\alpha)$, and the

direction of the magnetar's proper motion, $\rho_{\rm mag} = \tan^{-1}(\mu_\delta/(\mu_\alpha \cos(\delta)))$. The *H0* distribution of $\hat{g}_2$ is computed using mean angular differences $\Delta\rho = |\rho_{\rm SNR} - \rho_{\rm mag}|$ between the 95$^{\rm th}$ percentile of the observed distribution and 180°. p_3 uses the magnetar proper motion and the median magnetic field decay age $\mathcal{T}_{\rm decay}$ computed from the X-ray luminosity (see Appendix 2.11.4.1 and Ferrario & Wickramasinghe, 2008) to derive samples of the expected angular separation between magnetar and SNR, $\Delta\theta_{\rm mag} = |\vec{\mu}|/\mathcal{T}_{\rm decay}$. If the magnetar has no X-ray luminosity or magnetic field estimate, the spin-down age $\mathcal{T}_{\rm rot}$ from the McGill magnetar catalog is used instead. Samples of the true angular separation, $\Delta\theta_{\rm SNR}$ are derived using samples of the RA and declination of the magnetar and SNR. The search statistic $\hat{g}_2$ is the fraction of samples for which the difference in angular separation, $\Delta(\Delta\theta) = |\Delta\theta_{\rm SNR} - \Delta\theta_{\rm mag}|$ is outside the 95$^{\rm th}$ percentile from the *H1* case. p_3 is then derived from the *H0* distribution of $\hat{g}_3$, which assumes mean angular separations between the 95$^{\rm th}$ percentile and 1′.

Finally, we estimate p_4 based on the angular size $\Delta\theta$ of the SNR; we impose a lower limit on the angular size required to be associated with the magnetar given the magnetar's distance and age $\mathcal{T}_{{\rm decay}/rot}$. By sampling the magnetar distance d we compute samples of the physical radius of the SNR as $r_{\rm SNR} = d_{\rm mag}\Delta\theta$ and estimate the corresponding dynamical age $\mathcal{T}_{\rm dyn}$ from either free-expansion or Sedov-Taylor phase expansion as described in Appendix 2.11.4.2 (Sedov, 2018). For this we also sample the progenitor envelope mass from a uniform distribution between $2.75 - 120 M_\odot$[47] and use an explosion energy 10^{51} ergs [48](Morozova et al., 2017). We then draw samples of the magnetar age $\mathcal{T}_{{\rm decay}/rot}$ and compute the statistic $\hat{g}_3$ as the fraction of samples for which $\mathcal{T}_{{\rm decay}/rot} > \mathcal{T}_{\rm dyn}$. We impose only a loose lower limit since magnetar spindown and decay ages are uncertain. The p-value p_3 is taken as the percentile of $\hat{g}_3$ within the *H0* distribution which assumes mean ages between $\mathcal{T}_{\rm dyn}$ and the 95th percentile of the *H1* distribution. p_1, p_2, and p_3 are combined using Equations 2.5 and 2.6.

'By-Eye' Identification and Fitting of Candidates

[47]This range implicitly assumes that mass transfer to a binary companion or lost to stellar winds are negligible, which is not necessarily the case (Nomoto et al., 1995; Thielemann et al., 1996).

[48]Nomoto et al. (1995) suggest that gravitational binding energy $\sim 10^{53}$ ergs can increase the energy of supernovae. However, we use the observational constraint of $\sim 10^{51}$ erg from Type II CCSN lightcurves from (Morozova et al., 2017). Since Type II supernovae make up $\sim$ 90% of CCSNe, we find this assumption justified.

Optical, infrared, and radio sources identified 'by eye' which do not have known counterparts in public catalogs considered here were fit with ellipses parameterized by the RA and declination of the center (α_c, δ_c), major and minor axes (a, b), and position angle measured North of East (χ). Shifting the center of the ellipse to 0, the fit equation for the radius r as a function of polar angle θ is given by:

$$\begin{aligned} r(\theta) = ab((b^2\cos^2(\chi) + a^2 sin^2(\chi))\cos^2(\theta) + \\ (b^2 sin^2(\chi) + a^2\cos^2(\chi))sin^2(\theta) + \\ 2(b^2 - a^2)\cos(\chi)sin(\chi)\cos(\theta)sin(\theta))^{-1/2} \end{aligned} \tag{2.23}$$

For each source, the contour at one-half the maximum value within one arcminute (for radio sources; one arcsecond for optical and IR sources) of the identified center. The mean α and δ were recomputed from this contour prior to fitting with an ellipse using the equation above. The major and minor axes and position angle were then used identically to those of SNRs for the association test (see Section 2.11.2.3. Note that apparent magnitudes were not estimated for these sources, and p-values could not be estimated for the optical and IR searches. Any point sources of interest were queried in SIMBAD and public catalogs to determine the likelihood of association.

2.11.2.4 *Gaia* Search for Unbound Companions

Criteria for association of unbound *Gaia* sources with magnetars is based on their current positions, proper motion magnitudes and directions, and the consistency of the magnetar travel time with age estimates. *H0* is that the magnetar and source positions are not consistent with having an origin at the same location. For p_1, we assume the *Gaia* DR3 proper motion, parallaxes, and positions are Gaussian (or 2-sided Gaussian, where applicable) distributed, with standard deviation equal to the uncertainty. To account for bias in the conversion from parallax to distance ($d \approx \omega^{-1}$) we adopt the photo-geometric distance from the C. Bailer-Jones (2023) catalog.

For each magnetar, samples of the distance d, RA (α) and declination (δ) are drawn from their respective distributions to get samples of the position vector, $\overrightarrow{r}_{\mathrm{mag},i}$ (the subscript i indicates the quantity is Monte Carlo sampled). Magnetar proper motion measurements are often unavailable due to their reliance on Very Long Baseline Interferometry (VLBI) (e.g., Tendulkar et al., 2012). In such cases, we draw samples of the magnetar velocity magnitude from a Maxwellian distribution with

scale parameter $\sigma = 265\,\mathrm{km\,s^{-1}}$ as described in Hobbs et al. (2005). The velocity direction is drawn from a 3D uniform distribution to obtain $\overrightarrow{v}_{\mathrm{mag},i}$. If proper motions are known, the total velocity is still drawn from the truncated Hobbs et al. (2005) distribution, and the radial velocities are then computed from the velocity and proper motion samples with the sign chosen from a uniform distribution. Samples of the age τ_i, defined here as the time since the magnetar supernova would have occurred, are drawn from a uniform distribution from $1-10\,\mathrm{kyr}$. A sub-sample of *Gaia* sources within 5° of the magnetar-under-test are selected from the full sample to test for association. In a similar method to that above, samples of position $\overrightarrow{r}_i$ and velocity $\overrightarrow{v}_i$ are drawn for each *Gaia* source; here we sample the empirical walk/runaway velocity distribution from the fiducial simulation of Renzo et al. (2019) for which $\sim 95\%$ of simulated ejected massive stars have velocities $\lesssim 30\,\mathrm{km\,s^{-1}}$ (see also Blaauw, 1961; Feast & Shuttleworth, 1965; Sayers et al., 1996; Tetzlaff et al., 2010). We choose not to utilize the *Gaia* radial velocity measurements since they have not been confirmed through spectroscopic follow-up, and many ($\sim 10\%$) of sources within our sample do not have radial velocity measurements. This also prevents us from over-constraining the velocity samples while we impose the Renzo et al. (2019) distribution.

Next, the magnetar and source trajectories are traced for each sample from their current positions $\overrightarrow{r}_{\mathrm{mag},i}$ and $\overrightarrow{r}_i$ to their locations at time τ_i in the past:

$$\overrightarrow{r}_{\mathrm{o,mag,i}} = \overrightarrow{r}_{\mathrm{mag},i} - \tau_i \overrightarrow{v}_{\mathrm{mag},i} \tag{2.24}$$

$$\overrightarrow{r}_{o,i} = \overrightarrow{r}_i - \tau_i \overrightarrow{v}_i \tag{2.25}$$

We have utilized the `astropy` library's `apply_space_coord` method to perform this propagation, and use the `astropy.SkyCoord` object for conversion between Cartesian and Spherical coordinate systems. The initial RA and declination of source and magnetar, $\alpha_{o,i}$,$\delta_{o,i}$ and $\alpha_{o,\mathrm{mag},i}$,$\delta_{o,\mathrm{mag},i}$, are derived from $\overrightarrow{r}_{o,i}$ and $\overrightarrow{r}_{\mathrm{o,mag,i}}$, and are used to compute the angular separation at the time of the supernova, Θ_i. We compute this using `SkyCoord.angular_separation` method, which implements the Vincenty formula for the Great-circle distance between two points on a spherical surface (Vincenty, 1975). Additionally, using the G-band magnitude for each source, the $G-V$ color derived through Johnson-Cousins relations, and the distance samples

which are converted to distance moduli, we also derive samples of the V-band absolute magnitude $M_{V,i}$:

$$M_{V,i} = (m_G - A_G - (5\log_{10}(d_i) - 5)) - (G - V) \tag{2.26}$$

Θ_i and $M_{V,i}$ are used as the parameters of interest and compared to a threshold contour in $\{\Theta, M_V\}$ space. The contour is computed by injecting 100 positively-associated simulated sources with an OB-star-like absolute magnitude, $-10 \leq M_V \leq +3$. The 90$^{\text{th}}$ percentile contour of the 2D histogram is used as a threshold, and we define the search statistic $\hat{f}$ as the fraction of Monte Carlo samples falling outside the contour. A separate threshold contour is determined for each magnetar, using the position, distance, and proper motion of the magnetar as available. Critical values $\hat{f}_c$ were derived through a Receiver Operating Characteristic (ROC) analysis for each magnetar, which is summarized in Appendix 2.11.2.4. By comparing the final $\hat{f}$ to samples in the *H1* hypothesis (obtained during the ROC test), we estimate a p-value, p_1, as the percentile of $\hat{f}$ within the *H1* sample.

To further narrow down the candidate *Gaia* sources with $\hat{f} < \hat{f}_c$, we iteratively compute the true intersection points $\overrightarrow{r}_{\otimes,i}$ of the sampled trajectories with those of the magnetars, eliminating any samples with non-physical solutions. We then use the Monte Carlo sampled proper motions and positions to estimate the two-dimensional travel times for each magnetar-candidate pair:

$$\tau_{2\text{D},i} \approx \frac{\Delta\Phi_{\otimes,i}}{\sqrt{\mu^2_{\alpha,i}\cos^2(\delta_i) + \mu^2_{\delta,i}}} \tag{2.27}$$

$$\tau_{2\text{D,mag},i} \approx \frac{\Delta\Phi_{\otimes,\text{mag},i}}{\sqrt{\mu^2_{\alpha,\text{mag},i}\cos^2(\delta_{\text{mag},i}) + \mu^2_{\delta,\text{mag},i}}} \tag{2.28}$$

where $\Delta\Phi_{\otimes}$ is the angular separation between the intersection point and the current coordinate. Since we expect $\tau_{2\text{D,mag},i} = \tau_{2\text{D},i}$, we estimate a χ^2 statistic comparing the $\tau_{2\text{D,mag},i}$ vs. $\tau_{2\text{D},i}$ curve to a line with slope 1, taking the p-value p_2 as another measure of association. Similarly, we compute the physical travel time for the magnetar assuming it is at the *Gaia* source distance:

$$\mathcal{T}_{3\text{D,mag},i} \approx \frac{|\overrightarrow{r}_{\text{mag},i} - \overrightarrow{r}_{\otimes,i}|}{|\overrightarrow{v}_{\text{mag},i}|} \tag{2.29}$$

We expect each magnetar's travel time to be less than its age; if an SNR candidate with an age measurement is confidently associated with the magnetar, we use the SNR age, $\mathcal{T}_{\rm SNR}$. Five magnetars in our sample have $\mathcal{T}_{\rm SNR}$ estimates, four of which are measured assuming Sedov-Taylor plasma dynamics and the other which is computed kinematically using the magnetar proper motion (G. E. Anderson et al., 2012; Blumer et al., 2019; Borkowski & Reynolds, 2017; Dohm-Palmer & Jones, 1996; B. M. Gaensler et al., 1999; Lyman et al., 2022; Sedov, 2018). If no SNR association is known or its age is unconstrained, we estimate the age $\mathcal{T}_{\rm decay}$ from from continuum X-ray luminosity measurements using the crustal field decay model (see Ferrario & Wickramasinghe, 2008, and Appendix 2.11.4.1). This applies to 18 magnetars in our sample. If no SNR association is known and the X-ray luminosity or surface magnetic field strength are unknown, the spin-down age $\mathcal{T}_{\rm rot}$ reported in the McGill magnetar catalog is used in its place (Olausen & Kaspi, 2014). Five magnetars in the sample require spin-down ages to be used, decreasing confidence in their p-values since $\mathcal{T}_{\rm rot}$ is predicted to over-estimate magnetar ages (e.g., Kaspi & Beloborodov, 2017). For 5 magnetars, none of the three age estimates are known, and the final p-value is computed from p_1 and p_2 alone.

For p_4, we use samples of the magnetar and source distances from the initial Monte Carlo search to estimate the distribution of the difference, $\Delta d_i = d_i - d_{{\rm mag},i}$. The width of this distribution is dominated by the magnetar's distance error. We estimate the *H1* distribution, for which the magnetar and source are at the same distance, by shifting the Δd samples to have median 0. We then compute the search statistic as the fraction of Δd samples within the 3σ width ($0.15 - 99.85^{\rm th}$ percentiles) of the *H1* distribution. We compare this to 100 realizations of the $H0$ distribution which are shifted to have medians between $1 - 6\sigma_d$, where σ_d is the width of the *H1* distribution, and compute the search statistic for each trial. The p-value p_4 is computed as the percentile of the observed Δd statistic among the $H0$ distribution of statistics.

Receiver Operating Characteristic Analysis

The optimal critical threshold for the *Gaia* Monte Carlo search, $\hat{f_c}$, was derived through an ROC analysis. To compute the true positive rate (TPR) for trial thresholds from 0.1 to 1, 10,000 injection sources were simulated with randomly chosen ages between 1-10 kyr and velocity drawn from the fiducial simulation described in Renzo et al. (2019). A test magnetar was simulated with velocity drawn from the Hobbs et al. (2005), and both magnetar and source were propagated to present-day

Table 2.5: Critical Thresholds for Magnetar Association Tests

Magnetar	$\hat{\mathbf{f}}_{\mathbf{c}}$
CXOU J010	72.4%
4U 0142	5.7%
SGR 0418	87.2%
SGR 0501	91.2%
SGR 0526	80.4%
1E 1048	94.4%
1E 1547	8.4%
PSR J1622	98.5%
SGR 1627	11.4%
CXOU J1647	93.4%
1RXS J1708	99.2%
CXOU J1714	96.4%
SGR J1745	20.4%
SGR 1806	2.8%
XTE J1810	74.5%
Swift 1818	36.3%
SGR J1822	83.3%
SGR 1833	90.0%
Swift J1834	54.4%
1E 1841	14.3%
3XMM J1852	89.3%
SGR 1900	40.3%
SGR 1935	12.4%
1E 2259	54.5%
SGR 0755	63.7%
SGR 1801	11.2%
SGR 1808	64.4%
AX J1818	96.7%
AX J1845	91.0%
SGR 2013	84.3%
PSR J1846	39.3%

positions, starting from the same start position ($P_0 = P_{0,\mathrm{mag}}$). Each simulated source was given an OB-star-like absolute magnitude $M_V = -1.5$. The Monte Carlo search was conducted with 1,000 trials for each simulated source and the simulated magnetar. Search statistics $\hat{f}$ were computed for each source. The TPR for each trial $\hat{f}_c$ was computed as the fraction of sources with $\hat{f} < \hat{f}_c$. The false negative rate (FNR) is computed as FNR = 1-TPR.

To compute the false positive rate (FPR) for a given magnetar location, we tile the region nearby with 10′ pointings, starting at 10′ from the magnetar. For each tile, we pass all sources through the Monte Carlo association test, using the tile's center as the coordinates of the 'fake' magnetar. Since no magnetar is in the query region, these test samples are used as true negative injections. The FPR for each trial $\hat{f}_c$ was computed as the fraction of total sources (from all tiles) with $\hat{f} < \hat{f}_c$.

We expect differences in each magnetar's local environment, both in source density and, potentially, stellar types. Therefore, the ROC analysis is carried out for each magnetar individually. Note that in most cases, the FPR is very low; the FPR is higher for SGR 1801-23 because of its lack of distance measure and large position error. We choose the threshold for each magnetar where the TPR is maximized and the FPR is minimized; in cases where the FPR is consistently 0%, the threshold is $\hat{f}_c = 100\%$. In these cases, a *Gaia* source is a candidate for association if any Monte Carlo sample falls within the 90$^{\mathrm{th}}$ percentile contour in $\{\Theta, M_V\}$ space. Similarly, in cases where the FNR is consistently 0% (which occurs when the proper motion, position, and distance are well-constrained), the threshold is $\hat{f}_c = 0\%$. In these cases, a *Gaia* source is a candidate for association only if all Monte Carlo samples fall within the 90$^{\mathrm{th}}$ percentile contour in $\{\Theta, M_V\}$ space. Overall, we find this has little effect on the results, as most *Gaia* sources have either all or none of their samples within the contour region. We list $\hat{f}_c$ for each magnetar in Table 2.5.

2.11.3 False Positive Analyses

2.11.3.1 *Gaia* Search False Positives

In this section we discuss in detail the reasons that the candidates for unbound stellar companions of 3XMM J185246.6+003317 were rejected as false positives.

3XMM J185246.6+003317

For 3XMM J185246.6+003317, four candidates, *Gaia* DR3 4266311617807818624 (Source 1), *Gaia* DR3 4266313683745630080 (Source 2), *Gaia* DR3 4266315504811080748

(Source 3), and *Gaia* DR3 4258978601120897664 (Source 4), are identified with $p < 5\%$, all requiring the magnetar to have proper motion $\mu_\alpha \cos(\delta) \sim -5$ and $\mu_\delta \sim -3.5\,\mathrm{mas\,yr^{-1}}$. For Sources 1 and 2, the stellar velocities are consistent with walkaway stars with $|\overrightarrow{v}| \approx 28^{+8}_{-5}\,\mathrm{km\,s^{-1}}$ for Source 1 and $|\overrightarrow{v}| \approx 30^{+8}_{-5}\,\mathrm{km\,s^{-1}}$ for Source 2; the travel times are consistent with the magnetar's at the 1σ and 2σ levels, respectively. Higher velocities more consistent with runaway stars are required for Sources 3 and 4: $|\overrightarrow{v}| \approx 68^{+10}_{-15}\,\mathrm{km\,s^{-1}}$ and $|\overrightarrow{v}| \approx 143^{+6}_{-10}\,\mathrm{km\,s^{-1}}$, respectively. Without uncertainties on the distance of 3XMM J185246.6+00317, it is difficult to evaluate if each source is consistent with the magnetar's distance. However, the magnetar's estimated distance ~ 7.1 kpc far exceeds the four Sources' parallax distances, which are between $1 - 3$ kpc. 3XMM J185246.6+00317's distance was estimated from the nearby SNR Kes 79 based on their similar hydrogen column densities $N_H \approx 1.5 \times 10^{22}\,\mathrm{cm^{-2}}$ (Zhou et al., 2014). This is questionable given that Kes 79 is confirmed in association with a separate X-ray pulsar, CXOU 185238.6+004020 (Seward et al., 2003), although we explore a scenario in which both the pulsar and magnetar may be associated with the SNR in Section 2.4. It is also known that some X-ray sources have significant local extinction that can bias the foreground N_H estimate (e.g., Chaty & Rahoui, 2012; Predehl & Schmitt, 1995). However, the lack of notable IR emission from 3XMM J185246.6+003317 distinguish it from sources with significant local N_H such as HMXBs. Therefore, it is likely that N_H is indeed from the foreground and its similarity to that of Kes 79 suggests they are at the same distance ~ 7.1 kpc. If this is the case, then all five sources are in the foreground and cannot be associated with 3XMM J185246.6+003317. A precise proper motion measurement and independent distance measurement would allow more confident conclusions to be drawn.

2.11.3.2 Radio SNR Search False Positives

In this section we justify why candidates for SNR association with SGR 0755-2933 were rejected as false positives.

SGR 0755-2933 Eight radio sources were identified with $p < 5\%$ as potential SNRs

associated with SGR 0755-2933 Richardson et al. (2023) and Doroshenko et al. (2021) (see also Archibald et al., 2013; Barthelmy et al., 2016; Surnis et al., 2016). VLASS image cutouts with $1''$ pixels were obtained for each candidate, and four are ruled out as point sources. Two other sources are found to be coincident with known

stellar objects within $1'$ (an eclipsing binary and a Carbon star). The remaining two sources are each $\sim 14''$ across, or $\sim 0.22\,\mathrm{pc}$ at SGR 0755-2933's distance of $3.5 \pm 2\,\mathrm{kpc}$. Assuming the free-expansion phase, this corresponds to an SNR age range of $80 - 300$ years, which is marginally consistent with magnetar ages in general. If we accept the Doroshenko et al. (2021) association of SGR 0755-2933 with the X-ray source 2SXPS J075542.5-293353, we can use the X-ray luminosity $L_X \approx 10^{34}\,\mathrm{erg\,s^{-1}}$ to estimate $\mathcal{T}_{\mathrm{decay}}$ for a typical magnetic field strength $B \sim 10^{14}\,\mathrm{G}$ (see Appendix 2.11.4.1). From this method we estimate $\mathcal{T}_{\mathrm{decay}} \approx 60\,\mathrm{kyr}$ which is much larger than the free-expansion ages for the two SNR candidates. The detection of a subsequent burst resulting in more precise localization could confidently rule out one source which lies outside the 3σ error region of SGR 0755-2933. With the information at hand, we conclude that both sources are likely to be false positives based on the large position uncertainty and decay age estimate.

2.11.3.3 Bound Companion Search False Positives

In this section we justify why the bound companion candidates for PSR J1622-4950 and SGR J1822.3-1606 were rejected as false positives.

PSR J1622-4950

Through the optical search, the SkyMapper source SMSS J162244.99-495055.7 was recovered with p-value $p = 1\%$ as a potential bound companion of PSR J1622-4950. This magnetar lies along a highly extincted sightline, with $A_V \approx 30.17^{+8.94}_{-7.82}$ from the Predehl & Schmitt (1995) $N_H - A_V$ relation. From the $g-$ and $r-$band apparent magnitudes, we therefore estimate an absolute magnitude $M_V \sim -23.4$, which would be extremely bright for an OB star. From the mass-luminosity relation, this would correspond to a $\sim 10^{13} M_\odot$ star, which is unphysical. We also note that the candidate has a large angular separation $\sim 3.31''$, corresponding to 0.14 pc at the magnetar's 9 ± 1.35 kpc distance. This is impractical for the orbit of a neutron star ($\sim 1.4 M_\odot$) and massive star ($\lesssim 120 M_\odot$), suggesting an orbital period of $\sim 10^{18}$ years. Therefore, we conclude that this source is most likely a false positive. Chrimes et al. (2022a) identify a potential infrared counterpart for PSR J1622-4950 using HST data, but this is not recovered in either the optical or IR search in this work. This is consistent with their claim in Chrimes et al. (2022b) that this is more likely to be surface emission from the neutron star than a companion star.

SGR J1822.3-1606

Three distinct IR sources nearby SGR J1822.3-1606 are found to have $p < 5\%$: 2MASS 18221839-1604241 ($p < 0.1\%$; UKIDSS J182218.39-160424.0, UKIDSS J182218.39-160424.1), 2MASS 18221794-1604259 ($p < 0.1\%$; UKIDSS J182217.94-160425.9, UKIDSS J182217.94-160426.0), and 2MASS 18221797-1604360 ($p \approx 5\%$; UKIDSS J182217.97-160436.0, UKIDSS J182217.97-160435.9). The first is unlikely based on its angular separation $\sim 6.7'' \pm 0.7''$; at the magnetar's distance 1.6 ± 0.3 kpc, this corresponds to ~ 0.05 pc which is too large for a bound orbit. While this could be an unbound companion, it was not recovered in the *Gaia* search, and the absolute $J - H$ color is inconsistent with OB stars at the 5σ level when placed at the magnetar distance, with $J - H \approx 0.85 \pm 0.10$ (Chrimes et al., 2022b). The latter source was identified with $p < 5\%$ only for the UKIDSS counterparts ($p = 1\%, 2\%$), while the 2MASS source had a marginal $p \approx 5\%$. Again, we find it unlikely this is associated with SGR J1822 based on its angular separation $\sim 9.2'' \pm 0.7''$ and color $J - H \approx 1.69 \pm 0.14$. We conclude that both 2MASS 18221839-1604241 and 2MASS 18221797-1604360 are false positives for bound companions.

The second source, 2MASS 18221794-1604259, is much closer to the magnetar at $\sim 0.01'' \pm 0.7''$, or ~ 20 au at the magnetar's distance $\sim 1.6 \pm 0.3$ kpc, though this is still too distant for a bound system. This source was similarly identified as evidence that SGR J1822.3-1606 may be a Be star X-ray binary, like SGR 0755-2933, when initially discovered by e.g., J. Halpern (2011), Gogus & Gorosabel (2011), Gorosabel et al. (2011). The source's *Gaia* counterpart, *Gaia* DR3 4097826476059022848, has a negative parallax $\omega = -1.2 \pm 0.6$ mas which excluded it from the *Gaia* search (see Section 2.4 and Appendix 2.11.1). Its parallax distance is $d \approx 7.0^{+3.1}_{-2.8}$ kpc, which agrees with the magnetar's distance within 1σ. At the magnetar's distance, the intrinsic magnitude and color are $M_H \approx 2.5 \pm 0.1$ and $J - H \approx 1.5 \pm 0.1$, which are stellar in nature. However, the color is redder than expected for OB stars, and is more characteristic of an evolved supergiant star (Chrimes et al., 2022b). Notably, the star's proper motion from *Gaia* is $\mu_\alpha \cos(\delta) = -5.6 \pm 0.7$ mas yr^{-1}, $\mu_\delta = -8.2 \pm 0.6$ mas yr. Applying the *Gaia* Monte Carlo test results in a p-value $p = 79\%$ due to the significant travel time difference $\Delta\tau_{2D} \approx 0.3^{+0.7}_{-0.2}$ kyr required to trace trajectories to a common origin. While a magnetar proper motion measurement would motivate re-analysis, we conclude that the close proximity and companion's significant proper motion make it unlikely that the candidate is associated with SGR 1822.3-1606.

2.11.4 Magnetar Age Estimation

Magnetars' magnetic field decay and irregular outbursting and 'glitching' behavior make their characteristic spindown ages $\mathcal{T}_{\rm rot} = P(2\dot{P})^{-1}$ overestimates of their true age (Ferrario & Wickramasinghe, 2008; Kaspi & Beloborodov, 2017; Nakano et al., 2015; Olausen & Kaspi, 2014). In this section we provide a brief overview of two alternative estimates based on the X-ray luminosity and the dynamical plasma age of an associated SNR.

2.11.4.1 Derivation of Magnetar Age X-ray Luminosity Decay

We define $\mathcal{T}_{\rm decay}$ as the age of the magnetar estimated from the decaying crustal X-ray luminosity, L_x. This model is described in detail in Ferrario & Wickramasinghe (2008) and Ferrario & Wickramasinghe (2006) based on Pons & Geppert (2007). In this model, the dipole magnetic field component is responsible for spindown energy loss, but does not decay on timescales below $\sim 100\,$Myr. The toroidal component decay on timescales $\sim 1 - 10\,$kyr drives energy loss through quiescient crustal X-ray emission L_X. We assume the luminosity is modelled by an exponential decay following the initial cooling phase:

$$L_X(t) = L_0\left(\frac{B_d}{10^{13}\,\mathrm{G}}\right)e^{-t/\tau_d} \tag{2.30}$$

where B_d is the dipole field strength, $L_0 = 10^{33}\,\mathrm{erg\,s^{-1}}$, and τ_d is the decay timescale. The decay timescale is inversely proportional to the magnetic field, and is modelled as a power law dependence with $\delta = 1.3$:

$$\tau_d = \tau_{d0}\left(\frac{B_d}{10^{13}\,\mathrm{G}}\right)^{-\delta} \tag{2.31}$$

where $\tau_{d0} = 500\,$kyr. Plugging this into Equation 2.31 and solving for $t = \mathcal{T}_{\rm decay}$, which we take to be the present-day:

$$\mathcal{T}_{\rm decay} = \tau_{d0}\left(\frac{B_d}{10^{13}\,\mathrm{G}}\right)^{-\delta}\ln\left(\frac{L_X(t=\mathcal{T}_{\rm decay})}{L0}\frac{10^{13}\,\mathrm{G}}{B_d}\right) \tag{2.32}$$

where $L_X(\mathcal{T}_{\rm decay})$ is the X-ray luminosity at present-day. The constants L_0, τ_{d0}, and δ were determined through simulations by Ferrario & Wickramasinghe (2008). Figure 2.8 shows each magnetar's $\mathcal{T}_{\rm decay}$ as a function of L_X and B_d.

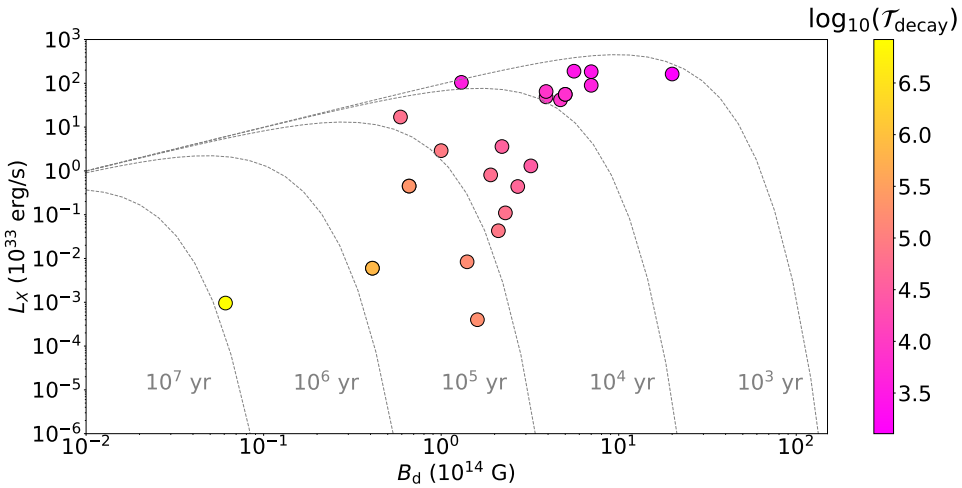

Figure 2.8: X-ray Luminosity (L_X) vs. Dipole Magnetic Field Strength (B_d) for Known Magnetars using the Decay Model of Ferrario & Wickramasinghe (2006, 2008). The magnetic field estimate is derived from the pulse period P and spindown rate $\dot{P}$ using $B_d \approx (3.2\times10^{19}G)\sqrt{P\dot{P}/1\,\mathrm{s}}$ as reported in the McGill catalog (Olausen & Kaspi, 2014). The X-ray luminosity is derived from the $2-10\,\mathrm{keV}$ flux and reported distance, also from the McGill catalog. The colorbar corresponds to the decay age $\mathcal{T}_{\mathrm{decay}}$ derived from Equation 2.32, and lines of constant age are shown in grey. This estimate is preferred to the spindown age, $\mathcal{T}_{\mathrm{rot}}$, which likely overestimates magnetar ages through neglect of field decay and glitching (e.g., Kaspi & Beloborodov, 2017; Nakano et al., 2015).

2.11.4.2 Derivation of Free-Expansion and Sedov-Taylor Expansion SNR Ages

In this section, we provide a brief description of the free-expansion and Sedov-Taylor expansion phases for SNRs as are relevant to this paper. We do not offer a detailed derivation, but refer the reader to Sedov (2018, Chapters IV. and V.), Truelove & McKee (1999), and Suzuki et al. (2021), from which this section is summarized. See also Taylor (1950) and Sedov (1946) for additional details. In this work, we are concerned with the age-radius relations for SNRs, and focus the discussion on this.

The earliest stage of a supernova explosion, which we refer to as 'free expansion', is dominated by the momentum of the ejecta mass, M_{ej}, rather than mass swept up from the surrounding medium (Truelove & McKee, 1999). This, coupled with the negligible radiative energy losses during this phase, allow the ejecta from the supernova to expand freely into the surrounding medium. During this phase, the radius of the expanding ejecta front is approximately linear with time:

$$\frac{R_{\rm FE}}{1\,{\rm km}} \approx (7090\,{\rm km}/s)\sqrt{\frac{E}{10^{51}\,{\rm ergs}}\frac{M_\odot}{M}}\frac{\mathcal{T}}{1\,{\rm s}} \tag{2.33}$$

where E is the energy of the supernova and $\mathcal{T}$ is the age of the remnant. The expansion velocity is lower than the sound speed in the surrounding medium, causing a 'blast wave' shock to precede the ejecta shell and inducing a reverse shock to oppose the ejecta. This marks the start of the transition to the Sedov-Taylor expansion phase, and occurs roughly on the characteristic timescale:

$$\mathcal{T}_{\rm ch} = \frac{M^{5/6}}{E^{1/2}(\mu n_{e,0})^{1/3}} \tag{2.34}$$

where $\mu \approx 1.4 m_p$ is the reduced mass of the ejecta and $n_{e,0}$ is the initial electron density, which increases with time through interaction with the ambient medium. The corresponding characteristic radius is

$$R_{\rm ch} = \left(\frac{M}{\mu n_{e,0}}\right)^{1/3} \tag{2.35}$$

(Sedov, 2018; Truelove & McKee, 1999).

Beyond this timescale and radius, the system enters the Sedov-Taylor expansion phase, in which the expansion is damped by the ambient medium. On late timescales, the ejecta expands as a power law with $R \propto \mathcal{T}^{2/5}$. To first order, we can form a piecewise model of $R(\mathcal{T})$ by joining the free expansion and Sedov-Taylor solutions at $R_{\rm ch}(\mathcal{T}_{\rm ch})$. Imposing this condition, we can derive the coefficient for the Sedov-Taylor solution:

$$\frac{R_{sT}}{1\,{\rm km}} \approx \left(\frac{R_{\rm ch}}{1\,{\rm km}}\right)\left(\frac{\mathcal{T}}{1\,{\rm s}}\right)^{-2/5} = (7090\,{\rm km}/s)\sqrt{\frac{E}{10^{51}\,{\rm ergs}}\frac{M_\odot}{M}}\left(\frac{\mathcal{T}_{\rm ch}}{1\,{\rm s}}\right)^{-3/5}\left(\frac{\mathcal{T}}{1\,{\rm s}}\right)^{-2/5} \tag{2.36}$$

which we note is independent of mass (Sedov, 2018; Truelove & McKee, 1999). We use this age estimate as an upper limit on the required age of a candidate SNR when deriving p_3 in the radio SNR search (see Section 2.11.2.3) and when considering the associations of SNRs in Section 2.6.3. We do not use this approximation for the SNR age estimates in Table 2.2, and opt only to use $T_{\rm SNR}$ for those with age estimates in the literature.

2.11.5 Past SNR and Neutron Star Companion Search Thresholds

Here we list references for the previous surveys used for comparison in Figure 2.6. For past radio SNR searches (see D. Green, 2019), we include the Canadian galactic plane Survey (CGPS; Gerbrandt et al., 2014; Kothes et al., 2006; Reich et al., 1990, *bottom*), the Parkes galactic plane Survey (PGPS; Duncan et al., 1997, *bottom left*), the Parkes-MIT-National Radio Astronomy Observatory (PMN; J. Condon et al., 1993; Stupar et al., 2007, *bottom left*), the 20 cm VLA supernova remnant search (VLA92; Sramek et al., 1992, *bottom middle*), the Multi-Array galactic plane Imaging Survey (MAGPIS; Helfand et al., 2006, *bottom middle*), The HI, OH, Recombination line (THOR) and VLA galactic plane Survey (VGPS) combined survey (THOR+VGPS; L. Anderson et al., 2017; Bihr et al., 2016, *bottom middle*), and the Molonglo Observatory Synthesis Telescope (MOST) galactic plane survey (MGPS; Whiteoak & A. Green, 1996, *bottom right*). We include limits from the Naval Observatory Merged Astrometric Dataset (NOMAD; Zacharias et al., 2005; Zacharias et al., 2004) and Tycho-2 (Høg et al., 2000b) point source and proper motion catalogs (*middle*), the former of which C. Kochanek (2018) use to search for stellar companions of the Crab and Cas A pulsars. We also include limits from the Asteroid Terrestrial-impact Last Alert System (ATLAS) Photometric All-Sky Survey (APASS; Tonry et al., 2018) and the HST used by C. Kochanek (2021) (in conjunction with 2MASS, UKIDSS, PS1, and *Gaia*) and Chrimes et al. (2022b), respectively, to search for pulsar and magnetar companions.

CHAPTER 2 BIBLIOGRAPHY

Acero, F. et al. (May 2016). "The First Fermi LAT Supernova Remnant Catalog". In: *The Astrophysical Journal Supplement Series* 224.1, 8, p. 8. DOI: 10.3847/0067-0049/224/1/8. arXiv: 1511.06778 [astro-ph.HE].

Akiyama, S. et al. (2003). "The magnetorotational instability in core-collapse supernova explosions". In: *The Astrophysical Journal* 584.2, p. 954.

Andersen, B. C. et al. (2023). "CHIME Discovery of a Binary Pulsar with a Massive Nondegenerate Companion". In: *The Astrophysical Journal* 943.1, p. 57.

Anderson, G. E. et al. (May 2012). "Multi-wavelength Observations of the Radio Magnetar PSR J1622-4950 and Discovery of Its Possibly Associated Supernova Remnant". In: *The Astrophysical Journal* 751.1, 53, p. 53. DOI: 10.1088/0004-637X/751/1/53. arXiv: 1203.2719 [astro-ph.HE].

Anderson, L. et al. (2017). "Galactic supernova remnant candidates discovered by THOR". In: *Astronomy & Astrophysics* 605, A58.

Andrae, R. et al. (2022). "Gaia Data Release 3: Analysis of the Gaia BP/RP spectra using the General Stellar Parameterizer from Photometry". In: *arXiv preprint arXiv:2206.06138*.

Archibald, R. F. et al. (2013). "An anti-glitch in a magnetar". In: *Nature* 497.7451, pp. 591–593.

Arras, P., A. Cumming, & C. Thompson (2004). "Magnetars: time evolution, superfluid properties, and the mechanism of magnetic field decay". In: *The Astrophysical Journal* 608.1, p. L49.

Avakyan, A. et al. (2023). "XRBcats: Galactic low-mass X-ray binary catalogue". In: *Astronomy & Astrophysics* 675, A199.

El-Badry, K. et al. (2023). "The fastest stars in the Galaxy". In: *arXiv preprint arXiv:2306.03914*.

Bailer-Jones, C. A. L. et al. (Mar. 2021). "Estimating Distances from Parallaxes. V. Geometric and Photogeometric Distances to 1.47 Billion Stars in Gaia Early Data Release 3". In: *The Astronomical Journal* 161.3, 147, p. 147. DOI: 10.3847/1538-3881/abd806. arXiv: 2012.05220 [astro-ph.SR].

Bailer-Jones, C. (2023). "Estimating Distances from Parallaxes. VI. A Method for Inferring Distances and Transverse Velocities from Parallaxes and Proper Motions Demonstrated on Gaia Data Release 3". In: *The Astronomical Journal* 166.6, p. 269.

Barker, B. L., E. P. O'Connor, & S. M. Couch (2023). "Inferring Type II-P Supernova Progenitor Masses from Plateau Luminosities". In: *The Astrophysical Journal Letters* 944.1, p. L2.

Barker, B. L. et al. (2022). “Connecting the Light Curves of Type IIP Supernovae to the Properties of Their Progenitors”. In: *The Astrophysical Journal* 934.1, p. 67.

Barthelmy, S. D. et al. (Mar. 2016). “Swift detection of a likely new SGR: SGR 0755-2933”. In: *The Astronomer’s Telegram* 8831, p. 1.

Bibby, J. L. et al. (May 2008). “A downward revision to the distance of the 1806-20 cluster and associated magnetar from Gemini Near-Infrared Spectroscopy”. In: *Monthly Notices of the Royal Astronomical Society* 386.1, pp. L23–L27. DOI: 10.1111/j.1745-3933.2008.00453.x. arXiv: 0802.0815 [astro-ph].

Bihr, S. et al. (Apr. 2016). “Continuum sources from the THOR survey between 1 and 2 GHz”. In: *Astronomy & Astrophysics* 588, A97, A97. DOI: 10.1051/0004-6361/201527697. arXiv: 1601.03427 [astro-ph.GA].

Blaauw, A. (1961). “On the origin of the O-and B-type stars with high velocities (the" run-away" stars), and some related problems”. In: *Bulletin of the Astronomical Institutes of the Netherlands, Vol. 15, p. 265* 15, p. 265.

Blumer, H. et al. (2019). “X-ray and radio studies of SNR CTB 37B hosting the magnetar CXOU J171405. 7- 381031”. In: *Monthly Notices of the Royal Astronomical Society* 487.4, pp. 5019–5028.

Bogdanov, S. (Aug. 2014). “Modeling the X-Rays from the Central Compact Object PSR J1852+0040 in Kesteven 79: Evidence for a Strongly Magnetized Neutron Star”. In: *The Astrophysical Journal* 790.2, 94, p. 94. DOI: 10.1088/0004-637X/790/2/94. arXiv: 1406.0515 [astro-ph.HE].

Borkowski, K. J. & S. P. Reynolds (2017). “Expansion of Kes 73, A Shell Supernova Remnant Containing a Magnetar”. In: *The Astrophysical Journal* 846.1, p. 13.

Bower, G. C. et al. (2015). “The proper motion of the galactic center pulsar relative to Sagittarius A”. In: *The Astrophysical Journal* 798.2, p. 120.

Bower, G. C. et al. (Jan. 2014). “The Angular Broadening of the Galactic Center Pulsar SGR J1745-29: A New Constraint on the Scattering Medium”. In: *The Astrophysical Journal Letters* 780.1, L2, p. L2. DOI: 10.1088/2041-8205/780/1/L2. arXiv: 1309.4672 [astro-ph.GA].

Brown, A. G. et al. (2021). “Gaia early data release 3-summary of the contents and survey properties”. In: *Astronomy & Astrophysics* 649, A1.

Burns, E. et al. (Feb. 2021). “Identification of a Local Sample of Gamma-Ray Bursts Consistent with a Magnetar Giant Flare Origin”. In: *The Astrophysical Journal Letters* 907.2, L28, p. L28. DOI: 10.3847/2041-8213/abd8c8. arXiv: 2101.05144 [astro-ph.HE].

Carretero-Castrillo, M., M. Ribó, & J. Paredes (2023). “Galactic runaway O and Be stars found using Gaia DR3”. In: *Astronomy & Astrophysics* 679, A109.

Casali, M. et al. (May 2007). “The UKIRT wide-field camera”. In: *Astronomy & Astrophysics* 467.2, pp. 777–784. DOI: 10.1051/0004-6361:20066514.

Chabrier, G. (2001). “The galactic disk mass budget. I. Stellar mass function and density”. In: *The Astrophysical Journal* 554.2, p. 1274.

Chambers, K. C. et al. (2019). *The Pan-STARRS1 Surveys*. arXiv: 1612.05560 [astro-ph.IM].

Chaty, S. & F. Rahoui (2012). “BROADBAND ESO/VISIR–SPITZER INFRARED SPECTROSCOPY OF THE OBSCURED SUPERGIANT X-RAY BINARY IGR J16318-4848”. In: *The Astrophysical Journal* 751.2, p. 150.

Chevalier, R. & A. W. Clegg (1985). “Wind from a starburst galaxy nucleus”. In: *Nature* 317.6032, pp. 44–45.

Chrimes, A. et al. (2022a). “New candidates for magnetar counterparts from a deep search with the Hubble Space Telescope”. In: *Monthly Notices of the Royal Astronomical Society* 512.4, pp. 6093–6103.

Chrimes, A. et al. (2022b). “Where are the magnetar binary companions? Candidates from a comparison with binary population synthesis predictions”. In: *Monthly Notices of the Royal Astronomical Society* 513.3, pp. 3550–3563.

Chrimes, A. et al. (2023). “Searching for ejected supernova companions in the era of precise proper motion and radial velocity measurements”. In: *Monthly Notices of the Royal Astronomical Society* 522.2, pp. 2029–2046.

Clark, J. S. et al. (2014). “A VLT/FLAMES survey for massive binaries in Westerlund 1-IV. Wd1-5–binary product and a pre-supernova companion for the magnetar CXOU J1647-45?” In: *Astronomy & Astrophysics* 565, A90.

Cline, T. et al. (Mar. 2000). “Observations of a Possible New Soft Gamma Repeater, SGR 1801-23”. In: *The Astrophysical Journal* 531.1, pp. 407–410. DOI: 10.1086/308470. arXiv: astro-ph/9909054 [astro-ph].

Cline, T. L. et al. (Apr. 1982). “Precise source location of the anomalous 1979 March 5 gamma-ray transient.” In: *The Astrophysical Journal Letters* 255, pp. L45–L48. DOI: 10.1086/183766.

Collaboration, G. et al. (2022). *Gaia Data Release 3: Summary of the content and survey properties*. arXiv: 2208.00211 [astro-ph.GA].

Condon, J. J. et al. (1998). “The NRAO VLA sky survey”. In: *The Astronomical Journal* 115.5, p. 1693.

Condon, J., M. R. Griffith, & A. E. Wright (1993). “The Parkes-MIT-NRAO surveys. IV-Maps for the Southern Survey covering delta in the range-88 to-37 deg”. In: *Astronomical Journal (ISSN 0004-6256), vol. 106, no. 3, p. 1095-1100.* 106, pp. 1095–1100.

Corbel, S. et al. (Nov. 1999). “The Distance to the Soft Gamma Repeater SGR 1627-41”. In: *The Astrophysical Journal Letters* 526.1, pp. L29–L32. DOI: 10.1086/312359. arXiv: astro-ph/9909334 [astro-ph].

Corbel, S. & S. S. Eikenberry (2004). “The connection between W31, SGR 1806–20, and LBV 1806–20: Distance, extinction, and structure”. In: *Astronomy & Astrophysics* 419.1, pp. 191–201.

Cotton, W. D. et al. (Apr. 2024). “The MeerKAT 1.3 GHz Survey of the Small Magellanic Cloud”. In: *MNRAS* 529.3, pp. 2443–2472. DOI: 10.1093/mnras/stae277. arXiv: 2401.11024 [astro-ph.GA].

Cross, N. J. et al. (2012). “The VISTA science archive”. In: *Astronomy & Astrophysics* 548, A119.

Cutri, R. M. et al. (June 2003). *VizieR Online Data Catalog: 2MASS All-Sky Catalog of Point Sources (Cutri+ 2003)*.

Davies, B. et al. (2009). “The Progenitor Mass of the Magnetar SGR1900+14”. In: *The Astrophysical Journal* 707.1, pp. 844–851. DOI: 10.1088/0004-637X/707/1/844. arXiv: 0910.4859 [astro-ph.SR].

Deller, A. T. et al. (Mar. 2012). “The Proper Motion of PSR J1550-5418 Measured with VLBI: A Second Magnetar Velocity Measurement”. In: *The Astrophysical Journal Letters* 748.1, L1, p. L1. DOI: 10.1088/2041-8205/748/1/L1. arXiv: 1201.4684 [astro-ph.SR].

Dinçel, B. et al. (2015). “Discovery of an OB runaway star inside SNR S147”. In: *Monthly Notices of the Royal Astronomical Society* 448.4, pp. 3196–3205.

Ding, H. et al. (2020a). “A magnetar parallax”. In: *Monthly Notices of the Royal Astronomical Society* 498.3, pp. 3736–3743.

Ding, H. et al. (2020b). “Probing magnetar formation channels with high-precision astrometry: The progress of VLBA astrometry of the fastest-spinning magnetar Swift J1818. 0–1607”. In: *Proceedings of the International Astronomical Union* 16.S363, pp. 271–275.

Dohm-Palmer, R. C. & T. W. Jones (1996). “Young supernova remnants in nonuniform media”. In: *The Astrophysical Journal* 471.1, p. 279.

Donati, J.-F. et al. (2006). “The surprising magnetic topology of τ Sco: fossil remnant or dynamo output?” In: *Monthly Notices of the Royal Astronomical Society* 370.2, pp. 629–644.

Doroshenko, V. et al. (2021). “SGR 0755- 2933: a new high-mass X-ray binary with the wrong name”. In: *Astronomy & Astrophysics* 647, A165.

Duarte-Cabral, A. et al. (Jan. 2021). *The SEDIGISM survey: molecular clouds in the inner Galaxy*. DOI: 10.1093/mnras/staa2480. arXiv: 2012.01502 [astro-ph.GA].

Dubner, G. & E. Giacani (2015). “Radio emission from supernova remnants”. In: *The Astronomy and Astrophysics Review* 23.1, p. 3.

Duncan, A. et al. (1997). “Supernova remnant candidates from the Parkes 2.4-GHz survey”. In: *Monthly Notices of the Royal Astronomical Society* 287.4, pp. 722–738.

Durant, M. & M. H. van Kerkwijk (Oct. 2006). “Distances to Anomalous X-Ray Pulsars Using Red Clump Stars”. In: *The Astrophysical Journal* 650.2, pp. 1070–1081. DOI: 10.1086/506380. arXiv: astro-ph/0606027 [astro-ph].

Dye, S. et al. (Nov. 2006). “The UKIRT Infrared Deep Sky Survey Early Data Release”. In: *Monthly Notices of the Royal Astronomical Society* 372.3, pp. 1227–1252. DOI: 10.1111/j.1365-2966.2006.10928.x. arXiv: astro-ph/0603608 [astro-ph].

Eden, D. J. et al. (Aug. 2017). “The JCMT Plane Survey: first complete data release - emission maps and compact source catalogue”. In: *MNRAS* 469.2, pp. 2163–2183. DOI: 10.1093/mnras/stx874. arXiv: 1704.02982 [astro-ph.GA].

Egret, D., M. Wenger, & P. Dubois (1991). “The SIMBAD astronomical database”. In: *Databases & On-line Data in Astronomy*. Springer, pp. 79–88.

Esposito, P. et al. (Sept. 2011). “Long-term spectral and timing properties of the soft gamma-ray repeater SGR 1833-0832 and detection of extended X-ray emission around the radio pulsar PSR B1830-08”. In: *Monthly Notices of the Royal Astronomical Society* 416.1, pp. 205–215. DOI: 10.1111/j.1365-2966.2011.19022.x. arXiv: 1105.1323 [astro-ph.HE].

Fahlman, G. G. & P. C. Gregory (Sept. 1981). “An X-ray pulsar in SNR G109.1-1.0”. In: *Nature* 293.5829, pp. 202–204. DOI: 10.1038/293202a0.

Farrow, D. J. et al. (2014). “Pan-STARRS1: Galaxy clustering in the Small Area Survey 2”. In: *Monthly Notices of the Royal Astronomical Society* 437.1, pp. 748–770.

Feast, M. & M. Shuttleworth (1965). “The kinematics of B stars, cepheids, galactic clusters and interstellar gas in the Galaxy”. In: *Monthly Notices of the Royal Astronomical Society* 130.4, pp. 245–280.

Fernie, J. (1983). “Relationships between the Johnson and Kron-Cousins VRI photometric systems.” In: *Publications of the Astronomical Society of the Pacific* 95.572, p. 782.

Ferrario, L. & D. Wickramasinghe (2006). “Modelling of isolated radio pulsars and magnetars on the fossil field hypothesis”. In: *Monthly Notices of the Royal Astronomical Society* 367.3, pp. 1323–1328.

– (2008). “Origin and evolution of magnetars”. In: *Monthly Notices of the Royal Astronomical Society: Letters* 389.1, pp. L66–L70.

Flewelling, H. A. et al. (2020). “The Pan-STARRS1 Database and Data Products”. In: *The Astrophysical Journal Supplement Series* 251.1, p. 7. DOI: 10.3847/1538-4365/abb82d. URL: https://doi.org/10.3847%2F1538-4365%2Fabb82d.

Fouesneau, M. et al. (2022). “Gaia Data Release 3: Apsis II–Stellar Parameters”. In: *arXiv preprint arXiv:2206.05992*.

Frail, D. A., S. R. Kulkarni, & J. S. Bloom (Mar. 1999). “An outburst of relativistic particles from the soft γ-ray repeater SGR1900+14”. In: *Nature* 398.6723, pp. 127–129. DOI: 10.1038/18163. arXiv: astro-ph/9812457 [astro-ph].

Frail, D. & T. Clifton (1989). “A kinematic distance to the supernova remnant G33. 6+ 0.1”. In: *The Astrophysical Journal* 336, pp. 854–860.

Frail, D., W. Goss, & J. Whiteoak (1994). “The radio lifetime of supernova remnants and the distribution of pulsar velocities at birth”. In: *arXiv preprint astro-ph/9407031*.

Frail, D. et al. (1995). “Does the Crab have a shell?” In: *The Astrophysical Journal* 454.2, p. L129.

Frederiks, D. et al. (2007). “On the possibility of identifying the short hard burst GRB 051103 with a giant flare from a soft gamma repeater in the M81 group of galaxies”. In: *Astronomy Letters* 33, pp. 19–24.

Fryer, C. et al. (1999). “What can the accretion-induced collapse of white dwarfs really explain?” In: *The Astrophysical Journal* 516.2, p. 892.

Fuller, J. & W. Lu (2022). “The spins of compact objects born from helium stars in binary systems”. In: *Monthly Notices of the Royal Astronomical Society* 511.3, pp. 3951–3964.

Gaensler, B. M., E. V. Gotthelf, & G. Vasisht (Nov. 1999). “A New Supernova Remnant Coincident with the Slow X-Ray Pulsar AX J1845-0258”. In: *The Astrophysical Journal Letters* 526.1, pp. L37–L40. DOI: 10.1086/312362. arXiv: astro-ph/9909400 [astro-ph].

Gaensler, B. M. et al. (Feb. 2005). “A Stellar Wind Bubble Coincident with the Anomalous X-Ray Pulsar 1E 1048.1-5937: Are Magnetars Formed from Massive Progenitors?” In: *The Astrophysical Journal Letters* 620.2, pp. L95–L98. DOI: 10.1086/428725. arXiv: astro-ph/0501563 [astro-ph].

Gaensler, B. (2014). “GRB 140705A/SGR 1935+ 2154: Probable association with supernova remnant G57. 2+ 0.8.” In: *GRB Coordinates Network* 16533, p. 1.

Gaensler, B. & S. Chatterjee (2008). “SGR 0501+ 4516: proximity to supernova remnant HB9.” In: *GRB Coordinates Network* 8149, p. 1.

Gaia Collaboration et al. (Nov. 2016). “The Gaia mission”. In: *Astronomy & Astrophysics* 595, A1, A1. DOI: 10.1051/0004-6361/201629272. arXiv: 1609.04153 [astro-ph.IM].

Gavriil, F. P., V. Kaspi, & P. Woods (2002). “Magnetar-like X-ray bursts from an anomalous X-ray pulsar”. In: *Nature* 419.6903, pp. 142–144.

Gelfand, J. D. & B. M. Gaensler (Oct. 2007). "The Compact X-Ray Source 1E 1547.0-5408 and the Radio Shell G327.24-0.13: A New Proposed Association between a Candidate Magnetar and a Candidate Supernova Remnant". In: *The Astrophysical Journal* 667.2, pp. 1111–1118. DOI: 10.1086/520526. arXiv: 0706.1054 [astro-ph].

Gerbrandt, S. et al. (2014). "The search for faint radio supernova remnants in the outer Galaxy: five new discoveries". In: *Astronomy & Astrophysics* 566, A76.

Giacani, E. et al. (Nov. 2009). "Radio and X-ray study of two multi-shell supernova remnants: Kes 79 and G352.7-0.1". In: *Astronomy & Astrophysics* 507.2, pp. 841–853. DOI: 10.1051/0004-6361/200912253. arXiv: 0907.2133 [astro-ph.GA].

Giacomazzo, B. & R. Perna (2013). "Formation of stable magnetars from binary neutron star mergers". In: *The Astrophysical Journal Letters* 771.2, p. L26.

Giacomazzo, B. et al. (2015). "Producing magnetar magnetic fields in the merger of binary neutron stars". In: *The Astrophysical Journal* 809.1, p. 39.

Gogus, E. & J. Gorosabel (Jan. 2011). "Swift J1822.3-1606: transient magnetar or Be X-ray binary?" In: *GRB Coordinates Network* 12170, p. 1.

Göğüş, E. et al. (July 2010a). "Discovery of a New Soft Gamma Repeater, SGR J1833-0832". In: *The Astrophysical Journal* 718.1, pp. 331–339. DOI: 10.1088/0004-637X/718/1/331. arXiv: 1005.3029 [astro-ph.HE].

Göğüş, E. et al. (Oct. 2010b). "Spatial, Temporal, and Spectral Properties of X-ray Emission from the Magnetar SGR 0501+4516". In: *The Astrophysical Journal* 722.1, pp. 899–908. DOI: 10.1088/0004-637X/722/1/899. arXiv: 1008.4089 [astro-ph.HE].

Gordon, A. C. et al. (2023). "The demographics, stellar populations, and star formation histories of fast radio burst host galaxies: implications for the progenitors". In: *The Astrophysical Journal* 954.1, p. 80.

Gordon, Y. A. et al. (Oct. 2020). "A Catalog of Very Large Array Sky Survey Epoch 1 Quick Look Components, Sources, and Host Identifications". In: *Research Notes of the American Astronomical Society* 4.10, 175, p. 175. DOI: 10.3847/2515-5172/abbe23.

Gordon, Y. A. et al. (Aug. 2021). "A Quick Look at the 3 GHz Radio Sky. I. Source Statistics from the Very Large Array Sky Survey". In: *The Astrophysical Journal Supplement Series* 255.2, 30, p. 30. DOI: 10.3847/1538-4365/ac05c0. arXiv: 2102.11753 [astro-ph.GA].

Gordon, Y. A. et al. (Aug. 2023). "A Quick Look at the 3 GHz Radio Sky. II. Hunting for DRAGNs in the VLA Sky Survey". In: *The Astrophysical Journal Supplement Series* 267.2, 37, p. 37. DOI: 10.3847/1538-4365/acda30. arXiv: 2303.12830 [astro-ph.GA].

Gorosabel, J. et al. (July 2011). "Swift J1822.3-1606: Optical/NIR counterpart candidate". In: *The Astronomer's Telegram* 3496, p. 1.

Gotthelf, E. V. & J. P. Halpern (Feb. 2008). "CCO Pulsars as Anti-Magnetars: Evidence of Neutron Stars Weakly Magnetized at Birth". In: *40 Years of Pulsars: Millisecond Pulsars, Magnetars and More*. Ed. by C. Bassa et al. Vol. 983. American Institute of Physics Conference Series, pp. 320–324. DOI: 10.1063/1.2900174. arXiv: 0711.1554 [astro-ph].

Gotthelf, E. V., J. P. Halpern, & J. Alford (Mar. 2013). "The Spin-down of PSR J0821-4300 and PSR J1210-5226: Confirmation of Central Compact Objects as Anti-magnetars". In: *The Astrophysical Journal* 765.1, 58, p. 58. DOI: 10.1088/0004-637X/765/1/58. arXiv: 1301.2717 [astro-ph.HE].

Gotthelf, E. V., J. P. Halpern, & F. D. Seward (July 2005). "Discovery of a 105 ms X-Ray Pulsar in Kesteven 79: On the Nature of Compact Central Objects in Supernova Remnants". In: *The Astrophysical Journal* 627.1, pp. 390–396. DOI: 10.1086/430300. arXiv: astro-ph/0503424 [astro-ph].

Gotthelf, E. V. et al. (Oct. 2000). "A 700 Year-old Pulsar in the Supernova Remnant Kesteven 75". In: *The Astrophysical Journal Letters* 542.1, pp. L37–L40. DOI: 10.1086/312923. arXiv: astro-ph/0008097 [astro-ph].

Green, D. (2019). "A revised catalogue of 294 Galactic supernova remnants". In: *Journal of Astrophysics and Astronomy* 40.4, p. 36.

Green, D. A. (1987). *A catalogue of galactic supernova remnants*. Mullard radio astronomy observatory.

Green, G. M. et al. (2015). "A three-dimensional map of Milky Way dust". In: *The Astrophysical Journal* 810.1, p. 25.

Green, G. M. et al. (2018). "Galactic reddening in 3D from stellar photometry–an improved map". In: *Monthly Notices of the Royal Astronomical Society* 478.1, pp. 651–666.

Green, G. M. et al. (2019). "A 3D Dust Map Based on Gaia, Pan-STARRS 1, and 2MASS". In: *The Astrophysical Journal* 887.1, 93, p. 93. DOI: 10.3847/1538-4357/ab5362. arXiv: 1905.02734 [astro-ph.GA].

Greisen, E. W. & M. R. Calabretta (2002). "Representations of world coordinates in FITS". In: *Astronomy & Astrophysics* 395.3, pp. 1061–1075.

Güver, T. & F. Özel (2009). "The relation between optical extinction and hydrogen column density in the Galaxy". In: *Monthly Notices of the Royal Astronomical Society* 400.4, pp. 2050–2053.

H. E. S. S. Collaboration et al. (Apr. 2018). "Extended VHE γ-ray emission towards SGR1806-20, LBV 1806-20, and stellar cluster Cl* 1806-20". In: *Astronomy & Astrophysics* 612, A11, A11. DOI: 10.1051/0004-6361/201628695. arXiv: 1606.05404 [astro-ph.HE].

Haberl, F. (2007). "The magnificent seven: magnetic fields and surface temperature distributions". In: *Astrophysics and Space Science* 308, pp. 181–190.

Hale, C. L. et al. (2021). "The Rapid ASKAP Continuum Survey Paper II: First Stokes I Source Catalogue Data Release". In: *arXiv preprint arXiv:2109.00956*.

Halpern, J. (Jan. 2011). "SGR J1834.9-0846: a neutron star in W41?" In: *GRB Coordinates Network* 12260, p. 1.

Halpern, J. P. & E. V. Gotthelf (2010a). "An Energetic Magnetar in HESS J1713-381/CTB 37B". In: *The Astrophysical Journal* 725.1, pp. 1384–1391. DOI: 10.1088/0004-637X/725/1/1384. arXiv: 1008.2558 [astro-ph.HE].

– (Feb. 2010b). "Two Magnetar Candidates in HESS Supernova Remnants". In: *The Astrophysical Journal* 710.2, pp. 941–947. DOI: 10.1088/0004-637X/710/2/941. arXiv: 0912.4985 [astro-ph.HE].

Halpern, J. P. et al. (Aug. 2007). "X-Ray Timing of PSR J1852+0040 in Kesteven 79: Evidence of Neutron Stars Weakly Magnetized at Birth". In: *The Astrophysical Journal* 665.2, pp. 1304–1310. DOI: 10.1086/519557. arXiv: 0705.0978 [astro-ph].

Hambly, N. C. et al. (Feb. 2008). "The WFCAM Science Archive". In: *Monthly Notices of the Royal Astronomical Society* 384.2, pp. 637–662. DOI: 10.1111/j.1365-2966.2007.12700.x. arXiv: 0711.3593 [astro-ph].

Hamuy, M. (2003). "Observed and physical properties of core-collapse supernovae". In: *The Astrophysical Journal* 582.2, p. 905.

Haschke, R., E. K. Grebel, & S. Duffau (Oct. 2012). "Three-dimensional Maps of the Magellanic Clouds using RR Lyrae Stars and Cepheids. II. The Small Magellanic Cloud". In: *The Astronomical Journal* 144.4, 107, p. 107. DOI: 10.1088/0004-6256/144/4/107. arXiv: 1209.3769 [astro-ph.GA].

Heinze, A. N. et al. (Nov. 2018). "A First Catalog of Variable Stars Measured by the Asteroid Terrestrial-impact Last Alert System (ATLAS)". In: *The Astronomical Journal* 156.5, 241, p. 241. DOI: 10.3847/1538-3881/aae47f. arXiv: 1804.02132 [astro-ph.SR].

Helfand, D. J. et al. (June 2007). "VLBA Measurement of the Transverse Velocity of the Magnetar XTE J1810-197". In: *The Astrophysical Journal* 662.2, pp. 1198–1203. DOI: 10.1086/518028. arXiv: astro-ph/0703336 [astro-ph].

Helfand, D. J. et al. (2006). "MAGPIS: a multi-array Galactic plane imaging survey". In: *The Astronomical Journal* 131.5, p. 2525.

Helfand, D. J., B. F. Collins, & E. V. Gotthelf (Jan. 2003). "Chandra X-Ray Imaging Spectroscopy of the Young Supernova Remnant Kesteven 75". In: *The Astrophysical Journal* 582.2, pp. 783–792. DOI: 10.1086/344725. arXiv: astro-ph/0209348 [astro-ph].

Hewett, P. C. et al. (Apr. 2006). "The UKIRT Infrared Deep Sky Survey ZY JHK photometric system: passbands and synthetic colours". In: *Monthly Notices of the Royal Astronomical Society* 367.2, pp. 454–468. DOI: 10.1111/j.1365-2966.2005.09969.x. arXiv: astro-ph/0601592 [astro-ph].

Hewitt, J. W. & F. Yusef-Zadeh (2009). "Discovery of New Interacting Supernova Remnants in the Inner Galaxy". In: *The Astrophysical Journal* 694.1, p. L16.

Hobbs, G. et al. (2004). "The Parkes multibeam pulsar survey–IV. Discovery of 180 pulsars and parameters for 281 previously known pulsars". In: *Monthly Notices of the Royal Astronomical Society* 352.4, pp. 1439–1472.

Hobbs, G. et al. (July 2005). "A statistical study of 233 pulsar proper motions". In: *Monthly Notices of the Royal Astronomical Society* 360.3, pp. 974–992. DOI: 10.1111/j.1365-2966.2005.09087.x. arXiv: astro-ph/0504584 [astro-ph].

Hodgkin, S. T. et al. (Apr. 2009). "The UKIRT wide field camera ZYJHK photometric system: calibration from 2MASS". In: *Monthly Notices of the Royal Astronomical Society* 394.2, pp. 675–692. DOI: 10.1111/j.1365-2966.2008.14387.x. arXiv: 0812.3081 [astro-ph].

Høg, E. et al. (Mar. 2000a). "The Tycho-2 catalogue of the 2.5 million brightest stars". In: *Astronomy & Astrophysics* 355, pp. L27–L30.

Høg, E. et al. (2000b). "Construction and verification of the Tycho-2 Catalogue". In: *Astronomy and Astrophysics, v. 357, p. 367-386 (2000)* 357, pp. 367–386.

Hulleman, F., M. Van Kerkwijk, & S. Kulkarni (2004). "The Anomalous X-ray Pulsar 4U 0142+ 61: Variability in the infrared and a spectral break in the optical". In: *Astronomy & Astrophysics* 416.3, pp. 1037–1045.

Hulleman, F. et al. (2001). "A Possible Faint Near-Infrared Counterpart to the Anomalous X-Ray Pulsar 1E 2259+586". In: *The Astrophysical Journal Letters* 563.1, pp. L49–L52. DOI: 10.1086/338478. arXiv: astro-ph/0110172 [astro-ph].

Hurley, K. et al. (Sept. 1999). "Where is SGR 1806-20?" In: *The Astrophysical Journal Letters* 523.1, pp. L37–L40. DOI: 10.1086/312256. arXiv: astro-ph/9906020 [astro-ph].

Ibrahim, A. Y. et al. (2024). *An X-ray and radio view of the 2022 reactivation of the magnetar SGRJ1935+2154*. arXiv: 2402.08596 [astro-ph.HE].

Irwin, M. J. et al. (2004). "VISTA data flow system: pipeline processing for WFCAM and VISTA". In: *Optimizing scientific return for astronomy through information technologies*. Vol. 5493. SPIE, pp. 411–422.

Israel, G. L. et al. (June 2003). "The Infrared Counterpart to the Anomalous X-Ray Pulsar 1RXS J170849-400910". In: *The Astrophysical Journal Letters* 589.2, pp. L93–L96. DOI: 10.1086/375832. arXiv: astro-ph/0304233 [astro-ph].

Israel, G. L. et al. (Apr. 2016). "The discovery, monitoring and environment of SGR J1935+2154". In: *Monthly Notices of the Royal Astronomical Society* 457.4, pp. 3448–3456. DOI: 10.1093/mnras/stw008. arXiv: 1601.00347 [astro-ph.HE].

Israel, G. et al. (2005). "Discovery and monitoring of the likely IR counterpart of SGR 1806-20 during the 2004 gamma-ray burst-active state". In: *arXiv preprint astro-ph/0506095*.

Jiao, W. et al. (2023). "Fragmentation of the High-mass "Starless" Core G10. 21-0.31: A Coherent Evolutionary Picture for Star Formation". In: *The Astrophysical Journal* 945.1, p. 81.

Jing, W. C. et al. (Aug. 2023). "Distance of PSR B0458+46 indicated by FAST H I absorption observations". In: *Monthly Notices of the Royal Astronomical Society* 523.4, pp. 4949–4956. DOI: 10.1093/mnras/stad1782. arXiv: 2306.01246 [astro-ph.HE].

Kaiser, N. (Oct. 2004). "Pan-STARRS: a wide-field optical survey telescope array". In: *Ground-based Telescopes*. Ed. by J. Oschmann Jacobus M. Vol. 5489. Society of Photo-Optical Instrumentation Engineers (SPIE) Conference Series, pp. 11–22. DOI: 10.1117/12.552472.

Kaiser, N. et al. (2002). "Pan-STARRS: a large synoptic survey telescope array". In: *Survey and Other Telescope Technologies and Discoveries*. Vol. 4836. SPIE, pp. 154–164.

Kargaltsev, O. et al. (Mar. 2012). "X-Ray Observations of the New Unusual Magnetar Swift J1834.9-0846". In: *The Astrophysical Journal* 748.1, 26, p. 26. DOI: 10.1088/0004-637X/748/1/26. arXiv: 1201.1894 [astro-ph.HE].

Karuppusamy, R. et al. (2020). "Detection of pulsed radio emission from new magnetar Swift J1818. 0-1607". In: *The Astronomer's Telegram* 13553, p. 1.

Kaspi, V. M. (Jan. 1996). "Pulsar/Supernova Remnant Associations". In: *IAU Colloq. 160: Pulsars: Problems and Progress*. Ed. by S. Johnston, M. A. Walker, & M. Bailes. Vol. 105. Astronomical Society of the Pacific Conference Series, p. 375.

Kaspi, V. M. & A. M. Beloborodov (2017). "Magnetars". In: *Annual Review of Astronomy and Astrophysics* 55.1, pp. 261–301.

Keane, E. F. & M. Kramer (2008). "On the birthrates of Galactic neutron stars". In: *Monthly Notices of the Royal Astronomical Society* 391.4, pp. 2009–2016.

Kirsten, F. et al. (2022). "A repeating fast radio burst source in a globular cluster". In: *Nature* 602.7898, pp. 585–589.

Klose, S. et al. (July 2004). "A Near-Infrared Survey of the N49 Region around the Soft Gamma Repeater SGR 0526-66". In: *The Astrophysical Journal Letters* 609.1, pp. L13–L16. DOI: 10.1086/422657. arXiv: astro-ph/0405299 [astro-ph].

Kobulnicky, H. A. & C. L. Fryer (2007). "A new look at the binary characteristics of massive stars". In: *The Astrophysical Journal* 670.1, p. 747.

Kochanek, C. S. (2009). "Stellar binary companions to supernova progenitors". In: *The Astrophysical Journal* 707.2, p. 1578.

Kochanek, C. (2018). "Cas A and the Crab were not stellar binaries at death". In: *Monthly Notices of the Royal Astronomical Society* 473.2, pp. 1633–1643.

– (2021). "Supernovae producing unbound binaries and triples". In: *Monthly Notices of the Royal Astronomical Society* 507.4, pp. 5832–5846.

– (2023). "A Search for Unbound Stellar Companions to Pulsar J1124- 5916". In: *Monthly Notices of the Royal Astronomical Society* 519.3, pp. 3865–3871.

Kochanek, C., K. Auchettl, & K. Belczynski (2019). "Stellar binaries that survive supernovae". In: *Monthly Notices of the Royal Astronomical Society* 485.4, pp. 5394–5410.

Kothes, R. & S. Dougherty (2008). "The distance and neutral environment of the massive stellar cluster Westerlund". In: *Revista Mexicana de Astronomía y Astrofísica* 33, p. 163.

Kothes, R. et al. (2006). "A catalogue of Galactic supernova remnants from the Canadian Galactic plane survey-I. Flux densities, spectra, and polarization characteristics". In: *Astronomy & Astrophysics* 457.3, pp. 1081–1093.

Kothes, R. et al. (2018). "A radio continuum and polarization study of SNR G57. 2+ 0.8 associated with magnetar SGR 1935+ 2154". In: *The Astrophysical Journal* 852.1, p. 54.

Kothes, R. & T. Foster (Feb. 2012). "A Thorough Investigation of the Distance to the Supernova Remnant CTB109 and Its Pulsar AXP J2301+5852". In: *The Astrophysical Journal Letters* 746.1, L4, p. L4. DOI: 10.1088/2041-8205/746/1/L4.

Kouwenhoven, M. B. N. et al. (Jan. 2005). "The primordial binary population. I. A near-infrared adaptive optics search for close visual companions to A star members of Scorpius OB2". In: *Astronomy & Astrophysics* 430, pp. 137–154. DOI: 10.1051/0004-6361:20048124. arXiv: astro-ph/0410106 [astro-ph].

Kramer, M., N. Wex, & R. Wielebinski (2000). "Pulsar Astronomy-2000 and beyond". In: *IAU Colloq. 177: Pulsar Astronomy-2000 and Beyond*. Vol. 202.

Krimm, H. A. et al. (Aug. 2020). "Swift Detection of an SGR-like flare from AX J1846.4-0258". In: *The Astronomer's Telegram* 13913, p. 1.

Kron, R. G. (1980). "Photometry of a complete sample of faint galaxies". In: *The Astrophysical Journal Supplement Series* 43, pp. 305–325.

Kroupa, P. (2002). "The initial mass function of stars: evidence for uniformity in variable systems". In: *Science* 295.5552, pp. 82–91.

Kroupa, P., C. A. Tout, & G. Gilmore (1993). "The distribution of low-mass stars in the Galactic disc". In: *Monthly Notices of the Royal Astronomical Society* 262.3, pp. 545–587. ISSN: 0035-8711. DOI: 10.1093/mnras/262.3.545. eprint: https://academic.oup.com/mnras/article-pdf/262/3/545/3370565/mnras262-0545.pdf. URL: https://doi.org/10.1093/mnras/262.3.545.

Kroupa, P. & C. Weidner (2003). "Galactic-field initial mass functions of massive stars". In: *The Astrophysical Journal* 598.2, p. 1076.

Kulkarni, S. R. et al. (Mar. 2003). "The Quiescent Counterpart of the Soft Gamma-Ray Repeater SGR 0526-66". In: *The Astrophysical Journal* 585.2, pp. 948–954. DOI: 10.1086/346110. arXiv: astro-ph/0209520 [astro-ph].

Kulkarni, S. R. et al. (1988). "A fast pulsar in radio nebula CTB80". In: *Nature* 331.6151, pp. 50–53.

Laha, S. et al. (Aug. 2020). "AX J1846.4-0258: Swift-BAT refined analysis". In: *GRB Coordinates Network* 28193, p. 1.

Lamb, D. et al. (Aug. 2003). "SGR 1808-20 (=H2802): A Possible new SGR". In: *GRB Coordinates Network* 2351, p. 1.

Lamb, R. C. et al. (July 2002). "Discovery of a Possible Anomalous X-Ray Pulsar in the Small Magellanic Cloud". In: *The Astrophysical Journal Letters* 574.1, pp. L29–L32. DOI: 10.1086/342352. arXiv: astro-ph/0205310 [astro-ph].

Lawrence, A. et al. (Aug. 2007). "The UKIRT Infrared Deep Sky Survey (UKIDSS)". In: *MNRAS* 379.4, pp. 1599–1617. DOI: 10.1111/j.1365-2966.2007.12040.x. arXiv: astro-ph/0604426 [astro-ph].

Lawrence, A. et al. (Mar. 2012). *VizieR Online Data Catalog: UKIDSS-DR8 LAS, GCS and DXS Surveys (Lawrence+ 2012)*. VizieR On-line Data Catalog: II/314. Originally published in: 2007MNRAS.379.1599L; 2012yCat.2314....0U.

– (Apr. 2013). *VizieR Online Data Catalog: UKIDSS-DR9 LAS, GCS and DXS Surveys (Lawrence+ 2012)*. VizieR On-line Data Catalog: II/319. Originally published in: 2007MNRAS.379.1599L.

Leahy, D. A. & W. W. Tian (Jan. 2008). "The Distances of SNR W41 and Overlapping H II Regions". In: *The Astronomical Journal* 135.1, pp. 167–172. DOI: 10.1088/0004-6256/135/1/167. arXiv: 0708.3377 [astro-ph].

Leahy, D. A. & W. Tian (2007). "The distance of the SNR Kes 75 and PWN PSR J1846-0258 system". In: *arXiv preprint arXiv:0711.4107*.

Leahy, D. A. & W. Tian (2008). "The distance of the SNR Kes 75 and PWN PSR J1846-0258 system". In: *Astronomy & Astrophysics* 480.2, pp. L25–L28.

Leung, S.-C., K. Nomoto, & T. Suzuki (2020). "Electron-capture supernovae of super-AGB stars: sensitivity on input physics". In: *The Astrophysical Journal* 889.1, p. 34.

Levin, L. et al. (Sept. 2010). "A Radio-loud Magnetar in X-ray Quiescence". In: *ApJ* 721.1, pp. L33–L37. DOI: 10.1088/2041-8205/721/1/L33. arXiv: 1007.1052 [astro-ph.HE].

Lima, R. C. R. de et al. (2024). *Evidence for 3XMM J185246.6+003317 as a massive magnetar with a low magnetic field*. arXiv: 2210.06648 [astro-ph.HE].

Lin, D., N. A. Webb, & D. Barret (Sept. 2012). "Classification of X-Ray Sources in the XMM-Newton Serendipitous Source Catalog". In: *The Astrophysical Journal* 756.1, 27, p. 27. DOI: 10.1088/0004-637X/756/1/27. arXiv: 1207.1913 [astro-ph.HE].

Lin, L. et al. (Oct. 2011). "Fermi/Gamma-Ray Burst Monitor Observations of SGR J0501+4516 Bursts". In: *The Astrophysical Journal* 739.2, 87, p. 87. DOI: 10.1088/0004-637X/739/2/87.

Lindegren, L. et al. (2021). "Gaia early data release 3-the astrometric solution". In: *Astronomy & Astrophysics* 649, A2.

Livingstone, M. A. et al. (2011a). "The Spin-down of Swift J1822. 3- 1606: A New Galactic Magnetar". In: *The Astrophysical Journal Letters* 743.2, p. L38.

Livingstone, M. A. et al. (Apr. 2011b). "Post-outburst Observations of the Magnetically Active Pulsar J1846-0258. A New Braking Index, Increased Timing Noise, and Radiative Recovery". In: *The Astrophysical Journal* 730.2, 66, p. 66. DOI: 10.1088/0004-637X/730/2/66. arXiv: 1007.2829 [astro-ph.HE].

Lorimer, D., A. Lyne, & F. Camilo (1998). "A search for pulsars in supernova remnants". In: *arXiv preprint astro-ph/9801096*.

Lorimer, D. R. (2008). "Binary and millisecond pulsars". In: *Living reviews in relativity* 11.1, p. 8.

Lower, M. E. et al. (2023). "The 2022 high-energy outburst and radio disappearing act of the magnetar 1e 1547.0–5408". In: *The Astrophysical Journal* 945.2, p. 153.

Lu, W., P. Beniamini, & P. Kumar (2022). "Implications of a rapidly varying FRB in a globular cluster of M81". In: *Monthly Notices of the Royal Astronomical Society* 510.2, pp. 1867–1879.

Lucas, P. et al. (2008). "The UKIDSS Galactic plane survey". In: *Monthly Notices of the Royal Astronomical Society* 391.1, pp. 136–163.

Lyman, J. et al. (2022). "The Fast Radio Burst-emitting Magnetar SGR 1935+2154—Proper Motion and Variability from Long-term Hubble Space Telescope Monitoring". In: *The Astrophysical Journal* 926.2, p. 121.

Lyne, A. et al. (2015). "The binary nature of PSR J2032+ 4127". In: *Monthly Notices of the Royal Astronomical Society* 451.1, pp. 581–587.

Malofeev, V. M. et al. (May 2005). "Discovery of radio emission from X-ray pulsar PSR J1852+0040". In: *The Astronomer's Telegram* 501, p. 1.

Maund, J. et al. (2016). “The possible detection of a binary companion to a Type Ibn supernova progenitor”. In: *The Astrophysical Journal* 833.2, p. 128.

Mazets, E. et al. (2008). “A giant flare from a soft gamma repeater in the Andromeda galaxy (M31)”. In: *The Astrophysical Journal* 680.1, p. 545.

McConnell, D. et al. (2020). “The Rapid ASKAP Continuum Survey I: design and first results”. In: *Publications of the Astronomical Society of Australia* 37, e048.

Mereghetti, S. et al. (2024). *A magnetar giant flare in the nearby starburst galaxy M82*. arXiv: 2312.14645 [astro-ph.HE].

Mereghetti, S. et al. (Oct. 2012). “The magnetar candidate AX J1818.8-1559”. In: *Astronomy & Astrophysics* 546, A30, A30. DOI: 10.1051/0004-6361/201219907. arXiv: 1208.0249 [astro-ph.HE].

Migliazzo, J. et al. (2002). “Proper-motion measurements of pulsar B1951+ 32 in the supernova remnant CTB 80”. In: *The Astrophysical Journal* 567.2, p. L141.

Miller, G. E. & J. M. Scalo (1979). “The initial mass function and stellar birthrate in the solar neighborhood”. In: *and JM Scalo. Astrophysical Journal Supplement Series, vol. 41, Nov. 1979, p. 513-547.* 41, pp. 513–547.

Minaev, P. Y. et al. (2024). *GRB 231115A – a magnetar giant flare in the M82 galaxy*. arXiv: 2402.08623 [astro-ph.HE].

Minter, A. H. et al. (Apr. 2008). “Neutral Hydrogen Absorption toward XTE J1810-197: The Distance to a Radio-emitting Magnetar”. In: *The Astrophysical Journal* 676.2, pp. 1189–1199. DOI: 10.1086/529005. arXiv: 0705.4403 [astro-ph].

Miyaji, S. et al. (1980). “Supernova triggered by electron captures”. In: *Publications of the Astronomical Society of Japan* 32.2, pp. 303–329.

Moe, M. & R. Di Stefano (2017). “Mind your Ps and Qs: the interrelation between period (P) and mass-ratio (Q) distributions of binary stars”. In: *The Astrophysical Journal Supplement Series* 230.2, p. 15.

Moisés, A. et al. (2011). “Spectrophotometric distances to Galactic H II regions”. In: *Monthly Notices of the Royal Astronomical Society* 411.2, pp. 705–760.

Mondal, T. (2021). “The life cycle of magnetars: A novel approach to estimate their ages”. In: *The Astrophysical Journal Letters* 913.1, p. L12.

Mori, K. et al. (June 2013a). “NuSTAR Discovery of a 3.76 s Transient Magnetar Near Sagittarius A*”. In: *The Astrophysical Journal Letters* 770.2, L23, p. L23. DOI: 10.1088/2041-8205/770/2/L23. arXiv: 1305.1945 [astro-ph.HE].

Mori, K. et al. (Apr. 2013b). “NuSTAR discovery of a 3.76 second pulsar in the Sgr A* region”. In: *The Astronomer’s Telegram* 5020, p. 1.

Morozova, V., A. L. Piro, & S. Valenti (2017). “Unifying type II supernova light curves with dense circumstellar material”. In: *The Astrophysical Journal* 838.1, p. 28.

Muno, M. P. et al. (Jan. 2006). "A Neutron Star with a Massive Progenitor in Westerlund 1". In: *The Astrophysical Journal Letters* 636.1, pp. L41–L44. DOI: 10.1086/499776. arXiv: astro-ph/0509408 [astro-ph].

Muno, M. et al. (2008). "A search for new Galactic magnetars in archival Chandra and XMM-Newton observations". In: *The Astrophysical Journal* 680.1, pp. 639–653.

Nakano, T. et al. (2015). "Suzaku studies of the supernova remnant CTB 109 hosting the magnetar 1E 2259+ 586". In: *Publications of the Astronomical Society of Japan* 67.1, p. 9.

Nakano, T. et al. (2017). "Study of the progenitor of the magnetar 1E 2259+ 586 through Suzaku observations of the associated supernova remnant CTB 109". In: *Publications of the Astronomical Society of Japan* 69.3, p. 40.

Nguyen, H. et al. (Oct. 2015). "The Three-mm Ultimate Mopra Milky Way Survey. II.Cloud and Star Formation near the Filamentary Ministarburst RCW 106". In: *The Astrophysical Journal* 812.1, 7, p. 7. DOI: 10.1088/0004-637X/812/1/7. arXiv: 1504.02246 [astro-ph.GA].

Nikzat, F. et al. (2022). "The VVV survey: Long-period variable stars-I. Photometric catalog of ten VVV/OGLE tiles". In: *Astronomy & Astrophysics* 660, A35.

Nomoto, K. (1987). "Evolution of 8-10 solar mass stars toward electron capture supernovae. II-Collapse of an O+ NE+ MG core". In: *Astrophysical Journal, Part 1 (ISSN 0004-637X), vol. 322, Nov. 1, 1987, p. 206-214.* 322, pp. 206–214.

Nomoto, K., K. Iwamoto, & T. Suzuki (1995). "The evolution and explosion of massive binary stars and Type Ib-Ic-IIb-IIL supernovae". In: *Physics Reports* 256.1-3, pp. 173–191.

Obergaulinger, M. et al. (Apr. 2009). "Semi-global simulations of the magneto-rotational instability in core collapse supernovae". In: *Astronomy & Astrophysics* 498.1, pp. 241–271. DOI: 10.1051/0004-6361/200811323. arXiv: 0811.1652 [astro-ph].

Obergaulinger, M., H.-T. Janka, & M. Á. Aloy (2014). "Magnetic field amplification and magnetically supported explosions of collapsing, non-rotating stellar cores". In: *Monthly Notices of the Royal Astronomical Society* 445.3, pp. 3169–3199.

Obergaulinger, M., O. Just, & M.-A. Aloy (2018). "Core collapse with magnetic fields and rotation". In: *Journal of Physics G: Nuclear and Particle Physics* 45.8, p. 084001.

Olausen, S. A. & V. M. Kaspi (May 2014). "The McGill Magnetar Catalog". In: *The Astrophysical Journal Supplement Series* 212.1, 6, p. 6. DOI: 10.1088/0067-0049/212/1/6. arXiv: 1309.4167 [astro-ph.HE].

Onken, C. A. et al. (2024). *SkyMapper Southern Survey: Data Release 4*. arXiv: 2402.02015 [astro-ph.CO].

Pagani, C., A. Beardmore, & J. Kennea (2011). “Swift J1822. 3-1606: Enhanced Swift-XRT position”. In: *The Astronomer’s Telegram* 3493, p. 1.

Park, S. et al. (2012). “An X-Ray Study of Supernova Remnant N49 and Soft Gamma-Ray Repeater 0526–66 in the Large Magellanic Cloud”. In: *The Astrophysical Journal* 748.2, p. 117.

Park, S. et al. (2020). “NuSTAR Detection of Quiescent Hard X-Ray Emission from SGR 0526–66 in the Large Magellanic Cloud”. In: *The Astrophysical Journal* 894.1, p. 17.

Petroff, E., J. Hessels, & D. Lorimer (2022). “Fast radio bursts at the dawn of the 2020s”. In: *The Astronomy and Astrophysics Review* 30.1, p. 2.

Pires, A. et al. (2009). “The isolated neutron star candidate 2XMM J104608. 7-594306”. In: *Astronomy & Astrophysics* 498.1, pp. 233–240.

Poelarends, A. J. et al. (2017). “Electron capture supernovae from close binary systems”. In: *The Astrophysical Journal* 850.2, p. 197.

Pons, J. A. & U. Geppert (2007). “Magnetic field dissipation in neutron star crusts: from magnetars to isolated neutron stars”. In: *Astronomy & Astrophysics* 470.1, pp. 303–315.

Ponti, G. et al. (2015). “The XMM–Newton view of the central degrees of the Milky Way”. In: *Monthly Notices of the Royal Astronomical Society* 453.1, pp. 172–213.

Popov, S. & M. Prokhorov (2006). “Progenitors with enhanced rotation and the origin of magnetars”. In: *Monthly Notices of the Royal Astronomical Society* 367.2, pp. 732–736.

Popov, S. B. (2020). “High magnetic field neutron stars and magnetars in binary systems”. In: *Proceedings of the International Astronomical Union* 16.S363, pp. 61–71.

Poveda, A., J. Ruiz, & C. Allen (Apr. 1967). “Run-away Stars as the Result of the Gravitational Collapse of Proto-stellar Clusters”. In: *Boletin de los Observatorios Tonantzintla y Tacubaya* 4, pp. 86–90.

Predehl, P. & J. H. Schmitt (1995). “X-raying the interstellar medium: ROSAT observations of dust scattering halos.” In: *Astronomy and Astrophysics, Vol. 293, p. 889-905 (1995)* 293, pp. 889–905.

Rajwade, K. et al. (2022). “Long term radio and X-ray evolution of the magnetar Swift J1818. 0-1607”. In: *Monthly Notices of the Royal Astronomical Society* 512.2, pp. 1687–1695.

Raynaud, R. et al. (2020). “Magnetar formation through a convective dynamo in protoneutron stars”. In: *Science Advances* 6.11, eaay2732.

Rea, N. et al. (Jan. 2014). “3XMM J185246.6+003317: Another Low Magnetic Field Magnetar”. In: *The Astrophysical Journal Letters* 781.1, L17, p. L17. DOI: 10.1088/2041-8205/781/1/L17. arXiv: 1311.3091 [astro-ph.GA].

Rea, N. et al. (2016). “Magnetar-like activity from the central compact object in the SNR RCW103”. In: *The Astrophysical Journal Letters* 828.1, p. L13.

Reich, W. et al. (1990). “A radio continuum survey of the Galactic Plane at 11 CM wavelength. II-The area L= 358-76 deg, B=-5 to 5 deg. III”. In: *Astronomy and Astrophysics Supplement Series (ISSN 0365-0138), vol. 85, no. 1, Oct. 1990, p. 633-690.* 85, pp. 633–690.

Renzo, M. et al. (2019). “Massive runaway and walkaway stars-A study of the kinematical imprints of the physical processes governing the evolution and explosion of their binary progenitors”. In: *Astronomy & Astrophysics* 624, A66.

Revnivtsev, M. & S. Mereghetti (2016). “Magnetic fields of neutron stars in X-ray binaries”. In: *The Strongest Magnetic Fields in the Universe*, pp. 299–320.

Richardson, N. D. et al. (2023). “A high-mass X-ray binary descended from an ultra-stripped supernova”. In: *Nature* 614.7946, pp. 45–47.

Roming, P. et al. (2008). “The first swift ultraviolet/optical telescope grb afterglow catalog”. In: *The Astrophysical Journal* 690.1, p. 163.

Ruiter, A. et al. (2019). “On the formation of neutron stars via accretion-induced collapse in binaries”. In: *Monthly Notices of the Royal Astronomical Society* 484.1, pp. 698–711.

Sakamoto, T. et al. (Apr. 2011). “Probing the nature of short swift bursts via deep INTEGRAL monitoring of GRB 050925”. In: *Advances in Space Research* 47.8, pp. 1346–1352. DOI: 10.1016/j.asr.2010.08.004. arXiv: 1008.0226 [astro-ph.HE].

Salpeter, E. E. (1955). “The luminosity function and stellar evolution.” In: *Astrophysical Journal, vol. 121, p. 161* 121, p. 161.

Sano, H. et al. (2023). “ALMA Observations of Supernova Remnant N49 in the Large Magellanic Cloud. II. Non-LTE Analysis of Shock-heated Molecular Clouds”. In: *The Astrophysical Journal* 958.1, p. 53.

Sathyaprakash, R. et al. (2024). *Long-term study of the 2020 magnetar-like outburst of the young pulsar PSRJ1846-0258 in Kes 75*. arXiv: 2401.08010 [astro-ph.HE].

Sato, T. et al. (June 2016). “Suzaku spectra of a Type-II supernova remnant, Kes 79”. In: *Publications of the Astronomical Society of Japan* 68, S8, S8. DOI: 10.1093/pasj/psv131. arXiv: 1512.04300 [astro-ph.HE].

Savage, B. D. & J. S. Mathis (1979). “Observed properties of interstellar dust”. In: *Annual review of astronomy and astrophysics* 17.1, pp. 73–111.

Sayers, S. L., P. J. Curran, & K. T. Mueser (1996). “Factor structure and construct validity of the Scale for the Assessment of Negative Symptoms.” In: *Psychological Assessment* 8.3, p. 269.

Schlafly, E. F. & D. P. Finkbeiner (2011). “Measuring reddening with Sloan Digital Sky Survey stellar spectra and recalibrating SFD”. In: *The Astrophysical Journal* 737.2, p. 103.

Schlafly, E. et al. (2015). “Three-dimensional Dust Mapping Reveals that Orion Forms Part of a Large Ring of Dust”. In: *The Astrophysical Journal* 799.2, p. 116.

Schneider, F. R. et al. (2019). “Stellar mergers as the origin of magnetic massive stars”. In: *Nature* 574.7777, pp. 211–214.

Schneider, F. et al. (2016). “Rejuvenation of stellar mergers and the origin of magnetic fields in massive stars”. In: *Monthly Notices of the Royal Astronomical Society* 457.3, pp. 2355–2365.

Scholz, P., V. Kaspi, & A. Cumming (2014). “THE LONG-TERM POST-OUTBURST SPIN DOWN AND FLUX RELAXATION OF MAGNETAR SWIFT J1822. 3-1606”. In: *The Astrophysical Journal* 786.1, p. 62.

Scholz, P. et al. (2017). “Spin-down evolution and radio disappearance of the magnetar PSR J1622–4950”. In: *The Astrophysical Journal* 841.2, p. 126.

Scholz, P. et al. (2012). “Post-outburst X-Ray Flux and Timing Evolution of Swift J1822.3-1606”. In: *The Astrophysical Journal* 761.1, 66, p. 66. DOI: 10.1088/0004-637X/761/1/66. arXiv: 1204.1034 [astro-ph.HE].

Schwope, A. et al. (1998). “The isolated neutron star candidate RBS1223 (1RXS J130848. 6+ 212708)”. In: *arXiv preprint astro-ph/9811326*.

Seaton, M. J. (Jan. 1979). “Interstellar extinction in the UV.” In: *Monthly Notices of the Royal Astronomical Society* 187, p. 73. DOI: 10.1093/mnras/187.1.73P.

Sedov, L. I. (1946). “Propagation of strong shock waves”. In: *Journal of Applied Mathematics and Mechanics* 10, pp. 241–250.

– (2018). *Similarity and dimensional methods in mechanics*. CRC press.

Seward, F. et al. (2003). “A Compact Central Object in the Supernova Remnant Kesteven 79”. In: *The Astrophysical Journal* 584.1, p. 414.

Shannon, R. M. & S. Johnston (Aug. 2013). “Radio properties of the magnetar near Sagittarius a* from observations with the australia telescope compact array.” In: *Monthly Notices of the Royal Astronomical Society* 435, pp. L29–L32. DOI: 10.1093/mnrasl/slt088. arXiv: 1305.3036 [astro-ph.HE].

Sharma, K. et al. (June 2023). “Deep Synoptic Array Science: A Massive Elliptical Host Among Two Galaxy-cluster Fast Radio Bursts”. In: *The Astrophysical Journal* 950.2, p. 175. DOI: 10.3847/1538-4357/accf1d. URL: https://dx.doi.org/10.3847/1538-4357/accf1d.

Shen, K. J. et al. (Sept. 2018). “Three Hypervelocity White Dwarfs in Gaia DR2: Evidence for Dynamically Driven Double-degenerate Double-detonation Type Ia Supernovae”. In: *The Astrophysical Journal* 865.1, 15, p. 15. DOI: 10.3847/1538-4357/aad55b. arXiv: 1804.11163 [astro-ph.SR].

Shenar, T. et al. (Aug. 2023). "A massive helium star with a sufficiently strong magnetic field to form a magnetar". In: *Science* 381.6659, pp. 761–765. ISSN: 1095-9203. DOI: 10.1126/science.ade3293. URL: http://dx.doi.org/10.1126/science.ade3293.

Shimwell, T. (2016). *LoTSS-PDR Image Archive*. URL: https://vo.astron.nl/lofartier1/q_img/imgs/info.

Shimwell, T. et al. (2022). "The LOFAR Two-metre Sky Survey-V. Second data release". In: *Astronomy & Astrophysics* 659, A1.

Simpson, R. J. et al. (Aug. 2012). "The Milky Way Project First Data Release: a bubblier Galactic disc". In: *Monthly Notices of the Royal Astronomical Society* 424.4, pp. 2442–2460. DOI: 10.1111/j.1365-2966.2012.20770.x. arXiv: 1201.6357 [astro-ph.GA].

Skrutskie, M. F. et al. (Feb. 2006). "The Two Micron All Sky Survey (2MASS)". In: *The Astronomical Journal* 131.2, pp. 1163–1183. DOI: 10.1086/498708.

Smith, L. et al. (2018). "VIRAC: the VVV Infrared Astrometric Catalogue". In: *Monthly Notices of the Royal Astronomical Society* 474.2, pp. 1826–1849.

Spangler, S. R., F. N. Owen, & R. Hulse (1977). "Radio survey of close binary stars". In: *Astronomical Journal, vol. 82, Dec. 1977, p. 989-997.* 82, pp. 989–997.

Sramek, R. A. et al. (Aug. 1992). "A VLA Search for Young Galactic Supernova Remnants". In: *The Astronomical Journal* 104, p. 704. DOI: 10.1086/116266.

Stairs, I. H. et al. (2001). "PSR J1740—3052: a pulsar with a massive companion". In: *Monthly Notices of the Royal Astronomical Society* 325.3, pp. 979–988.

Stamatikos, M. et al. (2020). "SGR Swift J1818. 0-1607: Swift-BAT refined analysis". In: *GRB Coordinates Network* 27384, p. 1.

Stetson, P. B. (July 2000). "Homogeneous Photometry for Star Clusters and Resolved Galaxies. II. Photometric Standard Stars". In: *Publications of the Astronomical Society of the Pacific* 112.773, pp. 925–931. DOI: 10.1086/316595. arXiv: astro-ph/0004144 [astro-ph].

Straal, S. M., J. D. Gelfand, & J. L. Eagle (Jan. 2023). "Discovery of GeV Gamma-Ray Emission from Pulsar Wind Nebula Kes 75 and PSR J1846-0258". In: *The Astrophysical Journal* 942.2, 103, p. 103. DOI: 10.3847/1538-4357/aca1a9. arXiv: 2211.08816 [astro-ph.HE].

Stupar, M. et al. (2007). "A statistical study of Galactic SNRs using the PMN survey". In: *Astrophysics and Space Science* 307, pp. 423–435.

Sun, M. et al. (Apr. 2004). "Chandra View of Kesteven 79: A Nearly Isothermal Supernova Remnant with Rich Spatial Structure". In: *The Astrophysical Journal* 605.2, pp. 742–750. DOI: 10.1086/382666. arXiv: astro-ph/0401165 [astro-ph].

Surnis, M. P. et al. (Apr. 2016). "Upper limits on the pulsed radio emission from SGR candidate SGR 0755-2933". In: *The Astronomer's Telegram* 8943, p. 1.

Suzuki, H., A. Bamba, & S. Shibata (2021). "Quantitative age estimation of supernova remnants and associated pulsars". In: *The Astrophysical Journal* 914.2, p. 103.

Svinkin, D. et al. (2021). "A bright γ-ray flare interpreted as a giant magnetar flare in NGC 253". In: *Nature* 589.7841, pp. 211–213.

Tam, C. R. et al. (Nov. 2006). "Chandra Observations of the Transient 7 s X-ray Pulsar AX J1845.0-0258". In: *The Astrophysical Journal* 652.1, pp. 548–553. DOI: 10.1086/507262. arXiv: astro-ph/0602522 [astro-ph].

Tan, C. M. et al. (Mar. 2020). "The LOFAR Tied-Array all-sky survey: Timing of 21 pulsars including the first binary pulsar discovered with LOFAR". In: *Monthly Notices of the Royal Astronomical Society* 492.4, pp. 5878–5896. DOI: 10.1093/mnras/staa113. arXiv: 2001.03866 [astro-ph.HE].

Taylor, G. I. (1950). "The formation of a blast wave by a very intense explosion I. Theoretical discussion". In: *Proceedings of the Royal Society of London. Series A. Mathematical and Physical Sciences* 201.1065, pp. 159–174.

Tendulkar, S. P., P. B. Cameron, & S. R. Kulkarni (2012). "PROPER MOTIONS AND ORIGINS OF SGR 1806- 20 AND SGR 1900+ 14". In: *The Astrophysical Journal* 761.1, p. 76.

– (2013). "Proper motions and origins of AXP 1E 2259+ 586 and AXP 4U 0142+ 61". In: *The Astrophysical Journal* 772.1, p. 31.

Tetzlaff, N., R. Neuhäuser, & M. Hohle (2010). "A catalogue of young runaway Hipparcos stars within 3 kpc from the Sun". In: *Monthly Notices of the Royal Astronomical Society* 410.1, pp. 190–200.

Tetzlaff, N. et al. (2011). "The origin of RX J1856. 5- 3754 and RX J0720. 4- 3125– updated using new parallax measurements". In: *Monthly Notices of the Royal Astronomical Society* 417.1, pp. 617–626.

Thielemann, F.-K., K. Nomoto, & M. Hashimoto (1996). *Core-collapse supernovae and their ejecta*.

Tian, W. W. & D. A. Leahy (Apr. 2008). "The Distance and Age of the Supernova Remnants Kes 73 and AXP 1E 1841-045". In: *The Astrophysical Journal* 677.1, pp. 292–296. DOI: 10.1086/529120. arXiv: 0709.4667 [astro-ph].

– (Apr. 2012). "Distances of the TeV supernova remnant complex CTB 37 towards the Galactic bar". In: *Monthly Notices of the Royal Astronomical Society* 421.3, pp. 2593–2597. DOI: 10.1111/j.1365-2966.2012.20491.x. arXiv: 1201.0731 [astro-ph.GA].

Tiengo, A. et al. (Feb. 2010). "The Dust-scattering X-ray Rings of the Anomalous X-ray Pulsar 1E 1547.0-5408". In: *The Astrophysical Journal* 710.1, pp. 227–235. DOI: 10.1088/0004-637X/710/1/227. arXiv: 0911.3064 [astro-ph.HE].

Tong, H. & L. Huang (2020). "Magnetar outburst and spin-down glitch". In: *Monthly Notices of the Royal Astronomical Society* 497.3, pp. 2680–2687.

Tonry, J. et al. (2012). "The Pan-STARRS1 photometric system". In: *The Astrophysical Journal* 750.2, p. 99.

Tonry, J. et al. (2018). "ATLAS: a high-cadence all-sky survey system". In: *Publications of the Astronomical Society of the Pacific* 130.988, p. 064505.

Torii, K. et al. (Aug. 1998). "Discovery of a 7 Second X-Ray Pulsar, AX J1845.0-0300". In: *The Astrophysical Journal* 503.2, pp. 843–847. DOI: 10.1086/306038.

Trigg, A. C. et al. (July 2024). "GRB 180128A: A second magnetar giant flare candidate from the Sculptor Galaxy". In: *Astronomy & Astrophysics* 687, A173, A173. DOI: 10.1051/0004-6361/202348858. arXiv: 2311.09362 [astro-ph.HE].

Truelove, J. K. & C. F. McKee (1999). "Evolution of nonradiative supernova remnants". In: *The Astrophysical Journal Supplement Series* 120.2, p. 299.

Turolla, R. (2009). "Isolated neutron stars: the challenge of simplicity". In: *Neutron stars and pulsars*. Springer, pp. 141–163.

Vallenari, A. et al. (2022). "Gaia Data Release 3: Summary of the content and survey properties". In: *arXiv preprint arXiv:2208.00211*.

van der Horst, A. J. et al. (Mar. 2010). "Discovery of a New Soft Gamma Repeater: SGR J0418 + 5729". In: *The Astrophysical Journal Letters* 711.1, pp. L1–L6. DOI: 10.1088/2041-8205/711/1/L1. arXiv: 0911.5544 [astro-ph.HE].

Vasisht, G. & E. V. Gotthelf (Sept. 1997). "The Discovery of an Anomalous X-Ray Pulsar in the Supernova Remnant Kes 73". In: *The Astrophysical Journal Letters* 486.2, pp. L129–L132. DOI: 10.1086/310843. arXiv: astro-ph/9706058 [astro-ph].

Velusamy, T., R. H. Becker, & F. D. Seward (Aug. 1991). "G33.6+0.1: A Shell Type Supernova Remnant With Unusual Structure". In: *The Astronomical Journal* 102, p. 676. DOI: 10.1086/115901.

Vincenty, T. (1975). "DIRECT AND INVERSE SOLUTIONS OF GEODESICS ON THE ELLIPSOID WITH APPLICATION OF NESTED EQUATIONS". In: *Survey Review* 23.176, pp. 88–93. DOI: 10.1179/sre.1975.23.176.88. eprint: https://doi.org/10.1179/sre.1975.23.176.88. URL: https://doi.org/10.1179/sre.1975.23.176.88.

Vrba, F. J. et al. (Apr. 2000). "The Discovery of an Embedded Cluster of High-Mass Stars near SGR 1900+14". In: *The Astrophysical Journal Letters* 533.1, pp. L17–L20. DOI: 10.1086/312602. arXiv: astro-ph/0002530 [astro-ph].

Wachter, S. et al. (Nov. 2004). "Precise Localization of the Soft Gamma Repeater SGR 1627-41 and the Anomalous X-Ray Pulsar AXP 1E1841-045 with Chandra". In: *The Astrophysical Journal* 615.2, pp. 887–896. DOI: 10.1086/424704. arXiv: astro-ph/0408266 [astro-ph].

Wang, Z. & D. Chakrabarty (Nov. 2002). "The Likely Near-Infrared Counterpart to the Anomalous X-Ray Pulsar 1E 1048.1-5937". In: *The Astrophysical Journal Letters* 579.1, pp. L33–L36. DOI: 10.1086/345077. arXiv: astro-ph/0207540 [astro-ph].

Wateren, E. van der et al. (2023). *PSR J0210+5845; An ultra wide binary pulsar with a B6V main-sequence star companion*. arXiv: 2312.01892 [astro-ph.HE].

Weidner, C. & P. Kroupa (2005). "The variation of integrated star initial mass functions among galaxies". In: *The Astrophysical Journal* 625.2, p. 754.

White, C. J. et al. (2022). "On the origin of pulsar and magnetar magnetic fields". In: *The Astrophysical Journal* 926.2, p. 111.

Whiteoak, J. & A. Green (1996). "The MOST supernova remnant catalogue (MSC)". In: *Astronomy and Astrophysics Supplement Series* 118.2, pp. 329–380.

Wolf, C. et al. (2018). "SkyMapper southern survey: First data release (DR1)". In: *Publications of the Astronomical Society of Australia* 35, e010.

Woodland, M. N. et al. (2023). "The Environments of Fast Radio Bursts Viewed Using Adaptive Optics". In: *arXiv preprint arXiv:2312.01578*.

Yalinewich, A., T. Piran, & R. Sari (2017). "Evolution of Supernova Remnants Near the Galactic Center". In: *The Astrophysical Journal* 838.1, p. 12.

Yao, J., R. Manchester, & N. Wang (2017). "A new electron-density model for estimation of pulsar and FRB distances". In: *The Astrophysical Journal* 835.1, p. 29.

Yeung, P. K. H. et al. (Aug. 2016). "Studying the SGR 1806-20/Cl* 1806-20 Region Using the Fermi Large Area Telescope". In: *The Astrophysical Journal* 827.1, 41, p. 41. DOI: 10.3847/0004-637X/827/1/41. arXiv: 1606.01707 [astro-ph.HE].

Younes, G. et al. (2023). "Magnetar spin-down glitch clearing the way for FRB-like bursts and a pulsed radio episode". In: *Nature Astronomy* 7.3, pp. 339–350.

Zacharias, N. et al. (2005). "VizieR Online Data Catalog: NOMAD Catalog (Zacharias+ 2005)". In: *VizieR Online Data Catalog*, pp. I–297.

Zacharias, N. et al. (2004). "The second US Naval Observatory CCD astrograph catalog (UCAC2)". In: *The Astronomical Journal* 127.5, p. 3043.

Zapartas, E. et al. (2017). "Delay-time distribution of core-collapse supernovae with late events resulting from binary interaction". In: *Astronomy & Astrophysics* 601, A29.

Zhong, S.-Q. et al. (2020). “On the Distance of SGR 1935+ 2154 Associated with FRB 200428 and Hosted in SNR G57. 2+ 0.8”. In: *The Astrophysical Journal Letters* 898.1, p. L5.

Zhou, P. et al. (Jan. 2014). “Discovery of the Transient Magnetar 3XMM J185246.6+003317 near Supernova Remnant Kesteven 79 with XMM-Newton”. In: *The Astrophysical Journal Letters* 781.1, L16, p. L16. DOI: 10.1088/2041-8205/781/1/L16. arXiv: 1310.7705 [astro-ph.HE].

Zhou, P. et al. (Nov. 2016). “Multi-wavelength Study of the Supernova Remnant Kes 79 (G33.6+0.1): On Its Supernova Properties and Expansion into a Molecular Environment”. In: *The Astrophysical Journal* 831.2, 192, p. 192. DOI: 10.3847/0004-637X/831/2/192. arXiv: 1612.03476 [astro-ph.HE].

Zhou, P. et al. (2019). “Spatially resolved X-ray study of supernova remnants that host magnetars: Implication of their fossil field origin”. In: *Astronomy & Astrophysics* 629, A51.

Zhou, P. et al. (2020). “Revisiting the distance, environment, and supernova properties of snr g57. 2+ 0.8 that hosts sgr 1935+ 2154”. In: *The Astrophysical Journal* 905.2, p. 99.

Chapter 3

MAGNETAR POPULATION SYNTHESIS UNDER THE STELLAR MERGER FORMATION HYPOTHESIS

3.1 Introduction

In Chapter 2 (Sherman et al., 2024), we concluded that the dearth of magnetars in binary systems or with ejected binary companions, given that $84 \pm 9\%$ of massive OB stars should start in binary or higher order systems (Moe & Di Stefano, 2017), could imply that magnetars preferentially form from isolated stars that result from binary mergers. This argument is purely statistical and based on observational completeness limits which may be superseded by future surveys. For example, the MeerKAT 1.3 GHz survey of the Small Magellanic Cloud (SMC) recently identified a new supernova remnant (SNR) associated with the SMC magnetar CXOU J010043.1-721134 which was not visible in the archival radio image data searched in Sherman et al. (2024). Upcoming telescopes such as the DSA-2000 and the Vera Rubin Observatory will have high sensitivities and near-realtime public access to image and point source datasets. In addition, the stability of stellar magnetic fields and their behavior under core-collapse are not well understood. Magneto-hydrodynamic (MHD) simulations from Schneider et al. (2019) have demonstrated amplification of the magnetic field through the merger process while Keszthelyi et al. (2021) use atmospheric modelling to reconstruct the magnetic star $\tau-$Sco's (which may be a merger product) magnetic field. However, the stability of stellar magnetic fields after merger are still uncertain, and core-collapse supernova models have not been developed to model the field through core-collapse, making it difficult to link a merger-amplified field to the neutron star remnant's field (R.-Y. Hu & Lou, 2009; Keszthelyi, 2023, and references therein).

Nonetheless, additional evidence supporting the magnetar-merger hypothesis has been presented by population synthesis simulations. Zapartas et al. (2017) used population synthesis to construct a core-collapse supernova (CCSN) delay-time distribution, identifying that $15^{+9}_{-8}\%$ occur at late times ($50-200$ Myr) after intermediate-mass stars ($4-8\,M_{\odot}$) interact with binary companions. Most of these late-time CCSNe (87%) result from binary mergers, while the remainder experience significant mass transfer without coalescence.

R.-C. Hu & Zhang (2026) also conduct a detailed population synthesis simulation to determine the frequency of single- and binary- star magnetar formation channels. They find that $\sim$ 57% of magnetars should form from disrupted binary systems while 19% form from stars that have merged before core-collapse. These more closely match the simulation-based and statistical predictions of Renzo et al. (2019), Kochanek et al. (2019), and Chrimes et al. (2022) than the observational constraints placed in Sherman et al. (2024). The discrepancy reflects the fact that the magnetar-merger hypothesis lacks convincing physical motivation, and is not naturally predicted by the most up-to-date models of stellar evolution.

The magnetar-merger formation scenario would alter, but not resolve, the birth-rate problem presented by Keane & Kramer (2008): the combined neutron star birth rate $\sim$ 11 per century exceeds the CCSNe rate $\sim$ 2 per century. To update this with more recent analyses, we use Rozwadowska et al. (2021) which combines constraints from massive star counts, observed CCSN, neutron star counts, and ^{26}Al enrichment to estimate a CCSN rate of $1.63 \pm 0.46\,\mathrm{century}^{-1}$. Sautron et al. (2024) then estimate a pulsar birth rate of $2.4\,\mathrm{century}^{-1}$ and Sautron et al. (2025) estimate a magnetar birth rate of $0.18^{+0.26}_{-0.06}\,\mathrm{century}^{-1}$ using simulation-based inference (see also Pardo-Araujo et al., 2026). Agarwal et al. (2026) recently updated the census of Rotating RAdio Transients (RRATs), estimating a reduced upper limit on the birth rate of $\lesssim 1.4\,\mathrm{century}^{-1}$. Using the X-ray Dim Isolated Neutron Star (XDINSs; $2.1 \pm 1.0\,\mathrm{century}^{-1}$) birth rates from Keane & Kramer (2008), the total neutron star birth rate is $4.7 - 6.1 \pm 1.0\,\mathrm{century}^{-1}$; even as an upper limit, this far exceeds the CCSN rate. Limiting magnetar formation to CCSNe from stellar mergers may lower their formation rate, but the total neutron star rate would still significantly exceed the CCSNe rate. However, confirming the magnetar-merger hypothesis could indicate that other neutron star species have similar selections on their progenitors, which would vary the birth rate more substantially.

In this chapter, we use population synthesis to estimate the Galactic magnetar population under the magnetar-merger progenitor hypothesis. In Section 3.2 we describe the Binary Population And Stellar Synthesis (BPASS) models and simulation procedure. Section 3.3 offers the resulting magnetar populations under four progenitor cases. Section 3.4 compares our results to the observed sample and previous population synthesis work, and extends the procedure to nearby galaxies. We conclude in Section 3.5 and offer guidance for future targeted surveys for magnetar-related transients in nearby galaxies.

3.2 Methods

3.2.1 Milky Way and BPASS Models

We utilize the Milky Way star formation history (SFH) from Mor et al. (2019), which estimates a present-day star formation rate of $\mathrm{SFR}_0 \sim 1 M_\odot\,\mathrm{yr}^{-1}$ using *Gaia* Data Release 2 (G. Collaboration, 2018). We convert the tabulated surface mass densities ($\Sigma\ [M_\odot\,\mathrm{pc}^{-2}]$) from Mor et al. (2019) to total star formation rate by assuming a disk radius $R_0 \approx 12\,\mathrm{kpc}$ at which the neutral Hydrogen gas mass exponentially declines (McMillan, 2016) time bins $0.1\,\mathrm{Gyr} \leq \Delta T \leq 1\,\mathrm{Gyr}$:

$$\mathrm{SFR}(T_i) = \frac{\Sigma \pi R_0^2}{\Delta T_i} \tag{3.1}$$

for bin number i. We adopt the Iron abundance [Fe/H] evolution history reconstructed in Snaith et al. (2015), linearly interpolating to each time bin and estimating the Milky Way metallicity as $Z_{\mathrm{MW}}(T_i) = Z_\odot 10^{[\mathrm{Fe/H}](T_i)}$.

To generate a stellar population, we use the Binary Population And Stellar Synthesis (BPASS, version 2.2) library of stellar models (Stanway & J. J. Eldridge, 2018), accessing it with the `hoki`[1] Python module and Evolution Explorer (EvE[2]; Stevance & Briel, 2022) database of stellar evolution tables compiled from BPASS's evolutionary model tracks. For each time bin, we query the EvE table for stellar models with Zero-Age Main Sequence (ZAMS) metallicity equal to the Milky Way value $Z_{\mathrm{MW}}(T_i)$. Selecting the subset that meet the magnetar formation criteria (discussed later in this section) we then obtain the primary and (if applicable) secondary ZAMS ($M_{1,\mathrm{ZAMS}}$, $M_{2,\mathrm{ZAMS}}$) and final (M_1, M_2) masses, as well as the total age τ_* of the system.

The `modelimf` and `mixedimf` (f_{model} and f_{mixed}) columns indicate, for each model, the number of such systems that will arise in a $10^6 M_\odot$ population at the ZAMS metallicity without and with feedback from prior stellar systems, respectively. We use these to compute the total number of systems within each time bin i as:

$$N_{\mathrm{sys}}(T_i) \approx \frac{\mathrm{SFR}(T_i)\Delta T_i}{10^6 M_\odot}\left(f_{\mathrm{model}}(T_i) + f_{\mathrm{mixed}}(T_i)\right) \tag{3.2}$$

Finally, we conduct a Monte Carlo simulation, sampling the time at which each system forms T_{start} from a uniform distribution within each time bin, and the time

[1] `https://heloises.github.io/hoki/intro.html`
[2] `https://doi.org/10.5281/zenodo.7341382`

for which the resulting magnetar is active $\tau_{\rm active}$ from a uniform distribution between $1-100\,$kyr. In addition, the current year, $T_{\rm obs}$, is sampled between the first magnetar discovery year (1979; Hewish et al., 1979; Mazets et al., 1979a,b) and present-day at time of writing (2026) to determine the likelihood that this range overlaps with the magnetar's lifetime. For each magnetar-terminated model, we determine the fraction of samples for which the magnetar is 'active' at $T_{\rm obs}$, i.e., that $T_{\rm age} + T_{\rm obs}$ (where $T_{\rm age} = 13.6\,$Gyr is the Milky Way age) is within the inclusive interval $[T_{\rm start} + \tau_*, T_{\rm start} + \tau_* + \tau_{\rm active}]$. This fraction, $f_{\rm active}$, is multiplied by $N_{\rm sys}(T_i)$ to obtain the number of magnetars produced by a given stellar model $N_{\rm mag,vis}$. We use 100 samples for each model and repeat the simulation 1,000 times for each criteria of the four criteria sets described later in this section.

3.2.2 Beaming Fraction Estimate

To account for magnetar emission's beaming, which may be directed away from our line-of-sight, we assume the emission's intensity follows a Hopf function with fourth approximation as discussed in Appendix C of C.-P. Hu et al. (2019), multiplying by $\cos\theta$ to account for foreshortening of the emission area. The Hopf function, shown in Figure 3.1, includes bending of light due to the neutron star's gravitational pull at large viewing angles, allowing a wide 205° visibility range. We conservatively assume that bursts within the $10^{\rm th}$ percentile of intensity will be detectable, which limits the visible range to 41°, or $f_{\rm beam} = 20\%$ of the full Hopf range. We multiply the magnetar population count by this fraction to determine the final number of visible active magnetars in each model.

3.2.3 Magnetar Formation Criteria

The conditions for CCSNe to occur and for neutron stars to form (as opposed to black holes) are still being actively explored[3] (e.g., Chrimes et al., 2022; J. Eldridge et al., 2017; J. J. Eldridge et al., 2008; J. J. Eldridge & Stanway, 2009; J. J. Eldridge & Tout, 2004; Fryer et al., 2012; Heger et al., 2003; Renzo et al., 2019; Stanway & J. J. Eldridge, 2018, and references therein). Here, we adopt conditions from Renzo et al. (2019), Chrimes et al. (2022), and J. Eldridge et al. (2017) to determine whether a CCSNe will produce a neutron star remnant:

1. The ZAMS mass of the primary (or sum of primary and secondary for a merger) is between $7.5-100 M_\odot$ (e.g., Renzo et al., 2019).

[3] J. J. Eldridge & Tout (2004) in fact described the determination of CCSN remnants as a "black art" given its poorly understood physics.

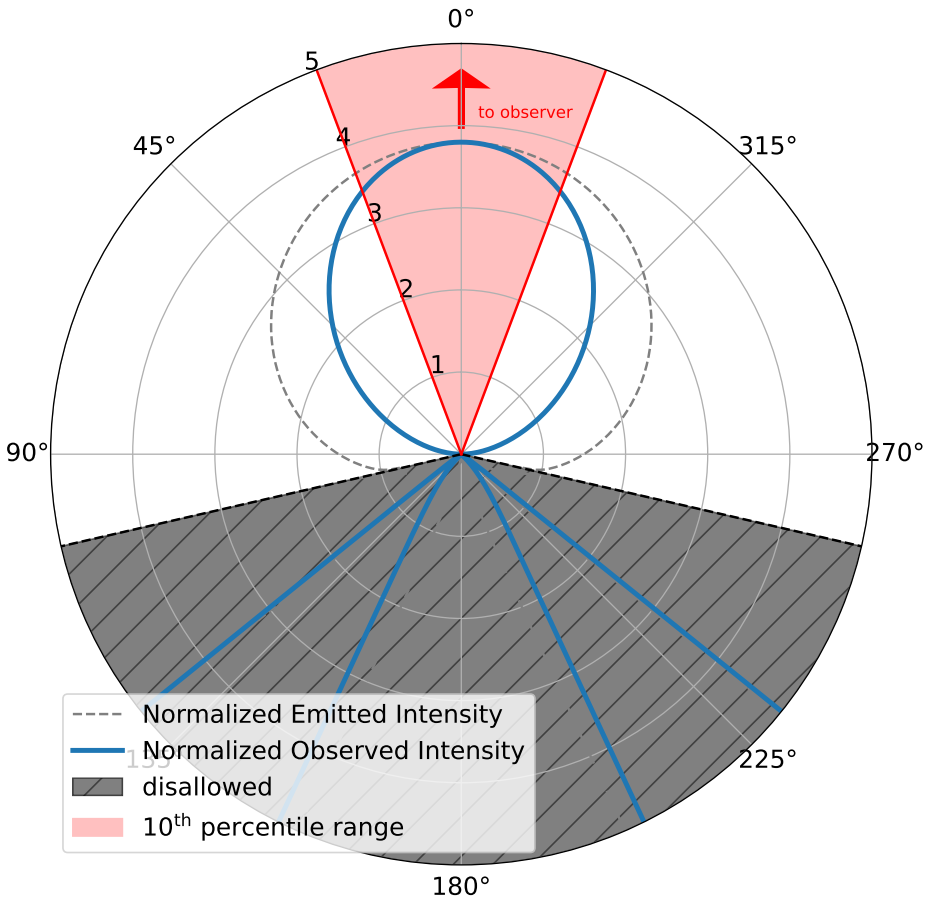

Figure 3.1: Hopf Function Beaming Model Centered on the Magnetar. The emitted intensity profile is shown as a grey dashed line while the foreshortened observed intensity profile is in blue. The angular range within which bursts will be in the 10^{th} percentile of intensity is shaded red, with the arrow indicating the observer's direction for peak intensity. The black shaded region highlights disallowed beaming directions for an emission area at 0°.

2. The final mass (obtained from the EvE `DEATH` table) of the primary (or sum of primary and secondary for a merger) is above $2M_{\odot}$ (Chrimes et al., 2022; J. Eldridge et al., 2017).

3. The final Carbon-Oxygen (CO) core mass exceeds $1.38M_{\odot}$ (Chrimes et al., 2022).

4. The final Oxygen-Neon (ONe) core mass is non-zero (Chrimes et al., 2022).

5. The final remnant mass is between $1.38 - 3M_{\odot}$ (Chrimes et al., 2022; J. Eldridge et al., 2017)

However, we acknowledge that the criteria above are oversimplified and incomplete; for example, Heger et al. (2003) and Poelarends et al. (2008) note that low-metallicity massive stars may have a tighter upper limit mass for neutron star formation than high-metallicity stars. We use the criteria above for consistency with recent population synthesis analyses (e.g., Chrimes et al., 2022; Renzo et al., 2019).

We then explore four possible magnetar progenitor scenarios to test the merger hypothesis:

1. Magnetars form from CCSNe of stellar mergers.
2. Magnetars form from CCSNe of mass-transfer binaries or stellar mergers.
3. Magnetars form from CCSNe of mass-transfer binaries, stellar mergers, or single stars.
4. Magnetars form from CCSNe of stellar mergers or single stars.

In each case, we select models from the EvE `SUMMARY` tables with the corresponding `type` parameter: 0 for mergers, -1 for single stars, and 1-3 for binaries.

3.3 Results

For each progenitor case in Section 3.2.3, the 90% confidence intervals for total active Milky Way magnetars and visible active Milky Way magnetars are reported in Table 3.1. The width of the confidence intervals most strongly depend on the magnetar age range ($1 - 100$ kyr) but also relate to uncertainties in the star formation history, metallicity, and time bins. We assess each model's likelihood based on the current sample of 26 confirmed magnetars and 30 candidate magnetars (see Chapter 1). If we include the candidates and assume the model likelihood is the number of samples with $26 \leq N_{\mathrm{mag,vis}} \leq 57$, then Case 2 (Mergers and Mass-Transfer Binaries) is preferred, with a $\sim 49\%$ probability. If we do not include candidates and assume the model likelihood is the number of samples with $26 \leq N_{\mathrm{mag,vis}}$, then Case 3 (Mergers, Binaries, and Single Stars) is preferred, with a $\sim 94\%$ probability. Case 1 (Mergers) and Case 4 (Mergers and Single Stars) predict far fewer magnetars than have been confirmed today. While we do not simulate the case in which only single stars form magnetars, Case 4's disagreement suggests that single stars alone could not reproduce the present-day magnetar population.

Table 3.1: Results of BPASS Monte Carlo Magnetar Generation

Progenitor	**(1) Mergers**	**(2) Mergers & Mass-Transfer Binaries**	**(3) Mergers, Single Stars, & Mass-Transfer Binaries**	**(4) Mergers & Single Stars**
Total	13 – 39	46 – 279	66 – 592	19 – 124
Visible	5 – 14	17 – 100	24 – 213	7 – 45
Likelihood (w/out Candidates; $26 \leq N_{\mathbf{mag,vis}} \leq 57$**)**	1%	49%	20%	24%
Likelihood (w/ Candidates; $N_{\mathbf{mag,vis}} \geq 26$**)**	1%	84%	94%	26%

3.4 Discussion

3.4.1 Implications for the Magnetar-Merger Hypothesis

Our results demonstrate that stellar mergers alone are unlikely to be responsible for the observed present-day magnetar population. Single stars contribute only a small fraction of magnetars in Cases 3 and 4, while mass-transfer binaries, in conjunction with mergers and, optionally, single stars, can reproduce the observed population of 26 magnetars and 30 candidates. Subtracting the samples in cases 2 and 1, we estimate that binaries alone produce $\sim 7 - 90$ visible magnetars with likelihood $\sim 70\%$; thus cases 2 and 3 still yield better fits. We conclude that while magnetars cannot form solely from mergers, but mergers contribute non-negligibly to the magnetar population.

Notably, in case 3 we see that roughly $50 - 70\%$ of the magnetars form from mergers or mass-transfer binaries, which exceeds the $\sim 15\%$ estimate from Zapartas et al. (2017) for all CCSNe. Thus, rather than forming from mergers, magnetars may preferentially form from the delayed Zapartas et al. (2017) CCSN channels, which include common-envelope evolution and stellar mergers. This could still generate a dearth of magnetars with binary or runaway companions, e.g., if significant mass transfer prior to CCSN leaves a much lighter white dwarf companion, it can be kicked at a higher velocity than was assumed for massive runaway stars in Sherman et al. (2024). Sherman et al. (2024) also did not search for white dwarf companions, which would harbor a unique spectrum excluded by magnitude cuts on the *Gaia* sample.

3.4.2 Comparison to Galactic Population Predictions

While we compared the simulated visible sample to the number of confirmed magnetars, we can also compare to past predictions from population synthesis. Gill &

Heyl (2007) used population synthesis with a small sample of 11 confirmed magnetars to predict only 15 – 17 visible magnetars are in the Milky Way; adopting our $f_{\rm beam} = 20\%$ implies 70 – 80 total magnetars. This offers $< 10\%$ likelihoods for each case (Case 4 is highest with 7.7%), demonstrating the impact of their limited sample size. Muno et al. (2008) apply non-detection limits from an archival search of *Chandra* and *XMM-Newton* to estimate 59^{+92}_{-32} total Galactic magnetars; this also most closely matches Case 4 (mergers and single stars). Ferrario & Wickramasinghe (2006) predict that 26 active, visible magnetars are detectable by *ROSAT* using population synthesis, yielding the $N_{\rm mag,vis} \geq 26$ likelihoods in Table 3.1 which prefer Case 3.

Other analyses predict the magnetar birth rate; Keane & Kramer (2008) estimate a $0.3^{+1.2}_{-0.2}\,{\rm century}^{-1}$ magnetars are born. For ages 1 – 100 kyr, this yields a wide range of $\sim 3 - 300$ total magnetars for which Cases 1, 2, and 4 are feasible with $\geq 90\%$ likelihoods. Case 3 is least-preferred with a $\sim 60\%$ probability, but the range in general is too wide for conclusions to be drawn. Beniamini et al. (2019) similarly predicts a wide range $0.23 - 2\,{\rm century}^{-1}$, directly from observations, or 2 – 2000 total magnetars. Most recently, Sautron et al. (2025) predict $0.18^{+0.26}_{-0.06}\,{\rm century}^{-1}$ through population synthesis, or $\sim 2 - 180$ total magnetars. This estimate prefers Case 1 (mergers) or Case 4 (mergers and single stars) with over 90% likelihoods.

The fact that the two best-constrained estimates, from Gill & Heyl (2007) and Muno et al. (2008), prefer Case 4 while the observed population prefers Case 2 or 3 is difficult to interpret. The observed magnetar population is a more reliable constraint, but it is also biased by telescope selection effects which may limit the total observing time, field-of-view, and sensitivity. Alternatively, the chosen beaming model may overestimate the beaming fraction, which could bring the Case 2 and 3 magnetar counts into the Gill & Heyl (2007) or Muno et al. (2008) ranges. While out-of-scope for this work, a more rigorous treatment of observational bias may lead to more robust constraints. Here, we continue to assume Cases 2 and 3 are preferred, while past models' preference for Case 4 likely results from their neglect of mergers and binary evolution channels and broad uncertainties in magnetar ages and birth rates.

3.4.3 Predictions for Magnetars and FRBs in Nearby Galaxies

Our predictions rely only on the Milky Way's metallicity and star formation history; therefore, we can estimate the number of magnetars in any galaxy for which these

parameters are known. The lifetimes of each stellar model prior to core-collapse range from $\sim 3 - 200$ Myr, and thus magnetars formed over 1 Gyr ago will not be active at present day. The present-day magnetar population in a given galaxy can therefore be predicted using only the present-day star formation rate and metallicity.

This can offer insight into the Fast Radio Burst (FRBs), bright, extragalactic bursts of millisecond-duration thought to originate from magnetars (e.g., Petroff et al., 2019). While $\sim 5,000$ FRBs have been detected to date (C. Collaboration et al., 2026), targeted radio surveys of nearby galaxies have been unsuccessful. CHIME/FRB Collaboration et al. (2020) observed 15 galaxies for $\sim 20 - 100$ hours, each, identifying no FRBs and placing an upper limit $\sim 0.4\,\mathrm{yr}^{-1}$ for bursts with energy $> 10^{34}$ erg. Pelliciari et al. (2023) used the Northern Cross Radio Telescope to observe 12 nearby (< 12 Mpc) galaxies, detecting one background FRB in the direction of M101, but no confident FRBs from their target galaxies. Both efforts used low frequency observations ($400 - 600$ MHz) where the FRB rate is higher, but scattering can significantly lower the signal-to-noise ratio. Higher frequency surveys attempted to mitigate these scattering effects by leveraging the ν^{-4} frequency dependence (Cordes et al., 1986). Despite this, Agarwal et al. (2019) identified no FRBs in 300 hours of L-band (1.4 GHz) observations of the Virgo galaxy cluster[4], and Wharton et al. (2025) detect no FRBs in ~ 100 hours of 8.4 GHz observations of M82 and M77. Each search targeted star-forming galaxies, where one expects magnetars to reside given their low ages (see Chapter 4).

Here we estimate the magnetar population in M82, using the star formation history from Schreiber et al. (2003) and the metal abundances from Origlia et al. (2004). Four time bins span lookback times from $0-34$ Myr, with starbursts of $\sim 1.2 M_\odot\,\mathrm{yr}^{-1}$ and $\sim 6.6 M_\odot\,\mathrm{yr}^{-1}$ at 5 and 10 Myr lookback times, respectively. We assume a constant metallicity $Z_{\mathrm{M82}} \approx 0.007$ since no detailed metallicity history is available for M82. Running the simulation in all four cases, we observe similar relative magnetar counts as for the Milky Way. For Case 3 (mergers, mass-transfer binaries, and single stars) we obtain the highest count, estimating that between $40 - 100$ total magnetars are within M82 with 90% confidence. Noting that only one of the 26 confirmed Galactic magnetars have produced an FRB-like burst (SGR J1935+2154) we expect only $\sim 1 - 4$ FRBs to be produced from M82. This indicates that the non-detection of FRBs by CHIME/FRB Collaboration et al. (2020) and Wharton et al. (2025) may result from the starburst history of M82. Most magnetar progenitors

[4]One candidate is identified, but was concluded to come from a background galaxy, not the Virgo cluster.

formed within the most recent starburst event, $\sim 5\,\mathrm{Myr}$ ago, and their remnants decayed past the death line well before present-day. Future targeted FRB surveys should not only focus on nearby starforming galaxies, but also account for the epoch of peak star formation to identify the most viable target galaxies.

3.5 Conclusion

In this chapter, we used BPASS stellar evolution models to investigate the magnetar-merger hypothesis. Our simulations demonstrate that while mergers and isolated stars cannot fully explain the observed magnetar population, only a subset of binaries must be included to do so. This may indicate that CCSNe in mass-transfer or common-envelope binaries can also lead to magnetars. We estimate that $\sim 70-600$ total magnetars are in the Milky Way, $\sim 50-280$ of which are from mergers and mass-transfer binaries, and 20% of which are beamed towards us. The $1-100\,\mathrm{kyr}$ age range is too broad to estimate a constraining birth rate, but if we naively assume magnetar SNR ages, $\sim 5\,\mathrm{kyr}$, we obtain $\sim 1-12\,\mathrm{century}^{-1}$, marginally higher than recent estimates by Sautron et al. (2025). Extending this population synthesis to the starburst galaxy M82, we finding that $\lesssim 100$ magnetars reside there, $\lesssim 4$ of which may produce FRBs. This may explain the lack of FRB detections from M82 in targeted surveys, and future efforts should consider galaxies with more recent startbursts or uniform star formation histories to maximize FRB detection probabilities.

CHAPTER 3 BIBLIOGRAPHY

Agarwal, D. et al. (2019). "A fast radio burst in the direction of the Virgo Cluster". In: *Monthly Notices of the Royal Astronomical Society* 490.1, pp. 1–8.

Agarwal, D. et al. (2026). "The RRATalog: a Galactic census of rotating radio transients". In: *Monthly Notices of the Royal Astronomical Society*, stag787.

Beniamini, P. et al. (2019). "Formation rates and evolution histories of magnetars". In: *Monthly Notices of the Royal Astronomical Society* 487.1, pp. 1426–1438.

CHIME/FRB Collaboration et al. (Nov. 2020). "A bright millisecond-duration radio burst from a Galactic magnetar". In: *Nature* 587.7832, pp. 54–58. DOI: 10.1038/s41586-020-2863-y. arXiv: 2005.10324 [astro-ph.HE].

Chrimes, A. et al. (2022). "Where are the magnetar binary companions? Candidates from a comparison with binary population synthesis predictions". In: *Monthly Notices of the Royal Astronomical Society* 513.3, pp. 3550–3563.

Collaboration, C. et al. (2026). "The Second CHIME/FRB Catalog of Fast Radio Bursts". In: *The Astrophysical Journal Supplement Series* 283.1, p. 34.

Collaboration, G. (2018). "VizieR online data catalog: Gaia DR2 (gaia collaboration, 2018)". In: *VizieR Online Data Catalog* 1345, pp. I–345.

Cordes, J., A. Pidwerbetsky, & R. Lovelace (1986). "Refractive and diffractive scattering in the interstellar medium". In: *Astrophysical Journal, Part 1 (ISSN 0004-637X), vol. 310, Nov. 15, 1986, p. 737-767. Research supported by the Alfred P. Sloan Foundation and Cornell University.* 310, pp. 737–767.

Eldridge, J. et al. (2017). "Binary population and spectral synthesis version 2.1: construction, observational verification, and new results". In: *Publications of the Astronomical Society of Australia* 34, e058.

Eldridge, J. J., R. G. Izzard, & C. A. Tout (2008). "The effect of massive binaries on stellar populations and supernova progenitors". In: *Monthly Notices of the Royal Astronomical Society* 384.3, pp. 1109–1118.

Eldridge, J. J. & E. R. Stanway (2009). "Spectral population synthesis including massive binaries". In: *Monthly Notices of the Royal Astronomical Society* 400.2, pp. 1019–1028.

Eldridge, J. J. & C. Tout (2004). "The progenitors of core-collapse supernovae". In: *Monthly Notices of the Royal Astronomical Society* 353.1, pp. 87–97.

Ferrario, L. & D. Wickramasinghe (2006). "Modelling of isolated radio pulsars and magnetars on the fossil field hypothesis". In: *Monthly Notices of the Royal Astronomical Society* 367.3, pp. 1323–1328.

Fryer, C. L. et al. (2012). "Compact remnant mass function: dependence on the explosion mechanism and metallicity". In: *The Astrophysical Journal* 749.1, p. 91.

Gill, R. & J. Heyl (2007). “The birthrate of magnetars”. In: *Monthly Notices of the Royal Astronomical Society* 381.1, pp. 52–58.

Heger, A. et al. (2003). “How massive single stars end their life”. In: *The Astrophysical Journal* 591.1, pp. 288–300.

Hewish, A. et al. (1979). “Observation of a rapidly pulsating radio source”. In: *A Source Book in Astronomy and Astrophysics, 1900–1975*. Harvard University Press, pp. 498–504.

Hu, C.-P., C. Ng, & W. C. Ho (2019). “A systematic study of soft X-ray pulse profiles of magnetars in quiescence”. In: *Monthly Notices of the Royal Astronomical Society* 485.3, pp. 4274–4286.

Hu, R.-Y. & Y.-Q. Lou (2009). “Magnetized massive stars as magnetar progenitors”. In: *Monthly Notices of the Royal Astronomical Society* 396.2, pp. 878–886.

Hu, R.-C. & B. Zhang (2026). “Formation Channels of Magnetars”. In: *The Astrophysical Journal* 999.1, p. 102.

Keane, E. F. & M. Kramer (2008). “On the birthrates of Galactic neutron stars”. In: *Monthly Notices of the Royal Astronomical Society* 391.4, pp. 2009–2016.

Keszthelyi, Z. et al. (June 2021). “The effects of surface fossil magnetic fields on massive star evolution - III. The case of τ Sco”. In: *Monthly Notices of the Royal Astronomical Society* 504.2, pp. 2474–2492. DOI: 10.1093/mnras/stab893. arXiv: 2103.13465 [astro-ph.SR].

Keszthelyi, Z. (2023). “Magnetism in High-Mass Stars”. In: *Galaxies* 11.2, p. 40.

Kochanek, C., K. Auchettl, & K. Belczynski (2019). “Stellar binaries that survive supernovae”. In: *Monthly Notices of the Royal Astronomical Society* 485.4, pp. 5394–5410.

Mazets, E. P., S. V. Golenetskij, & Y. A. Guryan (1979a). “Soft gamma-ray bursts from the source B1900+14”. In: *Soviet Astronomy Letters* 5, p. 343.

Mazets, E. P. et al. (1979b). “Observations of a flaring X-ray pulsar in Dorado”. In: *Nature* 282.5739, pp. 587–589. DOI: 10.1038/282587a0.

McMillan, P. J. (2016). “The mass distribution and gravitational potential of the Milky Way”. In: *Monthly Notices of the Royal Astronomical Society*, stw2759.

Moe, M. & R. Di Stefano (2017). “Mind your Ps and Qs: the interrelation between period (P) and mass-ratio (Q) distributions of binary stars”. In: *The Astrophysical Journal Supplement Series* 230.2, p. 15.

Mor, R. et al. (2019). “Gaia DR2 reveals a star formation burst in the disc 2–3 Gyr ago”. In: *Astronomy & Astrophysics* 624, p. L1.

Muno, M. et al. (2008). “A search for new Galactic magnetars in archival Chandra and XMM-Newton observations”. In: *The Astrophysical Journal* 680.1, pp. 639–653.

Origlia, L. et al. (2004). “Stellar and gaseous abundances in M82”. In: *The Astrophysical Journal* 606.2, pp. 862–868.

Pardo-Araujo, C. et al. (2026). “Magnetar fraction in Core-Collapse Supernovae”. In: *arXiv preprint arXiv:2601.16159*.

Pelliciari, D. et al. (2023). “The Northern Cross Fast Radio Burst project-III. The FRB–magnetar connection in a sample of nearby galaxies”. In: *Astronomy & Astrophysics* 674, A223.

Petroff, E., J. Hessels, & D. Lorimer (2019). “Fast radio bursts”. In: *The Astronomy and Astrophysics Review* 27.1, p. 4.

Poelarends, A. et al. (2008). “The supernova channel of super-AGB stars”. In: *The Astrophysical Journal* 675.1, pp. 614–625.

Renzo, M. et al. (2019). “Massive runaway and walkaway stars-A study of the kinematical imprints of the physical processes governing the evolution and explosion of their binary progenitors”. In: *Astronomy & Astrophysics* 624, A66.

Rozwadowska, K., F. Vissani, & E. Cappellaro (2021). “On the rate of core collapse supernovae in the milky way”. In: *New Astronomy* 83, p. 101498.

Sautron, M. et al. (2024). “The Galactic population of canonical pulsars-II. Taking into account several evolutionary paths: Interstellar medium interaction, Galactic potential, and a death valley”. In: *Astronomy & Astrophysics* 691, A349.

Sautron, M. et al. (2025). “The Galactic population of magnetars: a simulation-based inference study”. In: *The Astrophysical Journal* 986.1, p. 88.

Schneider, F. R. et al. (2019). “Stellar mergers as the origin of magnetic massive stars”. In: *Nature* 574.7777, pp. 211–214.

Schreiber, N. F. et al. (2003). “The nature of starburst activity in M82”. In: *The Astrophysical Journal* 599.1, pp. 193–217.

Sherman, M. B. et al. (2024). “Searching for magnetar binaries disrupted by core-collapse supernovae”. In: *Monthly Notices of the Royal Astronomical Society* 531.2, pp. 2379–2414. DOI: 10.1093/mnras/stae1289.

Snaith, O. et al. (2015). “Reconstructing the star formation history of the Milky Way disc (s) from chemical abundances”. In: *Astronomy & Astrophysics* 578, A87.

Stanway, E. R. & J. J. Eldridge (Sept. 2018). “Re-evaluating old stellar populations”. In: *Monthly Notices of the Royal Astronomical Society* 479.1, pp. 75–93. DOI: 10.1093/mnras/sty1353. arXiv: 1805.08784 [astro-ph.GA].

Stevance, H. F. & M. M. Briel (Nov. 2022). *BPASS-EvE database*. Version alpha. Zenodo. DOI: 10.5281/zenodo.7341382. URL: https://doi.org/10.5281/zenodo.7341382.

Wharton, R. S. et al. (2025). “High-frequency Fast Radio Burst Search of Nearby Star-forming Galaxies M77 and M82”. In: *The Astrophysical Journal* 984.2, p. 119.

Zapartas, E. et al. (2017). “Delay-time distribution of core-collapse supernovae with late events resulting from binary interaction”. In: *Astronomy & Astrophysics* 601, A29.

Chapter 4

AN UPDATED MAGNETAR SCALE HEIGHT AND IMPLICATIONS FOR THEIR STELLAR PROGENITORS

4.1 Introduction

The massive OB stars ($> 8M_\odot$) observed today are a subset of Population I stars, formed in star clusters (associations) with < 50 Myr lifetimes which end in Core-Collapse Supernovae (CCSNe) (e.g., Blaauw, 1964; Garmany, 1994; Lesh, 1969). While the remnants (neutron stars, black holes) of early Population II OB stars inhabit the Galactic bulge, young OB stars are born in the thin disk (e.g., Kroupa, 2004; Pantaleoni González et al., 2025; Quintana, 2024; Ward et al., 2020; Wright, 2020). Quintana et al. (2025) fit the z positions of the *Gaia* catalog of OB stars to an exponential distribution ($n(z) \propto e^{-z/h_e}$), measuring a scale height $h_{\rm e,OB} = 76 \pm 1$ pc. Their short lifetimes make present-day OB stars strong tracers of recent star formation, while their feedback (via stellar winds or CCSNe) of ionized gas into the Interstellar Medium relates them to the Galactic free electron distribution (Cordes & Lazio, 2002; Ocker & Cordes, 2024).

Much can be learned about the formation of neutron stars, which are formed from the CCSNe of OB stars between $8 - 100M_\odot$, by comparing their spatial distribution to that of OB stars. Slow radio pulsars ($P > 0.03$ s) follow an exponential distribution with scale height $h_{e,\rm psr} \approx 330$ pc, while recycled millisecond pulsars ($P < 0.03$ s) extend further from the plane with $h_{e,\rm msp} \approx 500$ pc (Levin et al., 2013; Lorimer et al., 2006). These are consistent with an origin from Population II OB stars in the Galactic Bulge (radius ~ 3 kpc) or thick disk (~ 1 kpc), as are the characteristic ages for slow ($\tau_C \equiv \dot{P}/2P \approx 100$ kyr-1 Gyr) and millisecond (MSPs; $\tau_C \approx 1 - 100$ Gyr) pulsars. Hobbs et al. (2004) constrained the proper motion distribution of neutron stars, determining that $\sim 100\,{\rm km\,s^{-1}}$ kicks from CCSNe can further broaden the scale height by up to 100 pc for slow pulsars and 10 kpc for MSPs based on their maximum ages. Thus slow pulsars and MSPs are likely a mixed population: MSPs and older slow pulsars form from Population II OB stars at large scale heights; younger slow pulsars are born from Population I OB stars within the disk and are kicked away from the plane by the CCSNe explosions. Indeed, only two pulsars with $\tau_C < 100$ kyr are more than 500 pc from the plane, supporting this scenario.

Magnetars, neutron stars with longer rotation periods (1 – 10 s) and stronger magnetic fields (10^{14-15}) than typical radio pulsars', are further intriguing due to their apparent preference for the galactic plane. Excluding the two magnetars in the Magellanic Clouds, Olausen & Kaspi (2014) find a low exponential scale height of 20 – 31 kpc for Galactic magnetars. First, this rules out the Population II formation scenario followed by the oldest MSPs and pulsars; magnetars appear to be an exclusively young species of neutron star formed from thin disk OB stars. Magnetars' low characteristic ages $\tau_C \approx 1 - 100$ kyr, which are likely overestimated due to their unique decaying magnetic fields (e.g., Ferrario & Wickramasinghe, 2006, 2008), support this scenario, and limit the distance magnetars can travel from the plane at typical kick velocities to $\lesssim 10$ pc. However, this does not explain the dearth of magnetars between $\sim 30 - 76$ pc from the plane. OB stars are found at over twice the distance from the galactic plane as magnetars; thus, it is unclear why magnetars would preferentially form only from OB stars closer to the plane.

Stellar metallicities could play a role; Schlesinger et al. (2014) use G dwarfs to constrain the Milky Way's metallicity gradient, with [Fe/H] decreasing further from the plane at a rate $-0.243^{+0.39}_{-0.053}$ dex kpc^{-1}. Observations of CCSNe in other galaxies suggest a preference for low metallicity environments (Pessi et al., 2023), and MESA simulations link this to a positive correlation between metallicity and the minimum stellar mass for CCSNe to occur (Ibeling & Heger, 2013). Therefore, the magnetar scale height could imply they prefer OB star progenitors with higher metallicities than typical neutron stars. Zapartas et al. (2017) also identify a population of late delay-time CCSNe from mass-transfer binaries, which would further alter the star's metallicity. However, with only a small sample of magnetars and varying levels of precision in distance estimates, Olausen & Kaspi (2014) can draw only limited conclusions on the magnetar formation from the measured scale height.

Olausen & Kaspi (2014) also estimate the vertical distance of the Sun from the galactic plane using the magnetar distribution, finding $z_{\odot,\mathrm{OK14}} = 13 - 22$ pc. This is only marginally consistent with recent constraints from the *Gaia* sample that place the Sun at $z_{\odot,\mathrm{BB19}} = 20.8 \pm 0.3$ pc above the disk (Bennett & Bovy, 2019). By improving the magnetar constraint, one can assess the significance of this discrepancy and determine whether or not the exponential model is well-fit to the magnetar sample. In Chapter 1, we defined the updated magnetar sample in detail; since Olausen & Kaspi (2014), 4 new magnetars have been confirmed (Swift J1818.0-1607, 3XMM J185246.6+003317, SGR J1830-0645, and Swift J1555.2-

Table 4.1: Magnetar Galactic Latitudes (b) with Errors (σ_b), Distances, and Vertical Distances (z) from galactic plane ($b = 0°$)

Magnetar	$b(°)$	$\sigma_b('')$	**Distance (kpc)**	**z (pc)**
4U 0142(+61)	-00°25′50.″7	0.5	3.6 ± 0.4	-27 ± 3
SGR 0418(+5729)	+05°07′08.″9	0.4	~ 2	~ 180
SGR 0501(+4516)	+01°57′04.″678	0.1	2.0 ± 0.3	~ 68
1E 1048.1(-5937)	-00°31′12.″50	0.07	9.0 ± 1.7	-82 ± 15
1E 1547.0(-5408)	-00°07′54.″029	0.004	3.91 ± 0.07	-9.0 ± 0.2
PSR J1622(-4950)	-00°06′06.″6	0.9	9.00 ± 1.35	-16 ± 2
SGR 1627(-41)	-00°06′41.″4	0.7	11.0 ± 0.3	-21.4 ± 0.5
CXOU J1647(10.2-455216)	-00°25′51.″0	0.4	3.9 ± 0.7	29 ± 5
1RXS J1708(49.0-400910)	+00°02′09.″9	1.0	3.8 ± 0.5	2.4 ± 0.3
CXOU J1714(05.7-381031)	+00°22′16.″3	0.7	9.8 ± 1.5	63 ± 10
SGR J1745(-2900)	-00°02′48.″42	0.06	8.3 ± 0.3	$-2.0^{+0.3}_{-0.2}$
SGR 1806(-20)	-00°14′31.″01	0.05	$8.7^{+1.8}_{-1.5}$	-37^{+8}_{-6}
XTE J1810(-197)	−00°09′30.″22497	0.00005	$2.5^{+0.4}_{-0.3}$	-10 ± 1
Swift 1818(.0-1607)	-00°08′16.″6684	0.0002	~ 4.8	-23^{+5}_{-4}
Swift J1822(.3-1606)	-01°01′15.″4	2.4	1.6 ± 0.3	-29 ± 5
Swift J1834(.9-0846)	-00°20′27.″6	0.80	4.2 ± 0.3	-25 ± 2
1E 1841(-045)	-00°00′18.″8	0.4	8.5 ± 1.3	$-0.77^{+0.12}_{-0.09}$
3XMM J1852(46.6+003317)	+00°02′42.3	3.2	~ 7.1	~ 5.6
SGR 1900(+14)	+00°45′56.″2	0.2	12.5 ± 1.7	167 ± 23
1E 2259(+586)	-00°59′44.″7	0.6	3.2 ± 2.0	-56 ± 3
SGR J1830(-0645)	-+01°30′16.″0	0.8	~ 4	~ 105
Swift J1555.2(-5402)	-00°20′11.″3	12000	~ 10	~ -59

Magnetars with boldfaced names have either been discovered or updated since Olausen & Kaspi (2014). See Chapter 1 for references.

5402) while improved distances and/or position measurements have been reported for four magnetars (PSR J1622-4950, CXOU J171405.7-381031, SGR J1745-2900, and 1E 1841-045). Table 4.1 shows updated z positions for each Galactic magnetar in the updated sample.

In this chapter, we re-estimate the magnetar scale height with an updated sample and discuss its implications for their formation. In Section 4.2 we describe the Markov-Chain Monte Carlo (MCMC) fit method and the models under test in addition to the exponential model. In Section 4.3 we relay the updated scale height estimates and evaluate the goodness-of-fit for each model. In Section 4.4 we discuss the implications of the low scale height on magnetar formation in detail. We conclude in Section 4.5, summarizing the analysis and considering next steps.

4.2 Methods

For each magnetar in Table 4.1, we compute the z coordinate (vertical distance measured from $b = 0°$, defined as the plane containing the Sun lying parallel to the galactic disk) as $z = d \sin(b)$, where d is the distance and b is the Galactic latitude. We compute errors using Gaussian error propagation as:

$$\sigma_z = \sqrt{(\sigma_d \sin(b))^2 + (d\sigma_b \cos(b))^2)} \tag{4.1}$$

accounting for upper and lower limits accordingly.

We consider four models for the magnetar z distribution: an exponential distribution as discussed in Section 4.1:

$$n_{\rm exp}(z) \propto \frac{-|z + z_\odot|}{h_e} \tag{4.2}$$

a self-gravitating isothermal disk as described by Bahcall (1984):

$$n_{\rm iso}(z) \propto {\rm sech}(\frac{|z + z_\odot|}{h_s}) \tag{4.3}$$

a Gaussian distribution:

$$n_{\rm norm}(z) \propto e^{\frac{-(z+z_\odot)^2}{2h_n^2}} \tag{4.4}$$

and a uniform distribution with minimum and maximum z values:

$$n_{\rm flat}(z) \propto \begin{cases} \text{constant} & z_{\rm min} < z < z_{\rm max} \\ 0 & \text{otherwise} \end{cases} \tag{4.5}$$

We use the Python `emcee` package to implement an MCMC simulation to fit the cumulative distribution function (cdf) of magnetar z coordinates. Gaussian likelihoods are adopted for each parameter, with systematic errors fit for z and the cdf. Flat priors are used for each scale height parameter, h_x, limiting it to $h_x < 100\,$pc. We consider two priors for $z_\odot$: in the first case we adopt a flat prior for $6\,{\rm pc} < z_\odot < 28\,{\rm pc}$ as estimated by Joshi (2007); in the second, we impose a Gaussian prior using the best-fit measurement, $z_{\odot,{\rm BB19}} = 20.8 \pm 0.3\,$pc Bennett & Bovy (2019).

After running the simulation with 32 walkers and 5,000 steps for each model, we compute χ^2 per degree of freedom ($\nu = 4$) to estimate the goodness of fit. We adopt the Beyesian Information Criterion (BIC) to determine which model is best-suited to the magnetar z distribution:

$$BIC = k\ln(N_{\rm mag}) - 2\ln(\hat{L}(\theta_{\rm fit})) \tag{4.6}$$

where $k = 4$ is the number of parameters, $N_{\rm mag} = 22$ is the number of magnetars, and $\hat{L}(\theta_{\rm fit})$ is the likelihood for the best-fit parameters. The best fit parameters are the median values with errors from the 16$^{\rm th}$ and 84$^{\rm th}$ percentiles.

As an initial test, we apply the MCMC pipeline using the exponential fit to the Olausen & Kaspi (2014) sample using the flat prior. We recover $z_\odot = 12.0^{+2.1}_{-1.5}$ pc and $h_e = 25.9^{+6.3}_{-2.2}$ pc in agreement with Olausen & Kaspi (2014) ($z_{\odot,\rm OK14} = 13.5 \pm 2.6$ pc and $h_{e,\rm OK14} = 30.7 \pm 5.7$ pc for the exponential fit).

4.3 Results

The results of the MCMC fit for each z-distribution model are shown in Table 4.2. While the best-fit model is the exponential with flat $z_\odot$ prior, no model is well-fit to the magnetar data; in all cases $\chi^2/\nu \gtrsim 20$. The BIC also indicates this model is the most preferred, resulting in a scale height of $h_{e,\rm flat} = 26.3^{+8.0}_{-2.0}$ pc. This is lower, though still in 1σ agreement with the Olausen & Kaspi (2014) result. We obtain a solar distance from the galactic plane of $z_{\odot,\rm flat} = 11.2 \pm 1.7$ pc, which also agrees with the Olausen & Kaspi (2014) result and is now a statistically significant $> 3\sigma$ difference from Bennett & Bovy (2019) *Gaia* estimate $z_{\odot,\rm BB19} = 20.8 \pm 0.3$ pc. The isothermal disk model with flat $z_\odot$ prior gives a similar goodness-of-fit as the exponential model (marginally worse) with a lower scale height estimate $h_{s,\rm flat} = 18.8^{+1.6}_{-1.7}$. The Gaussian and uniform models offer poor fits based on the χ^2/ν and BIC values. We focus here on the exponential model results, and discuss the possibility that magnetars follow a unique distribution in Section 4.4.

For the exponential model with $z_{\odot,\rm BB19} = 20.8 \pm 0.3$ pc prior, the distribution for h_e is distinctly bimodal with peaks at $h_{e,\rm BB19,1} = 49.5^{+2.0}_{-3.6}$ pc and $h_{e,\rm BB19,2} = 64.1^{+4.9}_{-3.7}$ pc. Splitting the MCMC samples for h_e above and below 55 pc does not change the median $z_\odot$ which is consistent with the Bennett & Bovy (2019) result as expected. However, visually, neither is well-fit to the magnetar empirical cdf, shown in Figure 4.1.

4.4 Discussion

The lack of reasonable fits to the exponential scale height prompts the question: is a different model required to describe the magnetar spatial distribution? Based on the BIC values, the exponential and isothermal disk models outperformed the Gaussian and uniform models, suggesting that the magnetar positions are not entirely agnostic to the shape of the galactic disk. Thus, the theory that magnetars form from young stellar populations remains viable. The low $\sim 100\,{\rm km\,s^{-1}}$ velocities and

Table 4.2: Results of MCMC Fit of Magnetar Scale Height

Model	Population[§]	$z_\odot$ prior[*]	$z_\odot$ (pc)	h_e (pc)	$f_z^\dagger$	$f_{\rm cdf}^\dagger$	χ^2/ν	BIC
Exponential	Galactic	$6\,{\rm pc} < z_\odot < 28\,{\rm pc}$ (flat)	11.2 ± 1.7	$26.3^{+8.0}_{-2.0}$	$2.0^{+0.8}_{-0.6}$	$0.18^{+0.08}_{-0.06}$	20	56
Exponential	Inner ($l > 90, l > 270$)	$6\,{\rm pc} < z_\odot < 28\,{\rm pc}$ (flat)	$12.8^{+1.4}_{-1.9}$	$24.7^{+1.8}_{-2.0}$	$1.6^{+0.6}_{-0.4}$	$0.18^{+0.08}_{-0.05}$	18	39
Isothermal Disk	Galactic $6\,{\rm pc} < z_\odot < 28\,{\rm pc}$ (flat)	$11.5^{+1.5}_{-1.2}$	$18.8^{+1.6}_{-1.7}$	$2.3^{+0.8}_{-0.6}$	$0.17^{+0.07}_{-0.05}$	21	58	
Gaussian	Galactic	$6\,{\rm pc} < z_\odot < 28\,{\rm pc}$ (flat)	$18.4^{+3.6}_{-6.5}$	$53.8^{+9.0}_{-4.6}$	$1.4^{+0.5}_{-0.3}$	$0.23^{+0.2}_{-0.1}$	74	72
Exponential[‡]	Galactic	$z_{\odot,{\rm BB19}} = 20.8 \pm 0.3\,{\rm pc}$	P1:20.8 ± 0.3 P2:20.7 ± 0.3	P1:$49.5^{+2.0}_{-3.6}$ P2:$64.1^{+4.9}_{-3.7}$	P1:$1.0^{+0.3}_{-0.2}$ P2:$1.0^{+0.5}_{-0.2}$	P1:$0.10^{+0.08}_{-0.06}$ P2:$0.08^{+0.07}_{-0.04}$	P1:78 P2:196	P1:68 P2:69
Exponential[‡]	Inner ($l > 90, l > 270$)	$z_{\odot,{\rm BB19}} = 20.8 \pm 0.3\,{\rm pc}$	P1:20.8 ± 0.3 P2:20.8 ± 0.3	P1:$38.1^{+1.8}_{-3.5}$ P2:$50.6^{+4.1}_{-3.3}$	P1:$1.0^{+0.4}_{-0.3}$ P2:$1.0^{+0.4}_{-0.2}$	P1:$0.17^{+0.15}_{-0.10}$ P2:$0.09^{+0.10}_{-0.05}$	P1:73 P2:209	P1:55 P2:57
Isothermal Disk	Galactic	$z_{\odot,{\rm BB19}} = 20.8 \pm 0.3\,{\rm pc}$	20.8 ± 0.3	$36.2^{+3.1}_{-6.5}$	$1.2^{+0.4}_{-0.3}$	$0.10^{+0.10}_{-0.06}$	107	72
Gaussian	Galactic	$z_{\odot,{\rm BB19}} = 20.8 \pm 0.3\,{\rm pc}$	20.7 ± 0.3	$55.7^{+3.5}_{-2.2}$	$1.3^{+0.4}_{-0.3}$	$0.3^{+0.2}_{-0.1}$	85	73
		$z_{\rm min}$ (pc)	$z_{\rm max}$ (pc)					
Uniform	Galactic	$6\,{\rm pc} < z_\odot < 28\,{\rm pc}$ (flat)	$-76.1^{+7.8}_{-10.7}$	$106.8^{+25.8}_{-22.3}$	$1.6^{+0.8}_{-0.4}$	$0.3^{+0.2}_{-0.1}$	157	79
Uniform	Galactic	$0.5(z_{\rm min} + z_{\rm max}) = 20.8 \pm 0.3\,{\rm pc}$	$-58.5^{+4.2}_{-28.6}$	$100.3^{+28.3}_{-4.6}$	$1.5^{+0.5}_{-0.3}$	$0.3^{+0.2}_{-0.1}$	85	85

[*]The flat $z_\odot$ prior uses limits from Joshi (2007), while the Gaussian prior (BB19) uses a Gaussian constrained by Bennett & Bovy (2019)

[†] f_z and $f_{\rm cdf}$ are the allowed systematic error in z position and cdf bin level, respectively, as fractions of the true values.

[‡]For the exponential model with $z_{\odot,{\rm BB19}} = 20.8 \pm 0.3\,{\rm pc}$ prior, we give the best-fit h_e, f_z, and $f_{\rm cdf}$ values using MCMC samples from each peak of the bimodal h_e distribution, labeled P1 ($h_e < 55$ for Galactic population, $h_e < 45$ for Inner population) and P2 ($h_e > 55$ for Galactic population, $h_e > 45$ for Inner population) .

[§]Population is either 'Galactic' when all Galactic magnetars are included or 'Inner' when only magnetars with longitude $l < 90°$ or $l > 270°$ are included to mitigate the effect of the outer disk warp.

SNR-inferred ages ($\sim 1-10\,$kyr) suggest that magnetars are born near ($\lesssim 1\,$pc) their present-day locations rather than being significantly kicked to larger scale heights by CCSNe explosions (e.g., Ding et al., 2024; Zapartas et al., 2017). However, this formation scenario is complicated by the presence of multiple $|z| > 90\,$pc outliers (SGR 0418+5729, SGR 1900+14, and SGR J1830-0645) and the significant offset of the magnetar distribution center from the well-constrained position of the disk. In this section, we consider the cause of the magnetars' $z_\odot$ offset, the reason for magnetars' low scale height compared to pulsars and OB stars, and the implications for magnetars' relationship to pulsars and long-period radio transients (LPTs or LPRTs; Beniamini et al., 2020).

4.4.1 Evidence of Disk Asymmetries

The observed $\Delta z_\odot = 9.6 \pm 1.7\,$pc offset may result from previously identified asymmetries in the Milky Way's stellar density distribution. Poggio et al. (2025), for example, constrain the 'warped' shape of the outer disk (galactocentric radius $r \gtrsim 10\,$kpc): stellar densities increase below the plane between longitudes $-60° \lesssim l \lesssim 0°$ and above the plane between $0° \lesssim l \lesssim 45°$ up to $z \sim 2\,$kpc from the plane. If magnetars follow this density model, those in the outer disk ($90° \lesssim l \lesssim 270°$) could bias the scale height, which would no longer reflect the birth sites of magnetars relative to the plane. If we remove the four magnetars in the outer disk from the sample, however, there is no significant change in the solar height $z_{\odot,\mathrm{inner}} = 12.8^{+1.4}_{-2.0}\,$pc from the exponential flat $z_\odot$ prior model, while the scale height is marginally lowered $h_{e,\mathrm{inner}} = 24.7^{+1.8}_{-2.0}\,$pc. The galactic plane offset is thus unrelated to the warp, while the scale height was biased as expected. When imposing the $z_{\odot,\mathrm{BB19}}$ prior, the bimodal h_e distribution persists, but is split at $\sim 45\,$pc instead of $\sim 55\,$pc. The results from the inner disk sample are in Table 4.1 as the 'Inner' population.

Poggio et al. (2025) also identify a corrugated wave structure from stellar density and vertical velocity perturbations in the z -direction on $\sim 25\,$pc scales (see also Yanny & Gardner, 2013). They constrain the density asymmetry to a factor ~ 0.05 difference above ($z \sim +12.5\,$pc) and below ($z \sim -12.5\,$pc) the plane, and propose this as the result of a gravitational interaction with a satellite galaxy over a few billion years ago. These density perturbations create a stellar overdensity above the plane and a stellar underdensity below the plane, which may result in more OB stars forming magnetars above the plane and ultimately, the $\Delta z_\odot = 9.6 \pm 1.7\,$pc magnetar plane offset. However, confirming the magnitude of the perturbation would require

analysis of the perturbation with higher spatial resolution.

If we take the offset at face value as evidence of the vertical corrugation, it would be the first probe of such asymmetry on sub-10 pc scales. The elevated density may also increase the contamination of Population I stars with heavy elements ejected from Population II stars' CCSNe or stellar winds into the ISM. An (2019) identify a reflective metallicity asymmetry that supports this (see also Long et al., 2025; Ness et al., 2013a,b; Schlesinger et al., 2014). From extragalactic observations, CCSNe are found to occur more frequently in low metallicity environments (Freeman, 2014; Ibeling & Heger, 2013; Pessi et al., 2023), thus more metal rich Population I stars would appear less likely to have CCSNe of their own to form magnetars. Therefore, the metallicity perturbation contradicts the magnetar offset, and they are likely unrelated. Alternatively, the boosted density may promote the formation of stellar binaries, whose interaction could form late-time CCSNe (Zapartas et al., 2017) or merge prior to a single CCSN (Renzo et al., 2019; Sherman et al., 2024), both of which have been proposed to explain magnetars' unique properties.

If magnetars are indeed centered on the disk ($z_{\odot,\mathrm{BB19}}$), the MCMC identifies a bimodal distribution in h_e. Limiting to the inner disk magnetars to eliminate the warp bias, we obtain $h_{e,\mathrm{BB19},1} = 38.1^{+1.8}_{-3.5}$ pc and $h_{e,\mathrm{BB19},2} = 50.6^{+4.1}_{-3.3}$ pc, neither of which minimize χ^2/ν. The χ^2/ν minimizing value with $z_{\odot,\mathrm{BB19}}$ prior is $\hat{h}_{e,\mathrm{BB19},1} \approx 30$ pc, nearly the same value obtained from the uniform $z_\odot$ prior case, which systematically underestimates z for each magnetar when imposing $z_{\odot,\mathrm{BB19}}$. The failure of MCMC to achieve a unimodal h_e distribution using the *Gaia* constraint on $z_\odot$, the visual inconsistency of both h_e peaks with the magnetar sample, and the systematic underestimation of z when using the best-fit h_e and $z_{\odot,\mathrm{BB19}}$ all indicate that the galactic plane offset is real and likely a result of the known vertical wave asymmetries. Constraining these asymmetries on $\lesssim 10$ pc scales would be the next step to investigating this hypothesis.

4.4.2 Magnetar Formation within OB Associations

Quintana et al. (2025) performed a census of OB stars, the likely progenitors of magnetars, in the solar neighborhood (within 1 kpc), estimating their scale height as $h_{e,\mathrm{OB}*} = 76 \pm 1$ pc. This far exceeds the magnetar scale height from the flat $z_\odot$ prior model, regardless of the correct $z_\odot$. If magnetars reside near their birth sites, as expected from their low ages and field decay models, one would expect their scale height to resemble that of their OB star progenitors. To investigate this, we must

understand the formation of OB stars.

O-type and B-type stars are generally thought to form in OB associations, gravitationally unbound star clusters that are kinematically related. Dynamical ejection produces a sub-sample of 'runaway' stars like ζ Oph traveling at high speeds away from their associations, while high stellar winds render the cluster unstable to gravitational unbinding. This scenario is thought to contribute to the present-day population of unbound field stars. With recent high-precision position and proper motion data from *Gaia*, some OB associations have been found to be kinematically unrelated, but most major, well-studied associations remain candidate star-forming locations (e.g., Garmany, 1994; Pantaleoni González et al., 2025; Quintana, 2024; Quintana et al., 2025; Ward et al., 2020; Wright, 2020).

Using the Wright (2020) population of confirmed[1] OB associations, we estimate the scale height using MCMC sampling with a uniform, unbound $z_\odot$ prior and limiting to the inner disk ($-90^\circ < l < 90^\circ$). We obtain a much lower scale height than the full OB star population: $h_{e,\mathrm{OB,assoc.}} = 33.8^{+1.6}_{-1.4}$ pc. This is in closer agreement with the magnetar scale height $h_{e,\mathrm{inner}} = 24.7^{+1.8}_{-2.0}$ pc. Magnetars may then originate from OB associations as opposed to dynamically-ejected field OB stars.

Both the offset and scale height could potentially be explained by a preference for OB associations which may be individually offset from the plane and range from $\sim 10-1,000$ pc in size. From Wright (2020), three OB associations in the inner disk (Gem OB1, Per OB2, and Cas OB7) lie between $10-14$ pc, matching the magnetar offset from the plane. Gem OB1 is approximately spherical with diameter $\lesssim 50$ pc, a similar extent to the magnetar scale height. Only two magnetars lie within 100 pc of known OB associations, none within 30 pc. This may be a selection bias since higher extinction within the plane could obscure some OB stars. Future OB star surveys and novel kinematic analysis methods may reveal more OB associations to cross-match with the magnetar population in search of formation sites.

4.4.3 Comparison to other Radio Transient Populations

Olausen & Kaspi (2014) noted the stark difference in scale height between Galactic magnetars and Galactic pulsars. Slow pulsars are well-fit by an exponential distribution with $h_{e,\mathrm{psr}} \approx 180-330$ pc (Lorimer et al., 2006); while also formed from OB stars, pulsars can travel up to ~ 1 kpc from their birth sites over their ~Myr ages,

[1]We exclude those which may not be associations based on more recent analyses. We also take the Sco-Cen and Ori OB1 associations as single clusters rather than counting their sub-groups separately.

making their large separations from the plane feasible with typical CCSN kicks (Hobbs et al., 2004). Similarly, MSPs follow an exponential distribution with scale height $h_{e,\mathrm{MSP}} \approx 500\,\mathrm{pc}$, with their longer lifetimes (∼Gyr) resulting in a larger scale height (Levin et al., 2013).

Magnetars escape this trajectory through their rapid magnetic field decay; coupled with their magnetically-powered emission, magnetars' energy reservoir is expected to deplete on $1-100\,\mathrm{kyr}$ timescales (e.g., Ferrario & Wickramasinghe, 2006, 2008). However, it is unclear how magnetars behave beyond this point, and whether they can enter a rotationally-powered phase more closely resembling pulsars. To check the consistency of this argument, we have re-fit the inner-disk pulsar population with the exponential model for different characteristic age ($\tau_C \equiv P/2\dot{P}$) groups. For the full slow pulsar ($P \lesssim 30\,\mathrm{ms}$) population we obtain $h_{e,\mathrm{psr}} \approx 321.4^{+0.3}_{-30.1}\,\mathrm{pc}$, consistent with Lorimer et al. (2006). Similarly, we obtain $h_{e,\mathrm{MSP}} = 460^{+30}_{-70}\,\mathrm{pc}$ for MSPs. We find scale heights $h_{e,\mathrm{psr},<100\,\mathrm{kyr}} = 38.0^{+0.1}_{-0.4}\,\mathrm{pc}$ for $\tau_C < 100\,\mathrm{kyr}$, $h_{e,\mathrm{psr},100\,\mathrm{kyr}-10\,\mathrm{Myr}} = 202.1^{+5.2}_{-25.2}\,\mathrm{pc}$ for $100\,\mathrm{kyr} < \tau_C < 10\,\mathrm{Myr}$, and $h_{e,\mathrm{psr},>10\,\mathrm{Myr}} = 460^{+4}_{-1}\,\mathrm{pc}$ for $\tau_C > 10\,\mathrm{Myr}$. This strong correlation with age and similarity of the $< 100\,\mathrm{kyr}$ scale height with that of magnetars indeed suggests that magnetars reside near their birth sites. Based on the arguments above, it may further suggest that both magnetars and young pulsars are born within OB associations while older pulsars can originate from field stars.

Beniamini et al. (2023) postulate that some magnetars may reach extremely long (minutes to hours) rotation periods through enhanced spin-down processes such as fallback accretion or glitching. Long Period Radio Transients (LPTs or LPRTs), which have rotation periods between 20 seconds−8.7 hours, were proposed as candidates for these Ultra-Long Period Magnetars (ULPMs), with 15 discovered so far. Two have been associated with White Dwarf-M-Dwarf binaries, while others exhibit sub-pulse structure, X-ray counterparts, and other neutron-star like behavior (de Ruiter et al., 2025; Dong et al., 2025a,b; Horváth et al., 2025; Rodriguez, 2025, see also Section 5).

No LPTs have had parallactic or spectroscopic distance measurements so far, leaving only dispersion measure (DM)-based estimates with $\sim 1\,\mathrm{kpc}$ uncertainties. For this reason, we do not attempt to fit for the LPT scale height, though we plot them for comparison in Figure 4.1. LPTs appear to reach larger scale heights than magnetars, and are more consistent with the White Dwarf population ($54 < h_{e,\mathrm{WD}} < 120\,\mathrm{pc}$ depending on mass; Wegg & Phinney, 2012). While this agrees with the White

Dwarf-M Dwarf binary model, Beniamini et al. (2020) predict that ULPMs should be older than typical magnetars, $\sim 10^{5.5-6}$ kyr. $\sim 1,000\,\mathrm{km\,s^{-1}}$ kick velocities imply they could reach up to $\sim 0.3 - 1$ kpc; thus the ULPM model is still viable.

4.5 Conclusion

In this chapter, we used MCMC to re-estimate the magnetar scale height $h_{e,\mathrm{mag}}$ = with an updated sample, accounting for the galactic disk warp by limiting to magnetars in the inner disk. We find the distribution is significantly offset from the *Gaia*-constrained solar scale height which may be evidence of the wave-like asymmetry on < 10 pc scales. It remains puzzling why magnetars' and young pulsars' scale heights are lower than that of OB stars, indicating a deference for formation from field OB stars. Instead, magnetars' and young pulsars' scale heights more closely resemble that of OB associations, suggesting they may form predominantly from stars within their star forming clusters rather than dynamically-ejected field stars. LPTs extend to a larger scale height than magnetars, though improved distance estimates are required to interpret this. In general, the exponential model is poorly fit to the magnetar distribution, with $\chi^2/\nu >> 1$ in all cases. In conjunction with the galactic plane offset and the presence of $|z| > 90$ pc outliers, this suggests that a novel spatial model is required to explain the magnetar sample. Magnetars' apparent agreement with OB associations further imply that any underlying spatial model may be 'patchy' or discontinuous rather than smooth, and need not be symmetrical about the galactic plane.

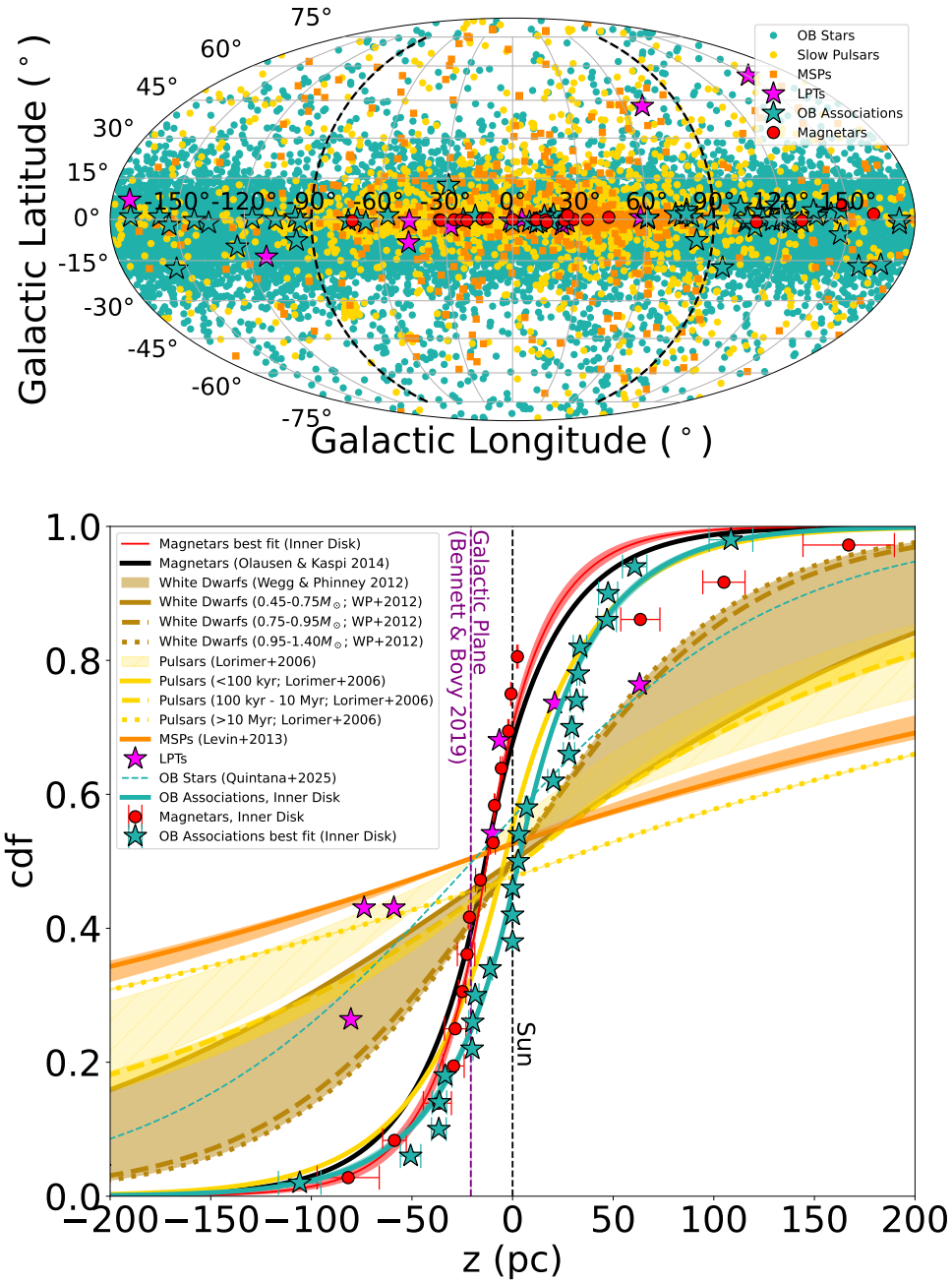

Figure 4.1: Spatial Distribution in Galactic Coordinates (Top), Cumulative Distribution Functions (cdfs), and Best-Fit Exponential Models (Bottom). Magnetars (red) and OB Associations (teal) are shown with best-fit curves from this work's MCMC analysis. LPTs are in magenta. 10% errorbars are assumed for sources without error estimates. Pulsar (gold; Levin et al., 2013; Lorimer et al., 2006) and White Dwarf (brown; Wegg & Phinney, 2012) scale height ranges are shaded, while the OB star scale height (teal; Quintana et al., 2025) is a dashed line. The cdf from Olausen & Kaspi (2014) is in black. The galactic plane position $z_{\odot,BB19}$ from (Bennett & Bovy, 2019) and Sun are indicated by purple and black dashed lines, respectively.

CHAPTER 4 BIBLIOGRAPHY

An, D. (2019). "Asymmetric Mean Metallicity Distribution of the Milky Way's Disk". In: *The Astrophysical Journal Letters* 878.2, p. L31.

Bahcall, J. N. (Jan. 1984). "The distribution of stars perpendicular to galactic disk". In: *The Astrophysical Journal* 276, pp. 156–168. DOI: 10.1086/161600.

Beniamini, P. et al. (2023). "Evidence for an abundant old population of Galactic ultra-long period magnetars and implications for fast radio bursts". In: *Monthly Notices of the Royal Astronomical Society* 520.2, pp. 1872–1894.

Beniamini, P., Z. Wadiasingh, & B. D. Metzger (2020). "Periodicity in recurrent fast radio bursts and the origin of ultralong period magnetars". In: *Monthly Notices of the Royal Astronomical Society* 496.3, pp. 3390–3401.

Bennett, M. & J. Bovy (2019). "Vertical waves in the solar neighbourhood in Gaia DR2". In: *Monthly Notices of the Royal Astronomical Society* 482.1, pp. 1417–1425.

Blaauw, A. (1964). "The O associations in the solar neighborhood". In: *Annual Review of Astronomy and Astrophysics, vol. 2, p. 213* 2, p. 213.

Cordes, J. M. & T. J. W. Lazio (2002). "NE2001. I. A new model for the galactic distribution of free electrons and its fluctuations". In: *arXiv preprint astro-ph/0207156*.

de Ruiter, I. et al. (May 2025). "Sporadic radio pulses from a white dwarf binary at the orbital period". In: *Nature Astronomy* 9, pp. 672–684. DOI: 10.1038/s41550-025-02491-0. arXiv: 2408.11536 [astro-ph.HE].

Ding, H. et al. (2024). "VLBA astrometry of the fastest-spinning magnetar Swift J1818. 0- 1607: a large trigonometric distance and a small transverse velocity". In: *The Astrophysical Journal Letters* 971.1, p. L13.

Dong, F. A. et al. (July 2025a). "CHIME/Fast Radio Burst Discovery of an Unusual Circularly Polarized Long-period Radio Transient with an Accelerating Spin Period". In: *The Astrophysical Journal Letters* 988.1, L29, p. L29. DOI: 10.3847/2041-8213/adeaab. arXiv: 2507.05139 [astro-ph.HE].

Dong, F. A. et al. (Sept. 2025b). "CHIME/Fast Radio Burst/Pulsar Discovery of a Nearby Long-period Radio Transient with a Timing Glitch". In: *The Astrophysical Journal Letters* 990.2, L49, p. L49. DOI: 10.3847/2041-8213/adfa8e. arXiv: 2407.07480 [astro-ph.HE].

Ferrario, L. & D. Wickramasinghe (2006). "Modelling of isolated radio pulsars and magnetars on the fossil field hypothesis". In: *Monthly Notices of the Royal Astronomical Society* 367.3, pp. 1323–1328.

Ferrario, L. & D. Wickramasinghe (2008). “Origin and evolution of magnetars”. In: *Monthly Notices of the Royal Astronomical Society: Letters* 389.1, pp. L66–L70.

Freeman, K. C. (2014). “The Galactic Bulge”. In: *Lessons from the Local Group: A Conference in honour of David Block and Bruce Elmegreen*. Springer, pp. 31–41.

Garmany, C. D. (1994). “OB associations: Massive stars in context”. In: *Publications of the Astronomical Society of the Pacific* 106.695, pp. 25–37.

Hobbs, G. et al. (2004). “The Parkes multibeam pulsar survey–IV. Discovery of 180 pulsars and parameters for 281 previously known pulsars”. In: *Monthly Notices of the Royal Astronomical Society* 352.4, pp. 1439–1472.

Horváth, C. et al. (2025). “A unified model for long-period radio transients and white dwarf binary pulsars”. In: *arXiv preprint arXiv:2507.15352*.

Ibeling, D. & A. Heger (2013). “The metallicity dependence of the minimum mass for core-collapse supernovae”. In: *The Astrophysical Journal Letters* 765.2, p. L43.

Joshi, Y. C. (2007). “Displacement of the Sun from the Galactic plane”. In: *Monthly Notices of the Royal Astronomical Society* 378.2, pp. 768–776.

Kroupa, P. (2004). “Massive stars: their birth sites and distribution”. In: *New Astronomy Reviews* 48.1-4, pp. 47–54.

Lesh, J. (1969). “Internal motions in the associations II Per and I Lac.” In: *Astronomical Journal, Vol. 74, p. 891-898* 74, pp. 891–898.

Levin, L. et al. (2013). “The High Time Resolution Universe Pulsar Survey–VIII. The Galactic millisecond pulsar population”. In: *Monthly Notices of the Royal Astronomical Society* 434.2, pp. 1387–1397.

Long, G. et al. (2025). “The Vertical Metallicity Gradient of the Galactic Disk for Mono-age Stellar Populations in LAMOST”. In: *The Astrophysical Journal* 983.1, p. 51.

Lorimer, D. R. et al. (2006). “The Parkes Multibeam Pulsar Survey–VI. Discovery and timing of 142 pulsars and a Galactic population analysis”. In: *Monthly Notices of the Royal Astronomical Society* 372.2, pp. 777–800.

Ness, M. et al. (2013a). “ARGOS–III. Stellar populations in the Galactic bulge of the Milky Way”. In: *Monthly Notices of the Royal Astronomical Society* 430.2, pp. 836–857.

– (2013b). “ARGOS–IV. The kinematics of the Milky Way bulge”. In: *Monthly Notices of the Royal Astronomical Society* 432.3, pp. 2092–2103.

Ocker, S. K. & J. M. Cordes (2024). “NE2001p: a native Python implementation of the NE2001 galactic electron density model”. In: *Research Notes of the AAS* 8.1, p. 17.

Olausen, S. A. & V. M. Kaspi (May 2014). "The McGill Magnetar Catalog". In: *The Astrophysical Journal Supplement Series* 212.1, 6, p. 6. DOI: 10.1088/0067-0049/212/1/6. arXiv: 1309.4167 [astro-ph.HE].

Pantaleoni González, M. et al. (2025). "The Alma catalogue of OB stars–III. A cross-match with Gaia DR3 and an extension based on new spectral classifications". In: *Monthly Notices of the Royal Astronomical Society* 543.1, pp. 63–82.

Pessi, T. et al. (2023). "A metallicity dependence on the occurrence of core-collapse supernovae". In: *The Astrophysical Journal Letters* 955.2, p. L29.

Poggio, E. et al. (2025). "The great wave-Evidence of a large-scale vertical corrugation propagating outwards in the Galactic disc". In: *Astronomy & Astrophysics* 699, A199.

Quintana, A. L. (2024). "OB associations: from stellar to galactic scales". In: *arXiv preprint arXiv:2412.10769*.

Quintana, A. L., N. J. Wright, & J. M. García (2025). "A census of OB stars within 1 kpc and the star formation and core collapse supernova rates of the Milky Way". In: *Monthly Notices of the Royal Astronomical Society* 538.3, pp. 1367–1383.

Renzo, M. et al. (2019). "Massive runaway and walkaway stars-A study of the kinematical imprints of the physical processes governing the evolution and explosion of their binary progenitors". In: *Astronomy & Astrophysics* 624, A66.

Rodriguez, A. C. (Mar. 2025). "Spectroscopic detection of a 2.9-hour orbit in a long-period radio transient". In: *Astronomy & Astrophysics* 695, L8, p. L8. DOI: 10.1051/0004-6361/202553684. arXiv: 2501.03315 [astro-ph.SR].

Schlesinger, K. J. et al. (2014). "The vertical metallicity gradient of the Milky way disk: transitions in [α/Fe] populations". In: *The Astrophysical Journal* 791.2, p. 112.

Sherman, M. B. et al. (2024). "Searching for magnetar binaries disrupted by core-collapse supernovae". In: *Monthly Notices of the Royal Astronomical Society* 531.2, pp. 2379–2414. DOI: 10.1093/mnras/stae1289.

Ward, J. L., J. D. Kruijssen, & H.-W. Rix (2020). "Not all stars form in clusters–Gaia-DR2 uncovers the origin of OB associations". In: *Monthly Notices of the Royal Astronomical Society* 495.1, pp. 663–685.

Wegg, C. & E. S. Phinney (Oct. 2012). "White dwarf kinematics versus mass". In: *Monthly Notices of the Royal Astronomical Society* 426.1, pp. 427–439. DOI: 10.1111/j.1365-2966.2012.21394.x. arXiv: 1206.1056 [astro-ph.GA].

Wright, N. J. (2020). "OB Associations and their origins". In: *New Astronomy Reviews* 90, p. 101549.

Yanny, B. & S. Gardner (2013). "The stellar number density distribution in the local solar neighborhood is north–south asymmetric". In: *The Astrophysical Journal* 777.2, p. 91.

Zapartas, E. et al. (2017). “Delay-time distribution of core-collapse supernovae with late events resulting from binary interaction”. In: *Astronomy & Astrophysics* 601, A29.

Chapter 5

SEARCHING FOR LONG DURATION RADIO TRANSIENTS WITH THE DSA-110

Sherman, M. B. et al. (2026). "Deep Synoptic Array Science: Searching for Long Duration Radio Transients with the DSA-110". In: *Publications of the Astronomical Society of the Pacific* 138.2, p. 024501. DOI: 10.1088/1538-3873/ae390e.

5.1 Abstract

We describe the design and commissioning tests for the DSA-110 Not-So-Fast Radio Burst (NSFRB) search pipeline, a 1.4 GHz image-plane single-pulse search sensitive to 134 ms−160.8 s radio bursts. Extending the pulse width range of the Fast Radio Burst (FRB) search by three orders of magnitude, the NSFRB search is sensitive to the recently-discovered Galactic Long Period Radio Transients (LPRTs or LPTs). The NSFRB search operates in real-time, utilizing a custom GPU-accelerated search code, `cerberus`, implemented in Python with JAX. We summarize successful commissioning sensitivity tests with continuum sources and pulsar B0329+54, estimating the 90% completeness 25σ flux (fluence) limit to be ~ 1200 mJy (~ 160 Jy ms). Future tests of recovery of longer timescale transients, e.g., CHIME J1634+44, are planned to supplement injection testing and B0329+54 observations. An offline DSA-110 NSFRB galactic plane Survey was conducted to search for LPRTs, covering $-3.5^\circ < b < 5.7^\circ$ and $141^\circ < l < 225^\circ$ (~ 770 square degrees) in Galactic coordinates. We estimate an upper limit Poissonian burst rate $\sim 2\,\mathrm{hr}^{-1}$ per square degree ($\sim 17\,\mathrm{hr}^{-1}$ per $3^\circ \times 3^\circ$ survey grid cell) maximized across the inner $|b| < 0.25^\circ$ of the surveyed region. By imposing the ~ 1200 mJy flux limit on two representative models (the magnetar plastic flow model and the White Dwarf-M Dwarf binary model), we reject with 95% confidence the presence of White Dwarf-M Dwarf binary LPRTs (beamed in a detectable direction) with periods between $\sim 10 - 50$ s within $\sim 95\%$ of the surveyed region. Combined with the prevalence of LPRTs in the galactic plane, our results motivate further consideration of both White Dwarf-M Dwarf binary models and isolated magnetar models. We will continue to explore novel LPRT search strategies during real-time operations, such as triggered periodicity searches and additional targeted surveys.

5.2 Introduction

Radio pulsar searching is entering a new exploratory phase; traditional single-dish telescope searches such as the Pulsar Arecibo L-band Feed Array (PALFA), Parkes Multi-beam Survey (PMBS), and Five-Hundred Metre Aperture Spherical Telescope (FAST) have utilized multi-beam receivers to discover roughly 2/3 of the $\sim$ 4000 known Galactic pulsars (Han et al., 2021; Y. Li et al., 2025; Manchester et al., 2005; Manchester et al., 2001). Over the past decade, the TRAnsients and PUlsars with MeerKAT (TRAPUM; Carli et al., 2024), the Canadian Hydrogen Intensity Mapping Experiment Pulsar (CHIME/PULSAR; Dong et al., 2023) backend, the LOw-Frequency ARray (LOFAR) Tied-Array All-Sky Survey (LOTAAS; Wateren et al., 2023), and Very Large Array (VLA) `realfast` system (C. Law et al., 2018), among others, have demonstrated that radio interferometers can achieve competitive sensitivities to single-dish telescopes with higher localization precision and less-costly antennas. Beyond contributing $\sim$ 500 additional pulsars, these arrays have been essential for follow-up imaging to identify and associate Supernova Remnants (SNRs), Pulsar Wind Nebulae (PWNe), long-duration afterglows, and Persistent Radio Sources (PRS) of both pulsars and extragalactic radio transients (e.g., Bruni et al., 2025; Cotton et al., 2024; Gaensler et al., 2005). However, these surveys have typically targeted pulsars with rotation periods $\lesssim$ 10 seconds out of necessity. Fast Fourier-domain search strategies require long integration times to remain sensitive to periods beyond second-scales, and suffer from low-frequency red noise, making them impractical targets (Ransom, 2001; Singh et al., 2022). Periodic transients with longer rotation periods (seconds to minutes), such as radio magnetars, Rotating Radio Transients (RRATs), and White Dwarf-M Dwarf binaries (either non-tidally-locked intermediate polars like AR Scorpii or tidally-locked non-accreting polars) were instead identified through serendipitous single-pulse surveys or follow-up of their high-energy counterparts (e.g., Caleb et al., 2022b; Hyman et al., 2005; Marsh et al., 2016).

The recent discovery of a dozen Galactic radio sources with unusually long pulse periods between $\sim$ 20 seconds$-$8.7 hours and low $\lesssim$ 10% duty cycles have begun to reveal an abundant unconstrained parameter space (e.g., de Ruiter et al., 2025; Horváth et al., 2025b; Hurley-Walker et al., 2022; Men et al., 2025; Tan et al., 2018). These so-called "Long-Period Radio Transients" (LPRTs, or LPTs) exhibit some properties characteristic of neutron stars, such as high polarization fractions, polarization position angle (PA) swings, temporal sub-structure, and un-detectable optical/IR (OIR) emission (Chrimes et al., 2022; Kramer et al., 2024;

Mitra et al., 2023; Radhakrishnan & Cooke, 1969). However, at least two LPRTs, ILT J1101+5521 (P = 2.1 hours) and GLEAM-X J0704-37 (P = 2.9 hours) reside in binaries with M-dwarf companions, with blue optical excess suggesting they are White Dwarfs (de Ruiter et al., 2025; Hurley-Walker et al., 2024). While the remaining sample have no clear M-Dwarf companions, the recent discovery of a secondary P = 8.74 hr period of GPM J1839-10 solely from radio timing suggests the White-Dwarf-M-Dwarf interpretation may extend to OIR-quiet candidates (Horváth et al., 2025b; Men et al., 2025). Nonetheless, a plethora of both neutron star and White Dwarf-M Dwarf binary models have been proposed to explain these new phenomena (e.g., Beniamini et al., 2023; Beniamini et al., 2020; Cooper & Wadiasingh, 2024; Qu & Zhang, 2025).

LPRTs' rapid emergence has spurred the development of novel search strategies on an accelerated timescale. The GaLactic and Extragalactic All-sky Murchison Wide-field Array (MWA)-Extended (GLEAM-X) survey's first discovery, GLEAM-X J1627-52, was found by comparing archival incoherently summed, low frequency (72 − 231 MHz) visibility data from 2 months apart (Horváth et al., 2025a; Hurley-Walker et al., 2022). These were followed by MeerKAT's (1284 MHz) PSR J0901-4046, LOFAR's (135 MHz) PSR J0250+5854, CHIME/FRB's (400-800 MHz) CHIME J0630+25 and CHIME J1634+44, all of which were discovered as single-pulses in second and millisecond resolution beamformed visibilities (Caleb et al., 2022a; Dong et al., 2025a,b; Tan et al., 2018). These beamformed discoveries resulted in higher resolution (∼arcsecond-to-arcminute) initial localizations, enabling immediate radio and multi-wavelength follow-up. In addition, ASKAP's and MeerKAT's L-band observations confirmed that LPRTs are detectable and discoverable at higher frequencies, where propagation effects like scattering in the Interstellar Medium (ISM) are less pronounced (e.g., J. Cordes et al., 1986; Jing et al., 2025; Ocker & J. M. Cordes, 2024). Notably, all LPRT discoveries have been via single-pulses or sub-pulses rather than folding on trial rotation periods[1].

Perhaps most promising is the discovery of four ASKAP LPRTs (ASKAP J1755-2527, ASKAP J1935+2148, ASKAP J1839-0756, ASKAP/DART J1832-0911), LOFAR's ILT J1101+5521, and the MWA's GPM J1839-10 and GLEAM-X J0704-37 using second-duration radio image differencing pipelines (Caleb et al., 2024; de Ruiter et al., 2025; Dobie et al., 2024; Hurley-Walker et al., 2023; Lee et al., 2025; D. Li et al., 2024; McSweeney et al., 2025; Wang et al., 2025b). Radio imaging

[1]Follow-up observations have used periodicity search and timing techniques for confirmation, but no LPRTs have been *discovered* initially using periodic search techniques.

consists of binning the U-V (East-West and North-South coordinates of each antenna pair's separation) visibility coordinates on a grid and applying a two-dimensional FFT. This is much faster than visibility beamforming and is mathematically identical, though some resolution and flux sensitivity are lost via the gridding process. The image-plane LPRT detections demonstrate that this sensitivity loss is negligible for LPRT timescales (seconds-to-minutes), motivating the development of real-time LPRT image plane search pipelines like the Commensal Real-time ASKAP Fast-Transients Coherent (CRACO) Upgrade (Wang et al., 2025a), in addition to upcoming beamformer-based searches such as the CHIME/SLOW pipeline (J. Huang et al., in prep.).

In this paper, we introduce the Deep Synoptic Array's (DSA-110) radio telescope's Not-So-Fast Radio Burst (NSFRB) pipeline, an image-plane single-pulse search for LPRTs on 0.134-160.8 second timescales. The NSFRB system builds on the existing real-time Fast Radio Burst (FRB) search, which has discovered $\sim$ 60 FRBs and localized $\sim$ 30 to host galaxies with arcsecond-scale precision (C. J. Law et al., 2024; Ravi et al., 2023; Sharma et al., 2024). In Section 5.3 we describe the NSFRB system design and search pipeline; in Section 5.4 we describe the commissioning NSFRB injection tests and observations of pulsar B0329+54; in Section 5.5 we report the results of a pilot DSA-110 NSFRB galactic plane Survey (DN-GPS); in Section 5.6 we discuss the sensitivity limits placed on LPRT emission in the galactic plane, and its implications for the White Dwarf binary model; in Section 5.7 we conclude with next steps, specifically the real-time search which is currently underway.

5.3 NSFRB System Design

The DSA-110 is a 96-antenna drift-scan (see e.g., Mantovanini et al., 2025; Wayth et al., 2015, for examples of drift-scan transient surveys with the MWA) radio interferometer at the Owens Valley Radio Observatory (OVRO) in Big Pine, CA. Details on the 64-antenna deployment and commissioning FRB survey can be found in Ravi et al. (2023). The array was completed in early 2025 by supplementing the East-West row of 47 "core" antennas with a 35-antenna North-South arm, enabling real-time localization of radio sources without incorporating the 14 long-baseline "outrigger" antennas. The antenna design, RF signal chain, baseband processing, and general compute resource layout remain largely similar to the 64-antenna deployment, and will not be detailed here. The revised visibility correlator, bandpass calibration procedures, and the FRB search pipeline will be

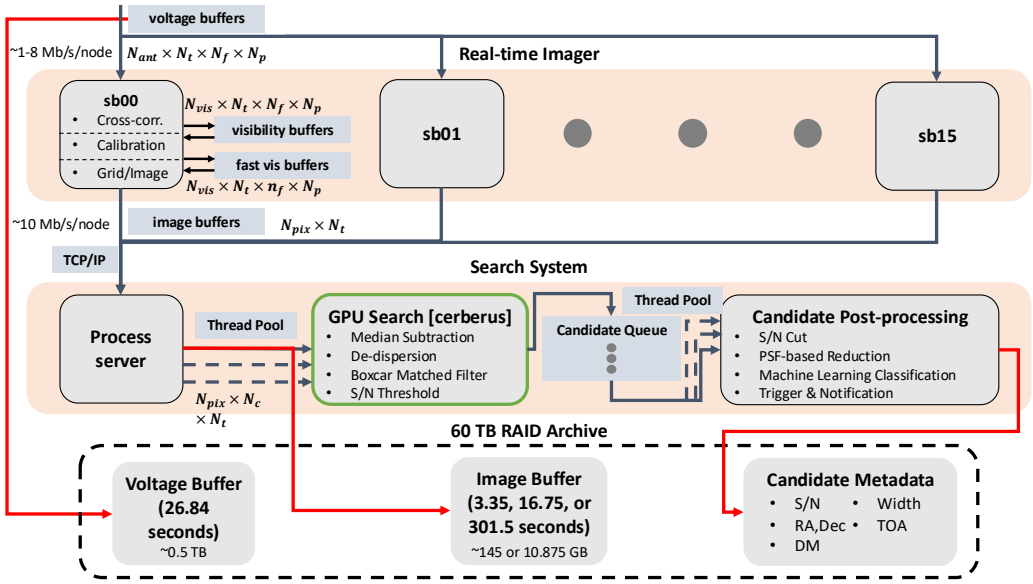

Figure 5.1: Diagram of the NSFRB Search System. Voltages for $N_{\text{ant}} = 97$ antennas, $N_t = 25$ time samples, $N_p = 2$ polarizations, and $N_f = 384$ frequency channels are pulled from a rotating PSRDADA buffer, cross-correlated, down-channelized to $n_f = 8$, and calibrated. $N_{\text{pix}} = 175 \times 175$ images are formed for each of $N_c = 16$ sub-bands and sent to the Process Server which assigns search and post-processing tasks. Image data and candidate metadata are saved to disk along with 26.8-second of voltage data triggered from the PSRDADA buffer if candidates above the 6σ threshold are identified. We outline in green the post-processor which is *not* required to operate in real-time.

discussed in detail elsewhere (Ravi et al., in prep.) For this work, we focus on components specific to the NSFRB system. Code for the NSFRB search is public at `https://github.com/dsa110/dsa110-nsfrb`, all of which is implemented using Python, leveraging the JAX[2] library to deploy GPU tasks. An ETCD[3] server is used to manage alerts and coordination between compute nodes. Figure 5.1 shows the full real-time system diagram, which we describe in the next sub-sections.

5.3.1 Fringe-Stopping and Imaging

The 187.5 MHz observing band, centered on 1.4 GHz, is split into 16×11.7 MHz sub-bands, each processed on a single compute node. Each node's correlator outputs dual-polarization $N_{\text{base}} = 4656$ cross-correlated visibilities as 384×30.5 kHz Nyquist-sampled (32.7μs) channels to a PSRDada buffer (Straten et al., 2021). For the NSFRB search, these are calibrated and fringe-stopped to the current meridian

[2] `https://docs.jax.dev/en/latest/index.html`
[3] `https://etcd.io/`

position in ∼ 3.35 second (102400 samples) chunks, down sampling to 134 ms resolution (25 samples) and 8×1.46 MHz channels. The 3.35 s fringe-stopping interval is selected to maintain point-source coherence; the fringe-timescale of the array is:

$$t_F = 648000\text{s}\frac{\lambda_c}{\pi b_{\max} 15 \cos(\delta)} \approx \frac{1.05\,\text{s}}{\cos(\delta)} \tag{5.1}$$

for the DSA-110, $b_{\max} = 2.6\,\text{km}$, $\lambda_c = 20\,\text{cm}$, where δ is the declination (e.g., Thompson et al., 2017). The array operates in drift-scan mode (no azimuthal slew) at $\delta = 71.6°$ during normal operations, making the nominal fringe rate $t_{F0} \approx 3.36\,\text{s}$.

Fringe-stopped visibilities are written to a 14.9 MB buffer read by the correlator node imager, which grids visibilities with baseline lengths $b > b_{\min} = 20\,\text{m}$ from the dense 82-antenna 'core' ($b < b_{\max} = 485\,\text{m}$) to a 175×175-pixel UV-grid. The core is assumed to be coplanar, so the W-term is neglected for normal operation; however, W-stacking is implemented and may be explored in the future (e.g., Gheller et al., 2023). Outrigger antenna data is included only for detailed manual inspection of candidates. The two visibility polarizations are summed, then approximately uniform weighting (Briggs robustness parameter $\mathcal{R} = -2$; Briggs, 1995) is applied to accumulate visibilities, and a two-dimensional inverse-FFT[4] is applied to form the final image with $\Delta\alpha = 10.3''(\cos\delta)^{-1}$, $\Delta\delta = 10.3''$ pixel scale (3 pixels per $31''$ synthesized beamwidth). The DSA-110 primary beam FWHM is roughly $\Omega = 1.5°(\cos\delta)^{-1} \times 1.5°$, while the 175×175 pixel image covers a $\Omega = 0.5°(\cos\delta)^{-1} \times 0.5°$ search region. Each of the 8 channels are imaged individually, then summed together to form a single image for each 134 ms time sample. Images on each node are then buffered (6.125 MB) for transport by an http client to a central search server.

5.3.2 `cerberus` Search Pipeline

Images are transferred from each correlator node to the search process server using TCP/IP via a 40 Gb ethernet switch, where they are associated and ordered based on their Modified Julian Date (MJD). The real-time search imposes a 3.35 second timeout to accommodate correlator node failure or high traffic from adjacent DSA-110 pipelines (e.g., the FRB search). The server manages and deploys search tasks on one of two NVIDIA GeForce RTX 2080 Ti GPUs, which are coordinated (concate-

[4]The NumPy Python Package implementation of `np.fft.ifft2d` is used for imaging. The visibility grid is first shifted using `np.fft.ifftshift` to properly order the zero-frequency component; `np.fft.ifftshift` is then applied to the resulting image.

nation, noise statistics, candidate identification, and post-processor queuing) with one of 15 reserved threads on the Intel(R) Xeon(R) Silver 4210 CPU.

The custom `cerberus` single-pulse search pipeline implements Python JAX Just-In-Time (JIT) compiled functions to de-disperse and boxcar filter images on the GPU. Data is first median subtracted in each pixel, then de-dispersed over 16 DM trials between $171-4,000\,\mathrm{pc\,cm^{-3}}$ (DM tolerance of 1.6). The JAX de-dispersion method is adapted from a custom PyTorch implementation, `PyTorchDedispersion`[5] (Kosogorov et al., 2025; Paszke et al., 2019), and allows shift indices for each frequency channel to be pre-computed and loaded onto the GPU to minimize latencies. The resulting de-dispersed time series are boxcar filtered on $\log_2$ spaced trials from 1-16 samples ($0.134-2.14\,\mathrm{s}$), and then normalized by the running standard deviation to compute the S/N. Final candidates are found by taking the maximum S/N (and its TOA) over time. A nominal 6σ signal-to-noise (S/N) threshold is imposed to identify candidates, which are pushed to the post-processor.

The search is performed at three sampling timescales: 0.134 s, 0.67 s (binned by 5 samples), and 10.05 s (binned by 75 samples). The process server bins images at each timescale as they are received, aligning them in the RA direction to account for the 25-sample fringe-stopping interval, and preserves batches for `cerberus` to re-search at the 0.67 s and 10.05 s timescales. For the real-time search, a single search iteration on the next shortest timescale (0.134 s, 0.67 s) is dropped to enable the longer timescale (0.67 s, 10.05 s) search iterations (the galactic plane data is not searched in real-time and thus does not drop iterations). The 0.67 s data is searched identically to the 0.134 s data, now probing DMs from $855-20000\,\mathrm{pc\,cm^{-3}}$ [6] with widths from $0.67-10.72\,\mathrm{s}$. The longest timescale data bypasses de-dispersion, leveraging the fact that the DM delay for DMs below $\sim 20000\,\mathrm{pc\,cm^{-3}}$ is now contained to a single sample across the 187.5 MHz band. They are then searched from $10.05-160.8\,\mathrm{s}$. The sensitivity of the search is shown in Figure 5.2, which indicates the full range of single-pulse widths the NSFRB search probes. The broad morphology of known LPRTs includes those with smooth profiles (e.g., McSweeney et al., 2025) and 'spiky' sub-pulses (e.g., Dong et al., 2025a; D. Li et al., 2024). By

[5] `https://github.com/nkosogor/PyTorchDedispersion`

[6] While it is not strictly necessary to search up to $20000\,\mathrm{pc\,cm^{-3}}$ since the peak DMs in the galactic plane typically only reach $\sim 5,000\mathrm{pc\,cm^{-3}}$, this range was selected because (1) the coarse time and frequency resolution, there is little benefit from finely sampled DM trials, and (2) extending the DM range by exactly 5× for data sampled at 5× lower resolution allows the GPU search code to utilize the same pre-computed shifts, thus saving GPU compute time and memory by only loading the the lookup table once.

searching at multiple timescales, `cerberus` will be sensitive to both morphologies.

Figure 5.3 shows the sensitivity as a function of DM for the de-dispersion schemes on each search timescale. We compute the total smeared pulse width by summing in quadrature the intrinsic pulse width $W_{\rm int}$, search timescale t_s, the dispersive smearing in the lowest frequency channel $t_{\Delta\nu} = (0.0083\,{\rm ms})\Delta\nu_{\rm MHZ}{\rm DM}\nu^{-3}_{\rm min,GHZ}$, and the dispersive delay across the full bandwidth after de-dispersion to the nearest trial DM $t_{\rm BW} = (4.15\,{\rm ms})|{\rm DM} - {\rm DM}_{\rm trial}|(\nu^{-2}_{\rm min,GHZ} - \nu^{-2}_{\rm max,GHz})$. The S/N relative to DM=0 is then:

$$ {\rm S/N}_{\rm rel}({\rm DM}) = \sqrt{\frac{\sqrt{W^2_{\rm int} + t^2_s + t^2_{\Delta\nu} + t^2_{\rm BW}}}{t_s}} \tag{5.2} $$

Thus ${\rm S/N}_{\rm rel}({\rm DM})$ is the S/N relative to that of a pulse with negligible $W_{\rm int}$ at DM = 0. Figure 5.3 shows ${\rm S/N}_{\rm rel}$ for each `cerberus` search timescale. We observe first that the relative S/N drops rapidly below 60% on the 134 ms timescale for ${\rm DM} \gtrsim 4,000\,{\rm pc\,cm^{-3}}$, and that pulses beyond ~ 540 ms (covered by the two longest trial widths) have $\lesssim 40\%$ even at DM = 0. This motivates the 670 ms search, which preserves $\gtrsim 60\%$ relative S/N for $670 - 1350$ ms timescales while minimizing S/N loss at high DM trials. Finally, the S/N loss flattens between trials for long trial widths, allowing the 10.05 s search to forego de-dispersion with minimal sensitivity loss while recovering the longest timescale bursts. Therefore, while binning to longer timescales loses raw fluence sensitivity as shown in Figure 5.2, it preserves sensitivity to the longest pulses at high DM trials relative to DM = 0.

5.3.3 Candidate Post-Processing

When candidates are identified, the image, S/Ns for all pixels, widths, and DM trials, and times-of-arrival (TOAs) for all pixels, widths, and DM trials are saved to disk. The candidate timestamp is pushed to ETCD which is monitored by the post-processing system. Standard post-processing is limited to the 10 highest S/N candidates, under the assumption that each image will have at most one candidate. To identify the most likely candidate, we compare the candidates' relative positions within the image to a simulated PSF. First, the PSF is thresholded at the $90^{\rm th}$ percentile to make a binary mask, which is centered on each candidate in turn. This candidate is treated as the central PSF lobe, and any other candidates within the binary mask are identified as possible sidelobes. The weighted mean S/N is computed over the central and sidelobe candidate S/Ns. After repeating with each

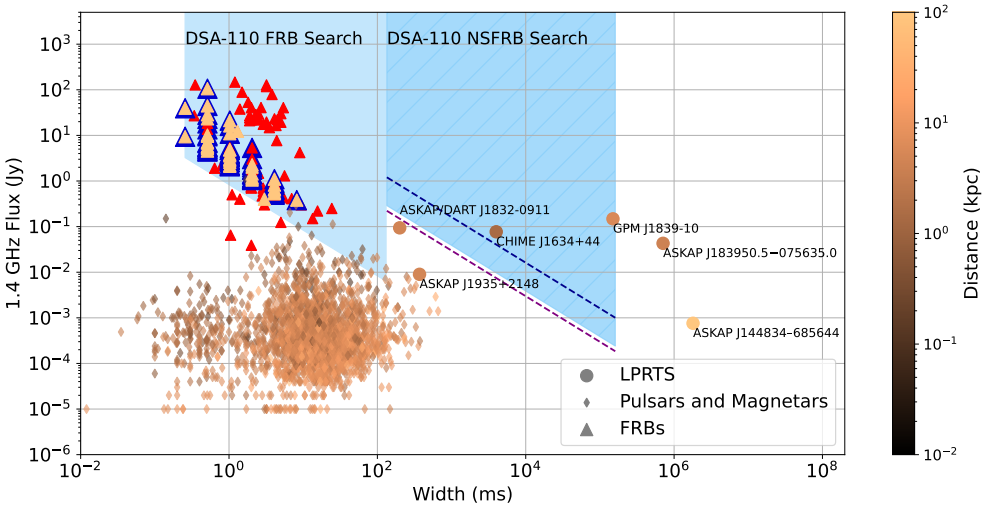

Figure 5.2: Pulse width and $6\sigma_{\rm srch}$ Fluence Sensitivity to $\Delta t = 134$ ms Bursts of the DSA-110 FRB (light blue; ~ 840 mJy ms) and NSFRB (dark blue hatched; ~ 40 Jy ms) searches. For each search we assume the fluence threshold is fixed; thus the lower border indicates the corresponding flux density threshold $6\sigma_{\rm th}\Delta t/W$ where W is the width measured at 1.4 GHz (note that in some cases (e.g., ASKAP J1832-09; D. Li et al., 2024; Wang et al., 2025b), only sub-pulses were detected at 1.4 GHz while a broader profile was detected at lower frequencies. In these cases, we still use the 1.4 GHz sub-pulse width). The dark blue dashed line shows the 90% completeness limit $25\sigma \approx 1200$ mJy ($25\sigma\Delta t \approx 160$ Jy ms; see Section 5.4.2). The purple dashed line shows the theoretical radiometer $6\sigma_{\rm th}$ sensitivity of the NSFRB survey. 1.4 GHz fluences and widths are shown for radio pulsars in the ATNF catalog (diamonds), FRBs from the literature (triangles), and LPRTs (circles). DSA-110 FRBs have dark blue outlines and show their detection pulse widths and S/N rather than refined estimates from baseband analysis. The colorbar indicates distance estimates in kpc (FRB luminosity distances are computed from host Galaxy redshifts; pulsar, magnetar, and LPRT distances are from parallaxes where available, and DM distance limits for the rest of the sample). Note that only pulsars, FRBs, and LPRTs with 1.4 GHz detections are shown.

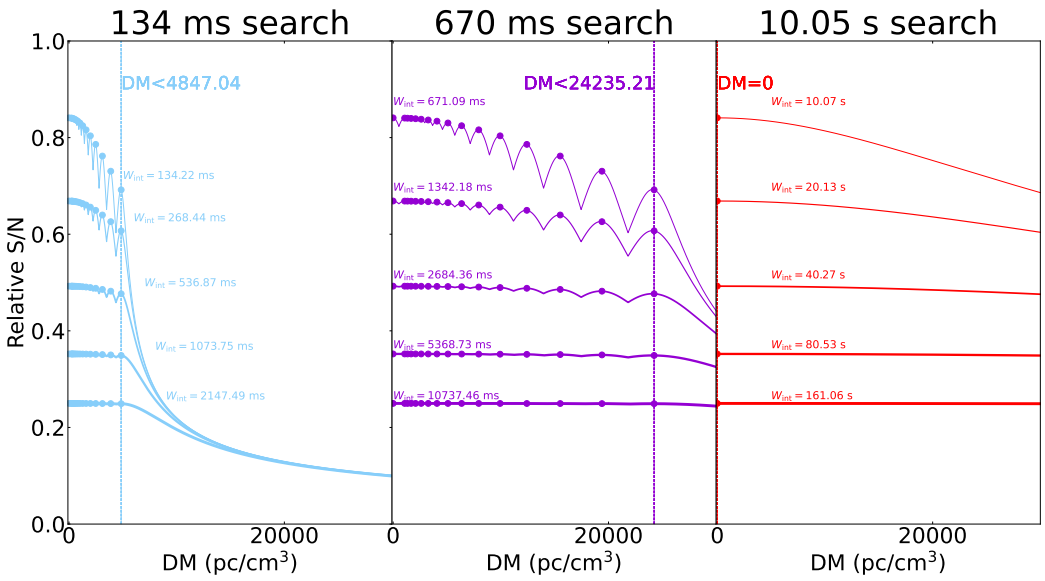

Figure 5.3: Relative S/N Loss (Equation 5.2) of NSFRB Search on the Three `cerberus` Timescales (134 ms, 670 ms, and 10.05 s) as a Function of DM. Each line corresponds to an intrinsic pulse width $W_{\rm int}$, and solid points indicate each trial DM.

candidate, the maximum S/N is identified and its central lobe candidate's width, DM, position, and TOA are taken as the final, most-likely candidate.

The second major post-processing stage is to apply a three-stage Convolutional Neural Network (CNN) classifier to the image (centered on the TOA) to identify and rule out Radio Frequency Interference (RFI). The CNN is trained on a set of simulated point sources, simulated near- and far-field RFI (examples of RFI are shown in Appendix 5.10.2), and field data sets of RFI and pulsar B0329+54 from NSFRB commissioning. The model consists of successive convolutional blocks with batch normalization, nonlinear activations, and max-pooling, followed by a small fully connected head with dropout; the CNN parameter learning rates are optimized with an Adaptive Moment Estimation (`Adam`; Adam, 2014) optimizer using a binary cross-entropy loss. After applying the trained model to the 3D image cube (position, time, frequency), the network outputs a single logit for each candidate which, after a sigmoid activation, we interpret as the RFI probability $p_{\rm rfi}$ (0 indicates likely astrophysical; 1 indicates likely RFI). Simulated injection tests and pulsar observations were used to verify classifier performance. Positively identified candidates are assigned a candidate name and metadata (RA, DEC, TOA, DM, width, and S/N) are saved to a `json` file. A candidate plot is saved and pushed as a Slack alert for human inspection; this shows the time and frequency averaged

image, the S/N as a function of trial DM and width for the final candidate pixel, the dynamic spectrum from the final candidate pixel, and the de-dispersed time series from the final candidate pixel. Finally, a trigger is sent to the correlator nodes to dump voltage data for a 26.85 second interval around the burst to disk for offline analysis and localization; voltage triggering is still being implemented. Code for the NSFRB pipeline, including imaging, data transfer, searching, and post-processing, is publicly available at `https://github.com/dsa110/dsa110-nsfrb`.

5.4 Commissioning Injection and Pulsar Tests

NSFRB commissioning observations took place from February — October, 2025, including injection testing, pulsar observations, continuum source observations, and an offline galactic plane Survey (February - April). The latter two are discussed in Section 5.5.

5.4.1 Initial S/N Threshold Optimization

We conducted a simulated pulse injection test to estimate an optimal S/N threshold which could be tuned further throughout commissioning. First, ~ 200 boxcar-shaped pulses with DMs between $0 - 4,000\,\mathrm{pc\,cm^{-3}}$, widths between $0.134 - 2.14\,\mathrm{s}$, and S/N between $0 - 10\sigma$ were generated. The amplitude of each burst is scaled based on noise estimates from imaged fast visibility data. These were sent to the process server and searched, with the peak S/N candidate identified and saved. We then compute a false-negative rate (fraction of missed injections) as a function of trial S/N thresholds from 0 to 20. Approximately two-thousand noise realizations without pulses were similarly sent through the search pipeline to estimate the false-positive rate as a function of S/N threshold. We simultaneously minimize the false-positive and false-negative rates with respect to S/N threshold, obtaining an optimal 6σ detection limit. This 6σ threshold was used for the galactic plane survey, while a more stringent 8.5σ has been adopted for the real-time pipeline to limit false positives while commissioning observations are completed. The threshold for the real-time search will be further tuned as we better characterize the RFI environment and noise statistics.

5.4.2 Detection Rate Injection Tests

We repeat the simulated injection test using the 6σ threshold and the complete post-processing pipeline, generating 50 injections per S/N bin between $1 - 40\sigma$ at randomly selected trial DMs and pulse widths. Figure 5.4 shows the resulting

detection rate, computed as the fraction of recovered injections in each S/N bin. The blue curve includes any candidates detected with S/N> 6σ; from this we estimate the search is > 90% complete for S/N> 25σ. In Section 5.5.4 we use this as the completeness flux limit for the NSFRB search.

As expected and shown by the red curves in Figure 5.4, the classifier reduces the search completeness by assessing each injection based on factors other than S/N (e.g., frequency extent, similarity to the point-spread function). The nominal search uses an RFI probability threshold $p_{\rm rfi} < 15\%$ for the CNN to reduce false-positives; for this we estimate an asymptotic detection rate of $\hat{f} \approx 40\%$. In Section 5.5.4, we incorporate this factor to estimate Poissonian burst rate limits.

Raising the threshold to $p_{\rm rfi} < 50\%$ recovers more injections but is less effective rejecting RFI. As new data is incorporated into the training set in future surveys, we expect this issue to improve gradually. The injection test also indicates some limitations of the search pipeline:

- The instantaneous noise estimate can be biased high for wider injections (8-16 samples) which lowers some candidates' S/N;
- Injections for which the burst (lowest frequency channel) is not at 50% phase are often rejected, which is mitigated by the centering method (see Section 5.3.3) but will limit detection of bursts with the incorrect TOA;
- In a small fraction of cases, the PSF clustering technique identifies "off-axis" candidates as opposed to the central candidate; further characterization of the clustering pipeline is needed to understand what properties cause this.

These limitations will be investigated in future work.

5.4.3 Pulsar Observations

Observations of pulsar B0329+54 ($P = 0.7145$ s, pulse profile FWHM= 6.6 ms, $S_{1.4\,\rm GHz} = 203$ mJy; Manchester et al., 2005) were used to monitor the system's sensitivity to transient pulsed emission which the NSFRB search is targeting. This pulsar is selected for its high pulse period ($\sim 5 \times 134$ ms samples), long pulse duration, and high flux; it is the only northern sky pulsar with an expected single-pulse S/N> $5\sigma_{\rm srch}$. Single pulses (filling the remaining samples with Gaussian noise) from initial observations were used to train the CNN classifier. Later observations then properly detected and classified the pulsar. Figure 5.5 shows a candidate

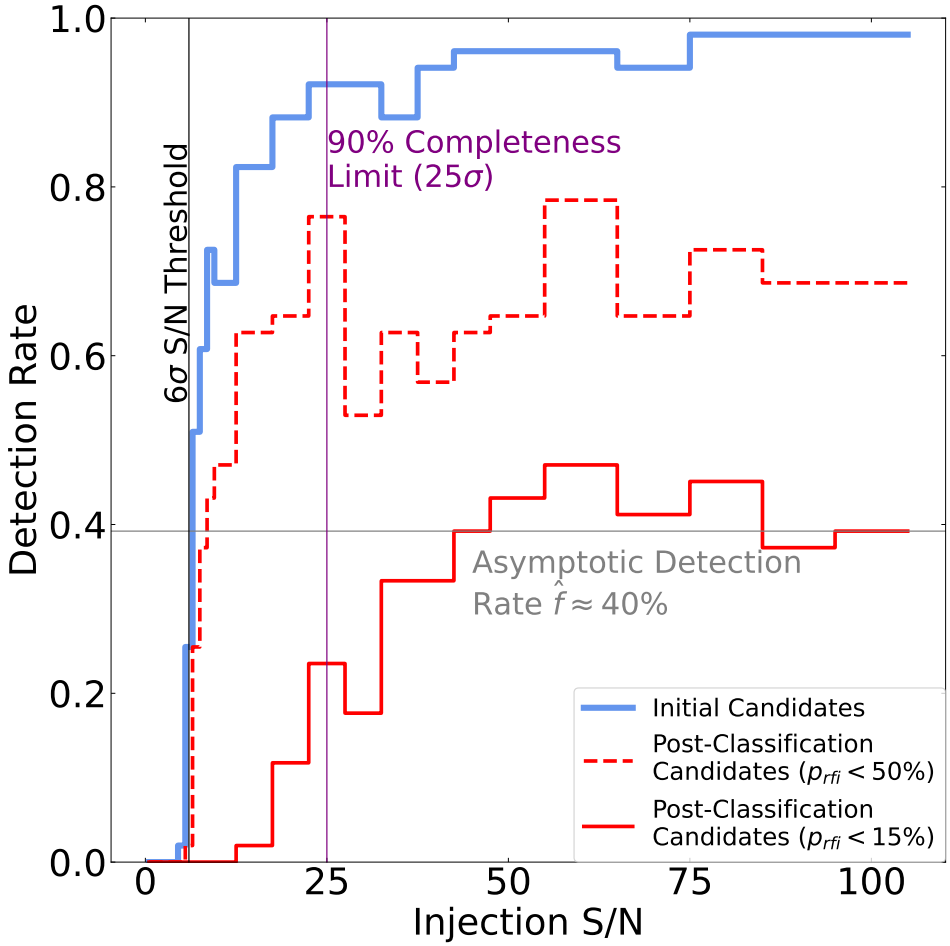

Figure 5.4: Detection Rate vs. Input S/N for Injection Test. The blue curve includes any candidates detected with S/N> 6σ while the red curves include only candidates classified as sources by the CNN classifier using probability thresholds $p_{\rm rfi} < 50\%$ (dashed) and $p_{\rm rfi} < 15\%$ (solid). The black line indicates the 6σ threshold determined in Section 5.4.1.

summary plot in which one of the five visible B0329+54 pulses was detected, demonstrating that the NSFRB search is sensitive to both single-pulsed and periodic emission. Note that pulsar B0329+54 has DM= 26.76410 pc cm^{-3}, but was detected at the DM=0 pc cm^{-3} trial bin due to the coarse trial DM spacing. The next DM trial is 213.72 pc cm^{-3}.

The pulsar was observed during its transit for four consecutive days (MJDs 60947 — 60950; September 29 — October 2, 2025) to characterize the search sensitivity at each stage of the pipeline. Figure 5.6 summarizes the results; 2039 total pulses were recorded, with 1,863 detected above $3\sigma_{\rm srch}$. The search is limited to report only one candidate per 3.35 s timeseries; therefore, we expect $2039 \times (134\,{\rm ms}/0.7145\,{\rm s}) \approx$ 382 final candidates from the 2,039 total pulses. 8,621 total candidates above the 8.5σ real-time threshold were detected; PSF-based reduction resulted in 1,511 candidates; the classifier then allowed through 33 final candidates for which alerts were sent, a roughly 9% detection rate. No final candidates were identified on October 1, 2025; inspection of the data implies this was due to higher-than-average RFI contamination and an unfortunately timed system restart. From the TOA histogram, it appears that the two brightest peaks of the B0329+54 profile are detected while the third is not, though we do not perform rigorous timing; the full profile shape is in part limited by the sampling time. The S/N distribution of pulses $> 3\sigma$ peaks near 19σ which is consistent expectations from the known 1.4 GHz flux and NSFRB sensitivity. The B0329+54 observations demonstrate the pipeline has sensitivity aligned with theoretical predictions, can decimate a large number of triggers to a manageable number of candidates, and can properly classify real astrophysical single-pulses.

5.5 The DSA-110 NSFRB galactic plane Survey (DN-GPS)

5.5.1 Survey Strategy

The NSFRB instrument conducted an inaugural survey of the galactic plane (GP) from February 18 - April 23, 2025 (MJD 60724 - 60788). The DSA-110 is a 'drift-scan' telescope, meaning that it cannot slew in the azimuthal direction. Visibilities are instead fringe-stopped to the meridian in 3.35 second (25×134 ms sampled) integrations as the sky drifts overhead. To track the galactic plane, antennas were slewed in elevation every hour, initially pointing south of the plane and recording data as the plane transited across the field-of-view. This method enables roughly 10 degrees coverage above and below the plane on each slew. This was repeated approximately daily starting 3 degrees further south each day, but slewing by the

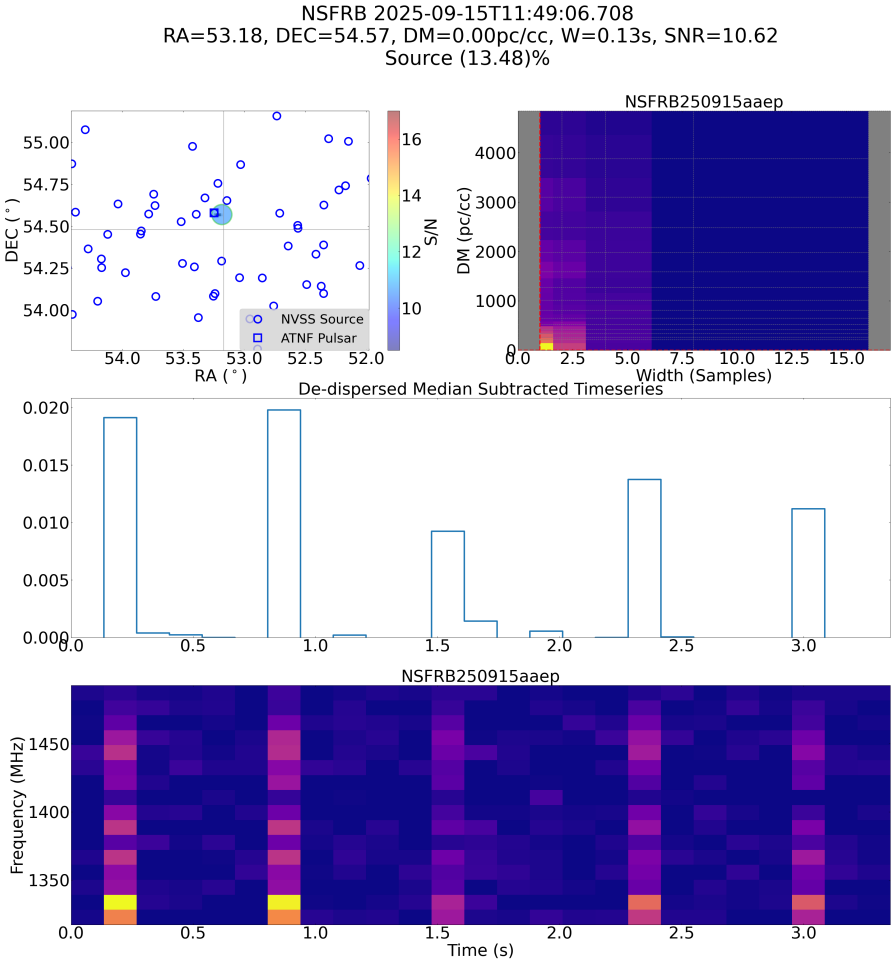

Figure 5.5: Example NSFRB candidate plot from detections of pulsar B0329+54. (top left) Position of the candidate (shaded circle) in reference to the pulsar's catalogued position (open blue square) and other field NVSS continuum sources (open blue circles). The colorbar corresponds to the S/N. (top right) S/N as a function of search DM and pulse width. (middle) DM=0 0.134 ms-sampled time series of the peak candidate in arbitrary units. (bottom) Dynamic spectrum of the peak candidate with coarse 12 MHz channels. The title gives the UTC time of the first time sample, RA and declination after systematic error correction, detected DM, pulse width, and S/N, and the CNN classifier's p-value.

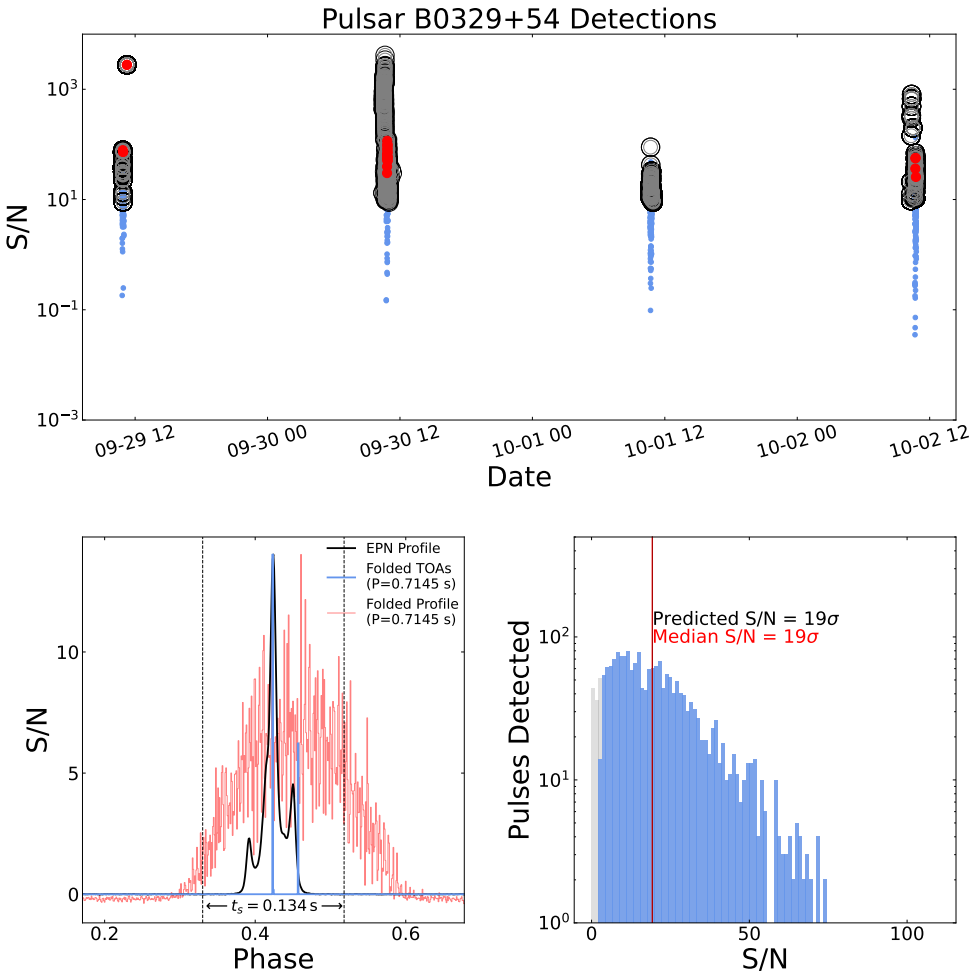

Figure 5.6: Summary of Pulsar B0329+54 Monitoring Observations. (Top) The S/N of all pulses measured from predicted Times-of-Arrival (TOAs) are in blue. Initial candidates above the 8.5σ threshold are in grey, remaining candidates after PSF-based reduction are in black, and final candidates after classification are in red. (Bottom right) The S/N distribution of all single-pulses above 3σ are in blue, while 'non-detections' below 3σ are in grey. The median of the > 3σ distribution is indicated in red and compared to the predicted S/N in black. (Bottom left) The folded pulse profile (S/N-weighted histogram of full timeseries) with 1,036 phase bins is shown in red while a histogram of peak TOAs is shown in blue. Note that the folded profile TOAs are not phase connected between days, nor are they phase connected to past observations (e.g., Deller et al., 2019). The profile from the European Pulsar Network (EPN) database is shown in black (Seiradakis et al., 1995). The TOA histogram is normalized such that the sum equals the mean TOA S/N, while the EPN and folded profiles are scaled to match the TOA histogram peak. The sampling time 134 ms, which limits the pulse profile resolution, is shown in phase units as black dashed lines.

same hourly step-size. This strategy maximizes the time between slews (roughly hourly), extends vertical plane coverage, and limits instrumental strain by spacing its observation over a 12-day span. The 12-day pattern was repeated six discrete times to ensure complete coverage of the plane in the presence of maintenance or observer error. Figure 5.7 shows the DN-GPS coverage maps for each pass; the final survey covers $-3.5^\circ < b < 5.7^\circ$ and $141^\circ < l < 225^\circ$ in Galactic coordinates.

5.5.2 Astrometric Calibration

Astrometric errors for candidates from the DN-GPS are estimated by comparing measured positions of sources from the Radio Fundamental Catalogue (RFC) to their milliarcsecond scale Very Long Baseline Interferometric (VLBI) localizations (Petrov & Kovalev, 2025). Sixteen RFC calibrators are selected as those that have 1.4 GHz flux measurements from the National Radio Astronomy Observatory (NRAO) VLA Sky Survey[7] (NVSS; Condon et al., 1998) and fall within the DN-GPS field (see Figure 5.7). We form 175×175 pixel images around each calibrator transit (between $1 - 30$ images, each averaged over 3.35 s) and use the `casatools` and `Astropy.WCS` modules to compute the RA and declination of each image pixel based on the current telescope pointing. Each image is fit with a 2D Gaussian around the main lobe of the RFC source to measure its position and align the images with each other, averaging over the full image set to maximize the signal-to-noise. This 'alignment solution' — the number of image pixels by which the source transits between each 3.35 s-fringestopped image — is also used to align images in the 0.67 s and 10.06 s search pipelines to correct small deviations from the expected transit due to the time and UV-grid resolution.

The final source position is measured from a 2D Gaussian fit of the full averaged image. We identify a statistically significant systematic position offset of $\epsilon_\alpha = -1.77' \pm 2''$, $\epsilon_\delta = -1.15' \pm 1''$ in RA and declination, respectively. After applying this correction, the remaining RMS position error is $\sigma_\alpha = 12''$, $\sigma_\delta = 7''$. Figure 5.8 (right) shows the final position offsets of the 16 calibrators with the 3σ position error circle.

[7]The NVSS survey is used because the VLA D-configuration synthesized beamsize ($\sim 46''$) is comparable to the DSA-110 core's ($\sim 31''$). Therefore, unresolved NVSS sources are most likely unresolved to the DSA-110, making flux measurements within a synthesized beam comparable.

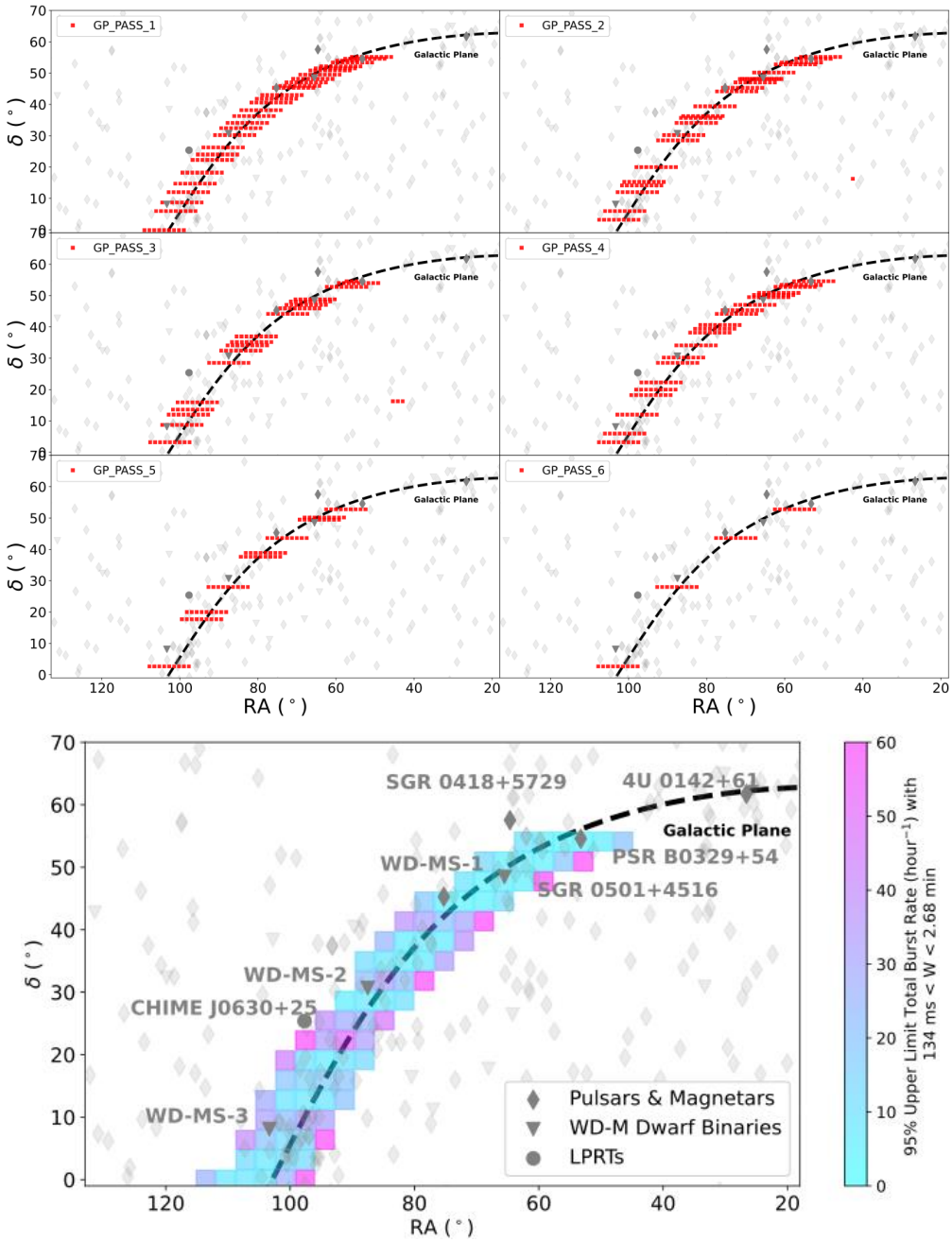

Figure 5.7: Coverage and Rate Limits for the DN-GPS pilot survey. (top) Each sub-plot shows one of six passes of the galactic plane (dashed black line). Center coordinates for each 3.35 s pointing are shown in red. The positions of known pulsars and magnetars are shown as diamonds; non-pulsar LPRTs detected to date are circles. A sample of White Dwarf-M Dwarf binaries from Rebassa-Mansergas et al. (2021) are shown as triangles. (bottom) 95% Poissonian burst rate upper limits are indicated by the colorbar for each $3° \times 3°$ grid region as discussed in Section 5.5. Sources of interest covered by the DN-GPS search region are labeled; of these, only B0329+54 is confidently detected.

5.5.3 Sensitivity and Flux Calibration

To estimate the flux sensitivity we convert the running standard deviation accumulated during the DN-GPS to flux units using 134 ms single-sample images of the 16 calibrators. The brightest source, J060351+215937 shown in Figure 5.9, is used to compute a conversion factor from arbitrary image pixel units to the NVSS catalog flux (2771.6 mJy). The same factor is applied to each calibrator observation as shown on the x-axis in Figure 5.8 (left). Applying this to an observing time-weighted average of the running standard deviation from each observing day, we estimate a sensitivity limit $\sigma_{\rm srch} \approx 50$ mJy, confirming that the calibrators follow an approximately linear relation down to the $3\sigma_{\rm srch}$ flux limit. Note the sensitivity ranged from $30 - 100$ mJy depending on the observation date. NVSS and RFC sources are observed daily during real-time observations to continuously update flux estimates; we include real-time NVSS observations in Figure 5.8 which show that fainter sources' measured flux flattens near $\sigma_{\rm srch}$ as expected.

As indicated in Figure 5.2, the measured $\sigma_{\rm srch} = 50$ mJy sensitivity exceeds the theoretical radiometer sensitivity estimate with approximately uniform $\mathcal{R} = -2$ image weights $\sigma_{\rm th} = 40$ mJy by roughly $1.3\times$. We attribute this in part to RFI excision. Both far- and near-field RFI have been observed, the former resulting from aircraft passing over the observatory and the latter from cellular networks transmitting near the center of the band. Near field RFI contributes to image-plane noise because it appears at all spatial scales rather than as a point source. The current pipeline adopts two visibility flagging criteria on the 1.5 MHz channels: (1) the mean visibility in the channel exceeds $5\times$ the running mean, (2) the peak median-subtracted visibility in the channel exceeds $10\times$ the running mean. These have proven effective in excising far-field RFI on a channel basis; however, near-field RFI may be leaking into adjacent channels, biasing the noise high in addition to the bandwidth reduction from channel flagging. Additional analysis is required to fully characterize RFI and devise techniques to recover sensitivity more robustly. Other potential effects that may lower sensitivity include primary beam attenuation, intrinsic flux calibrator variability, and poorly fit beamformer weights on a given day, which we do not investigate in detail here.

5.5.4 Results

No candidates were detected by the NSFRB pipeline from the DN-GPS data using a 6σ threshold. The data were re-searched multiple times with lower thresholds (as low as 2σ) in order to inspect low S/N candidates in more detail, resulting in no

marginal candidates. From the injection test in Section 5.4.2 we estimate the 90% completeness flux limit to be $25\sigma \approx 1200$ mJy.

As shown in Figure 5.7 (bottom), we partition the survey region into a grid of $3^\circ \times 3^\circ$ cells covering the total ~ 774 square degree survey area to estimate limits on the burst rate R_{95} from the NSFRB non-detection. Note that we neglect primary beam effects for this calculation. To do this, we first assume that $R_{95} < (\hat{f} T_{\rm obs})^{-1}$, where $T_{\rm obs} = 5$ minutes is the duration of a single pointing dataset, approximately the time for which a target remains in the DSA-110 NSFRB image field. $\hat{f}$ is the asymptotic detection rate shown in Figure 5.4, or the fraction of bursts we expect to be detected for high S/N, which we apply as an effective reduction in integration time. In this limit, we can use Poissonian statistics, adopting the weighted sum observing time from pointings that fall within each region, $T_{\rm tot,eff}$, using noise estimates from the date of observation ($\sim 40 - 60$ mJy) as inverse weights.

We estimate the upper limit on the total burst rate in each cell as $R_{95} = -(\hat{f} T_{\rm tot,eff})^{-1} \ln(0.05)$ with 95% confidence. The results are shown in Figure 5.7; we find that R_{95} ranges from $3 - 160\,{\rm hr}^{-1}$, with a weighted median $R_{95} < 14.1\,{\rm hr}^{-1}$. The tightest constraints are at low Galactic latitudes b and at declinations with the most complete coverage. For $|b| < 0.25^\circ$, the maximum burst rate upper limit among $3^\circ \times 3^\circ$ cells is $R_{95} < 17\,{\rm hr}^{-1}$ (or $< 2\,{\rm hr}^{-1}$ per square degree).

5.6 Discussion

While no candidates are detected, this is the first targeted search for LPRTs at 1.4 GHz, and the burst rate limit can be used to constrain models for LPRT emission. In this section, we contrast the detectability of two predominant models: the isolated neutron star model from Cooper & Wadiasingh (2024) and the White Dwarf-M Dwarf model from Qu & Zhang (2025).

5.6.1 Relevant Noise Estimates for Long and Short Periods

For this discussion, we partition the analysis at pulse period $P = \hat{f} T_{\rm obs} = \hat{f} \times (5\,{\rm minutes}) = 2\,{\rm minutes}$; for $P < \hat{f} T_{\rm obs}$, we assume that the LPRT is always "on", and thus if the flux exceeds the 90% completeness threshold 25σ (see Section 5.4.2) in any 5-minute observation, it will be detected. Therefore, for each $3^\circ \times 3^\circ$ grid cell, we take the minimum noise estimate among each contributing observing day as the relevant detection limit. The median among all grid cells is then $\sigma_{{\rm srch},P<2\,{\rm min}} \approx 40$ mJy.

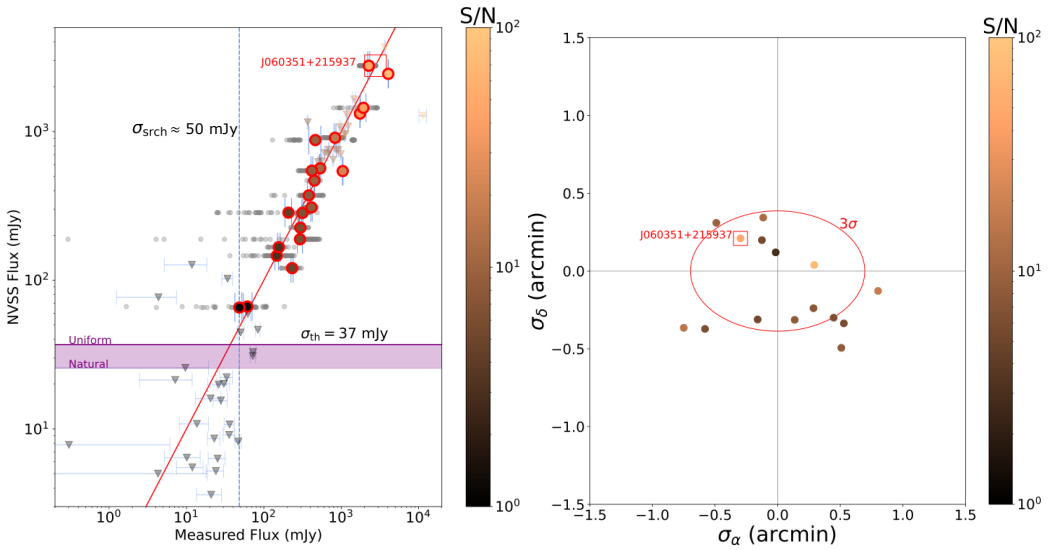

Figure 5.8: Flux and Astrometry Calibration Observations from the DSA-110 NS-FRB galactic plane Survey (DN-GPS). (Left) Measured vs. NVSS catalogued flux for the 16 calibrators selected from DN-GPS data are shown as circles. Individual measurements are in grey, while the mean measurements have colorbar equal to the observed signal-to-noise. Additional calibrator observations from the real-time pipeline are shown as triangles. The red line shows the conversion curve constrained from the brightest source, J060351+215937, and the sensitivity limit $\sigma_{\rm srch}$ is shown in blue. The range of theoretical sensitivity limits from natural to approximately uniform $\mathcal{R} = -2$ imaging weights is shown in purple. (Right) Measured position errors of the 16 calibrators, after subtracting the mean systematic offsets $\epsilon_\alpha = -1.77' \pm 2''$, $\epsilon_\delta = -1.15' \pm 1''$ from RFC positions, are shown as circles with colorbar equal to the observed signal-to-noise. The 3σ error ellipse ($72'' \times 42''$) is outlined in red.

For $P > \hat{f}T_{\rm obs}$, although the source is always "on", the long period allows us to treat it as a Poissonian process. Consider a source with $P > \hat{f}T_{\rm obs}$; since the source remains within the DSA-110 field-of-view ($\sim 1.5^\circ \cos(\delta)^{-1}$) for at most ~ 5 minutes (at the upper declination limit $\delta \approx 65^\circ$), only one pulse at most can be detected per day. The phase offset of this first pulse is effectively random since we have no prior information about the phase; subsequent bursts in contrast must be phase-connected to the first. Therefore, as we only perform a single-pulse search, the arrival of the first pulse is similar to a Poissonian random process with burst rate $\mathcal{R} \approx 1/P$. Just as the effective rate limit adopts a weighted sum observing time, $T_{\rm tot,eff}$, for each grid cell, we use the median noise estimate among each contributing observing day as the relevant detection limit. The median among all grid cells is then $\sigma_{{\rm srch},P>2\,{\rm min}} \approx 50\,{\rm mJy}$. In the next section we use $\sigma_{\rm srch} = \sigma_{{\rm srch},P<2\,{\rm min}}$ and $\sigma_{\rm srch} = \sigma_{{\rm srch},P>2\,{\rm min}}$ for $P < 2$ minutes and $P > 2$ minutes unless otherwise

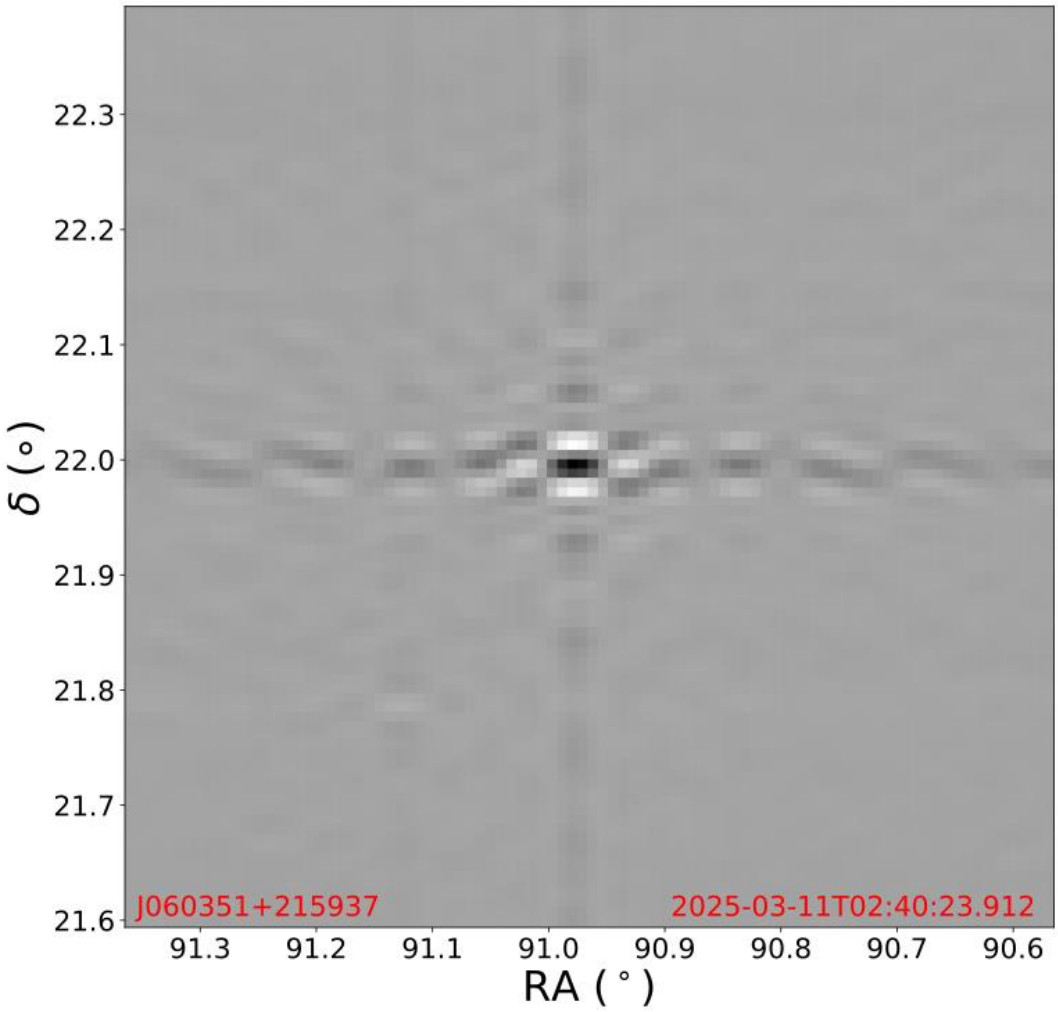

Figure 5.9: A Time- (3.35 s) and Frequency- (187.5 MHz) Averaged Dirty Image of Calibrator J060351+215937 where PSF and central sidelobes are visible. Dark regions are positive and light regions are negative in arbitrary units. J060351+215937 was the brightest calibrator observed during the DSA-110 NSFRB galactic plane Survey (DN-GPS) and was used to estimate the flux curve shown in Figure 5.8.

stated. The distinction is indicated in Figure 5.10 by a labeled vertical grey line at $P = 2$ minutes.

In the following analysis, we assume the LPRT sources are 'always active' for simplicity; some sources have appeared active for only months at a time (e.g., Hurley-Walker et al., 2022) while others have been active for decades (e.g., Hurley-Walker et al., 2023). Therefore, we leave a more detailed treatment of activity windows to future work.

5.6.2 Constraints on the White Dwarf-M Dwarf Binary and Neutron Star Models

In the Cooper & Wadiasingh (2024) neutron star model, plastic motion of the crust of a post-deathline magnetar induces twist in the magnetic field, storing magnetic energy. This energy is released over ~days, driving pair-plasma creation of charged particles. The resulting charges accelerate in a vacuum gap potential and coherently radiate via curvature radiation or inverse-Compton scattering. The maximum dissipation luminosity, which notably excludes the efficiency of pair-creation (e.g., Arendt Jr & Eilek, 2002), is below:

$$L_{\rm diss,NS} \approx \frac{v_{\rm p} B_S^2 A_{\rm fp} R_{NS}}{cP \sin^2(\theta_{\rm fp})} \tag{5.3}$$

where $v_{\rm p} \lesssim 10^6\,{\rm cm\,yr^{-1}}$ is the velocity of plastic flow, $B_S \approx 10^{15}\,{\rm G}$ is the surface magnetic field strength, $A_{\rm fp} \approx 10\,{\rm km}$ is the size of the crust 'footprint' undergoing plastic motion, and $\theta_{\rm fp}$ is the co-latitude of the footprint. By asserting that $L_{\rm diss,NS} > 25\sigma_{\rm srch} d^2 {\rm BW}$ for an LPRT at distance d within this model, and using the characteristic $B_S \gtrsim (3.2\times10^{19}\,G)\sqrt{P\dot{P}/2}$, we can solve for the maximum distance $d_{\rm max,NS}(P,\dot{P})$ to which the DN-GPS could detect the LPRT. Figure 5.10 (top) shows this result with $v_{\rm pl} = 10^4\,{\rm cm\,yr^{-1}}$; we see that for $\dot{P} > 10^{-13}$ and $P < R_{95}^{-1} = 4.3\,{\rm min}$ the search is complete to only 1 kpc. To the edge of the galaxy, approximately 30 kpc, the search is only sensitive to $\dot{P} > 10^{-10}$. Based on the $\dot{P}$ range of detected LPRTs with $P < R_{95}^{-1} = 4.3\,{\rm min}$, this indicates that the search is not sensitive to magnetar-LPRTs beyond 1 kpc. In addition, Cooper & Wadiasingh (2024) indicate that the plastic flow velocity can reasonably range from $1 < v_{\rm pl} < 10^6\,{\rm cm\,yr^{-1}}$, which is proportional to $L_{\rm diss,NS}$ and can significantly alter the horizon distance. Therefore, the search is not complete for magnetar-LPRT objects; we conclude that a population of ultra-long period magnetars may still be present within the galactic

plane despite our non-detection.

In the Qu & Zhang (2025) White Dwarf-M Dwarf binary model, the companion star orbits within the White Dwarf's magnetosphere, creating a voltage drop between the two stars via the unipolar inductor effect (Faraday disk). As charge flows between the stars due to the potential drop they create an electrical current, and the magnetosphere dissipates power via Ohmic heating, driving pair creation. Pair charges then radiate via the relativistic electron cyclotron maser mechanism. We adjust the derivation from Qu & Zhang (2025) to allow non-zero spin-down $\dot{P}$; a brief derivation is provided in Appendix 5.10.1, obtaining the following dissipation luminosity:

$$L_{\rm diss,WD} = \frac{4\pi}{c}\left(\frac{B_{\rm WD}R_{\rm WD}^3 R_c \zeta (4\pi^2)^{2/3}}{(G(M_{\rm WD}+M_c))^{2/3}}\right)^2 \left(\frac{1}{P^{14/3}} - \frac{14}{3}\frac{\dot{P}\tau}{P^{17/3}}\right) \tag{5.4}$$

where $B_{\rm WD} \approx 10^6$ G is the surface magnetic field strength of the White Dwarf star, M_{WD} and M_c are the stars' masses, R_{WD} and R_c are the stars' radii, and $\tau \lesssim 1$ Gyr is the timespan over which the White Dwarf radiates. Here we normalize $\zeta \equiv |P^{-1} - P_{\rm rot}^{-1}|P = 1$ where P is the orbital period and $P_{\rm rot}$ is the White Dwarf's rotation period; we assume $\tau \approx \tau_{\rm age} = 1$ Gyr, the typical White Dwarf age, as an upper limit, which will yield a more conservative range of $\dot{P}$ values (see Appendix 5.10.1 for justification of these assumptions). We apply the same detection condition, $L_{\rm diss,WD} > 25\sigma_{\rm srch} d^2$BW, and the resulting $d_{\rm max,WD}(P,\dot{P})$ is shown in Figure 5.10 (bottom). In this case, the DN-GPS is sensitive to WD-binary-LPRT objects within $d \lesssim 30$ kpc for $P \lesssim 50$ s. By this model, our non-detection determines that across 720 square degrees ($\sim 95\%$) of the survey region (excluding only 6 grid-points on the outskirts with $R_{95}^{-1} < 50$ s) there are no WD-binary-LPRTs with $S_{1.4\,GHz} > 25\sigma_{\rm srch,P<2\,min} \approx 1030$ mJy and $10 \lesssim P \lesssim 50$ s. While only a fraction of the allowed $P - \dot{P}$ parameter space is constrained, our results motivate further discussion of both the White Dwarf-M Dwarf binary and magnetar LPRT models.

5.7 Conclusion

We have developed and commissioned the DSA-110 NSFRB instrument, a GPU-accelerated image-plane single-pulse search sensitive to bright LPRTs with pulse widths between 134 ms−160.8 s. Initial continuum source observations have been largely successful and the pulsar B0329+54 is routinely detected. The inaugural DN-GPS survey recovered no candidates, placing limited constraints on the White Dwarf-

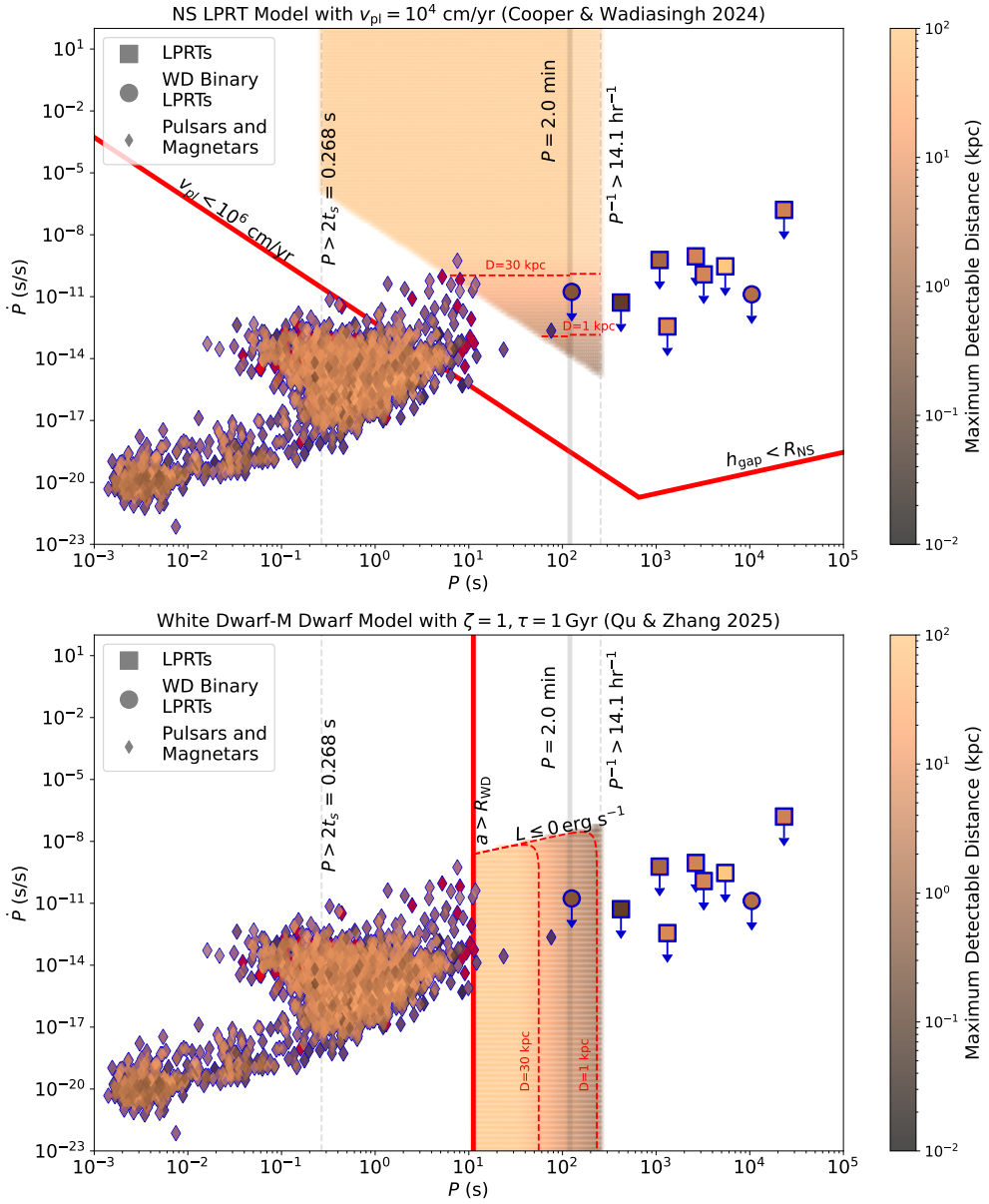

Figure 5.10: $P - \dot{P}$ Constraints from the DN-GPS Survey Using a Neutron Star Model (top; Cooper & Wadiasingh, 2024) and a White Dwarf Model (bottom; Qu & Zhang, 2025). In each plot the thick red lines bound the allowed emission ranges for each model. Vertical grey lines indicate hard limits from the DN-GPS search due to the sampling time and Poissonian burst rate. Pulsars (diamonds), WD binary LPRTs (squares) and all other LPRTs (circles) are colored with their distance estimates, while those without distances are in red. The colorbar also highlights the maximum detectable distance ($d_{\max}(P, \dot{P})$) for each model (see Section 5.5) given the DN-GPS $25\sigma_{\mathrm{srch},P<5\,\mathrm{min}} \approx 1030\,\mathrm{mJy}$ and $25\sigma_{\mathrm{srch},P>5\,\mathrm{min}} \approx 1200\,\mathrm{mJy}$ detection limits for $P < 2\,\mathrm{min}$ and $P > 2\,\mathrm{min}$, respectively. Red dashed lines are contours of constant $d_{\max}(P, \dot{P})$).

M Dwarf binary model. The real-time NSFRB search is online in drift-scan mode, adopting hourly source injections, daily calibrator and pulsar observations, and weekly construction of classifier re-training sets from false-positive detections for system health evaluation. Future work will explore triggered periodicity searching, further expansion of the pulse width range, and more DN-GPS-like surveys of the galactic plane, star-forming regions, and globular clusters.

5.8 Data Availability

The NSFRB code is publicly available at `https://github.com/dsa110/dsa110-nsfrb`.

5.9 Acknowledgments

The authors would like to thank Adam Dong, Maura McLaughlin, Duncan Lorimer, Scott Ransom, Bing Zhang, Tony Rodriguez, Assaf Horesh, Jayanta Roy, Bhaswati Bhattacharyya, Emmanuel Fonseca, Graham Doskotch, Natasha Hurley-Walker, and Kshitij Bane for creative discussions exploring the unique nature of LPRTs and novel ways to search for them. The authors thank the anonymous referee for offering constructive comments that improved the quality of the final manuscript. This work includes data from the Radio Fundamental Catalogue (RFC; `www.doi.org/10.25966/dhrk-zh08`) This material is based upon work supported by the National Science Foundation Graduate Research Fellowship under Grant No. 2139433. The authors thank staff members of the Owens Valley Radio Observatory and the Caltech radio group, whose tireless efforts were instrumental to the success of the DSA-110. The DSA-110 is supported by the National Science Foundation Mid-Scale Innovations Program in Astronomical Sciences (MSIP) under grant AST-1836018.

5.10 Appendix

5.10.1 Derivation of Time-dependent Dissipation Luminosity for the White Dwarf Model

In this appendix, we derive equation 5.4 incorporating time dependence. Starting from Equation 9 in Qu & Zhang (2025), the total voltage when the White Dwarf and M-dwarf are at a separation $a(t)$ is given by:

$$\Phi(t) = \frac{2\mu R_c}{ca(t)^2}\zeta\Omega(t) \tag{5.5}$$

where we introduce time-dependence in the orbital period $P = 2\pi/\Omega$ and orbital

separation a, and define $\zeta \equiv |\Omega - \Omega_{\rm rot}|/\Omega \sim$ constant where $\Omega_{\rm rot}$ is the rotational period of the White Dwarf. Recall the magnetic dipole moment $\mu \approx B_{\rm WD}R_{\rm WD}^3$, and Kepler's law $a(t)^3 = G(M_{\rm WD} + M_{\rm c})P(t)^2/(4\pi)$. Plugging these in for μ and $a(t)$, respectively:

$$\Phi(t) = \frac{2B_{\rm WD}R_{\rm WD}^3 R_c \zeta (4\pi^2)^{2/3}}{c(G(M_{\rm WD} + M_c)P^2(t))^{2/3}} \frac{2\pi}{P(t)} \tag{5.6}$$

$$\Phi(t) = \frac{2B_{\rm WD}R_{\rm WD}^3 R_c \zeta (4\pi^2)^{2/3}}{c(G(M_{\rm WD} + M_c))^{2/3}} \frac{2\pi}{P^{7/3}(t)} = KP(t)^{-7/3}, \quad K \equiv \frac{4\pi B_{\rm WD}R_{\rm WD}^3 R_c \zeta (4\pi^2)^{2/3}}{c(G(M_{\rm WD} + M_c))^{2/3}} \tag{5.7}$$

Let the resistance of the magnetosphere be $R_{\rm mag} = 4\pi/c$. The ohmic dissipation power is then written as:

$$\dot{E}_{\rm diss}(t) = \frac{c}{4\pi} K^2 P(t)^{-14/3} \tag{5.8}$$

If we assume the orbital period evolves slowly as $P(t) = P_0 + \dot{P}t$ to first order, we can write the dissipation power as:

$$\dot{E}_{\rm diss}(t) = \frac{c}{4\pi} K^2 (P_0 + \dot{P}t)^{-14/3} \tag{5.9}$$

$$\dot{E}_{\rm diss}(t) = \frac{c}{4\pi} K^2 P_0^{-14/3} (1 + \frac{\dot{P}}{P_0}t)^{-14/3} \tag{5.10}$$

If $\dot{P}t \ll P_0$, we can expand this to first order:

$$\dot{E}_{\rm diss}(t) = \frac{c}{4\pi} K^2 P_0^{-14/3} (1 - \frac{14}{3}\frac{\dot{P}}{P_0}t) \tag{5.11}$$

Then, substituting in for K and evaluating at the timespan over which the White Dwarf radiates $t = \tau$, we obtain equation 5.4:

$$L_{{\rm diss},WD} \equiv \dot{E}_{\rm diss}(\tau) = \frac{4\pi}{c}\left(\frac{B_{\rm WD}R_{\rm WD}^3 R_c \zeta (4\pi^2)^{2/3}}{(G(M_{\rm WD} + M_c))^{2/3}}\right)^2 (\frac{1}{P_0^{14/3}} - \frac{14}{3}\frac{\dot{P}\tau}{P_0^{17/3}}) \tag{5.12}$$

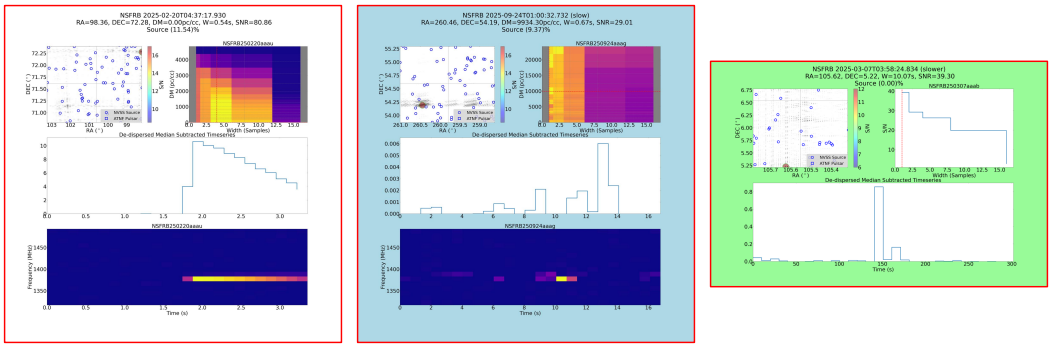

Figure 5.11: Candidate Plots for RFI Detected in the 134 ms (left) 670 ms (middle) and 10.07 s (right) Searches. Subplots for the left and middle plots are the same as described in Figure 5.5, while the right plot omits the dynamic spectrum since de-dispersion is omitted for the 10.07 s search.

Note that in general, we expect $\tau \ll \tau_{\rm age} \sim 1\,{\rm Gyr}$; for example, GPM J1839-10 was detected in archival data over the course of 36 years. Using its upper limit $\dot{P} < 3.6\times10^{-13}$ and measured $P = 31482.4$ s, we find $\dot{P}\tau/P \sim 10^{-8}$ for $\tau = 36$ years (Horváth et al., 2025b; Men et al., 2025). Even for $\tau = 1\,{\rm Gyr}$, we have $\dot{P}\tau/P \sim 10^{-1}$. Therefore we conclude the solution is valid in general for the LPRT case. Note also that ζ can vary over a wide range ($\zeta \sim 22$ for GPM J1839-10), but we normalize it to unity for this discussion as in Qu & Zhang (2025).

5.10.2 RFI Examples

Figure 5.11 shows example candidate plots for RFI on each search timescale, which was later added to the training set for the CNN classifier.

CHAPTER 5 BIBLIOGRAPHY

Adam, K. D. B. J. (2014). "A method for stochastic optimization". In: *arXiv preprint arXiv:1412.6980* 1412.6.

Arendt Jr, P. N. & J. A. Eilek (2002). "Pair creation in the pulsar magnetosphere". In: *The Astrophysical Journal* 581.1, p. 451.

Beniamini, P. et al. (2023). "Evidence for an abundant old population of Galactic ultra-long period magnetars and implications for fast radio bursts". In: *Monthly Notices of the Royal Astronomical Society* 520.2, pp. 1872–1894.

Beniamini, P., Z. Wadiasingh, & B. D. Metzger (2020). "Periodicity in recurrent fast radio bursts and the origin of ultralong period magnetars". In: *Monthly Notices of the Royal Astronomical Society* 496.3, pp. 3390–3401.

Briggs, D. S. (1995). "High fidelity deconvolution of moderately resolved sources". In: *Ph. D. Thesis*.

Bruni, G. et al. (2025). "Discovery of a persistent radio source associated with FRB 20240114A". In: *Astronomy & Astrophysics* 695, p. L12.

Caleb, M. et al. (May 2022a). "Discovery of a radio-emitting neutron star with an ultra-long spin period of 76 s". In: *Nature Astronomy* 6, pp. 828–836. DOI: 10.1038/s41550-022-01688-x. arXiv: 2206.01346 [astro-ph.HE].

Caleb, M. et al. (2022b). "Radio and X-ray observations of giant pulses from XTE J1810- 197". In: *Monthly Notices of the Royal Astronomical Society* 510.2, pp. 1996–2010.

Caleb, M. et al. (2024). "An emission-state-switching radio transient with a 54-minute period". In: *Nature Astronomy* 8.9, pp. 1159–1168.

Carli, E. et al. (2024). "The TRAPUM Small Magellanic Cloud pulsar survey with MeerKAT–I. Discovery of seven new pulsars and two Pulsar Wind Nebula associations". In: *Monthly Notices of the Royal Astronomical Society* 531.2, pp. 2835–2863.

Chrimes, A. et al. (2022). "New candidates for magnetar counterparts from a deep search with the Hubble Space Telescope". In: *Monthly Notices of the Royal Astronomical Society* 512.4, pp. 6093–6103.

Condon, J. J. et al. (1998). "The NRAO VLA sky survey". In: *The Astronomical Journal* 115.5, p. 1693.

Cooper, A. & Z. Wadiasingh (2024). "Beyond the rotational deathline: radio emission from ultra-long period magnetars". In: *Monthly Notices of the Royal Astronomical Society* 533.2, pp. 2133–2155.

Cordes, J., A. Pidwerbetsky, & R. Lovelace (1986). "Refractive and diffractive scattering in the interstellar medium". In: *Astrophysical Journal, Part 1 (ISSN 0004-637X), vol. 310, Nov. 15, 1986, p. 737-767. Research supported by the Alfred P. Sloan Foundation and Cornell University.* 310, pp. 737–767.

Cotton, W. D. et al. (Apr. 2024). "The MeerKAT 1.3 GHz Survey of the Small Magellanic Cloud". In: *MNRAS* 529.3, pp. 2443–2472. DOI: 10.1093/mnras/stae277. arXiv: 2401.11024 [astro-ph.GA].

de Ruiter, I. et al. (May 2025). "Sporadic radio pulses from a white dwarf binary at the orbital period". In: *Nature Astronomy* 9, pp. 672–684. DOI: 10.1038/s41550-025-02491-0. arXiv: 2408.11536 [astro-ph.HE].

Deller, A. et al. (2019). "Microarcsecond VLBI pulsar astrometry with PSRπ II. Parallax distances for 57 pulsars". In: *The Astrophysical Journal* 875.2, p. 100.

Dobie, D. et al. (2024). "A two-minute burst of highly polarized radio emission originating from low Galactic latitude". In: *Monthly Notices of the Royal Astronomical Society* 535.1, pp. 909–923.

Dong, F. A. et al. (2023). "The second set of pulsar discoveries by CHIME/FRB/Pulsar: 14 rotating radio transients and 7 pulsars". In: *Monthly Notices of the Royal Astronomical Society* 524.4, pp. 5132–5147.

Dong, F. A. et al. (July 2025a). "CHIME/Fast Radio Burst Discovery of an Unusual Circularly Polarized Long-period Radio Transient with an Accelerating Spin Period". In: *The Astrophysical Journal Letters* 988.1, L29, p. L29. DOI: 10.3847/2041-8213/adeaab. arXiv: 2507.05139 [astro-ph.HE].

Dong, F. A. et al. (Sept. 2025b). "CHIME/Fast Radio Burst/Pulsar Discovery of a Nearby Long-period Radio Transient with a Timing Glitch". In: *The Astrophysical Journal Letters* 990.2, L49, p. L49. DOI: 10.3847/2041-8213/adfa8e. arXiv: 2407.07480 [astro-ph.HE].

Gaensler, B. M. et al. (2005). "An expanding radio nebula produced by a giant flare from the magnetar SGR 1806–20". In: *Nature* 434.7037, pp. 1104–1106.

Gheller, C., G. Taffoni, & D. Goz (2023). "High performance w-stacking for imaging radio astronomy data: a parallel and accelerated solution". In: *RAS Techniques and Instruments* 2.1, pp. 91–105.

Han, J. et al. (2021). "The FAST Galactic Plane Pulsar Snapshot survey: I. Project design and pulsar discoveries". In: *Research in Astronomy and Astrophysics* 21.5, p. 107.

Horváth, C. et al. (Sept. 2025a). "A long period transient search method for the Murchison Widefield Array". In: *Publications of the Astronomical Society of Australia* 42, e129, e129. DOI: 10.1017/pasa.2025.10093. arXiv: 2509.06315 [astro-ph.IM].

Horváth, C. et al. (2025b). "A unified model for long-period radio transients and white dwarf binary pulsars". In: *arXiv preprint arXiv:2507.15352*.

Hurley-Walker, N. et al. (Jan. 2022). "A radio transient with unusually slow periodic emission". In: *Nature* 601.7894, pp. 526–530. DOI: 10.1038/s41586-021-04272-x. arXiv: 2503.08033 [astro-ph.HE].

Hurley-Walker, N. et al. (July 2023). "A long-period radio transient active for three decades". In: *Nature* 619.7970, pp. 487–490. DOI: 10.1038/s41586-023-06202-5. arXiv: 2503.08036 [astro-ph.HE].

Hurley-Walker, N. et al. (2024). "A 2.9 hr Periodic Radio Transient with an Optical Counterpart". In: *The Astrophysical Journal Letters* 976.2, L21, p. L21. DOI: 10.3847/2041-8213/ad890e. arXiv: 2408.15757 [astro-ph.SR].

Hyman, S. D. et al. (2005). "A powerful bursting radio source towards the Galactic Centre". In: *nature* 434.7029, pp. 50–52.

Jing, W. et al. (2025). "FAST Pulsar Database: II. Scattering profiles of 122 Pulsars". In: *arXiv preprint arXiv:2506.14519*.

Kosogorov, N. et al. (June 2025). "Implementing Continuous All-sky Monitoring with the OVRO-LWA to Identify Prompt and Precursor Counterparts of Gravitational Wave Events". In: *The Astrophysical Journal* 985.2, 265, p. 265. DOI: 10.3847/1538-4357/add014.

Kramer, M. et al. (2024). "Quasi-periodic sub-pulse structure as a unifying feature for radio-emitting neutron stars". In: *Nature Astronomy* 8.2, pp. 230–240.

Law, C. J. et al. (2024). "Deep synoptic array science: first FRB and host galaxy catalog". In: *The Astrophysical Journal* 967.1, p. 29.

Law, C. et al. (2018). "realfast: real-time, commensal fast transient surveys with the Very Large Array". In: *The Astrophysical Journal Supplement Series* 236.1, p. 8.

Lee, Y. et al. (2025). "The emission of interpulses by a 6.45-h-period coherent radio transient". In: *Nature Astronomy* 9.3, pp. 393–405.

Li, D. et al. (2024). "A 44-minute periodic radio transient in a supernova remnant". In: *arXiv preprint arXiv:2411.15739*.

Li, Y. et al. (2025). "Searching for pulsars in Globular Clusters with the Fast Fold Algorithm and a new pulsar discovered in M13". In: *arXiv preprint arXiv:2505.05021*.

Manchester, R. N. et al. (2005). "The Australia telescope national facility pulsar catalogue". In: *The Astronomical Journal* 129.4, p. 1993.

Manchester, R. N. et al. (2001). "The Parkes multi-beam pulsar survey–I. Observing and data analysis systems, discovery and timing of 100 pulsars". In: *Monthly Notices of the Royal Astronomical Society* 328.1, pp. 17–35.

Mantovanini, S. et al. (2025). "GaLactic and extragalactic all-sky Murchison Widefield Array survey eXtended (GLEAM-X) III: Galactic plane". In: *Publications of the Astronomical Society of Australia* 42, e137.

Marsh, T. et al. (2016). “A radio-pulsing white dwarf binary star”. In: *Nature* 537.7620, pp. 374–377.

McSweeney, S. J. et al. (2025). “A new long-period radio transient: discovery of pulses repeating every 1.16 h from ASKAP J175534. 9- 252749.1”. In: *Monthly Notices of the Royal Astronomical Society* 542.1, pp. 203–214.

Men, Y. et al. (2025). “A highly magnetized long-period radio transient exhibiting unusual emission features”. In: *Science Advances* 11.3, eadp6351.

Mitra, D., G. I. Melikidze, & R. Basu (2023). “Meterwavelength Single Pulse Polarimetric Emission Survey. VI. Toward Understanding the Phenomenon of Pulsar Polarization in Partially Screened Vacuum Gap Model”. In: *The Astrophysical Journal* 952.2, p. 151.

Ocker, S. K. & J. M. Cordes (2024). “NE2001p: a native Python implementation of the NE2001 galactic electron density model”. In: *Research Notes of the AAS* 8.1, p. 17.

Paszke, A. et al. (2019). “PyTorch: An Imperative Style, High-Performance Deep Learning Library”. In: *arXiv e-prints*, arXiv:1912.01703, arXiv:1912.01703. DOI: 10.48550/arXiv.1912.01703. arXiv: 1912.01703 [cs.LG].

Petrov, L. & Y. Y. Kovalev (2025). “The Radio Fundamental Catalog. I. Astrometry”. In: *The Astrophysical Journal Supplement Series* 276.2, p. 38.

Qu, Y. & B. Zhang (Mar. 2025). “Magnetic Interactions in White Dwarf Binaries as Mechanism for Long-period Radio Transients”. In: *The Astrophysical Journal* 981.1, 34, p. 34. DOI: 10.3847/1538-4357/adb1b5. arXiv: 2409.05978 [astro-ph.HE].

Radhakrishnan, V. & D. J. Cooke (Jan. 1969). “Magnetic Poles and the Polarization Structure of Pulsar Radiation”. In: *The Astrophysical Letters* 3, p. 225.

Ransom, S. M. (2001). *New search techniques for binary pulsars*. Harvard University.

Ravi, V. et al. (2023). “Deep synoptic array science: discovery of the host galaxy of FRB 20220912A”. In: *The Astrophysical Journal Letters* 949.1, p. L3.

Rebassa-Mansergas, A. et al. (Oct. 2021). “White dwarf-main-sequence binaries from Gaia EDR3: the unresolved 100 pc volume-limited sample”. In: *Monthly Notices of the Royal Astronomical Society* 506.4, pp. 5201–5211. DOI: 10.1093/mnras/stab2039. arXiv: 2107.06303 [astro-ph.SR].

Seiradakis, J. et al. (1995). “Pulsar profiles at high frequencies. I. The data.” In: *Astronomy and Astrophysics Supplement, v. 111, p. 205* 111, p. 205.

Sharma, K. et al. (2024). “Preferential occurrence of fast radio bursts in massive star-forming galaxies”. In: *Nature* 635.8037, pp. 61–66.

Singh, S. et al. (2022). "The GMRT High Resolution Southern Sky Survey for Pulsars and Transients. III. Searching for Long-period Pulsars". In: *The Astrophysical Journal* 934.2, p. 138.

Straten, W. van, A. Jameson, & S. Osłowski (2021). "PSRDADA: Distributed acquisition and data analysis for radio astronomy". In: *Astrophysics Source Code Library*, ascl–2110.

Tan, C. et al. (2018). "LOFAR Discovery of a 23.5 s Radio Pulsar". In: *The Astrophysical Journal* 866.1, p. 54.

Thompson, A. R., J. M. Moran, & G. W. Swenson (2017). *Interferometry and synthesis in radio astronomy*. Springer Nature.

Wang, Z. et al. (2025a). "The CRAFT coherent (CRACO) upgrade I: System description and results of the 110-ms radio transient pilot survey". In: *Publications of the Astronomical Society of Australia* 42, e005.

Wang, Z. et al. (June 2025b). "Detection of X-ray emission from a bright long-period radio transient". In: *Nature* 642.8068, pp. 583–586. DOI: 10.1038/s41586-025-09077-w. arXiv: 2411.16606 [astro-ph.HE].

Wateren, E. van der et al. (2023). "The LOFAR Tied-Array All-Sky Survey: Timing of 35 radio pulsars and an overview of the properties of the LOFAR pulsar discoveries". In: *Astronomy & Astrophysics* 669, A160.

Wayth, R. B. et al. (June 2015). "GLEAM: The GaLactic and Extragalactic All-Sky MWA Survey". In: *Publications of the Astronomical Society of Australia* 32, e025, e025. DOI: 10.1017/pasa.2015.26. arXiv: 1505.06041 [astro-ph.IM].

Chapter 6

POLARIMETRY OF 25 NEW FAST RADIO BURSTS PROVIDES INSIGHTS INTO THEIR ORIGINS

Sherman, M. B. et al. (2024). "Deep Synoptic Array Science: Polarimetry of 25 New Fast Radio Bursts Provides Insights into Their Origins". In: *The Astrophysical Journal* 964.2, p. 131. DOI: 10.3847/1538-4357/ad275e.

6.1 Abstract

We report on a full-polarization analysis of the first 25 as yet non-repeating FRBs detected at 1.4 GHz by the 110-antenna Deep Synoptic Array (DSA-110) during commissioning observations. We present details of the data-reduction, calibration, and analysis procedures developed for this novel instrument. Faraday rotation measures (RMs) are searched between $\pm 10^6\,\mathrm{rad\,m^{-2}}$ and detected for 20 FRBs with magnitudes ranging from $4 - 4670\,\mathrm{rad\,m^{-2}}$. 15/25 FRBs are consistent with 100% polarization, 10 of which have high ($\geq$ 70%) linear-polarization fractions and 2 of which have high ($\geq$ 30%) circular-polarization fractions. Our results disfavor multipath RM scattering as a dominant depolarization mechanism. Polarization-state and possible RM variations are observed in the four FRBs with multiple sub-components. We combine the DSA-110 sample with polarimetry of previously published FRBs, and compare the polarization properties of FRB sub-populations and FRBs with Galactic pulsars. Although FRB polarization fractions are typically higher than those of Galactic pulsars, and cover a wider range than those of pulsar single pulses, they resemble those of the youngest (characteristic ages $< 10^5$ yr) pulsars. Our results support a scenario wherein FRB emission is intrinsically highly linearly polarized, and propagation effects can result in conversion to circular polarization and depolarization. Young pulsar emission and magnetospheric-propagation geometries may form a useful analogy for the origin of FRB polarization.

6.2 Introduction

Fast Radio Bursts (FRBs) are energetic, millisecond-duration radio transients of extragalactic origin. There are now over 500 confirmed FRBs recorded in the Transient Name Server[1] (TNS) catalog (Petroff & Yaron, 2020). Several lines of

[1] https://www.wis-tns.org/

evidence point to neutron-star progenitors for FRBs, although models with, e.g., black-hole engines remain viable (e.g., B. Zhang, 2022b). Their exact emission mechanism is unknown, though multiple theories have been proposed. Some models predict emission from maser processes within the immediate plasma environments of neutron stars (Lyubarsky, 2014; Metzger et al., 2019). Others associate them with magnetospheric processes nearer to neutron-star surfaces, for example driven by crustal oscillations or magnetic reconnection (Beloborodov, 2021; Beniamini et al., 2020; Gu et al., 2016). Although both repeating and as yet one-off bursts can be described by these, other cataclysmic theories imply triggering in compact-object mergers and/or collapse that only produce one-off events (Falcke & Rezzolla, 2014; Totani, 2013). It is possible that multiple mechanisms are responsible for the FRB phenomenon, possibly even from the same source (e.g., Hewitt et al., 2023; Kirsten et al., 2023; Mckinven, 2022; Petroff, 2017). Perhaps relatedly, a remarkable diversity of progenitor host-galaxy systems is observed, including globular clusters (Kirsten et al., 2022), dwarf galaxies (Bhandari et al., 2023; Chatterjee et al., 2017), a variety of locations within galaxies on the star forming main sequence of galaxies (Gordon et al., 2023; Mannings et al., 2021), and massive quiescent galaxies (C. J. Law et al., 2024; Sharma et al., 2023).

The polarization of FRBs can be used to identify viable emission theories. Coupled with the observed high brightness temperatures $T_B \gg 10^{12}$ K, high linear polarization implies a coherent emission process such as curvature radiation, inverse-Compton scattering, or synchrotron-maser emission (e.g., C. Li et al., 2021; Qu & B. Zhang, 2023; Wang et al., 2022b). Smooth variations in the polarization position angle (PPA) over the burst durations can be associated with moving emission sites, in analogy with the rotating vector model applied to pulsar emission, or with propagation effects within or immediately outside the source magnetosphere (Cho et al., 2020; Luo et al., 2020; Oswald et al., 2023; Radhakrishnan & Cooke, 1969; Ravi & Lasky, 2016). Rapid jumps in PPA, observed in several pulsars, can indicate emission in different modes or from different locations within magnetospheres (e.g., Manchester et al., 1975; Stinebring et al., 1984). Circular polarization and depolarization from 100% linearly polarized bursts typically require mode conversion or absorption during propagation, multiple emission sites, or Faraday depolarization in a strongly magnetized, possibly inhomogeneous medium (Beniamini et al., 2022; Qu & B. Zhang, 2023). Faraday rotation measure (RM) variations observed in some FRBs also hint toward dynamic local environments of FRB progenitors (e.g., Anna-Thomas et al., 2023; D. Li et al., 2022; Mckinven et al., 2023). Each mechanism

places stringent physical constraints on the sources and near-source environments.

38 FRB sources have published polarization and/or RM data (see Appendix 6.8.1 for a detailed compilation). This small sample has limited the characterization of standard properties, although a few traits appear commonplace. Specifically, most repeating and non-repeating FRBs possess high linear polarization fractions ($\geq$ 70%) (e.g., Hilmarsson et al., 2021b; Mckinven et al., 2023; Nimmo et al., 2021). Some FRBs have exhibited non-negligible circular polarization ($\geq$ 30%, e.g., FRB 20190611B; Day et al., 2020). Repeaters appear non-uniform in their properties: some have stable polarization states like FRB 20190208A while others vary from burst to burst, like FRB 20121102A or FRB 20190520B (Anna-Thomas et al., 2023; Feng et al., 2022a; Mckinven et al., 2023). One-off bursts, for example FRB 20181112A, can have complex time-domain morphologies and polarization properties that evolve over the burst duration (Cho et al., 2020). Polarization properties so far do not appear to be a viable means of distinguishing repeaters from non-repeaters (e.g., B. Zhang, 2022b). Some repeaters exhibit smoothly time-varying RMs on week to month timescales, including FRB 20121102A, FRB 20190520B, and FRB 20180301 (Anna-Thomas et al., 2023; Hilmarsson et al., 2021a; Kumar et al., 2023). Strong burst to burst variability in linear- and circular-polarization fractions, as well as frequency-dependent oscillations in these quantities, were observed from the repeating source FRB 20201124A (Xu et al., 2022b). These were interpreted as originating during propagation through a strongly magnetized, evolving plasma environment within an AU of the FRB source. Frequency-dependent depolarization has also been observed in multiple FRBs (Feng et al., 2022b; Mckinven et al., 2023). This may be described by the stochastic RM model, in which spatial RM variations within a scattering screen depolarize FRB emission as it propagates along multiple pathways (Beniamini et al., 2022; Melrose & Macquart, 1998; Yang et al., 2022). No systematic studies of the polarization properties of as yet non-repeating FRBs have been published.

During the commissioning phase of the 110-antenna Deep Synoptic Array (DSA-110), an FRB survey at declination $\delta = 71^\circ$ at 1.4 GHz observing frequency was conducted. This paper reports on polarimetry of the first 25 FRBs detected with the DSA-110. The remainder of the paper will proceed as follows. Section 6.3 will describe the DSA-110 observations, polarization pipeline and methods for RM synthesis. We present linear- and circular-polarization fractions for 25 FRBs and RMs for 20 FRBs. Section 6.4 presents and discusses the physical implications of

Table 6.1: Table of Frequently Used Symbols and Abbreviations

Symbol/ Abbreviation	Units	Definition
PA, χ	$^\circ$	Observed linear-polarization position angle without correcting Faraday rotation
PPA, χ_0	$^\circ$	Intrinsic linear polarization position angle after correcting for all Faraday rotation
L/I	%	Frequency- and time-averaged debiased fractional linear polarization
$\|V\|/I$	%	Frequency- and time-averaged fractional absolute value circular polarization
V/I	%	Frequency and time-averaged fractional signed circular polarization
RVM		Rotating vector model
AP		Average profiles of Galactic pulsars
SP		Single pulses from Galactic pulsars
S/N		Signal to noise ratio

polarization subgroups based on the DSA-110 sample. In Section 6.5 we combine the DSA-110 sample with previously published FRBs to compare the polarization properties of repeaters and non-repeaters, and of FRBs with Galactic pulsars. The latter two sections include significant interpretation and discussion. We conclude in Section 6.6. We encourage the reader to peruse the extensive appendices for a detailed description of methodology in data reduction, analysis and interpretation, as well as a compilation of our data and literature data on FRB and pulsar polarization. We use a selection of symbols and common abbreviations summarized in Table 6.1. Calibrated full-polarization filterbank data and derived parameters in RMTable format[2] are made available on the CaltechDATA public repository[3]. These can be accessed through the DSA-110 archive (Morrell & C. J. Law, 2022).[4] Additional data will be made available upon request to the corresponding author.

6.3 Observations and data analysis

The DSA-110 array is currently in its commissioning phase. During the observations reported here, spanning January–November 2022, the array consisted of 48 core antennas for FRB searching, and 15 outrigger antennas to assist in FRB localization.

[2] `https://github.com/CIRADA-Tools/RMTable`

[3] `https://data.caltech.edu/`

[4] `https://code.deepsynoptic.org/dsa110-archive/`

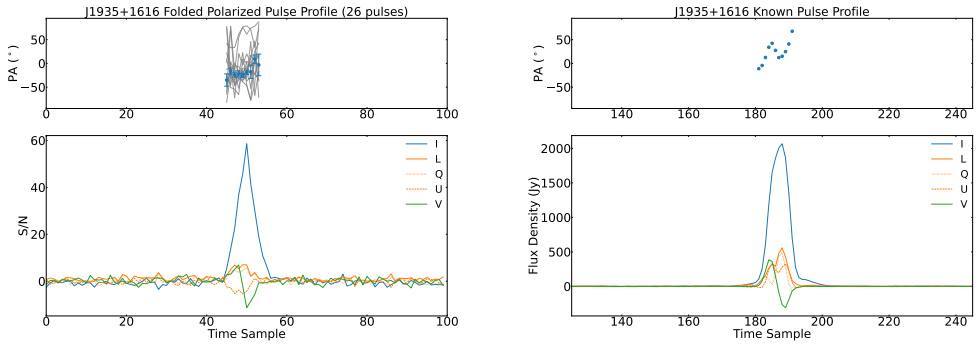

Figure 6.1: Comparison of the pulse profile of PSR J1935 + 1616 observed with the DSA-110 (left) to an archival profile from the European Pulsar Network (right). The observed profile was formed by centroiding and stacking 26 single-pulse detections automatically triggered and processed identically to DSA-110 FRBs. The top panels show the PA of the average profile (blue), and for the DSA-110 bursts, the PA of single pulses (grey). The bottom panels show the Stokes parameters and linear-polarization fraction (L/I) as labeled. Besides a PA offset of unknown origin, the profiles are otherwise similar.

Each 4.65-m antenna is equipped with dual orthogonal linearly polarized receivers, operating between 1280–1530 MHz. A linear basis using the IAU/IEEE handedness convention[5] is used for all polarimetry analysis discussed herein. The antennas are movable in elevation only, and are always pointed at the meridian. All FRBs we present here were detected during a survey at a declination of 71.6°. Ravi et al. in prep. will describe the instrument in detail, and some details have been included in previous publications on DSA-110 FRBs (e.g., C. J. Law et al., 2024; Ravi et al., 2023). None of the FRBs presented here have been observed to repeat by the DSA-110 in 150 hours of observing time during 2022 (C. J. Law et al., 2024), and we consider them as non-repeaters for the purposes of our analysis. Of the sample of 25 FRBs presented here, arcsecond-scale localizations, and secure host-galaxy association and characterization have been summarized for 11 events by C. J. Law et al. (2024). As this paper is focused on the intrinsic polarization properties of the DSA-110 and other FRBs, we do not utilize information (e.g., redshifts) derived from host-galaxy data. A discussion of the RMs of the localized DSA-110 and other FRBs are presented in the companion paper, Sherman et al. (2023).

The calibration and analysis of the full-polarization properties of the 25 FRBs

[5]The IAU/IEEE convention assumes that $V > 0$ is right-hand polarization, while $V < 0$ is left-hand polarization (Van Straten et al., 2010).

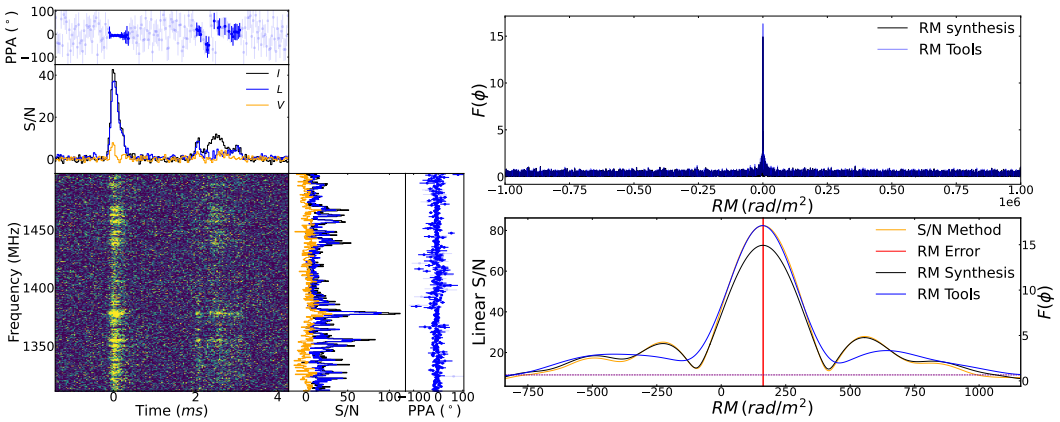

Figure 6.2: Summary of polarization and RM data on FRB 20220207C (***Zach***). Identical plots on all FRBs presented herein are shown in Appendix 6.8.12. *Left:* From top, we show the PPA (with 1σ errorbars) measured after correcting for RM, and frequency averaged time series of Stokes I, L, and V. The PPA is highlighted in bins with linear-polarization S/N $> 3\sigma$. The dynamic spectrum is shown at center, to the right of which are shown optimally summed spectra (Appendix 6.8.8) and the spectrally resolved PPA with $> 3\sigma$ bins highlighted. *Right:* The top panel shows the RM spectra evaluated over the full range of sensitivity using two different methods (Appendix 6.8.9), and the bottom panel shows a detailed analysis of the S/N of the peak.

described herein were carried out using standard techniques. The chief novelty of the present analysis is that it is developed from the ground up using a custom implementation on a new telescope. Novel methods were developed for certain aspects of the analysis, such as the estimation of accurate RMs and the corresponding uncertainties. A summary of the calibration and analysis techniques can be found in Appendix 6.8.2, and Appendices 6.8.3 to 6.8.9 justify them in detail.

In this section we show a single demonstration of the functioning of the polarization calibration and analysis pipeline. Figure 6.1 displays the calibrated, summed, polarized profile formed from 26 single-pulse detections of bright pulses from the PSR J1935+1616 (B1933). These pulses were detected and processed in exactly the same way as the DSA-110 FRBs. A comparison is made to the reported average profile from the European Pulsar Network (EPN) database of pulsar profiles (Gould & Lyne, 1998)[6]. Good agreement between the DSA-110 polarization profile and the EPN profile is found: note particularly the swing in Stokes V. A time offset in the linear polarization peak is observed, which is attributed to low signal-to-noise of the DSA-110 profile, and pulse summation based on simple centroiding and stacking.

[6] `http://www.epta.eu.org/epndb/`

An offset in PA is evident between the profiles: our method for deriving PAs is given in Appendix 6.8.4, and it is unclear exactly what method was used in calibrating the EPN profile. Additional details on verification of the polarization pipeline with J1935+1616 are given in Appendix 6.8.7.

We present polarization and RM results on all FRBs in Appendix 6.8.12. Figures 6.14 to 6.17 show calibrated and RM-corrected burst temporal profiles and dynamic spectra. Figures 6.18 to 6.20 show RM spectra for all FRBs with detectable RMs. Table 6.2 summarizes the various polarization fractions and RMs for each FRB. Throughout this paper we sometimes refer to DSA-110 FRBs by their internal natural names (e.g., FRB 20220207C is referred to as ***Zach***). Correspondence between the natural and formal names is noted in Table 6.2. Example plots for FRB 20220207C are shown in Figure 6.2.

6.4 Discussion of Individual Burst Polarization Properties

6.4.1 Motivation for Polarization-based Classification

The DSA-110 FRB sample spans a wide range of polarimetric and spectro-temporal properties. This is the largest uniform sample of FRB polarization, and motivates its use as a basis for a polarization-dependent classification scheme. The need for such classes stems from the ability of polarimetry to distinguish FRB emission and propagation models. The high brightness temperatures observed in FRBs require a coherent, highly polarized emission process (e.g., Luan & Goldreich, 2014). This could apply to pulsar-like 'antenna' mechanisms driven by charged particle bunches within the magnetosphere or synchrotron 'maser' emission via a shocked wind outside the magnetosphere (e.g., Metzger et al., 2019; Qu & B. Zhang, 2023; Wang et al., 2022a,b; B. Zhang, 2022a,b).

'Antenna' mechanisms appear more likely, since the observed circular polarization and de-polarization in FRBs require propagation through an extreme local plasma environment. For example. Faraday Conversion (FC) and cyclotron absorption each result in circular polarization; their presence would represent evidence of a highly magnetized, dense plasma nearby the source (e.g., Gruzinov & Y. Levin, 2019; Kumar et al., 2022; Qu & B. Zhang, 2023; Suresh & J. M. Cordes, 2019; Vedantham & Ravi, 2019). Similarly, depolarization can indicate either multi-path scattering through a screen with non-uniform RM (e.g., Melrose & Macquart, 1998), or the superposition of multiple emission modes (e.g., Mitra et al., 2023); these can be investigated through multi-band, high time-resolution polarization

Table 6.2: DSA-110 FRB Sample Polarization Properties

FRB Names	R.A. (°)	Decl. (°)	n_t	n_f	S/N	L/I	|V|/I	V/I	RM (rad m^{-2})	DM (pc cm^{-3})
FRB 20220121B / "Clare"	85.66°	64.39°	8	128	13.36	70.5 ± 20.6%	51.0 ± 12.7%	−51.0 ± 12.7%	−4.6 ± 15.5	313.5 ± 0.2
FRB 20220204A / "Fen"	278.27°	72.58°	6	32	17.68	62.8 ± 15.3%	7.5 ± 7.7%	−6.7 ± 7.7%	−11.0 ± 11.7	$612.2^{+0.005}_{-0.049}$
FRB 20220207C / "Zach"	310.2°	72.88°	1	16	72.57	74.9 ± 4.5%	14.8 ± 1.7%	11.1 ± 1.7%	162.48 ± 0.04	262.3 ± 0.01
FRB 20220208A / "Ishita"	322.58°	70.04°	32	256	10.70	114.3 ± 29.1%	11.4 ± 15.5%	−11.2 ± 15.5%	−23.3 ± 9.7	$437.0^{\pm}0.6$
FRB 20220307B / "Alex"	350.88°	72.19°	1	128	15.72	69.8 ± 16.0%	18.9 ± 8.0%	−10.3 ± 8.0%	−947.2 ± 12.3	499.15 ± 0.03
FRB 20220310F / "Whitney"	134.72°	73.49°	1	32	98.32	60.6 ± 4.7%	16.6 ± 1.6%	−7.4 ± 1.6%	11.4 ± 0.2	462.15 ± 0.004
FRB 20220319D / "Mark"	32.18°	71.04°	1	32	56.37	16.1 ± 4.0%	4.0 ± 2.0%	−3.0 ± 2.0%	59.9 ± 14.3	110.95 ± 0.01
FRB 20220330D / "Erdos"	163.75°	70.35°	40	64	17.98	73.2 ± 17.7%	15.8 ± 9.0%	3.1 ± 9.0%	−122.2 ± 4.5	$468.1^{+0.8}_{-0.9}$
FRB 20220418A / "Quincy"	219.11°	70.1°	2	128	16.84	64.1 ± 13.3%	21.4 ± 7.7%	2.7 ± 7.7%	6.1 ± 7.5	623.45 ± 0.01
FRB 20220424E / "Davina"	19.51°	71.8°	2	64	14.60	59.9 ± 16.2%	15.8 ± 7.4%	15.8 ± 7.4%	126.9 ± 13.4	$863.48^{+0.022}_{-0.036}$
FRB 20220506D / "Oran"	318.05°	72.83°	1	32	24.17	95.3 ± 10.9%	31.4 ± 4.6%	31.4 ± 4.6%	−32.4 ± 3.6	396.93 ± 0.01
FRB 20220509G / "Jackie"	282.67°	70.24°	1	32	40.32	98.5 ± 11.1%	6.0 ± 2.8%	5.4 ± 2.8%	−109.0 ± 1.2	269.5 ± 0.007
FRB 20220726A / "Gertrude"	73.95°	69.93°	2	64	18.25	93.5 ± 16.7%	13.8 ± 6.2%	−3.7 ± 6.2%	499.8 ± 7.2	686.55 ± 0.01
FRB 20220801A / "Augustine"	54.96°	70.18°	4	64	11.77	30.1 ± 18.0%	35.8 ± 13.7%	−1.3 ± 13.7%	–	412.6 ± 0.04
FRB 20220825A / "Ansel"	311.98°	72.59°	1	32	32.80	53.7 ± 11.4%	9.0 ± 5.9%	−7.4 ± 5.9%	750.2 ± 6.7	651.2 ± 0.02
FRB 20220831A / "Ada"	338.7°	70.54°	6	64	21.28	84.6 ± 12.8%	16.8 ± 5.3%	1.7 ± 5.3%	772.1 ± 7.2	1146.25 ± 0.2
FRB 20220914A / "Elektra"	282.06°	73.34°	1	64	17.43	16.3 ± 14.0%	20.5 ± 11.9%	11.9 ± 11.9%	–	631.05 ± 0.02
FRB 20220920A / "Etienne"	240.26°	70.92°	2	128	18.88	89.0 ± 16.2%	19.7 ± 8.1%	−14.9 ± 8.1%	−830.3 ± 8.3	315.0 ± 0.06
FRB 20220926A / "Celeste"	328.73°	72.86°	2	128	18.16	17.5 ± 21.0%	9.5 ± 14.2%	2.0 ± 14.2%	–	441.53 ± 0.03
FRB 20221002A / "Arni"	281.0°	71.6°	12	256	8.08	26.8 ± 22.7%	19.7 ± 18.1%	−12.5 ± 18.1%	–	322.5 ± 1.0
FRB 20221012A / "Juan" †	280.8°	70.52°	8	32	9.33	63.0 ± 21.4%	25.7 ± 11.0%	0.6 ± 10.9%	165.7 ± 17.7	441.2 ± 0.26
FRB 20221027A / "Koyaanisqatsi"	130.9°	71.6°	1	32	21.82	8.3 ± 7.0%	18.4 ± 5.2%	−2.2 ± 5.2%	–	452.5‡
FRB 20221029A / "Mifanshan"	143.8°	71.6°	4	128	17.12	85.7 ± 16.1%	15.6 ± 7.0%	6.8 ± 7.0%	−155.8 ± 9.7	1391.05‡
FRB 20221101B / "Nina"	342.0°	71.5°	4	32	14.21	99.3 ± 19.3%	24.5 ± 8.7%	−19.4 ± 8.7%	−32.2 ± 9.1	490.7‡
FRB 20221101A / "Ayo"	75.6°	71.6°	2	64	19.27	55.3 ± 11.3%	11.6 ± 6.2%	−5.5 ± 6.2%	4670.4 ± 10.8	1476.5‡

Notes: n_t and n_f are the downsampling factors in time and frequency from the native DSA-110 resolution (see Appendix 6.8.2) used to maximize S/N. The total, linear, absolute value of circular and signed circular polarization are given in columns 7, 8, 9, and 10. The right ascension and declination given are the ICRS frame coordinates of the beam in which the FRB was detected.

† FRB 20221012A's polarization is computed after derotating to the reported RM. This detection was marginal, with low linear-polarization S/N below the 9σ threshold. However, this is taken as a reliable measurement given the clear peak the RM spectrum (Figure 6.20) and apparent coherence when compared to the RMSF.

‡Detailed burst structure analysis used to estimate DM errors has not yet been performed for these FRBs. See G. Chen et al., in preparation for details.

studies of FRBs (e.g., Feng et al., 2022b; Hankins et al., 2003; Mckinven et al., 2023). A generalized classification scheme will help identify the characteristic FRB polarization properties to narrow the range of likely FRB theories.

To date, the predominant FRB categorization method was offered by Pleunis et al. (2021) based on observations of FRBs from the Canadian Hydrogen Intensity Mapping Experiment (CHIME). Their classes were based on the spectro-temporal morphology of FRBs detected in the 400-800 MHz band. However, we find these classes insufficient to describe the full DSA-110 sample's morphological properties. Furthermore, these classes do not include FRB polarization, for which we would like a straightforward and replicable classification framework. The DSA-110, whose polarization calibration scheme is verified in Appendices 6.8.5, 6.8.6, and 6.8.7, is well-equipped to define polarization sub-classes using the uniform sample of 25 FRBs presented here. However, we acknowledge that such a classification scheme would be limited by the DSA-110 sensitivity, and furthermore cannot be generalized beyond L-band detections. While we hope that these sub-groups will form the groundwork for a more general, polarization- and frequency-dependent classification scheme, we make no claims on its universality in the current iteration. Polarization properties are also difficult to distinguish from being intrinsic or the result of propagation effects. Therefore, while we identify classes based on total, linear, and circular polarization, we use them primarily to motivate a more detailed discussion of linear and circular polarization in the following section.

We define four unique polarization sub-groups which are applied in turn to the total, linear, and circular polarization fractions of each DSA-110 FRB:

1. **Consistent with 100% Polarized**: The polarization fraction falls within 3σ of 100% and beyond 3σ of 0%.

2. **Consistent with 0% Polarized**: The polarization fraction falls within 3σ of 0% and beyond 3σ of 100%.

3. **Intermediate**: The polarization fraction falls beyond 3σ of both 100% and 0%.

4. **Unconstrained**: The polarization fraction falls within 3σ of both 100% and 0%. This is equivalent to stating the polarization is not well-defined.

We then define two orthogonal sub-groups which generalize and place more quantitative limits on the morphological classes of Pleunis et al. (2021):

1. **Single Component**: Bursts exhibit one component (on approx. millisecond timescales).
2. **Multi-Component**: Bursts exhibit multiple components separated on millisecond timescales.

In Table 6.3, we sort the DSA-110 sample among these sub-classes using total, linear, and circular polarization fractions. For the remainder of the paper, the sub-groups **Consistent with 100% Polarized**, **Consistent with 0% Polarized**, **Intermediate**, and **Unconstrained** will refer only to the total polarization-based sub-groups unless otherwise noted. In the next section, we explore the specific properties of FRBs in each class. Figure 6.3 shows L/I and $|V|/I$ for the DSA-110 FRBs, grouped by their polarization class.

6.4.2 Single Component FRBs

A significant majority 21/25 of the DSA-110 sample are described by a single component on millisecond timescales, with most (13) of these being **Consistent with 100%** polarization. Three **Single Component** FRBs fall into each of the **Consistent with 0%** and **Intermediate** classes, while two have **Unconstrained** polarization properties. In this section we explore the characteristic polarization properties of **Single Component** FRBs.

6.4.2.1 Linear Polarization

As shown in Figure 6.3, all FRBs that are **Consistent with 100%** have $L/I > 50\%$, including 13 **Single Component** bursts; two-thirds of these (10) have $L/I > 70\%$. This is not uncommon among FRBs, as 36% of previously published repeaters and non-repeaters with L-band (1.4 GHz) polarization measurements also have $L/I > 50\%$. This large fraction of highly linearly polarized FRBs supports coherent radiation models such as curvature radiation from coherent charge bunches (Qu & B. Zhang, 2023; Wang et al., 2022b). While Feng et al. (2022b) demonstrate that repeaters become depolarized at lower frequencies, they associate this with stochastic RM scattering rather than intrinsic emission. Coherent radiation models are further supported by the relatively flat PPA's observed in this group. A χ^2 goodness-of-fit

Table 6.3: Polarization-based FRB subgroups from DSA-110 data.

	Consistent with 100%	**Consistent with 0%**	**Intermediate**	**Unconstrained**
Total Polarization ($\sqrt{(L/I)^2 + (V/I)^2}$)	FRB 20220121B (1) FRB 20220204A (1i) FRB 20220208A (1a) FRB 20220307B (1) FRB 20220330D (1i) FRB 20220424E (1i) FRB 20220506D (1ia) FRB 20220509G (1ia) FRB 20220726A (1a) FRB 20220831A (1a) FRB 20220920A (1) FRB 20221012A (1)‡ FRB 20221029A (1i) **FRB 20220418A (3a)** **FRB 20221101B (2)**	FRB 20220914A (1i) FRB 20220926A (1) FRB 20221027A (1i)†	FRB 20220319D (1i) FRB 20220825A (1ia) FRB 20221101A (1a) **FRB 20220207C (2ia)** **FRB 20220310F (2ia)**	FRB 20220801A (1ia) FRB 20221002A (1)
Linear Polarization (L/I)	FRB 20220121B (1) FRB 20220204A (1i) FRB 20220208A (1a) FRB 20220307B (1) FRB 20220330D (1i) FRB 20220424E (1i) FRB 20220506D (1ia) FRB 20220509G (1ia) FRB 20220726A (1a) FRB 20220831A (1a) FRB 20220920A (1) FRB 20221029A (1i) **FRB 20220418A (3a)** **FRB 20221101B (2)**	FRB 20220914A (1i) FRB 20220926A (1) FRB 20221027A (1i)† FRB 20220801A (1ia) FRB 20221002A (1)	FRB 20220319D (1i) FRB 20220825A (1ia) FRB 20221101A (1a) **FRB 20220207C (2ia)** **FRB 20220310F (2ia)**	FRB 20221012A (1)‡
Circular Polarization ($\lvert V\rvert/I$)	–	FRB 20220121B (1) FRB 20220204A (1i) FRB 20220208A (1a) FRB 20220307B (1) FRB 20220330D (1i) FRB 20220424E (1i) FRB 20220509G (1ia) FRB 20220726A (1a) FRB 20220920A (1) FRB 20221012A (1)‡ FRB 20221029A (1i) FRB 20220801A (1ia) FRB 20221002A (1) FRB 20220914A (1i) FRB 20220926A (1) FRB 20220319D (1i) FRB 20220825A (1ia) FRB 20221101A (1a) **FRB 20220418A (3a)** **FRB 20221101B (2)**	FRB 20220121B (1) FRB 20220506D (1ia) FRB 20221027A (1i)† **FRB 20220207C (2ia)** **FRB 20220310F (2ia)** FRB 20220831A (1a)	–

Notes: DSA-110 FRBs sorted into subgroups based on polarization significance as described in Section 6.4. Each burst is labeled with the number of resolved components, an "i" if the burst shows significant spectral striation, and an "a" if the burst shows significant scattering (G. Chen et al., in prep.). **Multi-Component** FRBs are boldfaced, while **Single-Component** FRBs are in regular font.

†FRB 20221027A is a unique FRB whose total polarization is **Consistent with 0%**, but which has **Intermediate** circular polarization. This is attributed to its insignificant linear polarization which adds noise to the total polarization estimate.

‡FRB 20221012A has a total polarization that is **Consistent with 100%** and a circular polarization that is **Consistent with 0%**, but its linear polarization is **Unconstrained**. From RM synthesis, we marginally detect an RM, although the peak in the RM spectrum has linear S/N below the 9σ threshold as shown in Figure 6.20. This suggests there is significant linear polarization which contributes to the total, though we cannot make more constraining statements within our current classification scheme.

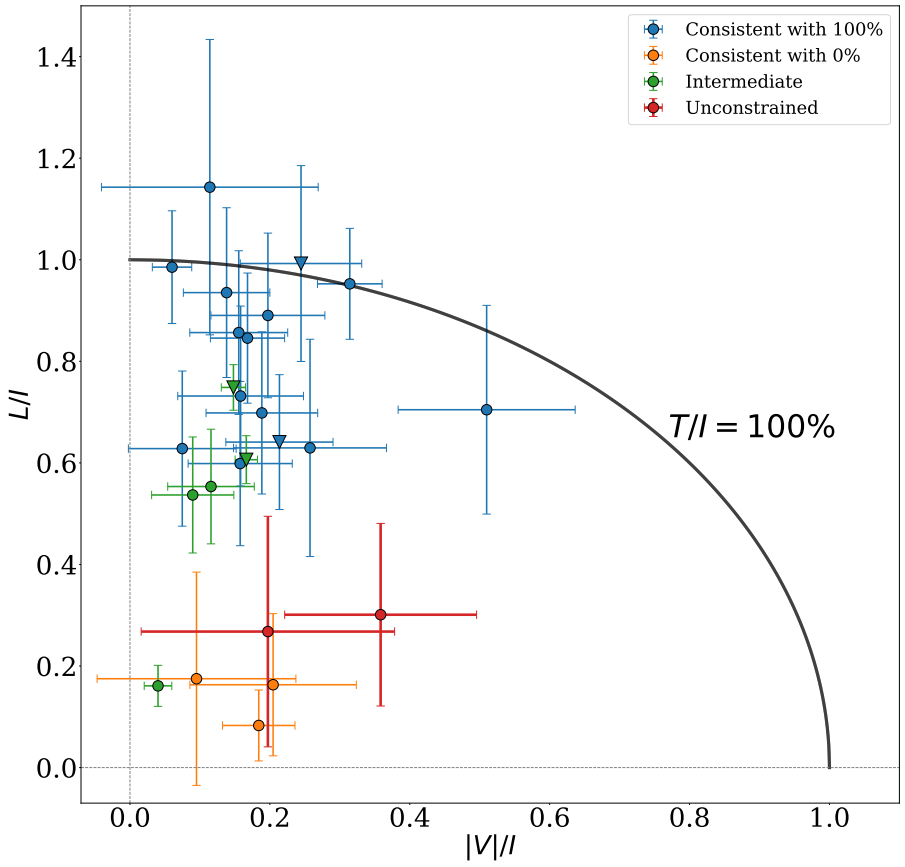

Figure 6.3: Linear and Absolute Value Circular Polarization for DSA-110 FRBs. Each FRB is color-coded by its polarization class as reported in Table 6.3. **Single Component** FRBs are shown as circles and **Multi-Component** FRBs are shown as triangles. The errorbars shown are 1σ uncertainties. The black line indicates where the total-polarization fraction $T/I = \sqrt{(|V|/I)^2 + (L/I)^2} = 100\%$. While all **Consistent with 100%** (blue) and most **Intermediate** (green) FRBs have $L/I > 50\%$, FRB 20220121B and FRB 20220506D also show significant circular polarization. FRB 20220319D is the only FRB in either class with less than 50% total polarization. All **Consistent with 0%** FRBs (orange) have L/I and $|V|/I$ below 25%.

test was conducted to compare the PPA in time bins with linear-polarization S/N $> 3\sigma$ to the weighted average PPA value (see Appendix 6.8.11). None of the 13 **Single Component** FRBs consistent with 100% polarization were found with significant variations ($p < 10\%$) in position angle. This may imply that there is a single dominant polarization mode in most FRBs, and resembles the behavior of young, high spin-down pulsars (Mitra et al., 2016; Ravi et al., 2010; Weltevrede & Johnston, 2008). In Section 6.5.2, we explore possible connections between FRBs and young pulsars in more detail. Notably, of FRBs in the **Consistent with 100%** and **Intermediate** sub-groups, only FRB 20220319D has a linear polarization fraction below 20%, a trait shared only by the 3 FRBs that are **Consistent with 0%**.

6.4.2.2 Circular Polarization

Circular polarization appears to be less common than linear polarization among the **Single Component** sample. Only two FRBs that are **Consistent with 100%** or **Intermediate** have $|V|/I > 30\%$: FRB 20220121B and FRB 20220506D. Both are **Consistent with 100%** and show no clear splitting of different signs of Stokes V. This is consistent with circular polarization originating through the propagation effects discussed above. A third FRB, FRB 20220801A, also has a high $|V|/I$, but falls into the **Unconstrained** subgroup, making any evident polarization difficult to confirm. We do not observe any changes in the sign of Stokes V within FRB 20220121B and FRB 20220506D, as are often observed at the centers of the main components in radio-pulsar APs (Radhakrishnan & Rankin, 1990). Furthermore, while most **Single Component** FRBs appear to have negligible circular polarization (evident from both $|V|/I$ fractions and polarized profiles in Figures 6.14-6.17), all four **Multi-Component** bursts appear to have significant circular polarization. We will explore this further in the next section.

The large fraction of FRBs that exhibit high linear polarization, as opposed to circular polarization, suggests that the intrinsic emission mechanism is often highly linearly polarized. Circular polarization and depolarization may then arise primarily from propagation effects. In this scenario, depolarization from the intrinsic mechanism due to unresolved micro or nano-second scale structure may be less significant than propagation effects, in contrast to pulsar radio emission (J. Cordes, 1976; Hankins et al., 2003; Mitra et al., 2015). However, this claim cannot be confirmed without higher time resolution observations of FRBs.

The limited 187 MHz bandwidth and 972 kHz resolution[7] of the DSA-110 spectra prevent detailed fits of frequency-dependent FC models. Instead, by assuming FC is significant in the region of interest, we can estimate the magnetic-field strength from frequency-averaged quantities as follows (Gruzinov & Y. Levin, 2019). One can estimate the Faraday Conversion Measure (CM) from the root mean squared circular polarization of each FRB, assuming the circular emission arises from FC at a single magnetic field reversal:

$$\sqrt{< V(\lambda^2)^2 >} = \sqrt{2(e^{-(\mathrm{CM}\lambda^2)^2/2} - e^{-(\mathrm{CM}\lambda^2)^2})} \tag{6.1}$$

The CM can be related to the RM and total magnetic field strength, B, by:

$$\mathrm{CM} \approx B\sqrt{\mathrm{RM}\left(\frac{8\pi^3 e^2}{m_e^3 c^4}\right)} \sim 10^{-2}\left(\frac{B}{1\,\mathrm{G}}\right)\left(\frac{\mathrm{RM}}{1\,\mathrm{rad}\,m^{-2}}\right)^{1/2}, \tag{6.2}$$

where e is the electron charge, m_e is the electron mass, and c is the vacuum speed of light. For FRB 20220121B and FRB 20220506D, we measure root mean squared circular polarization $\sqrt{< V(\lambda^2)^2 >} \approx 50\%$ and 40%, corresponding to conversion measures CM $\approx 10\,\mathrm{m}^{-2}$ in both cases. Given their RMs of $-4.60 \pm 15.48\,\mathrm{rad\,m}^{-2}$ and $-32.38 \pm 3.60\,\mathrm{rad\,m}^{-2}$, we estimate magnetic field strengths of $B \approx 510$ G and 150 G, respectively. These high field strengths are not consistent with supernova-remnant and plerionic environments, including those of the FRBs associated with persistent radio sources (e.g., Vedantham & Ravi, 2019). However, motivated by the likely FC observed during eclipses of the binary-system PSR B1744 − 24A (D. Li et al., 2023), the magnetized wind of a companion to the FRB progenitors is a reasonable possibility for the conversion site.

6.4.2.3 Depolarization

The DSA-110 sample reported here contains 3 **Single Component** FRBs that are **Consistent with 0%** and 3 that have **Intermediate** polarization. 9/16 FRBs in the published literature that have reported errorbars would also fall in these subgroups. Considering the circular polarization sub-groups, only FRB 20221027A has an **Intermediate** $|V|/I$ ($> 3\sigma$) among FRBs with **Intermediate** total polarization[8].

[7] Here we refer to the limited resolution of the spectra in Figures 6.14-6.17, which were binned by at least 32×30.4 kHz channels to maximize frequency structure.

[8] With $|V|/I = 18.4 \pm 5.2\%$, FRB 20221027A's linear polarization fraction is noise-dominated; therefore, its total polarization class (**Consistent with 0%**) is likely erroneous due to small errors in noise statistics. We will consider it as an **Intermediate** FRB for this discussion given its significant circular polarization fraction.

The lack of circular polarization in bursts with low total polarization implies that FC effects are less common, which one expects to depolarize the burst while producing residual circular polarization.

RM variations across a scattering screen are also unlikely to be the dominant depolarization mechanism for the DSA-110 FRBs. The variation in RM is captured by $\sigma_{\rm RM}$, the standard deviation of RM throughout the screen, and depolarization would be highly frequency dependent with the linear-polarization fraction of the form:

$$f_{\sigma_{\rm RM}} = 1 - e^{-2\sigma_{\rm RM}^2 \lambda^4} \tag{6.3}$$

This model has been found to match observations of 8 repeating FRBs from 0.1–10 GHz, with $\sigma_{\rm RM}$ values from $0.12\,{\rm rad\,m^{-2}}$ for FRB 20180916B to $218.9\,{\rm rad\,m^{-2}}$ for FRB 20190520B (Feng et al., 2022b; Mckinven et al., 2023). However, for $RM < 1,000\,{\rm rad\,m^{-2}}$, averaging over the DSA-110 frequency band (1.3 – 1.5 GHz) without RM correction is the dominant depolarization effect, which we quantify by:

$$f_{\rm avg} = 1 - \sqrt{< \cos({\rm RM}\lambda^2) >^2 + < \sin({\rm RM}\lambda^2) >^2} \tag{6.4}$$

where <> denotes the mean over frequency. Therefore, if we assume an FRB is intrinsically 100% polarized, we can write the observed polarization fraction as $L/I \approx f_{\sigma_{\rm RM}}({\rm RM})\, f_{\rm avg}(\sigma_{\rm RM})$; note that channel bandwidth depolarization is negligible in this RM range (see Appendix 6.8.9). Feng et al. (2022b) (see Figure 4) derives an empirical, linear relation between $\sigma_{\rm RM}$ and RM, which we adopt to write Equation 6.4 in terms of $\sigma_{\rm RM}$. We apply this model to the average polarization of the three bursts with insufficient L/I for RM measurements: FRB 20220914A, FRB 20220926A, and FRB 20221027A. We find that $\sigma_{\rm RM} \approx 0.3 - 1.0\,{\rm rad\,m^{-2}}$ could produce the observed polarization fractions for FRB 20220914A and FRB 20220926A, while $\sigma_{\rm RM} \approx 0.3 - 3.0\,{\rm rad\,m^{-2}}$ could produce the polarization of FRB 20221027A. From Feng et al. (2022b), these correspond to $RM \approx 200 - 900\,{\rm rad\,m^{-2}}$, which should be detectable with the DSA-110 RM synthesis pipeline; however, no significant RM was found for these three FRBs. Low S/N could prevent detection, but the low $\sigma_{\rm RM}$ suggests that RM synthesis would recover nearly 100% linear polarization, making the maximized linear S/N in each burst $\sim 20\sigma$ which exceeds the 9σ detection threshold (see Appendix 6.8.9).

We can perform a similar analysis for **Intermediate** FRBs, which do have RM measurements ranging from $10 - 4670\,{\rm rad\,m^2}$. We find that $\sigma_{\rm RM}$ in the range of

10–20 rad m^{-2} would be required for these FRBs. Apart from FRB 20221101A, this is around an order of magnitude higher than expected from Feng et al. (2022b) for these RM magnitudes, and the $\ll$ 1 ms scattering timescales of the DSA-110 FRBs (G. Chen et al., in prep.). Furthermore, assuming a common origin for the scattering and depolarization, the implied magnetic-field variations in the scattering screen are likely to be uncomfortably high, of order Gauss (Feng et al., 2022b; Yang et al., 2022, Section S4). A potential exception to these arguments is the event FRB 20220319D, as discussed in Appendix 6.8.10.

The significant fraction of FRBs in the DSA-110 sample that are **Consistent with 0%** or **Intermediate** poses an interesting challenge to theory (Qu & B. Zhang, 2023). The fact that depolarization has long been observed and puzzled over in pulsars, more significantly at high frequencies (> 1 GHz) than low, (e.g., Manchester et al., 1973; Manchester, 1971) should provide some hope that a common explanation may be found.

6.4.3 Multi-Component FRBs

4/25 of the DSA-110 sample exhibit multiple components on millisecond timescales[9]. FRB 20220418A and FRB 20221101B are **Consistent with 100% Polarization**, while FRB 20220207C and FRB 20220310F are **Intermediate**. In this section we explore the polarization properties of **Multi-Component** FRBs.

6.4.3.1 Stable Polarization States

Both FRB 20220207C and FRB 20220310F have two sub-components exhibiting significant linear polarization with $L/I > 50\%$. Significant circular polarization ($> 3\sigma$) is also evident, with $|V|/I \approx 15\%$. In FRB 20220207C, the first component has a flat PPA while the second fluctuates, although a $\chi^2_\angle$ test finds this variation is not significant (see Appendix 6.8.11 for details). In contrast, FRB 20220310F displays a flat PPA in both components, separated by $\sim 10^\circ$. If both components originate from a fixed region in a rotating magnetosphere, this suggests negligible rotation over the approximately millisecond burst durations. A potentially better way to quantify a constraint on the rotation periods of progenitor objects is by assuming emission from coherent charge bunches, as motivated by this specific

[9]We note that sub-microsecond-scale structures have been previously observed in FRBs (e.g., Majid et al., 2021; Nimmo et al., 2021, 2022), and indeed interesting structure within individual burst components is observed in some DSA-110 FRBs. We defer a high time resolution analysis of DSA-110 FRBs to future work.

categorization (Qu & B. Zhang, 2023; Wang et al., 2022b). For this analysis we assume a 'thin' bunch of charges, which aligns with the wide range of polarization properties observed in FRBs[10]. In this scenario, the burst duration must be much less than $(\gamma\Omega)^{-1}$, where $\gamma \sim 100$ is the bunch Lorentz factor[11], and Ω is the rotation angular frequency. Applying this condition for the ~ 0.3 ms duration of the first FRB 20220207C burst, we find required rotation periods $\gg 30$ ms. Similarly, the sub-bursts in FRB 20220310F span ~ 0.2 ms each, for which we find required rotation periods $\gg 20$ ms under the same curvature radiation assumptions. These estimates are of particular interest since 30 ms roughly demarcates the boundary between millisecond pulsar (MSPs) and slow canonical pulsar (CPs) rotation periods (e.g., Lorimer, 2008).

6.4.3.2 Polarization Variation

What is most striking about these bursts is that the different components appear to have different polarization properties, an effect that persists for non-repeating FRBs from at least the Australian Square Kilometre Array Pathfinder (ASKAP; Cho et al., 2020; Day et al., 2020). In contrast, none of the 21 single-component FRBs had statistically significant PPA variability, suggesting negligible polarization evolution across the burst. The variations between the polarization properties of the sub-components of FRB 20220207C, FRB 20220310F, FRB 20220418A, and FRB 20221101B defy a unified description. FRB 20220418A and FRB 20220207C exhibit multiple components with different polarization properties. FRB 20220207C's sub-components have very different profiles, although a $\chi^2_\angle$ test finds the PPA variation is not significant. Beyond this, the first sub-component is **Consistent with 100%** linear polarization while the second has $\sim$ 50% linear polarization and $\sim$ 20% circular polarization. FRB 20220418A is less constrained: while the first sub-component has high linear polarization, the second is **Unconstrained** and the third is **Consistent with 0%** linear and circular polarization.

FRB 20220310F's sub-components have more comparable properties, with L/I of $54.8 \pm 6.0\%$ and $67.4 \pm 7.2\%$, but while the circular-polarization fractions have a similar magnitude, the signs are opposite: V/I of $-16.7 \pm 1.3\%$ and $10.8 \pm 1.8\%$ respectively. Indeed, the polarization states of the two sub-components are

[10]For details, see Figures 2, 4, 5, and 6 of Wang et al. (2022b)

[11]We assume $\gamma\sim100$ based on the DSA-110 observing frequency 1.4 GHz and the expected curvature radius of magnetic field lines around a neutron star, $\rho \sim 10^{6-8}$ cm. Using Equation 18 of Qu & B. Zhang (2023), $58 \lesssim \gamma \lesssim 270$ are reasonable approximations for a coherent curvature radiation scenario.

individually well-defined, and the average locations of the two sub-components on the Poincaré sphere are almost orthogonal, with an angular separation of 71 ± 2 degrees (Figure 6.4). These are reminiscent of emission in orthogonally polarized modes observed in several pulsars (Manchester et al., 1975; Stinebring et al., 1984). However, the change in sign of Stokes V between the two components is rarely if ever observed in multi-component pulsar APs (Han et al., 1998). Changes in the sign of Stokes V between components can potentially be interpreted as emission from different magnetic hemispheres, potentially implying rapid rotation of the progenitor (Johnston & Kramer, 2019). Alternatively, the opposite signs in circular polarization may indicate that birefringence could be the cause of the split sub-components in FRB 20220310F (Qu & B. Zhang, 2023; Suresh & J. M. Cordes, 2019). While birefringent dispersive delay would require RM $\approx 10^7\,\mathrm{rad\,m^{-2}}$ to produce the observed 0.3 ms split in FRB 20220310F, birefringent refraction may be more plausible, requiring only RM $\approx 10^{1-2}\,\mathrm{rad\,m^{-2}}$. The closed loop formed on the Poincaré sphere by the polarization vector of the second component of FRB 20220310F is also reminiscent of the loop observed in the first component of FRB 20181112A by Cho et al. (2020), which was potentially ascribed to FC in a relativistic plasma. From equation 2, we estimate a magnetic field strength $B \approx 150\,\mathrm{G}$ would be required for FC, which is inconsistent with supernova-remnant and plerionic environments (e.g., Vedantham & Ravi, 2019).

6.4.3.3 RM Variation

We observe a significant 3.1σ variation in RM between the sub-components of FRB 20221101B ($-13.1 \pm 10.5\,\mathrm{rad\,m^{-2}}$ and $-75.9 \pm 17.5\,\mathrm{rad\,m^{-2}}$), and marginally significant 1.7σ and 2.7σ variations in FRB 20220207C ($161.5 \pm 0.4\,\mathrm{rad\,m^{-2}}$ and $173.5 \pm 7.2\,\mathrm{rad\,m^{-2}}$) and FRB 20220310F ($10.1 \pm 0.6\,\mathrm{rad\,m^{-2}}$ and $13.7 \pm 1.2\,\mathrm{rad\,m^{-2}}$), respectively. Figures 6.21-6.24 in Appendix 6.8.13 show the evolution of detected RM across across all four **Multi-Component** FRBs. No RM was detected for any but the strongest sub-component of FRB 20220418A, and intra-component RM variations were not observed for any other DSA-110 FRB. This effect is commonly observed in the APs of radio pulsars when sufficient S/N is available (Ilie et al., 2019), with magnitudes up to several tens of $\mathrm{rad\,m^{-2}}$, and is attributed to propagation effects in pulsar magnetospheres (e.g., Yang et al., 2023, Section 4.3). Similar propagation effects, if responsible for the RM variations we observe, may also be responsible for the multiple emission components as we only observe these effects (and significant variations in polarization state) for the FRBs that exhibit sub-components.

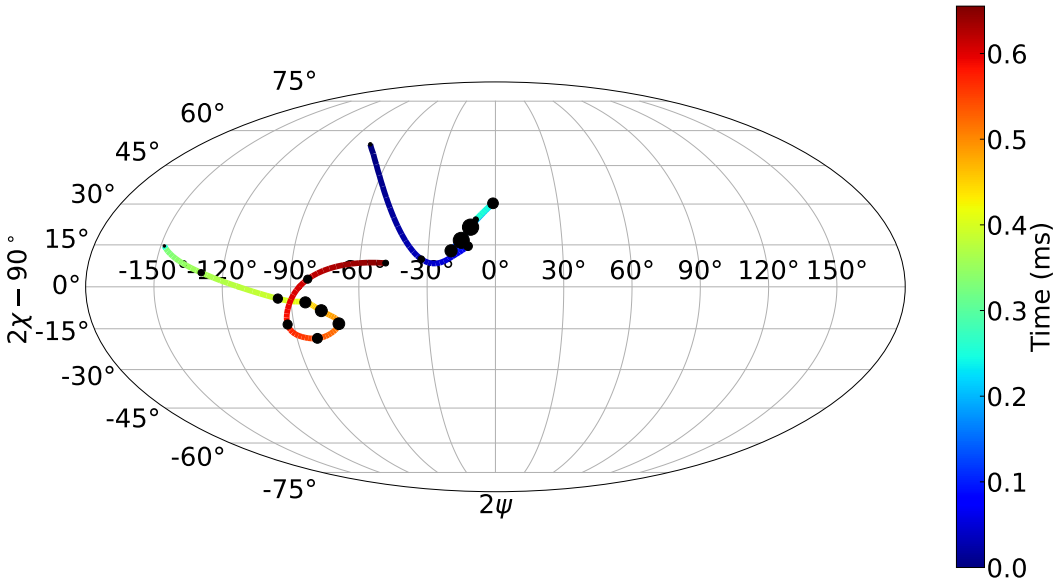

Figure 6.4: Projection of the polarization state of FRB 20220310F onto the Poincaré sphere. The position angle (χ) and longitude (ψ) are related to the Stokes parameters by $Q = \sin(2\psi)\sin(2\chi)$, $U = \sin(2\psi)\cos(2\chi)$, and $V = \cos(2\psi)$. Note the position angle axis has been shifted by 90° for ease of viewing. Data are displayed in windows of eight and ten 32.768 μs samples for the first and second components of the burst.

6.5 Comparisons

The polarization properties of FRBs provide insight into the nature of FRB emission and FRB sources, as has been the case for pulsars. We therefore present comparisons between the polarization properties of FRB sub-samples, and between FRBs and Galactic pulsars, to search for similarities and differences. Although emission from FRBs and pulsars is vastly different in energy scale (e.g., Nimmo et al., 2021), common propagation effects in magnetospheres and near-source environments may impact the polarization properties. We augment the DSA-110 FRB sample with a literature sample of 38 FRB sources with polarization data, described in detail in Appendix 6.8.1. The literature sample includes 19 repeating sources, for which we use the weighted mean of polarization measurements for the linear and circular fractions. When available, we use polarization measurements at L-band (1-2 GHz) for the literature sample in order to compare with the DSA-110 sample. A minimum S/N > 8σ is imposed on the literature sample of FRBs. For additional details, see Appendix 6.8.1. The DSA-110 sample thus more than doubles the total number of non-repeating FRBs with polarization measurements. In Section 6.5.1 we compare properties of different FRB sub-samples, and assess any frequency dependent or other selection effects. We then compare FRB polarization properties with those of

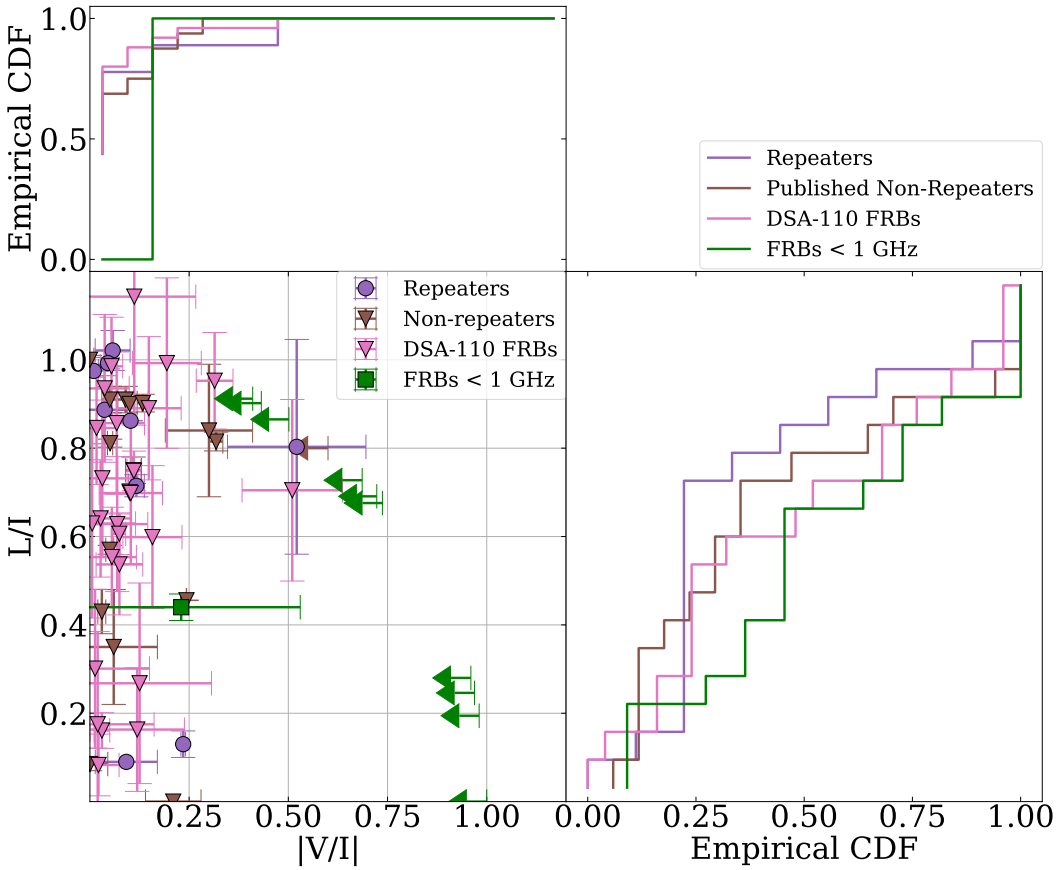

Figure 6.5: Comparison between the linear- and circular-polarization fractions of various FRB sub-samples. The top and right panels show empirical cumulative distribution functions (CDFs) for the DSA-110 sample (pink), published non-repeaters (brown), published repeaters (purple), and FRBs with measurements only at < 1 GHz (green). Arrows indicate upper limits in $|V/I|$ estimated from the measured values of L/I. See Appendix 6.8.1 for a summary of the literature data. In general, no significant differences between sub-samples are found.

various subsets of the Galactic pulsar population in Section 6.5.2.

6.5.1 Comparison between FRB sub-samples

In Figure 6.5 we compare the distributions of various FRB sub-samples in L/I and $|V|/I$. We consider the DSA-110 sample of 25 so far non-repeating events, along with published repeaters and non-repeaters, and measurements below 1 GHz. The literature sample contains 17 non-repeaters and 9 repeaters with polarization measurements at L-band (1 - 2 GHz), while there are 10 repeaters and 1 non-repeater with measurements only at lower frequencies (< 1 GHz). Six repeaters have measurements at multiple frequencies, for which we use the L-band observations where available. Sixteen non-repeaters (1 below 1 GHz) and 8 repeaters

(1 below 1 GHz) in the literature sample have circular polarization measurements. Kolmogorov-Smirnov (K-S) and Anderson-Darling (A-D) tests at 90% confidence (p-values below 10% reject the null hypothesis that the samples are drawn from the same distribution) reveal no significant differences in the distributions of DSA-110 and other FRBs in L/I. This holds when comparing with both previously published repeaters and non-repeaters, which themselves have no evident differences. We acknowledge however that this test is incomplete, and biases due to the resolution, sky coverage, and bandwidth of the DSA-110 survey may still exist. Further exploration of this however is outside the scope of this work, and we proceed on the assumption that such biases are negligible given the consistency of the DSA-110 sample with the published sample of FRBs.

A more detailed discussion is required to properly compare circular polarization. The circular polarization fraction can be defined either by averaging over the signed Stokes V fraction, V/I, or by taking the absolute value of Stokes V before averaging, $|V|/I$. The former preserves the sign (handedness) of circular polarization but neglects any significant sign changes across the burst. The latter accounts for sign changes, but introduces a bias which is not well-constrained. We provide both values for the DSA-110 bursts in Table 6.2, but most published FRBs use only V/I (e.g., Cho et al., 2020; Hilmarsson et al., 2021a). Therefore, we proceed by using V/I so that the sample is consistent, taking the absolute value ($|V/I|$) so that the already small sample is not further split by sign. With this definition, we find no significant difference when comparing the distribution of circular polarization of DSA-110 FRBs to previously detected non-repeaters. However, it is encouraged for future polarization surveys to report both V/I and $|V|/I$, as the latter is a more accurate representation of the magnitude of circular polarization. Furthermore, V/I and $|V|/I$ cannot be accurately compared due to the bias in $|V|/I$. For example, using $|V|/I$ for the DSA-110 sample and $|V/I|$ for the published sample, we find significant difference between the populations with p-value 1.2%. We conclude that the DSA-110 sample is not biased in its polarization properties with respect to published FRBs, and that polarization fractions do not appear to be a viable means of distinguishing repeaters and non-repeaters (see also Qu & B. Zhang, 2023).

We compare the sample of FRBs with polarization data at L-band to those measured at lower frequencies. No significant difference is found. This may suggest that other effects besides frequency-dependent stochastic RM depolarization (Feng et al., 2022b; Mckinven et al., 2023) generally determine the polarization properties

of the FRB population at different frequencies. Alternatively, if stochastic RM depolarization is dominant, this may imply that FRB progenitors can inhabit a wide variety of turbulent magneto-ionic environments. However, more robust conclusions would require a careful dissection of the population, for example into repeaters and non-repeaters; only two of the literature FRBs with polarization data reported below 1 GHz are apparent non-repeaters. We further note this method is primarily effective in characterizing the frequency-dependence of non-repeaters and repeaters detected in only one frequency band by analyzing the population as a whole. Feng et al. (2022b) and Mckinven et al. (2023) provide more detailed analyses of individual repeaters with measurements at multiple frequencies. For the remainder of the paper, we restrict the sample to the 18 non-repeaters and 9 repeaters with L-band polarization measurements.

6.5.2 Comparison between FRBs and pulsars

We next compare the linear- and circular-polarization fractions of FRBs with the Galactic and Magellanic-Cloud pulsar populations. We include RRATs, noting that no circular polarization data are available for RRATs at the time of writing. Radio-loud magnetars are also included, and are grouped with Canonical Pulsars (CPs, $P > 30$ ms) where necessary. We also consider both average-profile (AP) and single-pulse (SP) polarization fractions of pulsars.

Although the polarization properties of APs across the $P - \dot{P}$ diagram are well characterized (see Appendix 6.8.1 for a summary of existing observations), only a few SP polarization studies of substantial pulsar samples exist (e.g., Manchester et al., 1975; Mitra et al., 2023, 2016; Stinebring et al., 1984). Among the non-recycled pulsar population, significant trends in SP and AP polarization are observed with the spin-down energy loss rate, $\dot{E}$. For high-$\dot{E}$ pulsars, both SPs and APs typically exhibit high polarization fractions, and valid rotating vector model (RVM; Radhakrishnan & Cooke, 1969) fits can sometimes even be made to SPs. For lower-$\dot{E}$ pulsars, while SP polarization fractions remain high, AP polarization fractions decrease. The depolarization can have multiple causes: for example, a wider variance of polarization states of SPs, and SPs clustering into orthogonally polarized modes. These trends are driven by L/I; $|V|/I$ remains consistent with $\dot{E}$ and between SPs and APs. Here we compare the FRB polarization fractions to a collation of AP polarization fractions obtained around 1.4 GHz from the literature, and to the polarization fractions of SPs obtained with the Meterwavelength Single-pulse Polarimetric Emission Survey (MSPES) at 333 MHz and 618 MHz. The results are

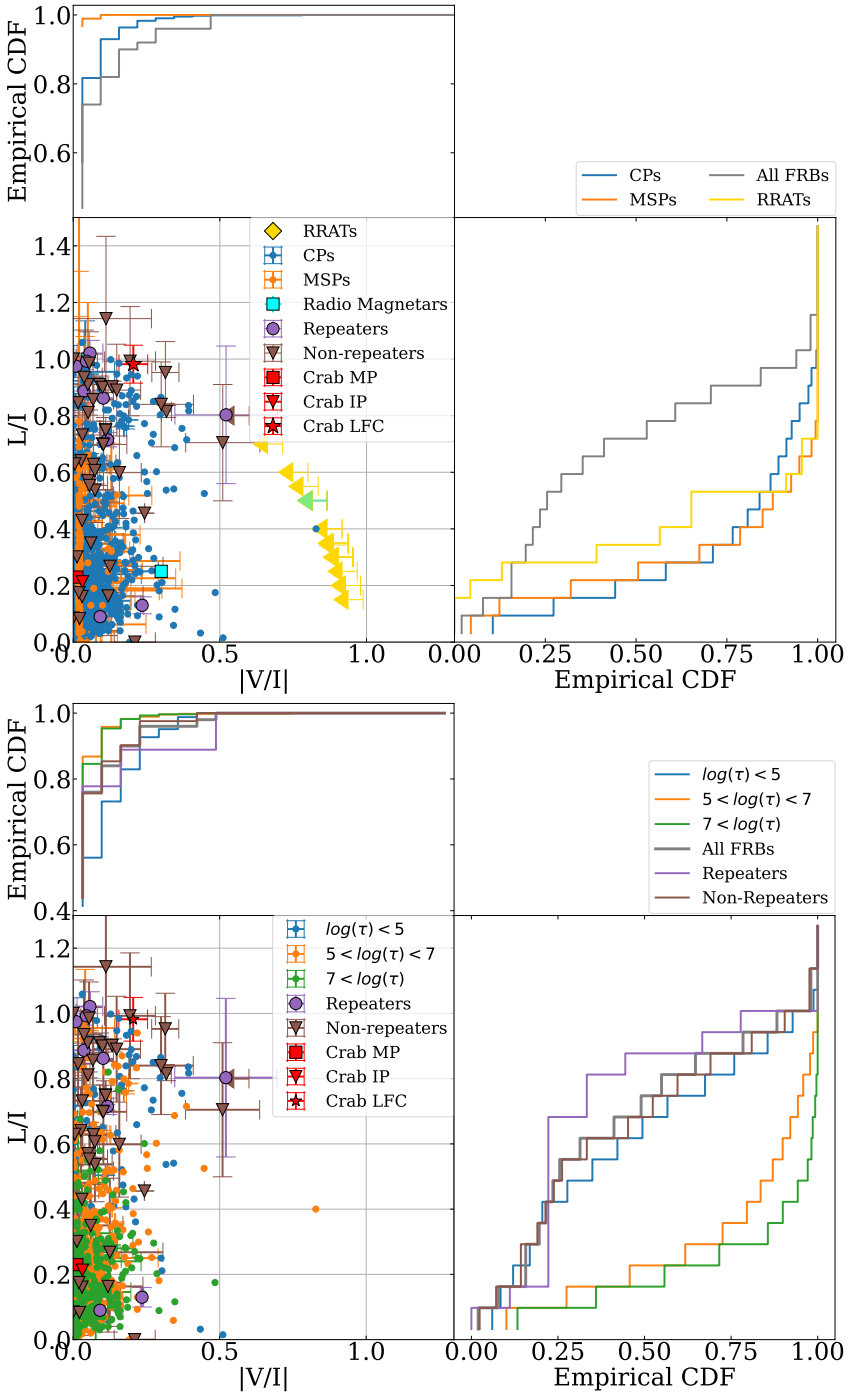

Figure 6.6: Comparison between the linear- and circular- polarization fractions of FRBs, pulsar APs, and RRATs. *Top:* FRBs (grey) are observed to have much higher linear-polarization fractions than MSPs (blue), CPs (orange) and RRATs (gold). Arrows indicate upper limits in $|V/I|$ estimated from the measured values of L/I. Somewhat higher circular-polarization fractions are also observed for FRBs. *Bottom:* We compare FRBs with canonical pulsars ($P > 30$ ms) with various characteristic ages. Young pulsars (blue) have remarkable similarity to FRBs (grey) in linear polarization, while older pulsars (orange, green) are more depolarized.

shown in Figures 6.6 and 6.7.

The distributions of polarization fractions of FRBs are largely dissimilar to those of pulsars. Pulsar APs and RRATs show characteristically smaller linear and circular polarization fractions than the FRB sample, both repeaters and non-repeaters. Of the 9 L-band repeaters we consider, only two have small ($\lesssim 30\%$) L/I, and the remainder have large ($\gtrsim 70\%$) L/I. Non-repeating FRBs have similar L/I and somewhat lower $|V/I|$ than repeaters, though small number statistics may limit concrete statements regarding repeaters. Although RRATs have slightly higher L/I than pulsar APs, this difference is marginal in comparison to the FRB-AP difference. A KS test indicates that repeating FRBs, unlike the non-repeaters, are not significantly different from CPs in $|V/I|$. Although interpretation of this is limited by small-number statistics with only seven repeaters with $|V/I|$ measurements.

Remarkably, FRBs (in particular non-repeating sources) have similar distributions of L/I and $|V|/I$ to the youngest (characteristic ages $\tau_c < 10^5$ yr) pulsar APs. The polarization properties of young, high-$\dot{E}$ pulsars are known to be drastically different to the remainder of the pulsar population (Weltevrede & Johnston, 2008), with high L/I, a lack of jumps in polarization position-angle and orthogonally polarized modes, and a close similarity between typical-SP and AP polarization profiles. The lack of depolarization in young pulsars is attributed to either magnetospheric propagation effects that cause only one of the modes (likely the O-mode) to be observed, or to the dominance of curvature radiation at high $\dot{E}$ (resulting in γ-ray emission) that may change the radio emission mechanism. Young pulsars, with emission likely from high in the magnetosphere (Ravi et al., 2010), may prove to be useful analogs for the production of FRB radiation even if the specific radio emission mechanisms differ. As an example, we refer the reader to recent work by Lin et al. (2023) on the importance of both extreme emission heights and relativistic motion in giant pulses emitted by the Crab pulsar.

Finally, we find that the MSPES SP distributions of L/I and $|V/I|$ are not consistent with the FRB distributions. The SP linear-polarization fractions are clustered around $\sim 60\%$, whereas the FRBs span a wider range of L/I. The SPs typically exhibit slightly higher values of $|V/I|$ than FRBs. The MSPES sample only contains seven SP measurements for $\dot{E} > 10^{34}\,\mathrm{erg\,s^{-1}}$, a threshold above which significant polarization changes are observed.

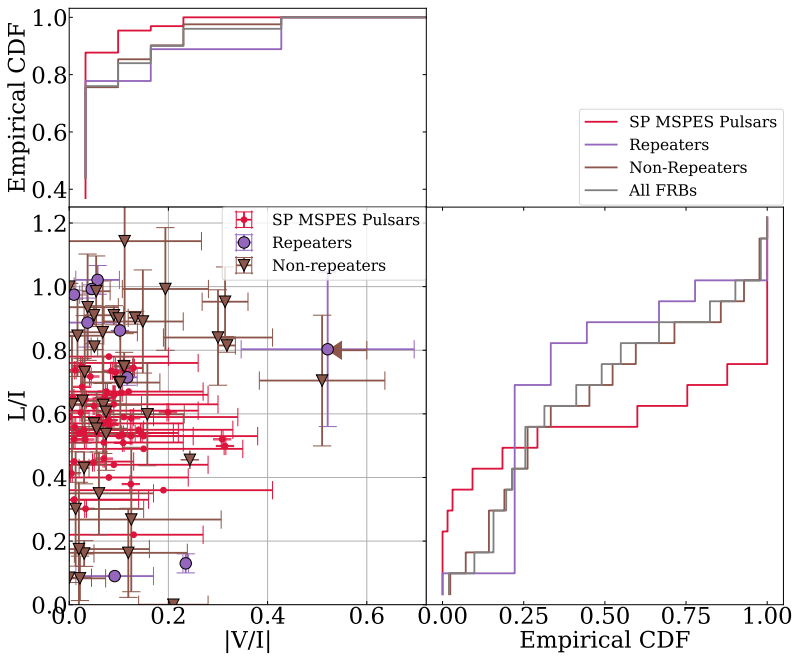

Figure 6.7: Comparison between the linear- and circular- polarization fractions of FRBs with pulsar single pulses (SPs). Pulsar SPs (red) have similar average linear polarization fraction ($\sim 60\%$), but cover a narrower range than FRBs (grey). Arrows indicate upper limits in $|V/I|$ estimated from the measured values of L/I.

6.6 Conclusions

We present a full-polarization analysis of the first 25 as yet non-repeating FRBs detected at 1.4 GHz with the DSA-110. This analysis includes a detailed description of data reduction and calibration for full-Stokes high time resolution data. We detect RMs for 20 FRBs, with magnitudes in the range $4 - 4670\,\mathrm{rad\,m^{-2}}$. We propose a classification according to polarization, S/N, and temporal properties. $15/25$ DSA-110 FRBs are labeled as **Consistent with 100% Polarization**, $3/25$ are labeled **Consistent with 0% Polarization**, $5/25$ are **Intermediate**, and $2/25$ have **Unconstrained** polarization properties due to their low S/N. Four FRBs that show multiple components on millisecond timescales are also unique in showing time-variable polarization properties, including RM.

We combine the DSA-110 sample with polarization measurements of previously published FRBs, and compare FRB sub-samples and FRBs with Galactic pulsars. We find no significant differences in the distributions of L/I and $|V/I|$ between the DSA-110 sample and the published samples; neither is there a significant difference between the repeater and non-repeater samples. We find that FRBs are typically far more polarized than the average profiles of pulsars and span a wider range

in polarization fractions than pulsar single pulses, which makes them remarkably similar to young (characteristic ages $< 10^5$ yr) pulsars.

We conclude the following.

1. The substantial fraction of highly linearly polarized FRBs ($15/25$ in the DSA-110 sample are **Consistent with 100%** and have $L/I > 50\%$) suggests that the FRB emission mechanism is often intrinsically linearly polarized. In the full DSA-110 sample, statistically significant variations in PPA are observed in $3/25$ events ($2/13$ **Consistent with 100%** events). This suggests modulation in some cases caused by a rapidly moving / rotating emission region.

2. Bursts with temporally separated components have variable polarization properties between the components. Of the $4/25$ such DSA-110 events, three have variable linear-polarization PPAs and fractions, two have variable signs and magnitudes of Stokes V, and three exhibit evidence for time-variable RMs. Together this suggests that the emission sites responsible for the different components originate from different regions of a magnetosphere, and are potentially viewed along different sightlines through magnetized plasma.

3. The origins of circular polarization and depolarization in FRBs remain mysterious. Faraday conversion in a highly magnetized near-source medium could explain the observed $|V|/I$ fractions. We disfavor bandwidth depolarization, RM scattering, and Faraday conversion as dominant depolarization mechanisms. We therefore have little evidence from polarimetry alone for the generic presence of dense, highly magnetized, inhomogeneous near-source plasma environments. Depolarization due to the superposition of multiple short bursts is possible.

4. The strong similarity between the L/I distributions of FRBs and the average profiles (and likely also single pulses) of the youngest pulsars suggests that the radio emission from young pulsars may form a useful analog to probe at least the depolarization mechanisms of FRBs. We note that the abrupt jump in PA observed in FRB 20220207C and the near-orthogonal positions on the Poincaré sphere of the two components of FRB 20220310F are uncommon for young pulsars.

Polarization studies have great promise in identifying characteristics of FRB emission that may prove useful in testing emission-mechanism and progenitor models. At

present, intrinsic emission-mechanism models favor high linear-polarization fractions, thus ascribing all other properties to propagation effects. In the future, studying FRB polarization properties in the context of other diagnostics of near-source environments, e.g., from accurate localizations, may be used to distinguish between intrinsic and extrinsic effects. At this point, we urge the further theoretical consideration of the intrinsic timescale(s) of FRB emission, and the causes of intrinsic depolarization. First, several of the DSA-110 FRBs are remarkably simple: the sample is characterized ($21/25$ events) by single emission components that are several tenths of a millisecond wide, with flat PPAs, and a wide range of linear-polarization fractions. We suggest that depolarization is likely intrinsic to the emission rather than a propagation effect; thus, the prospect of superposing several shorter bursts needs to be considered. At the same time, the existence of highly linearly polarized FRBs with flat PPAs over approx. millisecond timescales also requires an explanation. While not explored in this work, the scattering of FRBs over millisecond durations could be an alternate cause of flat PPAs. Third, our finding that multiple temporally separated emission components on approx. millisecond timescales tend to have different polarization properties poses an interesting additional challenge.

6.7 Acknowledgements

The authors would like to thank Jim Cordes, Dongzhi Li, Bing Zhang, Yuanhong Qu, Joel Weisberg, and Alexandra Mannings, for insightful and essential conversations on polarization theory and direction on the analysis conducted, as well as Paul Bellan and Yang Zhang for a comprehensive Plasma Physics course. We also thank Yi Feng, Dipanjan Mitra, Yuan-Pei Yang, Dylan Nelson, Reshma Anna-Thomas, and an anonymous referee for useful comments and recommendations on the early draft. This material is based upon work supported by the National Science Foundation Graduate Research Fellowship under Grant No. DGE-1745301. The authors thank staff members of the Owens Valley Radio Observatory and the Caltech radio group, including Kristen Bernasconi, Stephanie Cha-Ramos, Sarah Harnach, Tom Klinefelter, Lori McGraw, Corey Posner, Andres Rizo, Michael Virgin, Scott White, and Thomas Zentmyer. Their tireless efforts were instrumental to the success of the DSA-110. The DSA-110 is supported by the National Science Foundation Mid-Scale Innovations Program in Astronomical Sciences (MSIP) under grant AST-1836018.

6.8 Appendix

6.8.1 Literature samples of polarization observations of FRBs and pulsars

Previous analyses have yielded either RM or polarization measurements for at least 38 FRBs at time of writing; this sample was compiled using the Transient Name Server[12] (TNS), the FRB Catalog[13] (FRBcat), and the Canadian Hydrogen Intensity Mapping Experiment (CHIME) FRB Catalog 1[14] Petroff & Yaron (2020), (Amiri et al., 2021; Petroff et al., 2016). FRB polarization is often reported without uncertainties due to low resolution or low S/N that makes constraining the polarization difficult. In addition there is no standard method of computing the polarization fraction due to the wide range of morphologies in FRBs, and this should be held in mind when comparing polarimetry from multiple surveys. The FRBs in the literature sample compiled here were detected through the Apertif survey with the Westerbork Synthesis Radio Telescope (WSRT) and the Australian Square Kilometer Array Pathfinder (ASKAP) survey, as well as observations with the Parkes Telescope, CHIME, Green Bank Telescope, and Arecibo Observatory. Recent studies have observed frequency-dependent de-polarization thought to be the result of stochastic RM variations within a scattering screen (Feng et al., 2022b; Mckinven et al., 2023). A subset of 11 FRBs in this sample have polarization measurements at lower (< 1 GHz) frequencies.

Table 6.4 summarizes the polarization properties of each burst from the literature. Of the 38 bursts, 19 are repeaters, 34 have RM measurements, 15 have spectroscopic or photometric redshift measurements (9 repeaters, 6 non-repeaters), 25 have reported L-band linear polarization measurements, 11 have linear polarization measurements below 1 GHz, and 26 have reported circular polarization measurements. Below we describe the selection criteria and process for the FRB RMs used here:

1. Only RM measurements published before a 2023 April 10 cutoff date are considered for this sample.

2. For non-repeaters and repeaters with only 1 RM measurement, we use the available measurement.

3. For FRBs with RM measurements in the TNS or FRBcat databases, we defer to the catalogued value to maximize sample consistency.

[12] `https://www.wis-tns.org/`
[13] `https://www.frbcat.org/`
[14] `https://www.chime-frb.ca/catalog`

4. For repeaters with multiple RM measurements, we use the weighted mean, with the reciprocal of the errors as weights.

We make three exceptions based on the observed RM behavior:

- FRB 20190208A shows a secular evolution in RM which follows a 'U' shaped curve (Mckinven et al., 2023). Therefore, we use the most recent RM value rather than the weighted mean.
- FRB 20190231B has multiple RM measurements from Mckinven et al. (2023); however, CHIME reports difficulty in distinguishing RM detections near 0 from instrumental leakage. Therefore, we use the RM measurement with the lowest uncertainty to minimize propagation of any leakage errors.
- FRB 20191117A has 2 RM measurements from Mckinven et al. (2023) separated by $\sim 9\,\mathrm{rad\,m^{-2}}$, but it is unclear with only two bursts whether this variation is stochastic or secular. Therefore, we use the value with the smallest error to avoid improperly combining secularly evolved RMs.

We make three additional exceptions based on the conventions in the available literature; in cases where RM measurements are commonly compared to a well-constrained 'accepted' value which has not yet been superceded in accuracy, we use this accepted value. This affects the following FRBs:

- FRB 20121102A (e.g., Hilmarsson et al., 2021b; Michilli et al., 2018; Plavin et al., 2022); the value from Plavin et al. (2022) is used as it pre-dates other RM measurements and has a low relative error. However, since Sherman et al. (2023) compares the logarithm of the RM, deviations of the RM within an order of magnitude make little change to the analysis, and do not affect the analysis in this paper at all.
- FRB 20200120E (e.g., Bhardwaj et al., 2021; Nimmo et al., 2021); we use the value from the first detected burst in Bhardwaj et al. (2021).
- FRB 20201124A (e.g., Hilmarsson et al., 2021a; Kumar et al., 2022) we use the weighted mean value from Hilmarsson et al. (2021a)

We acknowledge that these constraints are not complete; secularly time-varying RMs are not properly represented either by the weighted mean or the value with the lowest error. In addition, while the weighted mean incorporates the signal-to-noise of individual bursts via the uncertainties, limitations due to the intrinsic bandwidth of the FRB are not explicitly accounted for. We proceed with our analysis, reasonably assuming that the reported RM's uncertainty properly quantifies the limitations of the measurement system. We leave additional revisions for variable RMs to future work.

We furthermore describe the selection criteria and process for the FRB polarization fractions used here:

1. Only polarization measurements published before the 2023 April 10 cutoff date are considered for this sample.
2. For non-repeaters and repeaters with only 1 polarization fraction measurement, we use the available measurement. If the polarization is reported for individual sub-components of the same burst, we use the weighted mean of the sub-components.
3. A minimum signal-to-noise $S/N > 8\sigma$ is imposed on all non-repeaters and individual bursts from repeaters included in this sample.
4. For FRBs with polarization measurements in the TNS or FRBcat databases, we defer to the catalogued value to maximize sample consistency.
5. For repeaters with multiple polarization measurements, we use the weighted mean, with the reciprocal of the errors as weights. If measurements are available at multiple frequencies, we use the L-band (1-2 GHz) if available. Otherwise, the observation with the nearest frequency below 1 GHz.
6. If only the signed circular polarization (V/I) is reported, then the absolute value circular polarization ($|V|/I$) is taken as the absolute value ($|V/I|$) (for further details, see Section 6.5). We make this condition given that most FRBs in the literature were reported with no $|V|/I$ measurement. If both L/I and V/I are reported but the total polarization $\sqrt{L^2 + V^2}/I$ is not explicitly stated, the total polarization is calculated as $\sqrt{(L/I)^2 + (V/I)^2}$.

Expanding on criteria 3, the minimum $S/N > 8\sigma$ applies both to non-repeaters and to the individual bursts of repeaters included in the reported weighted average

polarization fractions. Many studies fail to report the S/N of FRB detections (e.g., Feng et al., 2022a,b). In these cases, we estimate the S/N as the reported flux density S divided by the radiometer noise RMS σ_S of the detector (e.g., Condon & Ransom, 2016). If neither the S/N nor S are reported, we have chosen to include the FRB in our sample under the assumption that a reasonable detection threshold was used in the original survey.

As noted above, these selection criteria are not complete, as the weighted mean does not fully capture secularly time-varying polarization properties. We maintain the average FRB polarization fractions are sufficient for the cumulative distribution analysis presented here, and leave a fully time-dependent study to future work.

In the main text, we compare FRB properties to a sample of 1445 Galactic (and Magellanic Cloud) pulsars with published polarimetry of APs: 1305 canonical pulsars (CPs) with periods $P > 30$ ms, 137 millisecond pulsars (MSPs) with periods $P < 30$ ms, and 3 magnetars and 22 RRATs with published polarization or RM data at L-band. These are compiled from Johnston et al. (2022), Serylak et al. (2021), Wahl et al. (2022), Spiewak et al. (2022), Cameron et al. (2020), Olszanski et al. (2019), J. M. Weisberg et al. (1999), J. M. Weisberg et al. (1999), Johnston & Kerr (2018), Yan et al. (2011), Gould & Lyne (1998), Kramer et al. (2007), Camilo et al. (2007), Camilo et al. (2008), L. Levin et al. (2012), L. Levin et al. (2010), Keane & McLaughlin (2011), Caleb et al. (2019), Karastergiou et al. (2009), Xie et al. (2022). We use the following criteria and process for selecting the pulsar polarimetry and RM data:

1. Only polarization measurements published before the 2023 April 10 cutoff date are considered for this sample.

2. For each pulsar, we use the polarization fractions from the average profiles (APs) (except for the MSPES single-pulse sample discussed in Section 6.5).

3. Most pulsars are published with both $|V|/I$ and V/I; we record both values and use the absolute value of V/I for consistency as discussed in Section 6.5.

4. If multiple RM or polarization fractions are reported, the most recent measurement is used.

We note here that, as for the FRB literature sample, these criteria are not complete, as they do not capture time-varying RMs or polarization fractions in pul-

sars. A weighted average of measurements is not used for pulsars given the large amount of available data. Additionally, the most recent average profile is more well-constrained, and using average profile polarization fractions consistent the current literature on pulsar polarimetry. The average profile polarization fractions are sufficient for the analysis presented in this work, and we leave a fully time-dependent discussion to future work.

6.8.2 DSA-110 voltage data model and polarization processing

All polarization analysis of DSA-110 FRBs detected during the commissioning observations reported on herein, and the calibration of these data, are accomplished using automatically triggered voltage dumps. This refers to the storage of 61440 contiguous post-channelization complex (i.e., undetected) spectra for each antenna, with a time-resolution of 32.768 μs. The spectra consist of voltage measurements in two polarization channels for each of 63 antennas, in 6144 channels of 30.52 kHz width centered on 1405 MHz. Each complex sample is stored with 4-bit resolution for the real and imaginary parts. The four most significant bits are chosen using channel-dependent coefficients determined from the mean bandpass shapes of each antenna/polarization pair. For FRB data, the triggers are generated such that the arrival times of the bursts at 1498.75 MHz (the upper limit of the sampled band) correspond to exactly 0.5 s into the voltage dumps. Each voltage dump is stored in raw binary format, and is accompanied by a json header that includes all relevant descriptive information.

The voltage dumps are processed using a custom full-polarization beamforming pipeline (`dsa110-bbproc`). Post-correlation beamforming is implemented (Roy et al., 2018) with the addition of both auto- and cross-correlation terms to mitigate quantization noise in applying per-antenna beamforming weights. For FRB data, the weights are determined from visibility data on bright bandpass calibrators typically within 12 hr of detection. For voltage dumps on the continuum-source calibrators 3C48 and 3C286, the weights are determined from visibility data on the calibrators themselves. Ultimately, filterbank-format files are generated for each Stokes parameter by synthesizing beams in the directions of interest for each voltage dump. The polarization and Faraday-rotation definitions adopted here are summarized in Appendix 6.8.3.

The `dsa110-pol` module was developed to calculate FRB polarization and RM parameters offline from the polarized filterbank data. Major processing steps are as

Table 6.4: Previously Published FRB Sample Polarization Properties

FRB Names	Polarization Telescope/ Frequency	L/I	|V/I|	Polarization Reference	RM (rad m^{-2})	RM Reference	DM‡ (pc cm^{-3})
FRB 20201020A	Apertif/1375.0	–	–	–	110.0 ± 69.0	1	398.59 ± 0.08
FRB 20191108A	Apertif/1375.0	70.0%	10.0%	2	474.0 ± 3.0	3	588.1 ± 0.1
FRB 20190711A	ASKAP/1297.5	97.48 ± 1.39%†	0.96 ± 1.15% †	4	9.0 ± 2.0	4	593.1 ± 0.4
FRB 20190611B	ASKAP/1297.5	81.5 ± 2.1%†	31.8 ± 1.7%†	4	20.0 ± 4.0	4	321.4 ± 0.2
FRB 20190608B	ASKAP/1297.5	91.0 ± 3.0%	9.0 ± 2.0%	4	353.0 ± 2.0	4	338.7 ± 0.5
FRB 20181112A	ASKAP/1297.5	90.0%	10.0%	5	10.9 ± 0.9	5	589.27 ± 0.03
FRB 20180924B	ASKAP/1297.5	90.2 ± 2.0%	13.3 ± 1.4%	4	14.0 ± 1.0	6	361.42 ± 0.06
FRB 20180311A	Parkes/1382.0	75.0 ± 3.0%	11.0 ± 2.0%	7	4.8 ± 7.3	7	1570.9 ± 0.5
FRB 20171209A	Parkes/1382.0	100.0 ± 1.0%	0.0 ± 1.0%	7	121.6 ± 4.2	7	1457.4 ± 0.03
FRB 20150807A	Parkes/1382.0	80.0 ± 1.0%	–	8	12.0 ± 0.7	8	226.5 ± 0.1
FRB 20150418A	Parkes/1382.0	8.5 ± 1.5%	0.0 ± 4.5%	9	36.0 ± 52.0	9	776.2 ± 0.5
FRB 20150215A	Parkes/1382.0	43.0 ± 5.0%	3.0 ± 1.0%	10	1.5 ± 10.5	10	1105.6 ± 0.8
FRB 20190604A	CHIME/600.0	91.2 ± 8.1%	–	11	−20.0 ± 1.0	12	553.18 ± 3.23
FRB 20190303A	FAST/1250.0	88.7 ± 7.7%†	3.7 ± 5.8%†	13	−499.0 ± 0.7	11	223.21 ± 3.23
FRB 20190102C	ASKAP/1297.5	81.14 ± 0.91%†	5.08 ± 0.66%†	4	−110.0 ± 1.0	14	363.6 ± 0.3
FRB 20180916.J0158+65	Effelsburg/1700.0	102.1 ± 4.5%†	5.7 ± 4.4%†	15	−114.6 ± 0.6	16	347.76 ± 1.62
FRB 20180714A	Parkes/1382.0	91.0 ± 3.0%	5.0 ± 2.0%	7	−25.9 ± 5.9	7	1467.92 ± 0.3
FRB 20160102A	Parkes/1382.0	84.0 ± 15.0%	30.0 ± 11.0%	17	−220.6 ± 6.4	17	2596.1 ± 0.3
FRB 20110523A	GBT/800.0	44.0 ± 3.0%	23.0 ± 30.0%	18	−186.1 ± 1.4	18	623.3 ± 0.06
FRB 20121102A	Effelsburg, FAST/1700,1250.0	13.0 ± 3.0%	23.5 ± 0.6% †	19,20	127000.0 ± 800.0	19	557 ± 2
FRB 20191001A	ASKAP/1297.5	57.0 ± 1.0%	5.0 ± 1.0%	21	55.5 ± 9.0	21	506.92 ± 0.04
FRB 20201124A	Effelsburg, FAST/1360.0,1250.0	86.21 ± 0.01%†	10.23 ± 0.01%†	13,22,23,31	−601.0 ± 11.1†	22	410.83 ± 3.23
FRB 20180309A	Parkes/ 1382.0	45.56 ± 0.06%	24.33 ± 0.05%	7	–	–	263.42 ± 0.01
FRB 20200120E	Effelsburg/1400.0	99.3 ± 1.3%†	4.5 ± 0.9%†	30	−29.8 ± 5.0	24	88.96 ± 1.62
FRB 20151230A	Parkes/1352.0	35.0 ± 13.0%	6.0 ± 11.0%	25	–	–	960.4 ± 0.5
FRB 20140514A	Parkes/1352.0	0.0%	21.0 ± 7.0%	26	–	–	562.7 ± 0.6
FRB 20190520B	GBT/1450.0	9.0%	9.83 ± 0.68% †	27,20	−11000.0 ± 13100.0 †	27	1202 ± 10
FRB 20220912A	FAST/1400.0	80.3 ± 24.3%†	5.2 ± 0.2%†	28	0.6 ± 0.1	29	219.46 ± 0.04
FRB 20180814A	CHIME/600.0	69.1 ± 4.7%	–	11	699.8 ± 1.0	11	190.86 ± 3.23
FRB 20181030A	CHIME/600.0	72.75 ± 2.22%†	–	11	36.6 ± 0.2†	11	101.9 ± 1.62
FRB 20181119A	CHIME/600.0	67.58 ± 2.76%†	–	11	1340.0 ± 2.0 †	11	368.79 ± 6.47
FRB 20190222A	CHIME/600.0	24.61 ± 0.58%	–	11	571.0 ± 1.7	11	462.6 ± 3.23
FRB 20190208A	CHIME/600.0	86.52 ± 1.03% †	–	11	36.3 ± 0.7	11	579.06 ± 3.23
FRB 20190213B	CHIME/600.0	90.19 ± 2.68% †	–	11	−3.63 ± 0.41	11	302.47 ± 1.62
FRB 20180908B	CHIME/600.0	0.0%	–	11	0.18	11	197.33 ± 3.23
FRB 20190117A	CHIME/600.0	19.44 ± 0.40%†	–	11	76.31 ± 0.40	11	393.05 ± 1.62
FRB 20190417A	FAST/1250.0	71.5 ± 2.5%	11.7 ± 2.0%	13	4429.8 ± 3.5	11	1378.11 ± 6.47
FRB 20190907A	CHIME/600.0	28.0%	–	11	–	–	307.32 ± 3.23

Notes: Observation and polarization information for the compiled sample of previously published FRBs. The telescope and system observing frequency are those used for the polarization measurements. Names in boldface are repeaters, while non-boldfaced FRBs are non-repeating as of April 10th, 2023. For FRB 20220912A, the RM is that reported by CHIME while the polarization was measured from the DSA-110 detections. For repeaters with multiple RM or polarization measurements, values are the weighted average of observations. The sample was compiled with the use of the Transient Name Server (TNS), the FRB Catalog (FRBcat), and the Canadian Hydrogen Intensity Mapping Experiment (CHIME) FRB Catalog 1 (Amiri et al., 2021; Petroff et al., 2016; Petroff & Yaron, 2020). FRB 20180301 was excluded from this literature sample due to its inconsistent RM and L-band polarization properties, which are not accurately described by average values (Kumar et al., 2023; Luo et al., 2020). While Y.-K. Zhang et al. (2023) and Anna-Thomas et al. (2023) (While Version 1 of the ArXiv pre-print for Anna-Thomas et al. (2023) was available prior to the April 10th 2023 cutoff date, Version 2 and publication were not until May 2023.) presented additional polarization data, they were released after the data cutoff date and are excluded from this sample.

†Weighted mean of multiple bursts; ‡DM values are from the TNS catalog

Citations are listed below: (1)Pastor-Marazuela et al. (2022) (2)Connor et al. (2020) (3)Leeuwen et al. (2022) (4)Day et al. (2020) (5)Prochaska et al. (2019) (6)Bannister et al. (2019) (7)Osłowski et al. (2019) (8)Ravi et al. (2016) (9)Keane et al. (2016) (10)Petroff et al. (2017) (11)Mckinven et al. (2023) (12)Fonseca et al. (2020) (13)Feng et al. (2022b) (14)Macquart et al. (2020) (15)Nimmo et al. (2021) (16)Andersen et al. (2019) (17)Caleb et al. (2018) (18)Masui et al. (2015) (19)Plavin et al. (2022) (20)Feng et al. (2022a) (21)Bhandari et al. (2020) (22)Hilmarsson et al. (2021a) (23)Jiang et al. (2022) (24)Bhardwaj et al. (2021) (25)Bhandari et al. (2018) (26)Petroff et al. (2015) (27)Anna-Thomas et al. (2023)(28)Ravi et al. (2023) (29)McKinven & Chime/Frb Collaboration (2022) (30)Nimmo et al. (2022) (31)Xu et al. (2022a)

follows:

1. Polarimetric calibration is applied using the formalism described in Appendix 6.8.4. The stability of the calibration solutions is justified in Appendix 6.8.5, and critical assumptions on leakage are justified in Appendix 6.8.6.

2. Full-polarization spectra for each FRB are generated by optimally averaging over the burst temporal profiles (Appendix 6.8.8).

3. RM estimation then proceeds on these spectra as described in Appendix 6.8.9. If a significant RM is detected, the Stokes parameters are corrected for this RM.

4. Then, the total (T), linear (L) and circular (C) polarization spectra, as well as polarization position angle (χ) are computed. The average polarization fractions, referred to as L/I, $|V|/I$ and $\sqrt{L^2+V^2}/I$, are calculated as the weighted mean of $L_{\rm unbias}(t)/I(t)$, $C(t)/I(t)$, and $T(t)/I(t)$ across the FWHM of the burst using the optimal weights (Appendix 6.8.8). In addition, the sign-dependent circular polarization fraction V/I is computed as the weighted mean of $V(t)/I(t)$ across the burst. The mean position angle χ is calculated with a similar weighted mean across the FWHM.

6.8.3 Polarization and Faraday Rotation Background

The polarization of light is defined by the correlation properties of components of the propagating electric field. In a linear basis, where V_A and V_B refer to orthogonal linear components of the electric field, the Stokes parameters are one representation of the polarization state:

$$I = \frac{1}{2}(< V_A V_A^* > + < V_B V_B^* >) \tag{6.5}$$

$$Q = \frac{1}{2}(< V_A V_A^* > - < V_B V_B^* >) \tag{6.6}$$

$$U = \mathrm{Re}\{< V_A V_B^* >\} \tag{6.7}$$

$$V = -\mathrm{Im}\{< V_A V_B^* >\} \tag{6.8}$$

The DSA-110 uses the IAU/IEEE convention that $V > 0$ is right-hand polarization, while $V < 0$ is left-hand polarization (Van Straten et al., 2010). The linear, circular, and total polarization fractions as a function of time are computed as:

$$\frac{L_{\text{unbias}}(t)}{I(t)} = \begin{cases} \sqrt{L(t)^2 - \sigma^2}/I(t), \text{ for } \frac{L(t)}{\sigma} > 1 \\ 0, \text{ o/w} \end{cases} \tag{6.9}$$

$$\frac{C(t)}{I(t)} = \sqrt{V(t)^2}/I(t) \tag{6.10}$$

$$\frac{T(t)}{I(t)} = \sqrt{L_{\text{unbias}}(t) + V(t)^2}/I(t) \tag{6.11}$$

where $L_{\text{unbias}}(t)$ is the unbiased linear polarization following Simmons & Stewart (1985) and Everett & J. Weisberg (2001), and $L(t) = \sqrt{Q(t)^2 + U(t)^2}$ [15]. These are averaged across a burst to estimate the average polarization fractions. For all sources, $T \leq I$; in unpolarized sources, $T = 0$. In partially polarized sources, $T = pI < I$, where p is the polarization fraction. Finally, the position angle χ defines the phase difference between linearly polarized components:

$$\chi = 0.5 \tan^{-1}(\frac{U}{Q}) = 0.5 \angle P \tag{6.12}$$

where $P = Q + iU$ is the linear polarization vector. Errors in the position angle are estimated using a Monte Carlo simulation of 100 boxcar pulses with $\chi = 0$ and unity off-pulse standard deviation. The resulting error as a function of linear-polarization S/N is well-fit by a piecewise exponential with scale 28σ for $S/N > 19\sigma$, and 10σ for $S/N \leq 19\sigma$. Figure 6.8 shows the results of the simulation and best fit piecewise exponential; note these results imply that the Naghizadeh-Khouei & Clarke (1993) PA distribution significantly under-estimates the error, particularly for $S/N > 6\sigma$.

A different dispersion relation applies to orthogonal circularly polarized components for propagation through a plasma-filled region with a magnetic field, resulting in a rotation of the position angle of linearly polarized radiation. The position angle changes as a function of squared wavelength such that the RM is defined as:

$$\text{RM} = \frac{d\chi}{d\lambda^2} \tag{6.13}$$

[15] Note we adopt the convention used in equations 10 and 16 of Simmons & Stewart (1985) due to ambiguity in the unbiasing factor reported in Everett & J. Weisberg (2001).

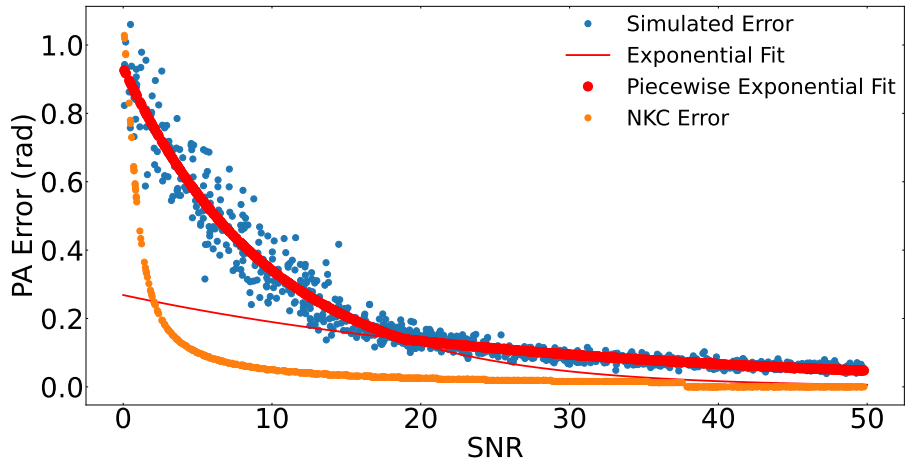

Figure 6.8: Simulated error in the linear polarization position angle (PA), as a function of linear-polarization S/N. See text for details of the simulation. The simulated error (blue) is taken as the standard deviation of the PA across the width of each boxcar pulse. The red lines indicate the piecewise exponential fit of the simulated error, while the red markers show the resulting error for each trial when computed using the fit. The error derived from the PA distribution of Naghizadeh-Khouei & Clarke (1993), shown in orange, appears to underestimate the error, especially at high S/N.

The RM characterizes the integrated line of sight magnetic field $\bar{B}_{||}$ that induces this rotation, weighted by the plasma electron number density n_e:

$$\mathrm{RM} = 0.81 \int \frac{n_e B_{||}}{(1+z(l))^2} dl \tag{6.14}$$

where z is the redshift of the dispersive material. Note that the $\bar{}$ indicates the field is averaged over the line-of-sight. In general, the RM has contributions from an FRB's host galaxy, the intergalactic medium (IGM), the Milky Way's circumgalactic medium (CGM) and interstellar medium (ISM), and the Earth's ionosphere due to the magnetic fields in these regions. This can, in addition to changing the magnitude of the RM, change the sign due to the direction dependence of the magnetic field. If the same plasma is assumed to contribute to both dispersion and RM:

$$\mathrm{DM} = \int_l^0 \frac{n_e}{1+z(l)} dl \tag{6.15}$$

the average line-of-sight magnetic field can be estimated as:

$$\bar{B}_{||}[\mu\mathrm{G}] \approx \frac{\mathrm{RM}}{0.81 \cdot \mathrm{DM}}(1+z) \tag{6.16}$$

Recent analyses imply a correlation between host RM (RM with contributions from the ionosphere, ISM, and IGM subtracted) and DM, implying that this approximation is reasonable (Mannings et al., 2022). We refer to position angle after correcting for RM is as the polarization position angle (PPA; χ_0), while PA, or χ, refer to the position angle measured without RM correction.

6.8.4 Derivation of Jones Matrix and Parallactic Angle Calibration for DSA-110

An effective Jones matrix for the coherently combined DSA-110 must be used to calibrate polarized observations, as described by, e.g., Robishaw & Heiles (2021). Calibration with a fully-defined Jones matrix accounts for cross-coupling between the orthogonal linearly polarized receptors, as well as gain and phase differences between the receptors (Heiles et al., 2001). Here we will choose a Cartesian basis aligned with the linearly polarized receptors. For the DSA-110, we operate in the 'ideal feed' assumption, that is, that there is zero cross-coupling between receptors. This requires that differences in gain or phase between the X and Y feeds are the dominant instrumental effect, which results in mixing among Stokes parameters. A difference between the X and Y gain will mix Stokes I and Q creating apparent linear polarization. A difference in phase corresponds to a time delay $\Delta t \approx \phi(\nu)(2\pi\nu)^{-1}$ between the X and Y feeds. This mixes Stokes U and V and creates residual circular polarization. Quantitatively, for the arbitrary Jones matrix below consisting of four complex terms:

$$J(\nu) = \begin{bmatrix} g_{xx}(\nu) & g_{xy}(\nu) \\ g_{yx}(\nu) & g_{yy}(\nu) \end{bmatrix} \tag{6.17}$$

we assume $|g_{xy}(\nu)| = |g_{yx}(\nu)| = 0$. We further simplify this by assuming $g_{yy}(\nu)$ is real and parameterize in terms of the absolute gain in the Y receptor, $|g_{yy}(\nu)|$, the ratio of the magnitudes of X and Y gains, $r(\nu) = |g_{xx}(\nu)|/|g_{yy}(\nu)|$, and the phase difference between the X and Y receptors, $\phi(\nu)$. The Jones matrix is then simplified to:

$$J(\nu) = \begin{bmatrix} r(\nu)|g_{yy}(\nu)|e^{i\phi(\nu)} & 0 \\ 0 & |g_{yy}(\nu)| \end{bmatrix} \tag{6.18}$$

One can estimate r by observing a known unpolarized source and assuming $Q = U = V = 0$. Similarly, one estimates ϕ by observing a known linearly polarized source and assuming $V = 0$. For DSA-110 observations, 3C48 was periodically observed as the unpolarized calibrator to estimate $r(\nu)$, while 3C286 was observed as the linearly polarized calibrator to estimate $\phi(\nu)$. Given the fixed declination (71.6°) of the DSA-110 commissioning survey, the affect of sky position on polarization calibration is left to future work. For this work, it is reasonable to assume that a single set of calibrators, 3C48 and 3C286, is sufficient for a constant pointing. At our 1.4 GHz observing frequency, 3C48 is known to be weakly polarized ($\sim 0.5\%$), which we assume is acceptable for use as an unpolarized calibrator within the error of the DSA-110[16] (Perley & Butler, 2013). 3C286 is known to have 9.5% linear polarization at 1.4 GHz, making it suitable as a linearly polarized calibrator (Perley & Butler, 2013). The absolute gain in the Y receptor, $|g_{yy}(\nu)|$, is estimated using 3C48 by comparing the observed flux to the polynomial fit (after correcting for the measured RM[17] of $-68\,\mathrm{rad\,m^{-2}}$ and estimated parallactic angle) defined by Perley & Butler (2017). $r(\nu)$, $\phi(\nu)$, and $|g_{yy}(\nu)|$ were determined after averaging over spurious peaks in Stokes parameters for each source as function of frequency, downsampling in frequency, then interpolating back to native resolution. For FRB observations, we calibrate by applying the inverse Jones matrix to the observed Stokes parameters, effectively setting the gain and phase of the X and Y feeds equal and minimizing the mixing of Stokes parameters.

Absolute position angles cannot be estimated with the current DSA-110 pipeline, as it would require tracking a calibrator source over a wide range of parallactic angles which the DSA-110, as a transit instrument, is not currently equipped for. In this work, an attempt to derive absolute position angle estimates by treating the DSA-110 as a single antenna; following Thompson et al. (2017) (Chapter 4), the elevation and azimuth of the array for a given FRB are estimated using the RA, α, and declination, δ, of the detected beam and observation time LST:

$$\sin(\theta) = \sin(b_{\mathrm{DSA}})\sin(\delta) + \cos(b_{\mathrm{DSA}})\cos(\delta)\cos(\mathrm{LST} - \alpha) \tag{6.19}$$

[16] In Appendix 6.8.6 we verify this assumption through leakage polarization tests. For additional information on polarized calibrators, see documentation for the Very Large Array (VLA) at `https://science.nrao.edu/facilities/vla/docs/manuals/obsguide/modes/pol`.

[17] Note the RM of 3C48 is measured at higher frequencies (1.6−30 GHz, or 1−18 cm wavelengths) where the polarization fraction is higher (Perley & Butler, 2013).

$$\sin(\phi + (b - 125)\delta\theta_b) = -\frac{\cos(\delta)\sin(\mathrm{LST} - \alpha)}{\cos(\theta)} \tag{6.20}$$

where l_{DSA} and b_{DSA} are the longitude and latitude of the DSA-110 (Owens Valley). b is the detected beam and $\delta\theta_b = 14$" is the synthesized beamwidth. The parallactic angle χ_{par} is then estimated as:

$$\sin(\chi_{\mathrm{par}}) = -\frac{\sin(\phi)\cos(b_{\mathrm{DSA}})}{\cos(\delta)} \tag{6.21}$$

and can be applied as a correction $\chi_{\mathrm{cal}} = \chi_0 + \chi_{\mathrm{par}}$.

6.8.5 Calibration Stability with Time and Primary-Beam Location

Four epochs of calibration observations were taken during the survey to apply to the sample of FRBs reported in this paper. Table 6.5 summarizes each observation. Each observation consists of multiple voltage dumps during the calibration-source transit. The transits nearest the center of the primary beam were used to derive Jones matrix parameters at each epoch. Figure 6.9 shows the Jones matrix solutions as a function of frequency for each epoch. From this, it is clear that the solution is stable, with standard deviation across epoch of 0.2%, 0.1 rad, and 3.6% for $r(\nu)$, $\phi(\nu)$, and $|g_{yy}(\nu)|$, respectively. Given this stability, the solutions were averaged together over all epochs and filtered in the frequency domain with a first order Savitsky-Golay filter, and this average solution was then used to calibrate all FRBs detected. The outlier $|g_{yy}(\nu)|$ solution from the 2022 April 14 observation was investigated and attributed to a software error which prevented the measurement set from being properly saved. The beamformer weights for this observation were therefore not gain calibrated resulting in a vertical offset in the measured Stokes parameters. Following the correction of this issue, no outliers were identified in subsequent calibration solutions, as shown in Figure 6.9. We therefore do not include the $|g_{yy}(\nu)|$ value from the 2022 April 14 observation in the average $|g_{yy}(\nu)|$ solution or the standard deviation reported above.

In addition to long-term stability, stability across the primary beam was estimated by using multiple Jones solutions from each epoch to calibrate the adjacent voltage dumps during the transits of 3C48 and 3C286. For each epoch, the gain solutions $r(\nu)$ and $|g_{yy}(\nu)|$ were taken as piecewise polynomial fits, while the phase solution $\phi(\nu)$ was taken as the median value across the band in order to reduce the impact of noise. The calibration is deemed stable if there is no systematic change in the

Table 6.5: Polarization Calibration Observations and Jones Matrix Parameters

3C48 observation name (Beam)	MJD	3C286 observation name (Beam)	MJD	$< r(\nu) >$	$< \phi(\nu) >$	$< \lvert g_{yy}(\nu) \rvert >$
2022/04/14, 2022/05/24 Observation						
kkz (46)	59683.829	dnz (18)	59723.215	1.00 ± 0.04	2.09 ± 0.14	1.48 ± 0.06
ane (197)	59683.837	fvn (57)	59723.217			
bzj (110)	59572.309	**kus** (135)	59723.221			
		oxr (174)	59723.223			
2022/09/14 Observation						
lck (107)	59835.417	mph (44)	59835.908	0.99 ± 0.02	2.11 ± 0.20	1.86 ± 0.02
bxc (182)	59835.422	**tnh** (122)	59835.912			
		ezb (200)	59835.916			
2022/10/21 Observation						
xtu (47)	59872.313	gbf (45)	59872.807	1.00 ± 0.03	2.15 ± 0.12	1.78 ± 0.04
eit (123)	59872.317	**lrp** (123)	59872.811			
jvp (198)	59872.321	fml (201)	59872.815			
2022/11/23 Observation						
xxc (22)	59906.219	quh (19)	59906.713	1.00 ± 0.03	2.29 ± 0.11	1.80 ± 0.04
fjr (72)	59906.222	xnr (71)	59906.716			
mia (123)	59906.224	**wtw** (123)	59906.718			
xol (173)	59906.227	vxo (175)	59906.721			
wsj (223)	59906.230	hwj (227)	59906.724			

Notes: Labels in bold are those nearest the center beam and are used to derive the Jones parameters in the last three columns. <> indicates the average value over frequency.

resulting polarization fraction and position angle as a function of each source's location within the primary beam. No significant variations in the recovered polarization properties, including RM, for 3C48 and 3C286 were observed. We therefore proceeded to use the beam-center voltage dumps to derive calibration parameters.

6.8.6 Calibration Leakage Estimates

In the above method, the off-diagonal terms characterizing leakage between the orthogonal receptors are assumed negligible, meaning that calibrated data will be uncertain up to the true magnitude of these terms. The above calibration corrects leakage between Stokes I and Q and between U and V. The leakage terms cannot be explicitly solved for without the observation of additional polarized sources over a wide range of position angles; this is not feasible with the DSA-110. Leakage between the other pairs of Stokes parameters is instead estimated by again calibrating adjacent voltage dumps on 3C48 and 3C286 on each observation epoch as described in the previous section. The remaining Q, U, and V fractions in calibrated 3C48 observations then estimate the remaining I leakage. Subtracting these leakages and the expected 9.6% linear polarization at position angle of $\chi = 33^\circ$ from calibrated 3C286 then allows for other leakage terms to be estimated. Specifically, the residual linear polarization above the expected 9.6% then corresponds to leakage from V into Q or U; the residual circular polarization is likewise leakage from Q and U into V. One can visualize this with the Mueller polarization matrix formalism (Heiles et al., 2001). The I-Q, I-U, I-V leakages then roughly estimate the first row and

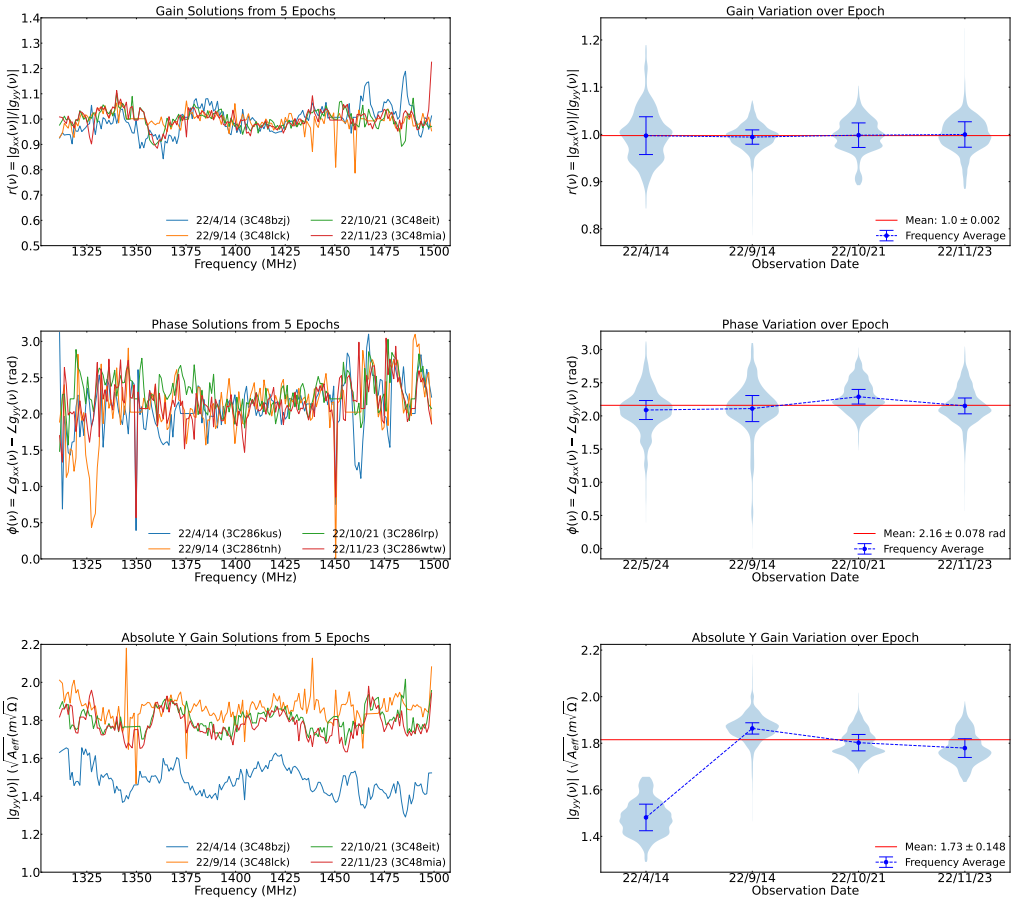

Figure 6.9: Jones matrix solutions on four epochs. *Left:* Frequency dependent $r(\nu)$, $\phi(\nu)$, and $|g_{yy}(\nu)|$ after removing birdies, downsampling and interpolating. *Right:* Solutions averaged over frequency for each observation. The violin plots show the distribution of the frequency dependent points while the red line shows the average value over all epochs.

first column of the Mueller matrix, while QU-V and V-QU roughly estimate the other off-diagonal terms, and the diagonal terms are derived from $r(\nu)$, $\phi(\nu)$, and $|g_{yy}(\nu)|$. While the matrix cannot be explicitly solved based on the 3C48 and 3C286 observations available, the leakage estimates reported here offer order of magnitude estimates.

Error bars are estimated by taking the standard error and subtracting the systematic standard error from beams within each voltage dump in which the source was not present, which characterizes the thermal noise. Leakage values for each epoch are summarized in Figure 6.10; the maximum leakage observed is 1.6% between I and U. This is within acceptable limits and justifies the ideal feed assumption above.

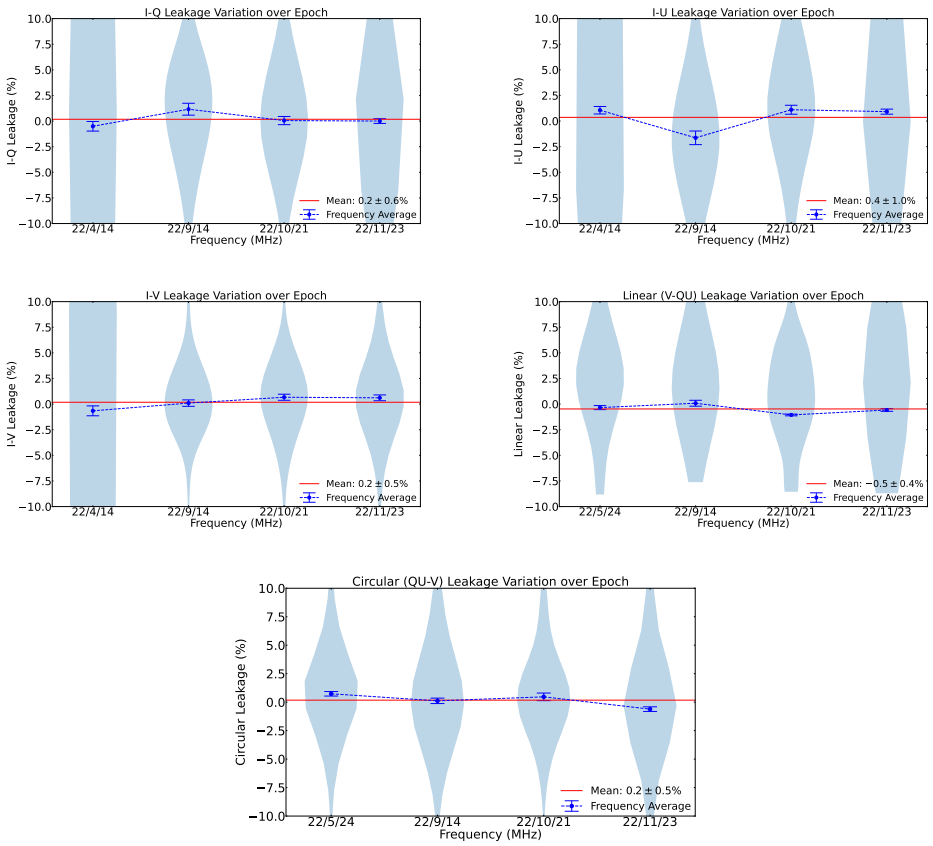

Figure 6.10: Violin plots of leakage estimates. The mean values are shown as markers, while the distributions are values from all calibrated voltage dumps and all frequency channels in each observation.

6.8.7 Example of Polarization Calibration with Pulsar J1935+1616

In Section 6.3, we presented the functioning polarization pipeline using the stacked profile of J1935+1616 shown in Figure 6.1. Here we further compute L/I, $|V|/I$, and V/I for each of the 26 pulses and for the folded profile to compare to the measured values from Gould & Lyne (1998). The linear polarization of the folded profile is $L/I = 14.6 \pm 5.6\%$, which is lower than the expected 18% but agrees within the 1σ errorbar. The absolute value circular polarization is $|V|/I = 16.9 \pm 5.7\%$ which is also within 1σ of the expected 15%. The signed circular polarization, $-2.5 \pm 21.6\%$ agrees with expected 2% within 1σ despite the opposite sign. From the pulse profiles in Figure 1 it is clear that this difference in sign is stochastic rather than a sign error in calibration[18]. From this we conclude that there is good agreement

[18]In this paper we adopt the IAU/IEE convention for Stokes V, in which $V > 0$ is right-handed and $V < 0$ is left-handed. Gould & Lyne (1998) use the PSR/IEE convention which has the opposite

between the DSA-110 polarization measurement of J1935+16 and expectation and find no significant systematic errors to apply. Figure 6.11 shows the polarization fractions of each of the 26 pulses as well as those of the average profiles. Note the low expected RM, $-2.3 \pm 0.5\,\mathrm{rad\,m^{-2}}$, and the low detected linear-polarization S/N prevent a confident RM measurement for verification.

6.8.8 Optimal Spectral Estimation

After calibration of each FRB, full-Stokes spectra are calculated by averaging over the burst time series. In order to prevent inclusion of noise in the spectrum, a window around each burst is first manually defined to contain all apparent emission components, over which the average spectrum is computed. Ideally, the pulse would then be weighted using the variance at each time step. These variances are estimated as the inverse of the frequency averaged S/N at each time step, i.e., the temporal profile of the burst. Previous studies have used a Gaussian fit and similar functions to estimate pulse profiles. However, the large variety in burst morphology among FRBs implies a Gaussian may not offer a reasonable fit. The pulse profile is determined by first averaging the total-intensity dynamic spectrum over frequency, then downsampling and linear interpolating to the desired time resolution to eliminate stochasticity and insignificant mid-pulse structure. Finally, to remove artifacts in due to the interpolation, the profile is filtered with a third-order Savitsky-Golay filter, with the filter width chosen specific to each burst. The profile is set to zero outside of the burst window defined above. The spectrum can then be computed as a weighted sum of the time series within the defined window using the profile as weights.

6.8.9 Detailed RM Synthesis Derivation and S/N Method Error

What follows is a detailed derivation of the RM Synthesis method and its variation, the S/N Method, utilized in this paper (Brentjens & De Bruyn, 2005; Burn, 1966; Heald, 2008). In the discrete case, Burn (1966) estimates the Faraday dispersion function (FDF) as the Fourier transform of the observed linear polarization vector $P_{\mathrm{obs}}(\lambda^2) = Q_{\mathrm{obs}}(\lambda^2) + iU_{\mathrm{obs}}(\lambda^2)$ from λ^2 space to RM space:

$$\hat{F}(\mathrm{RM}) = \frac{1}{N_{\lambda^2}} \sum_{\lambda^2} P_{\mathrm{obs}}(\lambda^2) W(\lambda^2)(\lambda^2) e^{-2i\mathrm{RM}(\lambda^2-\lambda_0^2)} \tag{6.22}$$

definition. Therefore, we have flipped the sign of Stokes V in both the EPN profile in Figure 1 and the expected V/I so that both are in the IAU/IEE convention for more accurate comparison.

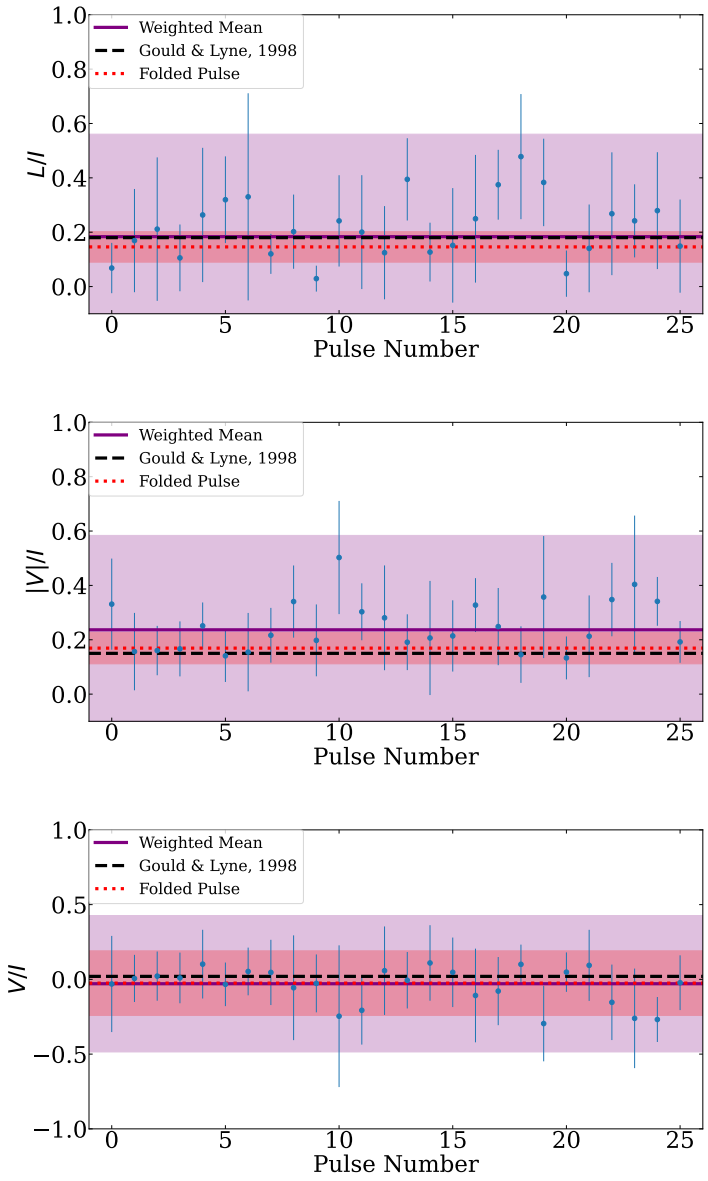

Figure 6.11: Linear (*top*), absolute value circular (*middle*), and signed circular polarization (*bottom*) measurements of J1935+1616. Polarization fractions for individual pulses are shown in blue, and the weighted mean is shown in purple, with the shaded area indicating the weighted error. The expected polarization fractions from Gould & Lyne (1998) (18%, 15%, and 2% from top to bottom) are shown in black. The linear and absolute value circular polarization fractions measured from the folded profiles, shown in red, are in good agreement with expectation within the 1σ errorbar.

where λ_0 is the mean of the λ^2 axis, and $W(\lambda^2)$ are weights applied to the spectra. Note that $Q_{\rm obs}(\lambda^2)$ and $U_{\rm obs}(\lambda^2)$ are the optimally weighted spectra of Q and U as described above. $\hat{F}(\mathrm{RM})$ is proportional to the linear polarization for a given RM correction, and this can therefore be interpreted as a linear polarization maximization method. The most probable value of the RM then occurs where $\hat{F}(\mathrm{RM})$ peaks; a parabola is fit to an oversampled RM range around the peak and its maximum taken to be the RM estimate. An error on this value is estimated as the full-width at half-max (FWHM) of the RM spread function (RMSF), divided by the linear-polarization S/N:

$$\sigma_{\rm RM1} = \frac{\mathrm{FWHM}\sigma_L}{\max(\hat{F}(\mathrm{RM}))} \tag{6.23}$$

where σ_L is the off-peak standard deviation in the linear-polarization signal, $|P(t)|$, after applying the ideal spectral weights described in the previous section. Sources here are assumed to be 'Faraday thin', meaning that for a small emitting volume, the amount of Faraday rotation that can occur is strictly limited; each FRB with significant RM is then assumed to have a dispersion function that peaks at only one value (e.g., Brentjens & De Bruyn, 2005).

RM synthesis is first performed with the `RM-tools` package[19], a Python implementation which also uses 'cleaning' to minimize sidelobes in the RM spectrum (Purcell et al., 2020). In order to exercise more control over the trial RM range, resolution, and synthesis method, an RM synthesis pipeline was implemented within the `dsa110-pol` library as `faradaycal`. In this function, the RM range and resolution can be specified, and since synthesis is implemented by brute force without optimization, the trial RM range can be arbitrarily wide and fine, and within arbitrary limits. Following synthesis with `RM-tools`, `faradaycal` is run on a fine RM trial grid (10^6 trial RMs from $\pm 10^6$ rad m^{-2} for a resolution 2 rad m^{-2}). A smaller region of $\pm 1,000$ rad m^{-2} is then defined around the peak in the FDF and run with 5,000 trial RMs for a resolution of 0.4 rad m^{-2} to obtain a better estimate.

The traditional RM synthesis methods described above operate on the time-averaged spectrum of an FRB, and therefore neglect any time-variation in polarization properties that could warp the measured RM. To address this, an additional RM synthesis function, `faradaycal_SNR` has been implemented within the `dsa110-pol` library. Rather than operating on the time-averaged spectrum, `faradaycal_SNR` instead

[19] `https://github.com/CIRADA-Tools/RM-Tools`

applies for each trial RM de-rotation at each time-step within the burst as shown below:

$$P_{\rm RM}(t,\lambda^2) = P_{\rm obs}(t,\lambda^2)(\lambda^2)e^{-2i{\rm RM}(\lambda^2-\lambda_0^2)} \tag{6.24}$$

The linear-polarization S/N for each trial RM, $\hat{F}_{\rm S/N}$, is then calculated by averaging $|P_{\rm RM}(t,\lambda^2)|$ over frequency, then taking the weighted average over the pulse, using the ideal spectral weights. The detected RM is taken to be the RM such that $\hat{F}_{\rm S/N}$ is maximized. This not only includes the time dependence of polarization properties, but also more closely matches how RM calibration is applied, i.e. de-rotation is applied at each time step. However, this method, referred to as the 'S/N Method' is more computationally expensive, and can therefore only be run on the smaller RM range of $\pm 1,000\,{\rm rad\,m^{-2}}$ around the peak determined from running `faradaycal`. In addition to obtaining the RM through synthesis with the time averaged S/N, the S/N method is performed on the spectrum at each timestep within the burst to investigate any time dependence on sub-millisecond timescales.

Brentjens & De Bruyn (2005) estimate the error in RM determined from RM synthesis to be equivalent to that estimated from QU-fitting, shown below, in the limit of high S/N:

$$\sigma_{\rm RM} = \frac{\sqrt{3}\sigma}{4|P|(\lambda^2_{\rm max}-\lambda^2_{\rm min})} \tag{6.25}$$

where $|P|$ is the linear polarization at the peak RM, and σ is the root-mean-squared (RMS) noise in the Q and U maps. However, many of the FRBs detected in this sample have low S/N, and this error is likely an underestimate. A more conservative error is estimated through a small simulation, in which 100 top-hat pulses are simulated at linear-polarization S/N trials between 1,2,...,20. The RM is then estimated for each trial and the error taken to be the standard deviation of all trials. The results of this simulation, as well as the error estimate from Brentjens & De Bruyn (2005) are shown in Figure 6.12. From this, it is clear that there is higher scatter in RM than implied by the formula above. Since a 9σ threshold is imposed on the peak $\hat{F}_{\rm S/N}$ based on the linear-polarization S/N needed to clearly resolve a peak in the RM spectrum[20], an exponential of the form:

[20]Note this threshold is determined through trial and error and was still subject to visual scrutiny in the reported results.

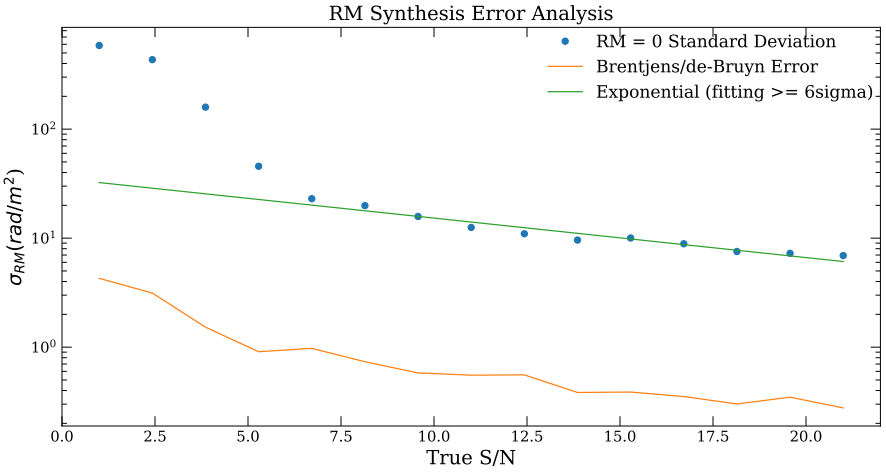

Figure 6.12: Simulated error in the recovered RM through RM Synthesis, as a function of linear-polarization S/N. See text for details of the simulation. For each true S/N, the mean analytic RM-uncertainty estimate from Brentjens & De Bruyn (2005) is shown as an orange curve. The blue points show the standard deviations of the recovered RMs, which are fit by the green line.

$$\sigma_{\mathrm{RM2}} = Ae^{B\hat{F}_{\mathrm{S/N}}} \tag{6.26}$$

is fit to the simulated error above $\sim 6\sigma$. A least-squares fit results in best-fit parameters $A = 35.17$, $B = -0.08$. This exponential is shown in Figure 6.12 .

We apply the standard RM synthesis methods to each FRB on the full range of sensitivity from $\pm 10^6\,\mathrm{rad\,m^{-2}}$. This range was estimated following the method outlined by Mckinven et al. (2021), which computes the maximum RM before the PA, χ can change significantly due to Faraday rotation. The change in PA that can occur within a frequency channel is given by Burke et al. (2019):

$$\Delta\chi = \frac{-2\mathrm{RM}c^2\Delta\nu}{\nu_c^3} \tag{6.27}$$

where $\Delta\nu$ is the width of each frequency channel and ν_c is the center frequency. The fraction of the initial polarization as a function of RM is then Schnitzeler & Lee (2015):

$$f = \frac{\sin(\Delta\chi)}{\Delta\chi} \tag{6.28}$$

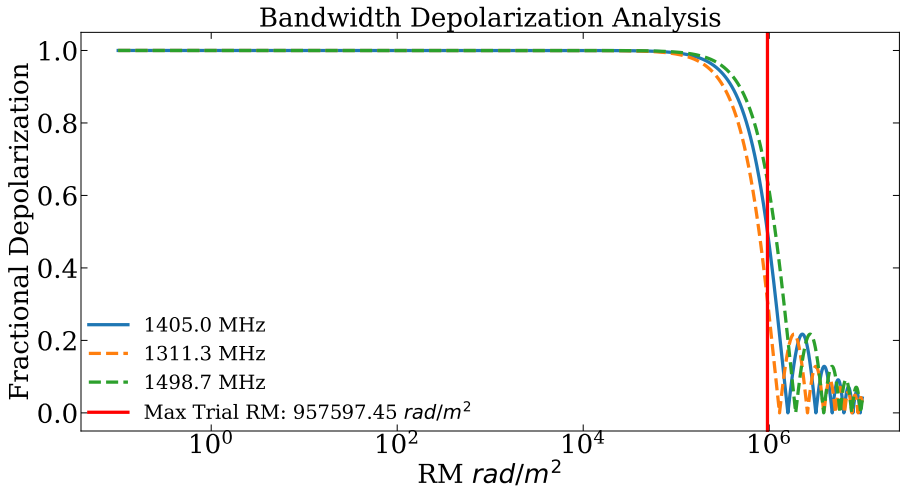

Figure 6.13: Fractional depolarization the DSA-110 as a function of RM, for different frequencies within the DSA-110 band.

Figure 6.13 shows a plot of f as a function of trial RM. The DSA-110's high frequency resolution means that it is sensitive to RM rotation up to $\mathrm{RM_{max}} = 9.6^{+2.0}_{-1.8} \times 10^5\,\mathrm{rad\,m^{-2}}$, making it well-equipped to detect RM's larger than the current maximum (FRB 20121102, which has an RM on the order of $\sim 10^5\,\mathrm{rad\,m^{-2}}$) (Hilmarsson et al., 2021b).

6.8.10 An RM-scattering scenario for FRB 20220319D (Mark)

Recall that for FRB 20220319D, $\mathrm{DM_{host}}$ and therefore $\bar{B}_{||}$ could not be accurately estimated given its close proximity to the Milky Way (Ravi et al., 2023). One can instead place limits on the host magnetic field by assuming the derived σ_{RM} and using a scattering timescale, τ_s, assuming that all depolarization is due to stochastic RM variation. A detailed derivation is described in the supplementary material of Feng et al. (2022b), and a short summary is provided here.

If all refractive scattering is contributed by a screen within the host galaxy at a distance R from the source, the scattering timescale τ_s is related to the refraction angle θ_s by:

$$\tau_s \approx \frac{R\theta_s^2}{2c} \tag{6.29}$$

The spatial scale of fluctuations in the electron density causing this refraction is then:

$$l_{\mathrm{scat}} \approx \theta_s R \approx \sqrt{2c\tau_s R} \tag{6.30}$$

If it is further assumed that the screen has stochastic RM variations with standard deviation $\sigma_{\rm RM}$ around mean $|{\rm RM_{scat}}|$, they can be written as:

$$\sigma_{\rm RM} \approx \sqrt{\frac{R}{l_{\rm scat}}}|{\rm RM_{scat}}|. \tag{6.31}$$

$|{\rm RM_{scat}}|$ is created by a perturbation in the electron-density or magnetic field. Assume for simplicity that only the electron density n_e is perturbed so that:

$$\sigma_{\rm RM} \approx \sqrt{R l_{\rm scat}}\frac{r_e^2}{2\pi e}\bar{B}_{||}\delta n_e \tag{6.32}$$

where r_e is the classical electron radius, and e is the electron charge. Solving for $\bar{B}_{||}\delta n_e$,

$$\bar{B}_{||}\delta n_e \approx \frac{2\pi\sigma_{\rm RM}e}{r_e^2(2c\tau_s R^3)^{1/4}}. \tag{6.33}$$

In FRB 20220319D's case, the low DM = $110.95\,{\rm pc\,cm^{-3}}$ suggests the scattering screen is not located near the source. Assume instead that $R \sim 1\,{\rm kpc}$. Consider first taking the estimated $\sigma_{\rm RM} = 20.81\,{\rm rad\,m^{-2}}$, and the upper limit on scattering derived for FRB 20220319D, $\tau_s \leq 0.061\,{\rm ms}$ (Ravi et al., 2023). This results in a lower limit of $\bar{B}_{||}\delta n_e \gtrsim 139.9\,\mu{\rm G\,cm^{-3}}$. For electron-density variations of order $\delta n_e \sim 0.01 - 0.1\ {\rm cm^{-3}}$ (estimated from DM and R), this would require a magnetic field $\bar{B}_{||} \lesssim 1399.0 - 13989.5\,\mu{\rm G}$, which would be relatively high compared to the typical ISM magnetic field, but consistent with a dense (e.g., star-forming) intervening environment.

Alternatively, Feng et al. (2022b) identifies a correlation of $\sigma_{\rm RM}$ with $|{\rm RM}|$ that can be approximated by $|{\rm RM}| \propto 100\sigma_{\rm RM}$. Following this rule, a more likely value for FRB 20220319D would be $\sigma_{\rm RM} \approx 0.73\ {\rm rad\,m^{-2}}$, implying the intrinsic emission is not 100% polarized[21]. Under this assumption, the upper limit becomes $\bar{B}_{||}\delta n_e \gtrsim 4.9\,\mu{\rm G\,cm^{-3}}$. Again using electron-density variations of order $\delta n_e \sim 0.01 - 0.1\ {\rm cm^{-3}}$, this would require a magnetic field $\bar{B}_{||} \lesssim 73.9 - 739.5\,\mu{\rm G}$. Although this is still large, it is more easily achievable in a Milky Way-like environment. The two scenarios give insignificant mean $|{\rm RM_{scat}}| << {\rm RM}$, equal to $3.9\times10^{-3}\ {\rm rad\,m^{-2}}$ and $0.1\times10^{-3}\ {\rm rad\,m^{-2}}$, respectively. In summary, an RM scattering scenario for the depolarization of FRB 20220319D is likely more plausible than for other DSA-110 FRBs, but would nonetheless require an unusually dense and magnetized intervening system.

[21] The RM value used here is derived from as host galaxy contribution to the RM, which is derived in the companion paper, Sherman et al. (2023).

6.8.11 PPA Variation Analysis

To estimate the significance of PPA (χ_0) variations, we conduct a variation of the χ^2 test that can be applied to circular data. For this we follow methods described in Mardia & Jupp (2000), which we refer to as MJ2000 (see also Mardia, 1972; Mardia & Zemroch, 1975a,b; Rao, 1972, and NCSS Technical Procedures Documentation)[22]. To determine if the PPA is constant, we assume a null hypothesis (H0) that the PPA is distributed as a von Mises random variable with mean angle $\hat{\mu}$ and concentration parameter $\hat{\kappa}$. For each FRB, we estimate $\hat{\mu}$ from the set of PPA $\{\chi_{0,i}\}$ in time bins with linear S/N > 3σ using equations 2.2.1-2.2.4 in MJ2000:

$$\hat{\mu} = \begin{cases} \tan^{-1}(\frac{\bar{S}}{\bar{C}}), & \text{for } \bar{C} \geq 0 \\ \tan^{-1}(\frac{\bar{S}}{\bar{C}}) + \pi, & \text{for } \bar{C} < 0 \end{cases} \tag{6.34}$$

where $\bar{C}$ and $\bar{S}$ are defined as:

$$\bar{C} = \frac{\sum \sigma_{\chi_{0,i}}^{-2} \cos(\chi_{0,i})}{\sum \sigma_{\chi_{0,i}}^{-2}} \tag{6.35}$$

$$\bar{S} = \frac{\sum \sigma_{\chi_{0,i}}^{-2} \sin(\chi_{0,i})}{\sum \sigma_{\chi_{0,i}}^{-2}} \tag{6.36}$$

where $\{\sigma_{\chi_{0,i}}\}$ are the uncertainties on each PA sample. From MJ2000 equation 5.3.5, the maximum likelihood estimate of $\hat{\kappa}$ is defined by the condition:

$$\frac{I_0(\hat{\kappa})}{I_1(\hat{\kappa})} = \bar{R} \tag{6.37}$$

where $\bar{R} = \sqrt{\bar{C}^2 + \bar{S}^2}$ and I_d is the d^{th} order modified Bessel function of the first kind. We use a spline linear interpolation to numerically solve for $\hat{\kappa}$. Finally the Score test statistic, which we refer to as $\chi^2_\angle$, is given by:

$$\chi^2_\angle = \begin{cases} 2N\hat{\kappa}(\bar{R}_{\hat{\mu}} - \bar{C}_{\hat{\mu}})(1 - (4N\hat{\kappa}\frac{I_0(\hat{\kappa})}{I_1(\hat{\kappa})})^{-1}), & \text{for } N < 5 \\ 4N\frac{\bar{R}^2_{\hat{\mu}} - \bar{C}^2_{\hat{\mu}}}{2-\bar{C}^2}, & \text{for } N \geq 5, \bar{C}_{\hat{\mu}} \leq 2/3 \\ \frac{2N}{1+\bar{C}^2_{\hat{\mu}}+3n^{-1}} \ln(\frac{1-\bar{C}^2}{1-\bar{R}^2}), & \text{for } N \geq 5, \bar{C}_{\hat{\mu}} > 2/3 \end{cases} \tag{6.38}$$

[22] https://www.ncss.com/wp-content/themes/ncss/pdf/Procedures/NCSS/Circular_Data_Analysis.pdf

where N is the number of PPA samples and we define:

$$\bar{C}_{\hat{\mu}} = N^{-1} \sum \cos(\chi_{0,i} - \hat{\mu}) \tag{6.39}$$

$$\bar{S}_{\hat{\mu}} = N^{-1} \sum \sin(\chi_{0,i} - \hat{\mu}) \tag{6.40}$$

$$\bar{R}_{\hat{\mu}} = \sqrt{\bar{S}^2_{\hat{\mu}} + \bar{C}^2_{\hat{\mu}}} \tag{6.41}$$

Through Monte Carlo simulations, we verify that $\chi^2_\angle$ follows a χ^2 distribution with one degree of freedom, and use this to compute a p-value for each FRB's $\chi^2_\angle$ estimate.

After computing $\chi^2_\angle$ for each FRB, we find no significant PPA variations at the 90% level or beyond. From visual inspection of some bursts, for example FRB 20220207C and FRB 20220310F (see Figures 6.14-6.17), that show evidence of variation without being identified as significant, we infer that the large PPA uncertainties and small N prevent rejection of the null hypothesis. We follow-up this analysis by computing the maximum difference in PPA across each FRB and its signficance, following a similar method to Jiang et al. (2022, Appendix C). With this we find a maximum 3.8σ PPA change across FRB 20220310F, which supports the mode change discussed in Section 6.4. A less significant 2σ PPA change is observeed for FRB 20220207C, supporting the $\chi^2_\angle$ result that its PPA variation is not significant.

6.8.12 Summary Plots for 25 DSA-110 FRBs

Figures 6.14-6.17 show the polarization summary plots for each of the 25 DSA-110 FRBs, including polarization profiles, PPAs, and dynamic spectra. Figures 6.18-6.20 show the RM summary plots for the 20 DSA-110 FRBs with RM detections.

6.8.13 RM Time Evolution Plots for Multicomponent FRBs

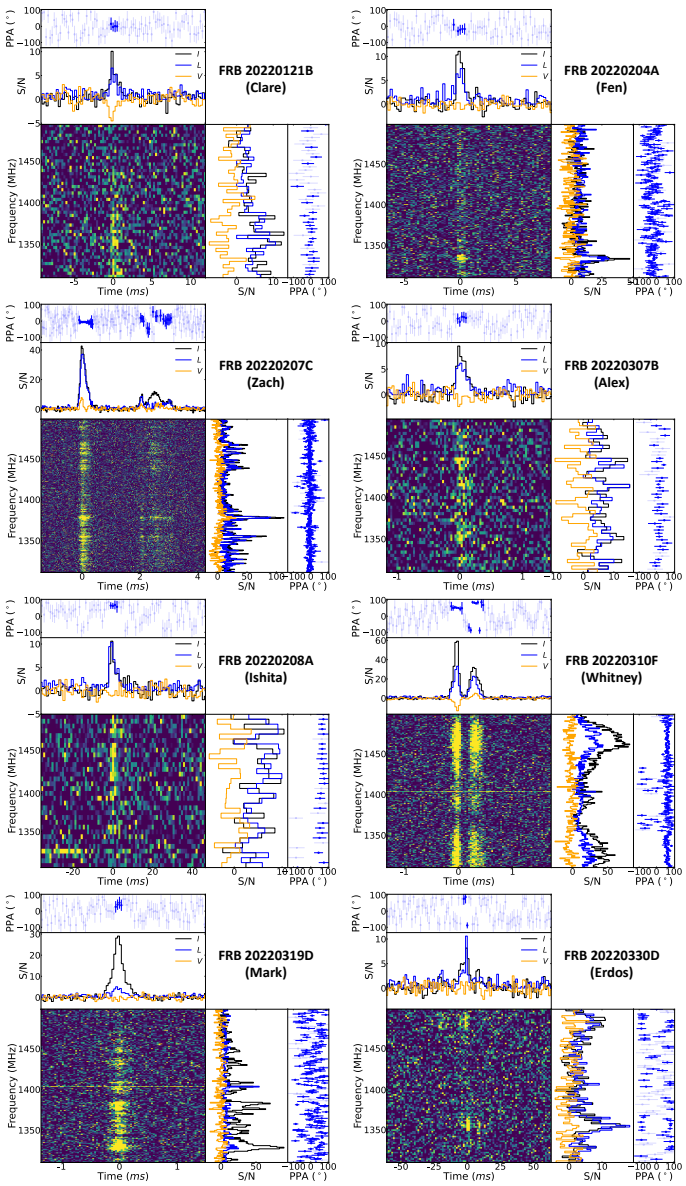

Figure 6.14: Summary of polarization data for each DSA-110 FRB. For each FRB, from top, we show the PPA (with 1σ errorbars) measured after correcting for RM, and frequency averaged time series of Stokes I, L, and V. The PPA is highlighted in bins with linear-polarization S/N $> 3\sigma$. The dynamic spectrum is shown at center, to the right of which are shown optimally summed spectra (Appendix 6.8.8) and the spectrally resolved PPA with $> 3\sigma$ bins highlighted. For FRBs with no measured RM, the PA without RM correction, rather than the PPA is shown.

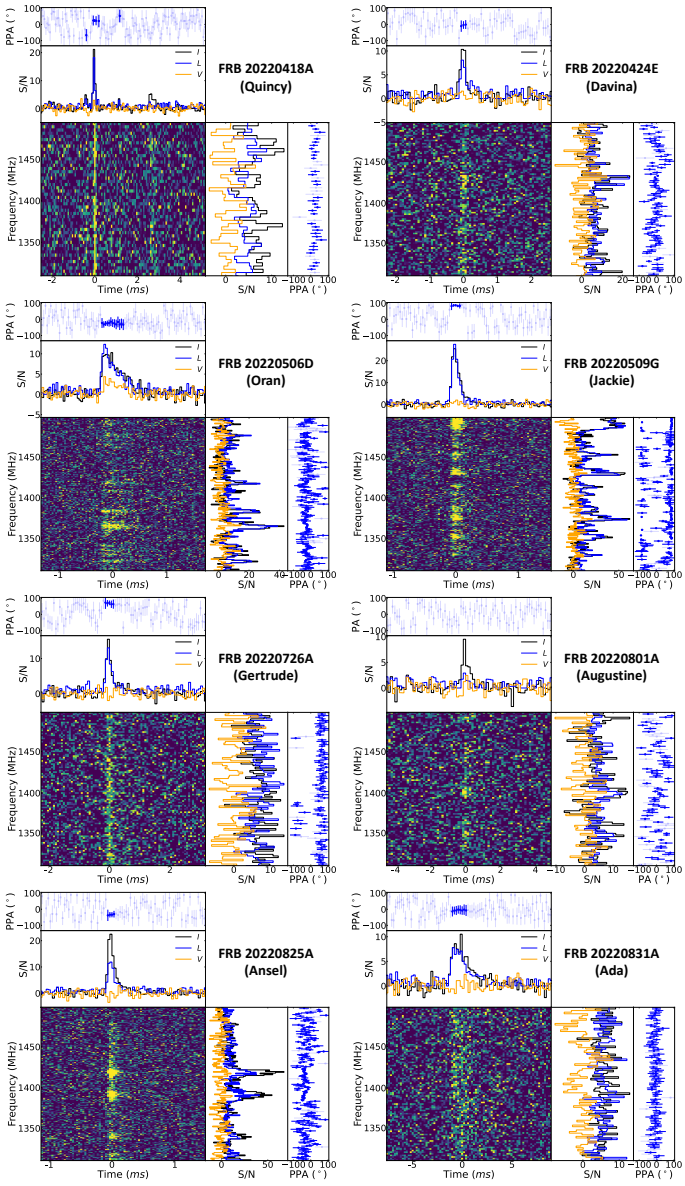

Figure 6.15: Same as Figure 6.14.

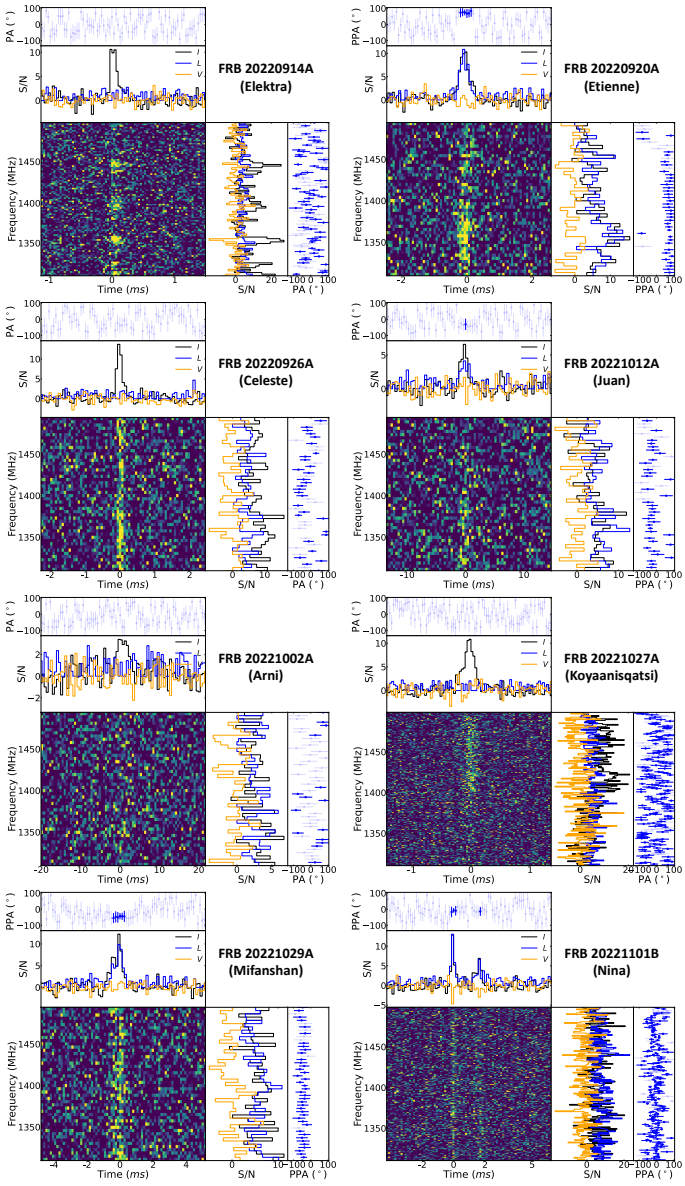

Figure 6.16: Same as Figure 6.14.

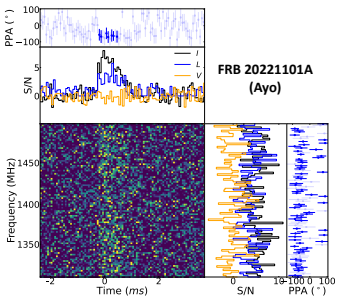

Figure 6.17: Same as Figure 6.14.

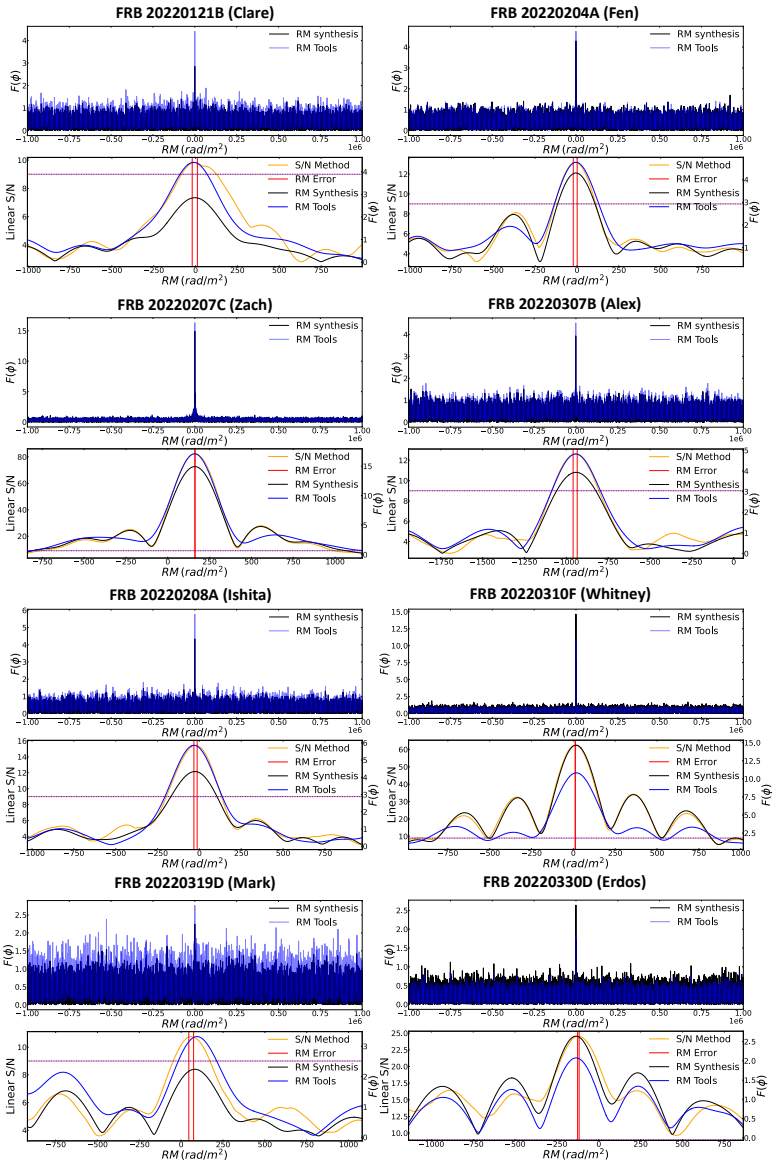

Figure 6.18: Summary of RM data on each FRB with significant detection. For each FRB, the top panel shows the RM spectra evaluated over the full range of sensitivity using two different methods (Appendix 6.8.9), and the bottom panel shows a detailed analysis of the S/N of the peak. The horizontal purple line indicates the 9σ significance threshold applied to the S/N Method spectrum (yellow).

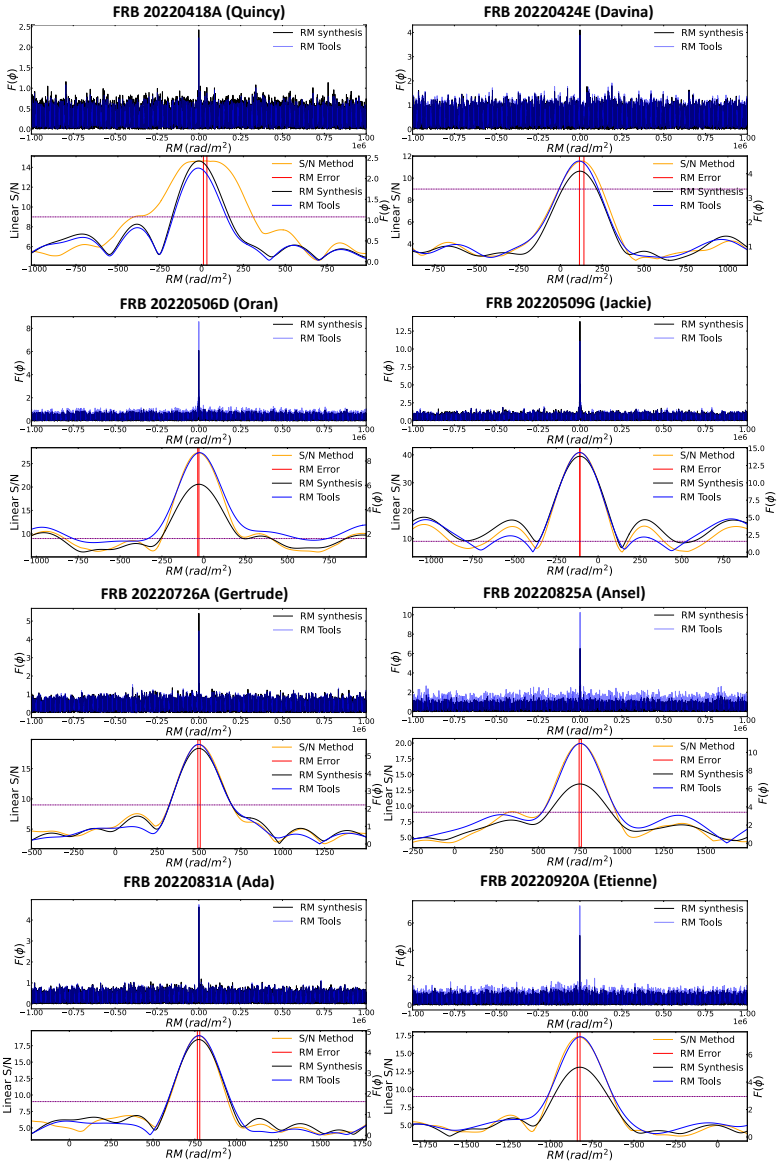

Figure 6.19: Same as Figure 6.18.

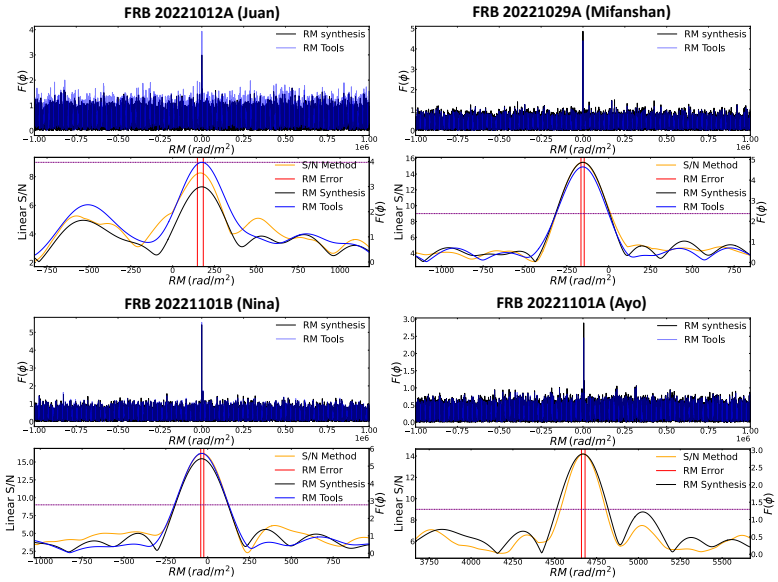

Figure 6.20: Same as Figure 6.18.

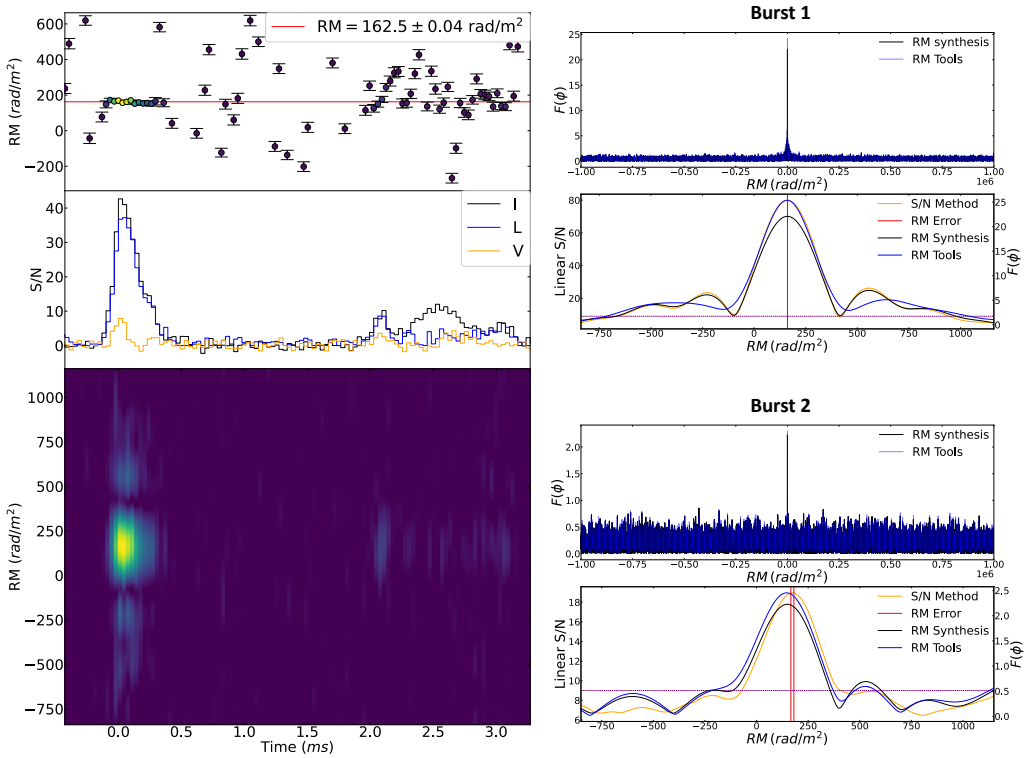

Figure 6.21: Time evolution of RM in FRB 20220207C; *Right:* The top plot shows the measured RM from the S/N method for each time bin; the polarized profile showing Stokes I (black), linear polarization (blue) and circular polarization (orange) is shown in the middle plot. The bottom plot shows the RM spectrum in each time bin, referred to as the Rotation Measure Transform. In the top plot, the color of each point corresponds to the peak S/N in the RM spectrum for that time bin, and correlates with the colormap in the RM transform. The red line is drawn at the average RM value from both sub-components, $162.48 \pm 0.04\,\mathrm{rad\,m^{-2}}$. *Right:* The RM synthesis summary plots are shown for sub-bursts 1 (top) and 2 (bottom) individually. See the caption for Figure 6.18 for a description of each trace in the RM synthesis plots.

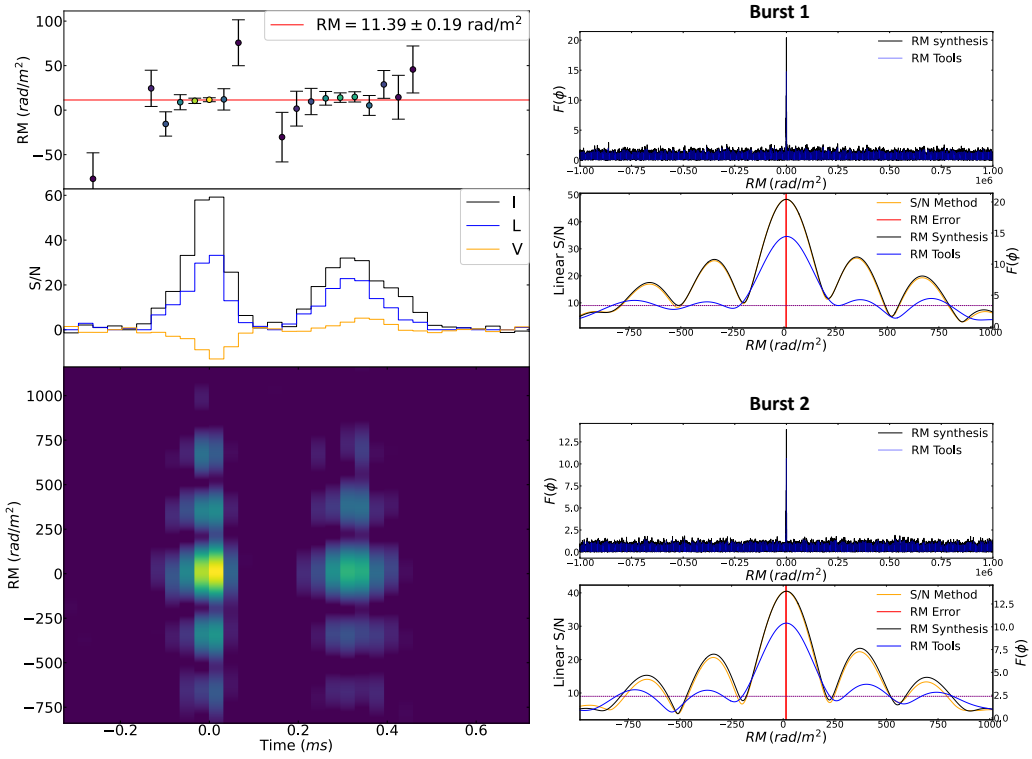

Figure 6.22: Same as Figure 6.21 for FRB 20220310F. The red line is drawn at the average RM value from both sub-components, $11.4 \pm 0.2\,\mathrm{rad\,m^{-2}}$.

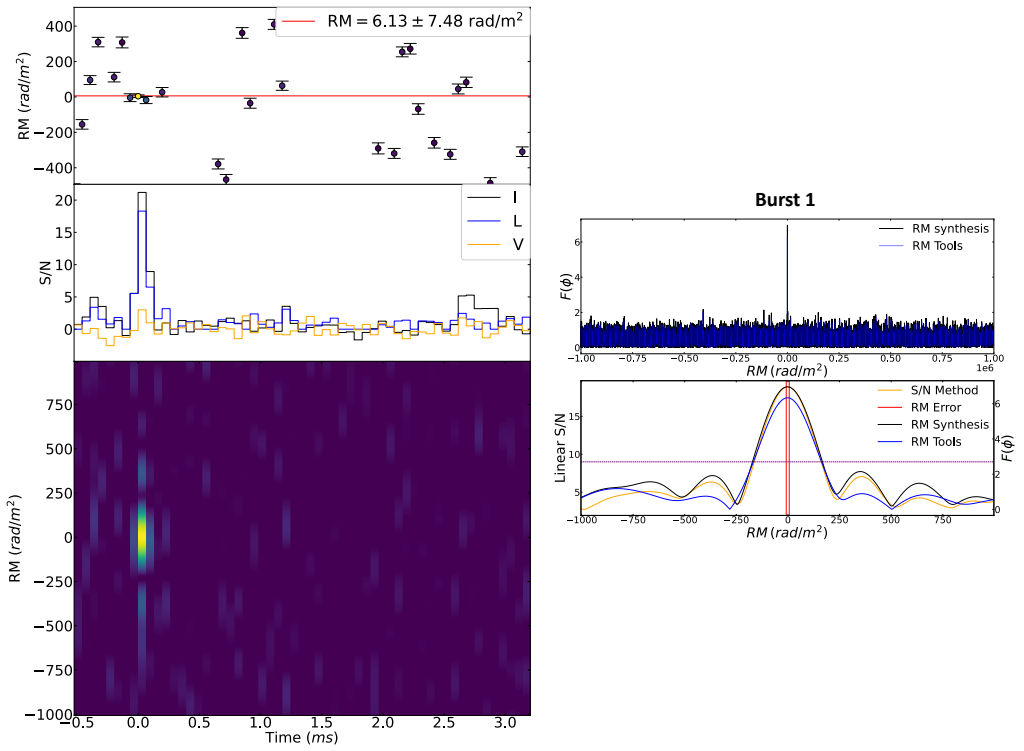

Figure 6.23: Same as Figure 6.21 for FRB 20220418A. The red line is drawn at the average RM value from all sub-components, $6.1 \pm 7.5\,\mathrm{rad\,m^{-2}}$. For the individual components, a significant RM is found only for the first.

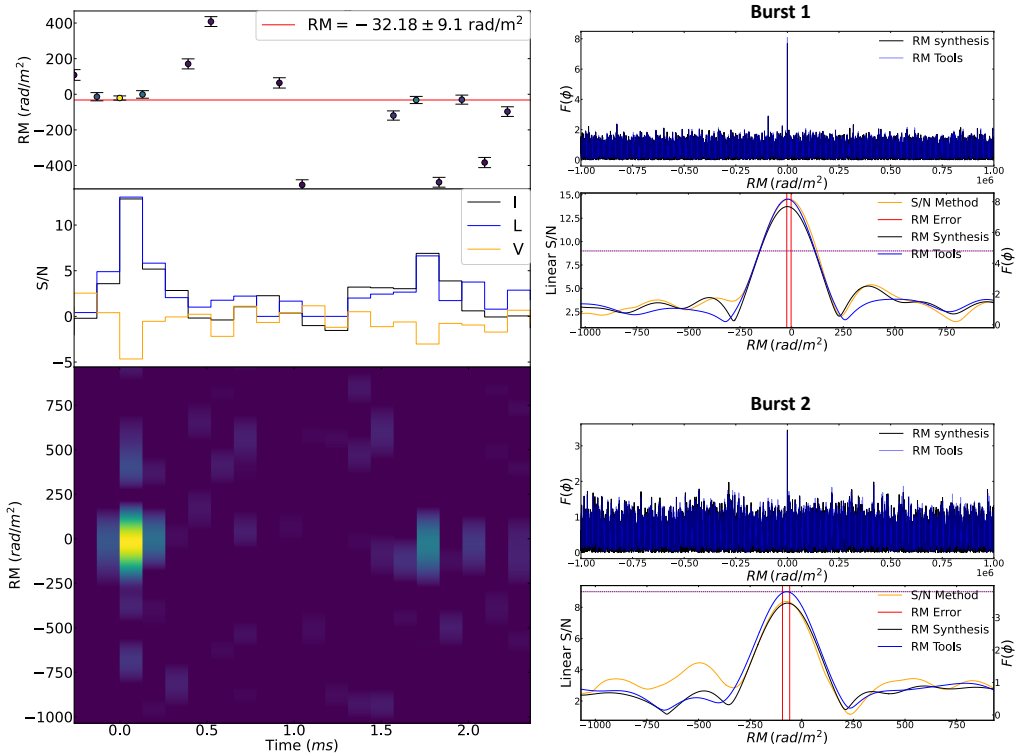

Figure 6.24: Same as Figure 6.21 for FRB 20221101B. The red line is drawn at the average RM value from both sub-components, $-13.1 \pm 10.5\,\mathrm{rad\,m^{-2}}$.

CHAPTER 6 BIBLIOGRAPHY

Amiri, M. et al. (2021). "The First CHIME/FRB Fast Radio Burst Catalog". In: *The Astrophysical Journal Supplement Series* 257.2, p. 59. DOI: 10.3847/1538-4365/ac33ab. URL: https://doi.org/10.3847%2F1538-4365%2Fac33ab.

Andersen, B. et al. (2019). "CHIME/FRB discovery of eight new repeating fast radio burst sources". In: *The Astrophysical Journal Letters* 885.1, p. L24.

Anna-Thomas, R. et al. (2023). "Magnetic field reversal in the turbulent environment around a repeating fast radio burst". In: *Science* 380.6645, pp. 599–603.

Bannister, K. W. et al. (2019). "A single fast radio burst localized to a massive galaxy at cosmological distance". In: *Science* 365.6453, pp. 565–570.

Beloborodov, A. M. (2021). "Can a strong radio burst escape the magnetosphere of a magnetar?" In: *The Astrophysical Journal Letters* 922.1, p. L7.

Beniamini, P., P. Kumar, & R. Narayan (2022). "Faraday depolarization and induced circular polarization by multipath propagation with application to FRBs". In: *Monthly Notices of the Royal Astronomical Society* 510.3, pp. 4654–4668.

Beniamini, P., Z. Wadiasingh, & B. D. Metzger (2020). "Periodicity in recurrent fast radio bursts and the origin of ultralong period magnetars". In: *Monthly Notices of the Royal Astronomical Society* 496.3, pp. 3390–3401.

Bhandari, S. et al. (2018). "The SUrvey for Pulsars and Extragalactic Radio Bursts–II. New FRB discoveries and their follow-up". In: *Monthly Notices of the Royal Astronomical Society* 475.2, pp. 1427–1446.

Bhandari, S. et al. (2020). "Limits on precursor and afterglow radio emission from a fast radio burst in a star-forming galaxy". In: *The Astrophysical Journal Letters* 901.2, p. L20.

Bhandari, S. et al. (May 2023). "A Nonrepeating Fast Radio Burst in a Dwarf Host Galaxy". In: *The Astrophysical Journal* 948.1, 67, p. 67. DOI: 10.3847/1538-4357/acc178. arXiv: 2211.16790 [astro-ph.HE].

Bhardwaj, M. et al. (2021). "A nearby repeating fast radio burst in the direction of M81". In: *The Astrophysical Journal Letters* 910.2, p. L18.

Brentjens, M. A. & A. De Bruyn (2005). "Faraday rotation measure synthesis". In: *Astronomy & Astrophysics* 441.3, pp. 1217–1228.

Burke, B. F., F. Graham-Smith, & P. N. Wilkinson (2019). *An introduction to radio astronomy*. Cambridge University Press.

Burn, B. (1966). "On the depolarization of discrete radio sources by Faraday dispersion". In: *Monthly Notices of the Royal Astronomical Society* 133.1, pp. 67–83.

Caleb, M. et al. (2018). “The SUrvey for Pulsars and Extragalactic Radio Bursts–III. Polarization properties of FRBs 160102 and 151230”. In: *Monthly Notices of the Royal Astronomical Society* 478.2, pp. 2046–2055.

Caleb, M. et al. (2019). “Polarization studies of rotating radio transients”. In: *Monthly Notices of the Royal Astronomical Society* 487.1, pp. 1191–1199.

Cameron, A. D. et al. (2020). “An in-depth investigation of 11 pulsars discovered by FAST”. In: *Monthly Notices of the Royal Astronomical Society* 495.3, pp. 3515–3530.

Camilo, F. et al. (2007). “Polarized Radio Emission from the Magnetar XTE J1810–197”. In: *The Astrophysical Journal* 659.1, p. L37.

Camilo, F. et al. (2008). “The Magnetar 1E 1547.0–5408: Radio Spectrum, Polarimetry, and Timing”. In: *The Astrophysical Journal* 679.1, pp. 681–686.

Chatterjee, S. et al. (Jan. 2017). “A direct localization of a fast radio burst and its host”. In: *Nature* 541.7635, pp. 58–61. DOI: 10.1038/nature20797. arXiv: 1701.01098 [astro-ph.HE].

Cho, H. et al. (2020). “Spectropolarimetric analysis of FRB 181112 at microsecond resolution: implications for fast radio burst emission mechanism”. In: *The Astrophysical Journal Letters* 891.2, p. L38.

Condon, J. J. & S. M. Ransom (2016). *Essential radio astronomy*. Princeton University Press.

Connor, L. et al. (2020). “A bright, high rotation-measure FRB that skewers the M33 halo”. In: *Monthly Notices of the Royal Astronomical Society* 499.4, pp. 4716–4724.

Cordes, J. (1976). “Pulsar radiation as polarized shot noise”. In: *The Astrophysical Journal* 210, pp. 780–791.

Day, C. K. et al. (Sept. 2020). “High time resolution and polarization properties of ASKAP-localized fast radio bursts”. In: *Monthly Notices of the Royal Astronomical Society* 497.3, pp. 3335–3350. DOI: 10.1093/mnras/staa2138. arXiv: 2005.13162 [astro-ph.HE].

Everett, J. & J. Weisberg (2001). “Emission beam geometry of selected pulsars derived from average pulse polarization data”. In: *The Astrophysical Journal* 553.1, p. 341.

Falcke, H. & L. Rezzolla (Feb. 2014). “Fast radio bursts: the last sign of supramassive neutron stars”. In: *Astronomy & Astrophysics* 562, A137, A137. DOI: 10.1051/0004-6361/201321996. arXiv: 1307.1409 [astro-ph.HE].

Feng, Y. et al. (2022a). “Circular polarization in two active repeating fast radio bursts”. In: *Science Bulletin* 67.23, pp. 2398–2401.

Feng, Y. et al. (2022b). “Frequency-dependent polarization of repeating fast radio bursts—implications for their origin”. In: *Science* 375.6586, pp. 1266–1270.

Fonseca, E. et al. (2020). “Nine new repeating fast radio burst sources from CHIME/FRB”. In: *The Astrophysical Journal Letters* 891.1, p. L6.

Gordon, A. C. et al. (2023). “The demographics, stellar populations, and star formation histories of fast radio burst host galaxies: implications for the progenitors”. In: *The Astrophysical Journal* 954.1, p. 80.

Gould, D. & A. Lyne (1998). “Multifrequency polarimetry of 300 radio pulsars”. In: *Monthly Notices of the Royal Astronomical Society* 301.1, pp. 235–260.

Gruzinov, A. & Y. Levin (2019). “Conversion measure of Faraday rotation–conversion with application to fast radio bursts”. In: *The Astrophysical Journal* 876.1, p. 74.

Gu, W.-M. et al. (June 2016). “A Neutron Star-White Dwarf Binary Model for Repeating Fast Radio Burst 121102”. In: *The Astrophysical Journal Letters* 823.2, L28, p. L28. DOI: 10.3847/2041-8205/823/2/L28. arXiv: 1604.05336 [astro-ph.HE].

Han, J. L. et al. (Oct. 1998). “Circular polarization in pulsar integrated profiles”. In: *Monthly Notices of the Royal Astronomical Society* 300.2, pp. 373–387. DOI: 10.1046/j.1365-8711.1998.01869.x. arXiv: astro-ph/9806021 [astro-ph].

Hankins, T. et al. (2003). “Nanosecond radio bursts from strong plasma turbulence in the Crab pulsar”. In: *Nature* 422.6928, pp. 141–143.

Heald, G. (2008). “The Faraday rotation measure synthesis technique”. In: *Proceedings of the International Astronomical Union* 4.S259, pp. 591–602. DOI: 10.1017/S1743921309031421.

Heiles, C. et al. (2001). “Mueller matrix parameters for radio telescopes and their observational determination”. In: *Publications of the Astronomical Society of the Pacific* 113.788, p. 1274.

Hewitt, D. M. et al. (2023). “Dense forests of microshots in bursts from FRB 20220912A”. In: *Monthly Notices of the Royal Astronomical Society* 526.2, pp. 2039–2057. DOI: 10.1093/mnras/stad2847. arXiv: 2308.12118 [astro-ph.HE].

Hilmarsson, G. et al. (2021a). “Polarization properties of FRB 20201124A from detections with the Effelsberg 100-m radio telescope”. In: *Monthly Notices of the Royal Astronomical Society* 508.4, pp. 5354–5361.

Hilmarsson, G. et al. (2021b). “Rotation measure evolution of the repeating fast radio burst source FRB 121102”. In: *The Astrophysical journal letters* 908.1, p. L10.

Ilie, C. D., S. Johnston, & P. Weltevrede (Feb. 2019). “Evidence for magnetospheric effects on the radiation of radio pulsars”. In: *Monthly Notices of the Royal Astronomical Society* 483.2, pp. 2778–2794. DOI: 10.1093/mnras/sty3315. arXiv: 1811.12831 [astro-ph.HE].

Jiang, J.-C. et al. (2022). "FAST Observations of an Extremely Active Episode of FRB 20201124A. III. Polarimetry". In: *Research in Astronomy and Astrophysics* 22.12, p. 124003.

Johnston, S. et al. (2022). "The thousand-pulsar-array programme on MeerKAT VII: polarisation properties of pulsars in the Magellanic Clouds". In: *Monthly Notices of the Royal Astronomical Society* 509.4, pp. 5209–5217.

Johnston, S. & M. Kerr (2018). "Polarimetry of 600 pulsars from observations at 1.4 GHz with the Parkes radio telescope". In: *Monthly Notices of the Royal Astronomical Society* 474.4, pp. 4629–4636.

Johnston, S. & M. Kramer (2019). "On the beam properties of radio pulsars with interpulse emission". In: *Monthly Notices of the Royal Astronomical Society* 490.4, pp. 4565–4574. DOI: 10.1093/mnras/stz2865. arXiv: 1910.04550 [astro-ph.HE].

Karastergiou, A. et al. (2009). "Radio polarization measurements from RRAT J1819-1458". In: *Monthly Notices of the Royal Astronomical Society: Letters* 396.1, pp. L95–L99.

Keane, E. & M. McLaughlin (2011). "Rotating radio transients". In: *arXiv preprint arXiv:1109.6896*.

Keane, E. et al. (2016). "The host galaxy of a fast radio burst". In: *Nature* 530.7591, pp. 453–456.

Kirsten, F. et al. (Feb. 2022). "A repeating fast radio burst source in a globular cluster". In: *Nature* 602.7898, pp. 585–589. DOI: 10.1038/s41586-021-04354-w. arXiv: 2105.11445 [astro-ph.HE].

Kirsten, F. et al. (June 2023). "Connecting repeating and non-repeating fast radio bursts via their energy distributions". In: *arXiv e-prints*, arXiv:2306.15505, arXiv:2306.15505. DOI: 10.48550/arXiv.2306.15505. arXiv: 2306.15505 [astro-ph.HE].

Kramer, M. et al. (2007). "Polarized radio emission from a magnetar". In: *Monthly Notices of the Royal Astronomical Society* 377.1, pp. 107–119.

Kumar, P. et al. (2022). "Circularly polarized radio emission from the repeating fast radio burst source FRB 20201124A". In: *Monthly Notices of the Royal Astronomical Society* 512.3, pp. 3400–3413.

Kumar, P. et al. (2023). "Spectro-Polarimetric variability in the repeating fast radio burst source FRB 20180301A". In: *arXiv preprint arXiv:2304.01763*.

Law, C. J. et al. (May 2024). "Deep Synoptic Array Science: First FRB and Host Galaxy Catalog". In: *ApJ* 967.1, 29, p. 29. DOI: 10.3847/1538-4357/ad3736. arXiv: 2307.03344 [astro-ph.HE].

Leeuwen, J. van et al. (2022). “The Apertif Radio Transient System (ARTS): Design, Commissioning, Data Release, and Detection of the first 5 Fast Radio Bursts”. In: *arXiv preprint arXiv:2205.12362*.

Levin, L. et al. (Sept. 2010). “A Radio-loud Magnetar in X-ray Quiescence”. In: *ApJ* 721.1, pp. L33–L37. DOI: 10.1088/2041-8205/721/1/L33. arXiv: 1007.1052 [astro-ph.HE].

– (2012). “Radio emission evolution, polarimetry and multifrequency single pulse analysis of the radio magnetar PSR J1622- 4950”. In: *Monthly Notices of the Royal Astronomical Society* 422.3, pp. 2489–2500.

Li, C. et al. (2021). “HXMT identification of a non-thermal X-ray burst from SGR J1935+ 2154 and with FRB 200428”. In: *Nature Astronomy* 5.4, pp. 378–384.

Li, D. et al. (2022). “A Highly Variable Magnetized Environment in a Pulsar Binary resembling Fast Radio Bursts”. In: *arXiv preprint arXiv:2205.07917*.

– (June 2023). “A highly magnetized environment in a pulsar binary system”. In: *Nature* 618.7965, pp. 484–488. DOI: 10.1038/s41586-023-05983-z. arXiv: 2205.07917 [astro-ph.HE].

Lin, R. et al. (Mar. 2023). “Resolving the Emission Regions of the Crab Pulsar’s Giant Pulses. II. Evidence for Relativistic Motion”. In: *The Astrophysical Journal* 945.2, 115, p. 115. DOI: 10.3847/1538-4357/acba95. arXiv: 2211.05209 [astro-ph.HE].

Lorimer, D. R. (2008). “Binary and millisecond pulsars”. In: *Living reviews in relativity* 11.1, p. 8.

Luan, J. & P. Goldreich (Apr. 2014). “Physical Constraints on Fast Radio Bursts”. In: *The Astrophysical Journal Letters* 785.2, L26, p. L26. DOI: 10.1088/2041-8205/785/2/L26. arXiv: 1401.1795 [astro-ph.HE].

Luo, R. et al. (2020). “Diverse polarization angle swings from a repeating fast radio burst source”. In: *Nature* 586.7831, pp. 693–696.

Lyubarsky, Y. (2014). “A model for fast extragalactic radio bursts”. In: *Monthly Notices of the Royal Astronomical Society: Letters* 442.1, pp. L9–L13.

Macquart, J.-P. et al. (2020). “A census of baryons in the Universe from localized fast radio bursts”. In: *Nature* 581.7809, pp. 391–395.

Majid, W. A. et al. (Sept. 2021). “A Bright Fast Radio Burst from FRB 20200120E with Sub-100 Nanosecond Structure”. In: *The Astrophysical Journal Letters* 919.1, L6, p. L6. DOI: 10.3847/2041-8213/ac1921. arXiv: 2105.10987 [astro-ph.HE].

Manchester, R. N., J. H. Taylor, & G. R. Huguenin (Jan. 1973). “Frequency Dependence of Pulsar Polarization”. In: *The Astrophysical Journal Letters* 179, p. L7. DOI: 10.1086/181105.

Manchester, R. N., J. H. Taylor, & G. R. Huguenin (Feb. 1975). "Observations of pulsar radio emission. II. Polarization of individual pulses." In: *The Astrophysical Journal* 196, pp. 83–102. DOI: 10.1086/153395.

Manchester, R. N. (1971). "Observations of pulsar polarization at 410 and 1665 MHz". In: *Astrophysical Journal Supplement, vol. 23, p. 283 (1971)* 23, p. 283.

Mannings, A. G. et al. (2021). "A high-resolution view of fast radio burst host environments". In: *The Astrophysical Journal* 917.2, p. 75.

Mannings, A. G. et al. (2022). "Fast Radio Bursts as Probes of Magnetic Fields in Galaxies at z< 0.5". In: *arXiv preprint arXiv:2209.15113*.

Mardia, K. V. (1972). *Statistics of directional data.* Probability and mathematical statistics. Academic Press. ISBN: 0124711502. URL: https://search.ebscohost.com/login.aspx?direct=true&AuthType=ip,sso&db=cat09073a&AN=cit.oai.edge.caltech.folio.ebsco.com.fs00001057.73b39503.802d.4a13.939f.ea01212e06c5&site=eds-live&scope=site&custid=s8984125.

Mardia, K. V. & P. E. Jupp (2000). *Directional statistics.* Wiley series in probability and statistics. J. Wiley. ISBN: 0471953334. URL: https://search.ebscohost.com/login.aspx?direct=true&AuthType=ip,sso&db=cat09073a&AN=cit.oai.edge.caltech.folio.ebsco.com.fs00001057.7399d9f8.d802.4ce0.8701.5afe7b791172&site=eds-live&scope=site&custid=s8984125.

Mardia, K. V. & P. J. Zemroch (1975a). "Algorithm AS 81: Circular Statistics". In: *Journal of the Royal Statistical Society. Series C (Applied Statistics)* 24.1, pp. 147–150. ISSN: 00359254, 14679876. URL: http://www.jstor.org/stable/2346721 (visited on 01/19/2024).

– (1975b). "Algorithm AS 86: The Von Mises Distribution Function". In: *Journal of the Royal Statistical Society. Series C (Applied Statistics)* 24.2, pp. 268–272. ISSN: 00359254, 14679876. URL: http://www.jstor.org/stable/2346578 (visited on 01/19/2024).

Masui, K. et al. (2015). "Dense magnetized plasma associated with a fast radio burst". In: *Nature* 528.7583, pp. 523–525.

Mckinven, R. et al. (2023). "Revealing the Dynamic Magneto-ionic Environments of Repeating Fast Radio Burst Sources through Multi-year Polarimetric Monitoring with CHIME/FRB". In: *arXiv preprint arXiv:2302.08386*.

Mckinven, R. (2022). "Spectropolarimetry of Fast Radio Bursts, Radio Galaxies, and the Milky Way". PhD thesis. University of Toronto (Canada).

McKinven, R. & Chime/Frb Collaboration (Oct. 2022). "Nine Bursts in Three Days from a Newly Discovered Repeating Source of Fast Radio Bursts". In: *The Astronomer's Telegram* 15679, p. 1.

Mckinven, R. et al. (2021). "Polarization Pipeline for Fast Radio Bursts Detected by CHIME/FRB". In: *The Astrophysical Journal* 920.2, p. 138.

Melrose, D. & J.-P. Macquart (1998). "Stochastic Faraday Rotation". In: *The Astrophysical Journal* 505.2, p. 921.

Metzger, B. D., B. Margalit, & L. Sironi (May 2019). "Fast radio bursts as synchrotron maser emission from decelerating relativistic blast waves". In: *Monthly Notices of the Royal Astronomical Society* 485.3, pp. 4091–4106. DOI: 10.1093/mnras/stz700. arXiv: 1902.01866 [astro-ph.HE].

Michilli, D. et al. (2018). "An extreme magneto-ionic environment associated with the fast radio burst source FRB 121102". In: *Nature* 553.7687, pp. 182–185.

Mitra, D., M. Arjunwadkar, & J. M. Rankin (2015). "Polarized quasiperiodic structures in pulsar radio emission reflect temporal modulations of non-stationary plasma flow". In: *The Astrophysical Journal* 806.2, p. 236.

Mitra, D., G. I. Melikidze, & R. Basu (June 2023). "Meterwavelength Single-pulse Polarimetric Emission Survey. VI. Towards understanding the Phenomenon of Pulsar Polarization in Partially Screened Vacuum Gap model". In: *arXiv e-prints*, arXiv:2306.02537, arXiv:2306.02537. DOI: 10.48550/arXiv.2306.02537. arXiv: 2306.02537 [astro-ph.HE].

Mitra, D. et al. (2016). "Meterwavelength single-pulse polarimetric emission survey". In: *The Astrophysical Journal* 833.1, p. 28.

Morrell, T. E. & C. J. Law (Feb. 2022). *DSA-110 Event Archive*. Version 0.0.1. URL: https://github.com/dsa110/dsa110-archive.

Naghizadeh-Khouei, J. & D. Clarke (1993). "On the statistical behaviour of the position angle of linear polarization". In: *Astronomy and Astrophysics, Vol. 274, p. 968 (1993)* 274, p. 968.

Nimmo, K. et al. (2021). "Highly polarized microstructure from the repeating FRB 20180916B". In: *Nature Astronomy* 5.6, pp. 594–603.

Nimmo, K. et al. (2022). "Burst timescales and luminosities as links between young pulsars and fast radio bursts". In: *Nature Astronomy* 6.3, pp. 393–401.

Olszanski, T. E., D. Mitra, & J. M. Rankin (2019). "Arecibo 4.5/1.4/0.33-GHz polarimetric single-pulse emission survey". In: *Monthly Notices of the Royal Astronomical Society* 489.2, pp. 1543–1555.

Osłowski, S. et al. (2019). "Commensal discovery of four fast radio bursts during Parkes Pulsar Timing Array observations". In: *Monthly Notices of the Royal Astronomical Society* 488.1, pp. 868–875.

Oswald, L. S., A. Karastergiou, & S. Johnston (July 2023). "Pulsar polarization: a partial-coherence model". In: *Monthly Notices of the Royal Astronomical Society*. DOI: 10.1093/mnras/stad2271. arXiv: 2307.14265 [astro-ph.HE].

Pastor-Marazuela, I. et al. (2022). "A fast radio burst with sub-millisecond quasi-periodic structure". In: *arXiv preprint arXiv:2202.08002*.

Perley, R. A. & B. J. Butler (May 2013). "INTEGRATED POLARIZATION PROPERTIES OF 3C48, 3C138, 3C147, AND 3C286". In: *The Astrophysical Journal Supplement Series* 206.2, p. 16. DOI: 10.1088/0067-0049/206/2/16. URL: https://doi.org/10.1088%2F0067-0049%2F206%2F2%2F16.

Perley, R. A. & B. J. Butler (2017). "An accurate flux density scale from 50 MHz to 50 GHz". In: *The Astrophysical Journal Supplement Series* 230.1, p. 7.

Petroff, E. et al. (2015). "A real-time fast radio burst: polarization detection and multiwavelength follow-up". In: *Monthly Notices of the Royal Astronomical Society* 447.1, pp. 246–255.

Petroff, E. et al. (2016). "FRBCAT: the fast radio burst catalogue". In: *arXiv preprint arXiv:1601.03547*.

Petroff, E. & O. Yaron (Aug. 2020). "Fast Radio Burst Catalogue on the TNS". In: *Transient Name Server AstroNote* 160, p. 1.

Petroff, E. (2017). "Fast radio bursts: recent discoveries and future prospects". In: *arXiv preprint arXiv:1709.02189*.

Petroff, E. et al. (2017). "A polarized fast radio burst at low Galactic latitude". In: *Monthly Notices of the Royal Astronomical Society* 469.4, pp. 4465–4482.

Plavin, A. et al. (2022). "FRB 121102: Drastic changes in the burst polarization contrasts with the stability of the persistent emission". In: *Monthly Notices of the Royal Astronomical Society* 511.4, pp. 6033–6041.

Pleunis, Z. et al. (2021). "Fast radio burst morphology in the first CHIME/FRB catalog". In: *The Astrophysical Journal* 923.1, p. 1.

Prochaska, J. X. et al. (2019). "The low density and magnetization of a massive galaxy halo exposed by a fast radio burst". In: *Science* 366.6462, pp. 231–234.

Purcell, C. R. et al. (May 2020). *RM-Tools: Rotation measure (RM) synthesis and Stokes QU-fitting*. Astrophysics Source Code Library, record ascl:2005.003. ascl: 2005.003.

Qu, Y. & B. Zhang (2023). "Polarization of fast radio bursts: radiation mechanisms and propagation effects". In: *Monthly Notices of the Royal Astronomical Society* 522.2, pp. 2448–2477.

Radhakrishnan, V. & D. J. Cooke (Jan. 1969). "Magnetic Poles and the Polarization Structure of Pulsar Radiation". In: *The Astrophysical Letters* 3, p. 225.

Radhakrishnan, V. & J. M. Rankin (Mar. 1990). "Toward an Empirical Theory of Pulsar Emission. V. On the Circular Polarization in Pulsar Radiation". In: *The Astrophysical Journal* 352, p. 258. DOI: 10.1086/168531.

Rao, J. S. (1972). "Some variants of chi-square for testing uniformity on the circle." In: *Zeitschrift für Wahrscheinlichkeitstheorie und Verwandte Gebiete* 22.1, pp. 33–44. ISSN: 0044-3719.

Ravi, V., R. N. Manchester, & G. Hobbs (June 2010). "Wide Radio Beams from γ-ray Pulsars". In: *The Astrophysical Journal Letters* 716.1, pp. L85–L89. DOI: 10.1088/2041-8205/716/1/L85. arXiv: 1005.1966 [astro-ph.HE].

Ravi, V. & P. D. Lasky (Jan. 2016). "A neutron star progenitor for FRBs? Insights from polarisation measurements". In: *arXiv e-prints*, arXiv:1601.06131, arXiv:1601.06131. DOI: 10.48550/arXiv.1601.06131. arXiv: 1601.06131 [astro-ph.HE].

Ravi, V. et al. (2016). "The magnetic field and turbulence of the cosmic web measured using a brilliant fast radio burst". In: *Science* 354.6317, pp. 1249–1252.

Ravi, V. et al. (2023). "Deep synoptic array science: discovery of the host galaxy of FRB 20220912A". In: *The Astrophysical Journal Letters* 949.1, p. L3.

Robishaw, T. & C. Heiles (May 2021). "The Measurement of Polarization in Radio Astronomy". In: *The WSPC Handbook of Astronomical Instrumentation*. WORLD SCIENTIFIC, pp. 127–158. DOI: 10.1142/9789811203770_0006. URL: https://doi.org/10.1142%2F9789811203770_0006.

Roy, J., J. N. Chengalur, & U.-L. Pen (Sept. 2018). "A Post-correlation Beamformer for Time-domain Studies of Pulsars and Transients". In: *The Astrophysical Journal* 864.2, 160, p. 160. DOI: 10.3847/1538-4357/aad815. arXiv: 1808.01088 [astro-ph.IM].

Schnitzeler, D. & K. Lee (2015). "Rotation measure synthesis revisited". In: *Monthly Notices of the Royal Astronomical Society: Letters* 447.1, pp. L26–L30.

Serylak, M. et al. (2021). "The thousand-pulsar-array programme on MeerKAT IV: Polarization properties of young, energetic pulsars". In: *Monthly Notices of the Royal Astronomical Society* 505.3, pp. 4483–4495.

Sharma, K. et al. (June 2023). "Deep Synoptic Array Science: A Massive Elliptical Host Among Two Galaxy-cluster Fast Radio Bursts". In: *The Astrophysical Journal* 950.2, 175, p. 175. DOI: 10.3847/1538-4357/accf1d. arXiv: 2302.14782 [astro-ph.HE].

Sherman, M. B. et al. (2023). "Deep Synoptic Array Science: Implications of Faraday Rotation Measures of Fast Radio Bursts Localized to Host Galaxies". In: *The Astrophysical Journal Letters* 957.1, p. L8. DOI: 10.3847/2041-8213/ad0380.

Simmons, J. & B. Stewart (1985). "Point and interval estimation of the true unbiased degree of linear polarization in the presence of low signal-to-noise ratios". In: *Astronomy and Astrophysics* 142, pp. 100–106.

Spiewak, R. et al. (2022). "The MeerTime Pulsar Timing Array: A census of emission properties and timing potential". In: *Publications of the Astronomical Society of Australia* 39. DOI: 10.1017/pasa.2022.19. URL: https://doi.org/10.1017%2Fpasa.2022.19.

Stinebring, D. R. et al. (June 1984). "Pulsar polarization fluctuations. I. 1404 MHz statistical summaries." In: *The Astrophysical Journal Supplement Series* 55, pp. 247–277. DOI: 10.1086/190954.

Suresh, A. & J. M. Cordes (2019). "Induced polarization from birefringent pulse splitting in magneto-ionic media". In: *The Astrophysical Journal* 870.1, p. 29.

Thompson, A. R., J. M. Moran, & G. W. Swenson (2017). *Interferometry and synthesis in radio astronomy*. Springer Nature.

Totani, T. (Oct. 2013). "Cosmological Fast Radio Bursts from Binary Neutron Star Mergers". In: *Publications of the Astronomical Society of Japan* 65, L12, p. L12. DOI: 10.1093/pasj/65.5.L12. arXiv: 1307.4985 [astro-ph.HE].

Van Straten, W. et al. (2010). "psrchive and psrfits: Definition of the Stokes Parameters and Instrumental Basis Conventions". In: *Publications of the Astronomical Society of Australia* 27.1, pp. 104–109.

Vedantham, H. & V. Ravi (2019). "Faraday conversion and magneto-ionic variations in fast radio bursts". In: *Monthly Notices of the Royal Astronomical Society: Letters* 485.1, pp. L78–L82.

Wahl, H. et al. (2022). "The NANOGrav 12.5 yr Data Set: Polarimetry and Faraday Rotation Measures from Observations of Millisecond Pulsars with the Green Bank Telescope". In: *The Astrophysical Journal* 926.2, p. 168.

Wang, W.-Y. et al. (2022a). "Magnetospheric curvature radiation by bunches as emission mechanism for repeating fast radio bursts". In: *The Astrophysical Journal* 927.1, p. 105.

Wang, W.-Y. et al. (2022b). "Polarization of magnetospheric curvature radiation in repeating fast radio bursts". In: *Monthly Notices of the Royal Astronomical Society* 517.4, pp. 5080–5089.

Weisberg, J. M. et al. (Mar. 1999). "Arecibo 1418 MHZ Polarimetry of 98 Pulsars: Full Stokes Profiles and Morphological Classifications". In: *The Astrophysical Journal Supplement Series* 121.1, pp. 171–217. DOI: 10.1086/313189.

Weltevrede, P. & S. Johnston (2008). "Profile and polarization characteristics of energetic pulsars". In: *Monthly Notices of the Royal Astronomical Society* 391.3, pp. 1210–1226.

Xie, J. et al. (2022). "The Emission Properties of RRAT J0139+ 3336 at 1.25 GHz". In: *The Astrophysical Journal Letters* 940.1, p. L21.

Xu, H. et al. (2022a). "A fast radio burst source at a complex magnetized site in a barred galaxy". In: *Nature* 609.7928, pp. 685–688.

Xu, H. et al. (Sept. 2022b). "A fast radio burst source at a complex magnetized site in a barred galaxy". In: *Nature* 609.7928, pp. 685–688. DOI: 10.1038/s41586-022-05071-8. arXiv: 2111.11764 [astro-ph.HE].

Yan, W. M. et al. (July 2011). "Polarization observations of 20 millisecond pulsars". In: *Monthly Notices of the Royal Astronomical Society* 414.3, pp. 2087–2100. DOI: 10.1111/j.1365-2966.2011.18522.x. arXiv: 1102.2274 [astro-ph.SR].

Yang, Y.-P., S. Xu, & B. Zhang (Apr. 2023). "Faraday rotation measure variations of repeating fast radio burst sources". In: *Monthly Notices of the Royal Astronomical Society* 520.2, pp. 2039–2054. DOI: 10.1093/mnras/stad168. arXiv: 2208.08712 [astro-ph.HE].

Yang, Y.-P. et al. (Apr. 2022). "Temporal Scattering, Depolarization, and Persistent Radio Emission from Magnetized Inhomogeneous Environments near Repeating Fast Radio Burst Sources". In: *The Astrophysical Journal Letters* 928.2, L16, p. L16. DOI: 10.3847/2041-8213/ac5f46. arXiv: 2202.09602 [astro-ph.HE].

Zhang, B. (2022a). "Coherent inverse compton scattering by bunches in fast radio bursts". In: *The Astrophysical Journal* 925.1, p. 53.

– (2022b). "The Physics of Fast Radio Bursts". In: *arXiv preprint arXiv:2212.03972*.

Zhang, Y.-K. et al. (Oct. 2023). "FAST Observations of FRB 20220912A: Burst Properties and Polarization Characteristics". In: *The Astrophysical Journal* 955.2, 142, p. 142. DOI: 10.3847/1538-4357/aced0b. arXiv: 2304.14665 [astro-ph.HE].

Chapter 7

IMPLICATIONS OF FARADAY ROTATION MEASURES OF FAST RADIO BURSTS LOCALIZED TO HOST GALAXIES

Sherman, M. B. et al. (2023). "Deep Synoptic Array Science: Implications of Faraday Rotation Measures of Fast Radio Bursts Localized to Host Galaxies". In: *The Astrophysical Journal Letters* 957.1, p. L8. DOI: 10.3847/2041-8213/ad0380.

7.1 Abstract

Faraday rotation measures (RMs) of fast radio bursts (FRBs) offer the prospect of directly measuring extragalactic magnetic fields. We present an analysis of the RMs of ten as yet non-repeating FRBs detected and localized to host galaxies with robust redshift measurements by the 64-antenna prototype of the Deep Synoptic Array (DSA-110). We combine this sample with published RMs of 15 localized FRBs, nine of which are repeating sources. For each FRB in the combined sample, we estimate the host-galaxy dispersion measure (DM) contributions and extragalactic RM. We find compelling evidence that the extragalactic components of FRB RMs are often dominated by contributions from the host-galaxy interstellar medium (ISM). Specifically, we find that both repeating and as yet non-repeating FRBs show a correlation between the host-DM and host-RM in the rest frame, and we find an anti-correlation between extragalactic RM (in the observer frame) and redshift for non-repeaters, as expected if the magnetized plasma is in the host galaxy. Important exceptions to the ISM origin include a dense, magnetized circum-burst medium in some repeating FRBs, and the intra-cluster medium (ICM) of host or intervening galaxy clusters. We find that the estimated ISM magnetic-field strengths, $\bar{B}_{||}$, are characteristically $\sim 1-2\,\mu$G larger than those inferred from Galactic radio pulsars. This suggests either increased ISM magnetization in FRB hosts in comparison with the Milky Way, or that FRBs preferentially reside in regions of increased magnetic-field strength within their hosts.

7.2 Motivation and background

The origins, evolution, and physical states of magnetic fields in galaxies remain poorly understood, despite their importance. During galaxy evolution, primordial seed fields are likely amplified through dynamo processes (Beck, 2016; Beck et

al., 1996; Rees, 1987), flux freezing in gas collapse (Marinacci et al., 2015) and fragmentation (Su et al., 2018), and turbulence (Ryu et al., 2008). In the Milky Way and nearby spiral galaxies, magnetic fields are dynamically important in the interstellar medium (ISM), with comparable energy density to turbulent gas motions and cosmic rays, and provide significant pressure support (Beck, 2016). Magnetism is critical to the processes of star formation in molecular clouds (Crutcher, 2012), and the propagation of cosmic rays and the resulting heating of the ISM and galaxy-scale winds (Zweibel, 2013). Estimates of the ISM magnetic-field strengths range from $\sim 5\,\mu$G in the Solar neighborhood (from direct Voyager-1 measurements; Burlaga et al., 2013), to $\sim 10\,\mu$G in denser regions of the galactic plane (Crutcher, 2012), to several tens of μG in the ISM of nearby starburst galaxies (Beck, 2016). Large-scale ordered fields are typically $\lesssim 30\%$ of the total field strengths (Beck, 2016; Haverkorn, 2015). Simulations suggest that the large-scale fields, likely found mostly in disk-dominated galaxies (Marinacci et al., 2018), saturate at several μG within a few Gyr after disk formation (Rodrigues et al., 2019; Su et al., 2018). Current estimates of magnetic-field strengths in external galaxies largely rely on equipartition analyses of synchrotron emission[1], which are subject to significant uncertainties in cosmic-ray energy losses (e.g., Ponnada et al., 2022). Direct measurements of magnetic-field strengths in external galaxies are required to test our understanding of the development of cosmic magnetism.

Fast radio bursts (FRBs) offer a direct probe of extragalactic magnetic fields through combined measurements of Faraday rotation measures (RMs) and dispersion measures (DMs) (e.g., Mannings et al., 2022; Masui et al., 2015; Ravi et al., 2016). RMs and DMs together enable the line-of-sight integrated magnetic field ($\bar{B}_{||}$) to be evaluated (Note the $\bar{}$ indicates this is integrated over the line-of-sight). Independent estimates of the Galactic RM and DM foreground can be used to identify extragalactic contributions, and host-galaxy components can be further isolated using models for the DM of the intergalactic medium (IGM; Macquart et al., 2020). In this work, we assume that FRB RMs and DMs include contributions as follows:

$$\mathrm{RM} = \mathrm{RM_{ion}} + \mathrm{RM_{MW}} + \mathrm{RM_{IGM}} + \frac{\mathrm{RM_{host}}}{(1+z)^2} \tag{7.1}$$

$$\mathrm{DM} = \mathrm{DM_{MW}} + \mathrm{DM_{MW,halo}} + \mathrm{DM_{IGM}}(z) + \frac{\mathrm{DM_{host}}}{(1+z)}. \tag{7.2}$$

Here, 'ion' refers to the ionosphere contribution (Sotomayor-Beltran et al., 2013), 'MW' refers to the Milky Way (estimated for RMs and DMs respectively using:

[1] Although see Robishaw et al. (2008) for observations of Zeeman splitting in OH megamasers.

Cordes & Lazio, 2002; Hutschenreuter et al., 2022), and 'host' refers to the FRB host galaxy. We assume a nominal Milky Way halo DM contribution of 10 pc cm^{-3} (Ravi et al., 2023, our results are largely insensitive to this assumption), and absorb host-halo RM and DM contributions in the host-galaxy terms. We further define $\mathrm{RM_{exgal}} \equiv \mathrm{RM_{IGM}} + \frac{\mathrm{RM_{host}}}{(1+z)^2}$, and

$$\bar{B}_{||} = \frac{\mathrm{RM}}{0.81 \cdot \mathrm{DM}}\,\mu\mathrm{G} \tag{7.3}$$

$$\bar{B}_{||,\,\mathrm{host}} = \frac{\mathrm{RM_{host}}}{0.81 \cdot \mathrm{DM_{host}}}\,\mu\mathrm{G}. \tag{7.4}$$

At present, 38 FRB sources have published polarization and/or RM data, of which just 15 (including six as yet non-repeating events) are localized to host galaxies (see Appendix A of the companion paper, Sherman et al. (2024), for a detailed compilation). The RMs of FRBs span an extraordinary range, both in magnitude and variability in the case of repeating sources. FRB 20121102A, for example, has an RM that varied from 1.3×10^5 rad m^{-2} to 7×10^4 rad m^{-2} (Michilli et al., 2018; Plavin et al., 2022) over three years, which with a modestly high host DM (around $50 - 225$ pc cm^{-3}; Tendulkar et al., 2017) indicates a dense, dynamic magnetoionic environment. Similar environments are inferred for a few repeating-FRB sources (Anna-Thomas et al., 2022; Mckinven et al., 2023; Xu et al., 2022), whereas others exist in entirely unremarkable magnetic environments (Feng et al., 2023; Kirsten et al., 2022). Frequency-dependent depolarization has also been observed in multiple repeating FRBs (Anna-Thomas et al., 2022; Feng et al., 2022; Mckinven et al., 2023), which may be described by the stochastic-RM model (Beniamini et al., 2022; Melrose & Macquart, 1998; Y.-P. Yang et al., 2022). A polarization analysis by Mannings et al. (2022) of five as yet non-repeating FRBs with host galaxy localizations could not disentangle any significant local RM contributions from broader host-ISM contributions. However, a tentative correlation between $\mathrm{DM_{host}}$ and $\mathrm{RM_{host}}$ suggested a significant contribution from ISM magnetic fields to the RMs of non-repeating FRBs.

Here we augment the existing sample of 15 localized FRB rotation measures with ten as yet non-repeating FRBs from the Deep Synoptic Array (DSA-110) sample compiled in Sherman et al. (2024) and C. J. Law et al. (2024). The chosen sample of FRBs contains those with detected RMs, host galaxy localizations, and robust redshift measurements. FRBs were detected using the 63 active antennas, while the 48-antenna core was used for arcsecond-scale localization. Polarimetry and RM estimation for these new events were presented in the companion paper by Sherman

et al. (2024), and host-galaxy analysis was presented in C. J. Law et al. (2024). Our goals in this paper are to identify extragalactic and host-galaxy contributions to FRB RMs, and to estimate and interpret $\bar{B}_{||,\,\mathrm{host}}$ along the FRB sightlines. In Section 7.3 we outline our methods for disentangling various RM and DM contributions. We then discuss the origins of FRB RMs in Section 7.4, and present and interpret measurements of $\bar{B}_{||,\,\mathrm{host}}$ in Section 7.5. We discuss limitations of our work and future prospects in Section 7.6, and conclude in Section 7.7. Throughout we adopt cosmological parameters from the *Planck* mission (Planck Collaboration et al., 2016). RM and polarization data for the DSA-110 FRBs can be accessed through the DSA-110 Archive[2], with additional data made available upon request to the corresponding author.

7.3 Estimation of host DM and RM

For each of the ten FRB sources in the sample under consideration, we estimate $\mathrm{DM_{host}}$ following the methods outlined in Connor et al. (2023a) (see also K. Yang et al., 2022). We derive the probability density function (PDF) of $\mathrm{DM_{host}}$ using the convolution of the PDFs of the observed DM with each DM component, as described in Connor et al. (2023a). Despite the small measurement uncertainty in the observed DMs ($< 0.06\%$), we assume for this analysis that the observed DM has a Gaussian distribution with standard deviation $0.1\,\mathrm{pc\,cm^{-3}}$ to account for any systematic errors (Chen et al., in prep). $\mathrm{DM_{MW}}$ is taken to have a Gaussian distribution with standard deviation $30\,\mathrm{pc\,cm^{-3}}$, $\mathrm{DM_{MW,halo}}$ is taken to have a uniform distribution between 0–$20\,\mathrm{pc\,cm^{-3}}$, and $\mathrm{DM_{IGM}}$ is distributed according to Z. Zhang et al. (2021) for each redshift; the redshift is treated as a constant given its negligible measurement uncertainty ($< 0.4\%$; Sharma et al., 2023). The distribution of $\mathrm{DM_{host}}$ (in the observer frame) is then given by the convolution below:

$$P\left(\frac{\mathrm{DM_{host}}}{1+z}\right) = P(\mathrm{DM}) * P(-\mathrm{DM_{MW}}) * P(-\mathrm{DM_{MW,halo}}) * P(-\mathrm{DM_{IGM}}(z)). \quad (7.5)$$

The quoted values of $\mathrm{DM_{host}}$ in Table 7.1 represent the expected values according to the PDFs.

We derive estimates of $\mathrm{RM_{host}}$ using a similar technique. The ionospheric contributions are estimated using the `ionFR` Python library, which uses ionospheric data from NASA's Archive of Space Geodesy Data[3] to estimate RM for a given

[2] `https://code.deepsynoptic.org/dsa110-archive/`
[3] `https://cddis.nasa.gov/`

time and line of sight with 12.5 deg^2 resolution (Sotomayor-Beltran et al., 2013). The module was modified slightly to account for the change in format of NASA's data files since 2014 to use 1-hr timesteps. In general, ionospheric RM is of order 1 rad m^{-2} with uncertainties of order 0.1 rad m^{-2}, but can change drastically in the presence of strong solar activity. The Galactic contribution is estimated using the Hutschenreuter et al. (2022) updated RM sky map, which has approximate resolution ~ 7 arcminutes[4]. While the Galactic contribution is more significant than ionospheric contributions, it remains small and is typically of order $10 - 20$ rad m^{-2} with uncertainties of order $5 - 15$ rad m^{-2}. In deriving RM$_{\rm host}$, we neglect RM$_{\rm IGM}$; this is justified below in Section 7.4. Table 7.1 summarizes estimates of RM and DM components for each FRB in the DSA-110 sample. Note that DM$_{host}$ (and by extension $\bar{B}_{||}$) could not be confidently constrained for FRB 20220319D due to its close proximity to the Milky Way, as discussed in Ravi et al. (2023). RM$_{\rm host}$ and DM$_{\rm host}$ estimates are obtained for nine repeating FRBs and six non-repeating FRBs from the published literature sample.

This analysis has several caveats. For example, host or intervening galaxy clusters can significantly affect some FRB DMs and RMs (Connor et al., 2023a; K.-G. Lee et al., 2023a; Ramesh et al., 2023), increasing the magnitudes of the estimated DM$_{\rm host}$ and RM$_{\rm host}$. Some repeating FRBs such as FRB 20121102A and FRB 20190520B show significant variation in RM (Anna-Thomas et al., 2022; Plavin et al., 2022). For these sources, a weighted mean value for the RM is used, as the local contribution cannot be confidently removed. We also note that estimates of DM$_{\rm host}$ can be refined through a consideration of host-galaxy observables such as Hα or UV luminosity (e.g., Mannings et al., 2022), as well as observations of intervening galaxies (e.g., Simha et al., 2023), but we defer such an analysis to future work.

Furthermore, we acknowledge that biases may be introduced by the non-detection of rotation measures in some FRBs. Five of the 25 FRBs reported in the companion paper, Sherman et al. (2024), have no significant RM detection due to low fractional linear polarization and S/N. If this is a result of intrinsically unpolarized emission, we cannot infer the magnitude of these missing RMs. If the depolarization is caused by high rotation measures, we would expect true RMs to be $\gtrsim 10^6$ rad m^{-2}, which are not detectable with the DSA-110 frequency resolution (see Sherman et al. (2024) Appendix H, Figure 10; Burke et al. (2019), Mckinven et al. (2021), and Schnitzeler

[4]The Hutschenreuter et al. (2022) map is published in healpix (`https://healpy.readthedocs.io/en/latest/`) format with NSIDE=512, which is a parameter describing the map resolution.

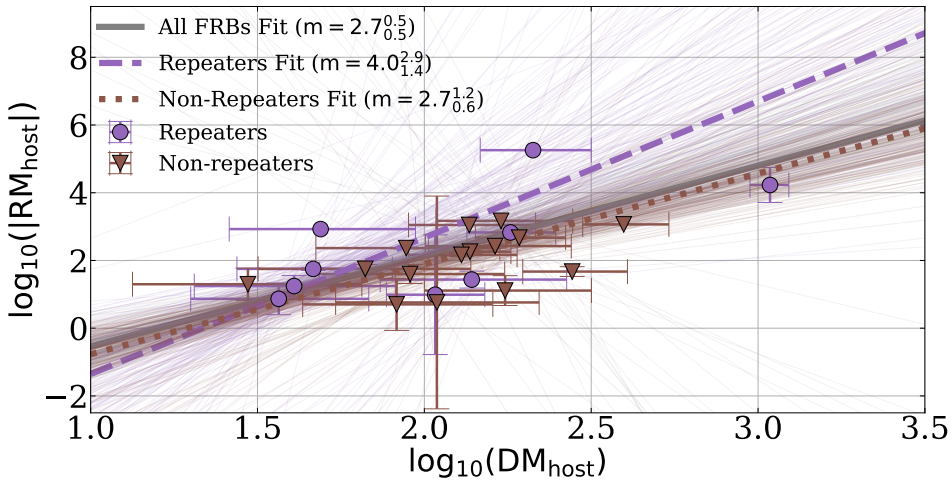

Figure 7.1: Estimates of RM_{host} and DM_{host} for as yet non-repeating (brown triangles) and repeating FRBs (purple circles). Solid lines show the best fit from a Markov-Chain Monte Carlo (MCMC) analysis for non-repeaters (brown), repeaters (purple), and the full sample (grey). Random draws from each MCMC simulation are shown by faint lines for non-repeaters (brown), repeaters (purple) and all FRBs (grey). The best fit slopes with 1-σ errors are displayed in the legend in each case.

& K. Lee (2015)). Similarly, some bursts exhibit non-negligible circular polarization that could result from Faraday Conversion; this would also suggest highly magnetic environments and therefore high RMs (e.g., Gruzinov & Levin, 2019; Kumar et al., 2022; Qu & B. Zhang, 2023; Suresh & Cordes, 2019; Vedantham & Ravi, 2019). Both of these latter affects could bias our population to low RM and $B_{||}$ measurements. We proceed under the assumption that such affects are negligible, and leave more rigorous analysis of non-detection statistics to future work.

7.4 The origin of FRB rotation measures

We first test the hypothesis that the host-galaxy ISM predominantly determines FRB RMs. We do this by searching for a correlation between RM_{host} and DM_{host}. Tentative evidence ($p = 0.06$, where p is the probability of the null hypothesis of no correlation) for such a correlation was identified by Mannings et al. (2022) using just nine FRBs (three repeaters and six non-repeaters). When considering all extragalactic contributions to the RMs and DMs of FRBs, such a correlation is the best motivated, both empirically and theoretically. Large-scale fields in the IGM are not evident in studies of the RMs of active galactic nuclei (Hammond et al., 2012). As such fields are likely no larger than several nano-Gauss, they will not contribute more than a few units of RM for typical FRBs (e.g., Akahori et al., 2016; Hackstein et al., 2019; Ravi et al., 2016). Furthermore, both observation of

Table 7.1: DSA-110 FRB Sample Rotation Measure Properties

FRB	Redshift	DM	$\mathrm{DM_{host}}$	RM	$\mathrm{RM_{MW}}$	$\mathrm{RM_{ion}}$	$\mathrm{RM_{host}}$	$\tilde{B}_{\parallel,\mathrm{host}}$ (μG)
20220207C	0.043040 ± 0.00012	262.3 ± 0.01	$136.98^{+39.31}_{-38.72}$	162.48 ± 0.04	-5.22 ± 16.93	1.35 ± 0.07	181.28 ± 18.42	$1.97^{+0.16}_{-0.84}$
20220307B	0.248123 ± 0.00013	499.15 ± 0.03	$169.77^{+76.15}_{-83.96}$	-947.23 ± 12.27	-4.11 ± 28.64	1.85 ± 0.09	-1477.8 ± 48.74	$-13.16^{+5.72}_{-5.3}$
20220310F	0.477958 ± 0.00042	462.15 ± 0.004	$66.5^{+49.16}_{-48.46}$	11.39 ± 0.19	-14.33 ± 7.43	0.51 ± 0.09	55.9 ± 16.26	$2.64^{+0.9}_{-2.1}$
20220319D	0.011228 ± 0.000041	110.95 ± 0.01	–	59.94 ± 14.33	-13.82 ± 17.68	2.07 ± 0.09	73.63 ± 23.26	–
20220418A	0.622000 ± 0.000098	623.45 ± 0.01	$109.04^{+76.21}_{-76.92}$	6.13 ± 7.48	7.96 ± 13.96	0.63 ± 0.1	-5.76 ± 41.67	$-0.17^{+0.61}_{-0.60}$
20220506D	0.30039 ± 0.00013	396.93 ± 0.01	$90.63^{+56.86}_{-59.16}$	-32.38 ± 3.6	-9.68 ± 14.72	1.16 ± 0.08	-39.75 ± 25.62	$-1.27^{+1.03}_{-0.38}$
20220509G	0.089400 ± 0.00013	269.5 ± 0.007	$129.16^{+47.13}_{-49.62}$	-109.0 ± 1.17	14.03 ± 14.05	0.69 ± 0.08	-146.54 ± 16.73	$-1.98^{+0.88}_{-0.33}$
20220825A	0.241397 ± 0.000098	651.2 ± 0.02	$395.77^{+112.01}_{-123.38}$	750.23 ± 6.67	-3.53 ± 15.26	0.32 ± 0.03	1161.38 ± 25.67	$4.49^{+0.63}_{-1.77}$
20220920A	0.158239 ± 0.00017	315.0 ± 0.06	$136.33^{+57.15}_{-62.41}$	-830.25 ± 8.29	0.72 ± 13.12	1.6 ± 0.09	-1117.08 ± 20.83	$-12.29^{+5.08}_{-4.34}$
20221012A	0.284669 ± 0.0007	441.2 ± 0.26	$162.95^{+78.21}_{-85.64}$	165.7 ± 17.66	3.07 ± 12.45	1.69 ± 0.13	265.86 ± 35.62	$3.27^{+0.65}_{-1.96}$

Notes: All DMs are expressed in units of $\mathrm{pc\,cm^{-3}}$, and all RMs are expressed in units of $\mathrm{rad\,m^{-2}}$. Redshifts and uncertainties were measured by the spectroscopic analysis procedure outlined in Sharma et al. (2023) and C. J. Law et al. (2024). See Chen (2024), for details on DM measurement and uncertainty.

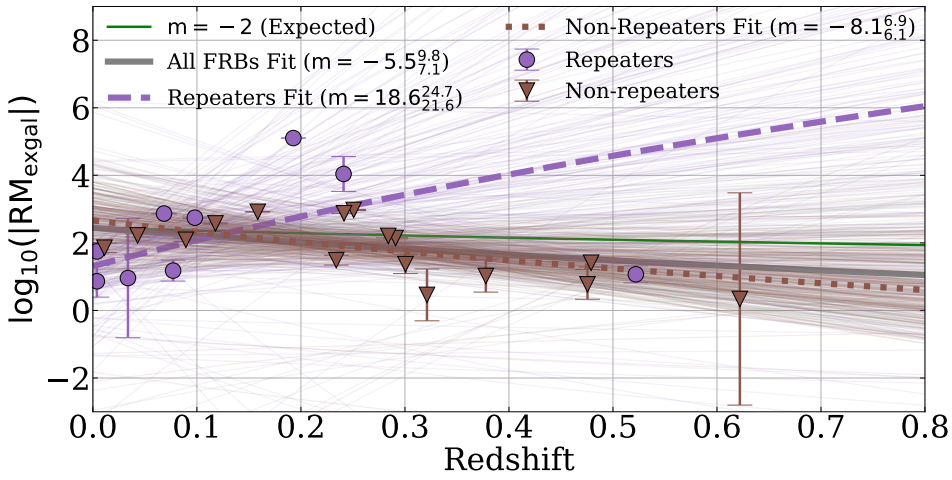

Figure 7.2: Estimates of RM_{exgal} at different redshifts for as yet non-repeating (brown triangles) and repeating FRBs (purple circles). Solid lines show the best fit from an MCMC analysis for non-repeaters (brown), repeaters (purple), and the full sample (grey). Note that redshift errorbars are omitted. The green line indicates the expected scaling from redshift suppression, i.e. $RM_{exgal} \propto (1+z)^{-2}$. Samples from each MCMC simulation are shown by faint lines for non-repeaters (brown), repeaters (purple) and all FRBs (grey). The best fit slopes with 1-σ errors are displayed in the legend in each case. Significant negative correlation is found for non-repeaters ($p = 0.006$) using a Spearman Rho test, although the median slope $m = -8.1^{6.9}_{6.1}$ is only marginally consistent with redshift suppression. The two repeaters with the highest values of RM_{exgal}, FRB 20121102A and FRB 20190520B, are known to have highly magnetized, dynamic local environments that may dominate their RMs (Anna-Thomas et al., 2022; Plavin et al., 2022).

nearby galaxies (Heesen et al., 2023) and IllustrisTNG simulations (Ramesh et al., 2023) imply the circum-galactic media (CGM) of intervening galaxies contribute negligibly to the observed RM (~ 0.01 rad m^2 at large impact parameters $\gtrsim 200$ kpc) compared to host ISM, local, and Milky Way contributions. Galaxy clusters, which will contribute significantly more RM (Connor et al., 2023a), likely affect on the order of 10% of FRB sightlines and may not dominate the IGM DM contributions. On the other hand, experience from Galactic pulsar observations suggests that pulsar RMs are excellent tracers of large-scale components of the Galactic magnetic field via correlations with DM (Han et al., 2018; Sobey et al., 2019). In the case of FRBs (and pulsars), a correlation between RM_{host} and DM_{host} can be masked if FRBs generally occupy dynamic local environments that contribute large RMs but little DM, like the environment of FRB 20121102A, because the DM component would be small with respect to other sources of DM.

We have conducted simple, physically motivated Monte Carlo simulations to demon-

strate how extreme (either dynamic or highly magnetized) local FRB environments could mask the correlation between $\mathrm{RM_{host}}$ and $\mathrm{DM_{host}}$. For a population of 24 FRBs, we draw samples of $\mathrm{RM_{ISM,host}}$ and $\mathrm{DM_{ISM,host}}$ assuming they have similar distributions to those of Milky Way pulsars. A subset of FRBs are then randomly selected to have extreme local environments; we consider cases in which the local magnetic field is (1) stochastically varying with Root Mean Squared (RMS) $\sigma_{\bar{B}_{||},\mathrm{local}} = 100\,\mu\mathrm{G}$, (2) smoothly varying with rate of change $d\bar{B}_{||,\mathrm{local}}/dt = 0.1\,\mu\mathrm{G\,day^{-1}}$, or (3) constant and of extreme magnitude $|\bar{B}_{||,\mathrm{local}}| = 100\,\mu\mathrm{G}$[5]. The local DM is drawn from a uniform distribution between $0 - 10\,\mathrm{pc\,cm^{-3}}$, and the local RM contribution computed as $\mathrm{RM_{local}} \approx 0.81 \bar{B}_{\|,\mathrm{local}} DM_{\mathrm{local}}$. The observed $\mathrm{RM_{host}}$ and $\mathrm{DM_{host}}$ are computed from the sum of the local and ISM contributions. We find that if the local field is either stochastically or smoothly varying, the correlation (for a Spearman Rho test with a 90% confidence level) between $\mathrm{RM_{host}}$ and $\mathrm{DM_{host}}$ can be masked if $\gtrsim 30 - 55\%$ of the sample ($\gtrsim 8 - 13$ FRBs) have extreme local environments, depending on the mean value of $\bar{B}_{||,\mathrm{local}}$. If the local field is constant, the correlation can be masked if only $\gtrsim 8\%$ of the sample ($\gtrsim 7 - 8$ FRBs) have $|\bar{B}_{||,\mathrm{local}}| = 100\,\mu\mathrm{G}$. Therefore, if a correlation is observed, one can conclude that the host ISM dominates the observed $\mathrm{RM_{host}}$ and $\mathrm{DM_{host}}$, while an upper limit $\lesssim 55\%$ of FRBs may reside in extreme local environments.

We conduct a Spearman Rho test for correlation using a 90% confidence level. The null hypothesis (p-value[6] $p > 10\%$) is that the variables are uncorrelated, which is rejected for significant p-values $p < 10\%$. Figure 7.1 shows a clearly detected correlation between $\mathrm{RM_{host}}$ and $\mathrm{DM_{host}}$. Significant correlations are found for repeaters ($p = 0.02$), non-repeaters ($p = 0.06$), and for all FRBs ($p = 0.004$). This confirms the tentative result of Mannings et al. (2022), and shows that it applies to both repeating and non-repeating FRBs. The existence of this correlation indicates that the RMs of both repeaters and non-repeaters are generally determined by large-scale fields in host-galaxy ISM. The ISM origin is bolstered by the weak correlation between host RM/DM and galactocentric offset found by Mannings et al. (2022), which ought not to exist if the magnetized plasma were in circumburst material.

An analysis of observed $\mathrm{RM_{exgal}}$ evolution with redshift z also demonstrates that RM originates in the host galaxy. As shown in Figure 7.2, we find a significant negative

[5]These nominal values are estimated to match the environments of FRBs with known dynamic local environments such as FRB 20121102A and FRB 20190520B (e.g., Mckinven et al., 2023).

[6]The p-value p should not be mistaken for the Spearman Rho test statistic ρ, which is not reported in this paper.

correlation ($p = 0.006$) between $\mathrm{RM_{exgal}}$ and z for non-repeaters. The result for repeating FRBs is significantly affected by FRB 20121102A and FRB 20190520B, which are known to have highly magnetized, dynamic local environments that may dominate their RMs (Anna-Thomas et al., 2022; Plavin et al., 2022). However, this does not contradict the conclusion that the host ISM dominates the RM and DM of repeaters. If repeating FRBs have higher variance in RM (both between sources and from burst-to-burst), then that variance could drown out the relatively weak $(1 + z)^{-2}$ effect. The lack of repeating FRBs at high redshift ($z > 0.3$) may also explain why local environments obscure the redshift suppression, but a significant correlation is still found between $\mathrm{RM_{host}}$ and $\mathrm{DM_{host}}$. For non-repeaters, a negative correlation between $\mathrm{RM_{exgal}}$ and z can most simply be attributed to the suppression of a characteristic $\mathrm{RM_{host}}$ by a $(1+z)^{-2}$ term, although this possibility is only marginally consistent with the measured slope of the anti-correlation. Cosmic evolution in host-galaxy field strengths may also play a role, although there is no theoretical basis for the observed $\mathrm{RM_{exgal}}$-z anti-correlation (e.g., Rodrigues et al., 2019).

7.5 Magnetic fields in FRB environments and host galaxies

Having established that estimates of $\mathrm{RM_{host}}$ for our FRB sample may trace the large-scale magnetic fields in the host-galaxy ISM, we can estimate and interpret $\bar{B}_{\parallel,\mathrm{host}}$ for the sample. The estimates for the DSA-110 sample are given in Table 7.1. We focus first on comparing estimates of $\bar{B}_{\parallel,\mathrm{host}}$ with estimates of $\bar{B}_{\parallel}$ for pulsars. This analysis is complementary to the investigation by Chrimes et al. (2021) of the physical locations of FRBs in their hosts relative to pulsars in the Milky Way. It is, however, similarly motivated by the prospect of determining whether or not Galactic pulsars are similarly located within the Milky Way as FRBs are within their hosts.

Figure 7.3 shows the distribution of $\mathrm{RM_{host}}$ and $\mathrm{DM_{host}}$ for FRBs in comparison with RMs and DMs of Galactic and Magellanic-Cloud pulsars, rotating radio transients (RRATs), and radio-loud magnetars. Using a Kolmogorov-Smirnov (K-S) consistency test, we find that the distributions of $\bar{B}_{\parallel,\mathrm{host}}$ for repeating and as yet non-repeating FRBs are significantly different to the $\bar{B}_{\parallel}$ distributions for pulsars and magnetars ($p \leq 0.089$ for repeaters; $p \leq 0.006$ for nonrepeaters when compared to CPs, MSPs, and all pulsars/magnetars), while the comparison to RRATs is inconclusive. Specifically, FRBs tend to have higher inferred values of $\bar{B}_{\parallel,\mathrm{host}}$ than Galactic neutron stars. There are two leading possibilities for this result. First, a significant fraction of FRBs, both repeating and non-repeating, may have important

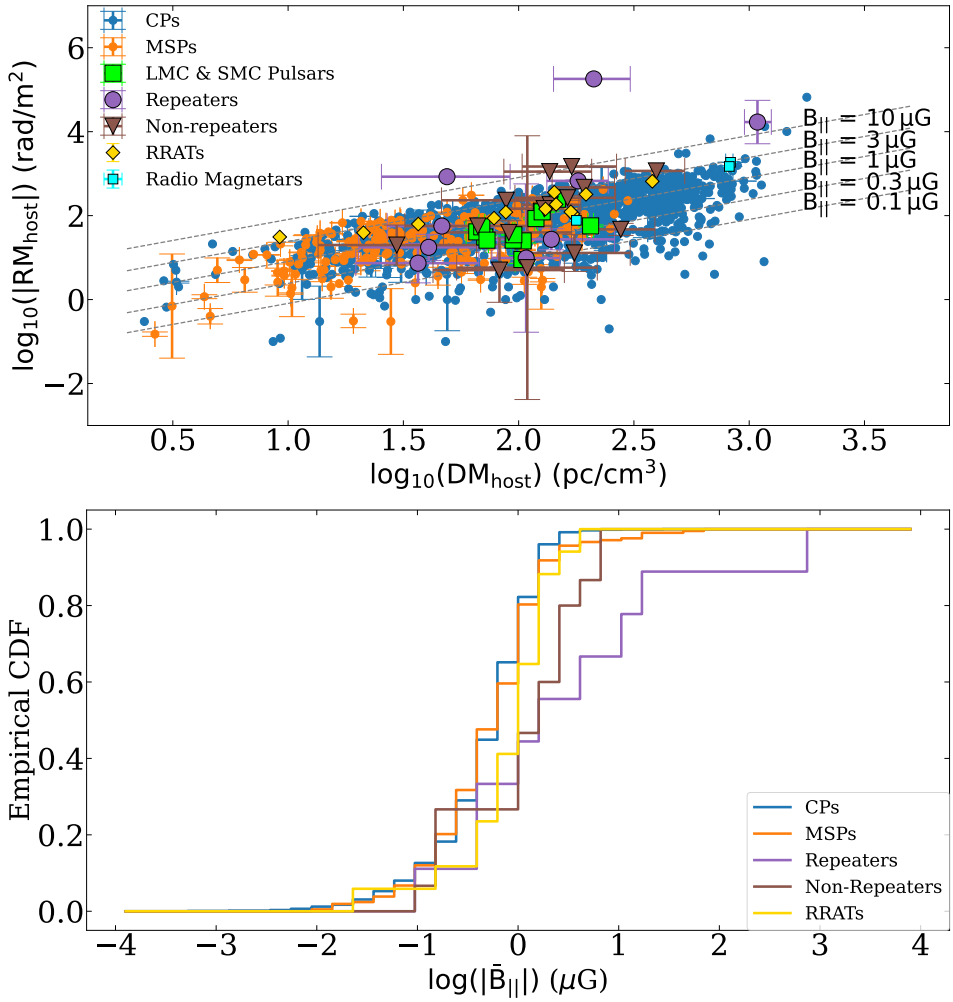

Figure 7.3: ***Top:*** Comparison of FRB $\mathrm{RM_{host}}$ and $\mathrm{DM_{host}}$ estimates with the RMs and DMs of pulsars, RRATs, and radio-loud magnetars. As yet non-repeating (brown triangles) and repeating FRBs (purple circles) are distinguished, as are canonical pulsars (CPs; $P > 30$ ms; blue circles) and millisecond pulsars (MSPs; $P < 30$ ms; orange circles). RRATs (yellow diamonds), pulsars in the Large and Small Magellanic Clouds (LMC, SMC; green squares), and radio magnetars (**cyan** squares) are included to complete the sample. Dotted grey lines of constant magnetic field, $\bar{B}_{\parallel,\mathrm{host}}$, are shown. *Bottom:* Empirical cumulative distribution functions (CDF) for the line-of-sight magnetic field $\bar{B}_{\parallel,\mathrm{host}}$. CDFs for CPs (blue) MSPs (orange), repeating (purple) and as yet non-repeating (brown) FRBs, and RRATs (yellow) are shown. Note that radio magnetars and Magellanic Cloud pulsars are included in the CP distribution. Both repeaters and non-repeaters are found to have distinct $\bar{B}_{\parallel,\mathrm{host}}$ from CPs and MSPs using a Kolmogorov-Smirnov (K-S) test and an Anderson-Darling (A-D) test with $> 99\%$ confidence. FRBs in general appear to occupy slightly more magnetized environments than pulsars. K-S and A-D tests find similarity between FRB and RRAT distributions. Data on literature samples of neutron stars were compiled according to Appendix A of the companion paper Sherman et al. (2024)

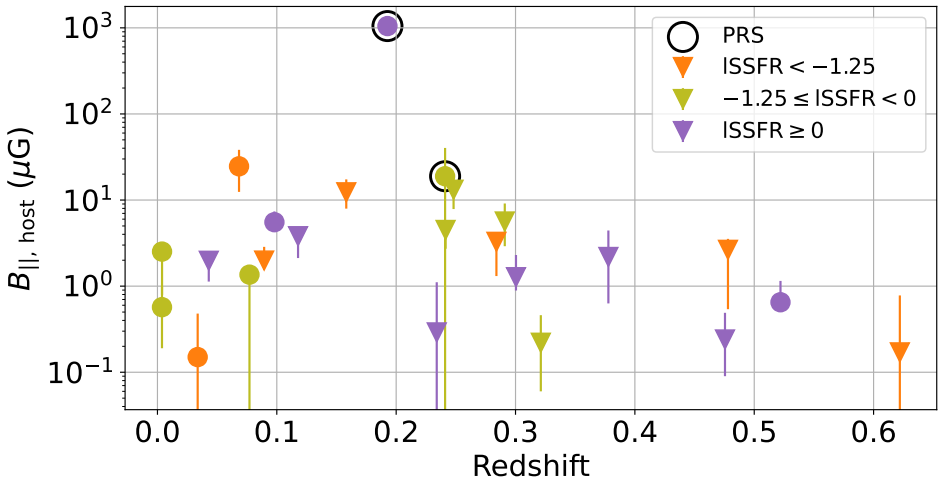

Figure 7.4: Estimates of $\bar{B}_{\parallel,\mathrm{host}}$ for FRBs at different redshifts, including as yet non-repeating sources (triangles) and repeaters (circles). FRBs are grouped by the (logarithmic) specific star-formation rates (lSSFR) of the host galaxies, scaled by $10^{10} M_\odot$: lSSFR < -1.25 (orange), $-1.25 \leq$ lSSFR < 0 (green) and lSSFR ≥ 0 (purple). FRBs 20121102A and 20190520B, both associated with persistent radio sources (PRSs; C. J. Law et al., 2022), are circled in black. No correlation is found between $\bar{B}_{\parallel,\mathrm{host}}$ and redshift for any subgroup, nor are there significant differences between the subgroups.

RM contributions from circum-source environments that contribute negligibly to their DMs (e.g., Y.-P. Yang et al., 2023). Such RM contributions would need to be significant enough to raise the inferred $\bar{B}_{\parallel,\mathrm{host}}$ values by some tens of percent, while not masking the $\mathrm{RM_{host}}$–$\mathrm{DM_{host}}$ correlation[7] . Alternatively, FRBs may be typically hosted by galaxies with larger large-scale ISM field strengths than observed in the Milky Way. This idea is consistent with observational and theoretical work establishing an increase in large-scale fields at fixed stellar mass with redshift, and the variation in field strength with star-formation activity (Beck, 2016; Rodrigues et al., 2019).

We can test the second scenario by investigating whether either redshift or specific star-formation rate (sSFR) are correlates of $\bar{B}_{\parallel,\mathrm{host}}$ (Figure 7.4). Estimates of sSFR for the literature sample of localized FRBs are derived from Gordon et al. (2023) where possible, and otherwise from Bhardwaj et al. (2021), Michilli et al. (2022), and Ravi et al. (2023). Estimates of sSFR for DSA-110 FRBs are sourced from C. J. Law et al. (2024). We find no significant correlation between $\bar{B}_{\parallel,\mathrm{host}}$ and either redshift or sSFR, either for repeaters or non-repeaters. This result disfavors cosmic evolution and a

[7]Note some outlier repeating FRBs such as FRB 20121102 and FRB 20190520B have less stringent requirements for significant RM given their already high inferred $\bar{B}_{\parallel,\mathrm{host}}$

biased host-galaxy population as explanations for the characteristically higher $\bar{B}_{\parallel,\mathrm{host}}$ values of FRBs in comparison with Galactic neutron stars. However, we cannot immediately favor the importance of circum-source environments in determining $\bar{B}_{\parallel,\mathrm{host}}$. First, we are not correcting for the location of the FRBs within their hosts, nor for the host-galaxy orientations, which may be also be important in determining FRB RMs (e.g., Kirsten et al., 2022; Mannings et al., 2022). Second, as is evident from Figure 7.3, it is possible that only some FRBs have characteristically higher $\bar{B}_{\parallel,\mathrm{host}}$ than Galactic pulsars. These objects, with $\bar{B}_{\parallel,\mathrm{host}} \gtrsim 10\,\mu\mathrm{G}$, likely do have significant circum-source RM contributions, additionally because large-scale fields are expected to saturate below $10\,\mu$G in most galaxies.

7.6 Discussion

Unlike with DM, the IGM and circum-galactic medium (CGM) of intervening galaxies are not expected to contribute significantly to the extragalactic RM of FRBs, due to small magnetic fields in those media (Hammond et al., 2012; Lan & Prochaska, 2020; Ponnada et al., 2022). For example, Amaral et al. (2021) found that the 3-σ upper limit on the RM from filaments in the IGM is $< 3.8\,\mathrm{rad\,m^{-2}}$, which is comparable to the Faraday column of Earth's ionosphere. Instead, the extragalactic RM of FRBs will typically be dominated by the host galaxy. For $\mathcal{O}(10\%)$ of sources, the magnetized ICM of galaxy clusters will contribute non-negligibly to the observed RM. This can happen when the FRB sightline intersects a foreground galaxy cluster by chance (K.-G. Lee et al., 2023b) as well as when the host galaxy is a cluster member (Connor et al., 2023b; Sharma et al., 2023). DM and RM estimates for a sample of FRBs impacted by galaxy clusters will allow for magnetic-field constraints in the intracluster medium (ICM), including beyond the virial radius where probes such as thermal X-ray emission are less sensitive.

The majority of FRB sightlines will *not* be impacted by the ICM. For such sources, the component of extragalactic DM that correlates with $\mathrm{RM_{exgal}}$ ought to come from the host galaxy. Thus, for a large sample of localized FRBs at low or moderate redshifts, the relationship between extragalactic DM and RM could be used to extract the distribution of $\mathrm{DM_{host}}$. The host galaxy DM distribution is currently poorly constrained, but has significant implications for FRB applications to cosmology as well as in our understanding of FRB host galaxies and progenitor environments. In this case, one must assume that the host-galaxy RM and DM originate from the same plasma.

In general, strong prospects remain for using FRBs to constrain or measure magnetic-field strengths in a variety of environments, including the ISM, galaxy groups, and galaxy clusters. If a sample of $z \gtrsim 1$ FRBs can be obtained, the suppression of $\mathrm{RM_{host}}$ may enable us to cleanly consider RM contributions external to galaxies in analogy to the estimation of DM contributions in the CGM and IGM (e.g., Connor & Ravi, 2022). Fortunately, a high-redshift sample of FRB RMs is likely to be discovered with upcoming surveys (Connor & Ravi, 2023), thanks to their large overall detection rate and increased sensitivity (e.g., Hallinan et al., 2019; Vanderlinde et al., 2019). Sub-arcsecond FRB localizations (e.g., Vanderlinde et al., 2019) and higher resolution RM maps from polarization surveys like ASKAP's Polarization Sky Survey of the Universe's Magnetism (POSSUM; Gaensler et al., 2010) will further assist in modeling and interpreting ISM RM contributions.

7.7 Conclusions

We present a study of the RMs of 25 FRBs localized to host galaxies, including ten new measurements from the DSA-110. The localizations enable a focused consideration of host-galaxy contributions to FRB RMs, and the resulting implications. We conclude the following.

1. The RMs of FRBs are predominantly contributed by the host-galaxy ISM. This is evidenced by an observed correlation between $\mathrm{RM_{host}}$ and $\mathrm{DM_{host}}$ for both repeating and as yet non-repeating FRBs (Figure 7.1), and supported by an anti-correlation between $\mathrm{RM_{exgal}}$ and z for non-repeating FRBs that suggests a characteristic value of $\mathrm{RM_{host}}$ (Figure 7.2). Important known exceptions include FRBs hosted by or viewed through galaxy clusters (e.g, FRB 20220509G; Connor et al., 2023a), and FRBs with highly magnetized circum-source environments (e.g, FRBs 20121102A and 20190520B; Anna-Thomas et al., 2022; Plavin et al., 2022).

2. The distribution of inferred $\bar{B}_{\parallel,\mathrm{host}}$ values for FRBs is generally inconsistent with the $\bar{B}_{\parallel}$ distribution for Galactic and Magellanic-Cloud pulsars (Figure 7.3). Higher values of $\bar{B}_{\parallel,\mathrm{host}}$ ($\sim 1 - 2\mu$G) are observed for FRBs in comparison with pulsars.

3. We test the possibility of the $\bar{B}_{\parallel,\mathrm{host}}$ excess being explained by a biased FRB host-galaxy population with stronger large-scale magnetic fields than the Milky Way. We find no evidence for this scenario (Figure 7.4); this result does not however exclude the possibility. The locations of FRBs within

their hosts, which we do not account for, may be important in interpreting host-ISM magnetic-field estimates. It also remains plausible that a significant subset of FRBs have substantially magnetized circum-source environments that contribute to but do not dominate estimates of $\bar{B}_{\parallel,\mathrm{host}}$.

7.8 Acknowledgments

The authors would like to thank Jim Cordes, Dongzi Li, Bing Zhang, Yuanhong Qu, Joel Weisberg, Alexandra Mannings, and Sam Ponnada for insightful and essential conversations on polarization theory and direction on the analysis conducted, as well as Paul Bellan and Yang Zhang for a comprehensive Plasma Physics course. We also thank Yi Feng, Dipanjan Mitra, Yuan-Pei Yang, Dylan Nelson, Reshma Anna-Thomas, and an anonymous referee for useful comments and recommendations on the early draft. The authors thank staff members of the Owens Valley Radio Observatory and the Caltech radio group, including Kristen Bernasconi, Stephanie Cha-Ramos, Sarah Harnach, Tom Klinefelter, Lori McGraw, Corey Posner, Andres Rizo, Michael Virgin, Scott White, and Thomas Zentmyer. Their tireless efforts were instrumental to the success of the DSA-110. The DSA-110 is supported by the National Science Foundation Mid-Scale Innovations Program in Astronomical Sciences (MSIP) under grant AST-1836018. This material is based upon work supported by the National Science Foundation Graduate Research Fellowship under Grant No. DGE-1745301.

CHAPTER 7 BIBLIOGRAPHY

Akahori, T., D. Ryu, & B. M. Gaensler (June 2016). "Fast Radio Bursts as Probes of Magnetic Fields in the Intergalactic Medium". In: *The Astrophysical Journal* 824.2, 105, p. 105. DOI: 10.3847/0004-637X/824/2/105. arXiv: 1602.03235 [astro-ph.CO].

Amaral, A. D., T. Vernstrom, & B. M. Gaensler (May 2021). "Constraints on large-scale magnetic fields in the intergalactic medium using cross-correlation methods". In: *Monthly Notices of the Royal Astronomical Society* 503.2, pp. 2913–2926. DOI: 10.1093/mnras/stab564. arXiv: 2102.11312 [astro-ph.CO].

Anna-Thomas, R. et al. (2022). "A highly variable magnetized environment in a fast radio burst source". In: *arXiv preprint arXiv:2202.11112*.

Beck, R. (2016). "Magnetic fields in spiral galaxies". In: *The Astronomy and Astrophysics Review* 24.1, pp. 1–57.

Beck, R. et al. (Jan. 1996). "Galactic Magnetism: Recent Developments and Perspectives". In: *Annual Review of Astronomy and Astrophysics* 34, pp. 155–206. DOI: 10.1146/annurev.astro.34.1.155.

Beniamini, P., P. Kumar, & R. Narayan (2022). "Faraday depolarization and induced circular polarization by multipath propagation with application to FRBs". In: *Monthly Notices of the Royal Astronomical Society* 510.3, pp. 4654–4668.

Bhardwaj, M. et al. (2021). "A nearby repeating fast radio burst in the direction of M81". In: *The Astrophysical Journal Letters* 910.2, p. L18.

Burke, B. F., F. Graham-Smith, & P. N. Wilkinson (2019). *An introduction to radio astronomy*. Cambridge University Press.

Burlaga, L. et al. (2013). "Evidence for a shock in interstellar plasma: Voyager 1". In: *The Astrophysical Journal Letters* 778.1, p. L3.

Chen, G. (2024). "Localized Fast Radio Bursts Using DSA-110". PhD thesis. California Institute of Technology.

Chrimes, A. A. et al. (2021). "The Galactic neutron star population - I. An extragalactic view of the Milky Way and the implications for fast radio bursts". In: *Monthly Notices of the Royal Astronomical Society* 508.2, pp. 1929–1946. DOI: 10.1093/mnras/stab2676. arXiv: 2105.04549 [astro-ph.GA].

Connor, L. & V. Ravi (July 2022). "The observed impact of galaxy halo gas on fast radio bursts". In: *Nature Astronomy* 6, pp. 1035–1042. DOI: 10.1038/s41550-022-01719-7. arXiv: 2107.13692 [astro-ph.GA].

– (May 2023). "Stellar prospects for FRB gravitational lensing". In: *Monthly Notices of the Royal Astronomical Society* 521.3, pp. 4024–4038. DOI: 10.1093/mnras/stad667. arXiv: 2206.14310 [astro-ph.CO].

Connor, L. et al. (June 2023a). “Deep Synoptic Array Science: Two Fast Radio Burst Sources in Massive Galaxy Clusters”. In: *The Astrophysical Journal Letters* 949.2, L26, p. L26. DOI: 10.3847/2041-8213/acd3ea. arXiv: 2302.14788 [astro-ph.HE].

– (June 2023b). “Deep Synoptic Array Science: Two Fast Radio Burst Sources in Massive Galaxy Clusters”. In: *The Astrophysical Journal Letters* 949.2, L26, p. L26. DOI: 10.3847/2041-8213/acd3ea. arXiv: 2302.14788 [astro-ph.HE].

Cordes, J. M. & T. J. W. Lazio (2002). “NE2001. I. A new model for the galactic distribution of free electrons and its fluctuations”. In: *arXiv preprint astro-ph/0207156*.

Crutcher, R. M. (Sept. 2012). “Magnetic Fields in Molecular Clouds”. In: *Annual Review of Astronomy and Astrophysics* 50, pp. 29–63. DOI: 10.1146/annurev-astro-081811-125514.

Feng, Y. et al. (2022). “Frequency-dependent polarization of repeating fast radio bursts—implications for their origin”. In: *Science* 375.6586, pp. 1266–1270.

Feng, Y. et al. (Apr. 2023). “An extreme active repeating fast radio burst in a clean environment”. In: *arXiv e-prints*, arXiv:2304.14671, arXiv:2304.14671. DOI: 10.48550/arXiv.2304.14671. arXiv: 2304.14671 [astro-ph.HE].

Gaensler, B. M. et al. (Jan. 2010). “Survey Science with ASKAP: Polarization Sky Survey of the Universe’s Magnetism (POSSUM)”. In: *American Astronomical Society Meeting Abstracts #215*. Vol. 215. American Astronomical Society Meeting Abstracts, 470.13, p. 470.13.

Gordon, A. C. et al. (2023). “The demographics, stellar populations, and star formation histories of fast radio burst host galaxies: implications for the progenitors”. In: *The Astrophysical Journal* 954.1, p. 80.

Gruzinov, A. & Y. Levin (2019). “Conversion measure of Faraday rotation–conversion with application to fast radio bursts”. In: *The Astrophysical Journal* 876.1, p. 74.

Hackstein, S. et al. (Sept. 2019). “Fast radio burst dispersion measures and rotation measures and the origin of intergalactic magnetic fields”. In: *Monthly Notices of the Royal Astronomical Society* 488.3, pp. 4220–4238. DOI: 10.1093/mnras/stz2033. arXiv: 1907.09650 [astro-ph.CO].

Hallinan, G. et al. (Sept. 2019). “The DSA-2000 — A Radio Survey Camera”. In: *Bulletin of the American Astronomical Society*. Vol. 51, 255, p. 255. DOI: 10.48550/arXiv.1907.07648. arXiv: 1907.07648 [astro-ph.IM].

Hammond, A. M., T. Robishaw, & B. M. Gaensler (Sept. 2012). “A New Catalog of Faraday Rotation Measures and Redshifts for Extragalactic Radio Sources”. In: *arXiv e-prints*, arXiv:1209.1438, arXiv:1209.1438. DOI: 10.48550/arXiv.1209.1438. arXiv: 1209.1438 [astro-ph.CO].

Han, J. L. et al. (Jan. 2018). "Pulsar Rotation Measures and Large-scale Magnetic Field Reversals in the Galactic Disk". In: *The Astrophysical Journal Supplement Series* 234.1, 11, p. 11. DOI: 10.3847/1538-4365/aa9c45. arXiv: 1712.01997 [astro-ph.GA].

Haverkorn, M. (Jan. 2015). "Magnetic Fields in the Milky Way". In: *Magnetic Fields in Diffuse Media*. Ed. by A. Lazarian, E. M. de Gouveia Dal Pino, & C. Melioli. Vol. 407. Astrophysics and Space Science Library, p. 483. DOI: 10.1007/978-3-662-44625-6_17. arXiv: 1406.0283 [astro-ph.GA].

Heesen, V. et al. (2023). "Detection of magnetic fields in the circumgalactic medium of nearby galaxies using Faraday rotation". In: *arXiv preprint arXiv:2302.06617*.

Hutschenreuter, S. et al. (2022). "The Galactic Faraday rotation sky 2020". In: *Astronomy & Astrophysics* 657, A43.

Kirsten, F. et al. (Feb. 2022). "A repeating fast radio burst source in a globular cluster". In: *Nature* 602.7898, pp. 585–589. DOI: 10.1038/s41586-021-04354-w. arXiv: 2105.11445 [astro-ph.HE].

Kumar, P. et al. (Apr. 2022). "Propagation of a fast radio burst through a birefringent relativistic plasma". In: *arXiv e-prints*, arXiv:2204.10816, arXiv:2204.10816. DOI: 10.48550/arXiv.2204.10816. arXiv: 2204.10816 [astro-ph.HE].

Lan, T.-W. & J. X. Prochaska (Aug. 2020). "Constraining magnetic fields in the circumgalactic medium". In: *Monthly Notices of the Royal Astronomical Society* 496.3, pp. 3142–3151. DOI: 10.1093/mnras/staa1750. arXiv: 2006.09369 [astro-ph.GA].

Law, C. J. et al. (2024). "Deep synoptic array science: first FRB and host galaxy catalog". In: *The Astrophysical Journal* 967.1, p. 29.

Law, C. J., L. Connor, & K. Aggarwal (Mar. 2022). "On the Fast Radio Burst and Persistent Radio Source Populations". In: *The Astrophysical Journal* 927.1, 55, p. 55. DOI: 10.3847/1538-4357/ac4c42. arXiv: 2110.15323 [astro-ph.HE].

Lee, K.-G. et al. (June 2023a). "The FRB20190520B Sightline Intersects Foreground Galaxy Clusters". In: *arXiv e-prints*, arXiv:2306.05403, arXiv:2306.05403. DOI: 10.48550/arXiv.2306.05403. arXiv: 2306.05403 [astro-ph.GA].

– (June 2023b). "The FRB20190520B Sightline Intersects Foreground Galaxy Clusters". In: *arXiv e-prints*, arXiv:2306.05403, arXiv:2306.05403. DOI: 10.48550/arXiv.2306.05403. arXiv: 2306.05403 [astro-ph.GA].

Macquart, J.-P. et al. (May 2020). "A census of baryons in the Universe from localized fast radio bursts". In: *Nature* 581.7809, pp. 391–395. DOI: 10.1038/s41586-020-2300-2. URL: https://doi.org/10.1038%2Fs41586-020-2300-2.

Mannings, A. G. et al. (2022). "Fast Radio Bursts as Probes of Magnetic Fields in Galaxies at z< 0.5". In: *arXiv preprint arXiv:2209.15113*.

Marinacci, F. et al. (Nov. 2015). "The large-scale properties of simulated cosmological magnetic fields". In: *Monthly Notices of the Royal Astronomical Society* 453.4, pp. 3999–4019. DOI: 10.1093/mnras/stv1692.

Marinacci, F. et al. (Nov. 2018). "First results from the IllustrisTNG simulations: radio haloes and magnetic fields". In: *Monthly Notices of the Royal Astronomical Society* 480.4, pp. 5113–5139. DOI: 10.1093/mnras/sty2206. arXiv: 1707.03396 [astro-ph.CO].

Masui, K. et al. (2015). "Dense magnetized plasma associated with a fast radio burst". In: *Nature* 528.7583, pp. 523–525.

Mckinven, R. et al. (2023). "Revealing the Dynamic Magneto-ionic Environments of Repeating Fast Radio Burst Sources through Multi-year Polarimetric Monitoring with CHIME/FRB". In: *arXiv preprint arXiv:2302.08386*.

Mckinven, R. et al. (2021). "Polarization Pipeline for Fast Radio Bursts Detected by CHIME/FRB". In: *The Astrophysical Journal* 920.2, p. 138.

Melrose, D. & J.-P. Macquart (1998). "Stochastic Faraday Rotation". In: *The Astrophysical Journal* 505.2, p. 921.

Michilli, D. et al. (Jan. 2018). "An extreme magneto-ionic environment associated with the fast radio burst source FRB 121102". In: *Nature* 553.7687, pp. 182–185. DOI: 10.1038/nature25149. arXiv: 1801.03965 [astro-ph.HE].

Michilli, D. et al. (2022). *Sub-arcminute localization of 13 repeating fast radio bursts detected by CHIME/FRB*. arXiv: 2212.11941 [astro-ph.HE].

Planck Collaboration et al. (2016). "Planck 2015 results - XIII. Cosmological parameters". In: *A&A* 594, A13. DOI: 10.1051/0004-6361/201525830. URL: https://doi.org/10.1051/0004-6361/201525830.

Plavin, A. et al. (2022). "FRB 121102: Drastic changes in the burst polarization contrasts with the stability of the persistent emission". In: *Monthly Notices of the Royal Astronomical Society* 511.4, pp. 6033–6041.

Ponnada, S. B. et al. (Nov. 2022). "Magnetic fields on FIRE: Comparing B-fields in the multiphase ISM and CGM of simulated L_* galaxies to observations". In: *Monthly Notices of the Royal Astronomical Society* 516.3, pp. 4417–4431. DOI: 10.1093/mnras/stac2448. arXiv: 2206.04764 [astro-ph.GA].

Qu, Y. & B. Zhang (2023). "Polarization of fast radio bursts: radiation mechanisms and propagation effects". In: *Monthly Notices of the Royal Astronomical Society* 522.2, pp. 2448–2477.

Ramesh, R. et al. (2023). *Azimuthal Anisotropy of Magnetic Fields in the Circumgalactic Medium Driven by Galactic Feedback Processes*. arXiv: 2305.11214 [astro-ph.GA].

Ravi, V. et al. (2016). "The magnetic field and turbulence of the cosmic web measured using a brilliant fast radio burst". In: *Science* 354.6317, pp. 1249–1252.

Ravi, V. et al. (2023). "Deep synoptic array science: discovery of the host galaxy of FRB 20220912A". In: *The Astrophysical Journal Letters* 949.1, p. L3.

Rees, M. J. (Sept. 1987). "The origin and cosmogonic implications of seed magnetic fields." In: *Quarterly Journal of the Royal Astronomical Society* 28, pp. 197–206.

Robishaw, T., E. Quataert, & C. Heiles (June 2008). "Extragalactic Zeeman Detections in OH Megamasers". In: *The Astrophysical Journal* 680.2, pp. 981–998. DOI: 10.1086/588031. arXiv: 0803.1832 [astro-ph].

Rodrigues, L. F. S. et al. (2019). "Evolution of galactic magnetic fields". In: *Monthly Notices of the Royal Astronomical Society* 483.2, pp. 2424–2440.

Ryu, D. et al. (May 2008). "Turbulence and Magnetic Fields in the Large-Scale Structure of the Universe". In: *Science* 320.5878, p. 909. DOI: 10.1126/science.1154923. arXiv: 0805.2466 [astro-ph].

Schnitzeler, D. & K. Lee (2015). "Rotation measure synthesis revisited". In: *Monthly Notices of the Royal Astronomical Society: Letters* 447.1, pp. L26–L30.

Sharma, K. et al. (June 2023). "Deep Synoptic Array Science: A Massive Elliptical Host Among Two Galaxy-cluster Fast Radio Bursts". In: *The Astrophysical Journal* 950.2, 175, p. 175. DOI: 10.3847/1538-4357/accf1d. arXiv: 2302.14782 [astro-ph.HE].

Sherman, M. B. et al. (2024). "Deep Synoptic Array Science: Polarimetry of 25 New Fast Radio Bursts Provides Insights into Their Origins". In: *The Astrophysical Journal* 964.2, p. 131. DOI: 10.3847/1538-4357/ad275e.

Simha, S. et al. (Mar. 2023). "Searching for the sources of excess extragalactic dispersion of FRBs". In: *arXiv e-prints*, arXiv:2303.07387, arXiv:2303.07387. DOI: 10.48550/arXiv.2303.07387. arXiv: 2303.07387 [astro-ph.GA].

Sobey, C. et al. (Apr. 2019). "Low-frequency Faraday rotation measures towards pulsars using LOFAR: probing the 3D Galactic halo magnetic field". In: *Monthly Notices of the Royal Astronomical Society* 484.3, pp. 3646–3664. DOI: 10.1093/mnras/stz214. arXiv: 1901.07738 [astro-ph.GA].

Sotomayor-Beltran, C. et al. (2013). "ionFR: Ionospheric Faraday rotation". In: *Astrophysics Source Code Library*, ascl–1303.

Su, K.-Y. et al. (Jan. 2018). "Stellar feedback strongly alters the amplification and morphology of galactic magnetic fields". In: *Monthly Notices of the Royal Astronomical Society* 473.1, pp. L111–L115. DOI: 10.1093/mnrasl/slx172. arXiv: 1710.05932 [astro-ph.GA].

Suresh, A. & J. M. Cordes (2019). "Induced polarization from birefringent pulse splitting in magneto-ionic media". In: *The Astrophysical Journal* 870.1, p. 29.

Tendulkar, S. P. et al. (2017). "The host galaxy and redshift of the repeating fast radio burst FRB 121102". In: *The Astrophysical Journal Letters* 834.2, p. L7.

Vanderlinde, K. et al. (Oct. 2019). "The Canadian Hydrogen Observatory and Radio-transient Detector (CHORD)". In: *Canadian Long Range Plan for Astronomy and Astrophysics White Papers*. Vol. 2020, 28, p. 28. DOI: 10.5281/zenodo.3765414. arXiv: 1911.01777 [astro-ph.IM].

Vedantham, H. & V. Ravi (2019). "Faraday conversion and magneto-ionic variations in fast radio bursts". In: *Monthly Notices of the Royal Astronomical Society: Letters* 485.1, pp. L78–L82.

Xu, H. et al. (Sept. 2022). "A fast radio burst source at a complex magnetized site in a barred galaxy". In: *Nature* 609.7928, pp. 685–688. DOI: 10.1038/s41586-022-05071-8. arXiv: 2111.11764 [astro-ph.HE].

Yang, K., Q. Wu, & F. Wang (2022). "Finding the missing baryons in the intergalactic medium with localized fast radio bursts". In: *The Astrophysical Journal Letters* 940.2, p. L29.

Yang, Y.-P., S. Xu, & B. Zhang (Apr. 2023). "Faraday rotation measure variations of repeating fast radio burst sources". In: *Monthly Notices of the Royal Astronomical Society* 520.2, pp. 2039–2054. DOI: 10.1093/mnras/stad168. arXiv: 2208.08712 [astro-ph.HE].

Yang, Y.-P. et al. (Apr. 2022). "Temporal Scattering, Depolarization, and Persistent Radio Emission from Magnetized Inhomogeneous Environments near Repeating Fast Radio Burst Sources". In: *The Astrophysical Journal Letters* 928.2, L16, p. L16. DOI: 10.3847/2041-8213/ac5f46. arXiv: 2202.09602 [astro-ph.HE].

Zhang, Z. et al. (2021). "Intergalactic medium dispersion measures of fast radio bursts estimated from IllustrisTNG simulation and their cosmological applications". In: *The Astrophysical Journal* 906.1, p. 49.

Zweibel, E. G. (May 2013). "The microphysics and macrophysics of cosmic rays". In: *Physics of Plasmas* 20.5, 055501, p. 055501. DOI: 10.1063/1.4807033.

Chapter 8

FORECASTS FOR PULSAR SEARCHING WITH THE DSA-2000

8.1 Introduction

Pulsars are neutron stars in the Milky Way and Magellanic Clouds with well-defined periodic radio pulsations. A catalog of ∼ 2700 slow, or canonical pulsars (CPs) and ∼ 600 recycled, or millisecond pulsars (MSPs) has been collected over the last 50 years, as reported by the Australia National Telescope Facility (ATNF) (R. N. Manchester et al., 2005). The pulsar emission mechanism has been well-constrained (e.g., Radhakrishnan & Cooke, 1969), making them invaluable as probes of the nuclear matter equation of state, the Galactic interstellar medium (ISM), and turbulent space-time via Pulsar Timing Arrays (PTAs) (e.g., Backer & Hellings, 1986; Cordes & Lazio, 2002; Lattimer, 2012). Additionally, the detection of more exotic pulsar species such as Double-Neutron Star binaries (DNS), Neutron Star-Black Hole binaries (NSBH), and MSPs with Main Sequence companions like Redbacks and Black Widows can provide a more holistic view of pulsar formation and evolution (Fruchter et al., 1988; Roberts et al., 2011). Modern radio interferometers, whose sensitivity scales with the number of antenna baselines in the array, have been instrumental to recovering the contribution of the collapsed Arecibo telescope, which had a 2.3 Jy System Equivalent Flux Density (SEFD). The Arecibo and Parkes single-dish telescopes have detected nearly two-thirds of pulsars in the ATNF catalog (R. N. Manchester et al., 1996, 2005; Spitler et al., 2014) while other single-dish telescopes, such as the Green Bank Telescope (GBT), the Giant Metrewave Radio Telescope (GMRT), and the Five-hundred meter Aperture Spherical Telescope (FAST) have contributed a ∼ 600 pulsars (e.g., Barr et al., 2013; Bhattacharyya et al., 2016; R. Manchester et al., 1978; Stovall et al., 2014). The success of interferometric surveys by the Canadian Hydrogen Intensity Mapping Experiment (CHIME; Amiri et al., 2022), the Karoo Array Telescope (MeerKAT; Bailes et al., 2020), the Low Frequency Array (LOFAR; Haarlem et al., 2013), and the 110-antenna Deep Synoptic Array precursor (DSA-110; Ravi et al., 2023) has presented the path forward in radio transient searching. MeerKAT and LOFAR have discovered 37 and 58 pulsars, respectively, in their inaugural and follow-up surveys (Dong et al., 2023; Thongmeearkom et al., 2024; Wateren et al., 2023). CHIME's 250 $\deg^2$ FOV allows for timing of up to 10 pulsars simultaneously, enabling the discovery of ∼ 20

new pulsars (Dong et al., 2023; Ng et al., 2020). The search for extragalactic Fast Radio Bursts (FRBs) further demonstrates the capabilities of radio interferometers. CHIME has compiled the largest uniform catalog of FRBs with 536 (Amiri et al., 2021), while the DSA-110's arcsecond scale localization accuracy has led to the identification of $\sim$ 30 FRB host galaxies (Law et al., 2024; Sharma et al., 2024). These surveys indicate the potential of large interferometers; however, they do not make up for the sensitivity and sky coverage of Arecibo, nor are they able to survey the sky at high rates.

Alongside the Square Kilometre Array (SKA; Smits et al., 2009; Weltman et al., 2020), the Deep Synoptic Array (DSA-2000) is expected to have a significant impact on pulsar science, utilizing 1650×6.15 m antennas to achieve an effective SEFD$\approx$ 1.6 Jy, comparable to that of Arecibo (Hallinan et al., 2019). The DSA-2000 also has a 7.3 deg^2 field-of-view (at 1100 MHz) that far exceeds that of Arecibo. These properties will enable a cadenced all-sky search strategy with the first ever real-time Radio Camera Instrument (RCI). While the bulk of resources are devoted to a Continuum All-Sky Survey (CASS), Deep Drilling Fields, and pulsar timing, a Fast Time Domain (FTD) search will be incorporated using an adjacent compute infrastructure (the Chronoscope), extending the search capabilities with little impact to the RCI pipeline. The large number of antennas, wide FOV, and high time resolution would make this a non-trivial compute task with modern GPU architectures. However, next-generation rack-based GPU clusters (e.g., the NVL series from NVIDIA) will revolutionize the speed and optimality of pulsar searching.

In this memo we present an early forecast of the performance of the DSA-2000 pulsar search. Section 8.2 describes the early pulsar search design **(which has been revised since completion of this memo)**. The remainder of the paper will proceed as follows: Section 8.3 provides forecasts for the pulsar detections from the DSA-2000 sensitivity; Section 8.4 uses multi-wavelength deep-field catalogs to model a continuum source targeting strategy; Section 8.5 describes how the unique survey cadence and pointing design can be optimized for pulsar follow-up; Section 8.6 provides conclusions and next steps in the FTD search design process.

8.2 DSA-2000 Pulsar Search Design

The DSA-2000 FTD search will run commensally with the CASS, operating on 2400×130.2 kHz tunable, Nyquist sampled channels output by the Radio Camera Frontend (RCF). The baseline search parameters are summarized in Table 8.1.

The pulsar search system will form synthesized beams of FWHM $22''(2\,\mathrm{GHz}/\nu)$ over the 2 GHz primary beam FWHM, 1.68°. Beams are formed at 0.1 ms time resolution over a variable integration time of order $\sim 1,800$ s, preserving sensitivity to both MSPs and CPs. Each beam will then be corrected for interstellar dispersion for $\sim 1,000$ Dispersion Measure (DM) trials up to a variable upper limit before searching for periodic signals for each beam and DM trial. The variable DM range can be tuned depending on pointing, since DMs can reach $\sim 5,000\,\mathrm{pc\,cm^{-3}}$ for galactic plane pulsars but are substantially lower at high Galactic latitudes. Allowing up to 10% signal-to-noise loss between DM trials (or a DM tolerance of 1.1), roughly 1,000 trials are required to search up to $\sim 5,000\,\mathrm{pc\,cm^{-3}}$.

The pulsar search will iterate over trial values of $\dot{f} = df/dt$ (where $f = 1/P$) to search for accelerated pulsar binaries. Using Kepler's law, we expect binaries to yield $\dot{f}$ values of order:

$$|\dot{f}| \approx \left(\frac{G(M_1 + M_2)}{cPa^2}\right) \tag{8.1}$$

where a is the semi-major axis and M_1 and M_2 are the pulsar and companion mass (e.g., Dimoudi et al., 2018; Ng et al., 2015; Ransom et al., 2002). While typical pulsar-Main Sequence star and pulsar-White Dwarf systems have $|\dot{f}| \lesssim 10^{-12}\,\mathrm{s^{-2}}$, more exotic double-Neutron Star or pulsar-Black Hole companions are expected to have $|\dot{f}| \lesssim 10^{-5}\,\mathrm{s^{-2}}$. The number of acceleration trials scales as below:

$$N_{\dot{f}} \approx \frac{|\dot{f}_{\mathrm{max}}|}{\delta \dot{f}} = |\dot{f}_{\mathrm{max}}|\frac{PT_{\mathrm{obs}}^2}{64 t_s} \tag{8.2}$$

(e.g., Equation 3 in Eatough et al., 2013). Thus $\sim 100 - 1,000$ trials are required to search up to $10^{-6} - 10^{-5}\,\mathrm{s^{-2}}$. However, $N_{\dot{f}}$ will be tuned depending on the available compute resources, integration time, and number of search targets for a given pointing.

8.3 Pulsar Detection Forecasts

To estimate the DSA-2000's pulsar detection yield, we conduct a Monte Carlo simulation wth PSRPop.py, a Python implementation of the PSRPop population synthesis software developed for pulsar forecasting (Bates et al., 2014). A Galactic population of 30605 MSPs and 209290 CPs was generated based on the known performances of the Parkes-Swinburne Multibeam Survey (PSMB), the Parkes Multibeam Survey

Table 8.1: Baseline Design Parameters for Pulsar Search

Bandwidth (MHz)	312.5
Frequency Channels	$2400 \times 130.2\,\mathrm{kHz}$
Synthesized Beamwidth	$2.2''(\frac{2\,\mathrm{GHz}}{\nu})$
Integration Time (s)	Variable (Nominal CASS pointings are 1800 s)
Sampling Time (ms)	0.1
Search Beams	$3,000 - 4,000$
Search Field of View (FOV)	1.68°
Maximum DM ($\mathrm{pc\,cm^{-3}}$)	$\sim 5,000$
DM Trials	1,000
Maximum $\dot{f}$ ($\mathrm{s^{-2}}$)	$10^{-6} - 10^{-5}$
$\dot{f}$ Trials	$\sim 100 - 1,000$

[1]While initial CASS epoch will use 1800 s pointings, subsequent epochs will have tunable integration times depending on the field.

(PKMBS), and the Parkes High Resolution Time Universe Survey (HTRU-S) (Edwards et al., 2001; Keith et al., 2010; R. N. Manchester et al., 2001). The pulsar forecast for the blind periodicity survey was simulated using the 'snapshot' method, which uses the equation below with provided survey parameters to estimate the radiometer signal-to-noise (S/N):

$$\mathrm{S/N} = \frac{GL_{1400}\sqrt{n_p T_{\mathrm{obs}} \Delta f}}{\beta D^2 (T_{\mathrm{sky}} + T_{\mathrm{sky}} + T_{\mathrm{CMB}})} \sqrt{\frac{P - W_{\mathrm{eff}}}{W_{\mathrm{eff}}}} \tag{8.3}$$

We adopt the parameters for the initial DSA-2000 design: $G \approx 4.17 e^{-0.5(\Delta\theta/1.68^\circ))^2}\,\mathrm{K\,Jy^{-1}}$ is the gain[1] scaled depending the pulsar's location $\Delta\theta$ in the primary beam; $n_p = 2$ is the number of polarizations; $\beta \approx 1$ is the survey degradation factor; $\Delta f = 130.2\,\mathrm{kHz}$is the channel bandwidth; $T_{\mathrm{sys}} = 25\,\mathrm{K}$ is the system temperature; $T_{\mathrm{sky}} = 25\,\mathrm{K}$ is the sky temperature estimated from the Haslam et al. (1982) sky map; $T_{\mathrm{CMB}} = 2.73\,\mathrm{K}$ is the blackbody temperature of the Cosmic Microwave Background (CMB); $A_e = 19.6\,\mathrm{m^2}$ is the dish area; $T_{\mathrm{obs}} = 660\,\mathrm{s}$ is the integration time; P is the pulse period; D is the distance to the pulsar; and W_{eff} is the effective pulse width (including scattering and scintillation). Recent updates to the array design use $N_{\mathrm{ant}} = 1650 \times 29.7\,\mathrm{m^2}$ dishes with $T_{\mathrm{sys}}/\eta = 28\,\mathrm{K}$ (where the aperture efficiency η is

[1]The original G=4.17 K/Jy estimate is conservative and assumes that an arbitrary fraction of baselines would be removed to reduce computation for the pulsar search (SEFD$\approx$ 6 Jy). The current design now assumes that all baselines will be included, leading to a significant improvement in gain ($G = 17.5\,\mathrm{K\,Jy^{-1}}$) in addition to the effect of hardware updates.

included) yielding total SEFD=1.6 Jy^{-1}. Despite these changes, the pulsar forecasts still demonstrate the impact of the DSA-2000.

Figure 8.1 shows the simulated population and the resulting detection estimates. Using a 9σ S/N threshold, the simulation forecasts the DSA-2000 is sensitive to 930^{+30}_{-140} MSPs ($\sim 3.1\%$ of the visible population i.e. pulsars within the survey area of the DSA-2000, which is limited to declinations above -30°) and 9930^{+90}_{-890} CPs ($\sim 4.7\%$ of the visible population). Appendix 8.7 describes how a spectrum folding search method may lower the sensitivity of a blind search, an effect incorporated into the negative uncertainties above. Figure 8.2 shows the detection forecast as a function of observing bandwidth, indicating that limiting the search to 312.5 MHz at low frequencies will negligibly affect search sensitivity. Thus, we expect the DSA-2000 to detect a significant portion of the Galactic population, roughly 3.2× the current known sample of pulsars in the ATNF catalog. Notably, the CASS, which has a $\sim 1.2\,\mu$Jy sensitivity will be sensitive to pulsars as continuum sources; with a 6σ ($\sim 7\,\mu$Jy) threshold, ~ 3322 MSPs and ~ 22580 CPs from the simulated population are detectable, through CASS. This indicates CASS can be used as a supplemental search tool and a prior to select continuum targets for the periodicity search. We discuss this strategy in detail in Section 8.4. Future work will more rigorously consider the DSA-2000's sensitivity to accelerated binary systems, including the effect of novel search methods such as "pruning" and hierarchical recursive searches (Men et al., 2023; Smith, 2016).

8.4 CASS Target Selection and Multi-Wavelength Cross-Matching

With the advent of rack-based GPU architectures that achieve $\sim 100\times$ faster compute speed ($\sim$ 10 PFLOPS) than the current state-of-the-art and revolutionary inter-GPU data transfer rates ($\sim$ 100 TB s^{-1}), the DSA-2000 pulsar search will face few limitations from compute resources. This freedom may enable a full-FOV pulsar search, previously limited to only a subset of beams. Alternatively, limiting the number of search beams could enable a dense sampling of the period, DM, and acceleration parameter space. The latter case is further motivated by the expectation of $\sim 4,000$ total pulsars in each pointing, far fewer than the maximum $\sim 10^6$ beams that can be formed. Over the first year of operation, the DSA-2000 CASS will build a radio image and continuum point source catalog to $\sim 1.2\,\mu$Jy. In this section, we describe a potential search strategy which targets continuum sources from the initial CASS epoch to limit the number of beams. Leveraging the continuum survey will also increase the probability of detecting pulsars in the blind search and recovering

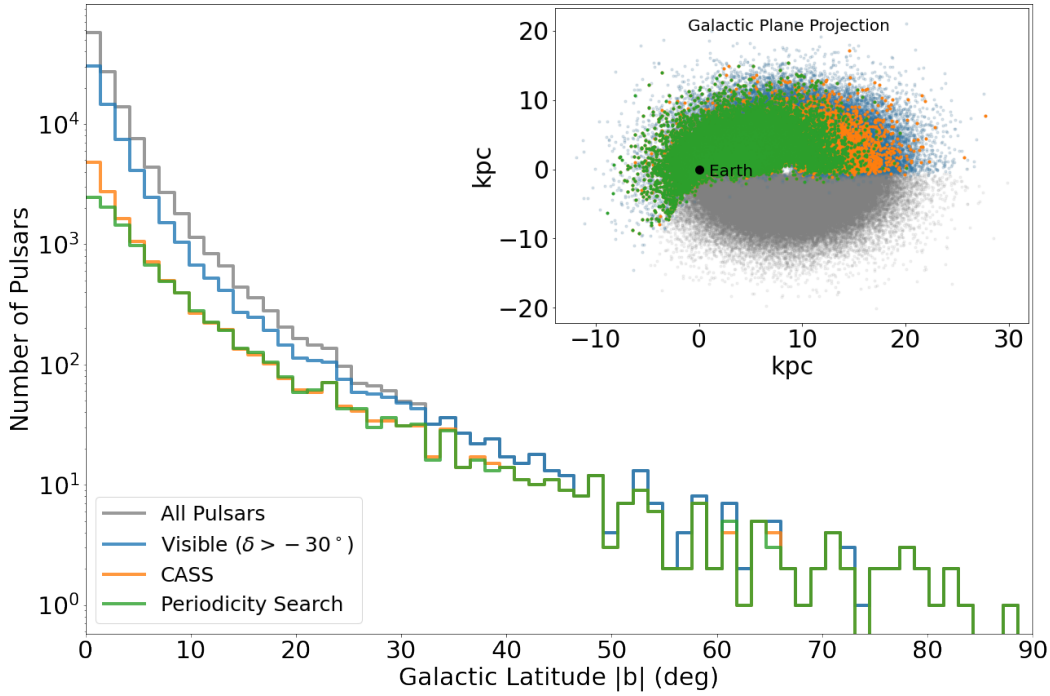

Figure 8.1: Histogram of Galactic Latitude of Simulated Pulsar Population. The inset plot shows the population in Cartesian coordinates projected into the galactic plane. For both plots, the full simulated sample is in grey, the $\delta > 30°$ population is in blue, the 25,902 pulsars detectable by CASS are in orange, and the 10,879 detectable by periodicity search are in green.

faint pulsars that are not detectable in the periodicity search.

After continuum point sources are identified (details on the photometry and detection pipeline will be detailed in Akeson et al., in prep), the target selection process will generally consist of removing extended sources and cross-matching with optical and IR (OIR) galaxy catalogs. Various methods have been developed to separate resolved objects from point sources in astrophysical images, such as PSF photometry and Kron magnitude comparisons. Full-band CASS images will have a resolution $\sim 3.02''$, enabling confident rejection of resolved false positives. Cross-matching will leverage all-sky OIR galaxy and extended source catalogs to rule out star-forming galaxies (SFGs) and active galactic nuclei (AGNs) that dominate at low flux (e.g., Condon et al., 2002). The DESI Legacy Imaging Surveys (Dey et al., 2019) and the Sloan Digital Sky Survey (SDSS; Ahumada et al., 2020) have conducted deep OIR imaging of over $\sim 10^5\,\mathrm{deg}^2$ of combined extragalactic sky, producing galaxy catalogs to AB magnitudes $\lesssim 22$. Next generation IR telescopes like the Roman (Bailey et al., 2023; Wang et al., 2022), Euclid (Scaramella et al., 2022),

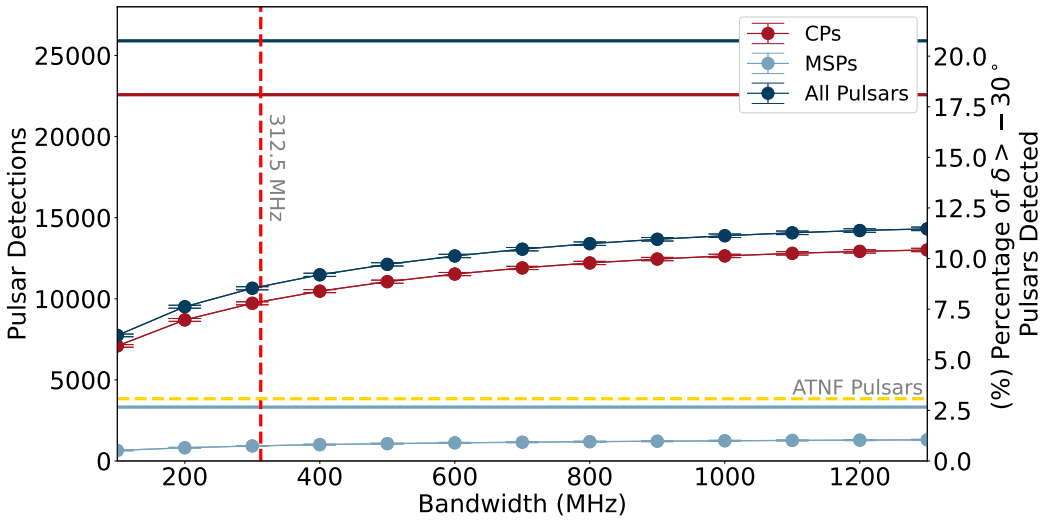

Figure 8.2: Simulated DSA-2000 Detections from a Blind Periodicity Search as a Function of Observing Bandwidth. 1σ errorbars are shown. Each trial bandwidth uses 700 MHz as the lower limit; the nominal 312.5 MHz design bandwidth is indicated in red. The right-hand axis indicates the percent of the total pulsar population detected. The solid horizontal lines indicate the number of pulsars detectable in the CASS. The known pulsar population (3838 total) from the ATNF catalog is shown in yellow, as of May 10$^{\text{th}}$, 2025.

and SPHERE-x (Alibay et al., 2023; Feder et al., 2024) telescopes will be launched concurrently with the DSA-2000 commissioning and first light, producing catalogs of $\sim 10^{6-8}$ galaxies imaged to $J \leq 20$, 24.5, and 26.7, respectively (Akeson, 2025; Akeson et al., 2024). These data sets will be essential for any targeted search to properly select Galactic pulsar candidates and rule-out extragalactic point sources from continuum images.

As a preliminary example, consider a source selection procedure for a single 0.63° (75% 2 GHz PSF) pulsar search radius using a CASS continuum image and a Roman telescope source catalog. We apply a prototype source selection pipeline to a 0.63° cutout of the COSMOS deep field, one of the only sky regions observed to a similar depth, spatial resolution, and wavelength coverage as enabled by the DSA-2000 and the Roman telescopes. Let the CASS catalog be modeled by the MeerKAT international GHz Tiered Extragalactic Exploration (MIGHTEE; Jarvis et al., 2017) survey and Very Large Array COSMOS 20 cm (VLAC20; Bondi et al., 2008; Schinnerer et al., 2007, 2010) source catalogs. With source catalog thresholds $\gtrsim 30\,\mu$Jy and $\gtrsim 6\,\mu$Jy, respectively, and spatial resolutions of 5″ and 1.5″, respectively, these approximate the 3.06″ CASS resolution and $7 \sim \mu$Jy (6σ)

detection threshold reasonably well. We approximate the Roman catalog using the Hubble Space Telescope (HST) COSMOS (Cosmos Team, 2020; Leauthaud et al., 2007; Scoville et al., 2007) source catalog and the COSMOS15 (Laigle et al., 2016) galaxy catalog. The former reaches survey depth $I \leq 26.5$ with $0.12''$ resolution, while the latter reaches $i^+ \lesssim 26.9$ with $\sim 0.15''$ resolution. These also compare well to the Roman $I \lesssim 28$ OIR sensitivity and $\sim 0.1''$ resolution.

We threshold the MIGHTEE/VLAC20 catalog at the $7\,\mu$Jy pulsar search threshold, remove sources fit with multiple Gaussian components or identified as radio galaxies in VLAC20, then cross match with HST extended sources and COSMOS15 galaxies brighter than $I \lesssim 28$. The final sample is highlighted in red in Figure 8.3, demonstrating that this simple selection strategy can reduce 11,537 initial continuum sources to 1901 search targets in a 0.63° radius field. Scaling the target count with the search area, we estimate the full 0.84° primary beam radius would result in $\sim 20,500$ initial sources and 3400 search targets. Notably, this example neglects the flux range from $7 - 30\mu$Jy on spatial scales from $3.06'' - 5''$. Using the (Condon et al., 2002) 1.4 GHz source count distributions and the Tiered Radio Extragalactic Continuum Simulation (TRECS) angular size distribution (Bonaldi et al., 2019, Figure 11), we estimate that an additional $\sim 3,200$ SFGs will be detected as unresolved point sources, while $\sim 1,400$ AGN will be detected, but ruled out as extended sources ($\sim 10''$). We conclude that for a pulsar search radius $\Delta\theta$, a total sample of $\sim 25,100(\Delta\theta/0.84^\circ)^2$ radio continuum sources can be narrowed to $6,600(\Delta\theta/0.84^\circ)^2$ pulsar search targets. Incorporating other selection criteria such as polarization and spectral index, or reducing the search radius, may further narrow the selected search beams (e.g., Kaplan et al., 2019). In Section 5, we discuss how reducing the search radius will impact survey planning and follow-up.

The strategy above is intended only as a simple demo; the cross-matching strategy will be improved during design, construction, and commissioning of the DSA-2000. For example, in-development custom point source detection algorithms leverage prior knowledge of DSA-2000 systematics to minimize extended source contamination (Akeson et al., in prep.). Learning-based pipelines like the Gradient Boosting algorithm XGBoost are also upgrading the classification process (C. Liu et al., 2025). A more detailed investigation of source confusion's sensitivity impact with forward modeling is currently underway (Huang & Hallinan, 2022, Rosero et al. in preparation). In general, we expect confusion limits in CASS images to be well-below the $7\,\mu$Jy search threshold used for pulsar target selection. Naturally, source

selection will be impeded within the galactic plane due to OIR source crowding, high interstellar extinction, diffuse radio synchrotron emission, and limited data for cross-referencing (extragalactic survey telescopes will maximize time at high Galactic latitudes). UV tapering, while effective at removing diffuse emission, introduces significant artifacts that further contaminate the source count. In Section 5, we briefly address how optimizing survey cadence can improve galactic plane observations, but a more rigorous study is left to future work (e.g., Faber et al., in preparation). This analysis nonetheless demonstrates the efficacy of the DSA-2000's unique pulsar search strategy.

While we have demonstrated that pulsar search targets can be selected via a robust classification and cross-matching strategy, additional source crowding and diffuse synchrotron emission motivate alternate strategies for the galactic plane, where most pulsars reside (see Figure 8.1). Fortunately, CASS pointings will be dynamically scheduled such that each search region will be visited with a flexible week-to-month cadence. By visiting the galactic plane more frequently (∼weekly), the same sensitivity of a targeted search can be recovered with randomly positioned search beams on a short timescale. Only ~ 30 such epochs with $\lesssim 4,500$ random beams each are required to sample all $\sim 10^5$ continuum sources per pointing, effectively matching the targeted search sensitivity.

8.5 Cadence, Follow-up, and Confirmation Strategy

By running commensally with the CASS, the pulsar search can leverage densely sampled pointings to recover sensitivity. As shown in Figure 8.4, CASS pointings are spaced by 1.68° in a hexagonal grid, with a minimum of 25 adjacent pointings within each scheduling block. In the current design, pulsar search beams will be confined to the 1.68° FWHM. The top plots in Figure 8.5 show that at low frequencies, a wider search field would allow some regions to be targeted on subsequent pointings, up to 12 times for a search field $\theta_{\rm psr} = 2\theta_{\rm PSF}$, where $\theta_{\rm PSF}$ is the primary beam FWHM. In these regions, one can recover the targeted search sensitivity by randomly forming beams in each pointing in only ~ 5 hours as opposed to waiting for the subsequent epochs. At higher frequencies, the smaller primary beam size minimizes pointing overlap, and the targeted search remains the optimal strategy.

An effective pulsar search also requires candidates to be followed-up and confirmed on later pointings. In the current design, a subset of beams will be formed on the outer part of the primary beam to follow-up pulsar candidates. This can either

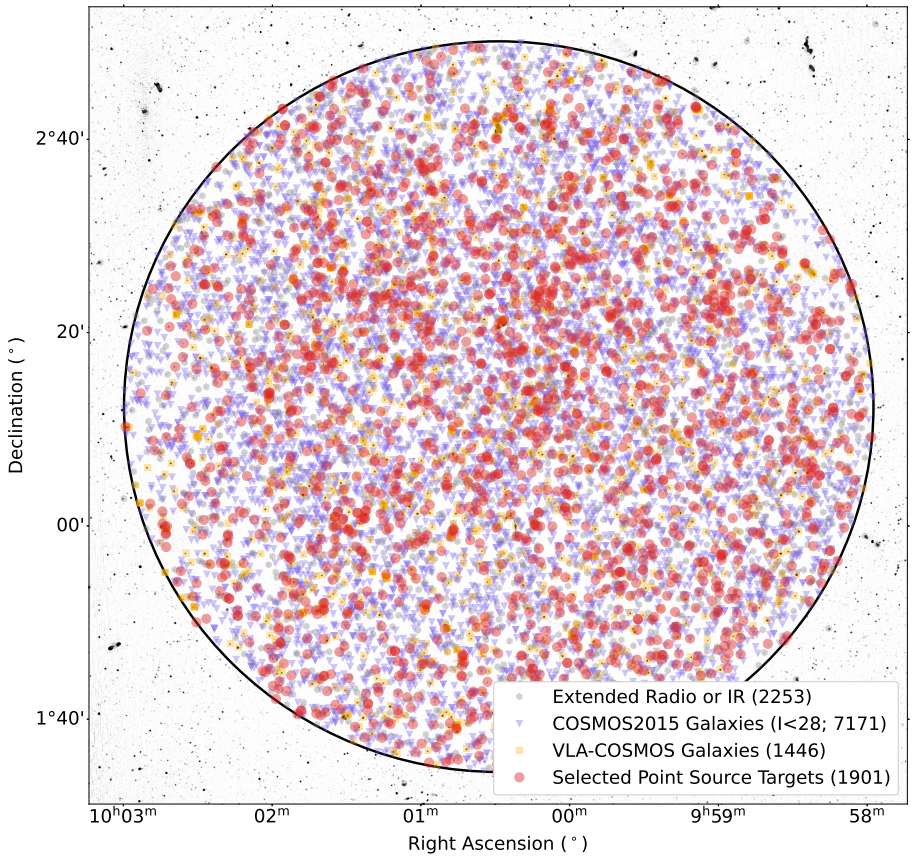

Figure 8.3: Example Pulsar Target Selection Using the COSMOS Deep Field. The underlying image is from the MeerKAT MIGHTEE survey. MIGHTEE/VLAC20 sources excluded as extended in radio or optical are grey circles. COSMOS2015 and VLAC20 Galaxies are marked with purple triangles and orange squares, respectively. The final target sample is indicated by red circles.

be done on later epochs or, as in the case above, on adjacent pointings within the same epoch. Notably, targeting the same search beam in a subsequent pointing will have a lower sensitivity since it will be formed at a larger offset from the pointing center. The bottom plot in Figure 8.5 shows the cumulative sensitivity if each beam is targeted with the maximum number of adjacent pointings. At the middle of the frequency band (1.35 GHz), revisiting the same beams improves the sensitivity by only a factor of two because they are outside of the FWHM of the adjacent beam. On the contrary, up to $\sim 7\times$ the on-axis sensitivity can be recovered for a small number of beams using a larger search field at low frequencies. Thus, follow-up and confirmation will be most effectively pursued by placing the tunable 312.5 MHz search band between $700 - 1100$ MHz.

The smaller FOV at mid- and high-frequency bands is still effective at reducing confusion from nearby continuum sources. While search beams cannot be re-visited as frequently, continuum point sources will appear narrower above 1.35 GHz due to the smaller PSF and can be more easily targeted. One potential survey strategy leveraging the full band is to run a targeted search over a single epoch at 1.35 GHz, and on the next epoch, follow-up candidates at 0.7 GHz with a larger search field. Each candidate can be observed in multiple adjacent pointings, maximizing the on-source time and increasing the chance of a re-detection for confirmation. Overlapping pulsar search fields will also have benefits for timing of known pulsars, as discussed in T. Liu et al. (2023); this will be investigated further in future work (Faber et al, in prep).

8.6 Conclusion

n this memo, we have considered the prospects for a DSA-2000 pulsar search, proposed a possible continuum source targeting strategy, and considered ways to optimize follow-up given the overlapping CASS pointing design. We have demonstrated that while the blind pulsar search will detect $\sim 10^4$ pulsars, sensitivity can be improved by targeting continuum sources from the CASS, extending the forecasted detections to $\sim$ 3000 MSPs and $\sim$ 20000 CPs. Overlapping adjacent pointings at low frequencies will enable rapid follow-up of candidates. Future work will investigate the DSA-2000's sensitivity to exotic, high acceleration pulsar binaries, and discuss the Generic-GPU-Project FTD search system in detail. With a flexible FTD architecture and unique search strategies, the DSA-2000 will make a lasting contribution to pulsar science, enabling population studies that will characterize their progenitors and probe intervening matter.

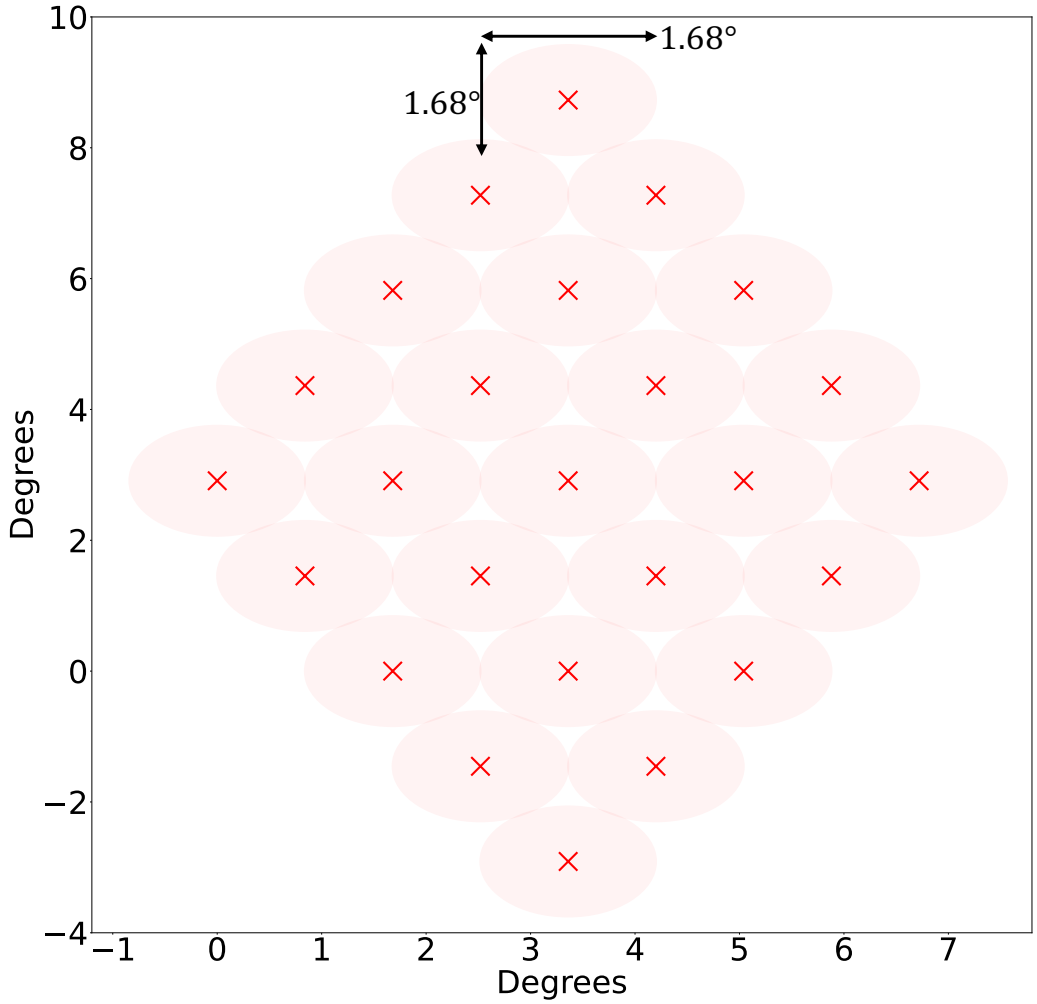

Figure 8.4: Example 25-Pointing Grid for DSA-2000 CASS. Pointing centers are indicated by an "x", and each circle indicates the FWHM of the primary beam at 2 GHz (1.68°).

8.7 Appendix

General practice for pulsar detection forecasting is to assume a constant S/N threshold, $S/N_{min} \approx 9$ (e.g., Cordes et al., 2006). However, Lazarus et al. (2015) use injection tests of Arecibo Pulsar-ALFA Survey (PALFA) pipeline to demonstrate that S/N_{min} cannot be fully described by the radiometer equation, especially at low pulse periods. Biases in the search algorithm can affect S/N_{min} resulting in overestimated pulsar detection predictions. It is essential to understand the baseline search performance, as future efforts will incorporate novel GPU-based optimization. To this end, a Monte Carlo simulation was conducted to characterize the true S/N_{min} as a function of the FFT size M, the pulse period P, and the sampling rate t_s. The method described follows a similar procedure to Smith (2016) to analyze novel

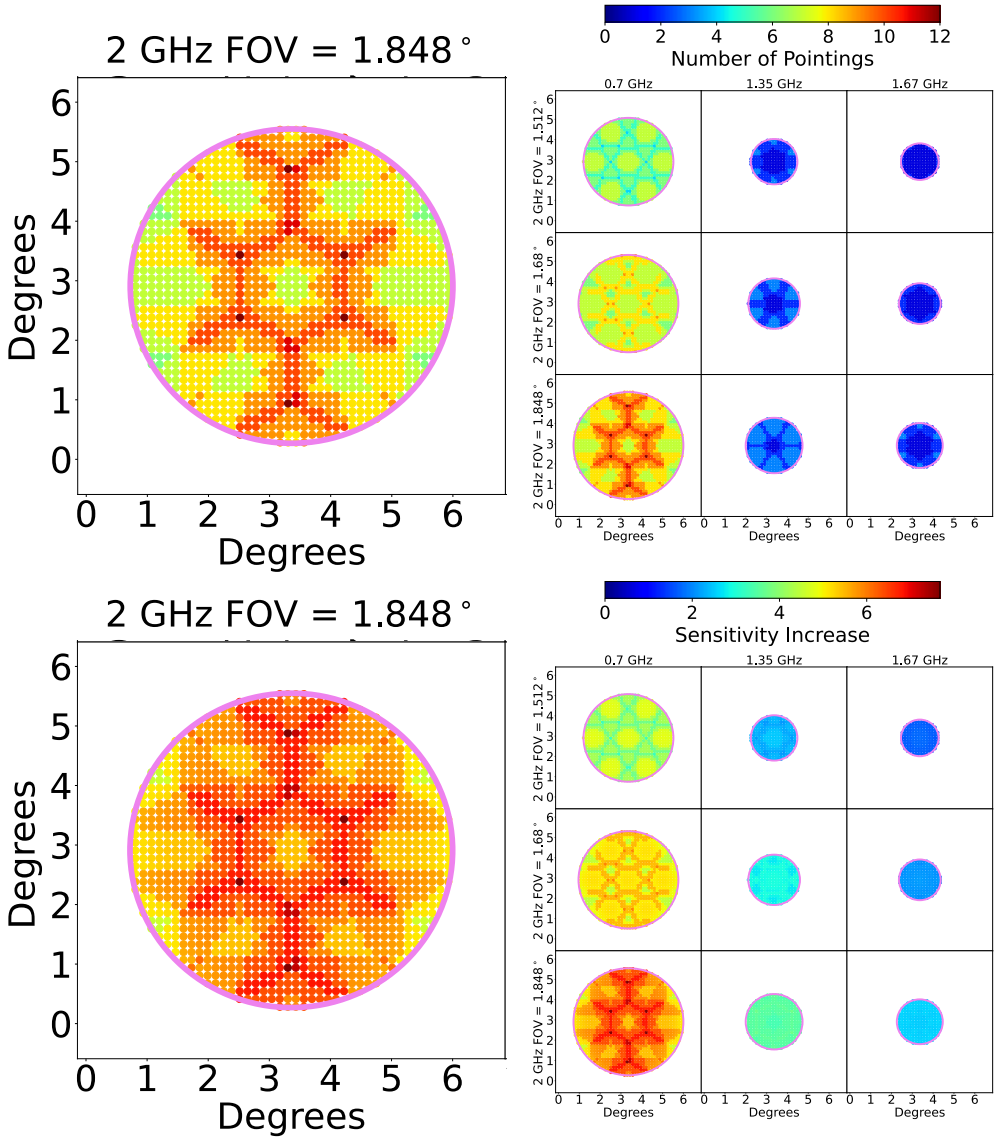

Figure 8.5: (top right) Number of adjacent pointings that overlap each point within example pulsar search FOVs. Each row corresponds to a different search region size and each column corresponds to a different frequency band. The pink circle indicates the edge of the search region, while the colorscale indicates the number of times a point can be visited within a 25-pointing grid. (bottom right) Sensitivity increase factor from re-visiting a point the maximum number of times. The rows and columns are identical to the bottom left plot. The top left and bottom left plots are zoomed in on the FOV= 1.848° example.

search algorithms. For a given trial FFT size, a Monte Carlo simulation was conducted by generating a population of pulsar timeseries with randomly selected pulse periods P, S/N, and duty cycle (estimated as $D = 1/n_{\text{harms}}$) drawn from uniform distributions ranging from $0.1Hz \leq 1/P \leq 1,000$ Hz (note here that the distribution is uniform in frequency rather than period for better interfacing with the algorithm) and $0 \leq \text{S/N} \leq 100$. Each timeseries is assumed to have radiometer noise RMS given by:

$$\sigma = \frac{T_{\text{sky}}}{\sqrt{2\Delta f t_{\text{int}}}} \tag{8.4}$$

where T_{sky}, Δf, and t_{int} are the system temperature, channel bandwidth, and integration time. For simplicity, the effects of scintillation, scattering, and dispersion were neglected. The generated pulsar was then assumed to be a perfectly de-dispersed timeseries averaged over frequency. Future work will involve incorporating more realistic effects (such as scintillation and scattering) into trial pulsars.

Each pulsar was then run through a prototype Python implementation of a power spectrum folding search, which takes as parameters the maximum number of harmonics to fold, nfolds, and an FFT size M. This is identical to a standard pulsar folding algorithm but sums only harmonics of the pulse period, which is known a-priori. A "detection" is defined as the case where the maximum search statistic $\hat{\epsilon}_{\text{max}}$ exceeds a critical threshold η, such that the probability of the search statistic exceeding η is:

$$\mathcal{P}(\hat{\varepsilon} > \eta) = N_{\text{trials}}^{-1} = \left(N_{\text{DM}} (\frac{f_{\text{max}} - f_{\text{min}}}{1/Mt_s}) N_{\text{sky}} \right)^{-1} \tag{8.5}$$

where the number of trials Ntrials is the total number of trials, including frequency trials ($Mt_s(f_{\text{max}} - f_{\text{min}})$), DM trials, and sky pointings. A histogram versus input S/N of each pulsar is created for total pulsars $H_{\text{tot}}(\text{S/N})$ and detected pulsars $H_{\text{det}}(\text{S/N})$, binning by $\Delta\text{S/N} = 1$, and the detection probability taken to be the ratio:

$$\mathcal{P}_{\text{det}}(\text{S/N}) = \frac{\mathcal{H}_{\text{det}}(\text{S/N})}{\mathcal{H}_{\text{tot}}(\text{S/N})} \tag{8.6}$$

as shown in Figure 8.6 (top). The S/N threshold estimate S/N_{min} is defined to be where $P_{\text{det}}(\text{S/N}_{\text{min}}) = 0.5 = 0.5$ after fitting a non-central χ^2 distribution. The resulting S/N threshold as a function of pulse frequency is shown in Figure 8.6

(bottom) for 0.1 ms sampling time and $M = 9 \times 10^6$. S/N_{min} is approximately constant with average value $S/N_{min,avg} = 9.4\sigma$. This suggests that the DSA-2000 search's high time resolution and sensitivity make it relatively robust against period-dependent effects, such as red noise (e.g., Singh et al., 2022), though a more detailed analysis is required to confirm this. S/N_{min} is extrapolated and applied to `PSRPop.py` by re-calculating the beam-averaged S/N for each pulsar and comparing it the S/N_{min} for the given pulse period. Figure 8.7 shows the revised detectable pulsar population compared to the original 9σ threshold sensitivity curves. The impact of the revised threshold is most prominent for MSPs with DM $\geq 200\,\mathrm{pc\,cm^{-3}}$, reducing the MSP blind search forecast by $\sim 12\%$, while CP detections are reduced by $\sim 8\%$. This effect is incorporated into the uncertainties reported in Section 8.3 for the blind search predictions.

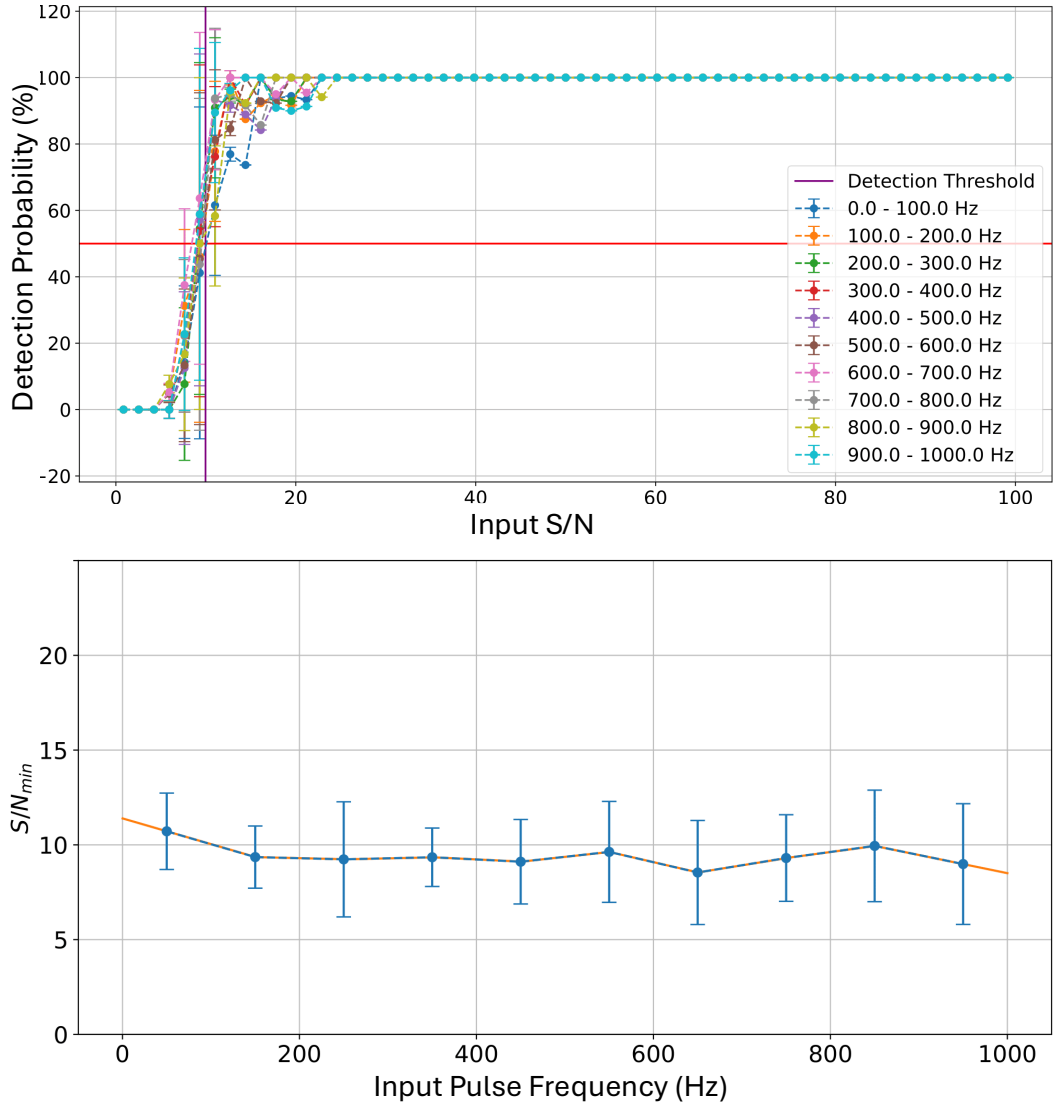

Figure 8.6: (top) Detection Probability Curves for the Baseline Search. The red line indicates the 50% detection probability corresponding to the S/N threshold. The purple line indicates the threshold η set by the false positive rate α used as the detection criteria on the search statistic. (bottom) S/N Threshold for Baseline Search. Linear interpolation is shown as a solid line, which is used for constraint of PSRPop.py simulations.

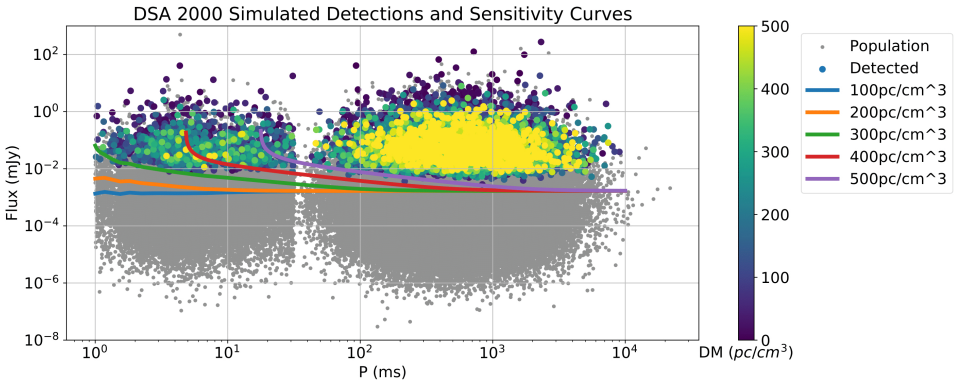

Figure 8.7: Baseline Search Sensitivity Plot and PSRPoppy Simulated Detections with Revised S/N Threshold. Sensitivity curves with the original constant S/N threshold of 9 are shown as solid lines.

CHAPTER 8 BIBLIOGRAPHY

Ahumada, R. et al. (July 2020). "The 16th Data Release of the Sloan Digital Sky Surveys: First Release from the APOGEE-2 Southern Survey and Full Release of eBOSS Spectra". In: *The Astrophysical Journal Supplement Series* 249.1, 3, p. 3. DOI: 10.3847/1538-4365/ab929e. arXiv: 1912.02905 [astro-ph.GA].

Akeson, R. (2025). "SPHEREx science data processing and archive products". In: *American Astronomical Society Meeting Abstracts*. Vol. 245, pp. 131–06.

Akeson, R. et al. (2024). "The DSA-2000 Public Archive and Photometry Pipeline". In: *American Astronomical Society Meeting Abstracts*. Vol. 56. 2, pp. 261–08.

Alibay, F. et al. (2023). "SPHEREx Preliminary Mission Overview". In: *2023 IEEE Aerospace Conference*. IEEE, pp. 1–18.

Amiri, M. et al. (2021). "The first CHIME/FRB fast radio burst catalog". In: *The Astrophysical Journal Supplement Series* 257.2, p. 59.

Amiri, M. et al. (2022). "An overview of CHIME, the Canadian hydrogen intensity mapping experiment". In: *The Astrophysical Journal Supplement Series* 261.2, p. 29.

Backer, D. & R. Hellings (1986). "Pulsar timing and general relativity". In: *Annual review of astronomy and astrophysics* 24.1, pp. 537–575.

Bailes, M. et al. (2020). "The MeerKAT telescope as a pulsar facility: System verification and early science results from MeerTime". In: *Publications of the Astronomical Society of Australia* 37, e028.

Bailey, V. P. et al. (2023). "Nancy Grace Roman Space Telescope coronagraph instrument overview and status". In: *Techniques and Instrumentation for Detection of Exoplanets XI* 12680, pp. 283–293.

Barr, E. D. et al. (2013). "The northern high time resolution universe pulsar survey–I. Setup and initial discoveries". In: *Monthly Notices of the Royal Astronomical Society* 435.3, pp. 2234–2245.

Bates, S. et al. (2014). "PsrPopPy: An open-source package for pulsar population simulations". In: *Monthly Notices of the Royal Astronomical Society* 439.3, pp. 2893–2902.

Bhattacharyya, B. et al. (2016). "The GMRT high resolution southern sky survey for pulsars and transients. I. Survey description and initial discoveries". In: *The Astrophysical Journal* 817.2, p. 130.

Bonaldi, A. et al. (2019). "The tiered radio extragalactic continuum simulation (T-RECS)". In: *Monthly Notices of the Royal Astronomical Society* 482.1, pp. 2–19.

Bondi, M. et al. (2008). "The VLA-COSMOS survey. III. Further catalog analysis and the radio source counts". In: *The Astrophysical Journal* 681.2, p. 1129.

Condon, J., W. Cotton, & J. Broderick (2002). "Radio Sources and Star Formation in the LocalUniverse". In: *The Astronomical Journal* 124.2, p. 675.

Cordes, J. M. & T. J. W. Lazio (2002). "NE2001. I. A new model for the galactic distribution of free electrons and its fluctuations". In: *arXiv preprint astro-ph/0207156*.

Cordes, J. M. et al. (2006). "Arecibo pulsar survey using ALFA. I. Survey strategy and first discoveries". In: *The Astrophysical Journal* 637.1, pp. 446–455.

Cosmos Team (Jan. 2020). *COSMOS ACS I-band Photometry Catalog*. DOI: 10.26131/IRSA169.

Dey, A. et al. (2019). "Overview of the DESI legacy imaging surveys". In: *The Astronomical Journal* 157.5, p. 168.

Dimoudi, S. et al. (2018). "A GPU implementation of the correlation technique for real-time Fourier domain pulsar acceleration searches". In: *The Astrophysical Journal Supplement Series* 239.2, p. 28.

Dong, F. A. et al. (2023). "The second set of pulsar discoveries by CHIME/FRB/Pulsar: 14 rotating radio transients and 7 pulsars". In: *Monthly Notices of the Royal Astronomical Society* 524.4, pp. 5132–5147.

Eatough, R. P. et al. (2013). "A coherent acceleration search of the Parkes multibeam pulsar survey–techniques and the discovery and timing of 16 pulsars". In: *Monthly Notices of the Royal Astronomical Society* 431.1, pp. 292–307.

Edwards, R. et al. (2001). "The Swinburne intermediate-latitude pulsar survey". In: *Monthly Notices of the Royal Astronomical Society* 326.1, pp. 358–374.

Feder, R. M. et al. (2024). "The Universe SPHEREx Will See: Empirically Based Galaxy Simulations and Redshift Predictions". In: *The Astrophysical Journal* 972.1, p. 68.

Fruchter, A., D. Stinebring, & J. Taylor (1988). "A millisecond pulsar in an eclipsing binary". In: *Nature* 333.6170, pp. 237–239.

Haarlem, M. P. van et al. (2013). "LOFAR: The low-frequency array". In: *Astronomy & astrophysics* 556, A2.

Hallinan, G. et al. (Sept. 2019). "The DSA-2000 — A Radio Survey Camera". In: *Bulletin of the American Astronomical Society*. Vol. 51, 255, p. 255. DOI: 10.48550/arXiv.1907.07648. arXiv: 1907.07648 [astro-ph.IM].

Haslam, C. et al. (1982). "A 408 MHz all-sky continuum survey. II-The atlas of contour maps". In: *Astronomy and Astrophysics Supplement Series, vol. 47, Jan. 1982, p. 1, 2, 4-51, 53-142.* 47, p. 1.

Huang, Y. & G. Hallinan (June 2022). “Forward Modeling the DSA-2000 Radio Camera”. In: *American Astronomical Society Meeting #240*. Vol. 240. American Astronomical Society Meeting Abstracts, 314.06, p. 314.06.

Jarvis, M. J. et al. (2017). “The MeerKAT international GHz tiered extragalactic exploration (MIGHTEE) survey”. In: *arXiv preprint arXiv:1709.01901*.

Kaplan, D. L. et al. (2019). “Serendipitous Discovery of PSR J1431-6328 as a Highly Polarized Point Source with the Australian SKA Pathfinder”. In: *The Astrophysical Journal* 884.1, p. 96.

Keith, M. et al. (2010). “The high time resolution universe pulsar survey–i. system configuration and initial discoveries”. In: *Monthly Notices of the Royal Astronomical Society* 409.2, pp. 619–627.

Laigle, C. et al. (2016). “The COSMOS2015 Catalog: Exploring the 1< z< 6 Universe with half a million galaxies”. In: *The Astrophysical Journal Supplement Series* 224.2, p. 24.

Lattimer, J. M. (2012). “The nuclear equation of state and neutron star masses”. In: *Annual Review of Nuclear and Particle Science* 62, pp. 485–515.

Law, C. J. et al. (May 2024). “Deep Synoptic Array Science: First FRB and Host Galaxy Catalog”. In: *ApJ* 967.1, 29, p. 29. DOI: 10.3847/1538-4357/ad3736. arXiv: 2307.03344 [astro-ph.HE].

Lazarus, P. et al. (2015). “Arecibo pulsar survey using ALFA. IV. Mock spectrometer data analysis, survey sensitivity, and the discovery of 40 pulsars”. In: *The Astrophysical Journal* 812.1, p. 81.

Leauthaud, A. et al. (2007). “Weak gravitational lensing with COSMOS: galaxy selection and shape measurements”. In: *The Astrophysical Journal Supplement Series* 172.1, p. 219.

Liu, C. et al. (2025). *A Morphological Model to Separate Resolved–unresolved Sources in the DESI Legacy Surveys: Application in the LS4 Alert Stream*. arXiv: 2505.17174 [astro-ph.IM]. URL: https://arxiv.org/abs/2505.17174.

Liu, T. et al. (2023). “Multi-messenger approaches to supermassive black hole binary detection and parameter estimation. II. Optimal strategies for a pulsar timing array”. In: *The Astrophysical Journal* 945.1, p. 78.

Manchester, R. N. et al. (1996). “The parkes Southern pulsar Survey—I. Observing and data analysis systems and initial results”. In: *Monthly Notices of the Royal Astronomical Society* 279.4, pp. 1235–1250.

Manchester, R. N. et al. (2005). “The Australia telescope national facility pulsar catalogue”. In: *The Astronomical Journal* 129.4, p. 1993.

Manchester, R. N. et al. (2001). “The Parkes multi-beam pulsar survey–I. Observing and data analysis systems, discovery and timing of 100 pulsars”. In: *Monthly Notices of the Royal Astronomical Society* 328.1, pp. 17–35.

Manchester, R. et al. (1978). “The second Molonglo pulsar survey–discovery of 155 pulsars”. In: *Monthly Notices of the Royal Astronomical Society* 185.2, pp. 409–421.

Men, Y. et al. (2023). “PulsarX: a new pulsar searching package-I. A high performance folding program for pulsar surveys”. In: *Astronomy & Astrophysics* 679, A20.

Ng, C. et al. (2015). “The High Time Resolution Universe Pulsar Survey–XII. Galactic plane acceleration search and the discovery of 60 pulsars”. In: *Monthly Notices of the Royal Astronomical Society* 450.3, pp. 2922–2947.

Ng, C. et al. (2020). “The Discovery of Nulling and Mode-switching Pulsars with CHIME/Pulsar”. In: *The Astrophysical Journal* 903.2, p. 81.

Radhakrishnan, V. & D. J. Cooke (Jan. 1969). “Magnetic Poles and the Polarization Structure of Pulsar Radiation”. In: *The Astrophysical Letters* 3, p. 225.

Ransom, S. M., S. S. Eikenberry, & J. Middleditch (2002). “Fourier techniques for very long astrophysical time-series analysis”. In: *The Astronomical Journal* 124.3, p. 1788.

Ravi, V. et al. (2023). “Deep synoptic array science: discovery of the host galaxy of FRB 20220912A”. In: *The Astrophysical Journal Letters* 949.1, p. L3.

Roberts, M. S., F. P. Search, & G. D. S. S. Collaborations (2011). “New black widows and redbacks in the Galactic field”. In: *AIP Conference Proceedings*. Vol. 1357. 1. American Institute of Physics, pp. 127–130.

Scaramella, R. et al. (2022). “Euclid preparation-I. The Euclid wide survey”. In: *Astronomy & Astrophysics* 662, A112.

Schinnerer, E. et al. (2007). “The VLA-COSMOS survey. II. Source catalog of the large project”. In: *The Astrophysical Journal Supplement Series* 172.1, p. 46.

Schinnerer, E. et al. (2010). “The VLA-COSMOS survey. IV. Deep data and joint catalog”. In: *The Astrophysical Journal Supplement Series* 188.2, p. 384.

Scoville, N. et al. (2007). “COSMOS: Hubble space telescope observations”. In: *The Astrophysical Journal Supplement Series* 172.1, p. 38.

Sharma, K. et al. (2024). “Preferential occurrence of fast radio bursts in massive star-forming galaxies”. In: *Nature* 635.8037, pp. 61–66.

Singh, S. et al. (2022). “The GMRT High Resolution Southern Sky Survey for Pulsars and Transients. III. Searching for Long-period Pulsars”. In: *The Astrophysical Journal* 934.2, p. 138.

Smith, K. M. (2016). “New algorithms for radio pulsar search”. In: *arXiv preprint arXiv:1610.06831*.

Smits, R. et al. (2009). “Pulsar searches and timing with the square kilometre array”. In: *Astronomy & Astrophysics* 493.3, pp. 1161–1170.

Spitler, L. et al. (2014). “Fast radio burst discovered in the Arecibo pulsar ALFA survey”. In: *The Astrophysical Journal* 790.2, p. 101.

Stovall, K. et al. (2014). “The green bank northern celestial cap pulsar survey. I. Survey description, data analysis, and initial results”. In: *The Astrophysical Journal* 791.1, p. 67.

Thongmeearkom, T. et al. (2024). “A targeted radio pulsar survey of redback candidates with MeerKAT”. In: *Monthly Notices of the Royal Astronomical Society* 530.4, pp. 4676–4694.

Wang, Y. et al. (2022). “The high latitude spectroscopic survey on the Nancy Grace Roman Space Telescope”. In: *The Astrophysical Journal* 928.1, p. 1.

Wateren, E. van der et al. (2023). *PSR J0210+5845; An ultra wide binary pulsar with a B6V main-sequence star companion*. arXiv: 2312.01892 [astro-ph.HE].

Weltman, A. et al. (2020). “Fundamental physics with the square kilometre array”. In: *Publications of the Astronomical Society of Australia* 37, e002.

Chapter 9

CONCLUSIONS AND OUTLOOK

In this thesis, we have explored observational evidence for the unique formation channels of magnetars, and considered whether they produce FRBs and LPTs using data from the DSA-110. While we have made vital progress to understand magnetars' nature, we uncover new questions that await growth of the magnetar and LPT populations and milliarcsecond-scale localization of FRBs. We draw the following conclusions:

9.1 Stellar Merger Channels and OB Associations Contribute to the Magnetar Population

With $\lesssim$ 24% of magnetars in unbound binary systems, a large fraction (48 – 86%) of magnetars must form from stellar mergers to uphold massive stars' preference for binary systems. Using BPASS simulations, we observe that mergers alone fail to produce the observed magnetar population, but are required alongside mass-transfer binaries to do so. Between 66 – 592 total magnetars may reside in the Milky Way with 90% confidence, $\sim$ 50 – 70% of which descend from mergers and mass-transfer binaries. Our result is relatively consistent with other population synthesis papers published since Sherman et al. (2024), which indicate that $\sim$ 15% of CCSNe come from delayed stellar mergers and mass-transfer binaries (Hu & Zhang, 2026; Zapartas et al., 2017). However, the excess neutron star birth rate identified by Keane & Kramer (2008) remains unsolved. In addition, OB associations more closely match the revised magnetar scale height, $h_e \approx 24\,\mathrm{pc}$, potentially linking magnetars to association stars rather than field OB stars. These dense, kinematically associated regions are known to dynamically eject massive stars, potentially creating an environment suitable for dynamical capture of binary companions and more exotic magnetar formation channels.

Future work will mull over the physical motivation for the magnetar-merger hypothesis. Magneto-hydrodynamic (MHD) simulations have not yet been developed to model the evolution of stellar magnetic fields through core-collapse, but Schneider et al. (2019)'s model 3D MHD merger simulation and Keszthelyi (2023)'s atmospheric modelling of τ Sco's magnetic field offer promising developments. Building the population of magnetars will enable pulsar current analyses (Lorimer

et al., 1993; Vranešević & Melrose, 2011) which can better predict the birth rate and test magnetic field decay models as well.

9.2 $10 - 50$ s White Dwarf-M Dwarf Binary LPTs are Rare in the galactic plane

The commensal DSA-110 NSFRB galactic plane survey successfully tested the novel image-plane search pipeline, which now operates in real-time alongside the FRB search. While the 1.2 Jy upper limit placed on LPT emission within 2° of the galactic plane is not significantly constraining, we demonstrate the method to apply this to the White Dwarf-M Dwarf binary and magnetar models. The search rules out White Dwarf-M Dwarf LPTs between $10 - 50$ s periods, but does not place meaningful constraints on the magnetar model. Still, it lays the foundation for future DSA-110 searches and surveys by other arrays to determine the origin of LPTs.

The primary area for improvement of the NSFRB pipeline is the sensitivity; while the search threshold is placed at 6σ, the 90% completeness limit is 25σ as a result of false negatives in the machine learning classifier and a lack of sensitivity to wide and high-DM LPTs. Additional testing since publication indicates this may result from incorrect noise estimation for 16-sample width trials. The 25 sample window may need to be widened to allow for more accurate noise estimates, or alternatively, the noise extrapolated from 1-sample width trials. Re-training the classifier with daily RFI detections would also improve false positive rejection and mitigate false negatives in the classifier, though this requires diligent monitoring and routine labeling of data. New spatial filtering algorithms (e.g., Andrew et al., 2026) can also be incorporated to improve RFI rejection, while the rapid development of novel single-pulse and periodicity search strategies will also inform future iterations of the NSFRB search (e.g., Andrade et al., 2025; Horváth et al., 2025; Singh et al., 2022; Wang et al., 2025).

9.3 FRBs Inhabit Highly-Magnetized Environments Resembling those of Young (< 10 kyr) Pulsars

The first sample of 25 DSA-110 FRBs demonstrates a preference for high linear polarization and flat polarization position angles. Upcoming work from the DSA-110 will expand this sample, reaffirming the polarizaiton distribution (Verdi et al., in preparation). Their similarity to young pulsars may imply they have similar local magneto-ionic environments, which are known to impede one polarization mode in young pulsars (Mitra et al., 2023). Since publication, Pandhi et al. (2024) and

Ng et al. (2025) have performed similar analyses on an additional 128 nonrepeaters and 28 repeaters from the CHIME FRB Baseband Catalog, and find a preference for high polarization fractions consistent with our results. The fact that the DSA-110 and CHIME identify similar polarization distributions at 1.4 GHz and 0.5 GHz, respectively, suggests that stochastic RM scattering is not the dominant affect among FRBs (Feng et al., 2022). However, the only way to truly test this is by detecting the same FRB burst at a wide range of frequencies. The early success of the Effelsberg Telescope's Ultra-Wideband Receiver (UBB; 1.3 – 6.0 GHz) with FRB 20240114A is promising, and full-polarization monitoring of active repeaters with UBB may definitively constrain the stochastic RM scattering model (Limaye et al., 2025). A sample of FRBs co-detected with the DSA-110 and CHIME, which reside at the same longitude, have illustrated ways to manufacture wide-bands from existing instruments (Pandhi et al., in preparation; Faber et al., in preparation).

FRB RMs display a preference for dense, highly magnetized regions of their host galaxies, but don't exhibit trends with specific star formation or galaxy type. Recent work by Sharma et al. (2024) uses the DSA-110 host galaxy sample to identify a preference for massive, high-metallicity host galaxies, which may result in elevated ISM magnetic fields. Gordon et al. (2025) use sub-arcsecond localization to identify that FRBs preferentially occur in spiral arms, disks, and other star-forming regions, even in quiescent galaxies. Such star forming regions are expected to host ionized gas from stellar feedback, and have been observed with elevated magnetic fields (Harvey-Smith et al., 2011). Thus FRBs' high local magnetic fields are most likely related to their residence in star forming regions, further supporting the magnetar origin model (see also Verdi et al., in preparation).

9.4 The DSA-2000 will Increase the Known Pulsar Population by Orders of Magnitude

Next-generation arrays like the DSA-2000 will increase the known pulsar and radio magnetar populations by orders of magnitude. In addition to forecasting that the DSA-2000 will detect $\sim 23,000$ northern-sky pulsars, the Square Kilometre Array (SKA) will detect $\sim 20,000 - 50,000$ southern-sky pulsars (Kramer & Stappers, 2015; Smits et al., 2009), and the Canadian Hydrogen Observatory and Radio-transient Detector (CHORD) will detect over $\sim 10,000$ pulsars (Vanderlinde et al., 2019). This will vastly reduce bias in pulsar birth rate analyses and enable rigorous tests of the magnetar-pulsar relationship. Furthermore, the DSA-2000 is will localize $\sim 10^4$ FRBs per year to less than $0.5''$ precision; coupled with the CHIME outriggers'

milliarcsecond localization precision, the local environments of nearby FRBs will be constrained to compare to polarization, RM, and DM properties.

The DSA-2000 currently does not have a dedicated search for LPTs planned. The FRB single-pulse search will target high-DM $1 - 256$ ms bursts to fluence limit $24\,\mu$Jy ms. As demonstrated by CHIME's discovery of two LPTs, substructure on $1 - 100$ ms timescales can be used to identify LPTs (Dong et al., 2025a,b). The DSA-2000 could attain a high sensitivity to LPTs simply by preserving low-DM FRB candidates for follow-up. Periodicity searches at > 20 s timescales will be infeasible for the DSA-2000 due to memory constraints and red noise limitations. But the non-uniform cadence of the Continuum All-Sky Survey (CASS) may enable image-differencing searches on hour or day timescales. This has also proven capable of detecting LPTs with the Murchison Widefield Array (Hurley-Walker et al., 2022). The flexible design and variety of public data products will help the DSA-2000 and other large-N telescopes revolutionize radio transient surveys and our understanding of magnetars in the near future.

CHAPTER 9 BIBLIOGRAPHY

Andrade, C. et al. (2025). "CHIME All-sky Multiday Pulsar Stacking Search (CHAMPSS): System Overview and First Discoveries". In: *The Astrophysical Journal* 990.1, p. 50.

Andrew, S. et al. (2026). "A spatial filter for mitigating radio interference and its application to CHIME/FRB Outriggers". In: *arXiv preprint arXiv:2603.25833*.

Dong, F. A. et al. (July 2025a). "CHIME/Fast Radio Burst Discovery of an Unusual Circularly Polarized Long-period Radio Transient with an Accelerating Spin Period". In: *The Astrophysical Journal Letters* 988.1, L29, p. L29. DOI: 10.3847/2041-8213/adeaab. arXiv: 2507.05139 [astro-ph.HE].

Dong, F. A. et al. (Sept. 2025b). "CHIME/Fast Radio Burst/Pulsar Discovery of a Nearby Long-period Radio Transient with a Timing Glitch". In: *The Astrophysical Journal Letters* 990.2, L49, p. L49. DOI: 10.3847/2041-8213/adfa8e. arXiv: 2407.07480 [astro-ph.HE].

Feng, Y. et al. (2022). "Frequency-dependent polarization of repeating fast radio bursts—implications for their origin". In: *Science* 375.6586, pp. 1266–1270.

Gordon, A. C. et al. (2025). "Mapping the Spatial Distribution of Fast Radio Bursts within their Host Galaxies". In: *The Astrophysical Journal* 993.1, p. 119.

Harvey-Smith, L., G. J. Madsen, & B. M. Gaensler (2011). "Magnetic fields in large-diameter H II regions revealed by the Faraday rotation of compact extragalactic radio sources". In: *The Astrophysical Journal* 736.2, p. 83.

Horváth, C. et al. (Sept. 2025). "A long period transient search method for the Murchison Widefield Array". In: *Publications of the Astronomical Society of Australia* 42, e129, e129. DOI: 10.1017/pasa.2025.10093. arXiv: 2509.06315 [astro-ph.IM].

Hu, R.-C. & B. Zhang (2026). "Formation Channels of Magnetars". In: *The Astrophysical Journal* 999.1, p. 102.

Hurley-Walker, N. et al. (Jan. 2022). "A radio transient with unusually slow periodic emission". In: *Nature* 601.7894, pp. 526–530. DOI: 10.1038/s41586-021-04272-x. arXiv: 2503.08033 [astro-ph.HE].

Keane, E. F. & M. Kramer (2008). "On the birthrates of Galactic neutron stars". In: *Monthly Notices of the Royal Astronomical Society* 391.4, pp. 2009–2016.

Keszthelyi, Z. (2023). "Magnetism in High-Mass Stars". In: *Galaxies* 11.2, p. 40.

Kramer, M. & B. Stappers (2015). "Pulsar Science with the SKA". In: *arXiv preprint arXiv:1507.04423*.

Limaye, P. et al. (2025). "A broadband study of FRB20240114A with the Effelsberg 100-m radio telescope". In: *arXiv preprint arXiv:2510.08367*.

Lorimer, D. et al. (1993). “Pulsar statistics: the birthrate and initial spin periods of radio pulsars”. In: *Monthly Notices of the Royal Astronomical Society* 263.2, pp. 403–415.

Mitra, D., G. I. Melikidze, & R. Basu (2023). “Meterwavelength Single Pulse Polarimetric Emission Survey. VI. Toward Understanding the Phenomenon of Pulsar Polarization in Partially Screened Vacuum Gap Model”. In: *The Astrophysical Journal* 952.2, p. 151.

Ng, C. et al. (2025). “Polarization properties of 28 repeating fast radio burst sources with CHIME/FRB”. In: *The Astrophysical Journal* 982.2, p. 154.

Pandhi, A. et al. (2024). “Polarization properties of 128 nonrepeating fast radio bursts from the first CHIME/FRB baseband catalog”. In: *The Astrophysical Journal* 968.2, p. 50.

Schneider, F. R. et al. (2019). “Stellar mergers as the origin of magnetic massive stars”. In: *Nature* 574.7777, pp. 211–214.

Sharma, K. et al. (2024). “Preferential occurrence of fast radio bursts in massive star-forming galaxies”. In: *Nature* 635.8037, pp. 61–66.

Sherman, M. B. et al. (2024). “Searching for magnetar binaries disrupted by core-collapse supernovae”. In: *Monthly Notices of the Royal Astronomical Society* 531.2, pp. 2379–2414. DOI: 10.1093/mnras/stae1289.

Singh, S. et al. (2022). “The GMRT High Resolution Southern Sky Survey for Pulsars and Transients. III. Searching for Long-period Pulsars”. In: *The Astrophysical Journal* 934.2, p. 138.

Smits, R. et al. (2009). “Pulsar searches and timing with the square kilometre array”. In: *Astronomy & Astrophysics* 493.3, pp. 1161–1170.

Vanderlinde, K. et al. (Oct. 2019). “The Canadian Hydrogen Observatory and Radio-transient Detector (CHORD)”. In: *Canadian Long Range Plan for Astronomy and Astrophysics White Papers*. Vol. 2020, 28, p. 28. DOI: 10.5281/zenodo.3765414. arXiv: 1911.01777 [astro-ph.IM].

Vranešević, N. & D. Melrose (2011). “Pulsar current revisited”. In: *Monthly Notices of the Royal Astronomical Society* 410.4, pp. 2363–2369.

Wang, Z. et al. (2025). “The CRAFT coherent (CRACO) upgrade I: System description and results of the 110-ms radio transient pilot survey”. In: *Publications of the Astronomical Society of Australia* 42, e005.

Zapartas, E. et al. (2017). “Delay-time distribution of core-collapse supernovae with late events resulting from binary interaction”. In: *Astronomy & Astrophysics* 601, A29.

Appendix A

PARSEC: A CUSTOM DSA-110 POLARIZATION ANALYSIS INTERFACE

In addition to the Python polarization analysis tools developed in Chapters 6 and 6, a user-friendly graphic user interface was developed for use with the 64-antenna DSA-110 prototype. The Polarization Analysis and Rotation Measure Synthesis Enabled for Calibration (PARSEC) dashboard allows new users to generate full-Stokes polarization calibrated filterbanks from baseband voltage data, tune the dispersion measure to optimize for FRB structure or S/N, compute polarization fractions, perform Faraday RM Synthesis, and query galaxy catalogs along FRB sightlines to construct RM and DM budgets. The dashboard was built using Mercury[1], and can be run as a service on DSA machines and accessed from code.deepsynoptic.org by authorized users. The code can be accessed at https://github.com/dsa110/dsa110-pol/tree/main/interface. In this section we include a tutorial for PARSEC with screenshots from the dashboard; note that the dashboard is not equipped for use with the full 96-antenna DSA-110.

[1] https://runmercury.com/

*P*olarization *A*nalysis and *R*M *S*ynthesis *E*nabled for *C*alibration

DSA-110 PARSEC Dashboard Tutorial

Last Updated: 2024-08-06 (M. Sherman)

This goal of this tutorial is to provide a brief overview of the most common use cases for the PARSEC dashboard during FRB baseband data analysis. Note this is not fully comprehensive; less-common functions and screens have been skipped over. Please refer to the Github page (https://github.com/dsa110/dsa110-pol) for additional documentation, or contact Myles Sherman at msherman@caltech.edu with questions

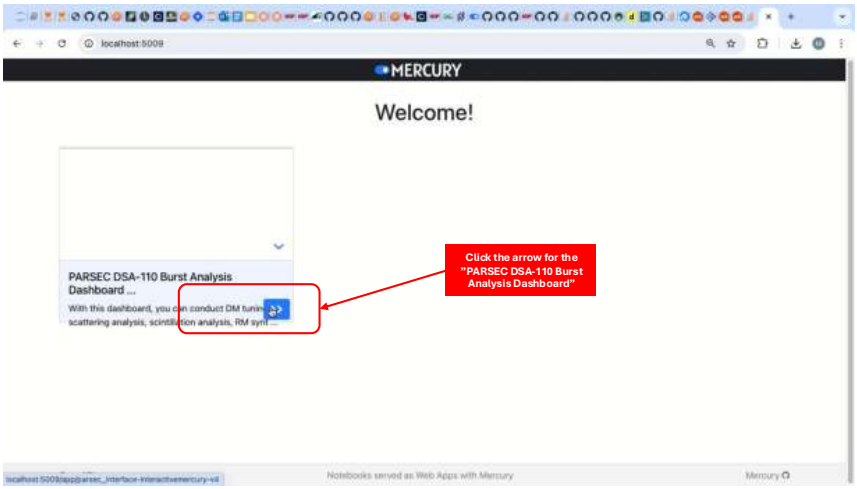
MERCURY
Welcome!
PARSEC DSA-110 Burst Analysis Dashboard ...
Click the arrow for the "PARSEC DSA-110 Burst Analysis Dashboard"
Notebooks served as Web Apps with Mercury

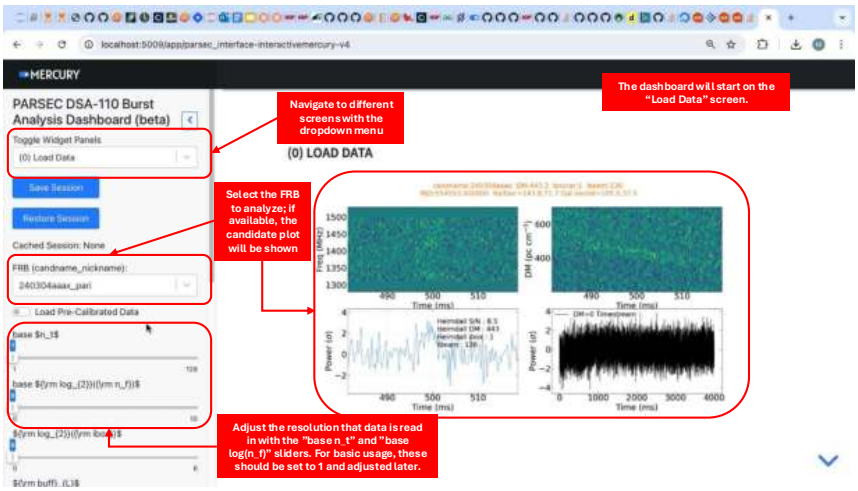
MERCURY
PARSEC DSA-110 Burst Analysis Dashboard (beta)
Navigate to different screens with the dropdown menu
The dashboard will start on the "Load Data" screen.
(0) LOAD DATA
Select the FRB to analyze; if available, the candidate plot will be shown
Adjust the resolution that data is read in with the "base n_t" and "base log(n_f)" sliders. For basic usage, these should be set to 1 and adjusted later.

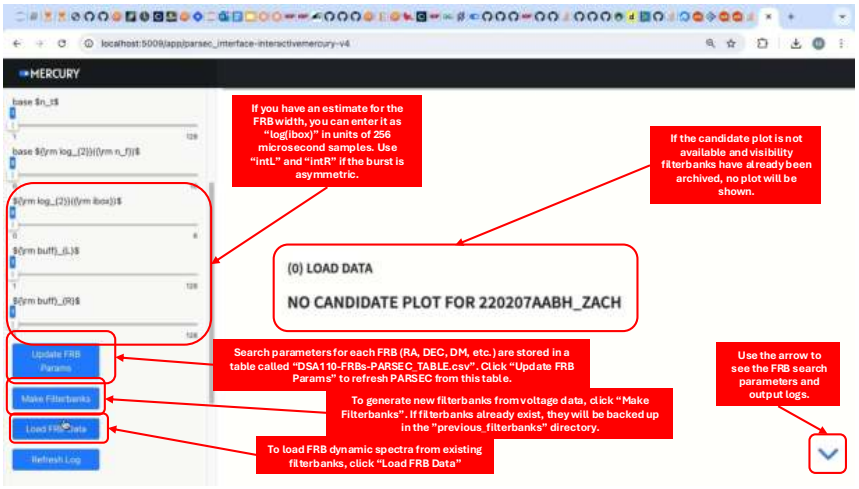
MERCURY
If you have an estimate for the FRB width, you can enter it as "log(ibox)" in units of 256 microsecond samples. Use "intL" and "intR" if the burst is asymmetric.
If the candidate plot is not available and visibility filterbanks have already been archived, no plot will be shown.
(0) LOAD DATA
NO CANDIDATE PLOT FOR 220207AABH_ZACH
Update FRB Params
Make Filterbanks
Load FRB Data
Refresh Log
Search parameters for each FRB (RA, DEC, DM, etc.) are stored in a table called "DSA110-FRBs-PARSEC_TABLE.csv". Click "Update FRB Params" to refresh PARSEC from this table.
To generate new filterbanks from voltage data, click "Make Filterbanks". If filterbanks already exist, they will be backed up in the "previous_filterbanks" directory.
To load FRB dynamic spectra from existing filterbanks, click "Load FRB Data"
Use the arrow to see the FRB search parameters and output logs.

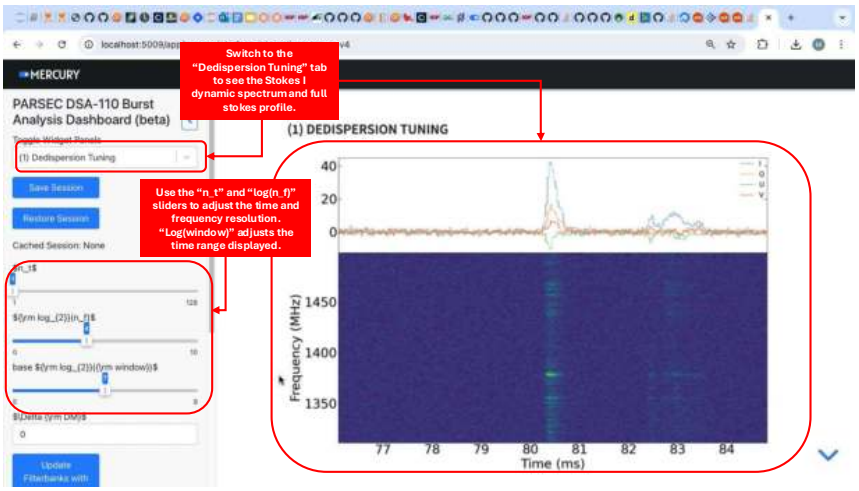
MERCURY
Switch to the "Dedispersion Tuning" tab to see the Stokes I dynamic spectrum and full stokes profile.
PARSEC DSA-110 Burst Analysis Dashboard (beta)
(1) Dedispersion Tuning
Save Session
Restore Session
Cached Session: None
Update Filterbanks with
Use the "n_t" and "log(n_f)" sliders to adjust the time and frequency resolution. "Log(window)" adjusts the time range displayed.
(1) DEDISPERSION TUNING
Frequency (MHz)
Time (ms)

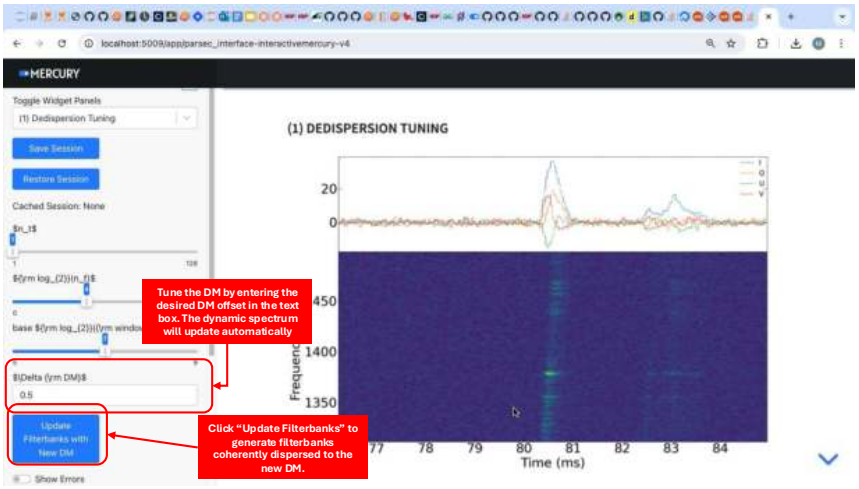
MERCURY
Toggle Widget Panels
(1) Dedispersion Tuning
Save Session
Restore Session
Cached Session: None
Δ (yrm DM)$
0.5
Update Filterbanks with New DM
Show Errors
(1) DEDISPERSION TUNING
Time (ms)
Tune the DM by entering the desired DM offset in the text box. The dynamic spectrum will update automatically
Click "Update Filterbanks" to generate filterbanks coherently dispersed to the new DM.

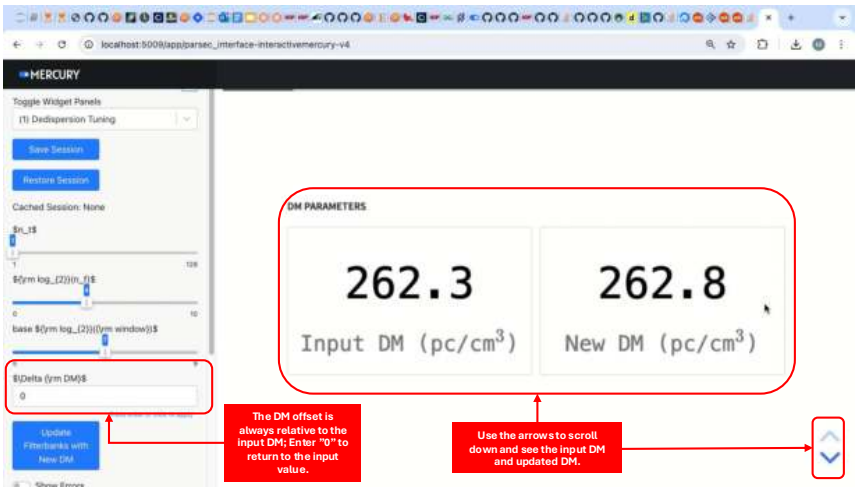
MERCURY
Toggle Widget Panels
(1) Dedispersion Tuning
Save Session
Restore Session
Cached Session: None
Δ (yrm DM)$
0
Update Filterbanks with New DM
DM PARAMETERS
262.3
Input DM (pc/cm^3)
262.8
New DM (pc/cm^3)
The DM offset is always relative to the input DM; Enter "0" to return to the input value.
Use the arrows to scroll down and see the input DM and updated DM.

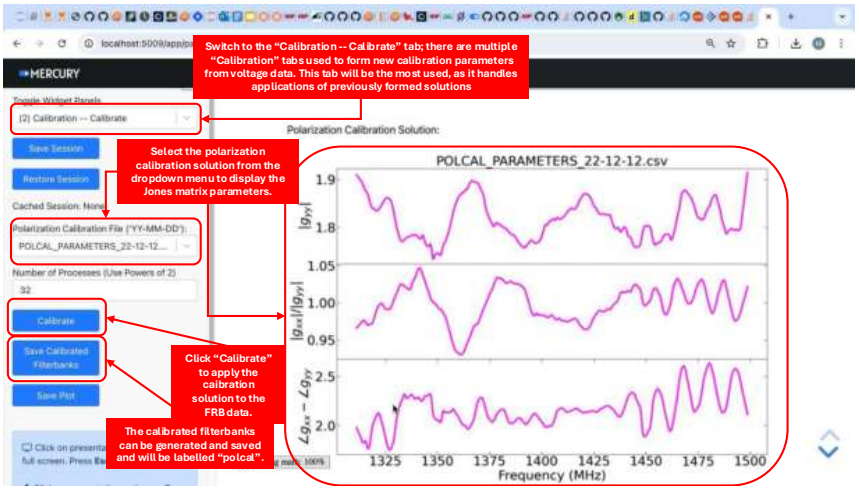
Switch to the "Calibration -- Calibrate" tab; there are multiple "Calibration" tabs used to form new calibration parameters from voltage data. This tab will be the most used, as it handles applications of previously formed solutions
Select the polarization calibration solution from the dropdown menu to display the Jones matrix parameters.
Click "Calibrate" to apply the caibration solution to the FRB data.
The calibrated filterbanks can be generated and saved and will be labelled "polcal".
MERCURY
(2) Calibration -- Calibrate
Save Session
Restore Session
Cached Session: None
Polarization Calibration File ('YY-MM-DD'):
POLCAL_PARAMETERS_22-12-12...
Number of Processes (Use Powers of 2)
32
Calibrate
Save Calibrated Filterbanks
Save Plot
Polarization Calibration Solution:
POLCAL_PARAMETERS_22-12-12.csv
Frequency (MHz)

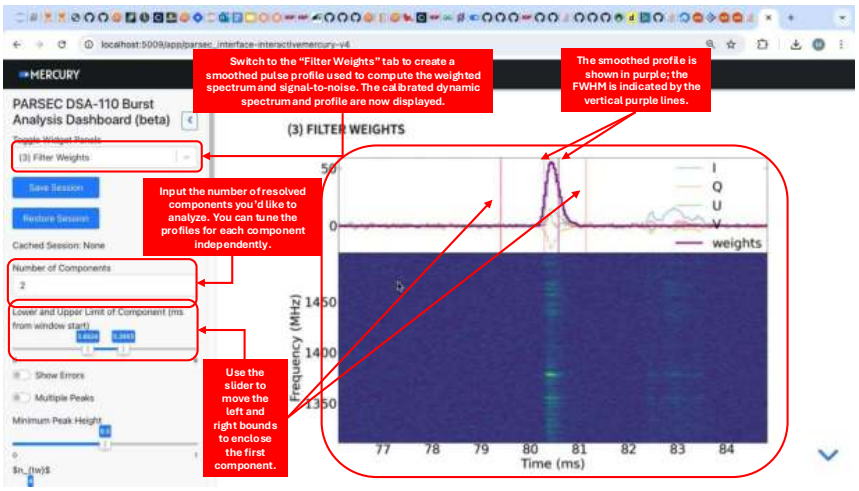
Switch to the "Filter Weights" tab to create a smoothed pulse profile used to compute the weighted spectrum and signal-to-noise. The calibrated dynamic spectrum and profile are now displayed.
The smoothed profile is shown in purple; the FWHM is indicated by the vertical purple lines.
Input the number of resolved components you'd like to analyze. You can tune the profiles for each component independently.
Use the slider to move the left and right bounds to enclose the first component.
MERCURY
PARSEC DSA-110 Burst Analysis Dashboard (beta)
(3) Filter Weights
Save Session
Restore Session
Cached Session: None
Number of Components
2
Lower and Upper Limit of Component (ms from window start)
Show Errors
Multiple Peaks
Minimum Peak Height
(3) FILTER WEIGHTS
I
Q
U
V
weights
Frequency (MHz)
Time (ms)

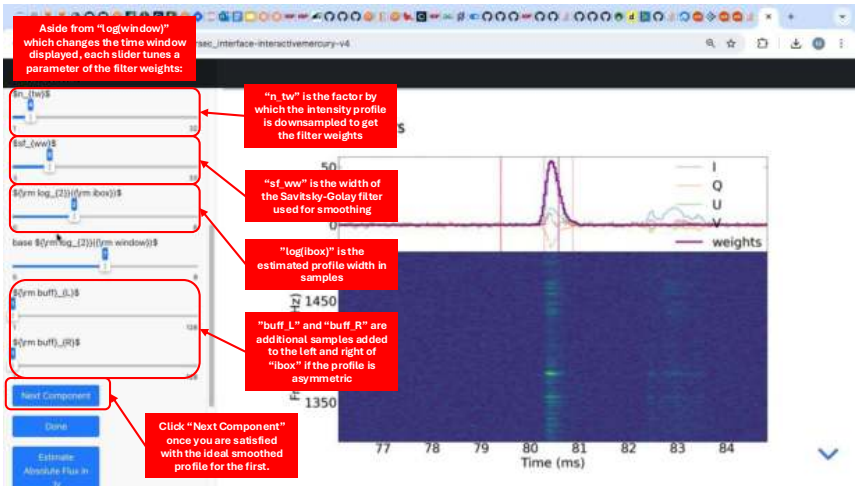
Aside from "log(window)" which changes the time window displayed, each slider tunes a parameter of the filter weights:
"n_tw" is the factor by which the intensity profile is downsampled to get the filter weights
"sf_ww" is the width of the Savitsky-Golay filter used for smoothing
"log(ibox)" is the estimated profile width in samples
"buff_L" and "buff_R" are additional samples added to the left and right of "ibox" if the profile is asymmetric
Click "Next Component" once you are satisfied with the ideal smoothed profile for the first.
Next Component
Done
I
Q
U
V
weights
Time (ms)

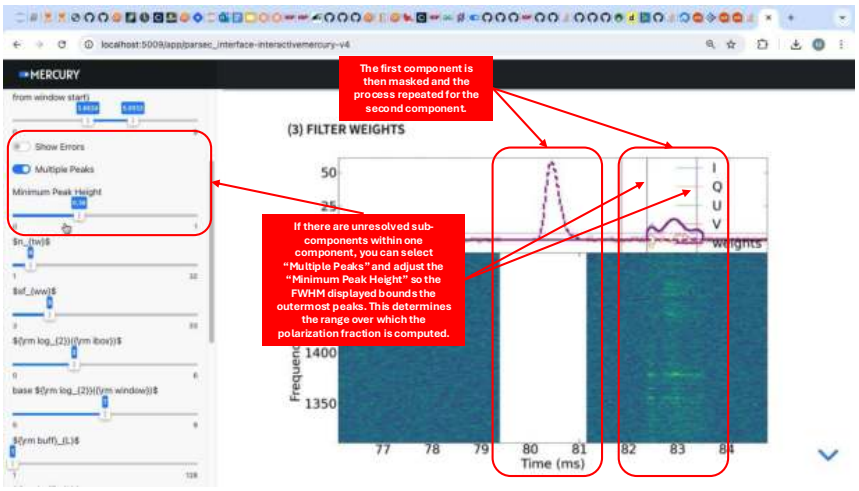
MERCURY
The first component is then masked and the process repeated for the second component.
(3) FILTER WEIGHTS
If there are unresolved sub-components within one component, you can select "Multiple Peaks" and adjust the "Minimum Peak Height" so the FWHM displayed bounds the outermost peaks. This determines the range over which the polarization fraction is computed.
Show Errors
Multiple Peaks
Minimum Peak Height
I
Q
U
V
weights
Time (ms)

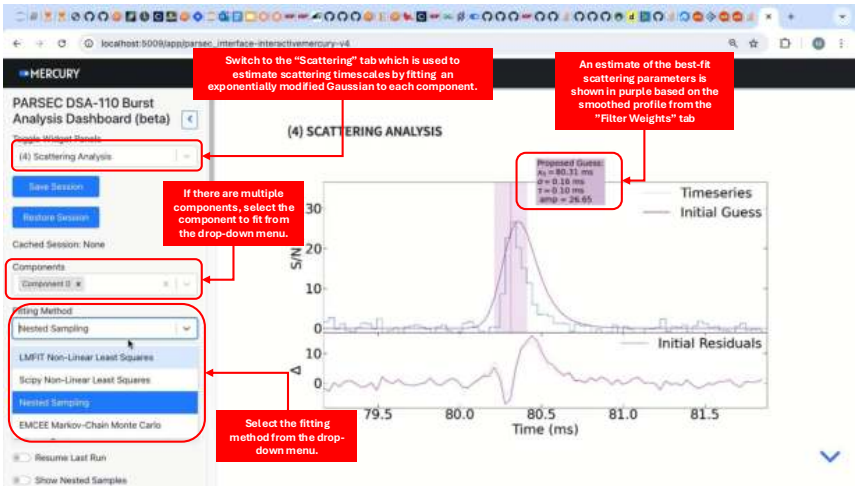
Switch to the "Scattering" tab which is used to estimate scattering timescales by fitting an exponentially modified Gaussian to each component.
An estimate of the best-fit scattering parameters is shown in purple based on the smoothed profile from the "Filter Weights" tab
If there are multiple components, select the component to fit from the drop-down menu.
Select the fitting method from the drop-down menu.
MERCURY
PARSEC DSA-110 Burst Analysis Dashboard (beta)
(4) Scattering Analysis
Save Session
Restore Session
Cached Session: None
Components
Fitting Method
Nested Sampling
LMFIT Non-Linear Least Squares
Scipy Non-Linear Least Squares
Nested Sampling
EMCEE Markov-Chain Monte Carlo
Resume Last Run
Show Nested Samples
(4) SCATTERING ANALYSIS
Timeseries
Initial Guess
Initial Residuals
S/N
Δ
Time (ms)

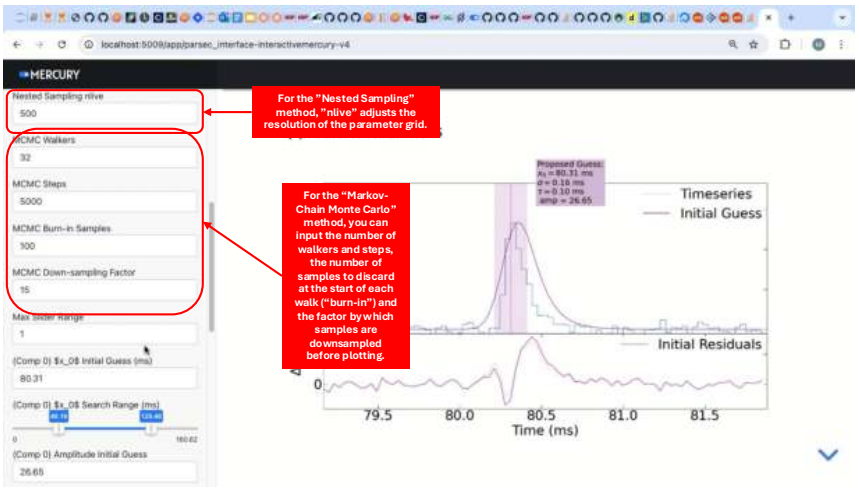
For the "Nested Sampling" method, "nlive" adjusts the resolution of the parameter grid.
For the "Markov-Chain Monte Carlo" method, you can input the number of walkers and steps, the number of samples to discard at the start of each walk ("burn-in") and the factor by which samples are downsampled before plotting.
MERCURY
Nested Sampling nlive
500
MCMC Walkers
32
MCMC Steps
5000
MCMC Burn-in Samples
100
MCMC Down-sampling Factor
15
(Comp 0) x_0 Initial Guess (ms)
80.31
(Comp 0) Amplitude Initial Guess
26.65
Timeseries
Initial Guess
Initial Residuals
Δ
Time (ms)

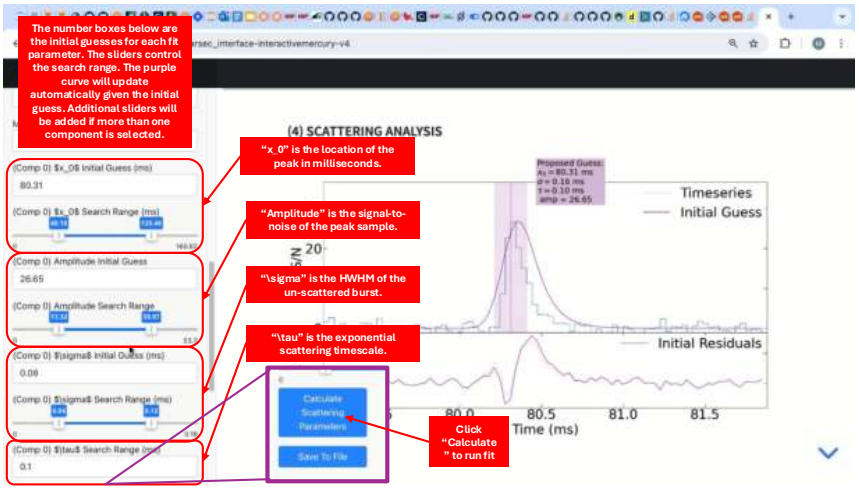
The number boxes below are the initial guesses for each fit parameter. The sliders control the search range. The purple curve will update automatically given the initial guess. Additional sliders will be added if more than one component is selected.
(4) SCATTERING ANALYSIS
"x_0" is the location of the peak in milliseconds.
"Amplitude" is the signal-to-noise of the peak sample.
"\sigma" is the HWHM of the un-scattered burst.
"\tau" is the exponential scattering timescale.
Click "Calculate " to run fit
Timeseries
Initial Guess
Initial Residuals
S/N
Time (ms)

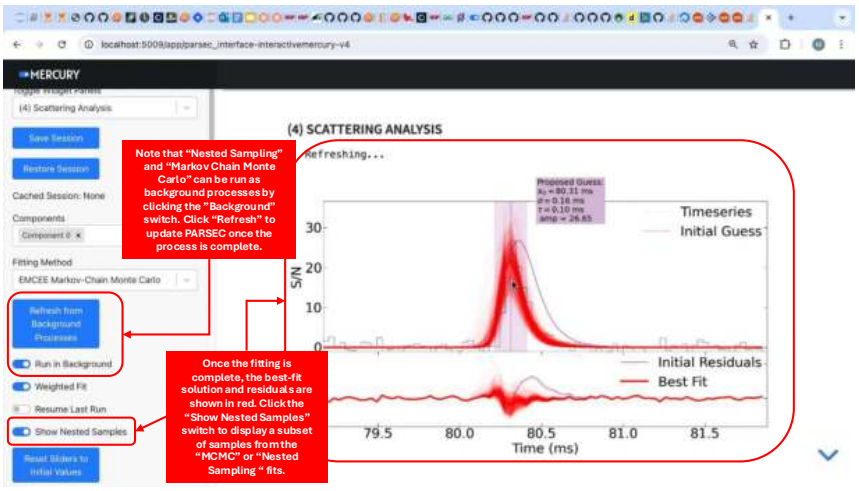
MERCURY
(4) Scattering Analysis
Save Session
Restore Session
Cached Session: None
Components
Fitting Method
EMCEE Markov-Chain Monte Carlo
Refresh from Background Processes
Run in Background
Weighted Fit
Resume Last Run
Show Nested Samples
Reset Sliders to Initial Values
Note that "Nested Sampling" and "Markov Chain Monte Carlo" can be run as background processes by clicking the "Background" switch. Click "Refresh" to update PARSEC once the process is complete.
Once the fitting is complete, the best-fit solution and residuals are shown in red. Click the "Show Nested Samples" switch to display a subset of samples from the "MCMC" or "Nested Sampling " fits.
(4) SCATTERING ANALYSIS
Refreshing...
Timeseries
Initial Guess
Initial Residuals
Best Fit
S/N
Time (ms)

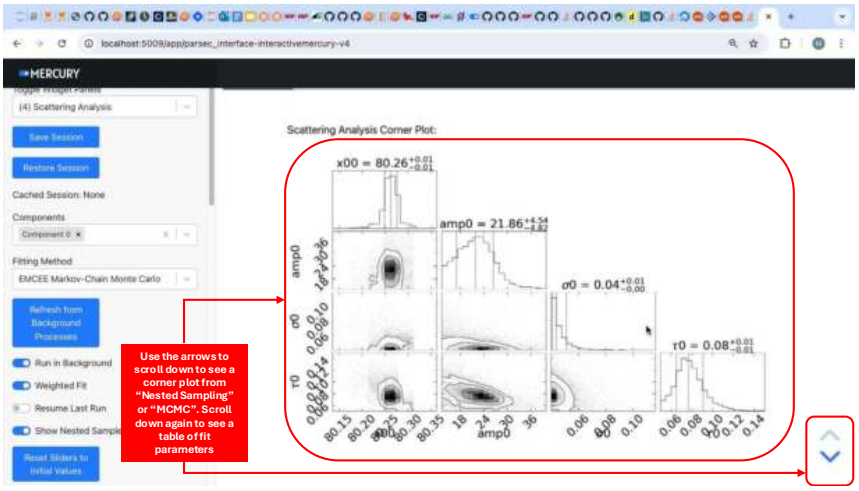
MERCURY
Scattering Analysis Corner Plot:
Use the arrows to scroll down to see a corner plot from "Nested Sampling" or "MCMC". Scroll down again to see a table of fit parameters

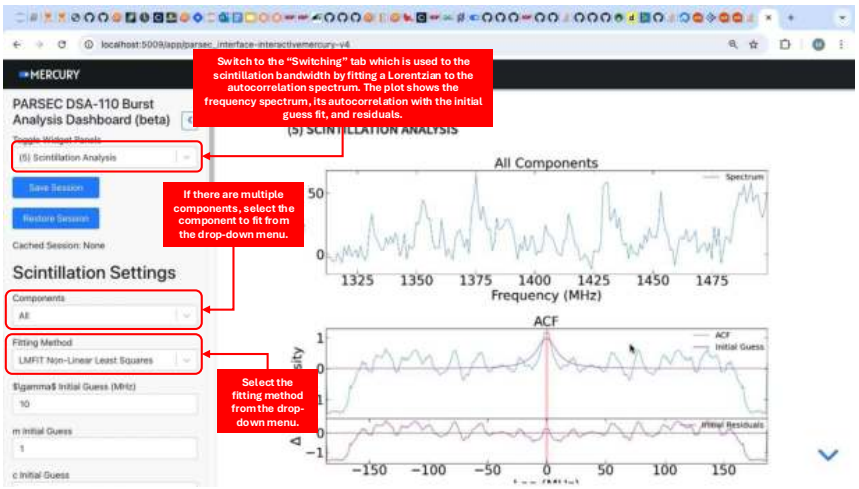
MERCURY
PARSEC DSA-110 Burst Analysis Dashboard (beta)
Switch to the "Switching" tab which is used to the scintillation bandwidth by fitting a Lorentzian to the autocorrelation spectrum. The plot shows the frequency spectrum, its autocorrelation with the initial guess fit, and residuals.
If there are multiple components, select the component to fit from the drop-down menu.
Select the fitting method from the drop-down menu.
Scintillation Settings
All Components
Frequency (MHz)
ACF

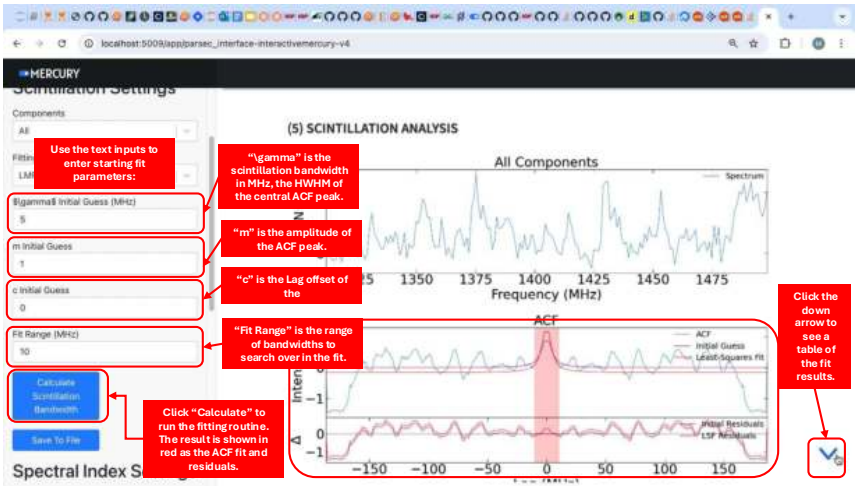
MERCURY
Components
All
Use the text inputs to enter starting fit parameters:
γ Initial Guess (MHz)
5
m Initial Guess
1
c Initial Guess
0
Fit Range (MHz)
10
Calculate Scintillation Bandwidth
Save To File
Spectral Index S
"\gamma" is the scintillation bandwidth in MHz, the HWHM of the central ACF peak.
"m" is the amplitude of the ACF peak.
"c" is the Lag offset of the
"Fit Range" is the range of bandwidths to search over in the fit.
Click "Calculate" to run the fitting routine. The result is shown in red as the ACF fit and residuals.
(5) SCINTILLATION ANALYSIS
All Components
Spectrum
S/N
1350
1375
1400
1425
1450
1475
Frequency (MHz)
ACF
Initial Guess
Least-Squares Fit
Initial Residuals
LSF Residuals
Intensity
Δ
−150
−100
−50
0
50
100
150
Click the down arrow to see a table of the fit results.

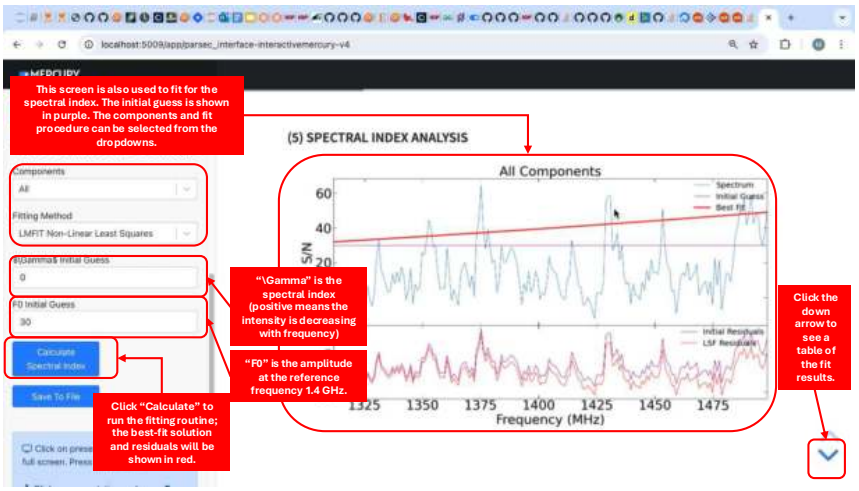
This screen is also used to fit for the spectral index. The initial guess is shown in purple. The components and fit procedure can be selected from the dropdowns.
Components
All
Fitting Method
LMFIT Non-Linear Least Squares
Γ Initial Guess
0
F0 Initial Guess
30
Calculate Spectral Index
Save To File
"\Gamma" is the spectral index (positive means the intensity is decreasing with frequency)
"F0" is the amplitude at the reference frequency 1.4 GHz.
Click "Calculate" to run the fitting routine; the best-fit solution and residuals will be shown in red.
(5) SPECTRAL INDEX ANALYSIS
All Components
Spectrum
Initial Guess
Best Fit
S/N
60
40
20
Initial Residuals
LSF Residuals
1325
1350
1375
1400
1425
1450
1475
Frequency (MHz)
Click the down arrow to see a table of the fit results.

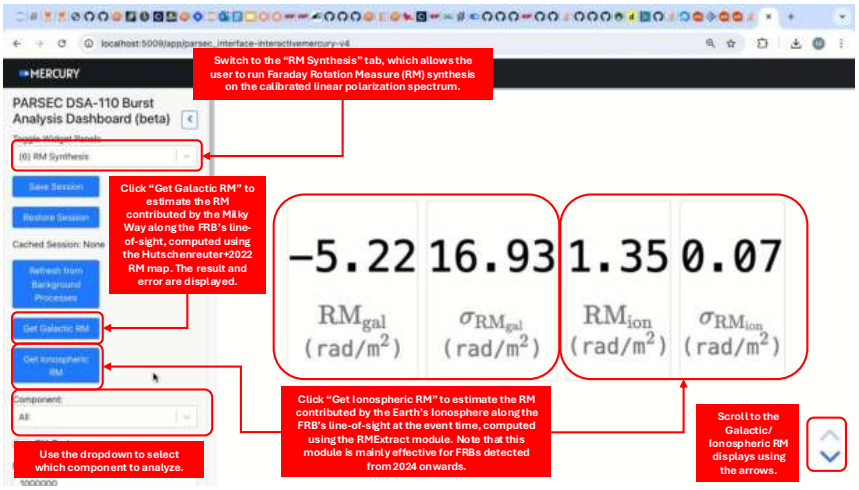
MERCURY
PARSEC DSA-110 Burst Analysis Dashboard (beta)
(6) RM Synthesis
Save Session
Restore Session
Cached Session: None
Refresh from Background Processes
Get Galactic RM
Get Ionospheric RM
Component:
All
Switch to the "RM Synthesis" tab, which allows the user to run Faraday Rotation Measure (RM) synthesis on the calibrated linear polarization spectrum.
Click "Get Galactic RM" to estimate the RM contributed by the Milky Way along the FRB's line-of-sight, computed using the Hutschenreuter+2022 RM map. The result and error are displayed.
−5.22
16.93
1.35
0.07
RM_{gal} (rad/m²)
$\sigma_{RM_{gal}}$ (rad/m²)
RM_{ion} (rad/m²)
$\sigma_{RM_{ion}}$ (rad/m²)
Click "Get Ionospheric RM" to estimate the RM contributed by the Earth's ionosphere along the FRB's line-of-sight at the event time, computed using the RMExtract module. Note that this module is mainly effective for FRBs detected from 2024 onwards.
Scroll to the Galactic/ Ionospheric RM displays using the arrows.
Use the dropdown to select which component to analyze.

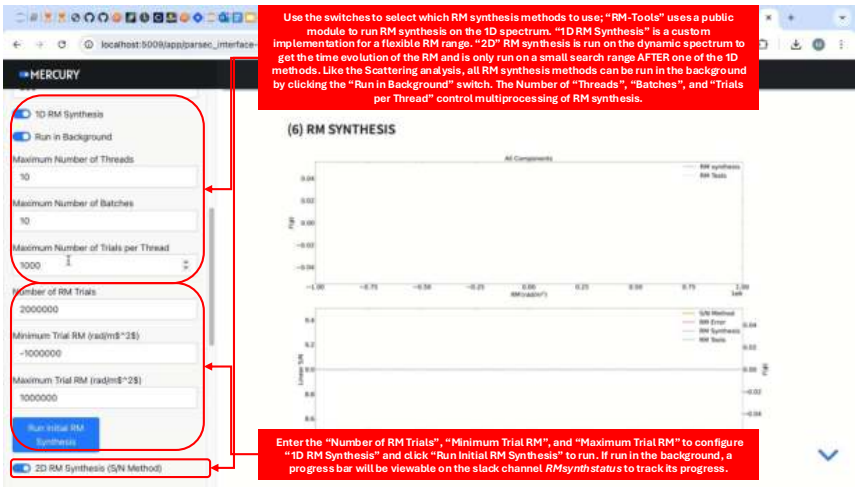
MERCURY
1D RM Synthesis
Run in Background
Maximum Number of Threads
10
Maximum Number of Batches
10
Maximum Number of Trials per Thread
1000
Number of RM Trials
2000000
Minimum Trial RM (rad/m^2)
-1000000
Maximum Trial RM (rad/m^2)
1000000
Run Initial RM Synthesis
2D RM Synthesis (S/N Method)
Use the switches to select which RM synthesis methods to use; "RM-Tools" uses a public module to run RM synthesis on the 1D spectrum. "1D RM Synthesis" is a custom implementation for a flexible RM range. "2D" RM synthesis is run on the dynamic spectrum to get the time evolution of the RM and is only run on a small search range AFTER one of the 1D methods. Like the Scattering analysis, all RM synthesis methods can be run in the background by clicking the "Run in Background" switch. The Number of "Threads", "Batches", and "Trials per Thread" control multiprocessing of RM synthesis.
(6) RM SYNTHESIS
Enter the "Number of RM Trials", "Minimum Trial RM", and "Maximum Trial RM" to configure "1D RM Synthesis" and click "Run Initial RM Synthesis" to run. If run in the background, a progress bar will be viewable on the slack channel *RMsynthstatus* to track its progress.

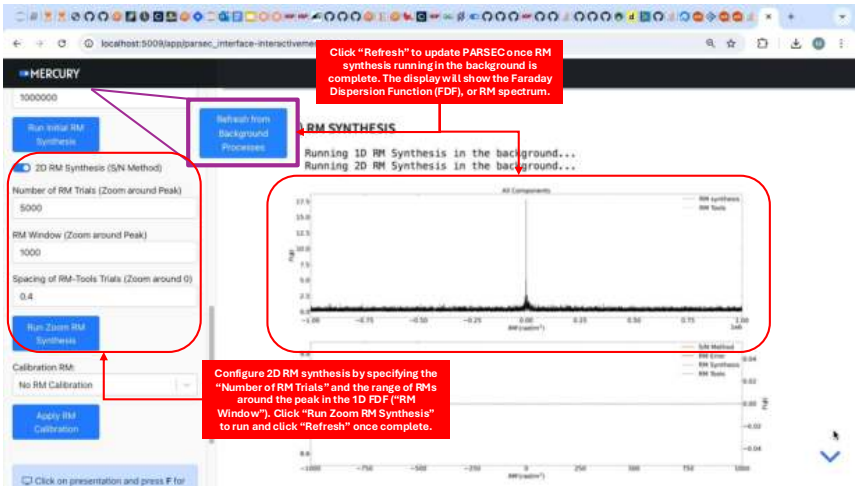
MERCURY
Click "Refresh" to update PARSEC once RM synthesis running in the background is complete. The display will show the Faraday Dispersion Function (FDF), or RM spectrum.
Refresh from Background Processes
RM SYNTHESIS
Running 1D RM Synthesis in the background...
Running 2D RM Synthesis in the background...
2D RM Synthesis (S/N Method)
Number of RM Trials (Zoom around Peak)
5000
RM Window (Zoom around Peak)
1000
Spacing of RM-Tools Trials (Zoom around 0)
0.4
Run Zoom RM Synthesis
Calibration RM:
No RM Calibration
Apply RM Calibration
Configure 2D RM synthesis by specifying the "Number of RM Trials" and the range of RMs around the peak in the 1D FDF ("RM Window"). Click "Run Zoom RM Synthesis" to run and click "Refresh" once complete.

MERCURY
Save Session
Restore Session
Cached Session: None
Refresh from Background Processes
Get Galactic RM
Get Ionospheric RM
Component:
All
RM-Tools
1D RM Synthesis
(6) RM SYNTHESIS
Refreshing...
Once complete, the RM spectrum in the zoomed region is displayed. Note that 1D synthesis will also be run in the zoomed range unless un-switched.
Use the arrow to scroll down to view the 2D spectrum and a table of peak RMs and Errors.

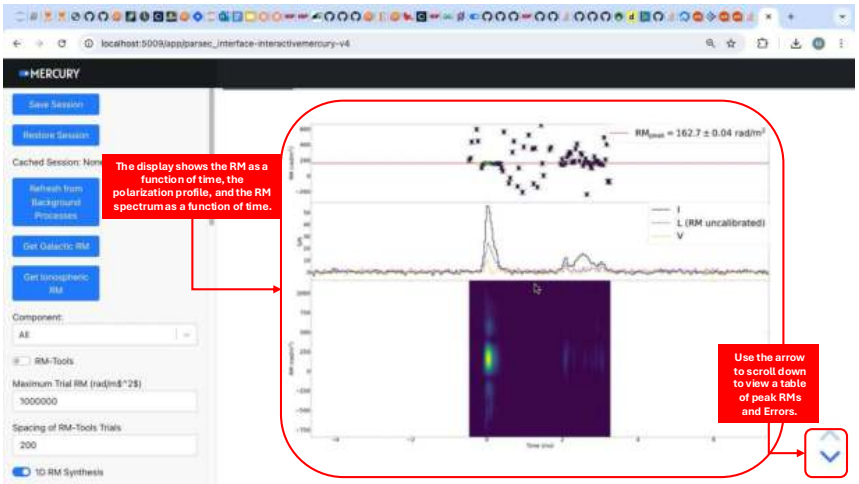

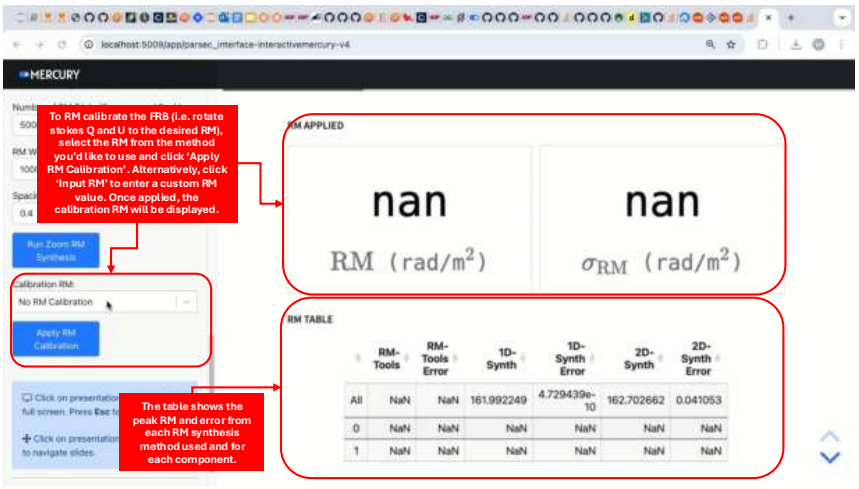

	RM-Tools	RM-Tools Error	1D-Synth	1D-Synth Error	2D-Synth	2D-Synth Error
All	NaN	NaN	161.992249	4.729439e-10	162.702662	0.041053
0	NaN	NaN	NaN	NaN	NaN	NaN
1	NaN	NaN	NaN	NaN	NaN	NaN

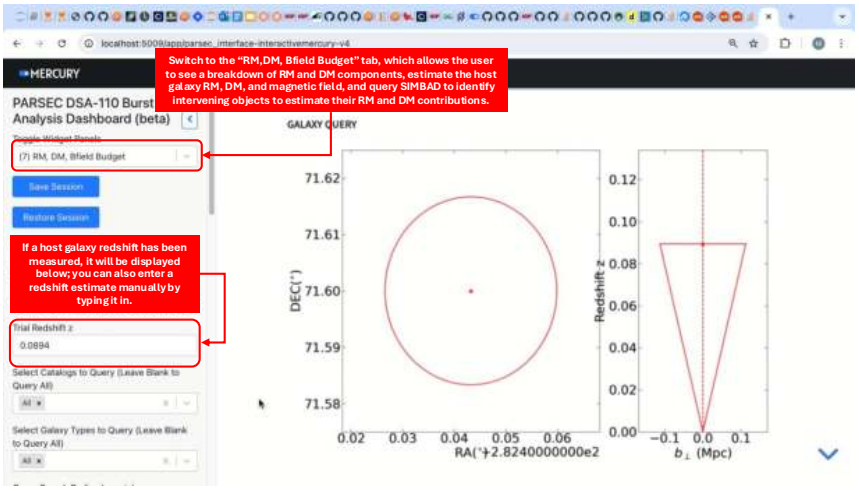
Switch to the "RM,DM, Bfield Budget" tab, which allows the user to see a breakdown of RM and DM components, estimate the host galaxy RM, DM, and magnetic field, and query SIMBAD to identify intervening objects to estimate their RM and DM contributions.
MERCURY
PARSEC DSA-110 Burst Analysis Dashboard (beta)
(7) RM, DM, Bfield Budget
Save Session
Restore Session
If a host galaxy redshift has been measured, it will be displayed below; you can also enter a redshift estimate manually by typing it in.
Trial Redshift z
0.0894
Select Catalogs to Query (Leave Blank to Query All)
Select Galaxy Types to Query (Leave Blank to Query All)
GALAXY QUERY
DEC(°)
RA(°)+2.8240000000e2
Redshift z
$b_\perp$ (Mpc)

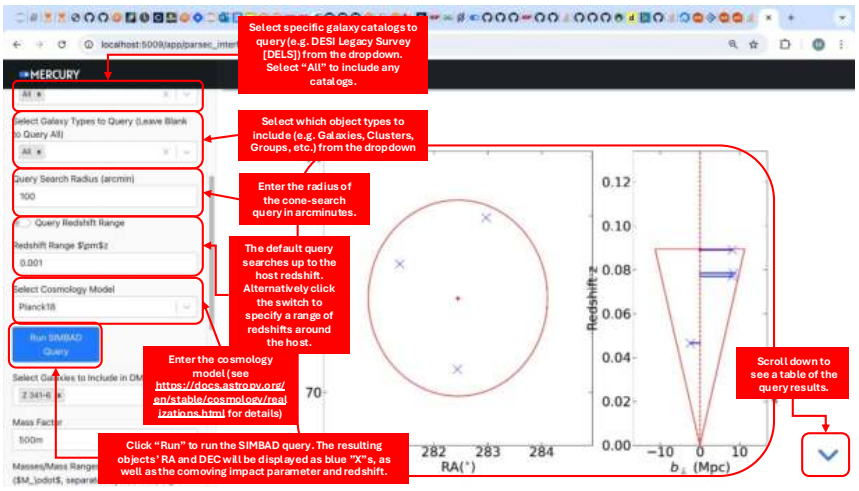
Select specific galaxy catalogs to query (e.g. DESI Legacy Survey [DELS]) from the dropdown. Select "All" to include any catalogs.
Select which object types to include (e.g. Galaxies, Clusters, Groups, etc.) from the dropdown
Enter the radius of the cone-search query in arcminutes.
The default query searches up to the host redshift. Alternatively click the switch to specify a range of redshifts around the host.
Enter the cosmology model (see https://docs.astropy.org/en/stable/cosmology/realizations.html for details)
Click "Run" to run the SIMBAD query. The resulting objects' RA and DEC will be displayed as blue "X"s, as well as the comoving impact parameter and redshift.
Scroll down to see a table of the query results.
MERCURY
Query Search Radius (arcmin)
100
Query Redshift Range
Redshift Range $\pm z$
0.001
Select Cosmology Model
Planck18
Run SIMBAD Query
Mass Factor
500m
RA(°)
Redshift z
$b_\perp$ (Mpc)

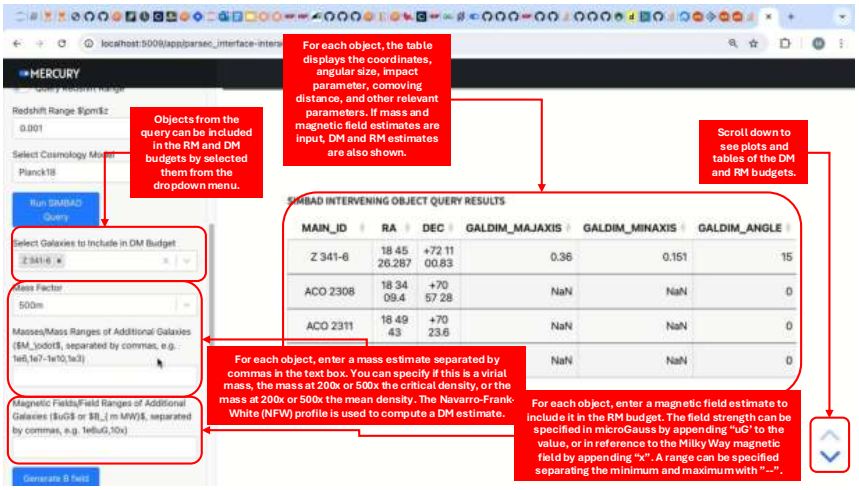
MERCURY
Objects from the query can be included in the RM and DM budgets by selected them from the dropdown menu.
For each object, the table displays the coordinates, angular size, impact parameter, comoving distance, and other relevant parameters. If mass and magnetic field estimates are input, DM and RM estimates are also shown.
Scroll down to see plots and tables of the DM and RM budgets.
SIMBAD INTERVENING OBJECT QUERY RESULTS
MAIN_ID | RA | DEC | GALDIM_MAJAXIS | GALDIM_MINAXIS | GALDIM_ANGLE
Z 341-6 | 18 45 26.287 | +72 11 00.83 | 0.36 | 0.151 | 15
ACO 2308 | 18 34 09.4 | +70 57 28 | NaN | NaN | 0
ACO 2311 | 18 49 43 | +70 23.6 | NaN | NaN | 0
NaN | NaN | 0
For each object, enter a mass estimate separated by commas in the text box. You can specify if this is a virial mass, the mass at 200x or 500x the critical density, or the mass at 200x or 500x the mean density. The Navarro-Frank-White (NFW) profile is used to compute a DM estimate.
For each object, enter a magnetic field estimate to include it in the RM budget. The field strength can be specified in microGauss by appending "uG" to the value, or in reference to the Milky Way magnetic field by appending "x". A range can be specified separating the minimum and maximum with "--".

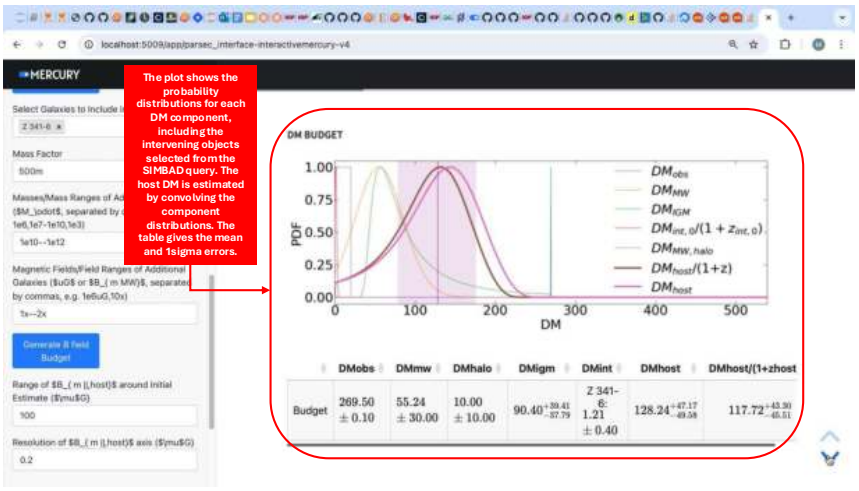
MERCURY
The plot shows the probability distributions for each DM component, including the intervening objects selected from the SIMBAD query. The host DM is estimated by convolving the component distributions. The table gives the mean and 1sigma errors.
DM BUDGET
PDF
DM
DMobs | DMmw | DMhalo | DMigm | DMint | DMhost | DMhost/(1+zhost
Budget | 269.50 ± 0.10 | 55.24 ± 30.00 | 10.00 ± 10.00 | 90.40 | Z 341-6: 1.21 ± 0.40 | 128.24 | 117.72

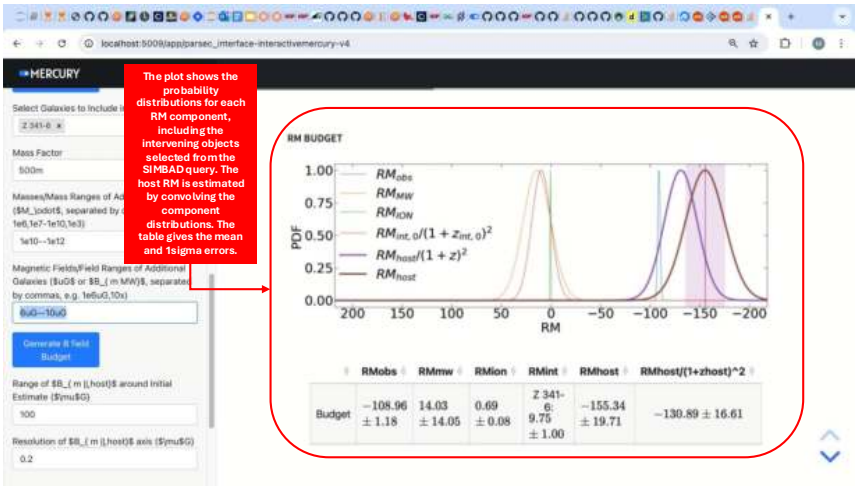
The plot shows the probability distributions for each RM component, including the intervening objects selected from the SIMBAD query. The host RM is estimated by convolving the component distributions. The table gives the mean and 1sigma errors.
RM BUDGET
PDF
RM
RMobs
RMmw
RMion
RMint
RMhost
RMhost/(1+zhost)^2
Budget
−108.96 ± 1.18
14.03 ± 14.05
0.69 ± 0.08
9.75 ± 1.00
−155.34 ± 19.71
−130.89 ± 16.61

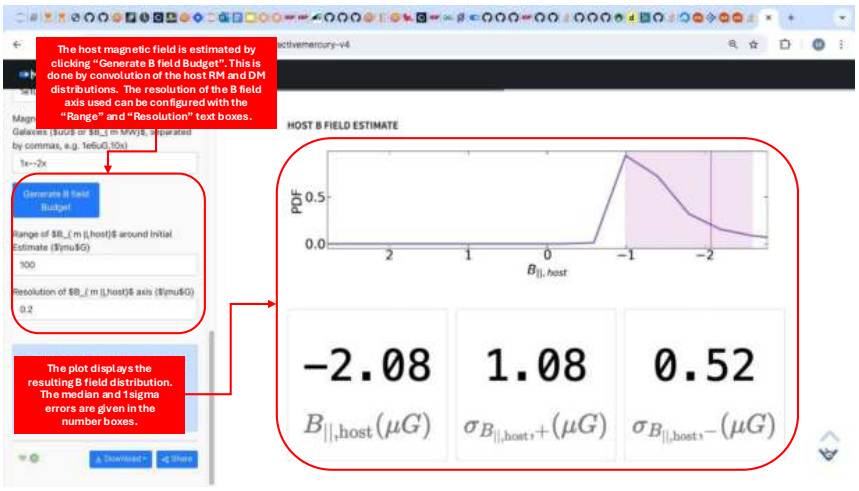
The host magnetic field is estimated by clicking "Generate B field Budget". This is done by convolution of the host RM and DM distributions. The resolution of the B field axis used can be configured with the "Range" and "Resolution" text boxes.
The plot displays the resulting B field distribution. The median and 1sigma errors are given in the number boxes.
HOST B FIELD ESTIMATE
PDF
−2.08
1.08
0.52

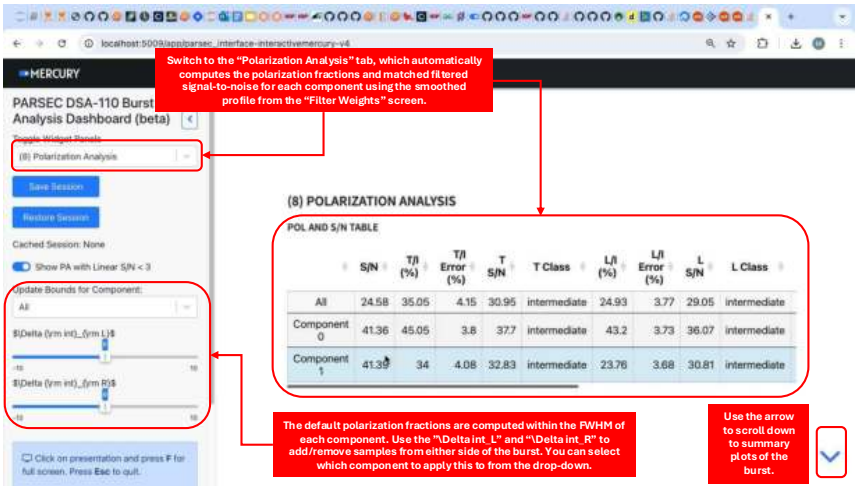
MERCURY
PARSEC DSA-110 Burst Analysis Dashboard (beta)
(8) Polarization Analysis
Save Session
Restore Session
Cached Session: None
Show PA with Linear S/N < 3
Update Bounds for Component:
All
Click on presentation and press F for full screen. Press Esc to quit.
Switch to the "Polarization Analysis" tab, which automatically computes the polarization fractions and matched filtered signal-to-noise for each component using the smoothed profile from the "Filter Weights" screen.
(8) POLARIZATION ANALYSIS
POL AND S/N TABLE
S/N | T/I (%) | T/I Error (%) | T S/N | T Class | L/I (%) | L/I Error (%) | L S/N | L Class
All 24.58 35.05 4.15 30.95 intermediate 24.93 3.77 29.05 intermediate
Component 0 41.36 45.05 3.8 37.7 intermediate 43.2 3.73 36.07 intermediate
Component 1 41.39 34 4.08 32.83 intermediate 23.76 3.68 30.81 intermediate
The default polarization fractions are computed within the FWHM of each component. Use the "\Delta int_L" and "\Delta int_R" to add/remove samples from either side of the burst. You can select which component to apply this to from the drop-down.
Use the arrow to scroll down to summary plots of the burst.

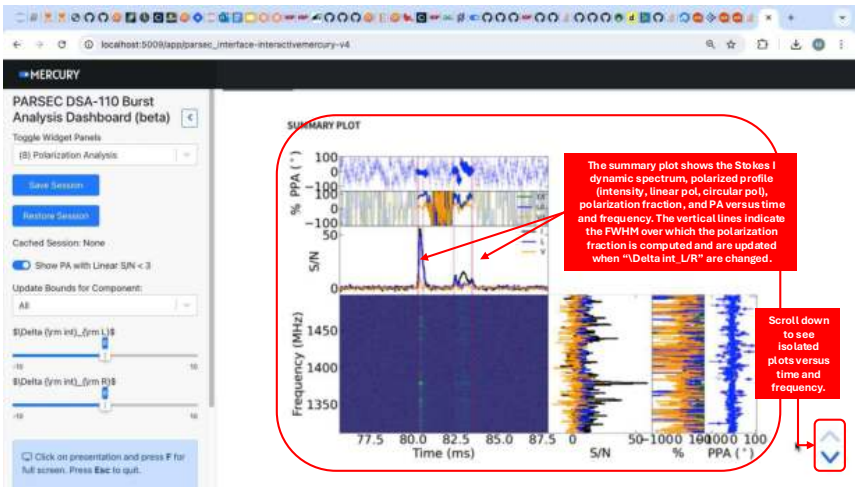
MERCURY
PARSEC DSA-110 Burst Analysis Dashboard (beta)
(8) Polarization Analysis
Save Session
Restore Session
Cached Session: None
Show PA with Linear S/N < 3
Update Bounds for Component:
All
Click on presentation and press F for full screen. Press Esc to quit.
SUMMARY PLOT
% PPA (°)
S/N
Frequency (MHz)
Time (ms)
PPA (°)
The summary plot shows the Stokes I dynamic spectrum, polarized profile (intensity, linear pol, circular pol), polarization fraction, and PA versus time and frequency. The vertical lines indicate the FWHM over which the polarization fraction is computed and are updated when "\Delta int_L/R" are changed.
Scroll down to see isolated plots versus time and frequency.

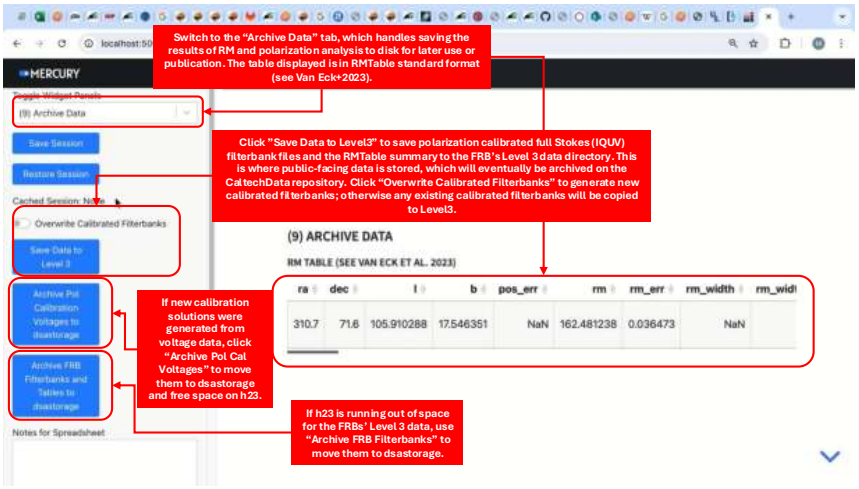
Switch to the "Archive Data" tab, which handles saving the results of RM and polarization analysis to disk for later use or publication. The table displayed is in RMTable standard format (see Van Eck+2023).
MERCURY
(9) Archive Data
Save Session
Restore Session
Cached Session: None
Overwrite Calibrated Filterbanks
Save Data to Level 3
Archive Pol Calibration Voltages to dsastorage
Archive FRB Filterbanks and Tables to dsastorage
Notes for Spreadsheet
Click "Save Data to Level3" to save polarization calibrated full Stokes (IQUV) filterbank files and the RMTable summary to the FRB's Level 3 data directory. This is where public-facing data is stored, which will eventually be archived on the CaltechData repository. Click "Overwrite Calibrated Filterbanks" to generate new calibrated filterbanks; otherwise any existing calibrated filterbanks will be copied to Level3.
(9) ARCHIVE DATA
RM TABLE (SEE VAN ECK ET AL. 2023)
ra dec l b pos_err rm rm_err rm_width rm_widt
310.7 71.6 105.910288 17.546351 NaN 162.481238 0.036473 NaN
If new calibration solutions were generated from voltage data, click "Archive Pol Cal Voltages" to move them to dsastorage and free space on h23.
If h23 is running out of space for the FRBs' Level 3 data, use "Archive FRB Filterbanks" to move them to dsastorage.

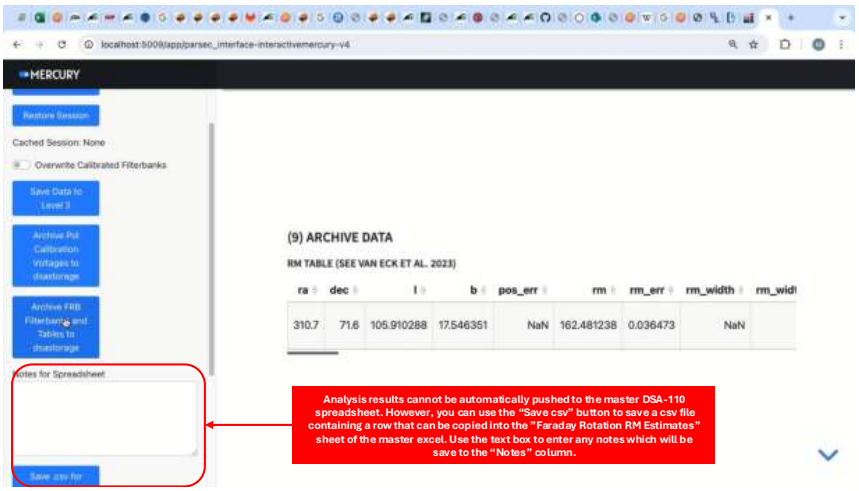
localhost:5008/app/parsec_interface-interactivemercury-v4
MERCURY
Restore Session
Cached Session: None
Overwrite Calibrated Filterbanks
Save Data to Level 3
Archive Pol Calibration Voltages to dsastorage
Archive FRB Filterbanks and Tables to dsastorage
Notes for Spreadsheet
Save csv for
(9) ARCHIVE DATA
RM TABLE (SEE VAN ECK ET AL. 2023)
ra dec l b pos_err rm rm_err rm_width rm_widt
310.7 71.6 105.910288 17.546351 NaN 162.481238 0.036473 NaN
Analysis results cannot be automatically pushed to the master DSA-110 spreadsheet. However, you can use the "Save csv" button to save a csv file containing a row that can be copied into the "Faraday Rotation RM Estimates" sheet of the master excel. Use the text box to enter any notes which will be save to the "Notes" column.

Appendix B

DSA-110 REAL-TIME NSFRB QUICK START GUIDE

In this section we summarize basic operation procedures for the real-time NSFRB search. Note this only covers the basic functionality: receive images, search, post-process, and monitor. More detailed functions are documented in detail in the T4 Concept of Operations, and in `README` files at `https://github.com/dsa110/dsa110-nsfrb`.

The NSFRB server runs on the `lxd110h24.pro.pvt` machine as four `systemctl` user services:

1. `procserver_RX.service`: Operates `http` server to receive image data from correlator nodes
2. `procserver_search.service`: Deploys `cerberus` search tasks on images received from correlator nodes
3. `T4manager.service`: Manages post-processing of candidates, including clustering, CNN classification, clustering, and triggering of voltage data
4. `rt_injector_test.service`: Coordinates injection tests

Users can start or stop all NSFRB services in the proper order by running `start_realtime_all.sh` or `stop_realtime_all.sh`, respectively. Log files can be monitored by running `get_status.sh [TIME] [LINES] [FILES]`, replacing `[TIME]` with the desired refresh time in seconds, `[LINES]` with the number of lines to output for each file, and optionally `[FILES]` with specific log file names (leaving empty will print all log files).

Arguments for `procserver_RX.service` (e.g., data packet size, correlator node flagging) can be changed in `run_proc_server_RX` on line 45, and arguments for the `procserver_search.service` (e.g., GPU usage, realtime search limits, S/N threshold) can be changed in `run_proc_server_search` on line 48. These arguments are described in the process server README. Similarly, arguments for `T4manager.service` (e.g., cluster size, triggering, periodicity search) can be changed in `run_T4_manager` on line 20 and are described in the T4 manager

README. Arguments for `rt_injector_test.service` (e.g., injection cadence, injection S/N) can be changed in `run_realtime_injector` on line 20 and are described in the T4 manager README.

NVSS and RFC calibrator source images are routinely monitored and saved for inspection to assess system health. To run the flux and astrometric calibration pipeline on new calibrator images, run `rt_daily_astrocal_run_once.sh [DATE]`, where [DATE] is replaced with the desired observation date (e.g., 2026-04-13). Then run `copy_cal_images.sh [DATE]` to update the server at `http://localhost:9090/plots/nsfrbcal` with plots of the measured vs. catalog flux and astrometric offsets, as well as time and frequency averaged images of calibrator sources. Refer to the README file therein for details.